Megaprojects vie to unlock the secrets of neutrinos p. 1480

Large-scale analysis of longevity genes pp. 1489 & 1508

Sex, gender, and diversity analysis in research p. 1492

Science

$15
30 SEPTEMBER 2022
science.org

AAAS



IGNEOUS MARS

Perseverance rover collects rocks in Jezero crater

pp. 1512 & 1513



The Welch Foundation Celebrates Outstanding Achievements in Chemistry

The Welch Award in Chemistry is presented annually by the Robert A. Welch Foundation to foster and encourage basic chemical research and to recognize the value of chemical research contributions for the benefit of humankind. The Welch Foundation proudly presents the 2022 award to Dr. Carolyn R. Bertozzi.

Dr. Bertozzi is a leading figure in the field of chemical biology who has made major strides with her study of cell surface sugars. With this award, she is being recognized for her innovative contributions to bioorganic chemistry and the development of bioorthogonal chemistry, all of which have instrumental applications in the study of human health and disease. Upon accepting the award, Dr. Bertozzi will receive $500,000 and a gold medallion.



CAROLYN R. BERTOZZI

Anne T. and Robert M. Bass Professor of Chemistry, Stanford University

THE Welch FOUNDATION

Advancing Chemistry. Improving Life.

Register now for the 2022 Welch Conference at welch1.org

HOUSTON, TX | OCTOBER 24–25, 2022

Genomics, Bio-Rad, and **YOU.**



PCR. qPCR. ddPCR.

Bio-Rad has the tools and support you need.

Take Your Gene Expression Research to the Next Level

At Bio-Rad, genomics innovation is in our DNA. Our technologies provide the robust, reliable results you need. With the leading advancements in both quantitative PCR (qPCR) and digital PCR (dPCR), you can unlock greater accuracy and reproducibility with easy-to-use instruments. See what you can discover with versatile nucleic acid quantification solutions from trusted experts.

Learn more about how Bio-Rad can support your genomics research at bio-rad.com/genomics-solutions

BIO-RAD



Advancing the future of scientific research

To help scientists accelerate scientific innovation, CAS, a division of the American Chemical Society, has developed the CAS SciFinder Discovery Platform™, a suite of powerful research tools.

With tens of thousands of scientific journals and millions of peer-reviewed articles published annually, finding the right information gets more complicated every year. CAS solves that problem with the CAS SciFinder Discovery Platform. "It's basically a search engine for scientists and for the different roles within a company," says Jian Wu, senior director of program management at CAS. "We have a suite of products that all come together in a platform that helps scientists do their research and development." That assistance includes powerful methods for searching the scientific literature and more.

With more than a century of experience in the information business, CAS makes the perfect partner for scientists seeking answers to questions. "We have over 100 years of knowledge in how to collect, aggregate, and organize information," Wu says. "We are a technology company that specializes in scientific information."

Although the amount of scientific information grows rapidly, scientists don't have the luxury of unlimited hours to explore it. So, CAS combines human curation from scientific experts with advanced technology, including artificial intelligence (AI), to "aggregate information and disseminate that information in a way that's efficiently digestible for the users," Wu explains.

In particular, the CAS SciFinder Discovery Platform was developed, Wu says, "to solve some very important pain points and problems that scientists face." For example, he explains that scientists often have questions that could already be answered using existing scientific information, but that information is not always easy to find. "We help by either pointing scientists to the right documents to read or we just flat out give them the answer within the products," Wu says.

To do this, the CAS SciFinder Discovery Platform provides three tools that can work together. In this way, it becomes a one-stop shop for scientists seeking information.

A trio of tools

"The big gorilla, called **CAS SciFinder**^{n}, contains a Google-like search engine that is specialized for scientists," Wu says. Based on the CAS Content Collection™—including articles, patent information, and more—scientists can use CAS SciFinder^{n} to explore chemical names, structures, regulatory information, and other scientific information. Life scientists also find many uses for CAS SciFinder^{n}. For example, it includes more than 54 million references related to biologics.

When a scientist has questions about a chemical reaction, the **CAS Analytical Methods™** solution can help. "This is built for analytical chemists," Wu says. Here, chemists can explore detailed methods for millions of chemical procedures and get step-by-step instructions for replicating a reaction. Also, methods can be compared to determine differences in conditions, reagents, and instrumentation. Currently, the CAS SciFinder Discovery Platform includes almost 150 million reactions, almost 200 million substances, and over 700 million genetic sequences that can be explored, and all of these numbers continue to increase.

Formulation scientists looking for approaches to producing paint, a pharmaceutical pill, shampoo, or other products can use **CAS Formulus®** to explore a database of formulations and associated workflows. In this way, formulators can more quickly find methods that are safe and effective, all while maintaining regulatory compliance.

In addition to all the power behind this trio of tools, the CAS SciFinder Discovery Platform includes an intuitive user interface. It's so easy to use that Wu says, "We've seen people comfortably using it within 30 minutes." That ease of use comes from the hard work CAS has done to develop this solution. "We are

PHOTO: © GETTY IMAGES/POBA

scientists making tools for other scientists," Wu says. "So we understand our users, talk to them all the time, and bounce ideas off each other." What Wu calls "heavy interaction with the end users" forms the foundation of this easy-to-use but designed-for-purpose platform.

Making new medicines

When a biotechnology or pharmaceutical company wants to make a new treatment, the CAS SciFinder Discovery Platform can simplify many steps. As an example, Wu discusses how it can be used in drug discovery. "When a company is trying to figure out how to create a compound—a chemical compound that's part of the drug—they need to do a lot of research on the different ways that have been tried already, including what has worked and what has not worked," he says. "So that's one very predominant use case."

Companies can even use the platform to map out the entire drug development process. "Our aspiration is to serve R&D with all of the information for the entire drug-discovery workflow all the way up to clinical trials," Wu says. "We're also investing heavily in building our predictive capabilities." As an example, CAS uses technology that predicts what questions companies might ask. Wu says that this includes "asking about the different effects of a compound on a target molecule, and what effect that target molecule has on a disease—based on existing publications, and accurate predictions of the future."

Those predictions come from expert knowledge plus computation. "There's AI and machine learning, but what fuels that is the data, and our data are expertly curated," Wu says. "So I'd say that's our secret sauce."

In addition, companies can apply the CAS SciFinder Discovery Platform to many other aspects of drug development. For instance, any intellectual property issues of a compound can be explored. "You can also source the materials to make something, because we have capabilities that can link you to chemical suppliers," Wu says. "One thing that is really cool is our tool that does retrosynthesis, which offers alternative paths for how to make something, and it provides the different reaction conditions, the byproducts, and so on."

Making science more efficient

By using the CAS SciFinder Discovery Platform, scientists can even improve the sustainability of their work. For example, a scientist might be planning an experiment but find through a search that it has already been done. "Maybe it didn't work out," Wu says. "All of our tools really highlight what's been experimented with before, and avoiding repeats of failed experiments saves time and materials and protects the environment, which is really crucial." CAS will enhance contributions to sustainability even more in the future. "We have plans to implement green sustainable features," Wu adds.

Beyond adding green chemistry, CAS is expanding the CAS SciFinder Discovery Platform to benefit all of the life sciences. "We're working on addressing information in biology and medicinal chemistry—things beyond core chemistry," Wu says. "That's going to expand over the next 5 to 10 years, and after that, we'll work on information in the material science of polymers."

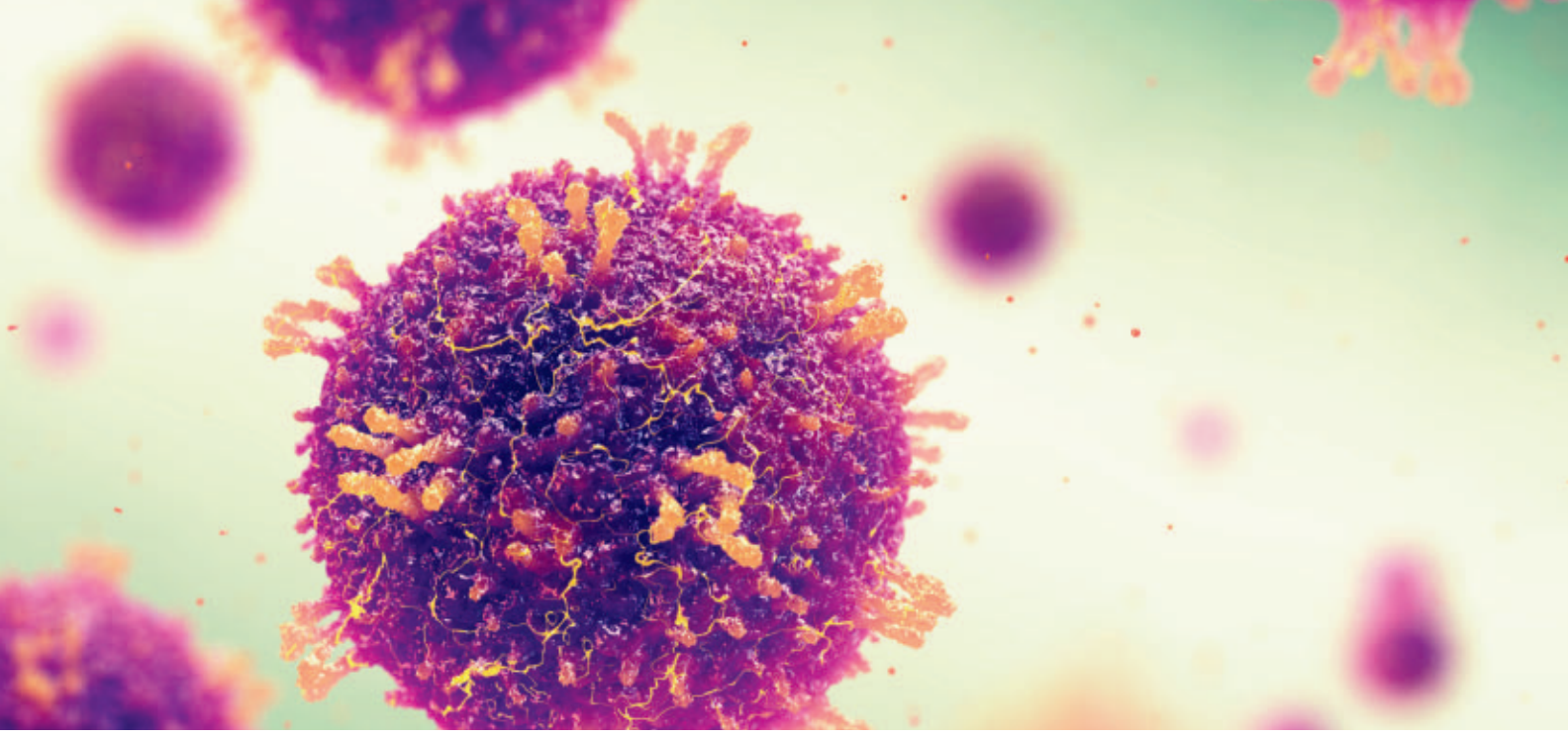
To summarize the value of the CAS SciFinder Discovery Platform, Wu says, "We get you all the information you need and minimize the time you need to spend before you go to the bench." That generates efficiency in time and finances. Even more important, that information helps generate better outcomes from experiments and even from new drug manufacturing.

Sponsored by

CAS
A division of the
American Chemical Society



PHOTO: © GETTY IMAGES/JOHNER IMAGES



It's time to think differently.

Find out how NEB can support your infectious disease research and development.

Gaining a better understanding of infectious diseases, including their characterization, evolution and transmission, continues to be a priority, both from an R&D standpoint and as a public health issue. The COVID-19 pandemic has demonstrated the need for a wide range of tools to research infectious diseases, and has highlighted the importance of speed and the ability to pivot as new problems arise. This has emphasized the need for innovation and thinking differently about where to access those critical materials, including genomics reagents.

Many scientists know NEB as a trusted reagent supplier to the life science community, but what you may not know is that we also offer a portfolio of products that can be used in infectious disease research, development of diagnostics and therapies, and in epidemiological studies and disease surveillance. In fact, many of our products have supported the development of COVID-19 diagnostics and vaccines, and can also be utilized with other infectious diseases, such as influenza and malaria.

- Benefit from almost 50 years of experience in molecular biology & enzymology
- Partner with our OEM & Customized Solutions team to find the best solution for your needs
- Take advantage of our expanded manufacturing capabilities
- Access product formats, such as GMP-grade*, lyophilized, lyo-ready and glycerol-free
- Be confident in your product performance with our expanded quality and regulatory systems

Ready to get started? Learn more at
www.neb.com/InfectiousDiseases

"GMP-grade" is a branding term NEB uses to describe reagents manufactured at our Rowley, MA facility, where we utilize procedures and process controls to manufacture reagents in compliance with ISO 9001 and ISO 13485 quality management system standards. NEB does not manufacture or sell products known as Active Pharmaceutical Ingredients (APIs), nor do we manufacture products in compliance with all of the Current Good Manufacturing Practice regulations.

One or more of these products are covered by patents, trademarks and/or copyrights owned or controlled by New England Biolabs, Inc. For more information, please email us at busdev@neb.com. The use of these products may require you to obtain additional third party intellectual property rights for certain applications.

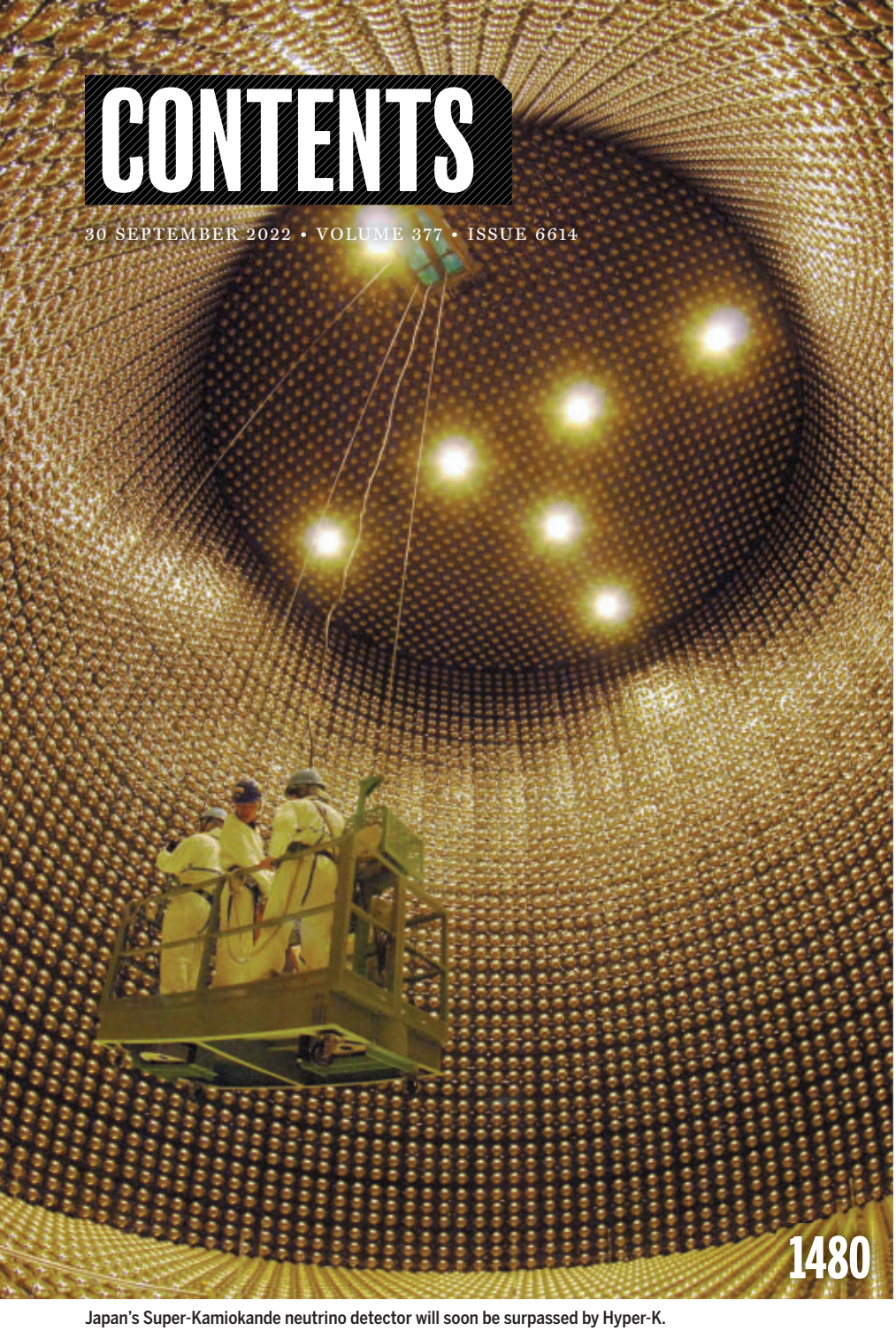
© Copyright 2022, New England Biolabs, Inc.; all rights reserved.

NEW ENGLAND BioLabs® Inc.

be INSPIRED
drive DISCOVERY
stay GENUINE

CONTENTS

30 SEPTEMBER 2022 • VOLUME 377 • ISSUE 6614



Japan's Super-Kamiokande neutrino detector will soon be surpassed by Hyper-K.

PHOTO: THE ASAHI SHIMBUN/GETTY IMAGES

NEWS

IN BRIEF

1472 News at a glance

IN DEPTH

1474 Room-temperature superconductivity claim retracted
After doubts grew, blockbuster *Nature* paper is withdrawn over objections of study team *By E. Hand*

1475 University pandemic policies raise equity worries
Tenure delays and pandemic impact statements could backfire, some fear *By K. Langin*

1477 Signs of state meddling seen in Russian academy election
Leader of Russia's largest chipmaker elected president after incumbent's sudden withdrawal *By O. Dobrovidova*

1478 Fraud charges crumble in China Initiative cases
Judges reject claims that defendants defrauded agencies by not disclosing China ties *By J. Mervis*

1479 New Omicron strains may portend big COVID-19 waves
Emerging subvariants are more immune evasive than ever *By G. Vogel*

FEATURES

1480 Clash of the titans
The United States and Japan are embarking on ambitious efforts to wring a key secret of the universe from the subatomic phantoms known as neutrinos *By A. Cho*

INSIGHTS

PERSPECTIVES

1486 Tackling unlit and inefficient gas flaring
Emissions from flaring threaten the global climate and the health of local communities
By R. Duren and D. Gordon
REPORT p. 1566

1488 Metabolite-driven antitumor immunity
An oncometabolite blocks T cell killing by inhibiting glycolysis *By J. A. Nathan*
REPORT p. 1519

1489 The genetics of a long life
Genetically diverse mice and cross-species comparison uncover links to longevity
By J. P. de Magalhães
RESEARCH ARTICLE p. 1508

1490 Earth was seasoned by countless blows
Earh's composition was shaped by collisions from external objects *By Z. M. Leinhardt*
REPORT p. 1529

POLICY FORUM

1492 A framework for sex, gender, and diversity analysis in research
Funding agencies have ample room to improve their policies *By L. Hunt* et al.

BOOKS ET AL.

1496 Revisiting the first dinosaur park
A once-ridiculed sculpture display is worth a second look *By I. Nieuwland*

1497 Spatial thinkers recieve their due
An insider's guide to visual reasoning celebrates those who think in pictures and patterns *By J. Wai*

BII | Prize for Science | Innovation

Bringing research to life–and science to market

Behind every life-changing solution is an entrepreneurial scientist–a creative mind who proved an idea in the lab and dared to carry it out in the world.

To encourage more scientists to translate their research, BioInnovation Institute (BII) and *Science* present a new annual award.

Our three winners will have their essays published in *Science* magazine and will be invited into BII's entrepreneurial ecosystem. In addition, the Grand Prize winner will receive a prize of USD 25,000, and each runner-up will receive USD 10,000 at a grand award ceremony in Copenhagen, Denmark.

The call for applications has just opened. Apply before November 1, 2022.
www.bii.dk/scienceprize

See film from the grand award ceremony 2022



Benedetto Marelli, Grand Prize Winner 2022

Presented by BII & *Science*

BII BioInnovation Institute Science

Apply before November 1, 2022
www.bii.dk/scienceprize

LETTERS

1498 Heat waves fuel fires on monoculture plantations
By J. Barquín et al.

1498 A low-carbon future for China's tech industry
By K. He et al.

1499 Standards needed for antibiotics in water
By D. Xu and R. Chen

RESEARCH

IN BRIEF

1504 From *Science* and other journals

REVIEW

1507 Human disease
Understanding pathogen survival and transmission by arthropod vectors to prevent human disease *C. Barillas-Mury* et al.
REVIEW SUMMARY; FOR FULL TEXT: DOI.ORG/10.1126/SCIENCE.ABC2757

RESEARCH ARTICLES

1508 Aging
Sex- and age-dependent genetics of longevity in a heterogeneous mouse population *M. Bou Sleiman* et al.
RESEARCH ARTICLE SUMMARY; FOR FULL TEXT: DOI.ORG/10.1126/SCIENCE.ABO3191
PERSPECTIVE p. 1489

1509 Drug design
Structure-based discovery of nonopioid analgesics acting through the α_{2A}-adrenergic receptor *E. A. Fink* et al.
RESEARCH ARTICLE SUMMARY; FOR FULL TEXT: DOI.ORG/10.1126/SCIENCE.ABN7065

1510 Immune signaling
Cyclic ADP ribose isomers: Production, chemical structures, and immune signaling *M. K. Manik* et al.
RESEARCH ARTICLE SUMMARY; FOR FULL TEXT: DOI.ORG/10.1126/SCIENCE.ADC8969

1511 Neuroevolution
Molecular and cellular evolution of the primate dorsolateral prefrontal cortex *S. Ma* et al.
RESEARCH ARTICLE SUMMARY; FOR FULL TEXT: DOI.ORG/10.1126/SCIENCE.ABO7257

Martian geology

1512 Aqueously altered igneous rocks sampled on the floor of Jezero crater, Mars *K. A. Farley* et al.
RESEARCH ARTICLE SUMMARY; FOR FULL TEXT: DOI.ORG/10.1126/SCIENCE.AB02196

1513 An olivine cumulate outcrop on the floor of Jezero crater, Mars *Y. Liu* et al.

1519 Cancer
Oncometabolite D-2HG alters T cell metabolism to impair $CD8^+$ T cell function *G. Notarangelo* et al.
PERSPECTIVE p. 1488

REPORTS

1529 Geochemistry
Earth's composition was modified by collisional erosion *P. Frossard* et al.
PERSPECTIVE p. 1490

1533 Cytoskeleton
Actin maturation requires the ACTMAP/C19orf54 protease *P. Haahr* et al.

1538 Superconductivity
Promotion of superconductivity in magic-angle graphene multilayers *Y. Zhang* et al.

1544 Ocean acidification
Climate change drives rapid decadal acidification in the Arctic Ocean from 1994 to 2020 *D. Qi* et al.



CREDITS: (PHOTO) CHRONICLE/ALAMY STOCK PHOTO; (ILLUSTRATION) ROBERT NEUBECKER



1550 Sea level change
A detection of the sea level fingerprint of Greenland Ice Sheet melt *S. Coulson* et al.

1555 Membranes
Hydrophobic polyamide nanofilms provide rapid transport for crude oil separation *S. Li* et al.

1561 Polymer chemistry
Catalytic deconstruction of waste polyethylene with ethylene to form propylene *R. J. Conk* et al.

1566 Methane emissions
Inefficient and unlit natural gas flares both emit large quantities of methane *G. Plant* et al.
PERSPECTIVE p. 1486; PODCAST

DEPARTMENTS

1471 Editorial
Better data, less gun violence
By A. R. Morrai and R. Smart

1574 Working Life
Let's talk about authorship *By N. Rashid*

ON THE COVER

Two samples of rock (top and bottom holes) were collected by the Perseverance rover from this outcrop of the Séítah geologic formation in Jezero crater, Mars. Also visible are a discarded sample attempt (middle hole), a rock abrasion patch (lower left depression), and the rover's tracks and shadow. Analysis of the Séítah formation shows that it consists of igneous rocks modified by liquid water. See pages 1512 and 1513. *Image: NASA/JPL-Caltech*



AAAS News & Notes.....1500
Science Careers..... 1572

SCIENCE (ISSN 0036-8075) is published weekly on Friday, except last week in December, by the American Association for the Advancement of Science, 1200 New York Avenue, NW, Washington, DC 20005. Periodicals mail postage (publication No. 484460) paid at Washington, DC, and additional mailing offices.

Copyright © 2022 by the American Association for the Advancement of Science. The title SCIENCE is a registered trademark of the AAAS.

Domestic individual membership, including subscription (12 months): $165 ($74 allocated to subscription). Domestic institutional subscription (51 issues): $2212; Foreign postage extra: Air assist delivery: $98. First class, airmail, student, and emeritus rates on request. Canadian rates with GST available upon request, GST #125488122. Publications Mail Agreement Number 1069624. **Printed in the U.S.A.**
Change of address: Allow 4 weeks, giving old and new addresses and 8-digit account number. **Postmaster:** Send change of address to AAAS, P.O. Box 96178, Washington, DC 20090–6178. **Single-copy sales:** $15 each plus shipping and handling available from backissues.science.org; bulk rate on request. **Authorization to reproduce** material for internal or personal use under circumstances not falling within the fair use provisions of the Copyright Act can be obtained through the Copyright Clearance Center (CCC), www.copyright.com. The identification code for *Science* is 0036-8075. *Science* is indexed in the *Reader's Guide to Periodical Literature* and in several specialized indexes.



RUTGERS
THE STATE UNIVERSITY OF NEW JERSEY

Building the Future, One City at a Time

Our WINLAB is taking tomorrow's tech out of the lab and into the streets of New York City

Building on their extensive research with wireless testbeds, radio technology, and mobile internet architecture, the Rutgers team at the Wireless Information Network Laboratory (WINLAB) is helping to implement COSMOS, a real-world outdoor lab putting next-generation wireless technology to work.

A major partnership between WINLAB and other local innovation leaders, with funding from the National Science Foundation, COSMOS will be deployed across a square mile in Manhattan's vibrant, densely populated West Harlem neighborhood.

These urban wireless networks of the future will support data-intensive applications for a smarter, safer world.

- **Smart intersections** that can safely process vital information in real time
- Cloud-based autonomous vehicles for **reliable driverless transportation**
- **Remote surgery** enabling doctors to operate on patients across great distances
- Augmented and virtual reality to **enhance interactivity** and provide new experiences

Excellence *is Earned*
excellence.rutgers.edu

EDITORIAL

Better data, less gun violence

For 25 years, the US government funded little research on firearm violence prevention. Although some dedicated researchers made important discoveries over this period, the scale of the research effort was not commensurate with the problem. Recently, however, there has been an unprecedented surge in research funding: the National Collaborative on Gun Violence Research, a private philanthropy, has awarded more than $21 million since 2018; the federal government has committed $25 million per year since 2019; and some states and other philanthropies have recently invested in such research programs.

The new opportunities this funding creates to understand and prevent firearm violence come at a critical moment. Firearm violence began increasing in 2015, with a sharp rise between 2019 and 2020, and again in 2021, resulting in firearm homicide rates not seen in the US since the end of the crack cocaine epidemic of the early 1990s. Although these increases occurred for nearly every demographic and geographic subgroup in the nation, they are highly concentrated among people who are Black, a group already facing firearm homicide rates 10 times greater than those of white people. Similarly, firearm suicides and suicides generally have soared in recent years, with preliminary 2021 counts showing a firearm suicide rate in the US greater than at any point in the past 43 years.

> "Research on gun violence that is supported by new funding is overdue..."

High and rising costs of firearm violence prompt an urgent need to use new research funding to test and evaluate violence prevention strategies, many of which—including community-based violence prevention interventions, state firearm laws, policing and criminal justice strategies, and health care interventions—have yielded promising initial results. However, mixed results across outcomes and contexts make it challenging to justify and sustain large-scale public investments in them.

Effective firearm violence prevention strategies require better understanding of the people, places, conditions, and antecedents of firearm violence, a line of research hampered by substandard federal data collection and laws that prohibit the federal government from sharing data with researchers. Given federal investments in other data systems that produce information on risk behaviors such as seat belt use and fruit juice consumption, it is notable that the US has had no federal system for estimating firearm ownership at the state level for more than 15 years. Furthermore, although the federal government has strong systems for counting the number of people killed by firearms, it fails at measuring nonfatal firearm injuries and crimes, which constitute the majority of firearm violence. There is no system that tracks hospitalizations for firearm injuries in every state and over time. The federal government does not produce estimates of all police shootings, mass shootings, or intimate partner violence. And although the Federal Bureau of Investigation (FBI) maintained a data series for 90 years that provided state information on use of firearms in violent crimes, it allowed that system to lapse in 2021 in expectation that enough police agencies would join the new (improved) National Incident-Based Reporting System. They have not. At last report, only 11,490 of 18,933 agencies contributed data through the new system, and the FBI has warned that it will be unable to produce 2021 crime rate estimates or crime trend information for all states. Without high-quality measures of nonfatal firearm injuries and crimes, the prevalence and costs of interpersonal firearm violence are underreported, and research efforts to understand relationships between firearm interventions and key outcomes are undermined.

In some cases, federal law needlessly prevents research on government data. For instance, in the late 1990s and early 2000s, a productive line of research used crime gun trace data collected by the Bureau of Alcohol, Tobacco, Firearms, and Explosives. These data revealed states and businesses where guns used in crimes originated, how crime guns moved across borders, the types of guns preferred for crime, and how policies affected crime gun flows. However, amendments to the Justice Department's appropriations bills (the Tiahrt Amendments) now prohibit the Bureau from sharing trace data with researchers. Other provisions of these amendments prohibit the federal government from retaining records verifying whether individuals passed federal background checks that are required to purchase a firearm.

If the United States is serious about fixing the escalating problem of firearm violence, the government needs to measure it. Research on gun violence that is supported by new funding is overdue but will be handicapped until federal and state firearm violence data systems improve.

–Andrew R. Morral and Rosanna Smart

Andrew R. Morral
is a senior behavioral scientist, director of the National Collaborative on Gun Violence Research, and director of the RAND Gun Policy in America Initiative at the RAND Corporation, Washington, DC, USA.
morral@rand.org

Rosanna Smart
is an economist at the RAND Corporation, Santa Monica, CA, USA.
rsmart@rand.org

10.1126/science.ade9060



NEWS

IN BRIEF

Edited by
Jeffrey Brainard

EARTH SCIENCE

European satellite duo will study oceans and warming

The European Space Agency (ESA) last week approved the $420 million Harmony mission as the next in its Earth Explorer line of science missions, following a competition. Harmony's two satellites will carry infrared sensors and radar receivers to observe the turbulent waves, winds, and eddies that govern the interchange of heat and gases between the oceans and atmosphere. Scientists know oceans soak up more than 90% of the excess heat of global warming, but they need Harmony's finer scale observations to explain how—and to calibrate climate models that predict the evolution of these dynamics decades ahead. "We want to study how the oceans and the atmosphere are talking to each other," says principal investigator Paco López-Dekker, a remote sensing scientist at the Delft University of Technology. After launch in 2029, the Harmony satellites will fly in formation with one of ESA's Sentinel-1 radar satellites, to be launched in 2025, while capturing its reflected beams at different angles. The mission will also be able to monitor 3D ground motions as small as 1 millimeter a year—of interest to scientists monitoring glacial ice loss, volcanic eruptions, and the seismic strain that leads to earthquakes.

Fiona ruins Puerto Rico research

FACILITIES | Scientists in Puerto Rico say they lost vital refrigerated samples and face delayed and ruined studies after Hurricane Fiona knocked out power across the island last week. The disruption continued this week, and authorities predict it may take workers weeks to restore a sustained power supply. Some researchers have transferred samples to other locations powered by generators. Ileana Rodríguez-Velez, a chemist at the University of Puerto Rico, Humacao, moved some still-viable samples of plants she is studying for their anticancer and antimicrobial activity to refrigerators at her and her mother's houses. Many researchers also endured outages when Hurricane María devastated the island in 2017. The restoration of the power grid has proceeded slowly, and after Fiona struck, some generators installed by researchers failed or lack enough fuel to operate reliably.

Donor absorbs pandemic institute

PUBLIC HEALTH | Eighteen months after vaccine specialist Rick Bright took the helm of a new institute with ambitious plans to help thwart future pandemics, he has left the job, and the young organization has been folded into the larger mission of its funder, the Rockefeller Foundation. During the administration of former President Donald Trump, Bright led a major U.S. funding agency that supports R&D for products to combat pandemics, but resigned from that job because of disagreements over the administration's COVID-19 response. Questioned about Bright's departure from the Pandemic Prevention Institute, a foundation spokesperson says, "The landscape has changed significantly" since its launch, "as there are now many different initiatives focused on creating a pandemic-free future." These include ones led by the World Health

PHOTO: ARTUR CARVALHO/GETTY IMAGES

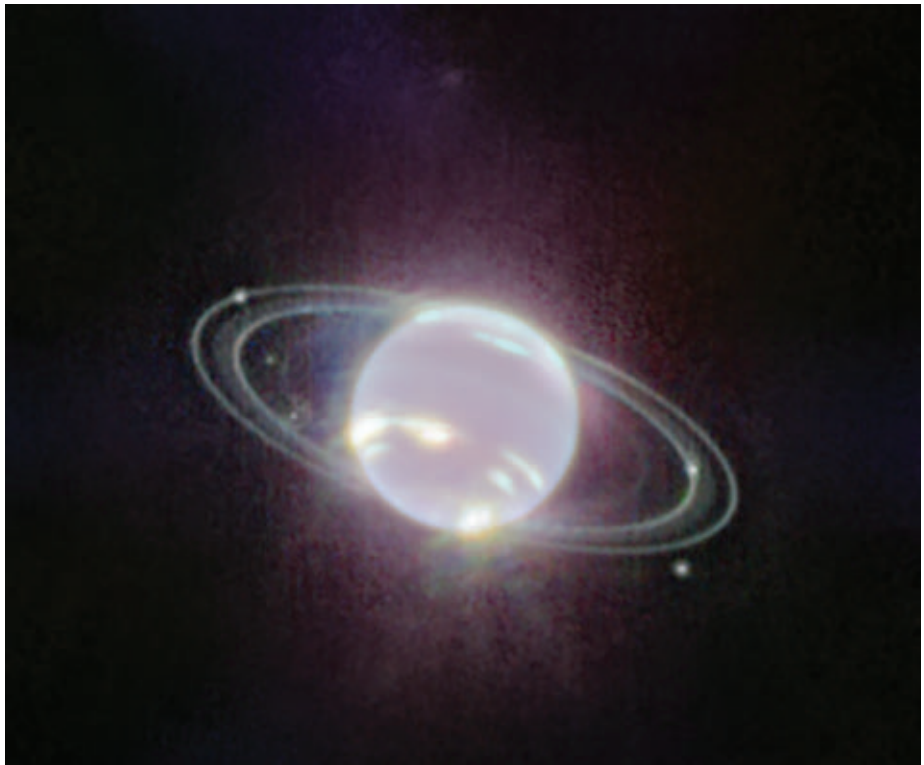
Organization and the U.S. Centers for Disease Control and Prevention. Rockefeller had pledged to invest $150 million over 3 years to support outside scientific efforts that do pathogen surveillance and establish a network to share data more efficiently. Bright says Rockefeller was pivoting to focus more on climate change. "I know their leadership and support in this area will make a huge impact," he says.

Global disease fund nets top haul

FUNDING | High- and low-income countries alike last week joined in pledging $14.25 billion to the Global Fund to Fight AIDS, Tuberculosis and Malaria, in the largest single fundraising push for global health. Supporters said the sum was necessary to help reverse setbacks in combating those diseases caused by the COVID-19 pandemic, although the amount fell short of the Global Fund's goal of $18 billion. The pledged amount may increase if Italy and the United Kingdom make contributions; changes this month in their governments delayed expected commitments. Many of the 45 countries that did pledge money, including low-income nations in Africa, upped their pledges by 30% or more despite inflation and other economic pressures. If achieved, the $18 billion could save 20 million lives and avoid 450 million new infections, the Global Fund estimates. The United States made the single largest commitment, up to $6 billion, but Congress must approve the money. The Bill & Melinda Gates Foundation made the largest private pledge, $912 million.

'Honorary' authors abound

PUBLISHING | Up to one-third of authors named on a large sample of scientific journal articles are "honorary" because they did not fulfill criteria for being listed as authors, a study has found. Some 1% of the authors provided only funding or other resources for the project, contributions that would not qualify a researcher for authorship under two standard definitions. The study, presented this month at the International Congress on Peer Review and Scientific Publication, examined more than 629,000 authors on 82,000 papers published in the PLOS family of journals from 2017 to 2021. It was unusual because it examined standardized statements, submitted by corresponding authors, that described each author's contribution. Previous studies have estimated the frequency of honorary authorship based on self-reports by scientists on surveys.



IN FOCUS NASA's James Webb Space Telescope has captured the clearest view of Neptune and its rings since the Voyager 2 probe briefly flew by in 1989. The new images, released last week, are the first recorded in infrared light—which explains why the planet does not appear blue, as it does in visible light. The gas giant's high-altitude, methane-ice clouds appear as streaks and spots, NASA said. The image also shows seven of Neptune's 14 known moons (not all of which are visible in the version above).

PHOTO: NASA/ESA/CSA/STScI

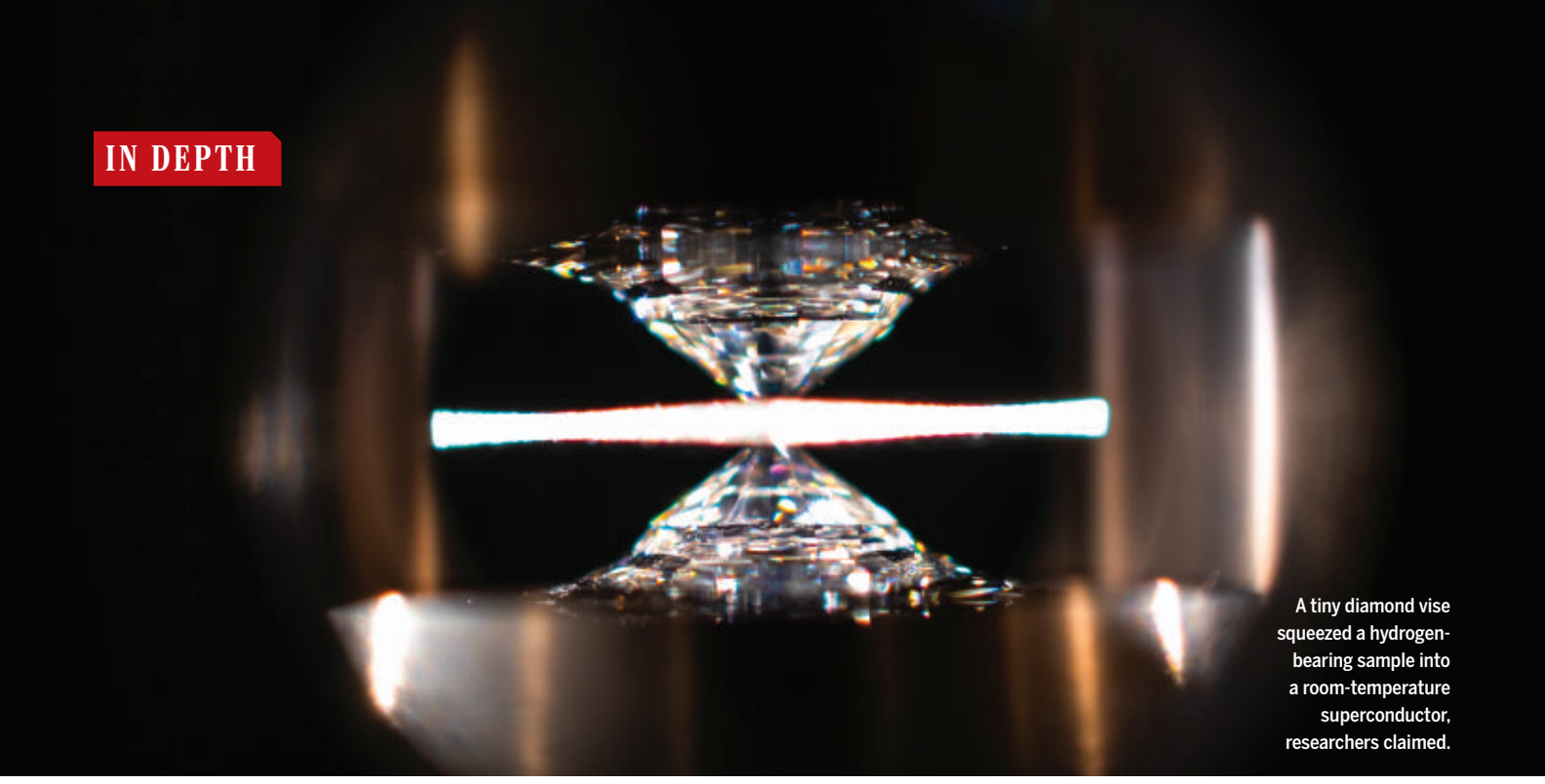
IN OTHER NEWS

U.S. SCIENCE ADVISER The U.S. Senate voted 56-40 to confirm Arati Prabhakar to lead the White House Office of Science and Technology Policy. Prabhakar, an applied physicist and former venture capitalist, will succeed Eric Lander, who resigned as the office's head in February after admitting he created a hostile work environment. She will also be the president's new science adviser, replacing Francis Collins, who had been acting in that role since Lander's departure. Prabhakar led the Defense Advanced Research Projects Agency from 2013 to 2017.

EBOLA OUTBREAK Uganda is battling an outbreak of the Sudan ebolavirus, one of six members of the genus *Ebolavirus*. The country declared an outbreak on 20 September and has since reported at least 36 confirmed or suspected cases, including 23 deaths. Two licensed Ebola vaccines exist, but neither one has been approved for use against the Sudan ebolavirus. Meanwhile, the Democratic Republic of the Congo declared on 27 September that its latest Ebola outbreak—a single infection with the Zaire ebolavirus confirmed on 22 August—has ended.

U.K. FRACKING The U.K. government lifted a 2019 moratorium on hydraulic fracturing ("fracking") to extract natural gas in England. A report last week by the British Geological Survey concluded that forecasting the small earthquakes triggered by fracking remains a challenge; it recommended drilling more test wells to obtain data.

GREENHOUSE GAS TREATY The U.S. Senate ratified the 2016 Kigali Amendment, joining 137 other countries in an effort to slash the production and use of hydrofluorocarbons, a class of potent greenhouse gases. Congress previously mandated reductions, and U.S. companies have begun to switch to alternatives. But the vote had symbolic importance as the first international climate treaty ratified by U.S. lawmakers since 1992.



A tiny diamond vise squeezed a hydrogen-bearing sample into a room-temperature superconductor, researchers claimed.

PHOTO: MIKE BRADLEY/BIG SLIDE

CONDENSED MATTER PHYSICS

Room-temperature superconductor claim retracted

After doubts grew, blockbuster *Nature* paper is withdrawn over objections of study team

By **Eric Hand**

In 2020, Ranga Dias, a physicist at the University of Rochester, and his colleagues published a sensational result in *Nature*, featured on its cover. They claimed to have discovered a room-temperature superconductor: a material in which electric current flows frictionlessly without any need for special cooling systems. Although it was just a speck of carbon, sulfur, and hydrogen forged under extreme pressures, the hope was that someday the material would lead to variants that would enable lossless electricity grids and inexpensive magnets for MRI machines, maglev railways, atom smashers, and fusion reactors.

Faith in the result is now evaporating. On Monday *Nature* retracted the study, citing data issues other scientists have raised over the past 2 years that have undermined confidence in one of two key signs of superconductivity Dias's team had claimed. "There have been a lot of questions about this result for a while," says James Hamlin, an experimental condensed matter physicist at the University of Florida. But Jorge Hirsch, a theoretical physicist at the University of California, San Diego (UCSD), and longtime critic of the study, says the retraction does not go far enough. He believes it glosses over what he says is evidence of scientific misconduct. "I think this is a real problem," he says. "You cannot leave it as, 'Oh, it's a difference of opinion.'"

The retraction was unusual in that *Nature* editors took the step over the objection of all nine authors of the paper. "We stand by our work, and it's been verified experimentally and theoretically," Dias says. Ashkan Salamat, a physicist at the University of Nevada, Las Vegas, and another senior member of the collaboration, points out the retraction does not question the drop in electric resistance—the most important part of any superconductivity claim. He adds, "We're confused and disappointed in the decision-making by the *Nature* editorial board."

The retraction comes even as excitement builds for the class of superconducting materials called hydrides, which includes the carbonaceous sulfur hydride (CSH) developed by Dias's team. Under pressures greater than at the center of the Earth, hydrogen is thought to behave like a superconducting metal. Adding other elements to the hydrogen—creating a hydride structure—can increase the "chemical pressure," reducing the need for external pressure and making superconductivity reachable in small laboratory vises called diamond anvil cells. As Lilia Boeri, a theoretical physicist at the Sapienza University of Rome, puts it, "These hydrides are a sort of realization of metallic hydrogen at slightly lower pressure."

In 2015, Mikhail Eremets, an experimental physicist at the Max Planck Institute for Chemistry, and colleagues reported the first superconducting hydride: a mix of hydrogen and sulfur that, under enormous pressures, exhibited a sharp drop in electrical resistance at a critical temperature (Tc) of 203 K (−70°C). That was nowhere near room temperature, but warmer than the Tc for most superconducting materials. Some theorists thought adding a third element to the mix would give researchers a new variable to play with, enabling them to get closer to ambient pressures—or room temperatures. For the 2020 *Nature* paper, Dias and colleagues added carbon, crushed the mix in a diamond anvil cell, and heated it with a laser to create a new substance. They reported that tests showed the telltale resistance drop at a Tc of 288 K (15°C)—roughly room temperature—and a pressure of 267 gigapascals, about 75% of the pressure at the center of the Earth.

But in a field that has seen many superconducting claims come and go, a drop in resistance alone is not considered suf-

ficient. The gold standard is to also provide evidence of another key attribute of superconductors: their ability to expel an applied magnetic field when they cross Tc and become superconducting. Measuring that effect in a diamond anvil cell is impractical, so experimentalists working with hydrides often measure a related quantity called "magnetic susceptibility." Even then they must contend with tiny wires and samples, immense pressures, and a background magnetic signal from metallic gaskets and other experimental components. "It's like you're trying to see a star when the Sun is out," Hamlin says.

The study's magnetic susceptibility data were what led to the retraction. The team members reported that a susceptibility signal emerged after they had subtracted a background signal, but they did not include raw data. The omission frustrated critics, who also complained that the team relied on a "user-defined" background—an assumed background rather than a measured one. But Salamat says relying on a user-defined background is customary in high-pressure physics because the background is so hard to measure experimentally.

"There have been a lot of questions about this result for a while."
James Hamlin, University of Florida

In response to some of the criticisms, Dias and Salamat in 2021 posted a paper to the arXiv physics preprint server. It contained raw susceptibility data and purported to explain how the background was subtracted. "It raised more questions than it answered," says Brad Ramshaw, a quantum materials physicist at Cornell University. "The process of going from the raw data to the published data was incredibly opaque."

Hirsch, a firebrand who has criticized other hydride superconductivity claims, has made stronger accusations. He says some of the published data presented by Dias and Salamat could be represented by a smooth polynomial curve—impossible for noisy laboratory measurements. "I think they were fabricated," Hirsch says. He also noted suspicious similarities to data in a 2009 *Physical Review Letters* paper on superconductivity in europium under high pressures. That study, which shared one author with the *Nature* paper, was retracted last year because of inaccurate magnetic susceptibility data.

In preprints, Hirsch kept hammering on the Dias study—so forcefully that in February, arXiv temporarily banned him from posting. He also complained to the University of Rochester, which in two inquiries found no evidence of scientific misconduct. This month, Hirsch and another critic, Dirk van der Marel, a condensed matter physicist at the University of Geneva, published their conclusion in a physics journal that the susceptibility data in the Dias study are "pathological." Van der Marel is heartened by the *Nature* retraction. "It is good to know you are not alone in believing something is seriously wrong," he says.

Dias says the team plans to resubmit the paper to *Nature* without any background subtraction; he says the raw data alone show the change in magnetic susceptibility. Salamat also notes that Hirsch and Van der Marel are not high-pressure experimentalists. "We believe that some of their actions have veered into personal attacks," he says. "We're just not going to have people throw mud at us from a distance." Dias sent "cease and desist" letters to Van der Marel and to Hirsch's department chair and dean at UCSD.

Eremets says the Dias study might still be right about CSH. But he has tried at least six times to replicate the results and failed. Although Dias's team has shared the basics of its experimental protocol, Eremets says they have been less forthcoming in the details, such as what type of carbon they used in their CSH mix. Boeri agrees. "There are a lot of people who are a lot more careful, and they share the data, and they share the samples," she says.

Salamat says colleagues are welcome to come to their labs and observe their methods and protocols. "We have an open-door policy." And he points to a CSH replication published in July. Critics question its independence, however, because it was led by Salamat's group and includes many of the same authors as the *Nature* paper.

Dias and Salamat are not slowing down. The duo has co-founded a company, Unearthly Materials, to pursue commercial room-temperature superconductors. At conferences this summer, Dias has presented claims of superconductivity in new hydride compounds. Although he declined to comment on those claims until they are published, he says, "We've moved on from the 2020 work." Salamat adds, "We're on the precipice of a new era of high-temperature superconductivity."

Eremets is skeptical that Dias's new superconductors will stand up to scrutiny. "How is this possible? Everything he touches turns to gold." But he is confident that the patient work of science, underpinned by painstaking replication, will sort the real promise of hydrides from the questionable claims. "Science is not afraid of these things," he says. "The truth, sooner or later, will come." ■

WORKFORCE

University pandemic policies raise equity worries

Tenure delays and pandemic impact statements could backfire, some fear

By **Katie Langin**

As the COVID-19 pandemic swept across the globe in 2020, calls began to ring out for universities to swiftly address concerns that interruptions to research, closure of schools and day cares, and other disruptions could widen existing inequities in academia and make it harder for women and researchers from other underrepresented groups to stay afloat. Many universities in the United States and elsewhere went on to institute new policies to support early-career faculty, including delaying tenure decisions and giving applicants for tenure and promotion a chance to disclose how COVID-19 disruptions had impeded their work. But despite the good intentions, many worry these moves fall short of what is needed—and if not properly implemented, they could end up infusing more bias into tenure and promotion decisions.

"These are complex problems in which a single pandemic impact statement or a tenure delay is not really going to address everything," says Dawn Culpepper, associate director of the ADVANCE Program for Inclusive Excellence at the University of Maryland, College Park. "We need more creative thinking on these issues."

Culpepper recently completed an analysis of policies for pandemic impact statements at 65 research-intensive universities in the United States and Canada. More than half didn't have publicly available campus-wide directives. Of the 27 that did, policies varied widely. At some universities, faculty were encouraged to write only single-paragraph statements; at others they were allowed to submit up to five pages. One university required all faculty going up for tenure or promotion to submit a statement; the others simply offered the option. Only 59% of institutions pro-

vided guidelines for reviewers about how to interpret the statements, and most of those that did only gave vague instructions. "I'm worried … that reviewers are making judgment calls about what kind of COVID impact statements are valid and legitimate and which ones aren't," says Culpepper, whose analysis will be published in a book chapter in 2023.

In all cases, faculty were instructed to focus their statements on professional disruptions, such as lab closures, travel restrictions, and increased teaching and advising workloads. Twenty-two percent of institutions prohibited faculty from mentioning personal circumstances such as increased caregiving responsibilities, but many others left the door open to such disclosures—a significant departure from standard tenure and promotion procedures. Normally, says Jessi Smith, a vice provost at the University of Colorado (CU), Colorado Springs, "The promotion and tenure process is really devoid of the human that is behind the package."

The decision to allow personal disclosures is well-intentioned, many argue, and could be an important step toward helping parents—the group that experienced the largest drop in productivity during the pandemic. But because stigma against motherhood lingers in academia, some worry that such disclosures could backfire. "In a healthy institution, where care is not seen as a negative thing … it should be easy enough for people to disclose," says Joya Misra, a professor of sociology and public policy and director of the ADVANCE program at the University of Massachusetts, Amherst. "But as long as people are at institutions where it is stigmatized, asking people to write about it could actually damage their long-term career prospects."

For some faculty members, it may also be risky to open up about any challenges, personal or professional. Black women, for example, "are expected to just do and be and show up no matter what's going on," says Christa Porter, an associate professor of higher education administration at Kent State University who has studied the experiences of Black women in academia. Their pandemic impact statements may not be viewed in the same light as similar statements written by, say, white men. Porter, who is also associate dean of the graduate college, took that concern into account during her own recent merit review. As a Black woman, she elected to not mention having children at home during the pandemic, even though some of her colleagues did so. "I just know it's going to be seen differently," she says.

> **"These issues are just going to get stickier and stickier."**
> **Dawn Culpepper**, University of Maryland, College Park

Misra has been leading workshops on her campus and elsewhere to train faculty to review pandemic impact statements equitably. She and her fellow trainers present case studies involving fictional professors and ask attendees to discuss how they would handle each case. "The idea is that if you think through enough cases before you start talking about colleagues in your department, you have a set of principles in mind," she says. That way, it's not about the person—it's about the situations they experienced. "I truly believe that every institution that has pandemic impact statements needs training on how to use them."

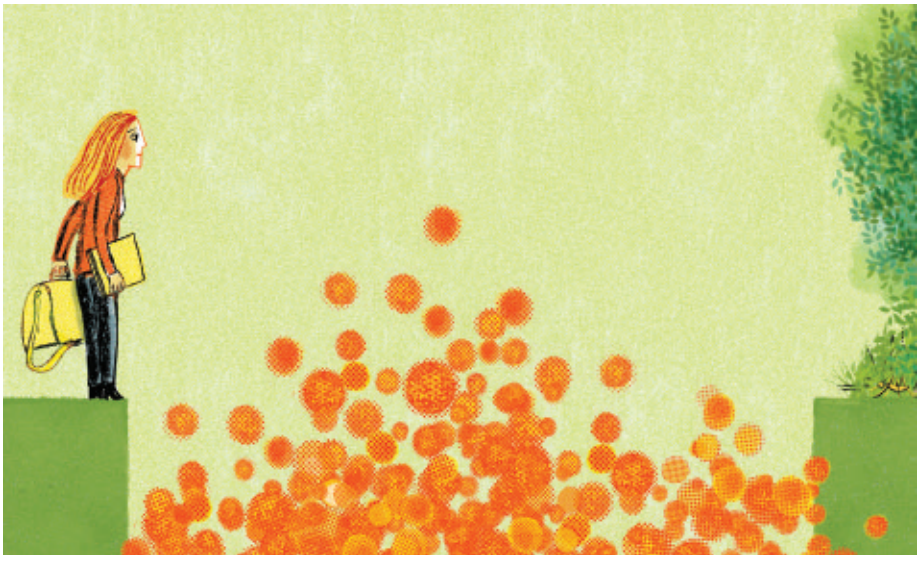


ILLUSTRATION: ROBERT NEUBECKER

Researchers are also concerned that inequities could arise from tenure delay policies, which went into place at more than 97% of research-intensive universities in the United States, according to a study by Culpepper and colleagues in press in the *ADVANCE Journal*. Proponents of these policies "really firmly believe that we just need to keep giving tenure delays, because people need to catch up," says a faculty member who requested anonymity to speak candidly about discussions with colleagues. They are "unable to pop out of this idea of how much people should have accomplished in a given time."

But others are pushing for a different approach: adjusting productivity expectations for tenure decisions. "The boat was not the same for everybody in the COVID storm," says Margaret Ptacek, a professor of biology and past director of the ADVANCE program at Clemson University. "We really need to look at how tenure and promotion policy and practices occur and make sure that there's a pathway for all different types of identities of faculty to have the potential for success." Critics also point to a 2018 study of tenure clock stoppage due to parental leave among economics professors, which found that when such policies were implemented from 1980 to 2005, they boosted tenure rates for men but reduced them for women—likely because some men continued to work during their leave.

"Continuing to wait until [a faculty member] 'catches up' just widens the power, access, and pay gaps that come with tenure and promotion," says Smith, whose research found that women and members of underrepresented racial and ethnic groups at her campus and CU Boulder were the most likely to accept tenure delays during the pandemic. "If we are going to do that," she continues, "then I would hope to see some sort of retroactive pay that gives those people the raise they would have received if they had gone up on time."

As things "return to normal," some worry that conversations about accounting for the pandemic's effects on academia, from current faculty to those still in training, are petering out prematurely. "We are still going to feel these impacts for a number of years, and in fact we probably haven't even seen them really play out. So there's even more reason to start paying attention to this and do so in a proactive way," Culpepper says. Going forward, "These issues are just going to get stickier and stickier."

"Universities did recognize that something needed to be done," Misra says. "But I don't see as much progress as I had hoped to see. I really hoped that it would lead to more of a transformation." ■



Gennady Krasnikov (left), with Russian President Vladimir Putin in 2015, is the new RAS president.

PHOTO: PAVEL GOLOVKIN/AP IMAGES

EUROPE

Signs of state meddling seen in Russian academy election

Leader of Russia's largest chipmaker elected president after incumbent's sudden withdrawal

By **Olga Dobrovidova**

The Kremlin tightened its control over the 300-year-old Russian Academy of Sciences last week when its current president, Alexander Sergeev, withdrew his bid for a second term a day before the election, citing the "administrative pressures" many RAS members face for "speaking out." The 67-year-old laser physicist, who was widely expected to win, declined to explain his withdrawal in more detail to members attending the RAS annual meeting in Moscow, but said it was a "forced decision." Instead, Gennady Krasnikov, who leads Mikron, Russia's biggest chipmaker, won the 20 September election.

The disruption shows how state meddling is weakening the once-powerful RAS, already hobbled under 2 decades of rule by President Vladimir Putin, says Michael Gordin, who studies the history of Russian science at Princeton University. Keeping candidates off the ballot through coercion is "part of a menu of actions that the Russian state takes to ensure favorable election outcomes," agrees Robert Moser, who studies Russian politics at the University of Texas, Austin.

Some outspoken RAS members tried to organize an election boycott on short notice. But a narrow quorum was present and willing to go ahead with a secret ballot for the two remaining candidates: Krasnikov and Dmitriy Markovich, who leads a thermophysics research institute in Siberia and is not well known outside the region. Krasnikov won by a comfortable 871-397 vote.

In the last RAS election, in 2017, Vladimir Fortov, the then–incumbent president running for reelection, also withdrew on the opening day of the meeting. "The difference is, back then everyone withdrew and elections were postponed," says Askold Ivantchik, an RAS member and historian at the RAS Institute of World History and France's national research agency, CNRS. Six months later, Sergeev won, with Krasnikov coming in third. This time, Ivantchik says, "The door was left open for the candidate preferred by the government."

Speaking the day before elections, Yuri Solomonov, chief designer for ballistic missiles at the Moscow Institute of Thermal Technology, threw his support behind Krasnikov because of what he said were "unfortunate" signals that Sergeev didn't have the support of the country's leadership. (Solomonov had endorsed Sergeev in 2017.) Krasnikov, 64, is a lifelong Mikron employee, and in 2016, after Russia's annexation of Crimea had triggered sanctions, Putin put him in charge of electronics as a national technological priority.

Markovich, Krasnikov's rival, was an unusually progressive candidate who talked about issues that rarely get attention in Russian science, such as gender imbalances. He used his final campaign speech to spotlight a scientist who he said was "mistakenly" charged with treason. (Since 2000, several dozen scientists, often working in fields related to hypersonic weapons, have been charged with treason and jailed.)

Irina Dezhina, a science policy researcher at the Institute for the Economy in Transition, says the election chaos will be "a blow" to RAS. The academy has always been "entirely a creation of the state," which pays its bills, Gordin notes. But in the turbulent 1990s it gained unprecedented influence over the nation's research budgets, which Putin then reversed in a 2013 change that stripped RAS of most of its control over research institutes. "It is now a shadow of its former self in terms of power and social influence," Gordin says.

At his first press briefing as president-elect, Krasnikov said the academy should be brought back into high-level decisions about science funding and policy. This echoes an academy call, published in August in its annual "state of the science" report, for a bigger role in the "operational management" of science. Dezhina thinks the government will ignore the vague calls and adds, "We've got enough managers in science, it's the managed that are the issue, with the number of researchers falling every year." R&D budgets in Russia have stagnated at about 1% of gross domestic product, well below the average for developed nations.

The invasion of Ukraine has isolated Russian science and triggered wide-ranging sanctions—including measures against Mikron. It has also fractured the scientific community. In his concluding remarks before the vote, Markovich wished for peace, a risky stance: Just 2 days later, public antiwar displays led to the detention of more than 1400 street protesters across Russia—with some reportedly drafted into the war effort on the spot.

In his election platform, Krasnikov blamed the recent technological constraints crippling Russian science on Western sanctions rather than Russia's own actions. After his election, he also said he would prioritize "technological sovereignty"—a cause touted by Putin, who formally relieved Sergeev of his duties and confirmed Krasnikov this week. ■

Olga Dobrovidova is a journalist who does climate communications work in Paris.

SCIENCE AND SECURITY

Fraud charges crumble in China Initiative cases

Judges reject claims that defendants defrauded agencies by not disclosing China ties

By **Jeffrey Mervis**

The U.S. government overplayed its hand in prosecuting U.S. academics under the controversial China Initiative, three federal courts ruled last week.

In separate cases, attorneys for the Department of Justice (DOJ) had maintained that chemist Franklin Tao, materials scientist Zhengdong Cheng, and mathematician Mingqing Xiao jeopardized the nation's security and defrauded the government by deliberately hiding ties to Chinese institutions from the federal agencies funding their research. But last week, judges in Kansas, Texas, and Illinois either invalidated some of the most serious charges or handed down relatively lenient sentences for lesser violations. One judge overturned Tao's fraud convictions, another accepted a plea deal that dropped nine fraud charges against Cheng, and the third sentenced Xiao to probation rather than prison for failing to report a foreign bank account.

Legal experts say DOJ's theory of what constitutes defrauding a funding agency has turned out to be untenable. "These [results] show that the government's [underlying] theory of the case was questionable," says Margaret Lewis, a law professor and China scholar at Seton Hall University who doubts prosecutors should have pursued criminal convictions for what are often treated as civil or administrative violations. "The primary duty of a prosecutor is to obtain justice, not a conviction," she says.

DOJ issued a statement after Xiao was sentenced saying the department had "recommended a sentence it believed appropriate under the law and facts of the case. [But] we respect the court's decision." It declined comment on the two other cases.

Launched by then-President Donald Trump's administration in 2018 to thwart economic espionage, the China Initiative led to charges against some two dozen academic scientists. Most were of Chinese ancestry, which civil rights groups said suggested anti-Asian bias. The initiative had a mixed track record: Although prosecutors won guilty pleas and prison terms for some defendants, they later dropped charges against many others or failed to win jury verdicts.

Last week brought new setbacks for DOJ. In the case of Tao, who is on unpaid leave from the University of Kansas, Lawrence, a jury in April found him guilty on one count of making a false statement by filing incomplete paperwork and three counts of fraud, while acquitting him of four related fraud charges. Prosecutors had argued that Tao committed fraud by hiding his work with Chinese institutions from his university and two funding agencies: the National Science Foundation and the Department of Energy.



At a March protest, Hong Peng (right) called for justice for her husband, Franklin Tao.

But last week U.S. District Judge Julie Robinson took the unusual step of throwing out the three fraud convictions. In her 61-page decision, Robinson noted that the U.S. Supreme Court has held fraud requires evidence that the defendant deprived someone of money or property. But Tao had in fact delivered the research he had promised to his funders and to his university, she wrote. "The evidence presented at trial showed that all three received what they bargained for."

"In any other case, the government would never have thought to bring the fraud charge," asserts Peter Zeidenberg, Tao's attorney. "But when it comes to Chinese American scientists and on anything related to China, [prosecutors] haven't applied the normal filtering process that they go through when deciding what is a meritorious case."

Tao is scheduled to be sentenced in January on the sole remaining count. Robinson's decision, meanwhile, echoes similar findings by judges in other China Initiative cases.

In September 2021, for example, U.S. District Judge Thomas Varlan acquitted mechanical engineer Anming Hu of the University of Tennessee, Knoxville, of six charges of defrauding NASA. "No rational jury could conclude that [Hu] acted with a scheme to defraud NASA by failing to disclose his affiliation" with a Chinese university, Varlan wrote in his 52-page ruling.

In April, U.S. District Judge Staci Yandle threw out two fraud charges against Xiao, a math professor at Southern Illinois University (SIU), Carbondale. A jury then acquitted him of making false statements but found him guilty of failing to disclose a foreign bank account on his tax returns.

Last week, however, the judge rejected the government's request that Xiao receive a 1-year prison sentence and a heavy fine. Instead, she ordered Xiao to serve 1 year of probation and pay a $600 fine. Now on paid administrative leave, Xiao hopes to be reinstated by SIU.

The tax charges "were more worthy of civil remedies—if they were worthy of any enforcement," says Xiao's lead attorney, Ryan Poscablo of Steptoe & Johnson.

Cheng, a former materials scientist at Texas A&M University (TAMU), College Station, was arrested and jailed in August 2020 on charges of making false statements and nine counts of fraud relating to a NASA grant. But last week the government dropped the fraud counts. Cheng then pleaded guilty to two counts of making false statements; he agreed to repay NASA $86,876 and pay a fine of $20,000. The two sides agreed on a prison sentence of time served; Cheng had already spent 13 months behind bars. (TAMU terminated Cheng in December 2020.)

It's not clear how many active China Initiative cases remain. In February, DOJ announced it was renaming the initiative because of the perception that the phrase has had a "chilling effect on U.S.-based scientists of Chinese origin [and] fueled a narrative of intolerance and bias." But Zeidenberg says he hasn't seen any substantive change in the government's approach to what it now calls "a strategy for countering nation-state threats" to the United States. ■

PHOTO: ALLISON KITE/*KANSAS REFLECTOR*



A woman receives an Omicron-specific booster at a pharmacy in Schwenksville, Pennsylvania.

PHOTO: HANNAH BEIER/REUTERS

COVID-19

New Omicron strains may portend big COVID-19 waves

Emerging subvariants are more immune evasive than ever

By **Gretchen Vogel**

Nearly 3 years into the pandemic, SARS-CoV-2 faces a formidable challenge: finding new ways around the immunity humans have built up through vaccines and countless infections. Worrisome new data show it is up to the challenge. Several new and highly immune-evasive strains of the virus have caught scientists' attention in recent weeks; one or more may well cause big, new COVID-19 waves this fall and winter.

"We can say with certainty that something is coming. Probably multiple things are coming," says Cornelius Roemer, who studies viral evolution at the University of Basel. Whether they will also lead to many hospitalizations and deaths is the big question.

"It's not surprising that we're seeing changes that yet again help the virus to evade immune responses," says molecular epidemiologist Emma Hodcroft of the University of Bern, who notes that SARS-CoV-2 faces "the same challenge that things like the common cold and influenza face every year—how to make a comeback."

The strains that look poised to drive the latest comeback are all subvariants of Omicron, which swept the globe over the past year. Several derived from BA.2, a strain that succeeded the initial BA.1 strain of Omicron but then was itself outcompeted in most places by BA.5, which has dominated in recent months. One of these, BA.2.75.2, seems to be spreading quickly in India, Singapore, and parts of Europe. Other new immune-evading strains have evolved from BA.5, including BQ.1.1, which has been spotted in multiple countries around the globe.

Despite their different origins, several of the new strains have chanced upon a similar combination of mutations to help scale the wall of immunity—a striking example of convergent evolution. They all have changes at half a dozen key points in the viral genome that influence how well neutralizing antibodies from vaccination or previous infection bind to the virus, says evolutionary biologist Jesse Bloom of the Fred Hutchinson Cancer Center.

To quickly gauge how well any new subvariant may evade immunity, researchers make copies of the viruses' spike proteins and expose them to monoclonal antibodies or sera from people to measure how well the antibodies can block the variants from infecting cells. Using such tests, researchers in China and Sweden have found that spike protein from BA.2.75.2 can effectively evade nearly all the monoclonal antibodies used for treating COVID-19, suggesting these treatments may become useless.

Both groups also found that BA.2.75.2 seems very good at evading immunity in humans. In a preprint posted on 19 September, immunologist Ben Murrell at the Karolinska Institute and his colleagues reported that serum samples from 18 blood donors in Stockholm—where vaccination rates are high and prior infections widespread—were less than one-sixth as effective at neutralizing BA.2.75.2 compared with BA.5. "This is the most resistant variant we've ever evaluated," says Karolinska virologist Daniel Sheward.

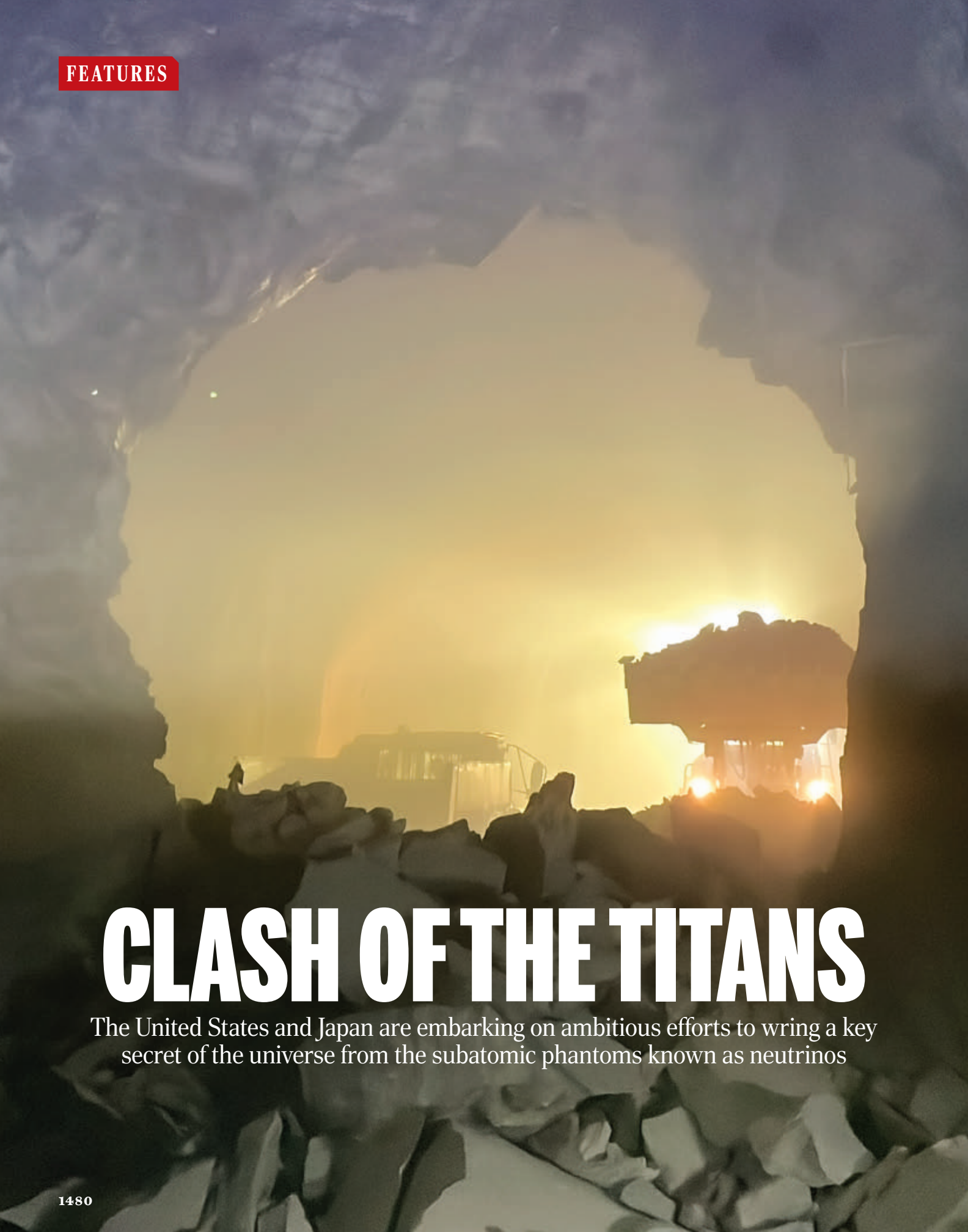
Immunologist Yunlong Richard Cao at Peking University and his colleagues found similar results for BA.2.75.2 after testing blood samples from 40 people who had been vaccinated with three doses of CoronaVac, a vaccine made from inactivated virus, and 100 more who had been vaccinated and then had breakthrough infections with BA.1, BA.2, or BA.5. The team found that BQ.1.1 had a similarly striking ability to evade antibodies.

In their preprint, updated on 23 September, Cao and his colleagues also report that the new variants do not seem to have lost any ability to bind tightly to the receptor on human cells that the virus uses to infect them, which means the variants' infectiousness has likely not decreased. And they report some evidence that infections with the variants trigger proportionally more of the wrong types of antibodies—those that bind tightly to the virus but don't blunt its ability to infect cells. All of that could portend a massive new wave, Cao says. "The scale of immune evasion has never been seen before, and the virus is still rapidly evolving," he says. "It's very bad."

Sheward and Murrell agree we should expect lots of infections in the next few months, as happened last winter when Omicron entered the scene. But they're less pessimistic than Cao, noting that many more people have recovered from an infection now or have received additional vaccine doses, including Omicron-specific boosters, whose rollout began this month. Those will boost overall antibody levels and will likely broaden the antibody repertoire, Sheward says: "I don't think we're quite back to square one."

"The choice to put BA.5 in the vaccine booster is still looking like a good one," Bloom adds. "The boosters are always going to be a step behind, but the good news is that the BA.5 booster is going to be one or two steps behind the virus' evolution, instead of five steps behind."

Just how brutal a comeback the coronavirus has managed will become clear once more people become infected with the new strains. The next wave may also provide better clues about what factors trigger or prevent severe disease, Murrell says: "I think we're going to learn a lot this winter." ■



CLASH OF THE TITANS

The United States and Japan are embarking on ambitious efforts to wring a key secret of the universe from the subatomic phantoms known as neutrinos

By **Adrian Cho**

Among physicists, those studying elusive particles called neutrinos may set the standard for dogged determination—or obdurate stubbornness. For 12 years, scientists in Japan have fired trillions of neutrinos hundreds of kilometers through Earth to a gigantic subterranean detector called Super-Kamiokande (Super-K) to study their shifting properties. Yet the nearly massless particles interact with other matter so feebly that the experiment, known as T2K, has captured fewer than 600 of them.

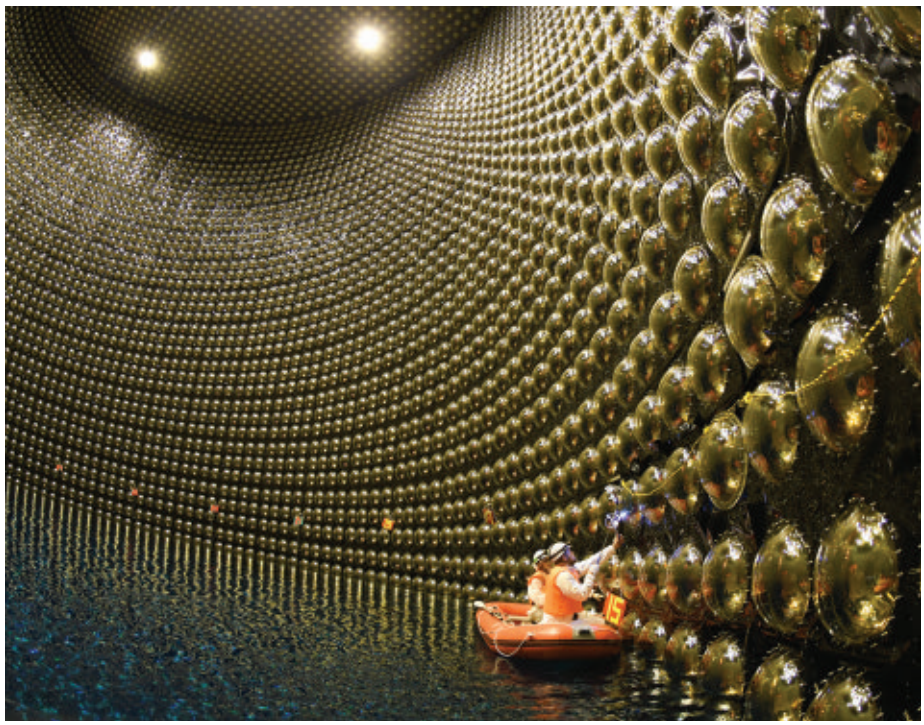
Nevertheless, so alluring are neutrinos that physicists are not just persisting, they are planning to vastly scale up efforts to make and trap them. At stake may be insight into one of the most profound questions in physics: how the newborn universe generated more matter than antimatter, so that it is filled with something instead of nothing.

That prospect, among others, has sparked a race to build two massive subterranean detectors, at costs ranging from hundreds of millions to billions of dollars. In an old zinc mine near the former town of Kamioka in Japan, physicists are gearing up to build Hyper-Kamiokande (Hyper-K), a gargantuan successor to Super-K, which will scrutinize neutrinos fired from a particle accelerator at the Japan Proton Accelerator Research Complex (J-PARC) in Tokai 295 kilometers away. In the United States, scientists are developing the Deep Underground Neutrino Experiment (DUNE) in a former gold mine in Lead, South Dakota, which will snare neutrinos from Fermi National Accelerator Laboratory (Fermilab) 1300 kilometers away in Batavia, Illinois.

Researchers with both experiments acknowledge they're in competition—and that Hyper-K may have an advantage because it will likely start to take data a year or two before DUNE. Yet aside from their goals, "Hyper-K and DUNE are vastly different," says Chang Kee Jung, a neutrino physicist at Stony Brook University and a T2K member who now also works on DUNE.

Hyper-K, which will be bigger but cheaper than DUNE, represents the next in a series of ever larger neutrino detectors of the same basic design developed over 40 years by Japanese physicists. It is all but certain to work as expected, says Masato Shiozawa, a particle physicist at the University of Tokyo and co-spokesperson for the 500-member Hyper-K collaboration. "Hyper-K is a more established technology than DUNE," he says. "That is why I proposed it."

DUNE will employ a relatively new technology that promises to reveal neutrino interactions in stunning detail and allow



PHOTOS: KAMIOKA OBSERVATORY/INSTITUTE FOR COSMIC RAY RESEARCH/UNIVERSITY OF TOKYO

A cavern being excavated in Japan (left) will house Hyper-Kamiokande. It will be an even bigger version of the famed Super-Kamiokande neutrino detector (right), a vast, water-filled tank lined with phototubes.

physicists to test their understanding of the particles with unprecedented rigor. "Without bragging too much, we are best in class," says Sergio Bertolucci, a particle physicist at the University of Bologna and Italy's National Institute for Nuclear Physics and cospokesperson for the 1300-member DUNE collaboration. However, that technological edge comes with a hefty price tag and, Bertolucci acknowledges, more risk.

How the rivalry plays out will depend on factors as mundane as the cost of underground excavation and as exciting as the possibility that neutrinos, always quirky, hold some surprise that will transform physicists' understanding of nature.

THE MOST COMMON PARTICLES in the universe besides photons, neutrinos exert no effect on the everyday objects around us. Yet they could carry clues to deep mysteries. Neutrinos and their antimatter counterparts both come in three types or flavors—electron, muon, and tau—depending on how they're generated. For example, electron neutrinos emerge from the radioactive decay of some atomic nuclei. Muon neutrinos fly from the decays of fleeting particles called pi-plus mesons, which can be produced by smashing a beam of protons into a target. These identities aren't fixed: A neutrino of one type can change into another, chameleonlike, as it zips along at near–light-speed.

Weirdly, a neutrino of a definite flavor has no definite mass. Rather, it is a quantum mechanical combination of three different "mass states." For example, a decaying pi-plus spits out the combination of mass states that makes a muon neutrino. However, like gears turning at different speeds, the mass states evolve at different rates, changing that combination. So, a particle that began as an electron neutrino might later appear as a tau neutrino—a phenomenon known as neutrino oscillation.

Theorists can explain all of this with a mathematical clockwork known as the three-flavor model. It has just a handful of parameters: roughly speaking, the probabilities with which one flavor will oscillate into another and the differences among the three mass states. The picture has gaps. Experiments show two mass states are close, but not whether the two similar states are lighter or heavier than the third—a puzzle known as the hierarchy problem.

Moreover, neutrinos and antineutrinos might oscillate by different amounts, an asymmetry called charge-parity (CP) violation. Measuring that asymmetry is the prize physicists seek, as it could help explain how the soup of fundamental particles in the early universe generated more matter than antimatter.

The wispy neutrinos themselves did not tilt the matter-antimatter balance. Rather, according to some theories, the familiar neutrinos are mirrored by vastly heavier "sterile" neutrinos that would interact with nothing except neutrinos. If sterile neutrinos and antineutrinos also behave asymmetrically, then in the early universe their decays could have generated more electrons than antielectrons (also called positrons), seeding the dominance of matter.

Seeing CP violation in ordinary neutrinos wouldn't prove this scenario played out, notes Patrick Huber, a theorist at Virginia Polytechnic Institute and State University. But not seeing CP violation among ordinary neutrinos would render it much less likely that the hypothetical heavyweights possess the key asymmetry, Huber says. "It's not impossible, but it's implausible," he says.

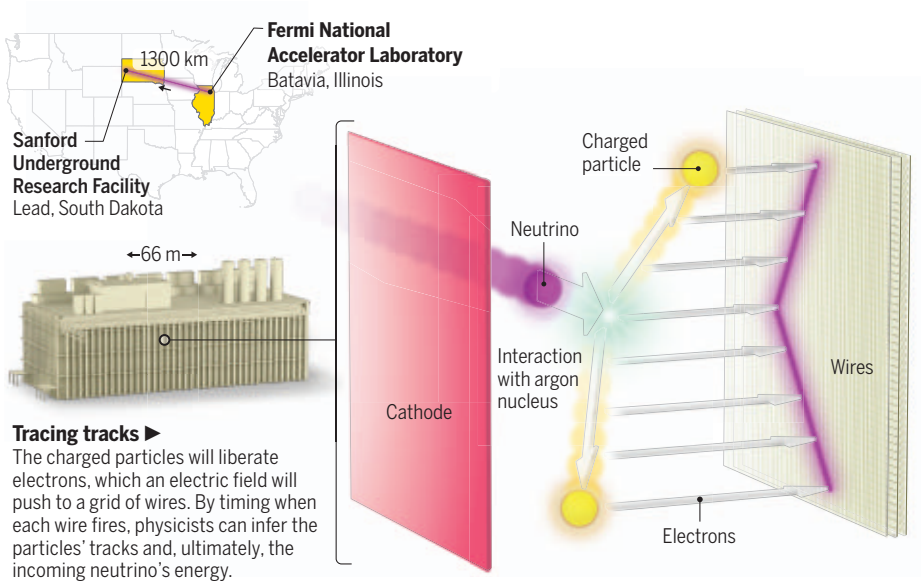
But, first, scientists must determine whether neutrinos really exhibit this asymmetry. The teams in Japan and the United States will both employ a well-established technique to probe neutrino behavior. By smashing energetic protons from a particle accelerator into a target to produce pi-pluses, they will generate a beam of muon neutrinos and shoot it toward a distant underground detector. There, researchers will count the surviving muon neutrinos and the electron neutrinos that have emerged along the way. Then they will switch to producing a beam of muon antineutrinos, by collecting pi-minuses instead of pi-pluses from the target. They'll repeat the measurements, looking for any differences.

The experiment is much harder than it sounds, as several other factors could create a spurious asymmetry. For example, the neutrino and antineutrino beams will inevitably differ slightly, both in intensity and in their energy spectrum. To account for such differences, the researchers must sample the particles as they start their journey by placing a small detector, preferably with a design as similar as possible to the distant detector, in front of the beam source.

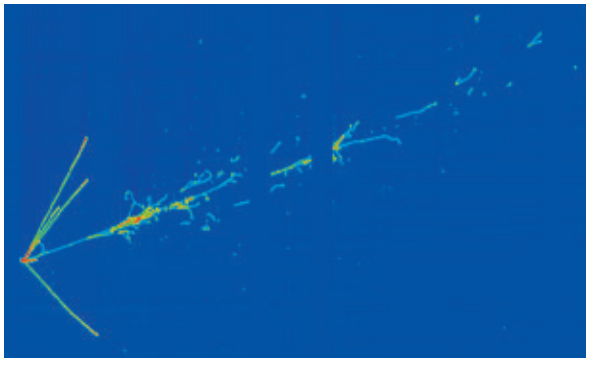
The physics of neutrinos themselves could also skew the results. For example, either neutrinos or antineutrinos will be absorbed more strongly by the matter they traverse on their flight to the detector. The

Neutrinos in high-def

Comprising two rectangular tanks, each filled with 17,000 tons of liquid argon, DUNE will precisely track all the charged particles produced when a high-energy neutrino fired from a distant laboratory strikes an argon nucleus.



Tracing tracks ▶
The charged particles will liberate electrons, which an electric field will push to a grid of wires. By timing when each wire fires, physicists can infer the particles' tracks and, ultimately, the incoming neutrino's energy.

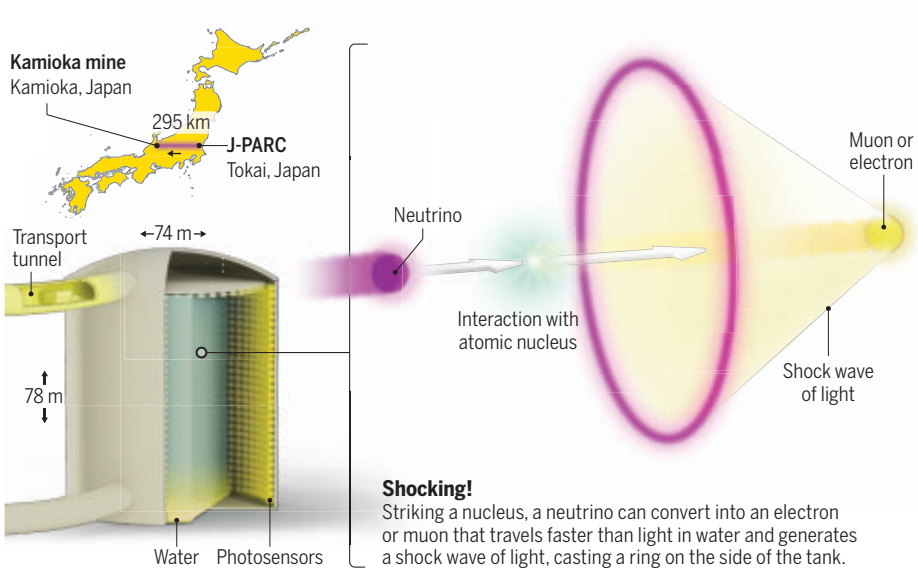


In MicroBOONE, a small liquid-argon detector at Fermilab, an energetic neutrino spawns charged particles, including an electron (long track).

CREDITS: (GRAPHIC) V. ALTOUNIAN/*SCIENCE*; (IMAGE) MICROBOONE COLLABORATION

Ring around a neutrino

An underground tank filled with 260,000 tons of water and lined with photodetectors, Hyper-Kamiokande will detect neutrinos shot from hundreds of kilometers away by exploiting the optical equivalent of a sonic boom.



Shocking! Striking a nucleus, a neutrino can convert into an electron or muon that travels faster than light in water and generates a shock wave of light, casting a ring on the side of the tank.

direction of that effect depends on the solution to the hierarchy problem. So, to spot CP violation, physicists will most likely have to solve the hierarchy problem, too.

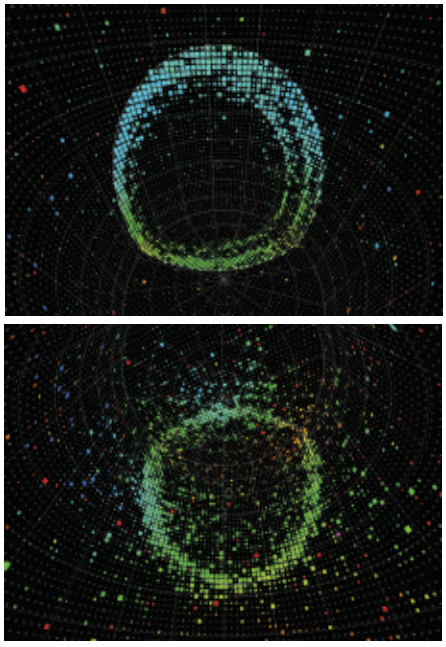
The biggest barrier to sorting all of this out, however, has been the measly harvest of neutrinos from even the biggest experiments. Like their counterparts in Japan, U.S. physicists already have a neutrino-oscillation experiment, NOνA, which shoots neutrinos from Fermilab to a detector 810 kilometers north in Minnesota. Like T2K, it has netted just several hundred neutrinos.

HYPER-K WILL TACKLE the scarcity primarily by providing a much bigger target for the neutrinos to hit. Proposed a decade ago, it's a scaled-up version of the storied Super-K detector and will consist of a cylindrical stainless steel tank 78 meters tall and 74 meters wide, holding 260,000 tons of ultrapure water—five times as much as Super-K.

To spot neutrinos, the detector will rely on the optical equivalent of a sonic boom. Rarely, a muon neutrino zipping through the water will knock a neutron out of an oxygen atom and change it into a proton, while the neutrino itself morphs into a high-energy muon. The fleeing muon will actually exceed the speed of light in water, which is 25% slower than in a vacuum, and generate a shock wave of so-called Cherenkov light, just as a supersonic jet creates a shock wave of sound. That conelike shock wave will cast a ring of light on the tank's side, which is lined with photodetectors.

Similarly, an electron neutrino can strike a neutron to produce a high-speed electron, which is lighter than a muon and will be buffeted more by the water molecules. The result will be a fuzzier light ring. Muon and electron antineutrinos can spawn detectable antimuons and antielectrons by striking protons, although with about half the efficiency of the neutrino interactions.

Hyper-K will be Japan's third great detector, all in the same mining area. From 1983 to 1995, the Kamioka Nucleon Decay Experiment (Kamiokande), a 3000-ton detector, tried to spot the ultrarare decays of protons that some theories predict. Instead, in 1987, it glimpsed neutrinos from a supernova—an advance that won a share of the Nobel Prize in Physics in 2002. In 1996, Super-K came online. It proved neutrinos oscillate by studying muon neutrinos generated when cosmic rays strike the atmosphere. Fewer come up from the ground than down from the sky, showing that those traversing Earth change flavor along the way. The discovery shared the Nobel in 2015. "It's spectacular what [Japanese physicists] have done," says Erin O'Sullivan, a neutrino astrophysicist at Uppsala University and a Hyper-K member who was drawn by "the dynasty of Super-K."



In Super-K, a muon neutrino turns into a muon, which radiates a tidy light ring (top). An electron neutrino spawns an electron and a fuzzier ring (bottom).

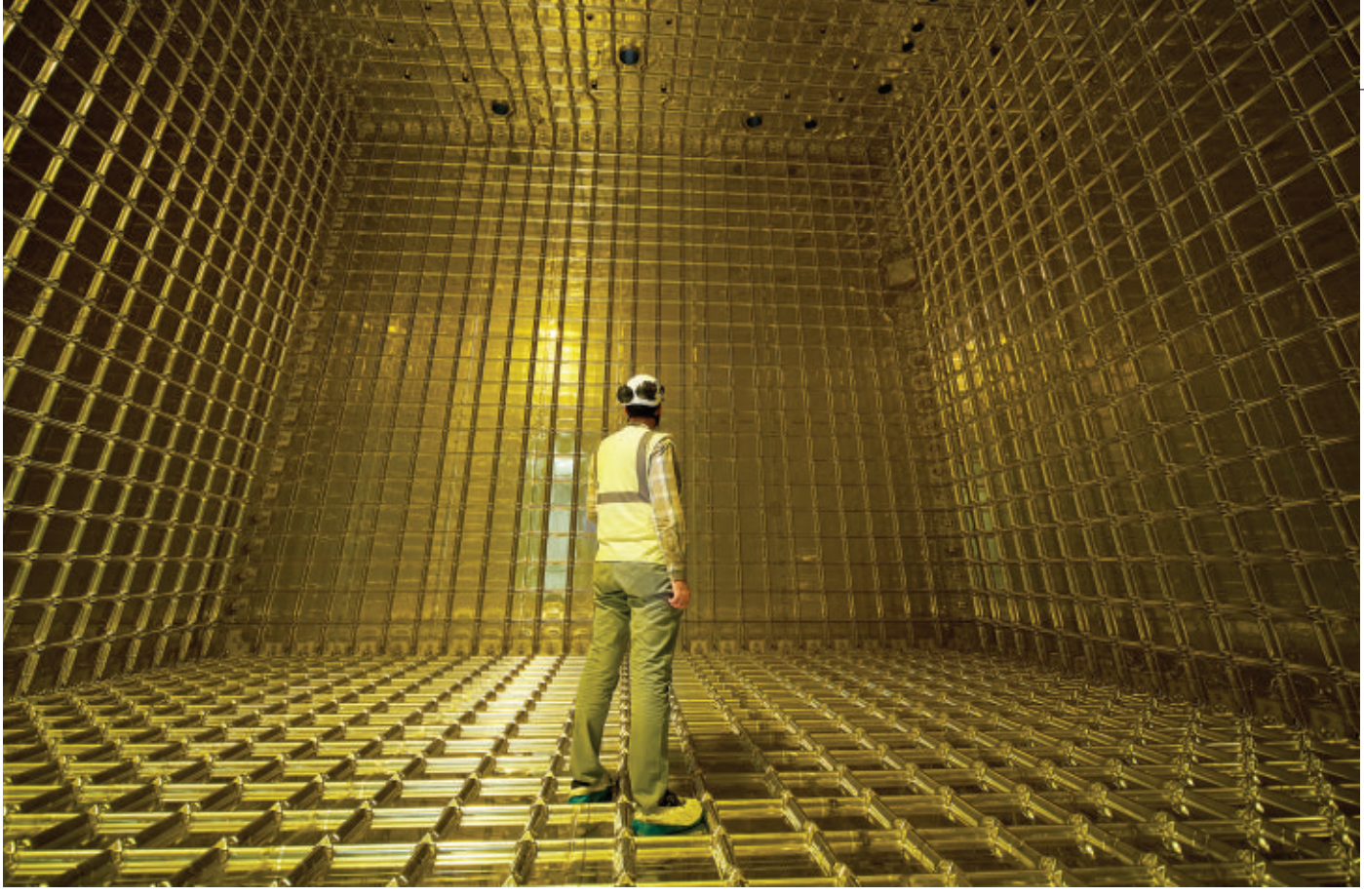
Hyper-K will reuse J-PARC's neutrino beam, which is now being upgraded to increase its power by a factor of 2.5. Overall, it should collect data at 20 times the rate of T2K, says Stephen Playfer, a particle physicist at the University of Edinburgh and the University of Tokyo and the project's lead technical coordinator. Before joining Hyper-K in 2014, he and his Edinburgh colleagues also considered joining DUNE. "When it came to comparing who was going to be first to see something, we thought Hyper-K was in a good position, just because it would have the statistics and it had a well-known technology," he says.

Hyper-K will have limitations. In particular, it won't measure the neutrinos' energies precisely. That matters because the rate at which a neutrino oscillates depends on its energy, and a beam contains neutrinos with a range or spectrum of energies. Without a way to pinpoint each neutrino's energy, the experiment would be unable to make sense of the oscillation rates.

To avoid this problem, Hyper-K, like current experiments, will rely on a trick. A neutrino beam naturally diverges, with lower energy neutrinos spreading more than higher energy ones. Thus, if a detector sits slightly to the side of the beam's path, it will see neutrinos with a narrower range of energies that should oscillate at roughly the same rate. So, like Super-K, Hyper-K will sit off the beam axis by an angle of 2.5°.

Physicists can then tune the energy of the beam so the neutrinos reach the detector when the oscillation is at its maximum. With the neutrinos' energy constrained, physicists basically count the number of arriving muon neutrinos, electron neutrinos, and their antimatter counterparts. Hyper-K's CP measurement comes down to comparing two ratios: electron neutrinos with muon neutrinos and electron antineutrinos with muon antineutrinos.

CREDITS: (GRAPHIC) V. ALTOUNIAN/*SCIENCE*; (IMAGES) KAMIOKA OBSERVATORY/INSTITUTE FOR COSMIC RAY RESEARCH/UNIVERSITY OF TOKYO



Since 2015, DUNE researchers have built prototypes at the European particle physics laboratory, CERN, which have performed even better than expected.

Workers have already begun the excavation for Hyper-K, which should take 2 years, Shiozawa says. The whole project will cost Japan about $600 million, with international partners chipping in an additional $100 million to $200 million, he says. The detector will be complete in 2027, Shiozawa says, and will start taking data a year later. So confident are Hyper-K researchers in their technology that they say the trickiest part of the project is the digging. "We need to construct probably the largest underground cavern" in the world, Shiozawa says. "In terms of technology and also cost, this is the biggest challenge."

IF, TECHNOLOGICALLY, Hyper-K amounts to much more of the same, DUNE aims to be something almost completely different. It will employ a technology that, until recently, was used in only one other large experiment but that should enable physicists to see neutrino interactions as never before. "To me, the draw of DUNE is its precision," says Chris Marshall, a particle physicist at the University of Rochester and DUNE's physics coordinator. "This is an experiment that will be world leading in just about everything that it measures."

Hunkering 1480 meters deep in a repurposed gold mine, DUNE will consist of two rectangular tanks 66 meters long, 19 meters wide, and 18 meters tall. Each will contain 17,000 tons of frigid liquid argon cooled to below –186°C. Just as in a water-filled detector, a neutrino can blast a neutron—in this case in an argon nucleus—to create a muon or an electron. But the neutrinos reaching DUNE from Fermilab will pack up to 10 times more energy than those flowing to Hyper-K. So, in addition to the muon or electron, a collision will typically produce a spurt of other particles such as pions, kaons, protons, and neutrons.

DUNE aims to track all those particles—or at least the charged ones—with a technology called a liquid argon time projection chamber. As a charged particle streaks through the argon, it will ionize some of the atoms, freeing their electrons. A strong electric field will push the electrons sideways until they hit three closely spaced planes of parallel wires, each plane oriented in a different direction. By noting when the electrons strike the wires, physicists can reconstruct with millimeter precision the original particle's 3D trajectory. And from the amount of ionization it produces, they can determine its type and energy.

The details are mind-boggling. The electrons will have to drift as far as 3.5 meters, driven by a voltage of 180 kilovolts. And unlike Hyper-K, DUNE will sit directly in the beam from Fermilab. So, it will capture a bigger but messier harvest of neutrinos, with ener-



Light glints off the planes of closely spaced, electron-catching wires within a DUNE prototype. The wires are 150 micrometers thick, like heavy hair.

PHOTOS: (TOP TO BOTTOM) BRICE MAXIMILLIEN/CERN; CERN

gies ranging from less than 1 giga-electron volt to more than 5 GeV.

DUNE's ability to precisely track all the particles should enable it to do something unprecedented in neutrino physics: Measure the energy of each incoming neutrino to construct energy spectra for each flavor of neutrino and antineutrino. Because of the flavor changing, a plot of each spectrum should itself exhibit a distinct wiggle or oscillation. By analyzing all of the spectra, physicists should be able to nail down the entire three-flavor model, including the amount of CP violation and the hierarchy, in one fell swoop, Bertolucci says. "It can measure all the parameters in the same experiment," he says.

Until now, the technology has never been fully developed. Italian Nobel laureate Carlo Rubbia dreamed up the liquid argon detector in 1977. But it wasn't until 2010 that one called ICARUS in Italy's subterranean Gran Sasso National Laboratory snared a few neutrinos shot from the European particle physics laboratory, CERN, near Geneva, Switzerland. Researchers at Fermilab and CERN have embarked on a crash program to build prototypes, which have worked even better than expected, says Kate Scholberg, a neutrino physicist and a DUNE team member at Duke University. "It's kind of an entrancing thing to look at the event displays" coming in, she says. "It's just incredible detail."

That precision comes at a price. For accounting purposes, the U.S. Department of Energy (DOE) splits the project in two. One piece, the Long Baseline Neutrino Facility (LBNF), includes the new neutrino beam at Fermilab and all the infrastructure. The second, DUNE, is an international collaboration that will build just the guts of the detectors. In 2015, DOE estimated LBNF/DUNE would cost $1.5 billion and come online in 2027. Last year, however, DOE reported that unexpected construction costs had raised the bill to $3.1 billion. The detector should be completed in 2028, says Christopher Mossey, project director for LBNF/DUNE-U.S. But the beam will lag until early 2031, potentially giving Hyper-K a head start of more than 2 years.

With contracts in hand and construction underway, DUNE developers are confident that the new cost and timeline will hold. Excavation has passed 40% and should be completed in May 2023, Mossey says. "We really are accomplishing big, tangible things." Still, DUNE physicists acknowledge that the project is riskier than Hyper-K. "It's a leap into the unknown, and that's the trade-off you make," Scholberg says. "Something that is more transformative is going to certainly entail more scariness."

BOTH EXPERIMENTS have other scientific goals, such as searching for proton decay. There, Hyper-K has an advantage, Huber says, as it is simply bigger and contains lots of lone protons in the hearts of the hydrogen atoms in water molecules. Another tantalizing payoff could come if a giant star collapses and explodes as a supernova near our Galaxy, as one did in 1987. The experiments would provide complementary observations, Scholberg says, as DUNE would see the electron neutrinos produced just as the core implodes and Hyper-K would see mainly electron antineutrinos released later in the explosion.



Hyper-Kamiokande will deploy new and improved phototubes, which must withstand pressures up to six atmospheres at the bottom of the tank.

PHOTO: KAMIOKA OBSERVATORY/INSTITUTE FOR COSMIC RAY RESEARCH/UNIVERSITY OF TOKYO

Nevertheless, the raison d'être for both experiments remains deciphering neutrino oscillations and searching for CP violation. So, how would a gambler handicap this race?

Given their head start, Hyper-K physicists could score major discoveries before DUNE even finds its feet. If CP violation is as big as it can possibly be, "then we may discover it in 3 years," Shiozawa says. "And also, we may discover proton decay in 3 years." But, he says, "It really depends on nature."

Hyper-K is optimized to measure CP violation assuming it's big and the three-flavor model is the final word on neutrino oscillations, Huber notes. Neither assumption may hold. And with its simpler counting technique and shorter baseline, the experiment may struggle to distinguish CP violation from the matter effect unless some other experiment independently solves the hierarchy problem. "Hyper-K certainly requires more external inputs," Huber says.

DUNE, in contrast, should be able to disentangle the whole mess on its own. Shiozawa, for one, is not counting out his rival. The Japanese project has experienced growing pains of its own, he notes, including being scaled back from an initial 1-million-ton design. And the Japanese government won't countenance any cost increase, putting project leaders in constant tension with contractors, he says. "The situation is not so different between the two projects."

Ultimately, the rivalry between Hyper-K and DUNE may be less a dash for glory than a decadeslong slog through uncertainty. If so, the two teams could end up collaborating as much as they compete, at least informally. "We'll have a long time where the most accurate results will come from a combination of the two [experiments]," Huber predicts.

Most tantalizing, instead of completing the current theory, the results could upend it. They might reveal deviations from the three-flavor model that could hint at new particles and phenomena lurking in the vacuum. After all, neutrinos have repeatedly surprised physicists, who once assumed that the particles came in only one type and were completely massless and inert. "Previously, neutrino experiments have taught us that we very rarely take data in a neutrino beam and get exactly what we expect," Marshall says.

The unexpected may be a long shot worth betting on. ■

INSIGHTS

PERSPECTIVES



Plant *et al.* found that the efficiency of methane removal by flaring at US oil and gas facilities is lower than expected.

METHANE EMISSION

Tackling unlit and inefficient gas flaring

Emissions from flaring threaten the global climate and the health of local communities

By **Riley Duren**[1,2] *and* **Deborah Gordon**[3,4]

Because of the outsized warming potential of methane, it is essential to limit this superpollutant to mitigate the worsening global climate emergency. More than 120 nations have signed the Global Methane Pledge to cut emissions by 30% by 2030 (*1*). Some 80 oil and gas (O&G) companies have joined the Oil and Gas Methane Partnership, which aims to establish a reporting framework for methane emissions (*2*), such as those from flaring—the practice of burning off unwanted gas. The World Bank has enlisted public and private stakeholders to commit to zero routine flaring by 2030 (*3*). On page 1566 of this issue, Plant *et al.* (*4*) report an average methane destruction removal efficiency of 87 to 94% by flaring in US-based O&G facilities. This number is much lower than what was previously assumed, and the authors attribute this to inefficient and unlit flares.

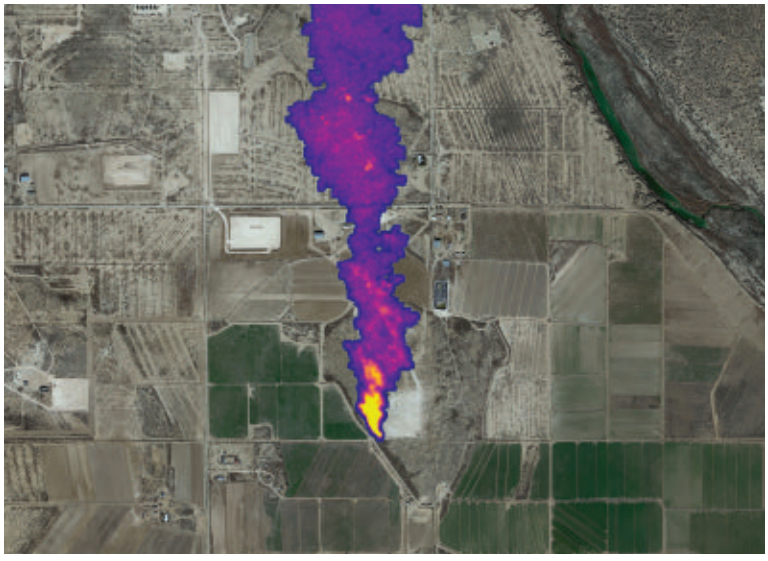
Flares are designed into O&G facilities as a safety precaution and should only be used in emergencies. Beyond safety, satellite data have shown that flaring may be resorted to for various reasons throughout O&G facilities globally (*5*). In 2021, an estimated 144 billion m^3 of gas was released through flaring—enough to generate two-thirds of the European Union's electricity needs. Currently, most O&G facilities provide no direct tracking of the methane removal efficiency (or even the operational status) of their flares. Until recently, it was assumed that most flares performed at nearly 100% efficiency, such that combustion effectively converted all of the flared gas into water and carbon dioxide (*6*). However, Plant *et al.* and other recent studies are providing a reality check on this overly optimistic view of flaring efficiency.

The authors studied more than 300 flares

[1]Carbon Mapper, Inc., Pasadena, CA, USA. [2]Arizona Institute for Resilient Environments and Societies and Research, Innovation and Impact, University of Arizona, Tucson, AZ, USA. [3]RMI, Basalt, CO, USA. [4]Watson Institute for International and Public Affairs, Brown University, Providence, RI, USA. Email: rduren@arizona.edu

PHOTO: H. ARMSTRONG ROBERTS/CLASSICSTOCK/GETTY IMAGES

from three major O&G production basins responsible for 80% of flaring in the US. The finding that a small number of inefficient or unlit flares are responsible for much higher than predicted emissions is not new. For instance, an earlier study found that ~1000 methane superemitters in the Permian basin (in New Mexico and Texas) were responsible for 60% of the region's methane emissions, with 12% of those emissions coming from inefficient flares, most of which were persistently unlit (*7*). The findings of Plant *et al*. reveal a broader trend for flaring across the US, which might be representative of the situation globally, indicating the need for broader observational studies. They also found that methane emissions from flaring in the US are five times as high as currently reported in the US Environmental Protection Agency's (EPA) greenhouse gas inventory.



Methane plume from an unlit flare in the Permian basin is detected by a remote sensing aircraft.

PHOTO: CARBON MAPPER/UNIVERSITY OF ARIZONA/ARIZONA STATE UNIVERSITY GLOBAL AIRBORNE OBSERVATORY

The International Energy Agency (IEA) estimated global average flaring efficiency at 92% in 2020 on the basis of satellite-derived flaring volumes and bottom-up operating data (*8*). In total, IEA estimated 8 million metric tons (Mt) of methane emitted from global flaring in 2020—equivalent to 660 Mt of CO_2 over 20 years (*9*). This is as large an emission footprint as that from half of all the cars in the US. To make matters worse, this estimate may be lower than reality because unlit flares are mostly unaccounted for. In addition to their global warming contribution, inefficient and unlit flarings also present air quality, health, and environmental justice concerns for local communities. Among the flares monitored by Plant *et al*., only 55 to 76% of the gas sent to flares was methane, and the remainder likely included volatile organic compounds and hazardous air pollutants, such as benzene. In the US, an estimated 18 million people live within 2 km of an O&G well (*10*), and ~500,000 people live within 5 km of an active flare in the Permian basin, the Eagle Ford basin (in Texas), and the Bakken basin (in North Dakota and Montana) (*11*). Unlit and incompletely combusted flares may expose nearby communities to a cocktail of copollutants that pose health risks.

A range of factors, including design flaws, perverse policies, operational negligence, and regulatory and enforcement gaps, all contribute to unlit and inefficient flaring. Although there are engineering solutions to increase the efficiency of flares, this problem largely lies with the lack of regulation and oversight. In some parts of the US, North Dakota for example, allowable efficiency for flaring is set as low as 90% (*12*). Exemptions in state and federal rules also allow routine flaring when "no sales line is available," which means that operators can simply burn their excess production as waste. In the Permian basin, for example, where pipeline capacity is limited, O&G operators routinely opt to burn the gas rather than sell it.

Better ways to monitor methane emissions may also be needed for operators and regulators to comply with and enforce the stricter emission standards if they are updated. Existing satellites can see the heat signatures of active flares but are mostly unable to detect unlit flares and have limited ability to directly quantify methane removal efficiency. Future satellites, such as the planned Carbon Mapper constellation (*13*), will offer more-comprehensive global flare tracking by having lower methane detection limits, higher spatial resolution, larger area coverage, and more-frequent sampling. Newer satellites, along with ground- and air-based monitoring systems, can be coordinated to focus on regions with the greatest risk for flaring issues. Monitoring systems can help direct further research studies to better characterize regional variations in flaring performance and evaluate previously unmonitored facilities in remote areas. Actionable methane data, when combined with rapid notification protocols, can alert operators for the expedited repair of inefficient and unlit flares and other malfunctions, such as gas and oil leaks. Requirements for self-reporting from operators, especially during the initial months when a production well comes online and during disruptions, could also improve oversight and reduce waste.

In addition to improved monitoring, there is a need for better models to guide improvements in flare design and operations. Observational data can be integrated with open-source engineering models like the Oil Climate Index plus Gas, which estimates O&G flaring and total life cycle emissions (*14*). Together, satellites, surface sensors, and models can provide more-accurate assessments of the role that improved flaring efficiency plays in overall O&G emissions and future mitigation efforts. The technology exists to prevent unlit and inefficient flares across O&G supply chains. Implementing flare fixes worldwide, however, will require further improvements in monitoring, regulations, and industry practices. As the global climate crisis continues to worsen, resolving the flaring problem in this decisive decade is among the easiest routes to help mitigate the problem. ■

REFERENCES AND NOTES

1. Global Methane Pledge (Climate & Clean Air Coalition Secretariat); www.globalmethanepledge.org/.
2. Oil & Gas Methane Partnership 2.0 (United Nations Environment Programme); www.ogmpartnership.com/.
3. Global Gas Flaring Reduction Partnership (World Bank); www.worldbank.org/en/programs/gasflaringreduction/about.
4. G. Plant *et al*., *Science* **377**, 1566 (2022).
5. C. D. Elvidge, M. Zhizhin, "Global Gas Flare Survey by Infrared Imaging, VIIRS Nightfire, 2012-2019" (ORNL DAAC, 2021); https://doi.org/10.3334/ORNLDAAC/1874.
6. M. McDaniel, "Flare Efficiency Study" (US EPA report, EPA-600/2-83-052, 1983).
7. D. H. Cusworth *et al*., *Environ. Sci. Technol. Lett.* **8**, 567 (2021).
8. International Energy Agency, "Flaring Emissions" (IEA, 2021); www.iea.org/reports/flaring-emissions.
9. IPCC, *Climate Change 2021: The Physical Science Basis. Working Group I Contribution to the Sixth Assessment Report of the Intergovernmental Panel on Climate Change*, V. Masson-Delmotte *et al*., Eds. (Cambridge Univ. Press, 2021).
10. E. D. Czolowski, R. L. Santoro, T. Srebotnjak, S. B. C. Shonkoff, *Environ. Health Perspect.* **125**, 086004 (2017).
11. L. J. Cushing, K. Chau, M. Franklin, J. E. Johnston, *Environ. Res. Lett.* **16**, 034032 (2021).
12. North Dakota Department of Environmental Quality; https://deq.nd.gov/aq/oilgas/.
13. Carbon Mapper constellation; https://carbonmapper.org; www.planet.com/carbon-mapper/.
14. D. Gordon, J. Koomey, A. Brandt, J. Bergerson, "Know your oil and gas: Generating climate intelligence to cut petroleum industry emissions" (RMI, 2022); https://rmi.org/insight/kyog/.

10.1126/science.ade2315

CANCER

Metabolite-driven antitumor immunity

An oncometabolite blocks T cell killing by inhibiting glycolysis

By **James A. Nathan**

Otto Warburg's observations that solid organ tumors preferentially use aerobic glycolysis, metabolizing glucose to lactate, to facilitate growth paved the way for our understanding of how nutrient availability and metabolism can promote cancer. A common theme is that proliferating tumor cells use a diverse array of mechanisms to acquire nutrients to grow rather than to simply support adenosine triphosphate (ATP) production (*1*). However, promoting cell growth is generally not sufficient for solid-organ tumors to develop because they must also evade cytotoxic T cells, raising the question of whether this immune evasion is linked to metabolism. On page 1519 of this issue, Notarangelo *et al.* (*2*) show that D-2-hydroxyglutarate (D-2HG), a metabolite secreted by tumors with mutations in isocitrate dehydrogenase (IDH) (*3*), functions within the tumor microenvironment (TME) to impair $CD8^+$ T cell–mediated tumor cell killing. These findings highlight the potential for metabolites within the TME to alter antitumor immune responses.

Somatic mutations in IDH occur in a wide range of tumors, including acute myeloid leukemia and ~80% of gliomas, the most common form of brain cancer (*4*). Disease-causing mutations disrupt the canonical action of IDH to convert isocitrate to α-ketoglutarate (αKG) in the tricarboxylic acid cycle and instead promote the formation of D-2HG from αKG (*3*). D-2HG acts as an "oncometabolite" within cells, contributing to tumorigenesis through inhibition of metabolite-sensitive enzymes (αKG-dependent dioxygenases) involved in modulating epigenetic marks and transcriptional reprogramming (*5*). However, D-2HG also accumulates to high levels within the TME (*6*). Notarangelo *et al.* investigate how extracellular D-2HG may be related to prior observations that IDH-mutant gliomas are protected from infiltrating T cells (*6*–*8*).

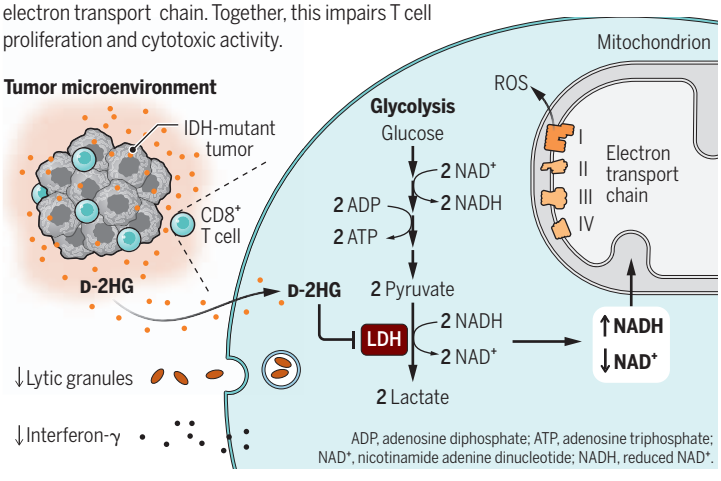
Notarangelo *et al.* find that treating isolated mouse $CD8^+$ T cells with D-2HG results in decreased proliferation, reduced lytic granule release, and impaired secretion of the cytokine interferon-γ (IFN-γ), leading to a functional loss of cytotoxic killing in vitro (see the figure). D-2HG needs to be present at the time of tumor cell recognition by $CD8^+$ T cells to impair killing, and removal of the metabolite restores T cell function. This rapidly reversible alteration in T cell function is not consistent with D-2HG–mediated changes in epigenetic marks (*5*), and no transcriptional reprogramming of T cells was found within 24 hours of treatment. Instead, the authors find that D-2HG exerts its effects by perturbing T cell glycolysis through direct inhibition of lactate dehydrogenase (LDH), which catalyzes the conversion of pyruvate to lactate, using reduced nicotinamide adenine dinucleotide (NADH) as a cofactor. Subsequently, this alters the balance between NAD^+ and NADH, which are important for maintaining redox levels in cells.

Prior studies have observed that D-2HG uptake by tumor-infiltrating macrophages and cytotoxic T cells can lead to suppression of antitumor immunity by altered tryptophan metabolism and calcium signaling (*6*, *9*). Notarangelo *et al.* show a distinct mechanism of evading T cell killing, demonstrating that regeneration of NAD^+ pools by LDH activity is central to $CD8^+$ T cell function. They find that D-2HG treatment of mouse $CD8^+$ T cells impairs glycolysis, resulting in a shift to respiration and shuttling of cytosolic NADH to the mitochondria. The resulting increase in activity of Complex I helps sustain $CD8^+$ T cell proliferation when glycolysis is impaired. Consistently, Notarangelo *et al.* show that treatment of cultured $CD8^+$ T cells with several LDH inhibitors phenocopies the effects of D-2HG treatment, and that resetting the NAD^+-NADH balance in vitro, by using a bacterial NADH oxidase to generate NAD^+ independently of LDH, prevents the shift to respiration.

The contribution of D-2HG to evading antitumor immunity was evident in both mouse models and tissue sections from patients with IDH-mutant tumors. Using single-cell studies and multiplexed immunofluorescence, Notarangelo *et al.* find that human IDH-mutant gliomas demonstrate an impaired IFN-γ signature comparable with that seen in mouse T cells treated with D-2HG, and they observe exclusion of $CD8^+$ T cells from regions with high D-2HG levels in IDH-mutant brain tumor sections from patients. The timing of exposure to D-2HG, and resulting LDH inhibition, may dictate the consequences for metabolic reprogramming of $CD8^+$ T cells. Earlier work that used a mouse model of melanoma found that pretreatment of T cells with an LDH inhibitor before their transfer into mice bearing melanoma actually improved antitumor immunity (*10*). These differential effects of LDH inhibition on cytotoxic T cells may need to be further resolved, but in the context of the TME, the findings of Notarangelo *et al.*

Suppressing T cell killing

D-2-hydroxyglutarate (D-2HG) is produced by isocitrate dehydrogenase (IDH) mutant tumors and accumulates in the tumor microenvironment. D-2HG uptake by surveilling $CD8^+$ T cells inhibits lactate dehydrogenase (LDH), which decreases glycolysis and disrupts the NAD^+-NADH balance. This drives respiration and thereby increases reactive oxygen species (ROS) produced by Complex I of the electron transport chain. Together, this impairs T cell proliferation and cytotoxic activity.



GRAPHIC: K. HOLOSKI/*SCIENCE*

Cambridge Institute of Therapeutic Immunology and Infectious Disease (CITIID), Department of Medicine, University of Cambridge, Cambridge, UK.
Email: jan33@cam.ac.uk

reveal a rapid LDH-dependent rewiring of CD8$^+$ T cell function.

The clinical use of inhibitors targeting IDH mutations suggests that drugs that decrease D-2HG levels may also confer clinical benefits through reversing T cell dysfunction. To date, small-molecule mutant IDH inhibitors are approved for clinical use in acute myeloid leukemia (*11*) and are being tested in IDH-mutant gliomas. Inhibitors of mutant IDH1 can improve antitumor T cell responses in mouse models (*6*, *12*), and it will be important to explore their potential enhancement of antitumor immunity in clinical disease.

The study of Notarangelo *et al*. highlights the role for metabolites in the TME to rewire immune cells but, more broadly, raises the question of how this rapid metabolic reprograming integrates with changes in epigenetic marks and immune cell function. In the context of D-2HG, this will be dependent on the relative contribution of active uptake and secretion, and how this flux is controlled in T cells remains to be fully determined. Moreover, the relative contribution to transcriptional programming will result from a complex interplay of the abundance of additional metabolites that can alter epigenetic marks (such as succinate, αKG, L-2HG, and itaconate), other nutrients within the TME, and oxygen availability. Notarangelo *et al*. also find that the effects of D-2HG on CD8$^+$ T cells are independent of the hypoxia-inducible factor pathway (which is regulated by αKG-dependent dioxygenases and transcriptionally up-regulates glycolysis), but how oxygen availability within the TME interplays with metabolic rewiring will be of interest to explore. As the technical challenges in determining metabolite concentrations within the TME begin to be overcome, non–cell-autonomous metabolic control of immune evasion by tumor cells can be further understood. ■

REFERENCES AND NOTES

1. M. G. Vander Heiden, L. C. Cantley, C. B. Thompson, *Science* **324**, 1029 (2009).
2. G. Notarangelo *et al*., *Science* **377**, 1519 (2022).
3. L. Dang *et al*., *Nature* **462**, 739 (2009).
4. L. Dang, K. Yen, E. C. Attar, *Ann. Oncol*. **27**, 599 (2016).
5. W. Xu *et al*., *Cancer Cell* **19**, 17 (2011).
6. L. Bunse *et al*., *Nat. Med*. **24**, 1192 (2018).
7. G. Kohanbash *et al*., *J. Clin. Invest*. **127**, 1425 (2017).
8. A. S. Berghoff *et al*., *Neuro-oncol*. **19**, 1460 (2017).
9. M. Friedrich *et al*., *Nat. Can*. **2**, 723 (2021).
10. D. Hermans *et al*., *Proc. Natl. Acad. Sci. U.S.A*. **117**, 6047 (2020).
11. G. C. Issa, C. D. DiNardo, *Blood Cancer J*. **11**, 107 (2021).
12. P. Chuntova *et al*., *J. Immunother. Cancer* **10**, e004644 (2022).

ACKNOWLEDGMENTS

J.N. is funded by a Wellcome Senior Fellowship (215477/Z/19/Z), Lister Fellowship, and Pfizer Innovative Target Exploration Network award.

10.1126/science.ade3697

AGING

The genetics of a long life

Genetically diverse mice and cross-species comparison uncover links to longevity

By **João Pedro de Magalhães**

Elucidating the genetics of complex traits and diseases is a major undertaking, one that can lead to biological insights and, because genetics increasingly informs drug discovery (*1*), new treatments. Longevity reflects aging and other processes affecting health and disease, so unraveling its genetic basis would have far-reaching implications. However, it has been a challenge to identify the genetic determinants of longevity in humans or animals (*2*) in part because longevity as a phenotype encompasses multiple other traits and disease risks. Tackling the complexity of the genetic component of longevity requires an integrated approach that leverages multiple sources of evidence. On page 1508 of this issue, Bou Sleiman *et al*. (*3*) use genetically heterogeneous mice to find new life-span loci and further perform cross-species comparisons to better understand the genetic basis of mammalian longevity.

Recent advances in identifying single genes that, when genetically manipulated, modulate longevity in animal models have been substantial (*4*). According to the GenAge database (*5*), there are more than 2000 longevity-associated genes in model organisms including mice, flies, yeast, and worms. One underappreciated limitation of such studies, however, is that they are mostly conducted in inbred, genetically homogeneous animal populations. This means that discoveries in the genetics of aging, as well as dietary and pharmacological manipulations, may be strain specific because there could be genetic background effects (*6*).

Given that most longevity studies in mice use isogenic stocks, the role of natural genetic variation in longevity in mice is not only poorly understood but largely unexplored. Bou Sleiman *et al*. genotyped 3276 mice from the Interventions Testing Program (ITP). The heterogeneous mice used in the ITP were derived by a four-way intercross of inbred strains. Therefore, one limitation of the work of Bou Sleiman *et al*. is that it will miss genetic variants absent from inbred strains. Further studies using wild-derived mouse populations with a larger genetic diversity would thus be of great value. Indeed, Bou Sleiman *et al*. found a small number of loci associated with life span using the ITP cross of inbred strains,

Genomics of Ageing and Rejuvenation Lab, Institute of Inflammation and Ageing, University of Birmingham, Birmingham, UK. Email: jp@senescence.info



PHOTO: XINHUA NEWS AGENCY/CONTRIBUTOR/GETTY IMAGES

Previously unknown loci associated with life span in mice may be relevant to humans living a long life, such as Emma Morano, who lived to 117 years.

suggesting that in more diverse mouse populations there could be many more genetic determinants of longevity.

The loci identified by Bou Sleiman *et al*. that modulate life span may contain dozens of genes. To further prioritize which genes may be causal, Bou Sleiman *et al*. obtained and integrated various other types of data. Specifically, they generated gene expression profiles of aged mice from the liver, a commonly studied organ in longevity owing to its essential functions for maintaining homeostasis, such as energy metabolism and detoxification. Mostly, however, they took advantage of multiple publicly available datasets to gain insights and score the genes in each locus that they identified. These included differential gene expression from the Tabula Muris Senis *(7)*, a single-cell transcriptomic atlas of mouse aging tissues, and longevity genes from mice and orthologs in other model organisms from the GenAge database (*5*). In addition, data on human orthologs were obtained from the Genotype-Tissue Expression (GTEx) project, with tissue-specific gene expression including aged tissues, and from the GWAS Catalog (*8*), which compiles data from genome-wide association studies. As such, the study of Bou Sleiman *et al*. showcases the value of these resources and the importance of integrating multiple types of data to help untangle complex phenotypes, such as life span.

The comparison of data from multiple organisms is also noteworthy. Given that longevity is a particularly time-consuming phenotype to study, research has relied on animal models, including worms (in which the first genes that modulate longevity were discovered), rodents, and, more recently, dogs (*4, 9*). After scoring and prioritizing the candidate genes in the loci modulating life span, Bou Sleiman *et al*. tested several *Caenorhabditis elegans* homologs for life-span effects. They found five genes from mice that modulated life span in worms when silenced: homeodomain interacting protein kinase 1 (*Hipk1*); dolichyl-di-phosphooligosaccharide-protein glycotransferase (*Ddost*); heparan sulfate proteoglycan 2 (*Hspg2*); FYVE, RhoGEF and PH domain containing 6 (*Fgd6*); and pyruvate dehydrogenase kinase 1 (*Pdk1*), although all except *Pdk1* reduced life span and hence may be pathological rather than aging related. *Hipk1* (*hpk-1* in *C. elegans*) acts as a regulatory node for chaperones and autophagy to preserve proteostasis in worms (*10*), a major longevity pathway. Furthermore, *Ddost* is involved in the processing of advanced glycation end products that accumulate with age and have been associated with several age-related diseases such as diabetes mellitus and cardiovascular diseases in various models and humans (*11*). Interestingly, a locus near *FGD6* has been found to influence health span, parental life span, and longevity in humans (*12*).

In line with other studies of the ITP revealing that life span is affected by dietary manipulations in a sex-specific manner (*13*), most loci that Bou Sleiman *et al*. found to modulate life span also exhibited sex dichotomy. It is unclear why this is the case. If a diet or allele slows aging, then why would this not be the case for males and females? It is possible that more specific processes or diseases (i.e., those with sex-specific effects) rather than aging-specific processes per se are altered when longevity is modulated. Moreover, Bou Sleiman *et al*. found many loci that only modulate life span after a given age and partial overlap between life-span loci and loci associated with growth or body weight, likely reflecting the multiple processes and traits that affect the longevity phenotype. Nonetheless, these sex-specific effects emphasize the heterogeneity of longevity and the need to study diverse populations (*14*).

The data generated by Bou Sleiman *et al*. will prove a valuable resource for the study of aging and longevity. Many genes are thought to contribute to mammalian longevity, yet only a (likely small) fraction of these are known, and there is still substantial unexplained heritability in human longevity. As such, data sharing and cross-species comparisons will foster and enhance future longevity studies and lead to more rapid progress. Candidates from animal models such as worms and mice provide a direction for further studies. The question of which genes in the loci identified by Bou Sleiman *et al*. contribute to longevity remains unanswered. Likewise, except for *FGD6*, whether the genes identified by the authors to modulate life span in worms are involved in human longevity remains to be established. Because longevity is a complex, multifactorial phenotype, it will also be important to elucidate in the future which processes and diseases are affected by genetic variants associated with longevity. ■

REFERENCES AND NOTES

1. D. Ochoa *et al*., *Nat. Rev. Drug Discov.* **21**, 551 (2022).
2. S. Dato *et al*., *Mech. Ageing Dev.* **165**, 147 (2017).
3. M. Bou Sleiman *et al*., *Science* **377**, eabo3191 (2022).
4. C. J. Kenyon, *Nature* **464**, 504 (2010).
5. R. Tacutu *et al*., *Nucleic Acids Res.* **46**, D1083 (2018).
6. J. P. de Magalhães, *Cell Cycle* **13**, 2671 (2014).
7. N. Almanzar *et al*., *Nature* **583**, 590 (2020).
8. A. Buniello *et al*., *Nucleic Acids Res.* **47**, D1005 (2019).
9. G. Taormina *et al*., *Genes* **10**, 518 (2019).
10. R. Das *et al*., *PLOS Genet.* **13**, e1007038 (2017).
11. R. S. Pinto *et al*., *Int. J. Mol. Sci.* **23**, 2404 (2022).
12. P. R. H. J. Timmers *et al*., *Nat. Commun.* **11**, 3570 (2020).
13. F. Macchiarini, R. A. Miller, R. Strong, N. Rosenthal, D. E. Harrison, in *Handbook of the Biology of Aging*, N. Musi, P. J. Hornsby, Eds. (Academic Press, ed. 9, 2021), pp. 219–235.
14. J. P. de Magalhães, J. Wang, *EMBO Rep.* **20**, e48054 (2019).

10.1126/science.ade3119

PLANET FORMATION

Earth was seasoned by countless blows

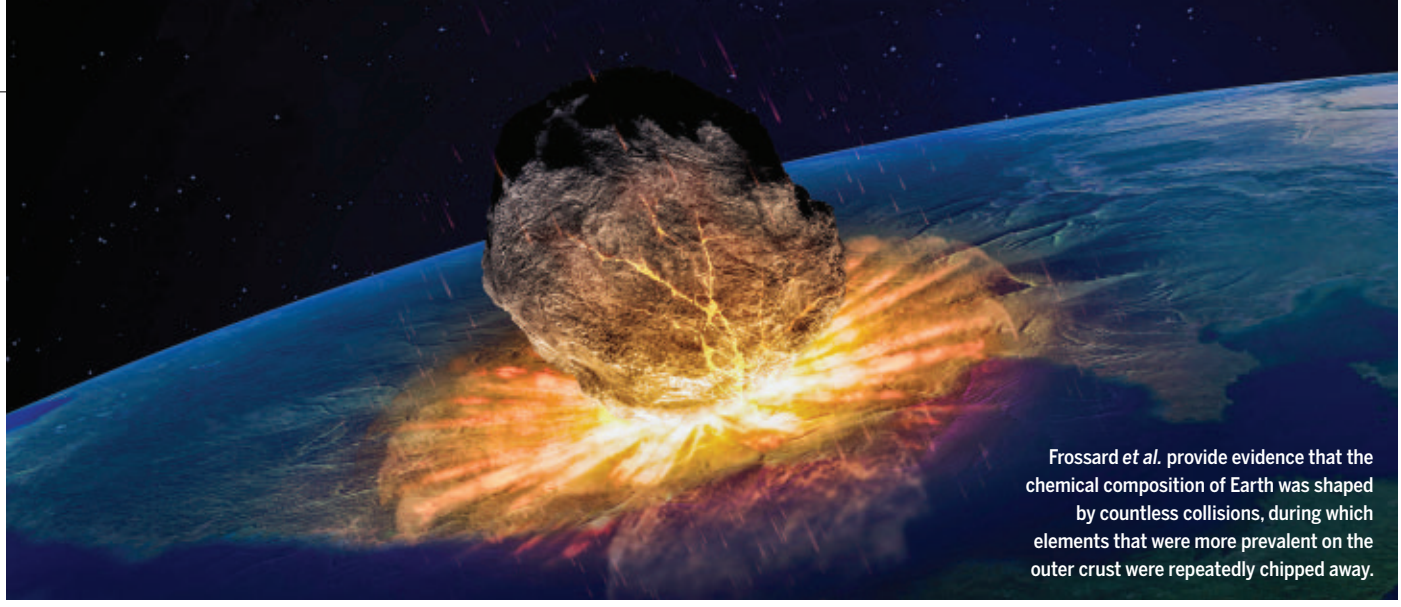
Earth's composition was shaped by collisions from external objects

By **Zoë Malka Leinhardt**

The formation of planets around distant stars is not uncommon. With more than 5000 planets detected outside of our Solar System, it is estimated that at least 25% of stars harbor planets. However, astronomers have yet to definitively find an Earth-like planet with the necessary characteristics to support life. Does this apparent rarity of Earth-like planets have something to do with the way Earth was formed? The history of Earth's formation and composition is an ongoing debate. Recent studies have found that Earth's current composition does not fully align with what would be expected if it was solely made up of the most primitive rocky meteorites. On page 1529 of this issue, Frossard *et al*. (*1*) show that the chemical makeup of Earth's crust has changed over time as the result of countless impacts with smaller rocky bodies.

At present, the favored formation model for rocky planets, such as Earth, revolves around collisions (*2*). According to this view, the process began with a swirling disk of dust and gas and a young Sun at the center. The dust and gas orbiting the Sun originated from a much larger, cooler cloud of molecular gas that collapsed to form the Sun. Some of the collapsing clouds had too much angular momentum to fall into the young Sun and instead formed a disk going around it. As the disk cooled, its solid components accumulated into many planetary building blocks, or "planetesimals." The planetesimals collided with each other often, which resulted in accretion and growth, and eventually formed rocky planets.

H.H. Wills Physics Laboratory, School of Physics, University of Bristol, Bristol BS8 1TL, UK.
Email: zoe.leinhardt@bristol.ac.uk



Frossard *et al.* provide evidence that the chemical composition of Earth was shaped by countless collisions, during which elements that were more prevalent on the outer crust were repeatedly chipped away.

IMAGE: MARC WARD/STOCKTREK IMAGES/GETTY IMAGES

During this period of planet formation, the accumulation of an entire planet required hundreds of thousands of collisions. As larger objects grew, they generated more gravitational pull on neighboring objects, which caused some collisions to be more violent, although even the gentlest collisions produced some debris (*3*). These collisions were pivotal in shaping the composition of planets and the structure of the Solar System. For instance, giant impacts are the favored explanation for the formation of massive moons, including Earth's Moon (*4*) and Pluto's largest satellite Charon (*5*). These collisions also played a role in other seemingly more subtle details, for example, the spin axial tilt of planets, such as that of Uranus (*6*), whose spin axis lies parallel to its orbital plane. So, it is not surprising to think that these collisions can also affect the composition of the planets.

The key to understanding how collisions could change the observed composition hinges on a planet's internal structure. Planets, including Earth, are not structurally uniform in composition. Instead, they are differentiated or separated into distinct layers. For instance, Earth contains a metal-rich iron-nickel core surrounded by a mantle of dense magnesium and iron silicate and capped with a floating crust of lighter silicate. This differentiation—with heavier compounds at the center and lighter ones on the outer layers—means that lighter material is more susceptible to removal by collisional events. This vulnerability is especially important for the gentler collisions that do not penetrate or expose the denser interior layers of the planet (*7*).

There is, however, an important nuance to this picture. Compositional differences found in Earth's crust and mantle are not solely based on the mass density of different elements but are also based on the elements' compatibility with each other to form molecules. For example, some rare Earth elements, such as samarium (Sm) and neodymium (Nd), are incompatible with mantle minerals and are thus "pushed" up to the crust despite being relatively heavy elements. Because of this detail, the radioactive decay of the isotope ^{146}Sm into ^{142}Nd has been used in geochemistry to study crust and mantle evolution. However, Earth has an excess of ^{142}Nd (relative to ^{144}Nd) compared with the meteorites that are considered representative of the planetesimals that built Earth (*8*).

There are three competing explanations for the apparent excess of ^{142}Nd. One idea suggests that the excess is only "apparent" and more ^{144}Nd exists deep within the mantle but is beyond the reach of current sampling techniques. Another idea is that the planetesimals that built Earth were not the same in composition because the accretion disk around the Sun was not uniform; it may actually be the planetesimals that are poor in ^{142}Nd. Another possibility—one supported by the findings of Frossard *et al.*—is that the crust of Earth was continuously eroded by impacts during its formation, which caused a greater loss of elements preferentially found in the crust.

Although both Sm and Nd are incompatible with the mantle, this discordance is slightly more pronounced with Nd. Therefore, as Earth formed, the ratio of Nd in the crust compared with Nd in the mantle is higher than the same ratio for Sm. Because of this, a larger fraction of ^{144}Nd than ^{146}Sm in Earth was removed from the crust through collisions. The ^{146}Sm left in the crust then eventually decayed into ^{142}Nd and produced the excess of ^{142}Nd over ^{144}Nd.

Frossard *et al.* argue that there is little evidence to support the hidden ^{144}Nd theory. They claim that because of the deep convective nature of the mantle during the final stages of Earth's accretion, ^{146}Sm and ^{144}Nd would have been too well mixed to completely explain the excess of ^{142}Nd. To determine the amount of compositional variation of Earth's building blocks, they used refined mass spectroscopy to analyze meteorites thought to be representative of the planetesimals that built Earth (*9*). According to the measurements, to explain the ^{142}Nd excess in the crust, up to 20% of Earth could have been removed by collision events during its formation. The authors point out that this collisional erosion would also remove other rare earth elements that tend to accumulate in the crust. This would provide an explanation for other mysteries, such as the apparent lack of uranium, potassium, and thorium in Earth's crust.

There are clues that Earth is not alone in suffering collisional compositional modification. For instance, within the Solar System, a single large collision is, at present, the favored explanation for the lack of a crust and mantle on Mercury (*10*). Looking beyond the Solar System, giant impacts may also be responsible for the high mass density of some exoplanets, such as GJ 376 (*11*) and Kepler-107c (*12*). Although the findings of Frossard *et al.* do not directly explain why Earth is perhaps distinctive in its ability to support life, it highlights the rich diversity among rocky planets and how little is known about the events that shape them. ■

REFERENCES AND NOTES

1. P. Frossard, C. Israel, A. Bouvier, M. Boyet, *Science* **377**, 1529 (2022).
2. E. Kokubo, S. Ida, *Astrophys. J.* **581**, 666 (2002).
3. P. Carter, Z. M. Leinhardt, T. Elliott, M. J. Walter, S. T. Stewart, *Astrophys. J.* **813**, 72 (2015).
4. M. Ćuk, S. T. Stewart, *Science* **338**, 1047 (2012).
5. R. M. Canup, *Science* **307**, 546 (2005).
6. Z. Rogoszinski, D. Hamilton, *PSJ* **2**, 78 (2021).
7. P. Carter, Z. M. Leinhardt, T. Elliott, S. T. Stewart, M. J. Walter, *Earth Planet. Sci. Lett.* **484**, 276 (2018).
8. M. Boyet, R. W. Carlson, *Science* **309**, 576 (2005).
9. M. Garçon *et al.*, *Chem. Geol.* **476**, 493 (2018).
10. A. Chau, C. Reinhardt, R. Helled, J. Stadel, *Astrophys. J.* **865**, 35 (2018).
11. K. W. F. Lam *et al.*, *Science* **374**, 1271 (2021).
12. A. Bonomo *et al.*, *Nat. Astron.* **3**, 416 (2019).

10.1126/science.add3199

POLICY FORUM

DIVERSITY

A framework for sex, gender, and diversity analysis in research

Funding agencies have ample room to improve their policies

By **Lilian Hunt[1], Mathias Wullum Nielsen[2], Londa Schiebinger[3,4]**

National research agencies are responsible for promoting excellent research that benefits all of society (*1*). Integrating sex, gender, and diversity analysis (SG&DA) into the design of research, where relevant, can improve research methodology, enhance excellence in science, and make research more responsive to social needs (*2*). National funding agencies—encouraged by scientists and social movements—have thus begun to implement policies to integrate sex, gender, and, more recently, diversity analysis into the grant proposal process, where these factors have been shown to play a role. We develop a five-part analytical framework for implementing and evaluating SG&DA policies, and use it to evaluate the quality of SG&DA policies for 22 major national funding agencies across six continents. By collecting emerging global practices for policy implementation, we seek to improve understanding of these policies and practices in efforts to enhance international collaborations and research excellence.

SG&DA is highly developed in health and biomedicine, machine learning, and artificial intelligence, and is emerging in other fields. Incorporating SG&DA into research design has enabled advancements across numerous disciplines. For example, research on pain documents both biological aspects (i.e., sex differences in electrical, ischemic, thermal, pressure, and muscle pain sensitivity) and cultural aspects (differences in how people report pain and how physicians understand and treat pain). Consensus analyses now include sex-based analysis in nonhuman animal and human preclinical and clinical research, gender-based analysis in patient–physician relationships and, more recently, analysis of different racialized groups and ethnicities in clinical treatment (*3*, *4*).

SG&DA informs each phase of the research process—from establishing project objectives (e.g., considering the characteristics of target populations and the social implications of the project), to developing methodologies (e.g., ensuring appropriate and unbiased measures and instruments), gathering data (e.g., sampling sufficient participant numbers across categories), analyzing data (e.g., considering within- and between-group differences and intersecting factors) to reporting results (e.g., considering language use and specifying how categorical data were collected and annotated) (*5*).

There are three pillars of the science infrastructure that need to coordinate policies to achieve excellence in science (*2*). The first, funding agencies, encourage integrating SG&DA at the beginning of the research process. In 2003, the European Commission (EC) endorsed "questioning systematically whether, and in what sense, sex and gender are relevant in the objectives and methodology of projects." Other public-funding agencies followed suit with policies implemented at the Canadian Institutes of Health Research (CIHR; 2010), German Research Foundation (DFG; 2020), and National Research Foundation of Korea (NRF; 2021), among others (*6*).

Pillar two, peer-reviewed journals, increasingly consider SG&DA when selecting manuscripts for publication (*7*). Pillar three, universities and research institutions, are responsible for developing methods for this type of analysis and for providing this expertise to future generations. Many faculties of science, medicine, and engineering have not yet integrated knowledge of SG&DA into their core curricula; hence, many researchers and research evaluators lack training in these types of analyses, and new guidance is needed to improve this.

This study focuses on funding agencies and develops an analytical framework to evaluate the uptake of policies for integrating sex, gender, and diversity—which covers intersectional characteristics such as age or life course, indigeneity, race and ethnicity, sexuality, socioeconomic status, and other axes of inequality—into research design. Previous studies have analyzed single funding agencies in depth (*1*, *8*–*9*) or focused narrowly on particular regions such as sub-Saharan Africa, or more often Europe and North America (*10*, *11*). One international study included questions on SG&DA policies in their larger survey focused on gender equity in research teams (*12*). Ours is the first to develop a cross-disciplinary analytical framework for policy development and to apply it globally.

DEVELOPING THE POLICY FRAMEWORK

We conducted an investigation in three stages: (i) document analysis, (ii) global survey, and (iii) policy analysis. Based on a documented analysis of SG&DA-related policies and guidelines and prior research (*6*), we developed our analytical framework, a five-part guide for implementing and evaluating SG&DA policy (see the box) (for a full outline of the development process, see supplementary materials (SM) S1). We convened an international advisory group that included representatives from public funders, expert researchers, and policy specialists from five global areas—Africa and the Middle East, Europe and Central Asia, Latin America and the Caribbean, North America, and South and East Asia and the Pacific—to discuss and improve the framework's clarity, specificity, applicability, and global representativeness (SM S2).

We tested the applicability of our framework for evaluating SG&DA policies through a pilot survey targeting six large public funding agencies in Europe, East Asia, and North America—the CIHR, DFG, EC, Irish Research Council, US National Institutes of Health (NIH), and NRF Korea—four of which had representation on our advisory board. The survey was designed to collect all relevant information on SG&DA-related activities done by the agencies. Evidence consisted of publicly available policies and guidance documents, and, where agencies were in the process of developing policy, internal documents. We checked all self-reported responses against agency documents. The pilot study confirmed the applicability of our evaluation tool and also led to minor revisions in item phrasing.

For the global evaluation, we consulted with our advisory board to select 39 ad-

[1]Equality, Diversity and Inclusion in Science and Health (EDIS), Culture, Equity, Diversity, and Inclusion, Wellcome Trust, London, UK. [2]Department of Sociology, University of Copenhagen, Copenhagen, Denmark. [3]History of Science, Stanford University, Stanford, CA, USA. [4]Gendered Innovations in Science, Health and Medicine, Engineering, and Environment, Stanford, CA, USA. Email: schiebinger@stanford.edu

ditional funding agencies based on geographic spread with the goal of covering agencies from all continents that host such agencies (SM S4). We focused on public agencies as these are typically the largest, most prestigious, and agenda-setting funders at the national level. Of the 39 invited, 16 agreed, yielding a final sample of 22 (SM S5).

Response rates differed across regions. In North America, all 5 invited agencies participated; in Europe and Central Asia, 9 of 14 agencies responded; in Latin America and the Caribbean, 2 of 3 agencies responded; in South and East Asia and the Pacific, 4 of 7 agencies responded; and in Africa and the Middle East, only 3 of the 11 invited responded (table S1).

As part of our participatory design, funders were invited to complete an online questionnaire (SM S8 to S11) and asked to provide evidence (either publicly available or internally agreed upon) for each answer. Each agency was scored on their performance across the five parts of the policy framework by at least two evaluators using a scoring matrix (SM S6 and S12) vetted by the advisory board. The scores of individual funding agencies are kept confidential per agreement.

Overall, one agency scored in the first tier (81+ points out of 100) in SG&DA policies and measures; six agencies scored in the second tier (61 to 80 points), five in the third tier (41 to 60 points), two in the fourth tier (21 to 40 points), and nine are just beginning (0 to 20 points) (see the figure). Globally, almost half of agencies (9 of 22) provided definitions of terms of reasonable quality (first and second tiers) (see the figure) (table S2). Similarly, almost half of agencies (9 of 22) provided quality proposal guidelines for applicants. Only about a third of agencies (7 of 22) provided quality instructions to evaluations, and even fewer (5 of 22) provided quality trainings for applicants, evaluators, and staff. Evaluation of policy implementation was the weakest, with only two agencies scoring in the second tier and none in the first. Many agencies have begun implementing policy, but most have not considered evaluation. It is important that agencies plan to evaluate policies from the very beginning.

One complicating factor in comparing agencies is that some agencies span all fields of the human and natural sciences, technology, and health and biomedicine, whereas others are more specialized. When we divided our data by agency type, however, we found no pronounced differences, suggesting that funders with wide remits can successfully implement these policies (fig. S1).

Each component of our five-part framework process for policy development is important to the success of policy implementation. A simple policy mandate to include SG&DA in research is itself not enough, and, when poorly executed, SG&DA can lead to harm (*13*). Further, funding agency policies are but one part of behavioral and cultural shifts in the research endeavor and need to be supported by coordinated change across the broader science infrastructure.

A framework to implement and evaluate policies

The framework covers five aspects of public funding agencies' efforts to promote sex, gender, and diversity analysis (SG&DA).

Definition of terms
- Clear and quality definitions
- Definitions readily available

Proposal guidelines for applicants
- Instructions to applicants to include SG&DA
- Encourage or require?
- Examples given
- Specify how SG&DA is included at each stage of the research cycle—detail for yes and justify for no

Instructions for evaluators
- Instructions for reviewers to include SG&DA in their evaluations
- Assessment at each stage of the research process
- Monitoring

Trainings for applicants, evaluators, and staff
- Training, resources, and support available for applicants
- Training, resources, and support available for proposal evaluators
- Training, resources, and support available for relevant agency staff
- Training mandatory through certification
- Development of open access resources: courses and high-quality materials

Evaluation of policy implementation
- Number and proportion of proposals that include SG&DA
- Number and proportion of proposals that include quality SG&DA
- Quality of evaluators' scoring & comments
- Number of applicants, evaluators, & staff who engaged in training
- Number and proportion of publications from funded proposals that include SG&DA

EMERGING GLOBAL PRACTICES

Each agency will develop country-specific policies that accommodate their cultural practices and regulatory landscapes. At the same time, agencies can share policies and practices to enhance research collaboration across regions. Here we explore key considerations for each part of our policy framework and track emerging policies. These considerations are drawn from agencies' responses to our questionnaire (SM S7).

Overall, we found differences across countries as to where these policies sit within agencies, how they are implemented, and where accountability for them lies. Most funders in our study—for example, the DFG and EC—include SG&DA under their "excellence" criteria; i.e., SG&DA is judged in relation to its potential to create new knowledge. CIHR, for example, found that once their SG&DA policy was established, applicants who scored well on the SG&DA question scored well overall, i.e., SG&DA improved the overall quality of the proposal, and the proposal was more likely to be funded (*9*).

Definition of terms

The first step in policy development is definition of terms (see the box). It is important that the same definitions are shared with applicants, evaluators, and staff to support consistency across the agency. For example, the Canadian Tri-Agency provides guidance in both English and French describing Gender-Based Analysis Plus (GBA+) that links across agency materials (all references to policy documents are available in table S3). Which terms and how they are defined will be country specific. For "diversity," for example, each agency will determine which factors to prioritize and for which funding areas. Some agencies, such as those in Australia, synchronize their guidelines with those set through national legislation. [See (*14*) for example definitions of key terms, and links between agency policies and this five-part framework.]

We chose to evaluate agencies on "sex" and "gender" analysis because sex and gender were historically the categories included in agency policy—for example, by the EC. Although sex is a biological characteristic of humans and numerous nonhuman organisms and is an important category to continue to call out, gender is at the same epistemic level as other aspects of sociocultural diversity and may, in the future, be folded into diversity analysis. We included both gender and diversity to allow us to evaluate developed and emerging policy practices. Second, we considered evaluating on "intersectional" analysis but, after policy reviews and consultation with our advisory board, judged "diversity" a more generally used term.

Proposal guidelines for applicants

Agencies take three basic approaches in their request to applicants to integrate SG&DA into their proposal, where relevant:

Most encourage applicants to integrate SG&DA; a few require this type of analysis; some only encourage applicants but instruct evaluators to score this element. In this study, more points were awarded to funders who required SG&DA; however, more research is needed to determine the differential impact of these various approaches. In all cases, the "where relevant" is crucial. No agency asks for SG&DA in pure mathematics, for example, where no body of literature has established its relevance.

The trajectory of the EC is of interest. Since 2003, the Commission has encouraged sex and gender analysis, referred to as the "gender dimension," in research. To strengthen the policy, in 2014, Horizon 2020 flagged topics for which taking the gender dimension into account was mandatory. Since 2021, Horizon Europe has required all proposals to consider sex, gender, and/or intersectional analysis in research, unless otherwise specified.

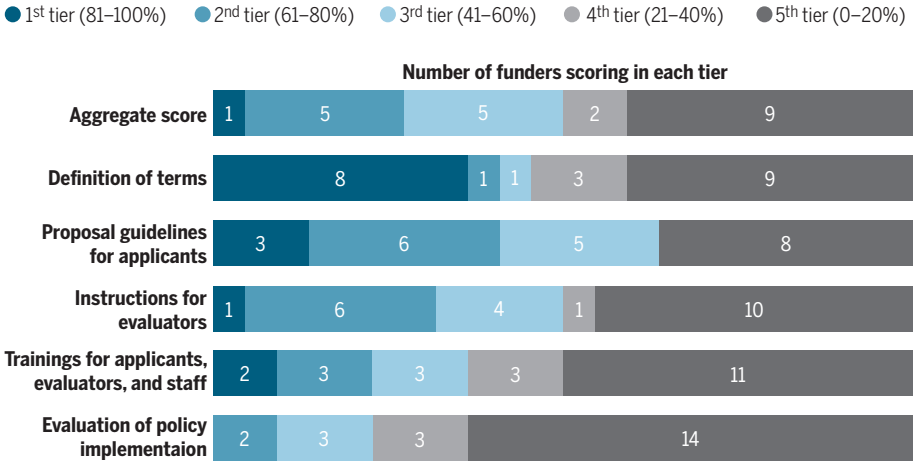
The US NIH has, since 2016, required all applicants to consider "sex as a biological variable" (SABV) and has detailed how this type of analysis supports excellence in science (*1*). This requirement supplements policies for inclusion of sex and gender, race, and ethnicity in clinical trials launched in the 1990s and inclusion of age (Inclusion Across the Lifespan) added in 2019.

The DFG implemented its SG&DA guidelines in 2020 after a 2-year study period. The DFG encourages but does not require applicants to consider SG&DA, emphasizing that it funds "proposals in curiosity-driven basic research" in fields selected by applicants where freedom of research is core. In so doing, the DFG taps into the issue of academic freedom, where principal investigators set their own research agendas. Notably, SG&DA is one methodological tool among many that researchers may employ. Like any other methodology, appropriate application is key to research outcomes. It is the job of researchers and research evaluators to determine when SG&DA may enhance research outcomes. Interestingly, the DFG requires research evaluators to take SG&DA into account, making SG&DA analysis de facto required if relevant to research outcomes.

In many countries, agency policy is governed by national legislation. In Japan, where the government renews the basic plans for Science, Technology, and Innovation (STI) every 5 years, the sixth STI Basic Plan in 2021 included integrating the gender perspective and gender analysis into research and technology development. Similarly, in 2021, the Republic of Korea passed an amendment of the Framework Act on Science and Technology to include integrating sex and gender into research, which allowed the NRF Korea to develop new policies.

Agencies' performance on the policy framework

Using a scoring matrix (see supplementary materials), funding agencies were awarded points reflective of their performance on each of five parts of the sex, gender, and diversity analysis (SG&DA) policy framework (bottom five bars). Those five component-level scores were aggregated into an overall score (top bar). For each component and the aggregate, agencies were assigned to five tiers based on the percentage of the total possible points that they received for that component or aggregate. Bars reflect the number of agencies (out of 22 in total) whose scores fall within a given tier for that component or aggregate.



GRAPHIC: N. CARY/*SCIENCE*

In our study, we evaluated whether applicants are instructed to detail how SG&DA analysis is incorporated into all phases of research. If SG&DA is not relevant to the proposed research, applicants should be asked to provide literature to demonstrate that no sex, gender, or relevant diversity differences have been found.

Instructions for evaluators

Evaluators are crucial to the success of SG&DA policies. CIHR found that "targeting applicants alone to adopt new science policies without concomitant pressure by evaluators…may not be effective" (*9*). Since 2018, CIHR has required evaluators to rate the quality of the SG&DA as a "strength," "weakness," or "not applicable" and to provide a rationale for their rating along with recommendations to applicants for improvement.

Funders should provide applicants and evaluators similar forms and instructions for consistency across the research process. Some agencies, such as the EC, are limited in the overall instructions they can provide on this particular requirement given the number of topics that need to be covered. Agencies may provide "good research guides" that reference assessing SG&DA alongside other elements of peer review, such as ethics and reproducibility.

Agencies must monitor the evaluation process to confirm that SG&DA is addressed in reviewer comments and that those comments are high quality.

Trainings for applicants, evaluators, and staff

SG&DA is not yet consistently part of university curricula in the physical and life sciences, health and biomedicine, and engineering. Until universities step up to the task, funding agencies need to fill this gap. The most comprehensive online, interactive agency trainings to date are in health and biomedicine. Trainings are also available for certain areas of the natural sciences, engineering, computer science, and environmental sciences, but more are needed. Agencies can evaluate the effectiveness of the training by including a pre-test and a post-test. CIHR, for example, found that the majority of participants who completed training modules demonstrated improved knowledge of sex and gender analysis (*15*). Most trainings are voluntary; however, some funders require applicants to submit a certificate of completion for large, strategic competitions.

Use of the same training materials by applicants, evaluators, and agency staff helps to ensure consistency in policies, terminology, and expectations. Agencies can coordinate and share trainings internationally; there is no need to duplicate efforts, except where specific cultural practices require a particular approach.

Some agencies foster training in this area through research institutions. The US NIH, for example, has invested $160 million in

Specialized Centers of Research Excellence across 25 research institutions to "train researchers in experimental design and analyses that consider sex and/or gender" (*1*).

Evaluation of policy implementation

Only three agencies in our study had performed policy implementation evaluations. A further nine were in the planning stages; 10 had no plans in place. We strongly recommend that agencies implement evaluation plans as they develop policies to facilitate appropriate quantitative and qualitative evaluation.

Our framework sets out five aspects for the evaluation of policy implementation:

1) The number and proportion of proposals that include SG&DA. CIHR found that from 2011 to 2019, the proportion of grants including sex analysis increased from 22 to 83% and grants including gender analysis from 12 to 33%. The level of integration differed across sectors, with the lowest in biomedical and the highest in clinical research (*8*).

2) The number and proportion of proposals that include quality SG&DA. The EC conducted a mid-term evaluation of sex and gender analysis for Horizon 2020 in 2017 to consider the proposal quality, methods, impacts, dissemination, and also whether the project advanced methodology for sex and gender analysis in the particular field in which the proposal was submitted. Overall, the EC concluded that the quality of the gender dimension in project proposals was not high and that more training was needed (*9*). The EC also experimented with computer-assisted textual analysis given the volume of applications per year. These evaluation methods are in their infancy and require further development.

3) The quality of evaluators' scoring and comments. This aspect emerged as a central point in the analysis of agencies' self-reported activities. We did not score funders on this point but will in future iterations. CIHR manually sampled 5% of evaluators' comments to check the quality of responses (*9*). The EC reviewed the effectiveness of review panels and found that only 36% considered the gender dimension and, of those, 70% included a gender expert, suggesting that review panels require guidance from experts (*8*).

4) The number of applicants, evaluators, and staff who engaged in trainings and in what type of training. If possible, the correlation between applicant training and the success of applicant proposals should be assessed. Some funders, such as the Spanish Carlos III Health Institute, reported in our questionnaire that they monitor the number of applicants who participate in SG&DA training and are setting targets for improvement.

5) The number and proportion of peer-reviewed publications (or other recognized modes of dissemination) that result from funded proposals that incorporated SG&DA. To monitor this, funders will need to track papers and research outputs using grant numbers. The Science Foundation Ireland reported in our study that they collect researcher-reported publication data to check that proposals that included sex and/or gender analysis reported those results in publications.

A trend that we continue to watch is the broadening of sex and gender analysis to include other social dimensions. Already, the EC has added "intersectional" analysis to their gender dimension; these policies, however, remain under the broader gender equality strategy. The DFG started with sex, gender, and "diversity" on equal terms. The US NIH has included "age," which they term "Inclusion Across the Lifespan." A number of funding agencies, such as the Natural Sciences and Engineering Research Council of Canada, incorporate research design policies under a broader equity, diversity, and inclusion (EDI) umbrella. In the past, EDI has typically focused on "who" is doing the research, not on "how" research is done. This means that special care will be needed to expand EDI to include research methodologies.

FUTURE FRAMEWORK DEVELOPMENT

Our evaluation of SG&DA policy implementation has some limitations that restrict its generalizability. First, our coverage of public funding agencies, though geographically comprehensive, is not exhaustive. Participation rates were especially low for agencies in Africa and the Middle East, and we were unable to establish contacts with funding agencies in Russia and China. Second, we excluded private funders in this first round. Future studies might consider large international private funders, such as the Bill and Melinda Gates Foundation, Novo Nordisk Foundation, Oswaldo Cruz Foundation, and Wellcome Trust. Third, we might add elements to each of the five parts of our framework. For example, are applications that include SG&DA funded at rates and amounts comparable to those of other similar projects? Fourth, policies that encourage scientists to change their practices can spur resistance. Future frameworks might include assessing how funding agencies deal with such resistance. Finally, our study details how well and how consistently SG&DA policies are implemented, but further quantitative and qualitative analysis is needed to correlate the framework's scoring with the impact of agency policies on research outputs. Current funder evaluation policies do not support this type of analysis.

CONCLUSION

National public funding agencies seek different ways to support the progress of science and technology and advance health, prosperity, and well-being by promoting discovery and innovation, excellence, and societal relevance in research. SG&DA is one set of methods among many that researchers will deploy to help achieve these goals. Funding agencies are rapidly developing policies to promote SG&DA. The goal of our work is to assist in collaboratively achieving efficient implementations of SG&DA-related funding policies globally. ■

REFERENCES AND NOTES

1. M. E. Arnegard, L. A. Whitten, C. Hunter, J. A. Clayton, *J. Womens Health* **29**, 858 (2020).
2. C. Tannenbaum, R. P. Ellis, F. Eyssel, J. Zou, L. Schiebinger, *Nature* **575**, 137 (2019).
3. K. E. Boerner *et al*., *Pain* **159**, 2137 (2018).
4. M. R. Janevic *et al*., *J. Pain* **23**, 707 (2022).
5. L. Schiebinger *et al*., "Methods of sex, gender, and intersectional analysis," Gendered Innovations; http://genderedinnovations.stanford.edu/methods-sex-and-gender-analysis.html.
6. L. Schiebinger *et al*., "Sex and gender analysis policies of major granting agencies," Gendered Innovations; http://genderedinnovations.stanford.edu/sex-and-gender-analysis-policies-major-granting-agencies_8_6_21.html.
7. R. Merriman *et al*., *BMJ Glob. Health* **6**, e005672 (2021).
8. Directorate-General for Research and Innovation (European Commission), "Interim evaluation: gender equality as a crosscutting issue in Horizon 2020" (Publications Office of the European Union, Luxembourg, 2017).
9. J. Haverfield, C. Tannenbaum, *Health Res. Policy Syst.* **19**, 94 1 (2021).
10. J. C. Jackson, J. G. Payumo, A. J. Jamison, M. L. Conteh, P. Chirawu, *Front. Res. Metr. Anal.* **7**, 814600 (2022).
11. S. Y. Håkansson, J. Sand, "The gender dimension in research and innovation: Results from a global survey on research funding organisations" (Swedish Secretariat for Gender Research University of Gothenburg, Gothenburg, 2021).
12. GRC Gender Working Group, "Gender-disaggregated data at the participating organisations of the global research council: Results of a global survey" (Global Research Council, 2021).
13. J. W. Rich-Edwards, U. B. Kaiser, G. L. Chen, J. E. Manson, J. M. Goldstein, *Endocr. Rev.* **39**, 424 (2018).
14. L. Schiebinger *et al*., "Mapping emerging policy practices of public granting agencies," Gendered Innovations; http://genderedinnovations.stanford.edu/sex-and-gender-analysis-policies-major-granting-agencies.html.
15. C. Tannenbaum, K. van Hoof, *Biol. Sex Differ.* **9**, 1 (2018).

ACKNOWLEDGMENTS

We thank the members of our advisory board for their guidance and the participating funding agencies for their time.

SUPPLEMENTARY MATERIALS

science.org/doi/10.1126/science.abp9775

10.1126/science.abp9775



Visitors take in the Crystal Palace Dinosaurs, the first 3D models of prehistoric creatures.

PHOTO: CHRONICLE/ALAMY STOCK PHOTO

PALEONTOLOGY

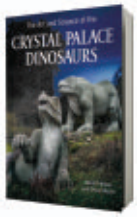
Revisiting the first dinosaur park

A once-ridiculed sculpture display is worth a second look

By **Ilja Nieuwland**

The Crystal Palace Dinosaurs—a series of life-size statues that rendered extinct prehistoric species three-dimensionally for the first time—made their public debut in 1854 on the grounds of the Crystal Palace in the London suburb of Sydenham. Despite its moniker, the 30-piece collection includes only four dinosaurs: two iguanodons, a megalosaurus, and a hylaeosaurus. Based on fragmentary fossil material, the models were later revealed to be wildly inaccurate, and the installation was widely ridiculed in the following decades. In recent years, however, the statues have experienced a reappraisal as historically important objects.

The story of the Crystal Palace Dinosaurs has been told, embellished, and retold to the point where mythology and facts start to merge. A new book, *The Art and Science of the Crystal Palace Dinosaurs*, seeks to set the record straight on these important reconstructions. Written by Mark Witton, a paleontologist and paleoartist at the University of Portsmouth, and Ellinor Michel, a conservator at London's Natural History Museum, it succeeds in compiling various narratives about the collection and critically comparing them with archival documentary evidence and physical analyses of the sculptures.



The Art and Science of the Crystal Palace Dinosaurs
Mark P. Witton and Ellinor Michel
The Crowood Press, 2022. 192 pp.

One oft-repeated myth surrounding the collection concerns the alleged close collaboration between Benjamin Waterhouse Hawkins, the sculptor who created the statues, and paleontologist Richard Owen, who was hired as a professional consultant on the project. As Witton and Michel demonstrate, Owen showed only very occasional interest in the project, and Waterhouse Hawkins should be considered the main, if not the sole, creator of the statues.

The book also examines other aspects of the exhibition, including its construction and preservation. The authors purposely de-emphasize the dinosaur sculptures, by far the most frequently discussed of the collection, a strategy likely meant to prevent the more famous denizens of the park from overwhelming the others.

Witton's interest in the Crystal Palace Dinosaurs is not coincidental; as a paleoartist, he is part of a movement that seeks to promote "greater originality and bolder speculation in paleoartworks" (*1*). As such, he is sympathetic to Waterhouse Hawkins's plight, noting that the artist had to extrapolate from fragmentary material and limited data.

Each of the installation's animal statues is subjected to an analysis of its conception, construction, reception, and preservation. The statues are also considered against contemporary reconstructions rendered by Witton. This serves to emphasize how fundamentally reconstructions have changed in some cases, such as the dinosaurs iguanodon and megalosaurus (chapter 7). In other cases, the differences are more superficial (e.g., Megatherium, chapter 4).

Although the book discusses the public reception of the exhibition, it tends to undersell the staging of the exhibits and its influence on the public. What it gets right, however, is its discussion of the connections between modern popular paleontology and that of the late 19th century. A prime example is the exhibition's accompanying merchandise, which included scale models of extinct animals. This practice is now ubiquitous in modern natural history museums.

The book's final chapter, which discusses the preservation of the Crystal Palace Dinosaurs, is perhaps the most urgent. Up until the end of the 20th century, the authors note, the models were subjected to "relatively callous treatment," resulting in substantial damage, and by the time the collection achieved heritage status in 1973, seven statues had vanished. Meanwhile, the condition of the remaining statues continues to deteriorate as a result of vandalism, weeds, moisture, and a general lack of preservation. The authors argue passionately for greater investment in this consequential collection, pledging to donate the proceeds of this book to a charity dedicated to their conservation and interpretation. ■

The reviewer is at the Huygens Institute, Royal Netherlands Academy of Arts and Sciences, Amsterdam, Netherlands. Email: ilja.nieuwland@huygens.knaw.nl

REFERENCES AND NOTES

1. I. Nieuwland, *Science* **369**, 148 (2020).

10.1126/science.ade4444

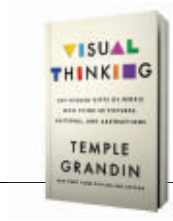
PSYCHOLOGY

Spatial thinkers receive their due

An insider's guide to visual reasoning celebrates those who think in pictures and patterns

By **Jonathan Wai**

Visual Thinking: The Hidden Gifts of People Who Think in Pictures, Patterns, and Abstractions
Temple Grandin
Riverhead, 2022. 352 pp.



How we come to see the world can sometimes prevent us from seeing it in other ways. This idea is at the heart of Temple Grandin's new book, *Visual Thinking*, in which she explains how she sees the world. Leading readers through a dizzying array of scientific and other literature, she argues that we are not identifying and developing the talents of those who are visual thinkers ("people who think in pictures and patterns"), giving preference instead to verbal thinkers ("people who think in words"), and this has consequences for many areas of society. This idea is supported by a long history of research on spatial reasoning and spatial thinking (*1*–*4*). She notes that her inspiration for *Visual Thinking* came from Thomas West's influential 1990 treatise *In the Mind's Eye*, which profiled some of the most notable visual thinkers in history and connected visual thinking with neurodiversity (*5*).

Grandin discusses a wide array of visual thinking engineers and inventors, including famous examples such as Thomas Edison (a lifelong hero of hers), as well as builders and innovators she has met in her work. She writes, for example, about a man with dyslexia who reports that he was saved by a welding class in high school. He now owns a metal fabrication company, has multiple patents, and can build just about anything without needing to sketch out designs in advance.

A core theme that threads the book's chapters is how diverse perspectives are useful for scientific and societal problem-solving and how people with different talents are often necessary for seeing a problem's various facets. Here, she describes the accomplishments of American inventors Russell and Sigurd Varian. Russell's theoretical and technical knowledge complemented Sigurd's mechanical skill, allowing the brothers to pioneer microwave and radiation therapy devices. The key, she argues, is to ensure that there is mutual respect for different viewpoints, which improves productive communication in teams.

The reviewer is at the Department of Education Reform and Department of Psychology, University of Arkansas, Fayetteville, AR 72701, USA. Email: jwai@uark.edu

The book also reviews research on genius and neurodiversity and offers an update on how Grandin's thinking has evolved regarding the importance of understanding and appreciating animal consciousness. She argues here that animal thinking and sensing are largely visual and that this shared perspective helps her forge deep connections with them.

In chapter 6, Grandin provides an incredible look into how visual thinkers, and specifically those she calls "object thinkers"—individuals like herself who conceive of the world through photorealistic images—are able to visualize systems and troubleshoot an array of problems, ranging from those that emerge on mechanical assembly lines and during plane flight disasters to those that arise from decaying building infrastructure and precede bridge collapse. Here she describes how the James Webb telescope was delayed, in part, because of poor workmanship. When subjected to a shake test, bolts and fasteners fell off. She argues that a good object visualizer could have predicted this and designed more appropriate fasteners.

Building on Grandin's rich examples and emphasis on helping visual thinkers, especially those who are neurodiverse, it is important to consider ways we might help spatially talented students in K–12 schools, where roughly 2 to 3 million have talents that go relatively underdeveloped by curriculum that emphasizes mathematical and verbal reasoning over spatial and visual thinking (*2*, *4*, *6*). Such individuals could fill the ranks of the hands-on occupational needs that Grandin highlights throughout her book.

Despite its strengths, the book misses the opportunity to connect to the broader literature on spatial reasoning [e.g., (*1*–*4*, *6*)], and almost everything is filtered through the particular way that Grandin sees the world. Grandin's writing is rich in description, however, and I could almost fully imagine many of the things she set out to explain, even if my capacity to do so as a primarily verbal thinker was limited.

All of us could benefit from realizing that we need different kinds of minds to solve society's biggest problems. Hopefully this book will inspire readers to look at the world in different ways so that we might better recognize the many assets each of us brings to the table. ■

REFERENCES AND NOTES

1. I. M. Smith, *Spatial Ability* (Univ. of London Press, 1964).
2. N. S. Newcombe, *Am. Educ.* **34**, 29 (2010).
3. D. E. Super, P. B. Bachrach, *Scientific Careers and Vocational Development Theory* (Bureau of Publications, Teachers College, Columbia Univ., 1957).
4. D. Lubinski, *Pers. Individ. Dif.* **49**, 344 (2010).
5. T. G. West, *In the Mind's Eye* (Prometheus Books, 1997).
6. J. M. Lakin, J. Wai, *Br. J. Educ. Psychol.* **90**, 1015 (2020).

10.1126/science.ade5504

SCIENCE & FOOD



PHOTO: FOODFOLIO/ALAMY STOCK PHOTO

Black-eyed peas appear in many cuisines in the African diaspora.

PODCAST

High on the Hog: A Culinary Journey from Africa to America
Jessica B. Harris
Bloomsbury, 2011. 304 pp.

Understanding how and why crops, cuisines, and cooking practices spread around the world is a topic of interest to anthropologists and agricultural scientists alike. This week on the *Science* podcast, Jessica Harris explores the food practices of the African diaspora, offering insight into the roles played by the transatlantic slave trade, a discussion of power and reclaiming history, and lessons in food sustainability. https://bit.ly/3LmnOut

10.1126/science.ade8448



LETTERS

Edited by **Jennifer Sills**

Heat waves fuel fires on monoculture plantations

This summer, Europe broke high temperature records across the continent (*1*) and experienced the largest widespread drought in 500 years (*2*). The extreme climatic conditions contributed to an increased number and extent of forest fires across Europe (*3*). Large forest fires are boosted not only by warmer and dryer conditions but also by the type and state of the vegetation (i.e., fuel models) (*4*). Many recent forest fires worldwide have been fueled by large areas of evergreen monoculture plantations, such as *Eucalyptus spp*. in Chile and Portugal in 2017 (*5*) and *Pinus spp*. in France this past summer (*6*). Given increasing temperatures and fire risks, the traditional practices for evergreen tree plantations are no longer a responsible forest management strategy.

Evergreen trees have been shown to serve as efficient fuel for fires. Specific plant traits, such as essential oils or enhanced terpene content in *Eucalyptus spp*. and *Pinus spp*. leaves, respectively, increase the trees' flammability (canopy ignition and the subsequent resprout or seed release help the species to outcompete others) (*7*). The higher evapotranspiration rates of evergreens compared with native forests translate to lower soil humidity and dryer conditions (*8*). In addition, monoculture plantations often suffer from poor or nonexistent design and forest management, which translates into high tree densities, species homogeneity, and increased continuity of fuel loads (*9*).

Evergreen monoculture plantations have increased worldwide over the past two centuries (*10*). In many cases, they are the selected species for large-scale reforestation for erosion control, carbon sequestration, or restoration of burned areas. Current environmental policies continue to favor these strategic responses, so additional monoculture plantations are likely [e.g., (*11*)]. However, given the fire risks they pose and the increasing probabilities of heatwaves, the lack of innovative design and management strategies for these evergreen monocultures is creating the perfect conditions for larger and more devastating forest fires worldwide.

Scientists, public administrations, and the forestry industry must reconsider tree planting design, strategies, and management actions when dealing with evergreen monoculture plantations. Otherwise, we might be just casting more wood on the bonfire.

J. Barquín*, L. Concostrina-Zubiri, I. Pérez-Silos, G. Hernández-Romero, A. Vélez-Martín, J. M. Álvarez-Martínez
IHCantabria–Instituto de Hidráulica Ambiental de la Universidad de Cantabria, 39011 Santander, Spain.
*Corresponding author. Email: barquinj@unican.es

REFERENCES AND NOTES

1. A. Fowle, "Weather tracker: Record-breaking heat continues to scorch western Europe," *The Guardian* (2022).
2. "Europe's drought the worst in 500 years—report,' BBC (2022).
3. European Forest Fire Information System, "EFFIS Estimates for EU Countries" (2022); https://effis.jrc.ec.europa.eu/apps/effis.statistics/estimates.
4. D. M. J. S. Bowman *et al*., *Science* **324**, 481 (2009).
5. S. Gómez-González, F. Ojeda, P. M. Fernandes, *Environ. Sci. Pol.* **81**, 104 (2018).
6. European Commission, Copernicus, "EMSR619: Forest fires in South West, Gironde and Landes, France" (2022); https://emergency.copernicus.eu/mapping/list-of-components/EMSR619.
7. J. G. Pausas, J. E. Keeley, D. W. Schwilk, *J. Ecol*. **105**, 289 (2017).
8. J. A. Rodriguez Suarez, F. Diaz-Fierros, R. Perez, B. Soto, *Hydrology* **22**, 5561 (2014).
9. M. P. North *et al*., *For. Ecol. Manag*. **432**, 15 (2019).
10. T. K. Rudel *et al*., *Ambio* **49**, 74 (2020).
11. European Commission, "European Green Deal: Commission proposes new strategy to protect and restore EU forests" (2021); www.ec.europa.eu/commission/presscorner/detail/en/ip_21_3723.

10.1126/science.ade5923

A low-carbon future for China's tech industry

The information and communications technology (ICT) industry, which includes telephone and computer networks and devices, has the potential to reduce emissions and increase efficiency in other industries by using internet platforms to connect equipment, production lines, factories, suppliers, products, and customers

PHOTO: BENOIT TESSIER/POOL/AFP VIA GETTY IMAGES



In these maritime pine (*Pinus pinaster*) plantations in southwest France, older trees have withstood fire better than younger trees, indicating that tree age and management practices could affect flammability.

(*1*). The ICT industry is expected to help reduce global carbon emissions by 20% by 2030 (*2*). However, the industry's own carbon emissions could undermine its positive contributions. Although carbon emissions produced by the ICT industry accounted for only about 1% of total global carbon emissions in 2007, without interventions, the number could reach 14% by 2040 (*3*). In China, where the ICT industry is growing rapidly (*4*), the government must ensure an environmentally responsible transition.

In August, to accelerate the low-carbon transformation of the ICT industry, the Chinese government issued the Action Plan for Green and Low-Carbon Development in the Information and Communication Industry (2022–2025), which puts forward a series of targets (*5*). For example, the plan proposes that China's 5G operators increase the network infrastructure (such as fiber optic cables, ducts, and towers) that they share from 58.9% in 2021 (*6*) to no less than 80% in 2025. This goal will help to prevent redundant construction by multiple companies. The plan also provides efficiency targets for data centers, which currently consume large amounts of energy for cooling and lighting.

To meet the proposed targets, China must make strategic decisions about the ICT industry's growth. To improve the energy efficiency of ICT infrastructure and reduce carbon emissions from duplicate construction, the country should continue to promote the sharing of an appropriate number of large data centers, communication base stations for wireless equipment, and communication equipment rooms. In addition, China should ensure that the ICT industry's supply chain uses low-carbon technology. Suppliers should be encouraged to adopt efficient technologies, such as intelligent temperature controls, and to use Internet of Things technology to automate and digitally manage the production and transportation of equipment. All steps in the supply chain should use clean energy, including biomass (*7*), as much as possible. Finally, the ICT industry should take advantage of the possibilities it offers to other industries. For example, ICT enterprises should embrace online meetings and telehealth visits.

Addressing climate change requires broad global participation and joint action. China has become one of the world's leading countries in information technology (*8*). Developing its ICT industry with intention, and supporting other developing countries facing similar ICT challenges, can lay a solid foundation for achieving national and global emission reduction targets.

Ke He[1,2], Fanlue Li[1], Hao Wang[1], Ruoyu Ming[1], Junbiao Zhang[3]*
[1]College of Economics & Management, Huazhong Agricultural University, Wuhan, Hubei 430070, China. [2]School of Agricultural Economics and Rural Development, Renmin University of China, Beijing 100872, China. [3]Laboratory of Green and Low-carbon Development in Agriculture, Huazhong Agricultural University, Wuhan 430070, China.
*Corresponding author.
Email: zhangjb513@126.com

REFERENCES AND NOTES

1. Y. Wang *et al.*, *Renew. Sust. Energ. Rev.* **160**, 112344 (2022).
2. GeSI, "#SMARTER2030 ICT solutions for 21st century challenges" (2015); www.gesi.org/research/smarter2030-ict-solutions-for-21st-century-challenges.
3. Greenpeace, "Towards carbon neutrality: China's internet technology industry roadmap to 100% renewable energy" (2022); www.greenpeace.org.cn/2021/01/12/pr-china-internet-tech-carbon-neutral/ [in Chinese].
4. H. Sun *et al.*, *Technol. Soc.* **66**, 101661 (2021).
5. Ministry of Industry and Information Technology of the People's Republic of China, "Action plan for green and low-carbon development in the information and communication industry (2022–2025)" (2022); www.miit.gov.cn/jgsj/txs/wjfb/art/2022/art_f843aa7e249445bbbf3e6796f6ab7236.html [in Chinese].
6. Ministry of Industry and Information Technology of the People's Republic of China, "Interpretation of the statistical bulletin of the communications industry in 2021" (2022); www.miit.gov.cn/jgsj/yxj/xxfb/art/2022/art_b6578e7993bf4c999b28e88b53037044.html [in Chinese].
7. K. He, in *Ecological Compensation for Agricultural Wastes Recycling* (People's Publishing House, Beijing, 2019), pp. 83–88 [in Chinese].
8. Y. Huang *et al.*, *Rev. Dev. Econ.* **26**, 510 (2022).

10.1126/science.ade7583

Standards needed for antibiotics in water

Antibiotics are frequently used to treat or prevent bacterial infections in humans, animals, and crops. Later, the drugs end up in the environment, particularly the water supply, through wastewater, excrement, or groundwater. Because testing for antibiotics in drinking water (even bottled water) is rare, people consume them unknowingly (*1*). Extensive human exposure to low-dose antibiotics can lead to decreased response to antibiotics when they are needed (*2*), and antimicrobial resistance is growing (*3*). Therefore, governments worldwide should work to identify, prevent, and remediate antibiotic contamination of water sources (*4*).

Antibiotics in water have been found across the world. Commonly used antibiotics have been identified in rivers in 75 countries across six continents, in concentrations as much as 300 times the level deemed safe for human consumption (*5*). In China, thousands of tons of antibiotics are released into the environment annually (*6*), and the numbers could double by 2030 (*7*). Antibiotics used by the agriculture, aquaculture, and livestock industries, as well as those consumed by humans for medicinal purposes or in food (*2*), eventually end up in waterways (*8*).

To prevent further antibiotics contamination, national governments should limit antibiotic use in livestock and aquaculture (*9*). In addition, national governments should draw up strict, quantitative standards for commonly used antibiotics, develop low-cost technologies to test for them, and conduct routine monitoring of rivers, lakes, and drinking water sources to identify contamination. By collecting detailed information about which antibiotics are in the water and in what quantities, governments can pinpoint the water sources that should be avoided and install filters to remove antibiotics from drinking water.

Di Xu[1] and Ruishan Chen[2]*
[1]School of Environmental and Geographical Sciences, Shanghai Normal University, Shanghai 200234, China. [2]School of Design, Shanghai Jiao Tong University, Shanghai 200240, China.
*Corresponding author. Email: rschen@sjtu.edu.cn

REFERENCES AND NOTES

1. Y. Ben *et al.*, *Wat. Res.* **175**, 115699 (2020).
2. K. M. M. Pärnänen *et al.*, *Sci. Adv.* **5**, eaau9124 (2019).
3. M. Qiao *et al.*, *Environ. Int.* **110**, 160 (2018).
4. R. P. Schwarzenbach *et al.*, *Science* **313**, 1072 (2006).
5. J. L. Wilkinson *et al.*, *Proc. Natl. Acad. Sci. U.S.A.* **119**, e21139471119 (2022).
6. C. Larson, *Science* **347**, 704 (2015).
7. T. P. Van Boeckel *et al.*, *Proc. Natl. Acad. Sci. U.S.A.* **112**, 5649 (2015).
8. R. Hao *et al.*, *Science* **348**, 1100 (2015).
9. M. Cully, *Nature* **509**, S16 (2014).

10.1126/science.ade6856



Schoolchildren in Puerto Maldonado, Peru, use Foldscopes to inspect plant material they collected on their playground.

PHOTO: JON COX/ACEER FOUNDATION

2022 Golden Goose Award honors serendipitous science

Ceremony recognizes unexpected breakthroughs on pain relievers, microscopes, and laser surgery

By **Andrea Korte**

A powerful pain reliever called ziconotide, which serves as an alternative treatment to opioids, is derived from an unusual source: the venom of cone snails.

The roots of the discovery of ziconotide stretch back to the Philippines in the 1970s. However, "we weren't aiming to develop a pain compound," said researcher Michael McIntosh.

Studying cone snails was initially a detour for researchers Baldomero Olivera and Lourdes Cruz. Olivera, who was splitting his time between the United States and the Philippines, found his research on DNA synthesis hampered by a lack of access to equipment and supplies in Manila. He found inspiration in his childhood interest in shell collecting. Cone snails are abundant in the Philippines, and their venom, which they use to trap fish, worms, and other mollusks, could be a rich avenue for research.

A number of breakthroughs emerged from the multidecade, multinational collaboration begun by Olivera and Cruz, which was bolstered by access to raw materials in their Philippines lab and leading-edge technology for analysis of the venom at their University of Utah lab. Among their findings: determining that the venom itself was made of peptides—very small, tightly bound proteins.

Building upon this work were other researchers, including McIntosh and Craig Clark, both of whom joined the lab as undergraduates. Pursuing his interest in brain science, Clark injected different combinations of cone snail venom peptides directly into the brains of lab mice to a surprisingly wide range of results: Some combinations caused shaking, others made mice lethargic, others made them excitable. McIntosh homed in on the particular peptide that caused shaking—purifying it, identifying its chemical structure, and dubbing it omega-conotoxin.

Over the years, the lab, in partnership with collaborators, uncovered more about omega-conotoxin and its effects—including its use as a potent pain reliever for patients with chronic illnesses. Observing the effects of conotoxins in animals has also helped researchers find new ways to map the body's nervous system.

Now, the researchers have been recognized with the 2022 Golden Goose Award, which honors federally funded research that unexpectedly benefits society.

Funding from the National Institute of General Medical Sciences of the National Institutes of Health as well as the Department of Defense was indispensable to their discoveries, the researchers acknowledged.

"It wasn't that easy to analyze small amounts of proteins at the time," said Olivera. "But the fact that we finally got an NIH grant, *that* I would say was what really allowed us to discover things that were unexpected."

"Tiny Snail, Big Impact: Cone Snail Venom Eases Pain and Injects New Energy into Neuroscience" was one of three Golden Goose Award–winning research projects recognized at the 14 September ceremony hosted by the American Association for the Advancement of Science. In attendance at the Washington, D.C., ceremony were Olivera and McIntosh, who continue to work together at the University of Utah, and Cruz, who was named a National Scientist of the Philippines in 2006. (Clark passed away in 1994.)

"This is that wonderful time of year when we shine a light on the unforeseen yet completely predictable major impacts of federally funded scientific research," said Sudip S. Parikh, chief executive officer at AAAS and executive publisher of the *Science* family of journals, in remarks at the ceremony. "AAAS is proud to be a Golden Goose Award founding organization and to have the opportunity to share with all of you the stories of these incredible scientists whose

research went in amazing and valuable directions that will benefit all Americans."

This year's award comes weeks after Congress's passing and President Biden's signing of the bipartisan CHIPS and Science Act, which reauthorizes the key federal agencies whose projects will propel the very innovations honored by the Golden Goose Award.

The award was launched in 2012, but like much of the research it recognizes, its inspiration emerged much earlier. In the 1970s and 1980s, the late Senator William Proxmire (D–WI) bestowed the dubious honor of the Golden Fleece Award. His awards were intended to highlight wasteful government spending, and basic scientific research was often in his crosshairs. Representative Jim Cooper (D–TN), however, recognized that esoteric, often silly-sounding scientific research can yield significant impacts. To recognize and celebrate the scientists pursuing federally funded research with often unexpectedly beneficial results, Cooper's vision was brought to life by a coalition of businesses, universities, and scientific organizations, including AAAS.

Since its inception, the award has honored more than 70 researchers for breakthroughs deriving from sources as wide-ranging and seemingly obscure as horseshoe crab blood and rat massage.

Also joining the ranks of honorees with the 2022 Golden Goose Award are two more teams of researchers.

Manu Prakash of Stanford University and Jim Cybulski of Foldscope Instruments, Inc., earned the award for creating the Foldscope—an innovative new microscope made of folded paper. Powerful enough to magnify 140 times, inexpensive to manufacture, and accessible in conditions where a bulky yet delicate and expensive microscope might not be practical, the tool was born of Prakash's fieldwork in a Thai rainforest studying infectious disease diagnostics, where a standard microscope was going unused.

To develop an accessible microscope that could be toted anywhere, Prakash's lab received support from NIH, while Cybulski received the NIH Fogarty International Center Global Health Equity Scholars Fellowship and a National Science Foundation grant allowed them to manufacture and distribute Foldscopes.

A multinational team consisting of Tibor Juhasz, Ron Kurtz, Detao Du, Gérard Mourou, and Donna Strickland also received the Golden Goose Award for paving a path to bladeless LASIK eye surgery.

The serendipitous results stem from Mourou and Strickland's research on short, intense laser pulses—their development of the optical technique known as chirped pulse amplification earned them half of the 2018 Nobel Prize in Physics.

When Du was a graduate student in Mourou's lab—the Center for Ultrafast Optical Science at the University of Michigan—he accidentally lifted his goggles and exposed his eye to a stray beam. While Du had no visible damage to his eye, Kurtz, then a medical resident, checked his eyes to find a series of perfectly circular laser burns on his retina. The damage was not serious, but the laser left much more precise marks than the lasers in medical use at the time. Along with Juhasz, they collaborated to pursue clinical uses for these femtosecond laser pulses. Their research was supported by funding from the Department of Energy and NSF.

Today, this laser approach has supplanted the precision scalpel for surgery to improve patients' vision, from which millions have benefited.

Cooper—the award's "Father Goose"—retires this year after 32 years of service in Congress, but his vision of recognizing and celebrating that serendipitous science can change lives persists.

Said Cooper at the award ceremony, "Tell me a fact, and I may remember it. Tell me the truth, and I may believe. But tell me a story, and I will carry it in my heart forever. And that's what Golden Goose is all about."

Meredith Asbury, Gwendolyn Bogard, and Haylie Swenson contributed to this report.

NEWS FROM Science
AAAS

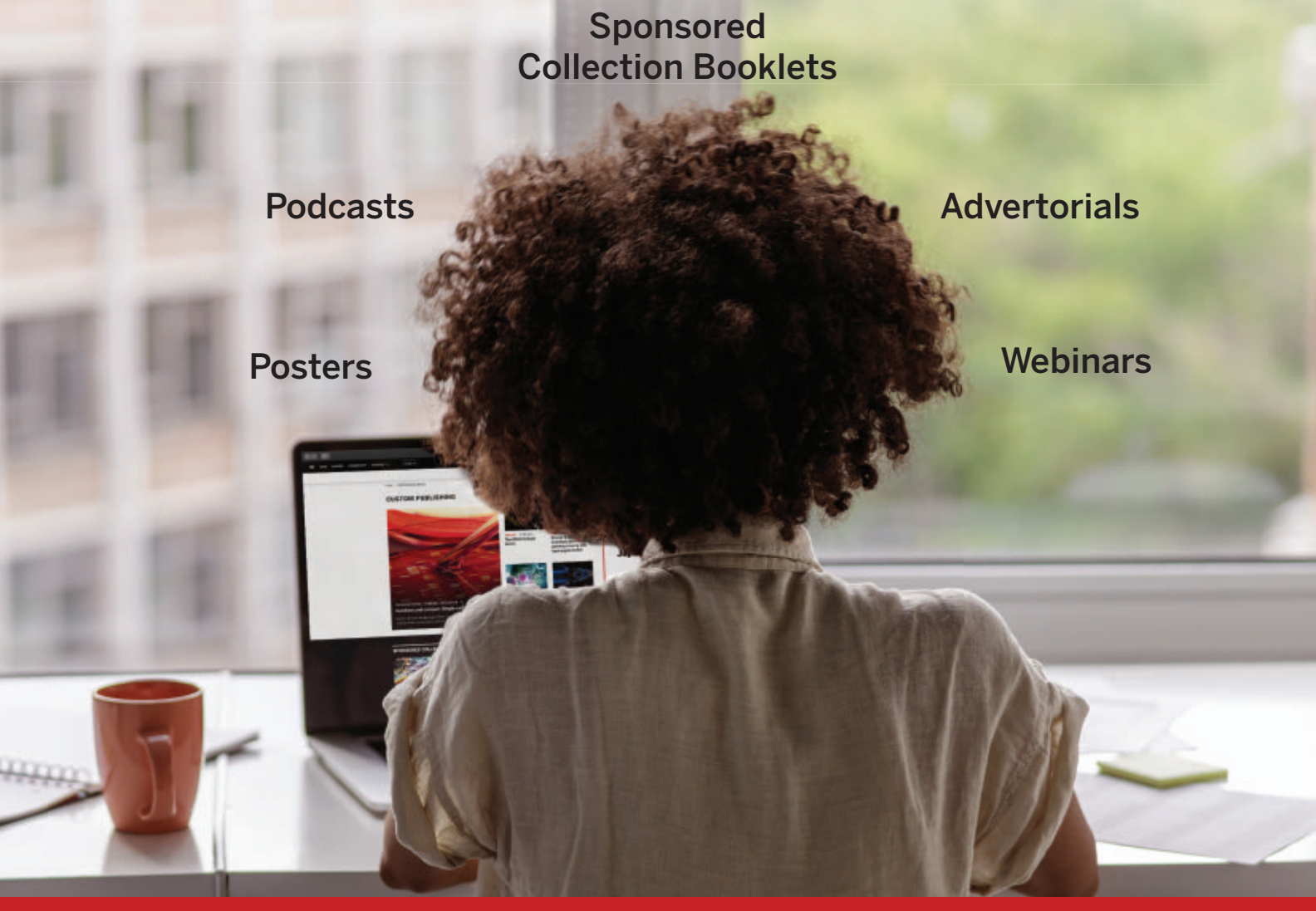
Subscribe to **News from Science** for unlimited access to authoritative, up-to-the-minute news on research and science policy.



bit.ly/NewsFromScience

QUALITY CONTENT FOR THE GLOBAL SCIENTIFIC COMMUNITY

Multiple ways to stay informed on issues related to your research



Science
AAAS

Scan the code and start exploring the latest advances in science and technology innovation!

Science.org/custom-publishing

Brought to you by the *Science*/AAAS Custom Publishing Office.

Posters | **Podcasts** | **Sponsored Collection Booklets** | **Advertorials** | **Webinars**

CALL FOR PAPERS

SPJ
SCIENCE PARTNER JOURNALS



Plant Phenomics

OPEN ACCESS

Plant Phenomics is a Science Partner Journal published in affiliation with the State Key Laboratory of Crop Genetics & Germplasm Enhancement, Nanjing Agricultural University (NAU) and distributed by the American Association for the Advancement of Science (AAAS). *Plant Phenomics* publishes novel research that advances both in field and indoor plant phenotyping, with focus on data acquisition systems, data management, data interpretation into structural or functional traits, integration into process based or machine learning based models, and connects phenomics to applications and other research domains.

Submit your research to *Plant Phenomics* today!
Learn more: **spj.sciencemag.org/plantphenomics**

The Science Partner Journals (SPJ) program was established by the American Association for the Advancement of Science (AAAS), the non-profit publisher of the *Science* family of journals. The SPJ program features high-quality, online-only, Open-Access publications produced in collaboration with international research institutions, foundations, funders, and societies. Through these collaborations, AAAS furthers its mission to communicate science broadly and for the benefit of all people by providing top-tier international research organizations with the technology, visibility, and publishing expertise that AAAS is uniquely positioned to offer as the world's largest general science membership society.

Learn more at **spj.sciencemag.org**

@SPJournals **@SPJournals**

ARTICLE PROCESSING CHARGES WAIVED UNTIL 2022

RESEARCH

IN *SCIENCE* JOURNALS

Edited by
Michael Funk



SEA LEVEL CHANGE

Leveling up and down

Rapid melting of ice sheets and glaciers raises the global average sea level but does so in a complex pattern of regional increases and decreases called a sea level fingerprint. Coulson *et al.* found that the fingerprint of melting near the Greenland Ice Sheet can be detected using ice mass loss estimates made from radar altimetry and model reconstructions of nearby glaciers. Their data provide an independent confirmation of the acceleration of Greenland Ice Sheet mass loss and reveal the impact of this mass flux on sea surface heights around Greenland. —HJS *Science*, abo0926, this issue p. 1550

New estimates of ice mass loss can provide an independent sea level change fingerprint for the Greenland Ice Sheet.

PHOTO: JONATHAN NACKSTRAND/AFP/GETTY IMAGES

SUPERCONDUCTIVITY

Superb graphene multilayers

Graphene bilayers and trilayers consisting of monolayers twisted at just the right angle have been shown to be superconducting. To acquire a unified understanding of superconductivity in these moiré superlattices, it is desirable to increase the number of known graphene moiré superconductors. Zhang *et al*. fabricated samples consisting of three, four, and five graphene layers that were twisted with respect to each other in an alternating sequence. These graphene multilayers were coupled to an underlying monolayer of tungsten diselenide. The researchers observed robust superconductivity in all three types of samples, with the superconducting portion of the phase diagram becoming more prominent as the number of layers increased. —JS

Science, abn8585, this issue p. 1538

MEMBRANES

Filtering hydrocarbons

Thin-film composite membranes synthesized through interfacial polymerization on a porous supports are used for water filtration on an industrial scale. Li *et al.* incorporated hydrophobic vesicles into the synthesis process to act as carriers to bring pure hydrocarbon or fluorinated hydrocarbon molecules into the thin top layer of the polymer film. This approach boosts the permeance for hydrophobic solvents, enabling the membranes to combine high permeance and high rejection rates when dealing with mixtures of organic molecules. The authors were able to demonstrate the separation of realistic crude oil mixtures. —MSL

Science, abq0598, this issue p. 1555

CYTOSKELETON

Making a mature cell skeleton

Actin molecules are critical components of the cytoskeleton, controlling processes such as cellular organization, organelle trafficking, and force generation. Actin proteins contain an N-terminal acetylated methionine that gets removed during maturation by a specific and previously unknown enzyme. Haahr *et al*. identified it as the protease ACTMAP, which modifies all actin molecules in all cell types. Ablation of this factor converts the actin cytoskeleton to a permanent immature state that supports life but comes at the expense of muscle weakness. —SMH

Science, abq5082, this issue, p. 1533

POLYMER CHEMISTRY

Making propylene from polyethylene

Polyolefins are the most abundantly produced plastics but are

unfortunately also among the hardest to break back down into their building blocks. Conk *et al*. developed a preliminary method to produce propylene from a sequence of reactions between waste polyethylene and fresh ethylene. Specifically, the process involves a small extent of desaturation of each polyethylene chain by a dehydrogenation catalyst, followed by steady breakdown of the chains into propylene through catalytic isomerization and metathesis reactions with ethylene. Subject to cost and process optimization, the method shows promise for generating a valuable feedstock chemical from waste plastic. —JSY

Science, add1088, this issue p. 1561

GEOCHEMISTRY

Eroding Earth's early crust

The composition of Earth can in part be explained by simply looking at meteorites that did not accrete into planets. Despite the broad agreement between the composition of certain meteorites and Earth, differences in isotopes such as 142 neodymium suggest a more complicated process for planetary formation. Frossard *et al*. looked at some of these ancient meteorites to disentangle the origin of the isotope differences (see the Perspective by Leinhardt). Collisional erosion of primordial crusts played an outside role, which may help to explain the total amount of more volatile elements in the Earth. —BG

Science, abq7351, this issue p. 1529; see also add3199, p. 1490

CANCER

Oncometabolite targets T cells

Cancer-causing mutations in isocitrate dehydrogenase cause accumulation of the metabolite D-2-hydroxyglutarate (D-2HG). Notarangelo *et al*. showed that such high concentrations of D-2HG could act as a direct inhibitor of lactate dehydrogenase in mouse T cells (see the Perspective by Nathan). Inhibition of this metabolic enzyme altered glucose metabolism in the T cells and inhibited their proliferation, cytokine production, and ability to kill target cells. The authors propose that in addition to its known cell-autonomous cancer-promoting effects, D-2HG may also have immunosuppressive activity. —LBR

Science, abj5104, this issue p. 1519; see also ade3697, p. 1488

FUNGAL INFECTIONS

A new trick for CAR T cells

Chimeric antigen receptor (CAR) T cells are most commonly thought of as a cancer therapy, but there is recent work testing their use in treating nonmalignant diseases. Seif *et al*. developed and tested a CAR T cell construct that targeted hyphae of *Aspergillus fumigatus*, a ubiquitous mold that can cause invasive pulmonary aspergillosis in immunocompromised individuals. *A. fumigatus*–specific CAR T cells had potent and selective antifungal activity in vitro and in preclinical animal models, supporting further clinical development. —CSM

Sci. Transl. Med. **14**, eabh1209 (2022).

NEUROSCIENCE

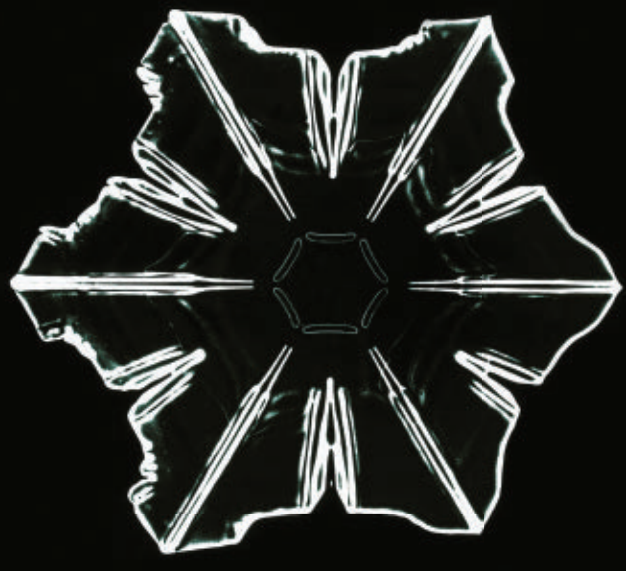
Damaged neurons send glia immune signal

In neurodegenerative diseases, neurons accumulate DNA double-strand breaks (DSBs). In a mouse model of neurodegeneration and in brains from humans with Alzheimer's disease, Welch *et al*. showed that DSB-bearing neurons elevate senescent and antiviral immune responses, which in turn elicit microglia activation. Although microglia are known resident immune cells, these findings highlight immune responses originating from damaged neurons as a distinct mechanism of disease-associated neuroinflammation. —LG

Sci. Adv. 10.1126/sciadv.abo4662 (2022).

IN OTHER JOURNALS

Edited by **Caroline Ash** *and* **Jesse Smith**



MACHINE LEARNING

Learning how water freezes

Machine learning (ML) is becoming an essential tool for modeling physical systems. It all started with a cautious attitude because ML comes from a different field, but over time, ML has gained more and more trust from researchers who bring their knowledge of physics to its development. Piaggi *et al.* present a prime example of the successful application of ML to a fundamental physical phenomenon, ice nucleation, the initial step in freezing water that occurs on time scales longer than traditional first-principles simulations can afford. The deep neural network that the authors developed to model quantum-mechanical interatomic forces substantially accelerated molecular dynamics simulations of this rare event, propagating it for previously unthinkable time spans and thus revealing important atomic-level details of what happens when water freezes. —YS

Proc. Natl. Acad. Sci. U.S.A. **119**, e2207294119 (2022).

Machine learning can be used to reveal atomic-level details of ice nucleation, the initial step in freezing water (such as in the snow crystal shown).

BLACK HOLES

Microlensing by an isolated black hole

Black holes emit no light of their own, so stellar mass black holes have only been identified in binary systems. Sahu *et al*. searched for an isolated black hole using the astrometric microlensing technique, which occurs when a foreground black hole (the lens) passes precisely in front of a background star (the source) as seen from Earth. Gravitational lensing causes the apparent brightness of the source to increase for a few months and its apparent position to shift by a few milliarcseconds over several years. By monitoring the astrometry of a microlensing event, the authors were able to determine that it

PHOTO: DE AGOSTINI PICTURE LIBRARY/GETTY IMAGES



GENETICS

Genetics of chimpanzee conservation

Genetics can be applied to conservation efforts to better understand the population dynamics of endangered species. However, sample collection from wild species can be invasive and difficult to achieve. Fontsere *et al.* used noninvasive, low-coverage genomic sequence capture of fecal samples from 828 wild chimpanzees across 48 sites in Africa to illuminate their population history. They found that chimpanzee groups have been historically isolated, but there is evidence of limited admixture between chimpanzee subspecies and their close relatives, bonobos. Although it is not a complete sampling of chimpanzee populations, this catalog of genetic variation can also aid in efforts to return poached chimpanzees to their countries of origin, in agreement with international standards. —CNS

Cell Genom. 10.1016/j.xgen.2022.100133 (2022).

Chimpanzee diversity can be monitored by noninvasive fecal sampling.

was due to an isolated black hole of seven solar masses. —KTS

Astrophys. J. 10.3847/1538-4357/ac739e (2022).

MICROBIOME

Impersonating insulin

Type 1 diabetes (T1D) is a complex autoimmune disease that leads to the destruction of pancreatic beta cells. Production of the glucose-regulating hormone insulin becomes compromised, and T1D usually presents early in life. The causes of T1D are not clear. However, Girdhar *et al.* have identified a link between a human gut microbe and T1D onset. The researchers found that the bacterium *Parabacteroides distasonis* produced an insulin-like peptide with structural similarity to human insulin. This molecular mimicry tricked the immune system into making insulin antibodies that then attacked the pancreas and enhanced T1D onset in an animal model. —PNK

Proc. Natl. Acad. Sci. U.S.A. **119**, e2120028119 (2022).

ANTIBIOTICS

Antibiotics shape lifetime health

Premature infants are vulnerable to infection and consequently are frequently given antibiotics prophylactically. However, antibiotic treatment in the very young can interfere with the establishment of a complete gut microbiota community. Poon *et al.* investigated the longer-term consequences of vancomycin treatment on neonatal mice. In addition to sustained disruption to the microbiota, the authors also noted changes in gut transit times, and found that the activity of myenteric and submucosal neurons differed between treated and untreated mice as they reached adulthood. Furthermore, neonatal vancomycin treatment was associated with lifetime depletion of mucosal serotonin levels. Although male mice showed greater myenteric neural disruption, serotonin depletion was seen in both sexes. Such profound physiological changes in response to early-life antibiotic treatment may have sex-specific and lifetime consequences for mammalian health. —CA

J. Physiol. 10.1113/JP282939 (2022).

ANIMAL COMMUNICATION

Rock on hyrax!

Anyone who has been captivated by a tune—or more precisely by a singer belting out a good song—knows the power of a rhythmic performance. Many animals sing in courtship, notably birds, but also whales, rodents, primates, and hyraxes. Demartsev *et al.* studied hyrax song and its rhythms for more than a decade and found that males that sing more often and have more rhythm tend to have higher reproductive success. That hyraxes sing alone and with rhythm suggests that their songs are shaped by female choice and reflect male quality rather than being a group coordination. Therefore, sexual selection may play a role in the evolution of song and rhythm more widely. —SNV

J. Anim. Ecol. 10.1111/1365-2656.13801 (2022).

ORGANIC CHEMISTRY

Palladium protection during amination

Palladium catalysis is widely used in pharmaceutical and agrochemical synthesis to forge bonds between carbon and nitrogen centers. However, in the case of amination adjacent to olefins, the amine reactants often disrupt the catalysis by coordinating more strongly to the metal than the olefins. Jin *et al.* report that the use of bidentate phosphine ligands can protect palladium from deactivation by amines during oxidative allylic amination. Simulations suggested that the benzoquinone oxidant further protects the metal by weakening the amine's coordination affinity through hydrogen bonding. —JSY

Nat. Chem. 10.1038/s41557-022-01023-x (2022).

PHOTO: SERGEY URYADNIKOV/SHUTTERSTOCK

ALSO IN *SCIENCE* JOURNALS

Edited by **Michael Funk**

HUMAN DISEASE

Vanquishing vexing vectors

Many major human and animal diseases are transmitted by blood-feeding insects and ticks. Because pathogens are ingested when these vectors feed, interactions with the vector's gut microbiome, midgut secretions, and epithelial cells are key factors in the transmission of disease. Barillas-Mury *et al.* reviewed recent research bolstering our understanding of how pathogens interact with both vectors and their microbiomes, as well as with vector-derived factors and vertebrate hosts after vector bites. The authors also discuss how these advances are being translated into next-generation strategies to control natural vector populations and inform the development of biomarkers of vector exposure. —STS

Science, abc2757, this issue p. 1507

AGING

Long live the mice (and humans)

The question of what determines our longevity has preoccupied humans throughout the ages, and different researchers have tried to address this in a variety of ways. Bou Sleiman *et al.* approached this question on a large scale, examining the growth patterns and genetics of thousands of mice from a multicenter study of aging (see the Perspective by Magalhães). From this analysis, the authors identified the contributions of various genes to the animals' longevity, which differed between male and female mice. The genes involved were well conserved between species, as evidenced by the finding of similar effects in humans and worms. In addition to genetics, early-life nutrition appeared to play a major role. —YN

Science, abo3191, this issue p. 1508; see also ade3119, p. 1409

IMMUNE SIGNALING

Production of small signaling isomers

Isomers of the small signaling molecule cyclic ADP ribose (cADPR) are produced when bacteria and plants respond to pathogens. Manik *et al.* found that cyclization is managed by Toll/interleukin-1 receptor (TIR) domain proteins that are themselves activated by conformational changes. One cyclic isomer, 3′cADPR, activates bacterial antiphage defense systems in bacteria and suppresses immunity in plants. —PJH

Science, adc8969, this issue p. 1501

DRUG DESIGN

A path to pain relief

The serious problems associated with opioid addiction have motivated the search for non-opioid pain-relief drugs. The α2A-adrenergic receptor (α2AAR) is a validated pain receptor that is targeted by the drug dexmetadomine. This drug is used in hospitals but is unsuitable for broader use because it causes sedation and is not orally bioavailable. Fink *et al.* screened more than 300 million virtual molecules and identified agonists that bind α2AAR with reasonable affinity and are structurally unrelated to known agonists. Crystal structures of two of the compounds bound to α2AAR allowed optimization to improve potency. The optimized compounds were effective in a neuropathic pain model without causing sedation, making them promising leads for further development. —VV

Science, abn7065, this issue p. 1509

NEUROEVOLUTION

Primate brain diversity

Primate brains benefit from an evolutionary specialization of the cortex that supports cognition. Ma *et al.* tracked transcriptomes from cellular nuclei sampled from human, chimpanzee, macaque, and marmoset brain cortices. The transcriptomes define groups of cell types, some of which are conserved and some that differ between these species. Several human-specific specializations were identified. Expression patterns of more than 900 genes associated with brain disorders revealed a variety of conserved, divergent, group-specific patterns. —PJH

Science, abo7257, this issue p. 1511

MARTIAN GEOLOGY

Igneous rocks in Jezero crater

The Perseverance rover landed in Jezero crater on Mars in February 2021. Farley *et al.* describe the geologic units investigated by the rover as it began to traverse the crater floor, based on images and spectroscopy. The authors found that the rocks are of igneous origin, later modified by reactions with liquid water. They also describe the collection of drilled samples for potential return to Earth by another spacecraft. Liu *et al.* present compositional data for these igneous rocks based on x-ray fluorescence measurements. They found similarities with some Martian meteorites and conclude that the igneous rocks formed from crystals that sank in a thick sheet of magma. Together, these studies constrain the history of Jezero crater and provide geological context for analysis of the drill samples. —KTS

Science, abo2196, abo2756 this issue, p. 1512 p. 1513

OCEAN ACIDIFICATION

Acceleration in the Arctic

The Arctic is warming at a rate faster than any comparable region on Earth, with a consequently rapid loss of sea ice there. Qi *et al.* found that this sea ice loss is causing more uptake of atmospheric carbon dioxide by surface water and driving rapid acidification of the western Arctic Ocean at a rate three to four times higher than that of the other ocean basins. They attribute this finding to melt-driven addition of freshwater and the resulting changes in seawater chemistry. —HJS

Science, abo0383, this issue p. 1544

METHANE EMISSIONS

Fueling global warming

Flaring, the process of burning natural gas escaping from oil and gas wells, is primarily intended to combust the powerful greenhouse gas methane to minimize its emission. But is flaring as effective as is claimed? Plant *et al.* used airborne sampling to measure flare efficiency in three major gas production regions in the United States and found that methane emissions were five times higher than currently thought (see the Perspective by Duren and Gordon). Therefore, flaring is often not as efficient as presumed—or methane plumes simply are not combusted at all. —HJS

Science, abq0385, this issue p. 1566; see also ade2315, p. 1486

BIOCHEMISTRY

Protecting PKCγ for neurodegeneration

Mutations in protein kinase Cγ (PKCγ) cause a hereditary neurodegenerative disease called spinocerebellar ataxia type 14. Pilo *et al.* found that these mutations increase basal activity by disrupting autoinhibitory contacts within the kinase. This structural change also impairs quality control pathways that would normally lead to the degradation of aberrant PKC. Transgenic mice expressing a disease-associated mutant exhibited ataxia-associated loss of Purkinje cells and increased phosphorylation of PKCγ target proteins in the cerebellum. —LKF

Sci. Signal. **15**, eabk1147 (2022).

IMMUNODEFICIENCY

Subpar sustenance for lymphocytes

WHIM syndrome, a human inborn error of immunity featuring reduced numbers of circulating lymphocytes, is caused by gain-of-function mutations in the chemokine receptor CXCR4. Zehentmeier *et al.* investigated stromal cell abnormalities contributing to lymphopenia by analyzing gene expression by bone marrow mesenchymal stem cells (MSCs) in a mouse model of a WHIM-inducing mutation. These cells exhibited reduced expression of the gene for interleukin-7 (IL-7), a cytokine critical for early B cell differentiation because of excess signaling through the lymphotoxin beta receptor (LTβR). Reduced expression of the genes for IL-7 and B cell–activating factor by lymph node stromal cells contributed to the lymphopenia. These findings demonstrate that CXCR4 and LTβR are viable targets for therapies to ameliorate the immunodeficiency of WHIM syndrome. —IRW

Sci. Immunol. **7**, eabo3170 (2022).

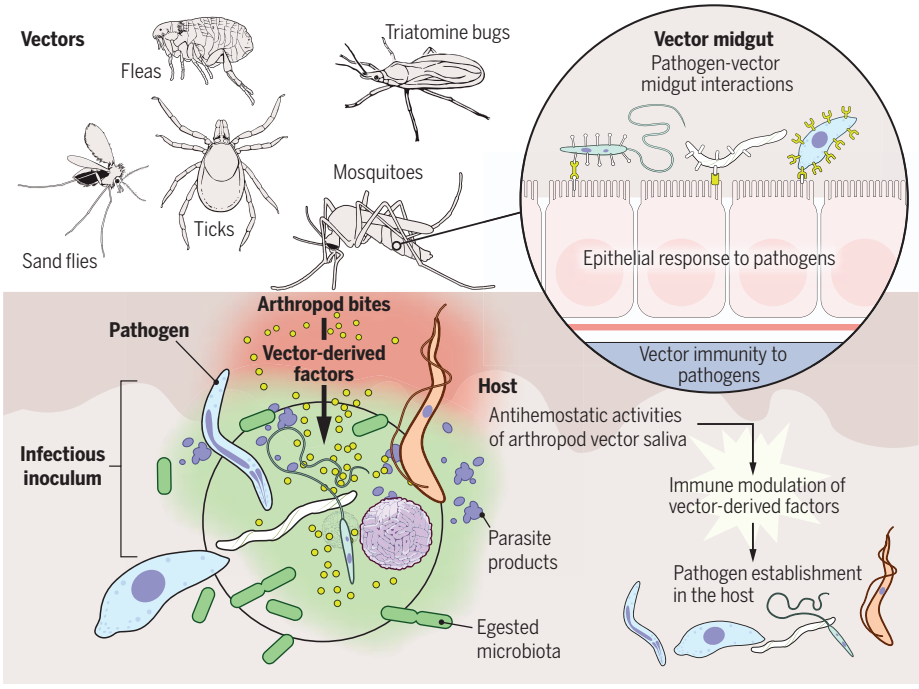
REVIEW SUMMARY

HUMAN DISEASE

Understanding pathogen survival and transmission by arthropod vectors to prevent human disease

Carolina Barillas-Mury*†, José M. C. Ribeiro*†, Jesus G. Valenzuela*†

BACKGROUND: Many endemic human and animal diseases caused by viruses, bacteria, protozoa, or nematodes are transmitted by blood-feeding insects or ticks. Because pathogens are ingested with the blood meal, their interactions with the vector's gut microbiome, midgut secretions, and epithelial cells are key determinants of disease transmission. Most pathogens must infect the vector and multiply to be transmitted, and this amplification greatly increases their chances of infecting a new vertebrate host. Accordingly, how pathogens survive or invade the midgut, and their interactions with the invertebrate immune system, are areas of great interest in vector biology. Blood-feeding arthropods secrete saliva while probing for blood, and saliva from many different vectors has been shown to have antihemostatic, anti-inflammatory, and immunomodulatory activities that allow successful blood feeding. Other vector-derived factors, including exosomes, egested microbiota, and pathogen-derived molecules, are injected at the bite site where pathogens are delivered and modulate the local environment and the innate immune responses of the host skin, promoting pathogen establishment and disease progression. Thus, functional studies of vector saliva and other vector-derived factors, their roles in pathogen establishment and transmission, the potential use of specific protein targets to prevent vector-borne diseases, and the use of vector salivary proteins as biomarkers of exposure to vector bites are also of great importance.



Interaction of pathogens with arthropod vector molecules promotes pathogen survival and transmission. Vector-borne pathogens interact with the gut microbiota and with secreted molecules and midgut receptors necessary for survival or for cell invasion. This allows them to circumvent the vector immune system to avoid elimination, multiply, and be transmitted. Pathogens also interact with vector-secreted molecules that are coinjected into the skin of the vertebrate host during disease transmission by the bite of an infected vector. These vector-derived factors—which include salivary proteins, parasite exosomes, parasite molecules, and egested microbiota—modify the hemostatic and innate immune response of the host skin, resulting in enhanced pathogen transmission.

ADVANCES: Over the past 20 years, the study of vector biology has been revolutionized by many new molecular, cell biology, and genomic tools. For example, the advent of genomics and third-generation sequencing has allowed for high-density de novo transcriptome assembly and single-cell RNA transcriptome analysis, even without a reference genome. Perturbations in vector gene expression in response to infection with specific pathogens can now be studied at a genome-wide level. The expression of recombinant proteins derived from genomics or transcriptomic studies has enabled structure-function studies, the discovery of salivary biomarkers to measure vector exposure in humans, and the generation of specific antibodies for subcellular localization of pathogen receptors or of vector-derived proteins that interact with specific pathogens. Transient gene silencing has revealed the participation of specific genes or signaling pathways in both vector physiology and in vector immunity against pathogens. There have also been great advances in the genetic manipulation of insects with the CRISPR-Cas9 system and the development of gene-driven strategies, such as CRISPR-Cas9–directed homologous repair. The symbiotic proteobacteria *Wolbachia* has been introduced into natural populations of *Aedes aegypti* mosquitoes to reduce viral replication and transmission of dengue, Zika, and Chikungunya with promising results. Such approaches may hold the long-awaited promise of permanently modifying natural vector populations to render them unable to transmit disease.

OUTLOOK: In this Review, we highlight recent progress in our understanding of the basic molecular and cell biology of pathogen interactions with vectors and their microbiomes, as well as the interactions between vector-derived factors and pathogens with their vertebrate hosts during the establishment of infection after a vector bite. We discuss how these advances in the biology of disease transmission have also translated into next-generation strategies to control natural vector populations and to modify them to disrupt their capacity to transmit disease. Moreover, we review the development of salivary biomarkers of vector exposure as a tool for evaluating both epidemiological studies and vector control strategies by measuring vector biting activity in humans. ■

Laboratory of Malaria and Vector Research, National Institute of Allergy and Infectious Diseases, Rockville, MD 20852, USA.
*Corresponding author. Email: cbarillas@niaid.nih.gov (C.B.-M.); jribeiro@niaid.nih.gov (J.M.C.R.); jvalenzuela@niaid.nih.gov (J.G.V.)
†These authors contributed equally to this work.
Cite this article as C. Barillas-Mury *et al.*, *Science* **377**, eabc2757 (2022). DOI: 10.1126/science.abc2757

READ THE FULL ARTICLE AT
https://doi.org/10.1126/science.abc2757

REVIEW

HUMAN DISEASE

Understanding pathogen survival and transmission by arthropod vectors to prevent human disease

Carolina Barillas-Mury*†, José M. C. Ribeiro*†, Jesus G. Valenzuela*†

Many endemic poverty-associated diseases, such as malaria and leishmaniasis, are transmitted by arthropod vectors. Pathogens must interact with specific molecules in the vector gut, the microbiota, and the vector immune system to survive and be transmitted. The vertebrate host, in turn, is infected when the pathogen and vector-derived factors, such as salivary proteins, are delivered into the skin by a vector bite. Here, we review recent progress in our understanding of the biology of pathogen transmission from the human to the vector and back, from the vector to the host. We also highlight recent advances in the biology of vector-borne disease transmission, which have translated into additional strategies to prevent human disease by either reducing vector populations or by disrupting their ability to transmit pathogens.

Blood-feeding insects are vectors of some of the most devastating diseases in low-income areas, such as malaria, Zika, dengue, and leishmaniasis. Vector-pathogen interactions, particularly those mediated by the midgut, the gut microbiota, and the vector immune system, are intense areas of study because they are major determinants of disease transmission by limiting pathogen survival. Molecular interactions between vector-derived factors—such as salivary proteins, exosomes, and egested microbiota—and the mammalian host modulate local skin immunity and are critical for pathogen establishment. Thus, it is very important to understand how saliva and other vectors or pathogen-derived factors affect disease transmission and to understand their potential as vaccine targets to prevent diseases or as biomarkers of vector exposure.

Interaction of pathogens with vector midgut proteins

Ingested pathogens need to survive the harsh environment of the midgut lumen, where blood digestion takes place. The blood meal is surrounded by a chitinous peritrophic matrix (PM), which prevents direct contact between the gut microbiome and epithelial cells (Fig. 1). In *Anopheles gambiae* mosquitoes, the permeability of the ectoperitrophic space (between the PM and the midgut epithelium) is tightly modulated by secretion of an immune-modulatory peroxidase (IMPer) (*1*). This enzyme cross-links proteins in the ectoperitrophic space, allowing commensal bacteria to proliferate in the gut lumen without eliciting epithelial immunity. This also allows early stages of *Plasmodium* to develop within the gut without detection. In tsetse flies, *Trypanosoma brucei* takes advantage of the immature and fluid PM to move into the ectoperitrophic space. There, it colonizes the proventriculus to later establish midgut infection (*2*).

Some pathogens must bind to specific midgut receptors to survive. *Leishmania major* parasites, for example, are covered with lipophosphoglycans that specifically bind to PpGal, a sand fly midgut galectin receptor required for parasite survival and development (Fig. 1) (*3*). The Borrelia surface protein OSP A binds to TROSPA, a receptor in the gut of the *Ixodes scapularis* tick (Fig. 1), an interaction required for tick colonization by spirochetes (*4*). Thus, arthropod midgut receptors are attractive potential vaccine targets to block disease transmission.

Effect of gut microbiota and multiple blood meals in vectorial capacity

Commensal gut bacteria proliferate extensively as the blood meal undergoes digestion and affect pathogen establishment. In *A. gambiae*, the mosquito gut microbiota limits *Plasmodium* infection, and oral antibiotics increase *Plasmodium* survival (*5*). By contrast, the gut microbiota of sand flies is essential for *Leishmania*, and antibiotics inhibit their development into infective metacyclics (*6*). The close interaction of pathogens with the insect gut microbiota has been exploited by using an enterobacterium isolated from wild-caught *Anopheles* to limit *Plasmodium* development in mosquitoes (*7*) and *Chromobacterium* sp. from field-caught *Aedes* to impair *Plasmodium* and dengue virus infection (*8*).

Recent findings show that ingestion of multiple blood meals can enhance pathogen transmission by infected vectors (Fig. 1). When *Leishmania*-infected sand flies take a second blood meal, parasites dedifferentiate into a multiplicative stage called retroleptomonad, which expands the population of infective metacyclics in the vector gut (*9*). Similarly, dengue virus–infected mosquitoes fed a second uninfected blood meal exhibit higher systemic virus dissemination that enhances viral transmission (*10*). This increase in vectorial capacity after the ingestion of blood from a healthy host may explain why disease transmission is so effective in the field.

Insect innate immunity and vector competence

Antiplasmodial responses of anopheline mosquitoes can limit malaria transmission. In *A. gambiae*, these responses involve the sequential and coordinated activation of epithelial immunity by invaded midgut cells (*11*–*15*), microvesicle release by circulating hemocytes (*16*, *17*), and activation of the mosquito complement system (*15*, *18*). Genetic studies have revealed that Pfs47, a protein on the surface of the parasite *Plasmodium falciparum*, mediates immune evasion (*19*, *20*) by interacting with a receptor in the mosquito midgut (*21*). The receptors have diverged in evolutionarily distant mosquitoes (*21*, *22*) and constantly select for parasites with a *Pfs47* haplotype compatible with their receptor (*22*).

Antiviral immunity in *Drosophila* and mosquitoes is mediated by the RNA interference (RNAi) pathway, whereas the Piwi-interacting RNA (piRNA) pathway appears to be active only in mosquitoes (*23*–*25*). Silencing key components of the RNAi pathway in *Aedes aegypti* mosquitoes increases *Dengue* (*26*) and *Sindbis* virus replication (*27*) and, in *A. gambiae*, enhances the infection and dissemination of *O'nyong-nyong* virus (*28*).

piRNAs range in size between 26 and 31 base pairs and have been mostly linked to the silencing of retrotransposons (*29*) and other genetic elements in the germ line (*30*). However, an antiviral role in mosquito cell lines has been proposed, where viral DNAs (vDNAs) are integrated into the *A. aegypti* genome as endogenous viral elements (EVEs) and serve as templates to produce piRNAs (*31*–*33*). EVEs may therefore represent a type of immune memory by providing a record of past infections (*32*). EVE-derived piRNAs are specifically loaded onto Piwi4 and inhibit virus replication (*33*). Inhibition of vDNA in *Aedes albopictus* and *A. aegypti* mosquitoes infected with two arboviruses (*Dengue* or *Chikungunya*) reduces viral small RNAs and results in high susceptibility to viral infection and loss of tolerance. Thus, vDNA is an important mechanism for persistent viral infections in mosquitoes, which makes these insects highly efficient disease vectors (*34*).

Furthermore, overactivation of the JAK–STAT pathway decreases *A. aegypti* susceptibility to dengue virus infection, whereas silencing key

Laboratory of Malaria and Vector Research, National Institute of Allergy and Infectious Diseases, Rockville, MD 20852, USA.
*Corresponding author. Email: cbarillas@niaid.nih.gov (C.B.-M.); jribeiro@niaid.nih.gov (J.M.C.R.); jvalenzuela@niaid.nih.gov (J.G.V.)
†These authors contributed equally to this work.

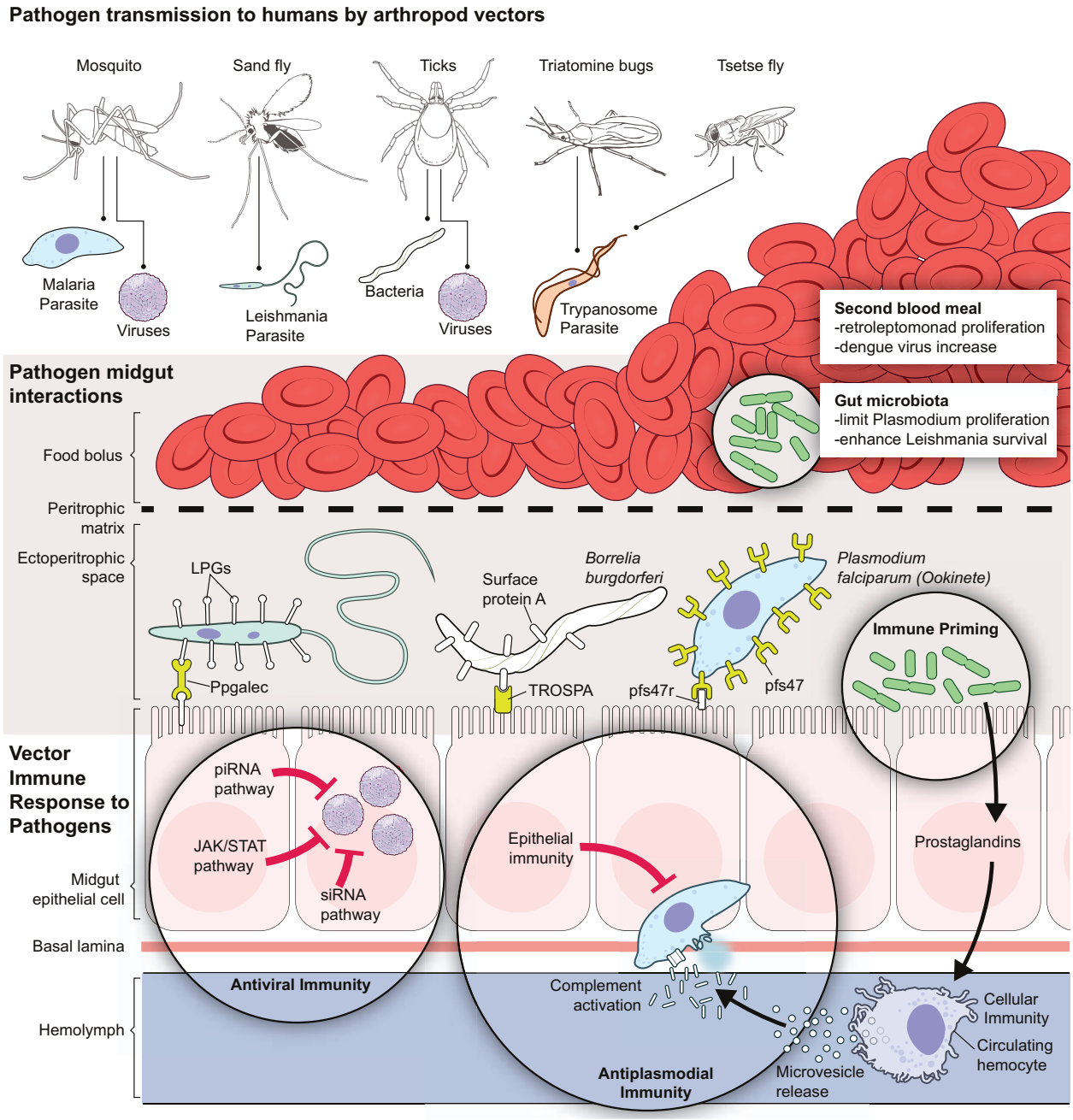


Fig. 1. Pathogens ingested by arthropod vectors interact closely with the gut microbiota and with midgut epithelial cells. They traverse the PM, and some interact with specific receptors, such as *P. papatasi* galectin (PpGal), *I. scapularis* TROSPA, and the *P. falciparum* Pfs47 receptor. Epithelial cells activate antiviral responses mediated by the piRNA, small interfering RNA (siRNA), and JAK–STAT pathways. At the same time, caspase-mediated nitration responses of ookinete-invaded midgut cells activate hemocyte microvesicle release, which promotes the activation of complement-mediated *Plasmodium* elimination. Ingestion of a second blood meal can also provide nutritional and/or differentiation signals that enhance pathogen transmission. LPGs, lipophosphoglycans.

components for activation of the pathway enhances susceptibility to infection (*35*). Activation of the Toll pathway and the gut microbiota reduces *A. aegypti* susceptibility to dengue infection (*36*), whereas constitutive activation of the immunodeficiency (IMD) pathway decreases microbiota bacterial loads and increases Sindbis virus infection (*37*). By contrast, elimination of the gut microbiota in *A. gambiae* decreases infectivity with O'nyong-nyong virus (*38*). The *A. gambiae* midgut activates local antiviral responses to O'nyong-nyong virus infection, which involve the IMD and JAK–STAT signaling pathways, whereas the RNAi pathway mediates systemic responses (*38*). Loquacious 2 (Loqs2) is required to control systemic replication of dengue virus and Zika virus in *A. aegypti*. Loqs2 is not expressed in the midgut, but ectopic midgut expression in transgenic mosquitoes limits dengue virus replication and dissemination (*39*).

Innate immune priming

Insect immunity relies on innate immune responses that were thought to be hardwired. However, studies in *A. gambiae* have revealed that mosquitoes previously exposed to *Plasmodium* infection mount a more effective response to subsequent infections (*1*). The priming response is established when ookinete invasion allows direct contact of the gut microbiota with midgut cells, activating prostaglandin

synthesis mediated by two heme peroxidases (HPx7 and HPx8) (*16*). This triggers the systemic release of a hemocyte differentiation factor (HDF) that increases the proportion of circulating granulocytes (*1*). HDF is a complex of lipoxin A_4 bound to Evokin, a carrier from the lipocalin family. Immune priming involves increased ability of mosquitoes to synthesize lipoxins, predominantly lipoxin A_4 (*40*). Primed hemocytes then release more microvesicles in response to ookinete invasion, which enhances the activation of the mosquito complement system (*17*).

Vector saliva

The saliva of blood-feeding arthropods has antiplatelet, anticlotting, and vasodilatory properties and contains modulators of inflammation and immunity (*41*, *42*) (Fig. 2). Despite similar functions, these proteins are highly divergent among insect species because blood feeding evolved independently, and these genes evolve rapidly. For example, most vectors that feed on mammalian blood have high levels of adenosine 5′-diphosphate (ADP)–hydrolyzing enzymes to inhibit platelet aggregation, but these levels are achieved using different strategies. A 5′-nucleotidase family exists in ticks (*43*), triatomine bugs (*44*), and mosquitoes (*45*); a CD39 family is present in fleas (*46*); and a Cimex-type apyrase is found in sand flies (*47*) and bed bugs (*48*). The most potent vasodilator known, the peptide maxadilan, was discovered in the sand fly *Lutzomyia longipalpis* (*49*). Several "kratagonists" (from the Greek "kratos" meaning "to seize") in vector saliva, such as lipocalins and odorant-binding proteins, act as scavengers of histamine, serotonin, leukotrienes, thromboxane A_2, and inflammatory cytokines (*50*), whereas other protein families inhibit the activation of the complement system (*51*–*54*).

The advent of third-generation sequencing has revealed the existence of many previously unknown salivary proteins—~50 different salivary polypeptides in sand flies, >100 in mosquitoes and triatomine bugs, and thousands in hard ticks (*55*, *56*). The function of most of these proteins remains unknown. The increased number of salivary transcripts in ticks is the result of a large expansion of several protein families. However, only a few members of each family are expressed at a given time, and the composition of saliva changes over time (*57*). This phenomenon, which we refer to as sialome switching, may be an immune evasion strategy, but how it is regulated remains a mystery.

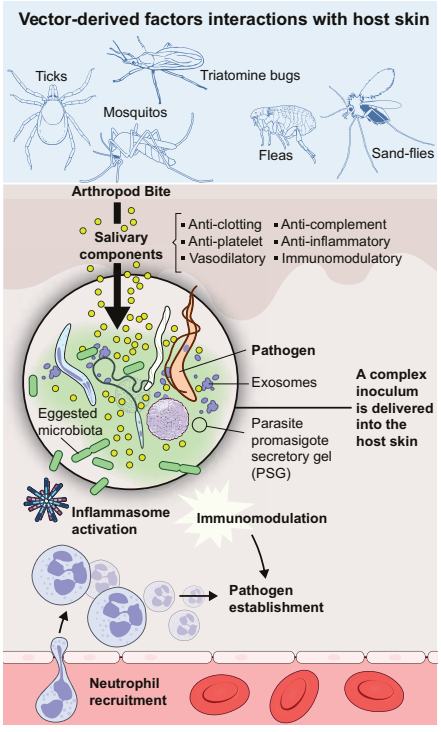


Fig. 2. In addition to pathogens, blood-feeding arthropods deliver a series of vector-derived factors, such as salivary components and gut microbiota, and pathogen components, such as exosomes and proteophosphoglycans, into the host skin. Vector-derived factors counteract the hemostatic system and modulate host skin immunity, including activation of the inflammasome, which favors the establishment of some parasitic and viral infections.

The effect of vector saliva and vector-derived factors on pathogen establishment

Needle inoculation of pathogens does not mimic their natural delivery by an insect bite. For example, West Nile virus delivered to mice by mosquito *Culex tarsalis* bites results in higher viremia and neuroinvasion compared with needle inoculation (*58*). Likewise, injection of Semliki Forest virus in a skin site previously bitten by *Aedes* mosquitoes results in higher viremia and increased mortality in rodents (*59*), mediated by interleukin-1β (IL-1β) activation and recruitment of neutrophils to the dermis (*59*). Similarly, *Leishmania donovani* transmission by sand fly bites induces the activation of the inflammasome, production of IL-1β, recruitment of neutrophils, and parasite visceralization (Fig. 2). By contrast, no parasite visceralization occurs with needle-injected parasites (*60*). Activation of IL-1β and neutrophil recruitment was triggered by the gut microbiota egested during the sand fly bite (*60*). *Plasmodium* sporozoites injected at the bite site by *Anopheles stephensi* result in higher parasitemias, enhanced progression to cerebral malaria, and death (*61*). SALP15, a tick salivary protein, is essential for establishment and dissemination of infection by inhibiting T cell activation and protecting *Borrelia* from the host complement (*62*). Thus, vector-derived factors from different disease vectors appear to activate innate immune responses and to recruit cells, such as neutrophils, that facilitate pathogen establishment (Fig. 2).

There are other mechanisms by which vector saliva facilitates pathogen transmission. For example, the sand fly salivary endonuclease LunDep destroys neutrophil extracellular traps (NETs), increasing survival of *L. major* parasites (*63*). The sand fly salivary hyaluronidase enhances *Leishmania* infection in mice by working as a so-called spreading factor and by increasing neutrophil recruitment to the bite site (*64*, *65*). The *A. aegypti* salivary protein NeSt1 increases *Zika* virus pathogenesis by activating neutrophils (*66*), whereas the salivary protein AaVA-1 enhances *Zika* and *Dengue* transmission in rodents by activating autophagy in immune cells (*67*). In addition to salivary proteins, *Leishmania* proteophosphoglycans and exosomes as well as egested microbiota are part of the infectious inoculum of sand flies (*60*, *68*, *69*).

Arthropod salivary proteins as vaccine targets to prevent disease transmission

Arthropod salivary proteins are promising vaccine candidates to disrupt transmission of vector-borne diseases (*70*, *71*). Vaccination of rhesus macaques with the sand fly salivary protein PdSP15 confers protection from *L. major* transmitted by sand fly bites, which correlates with the development of a PdSP15-specific type 1 T helper (T_H1) cell immunity and anti-*Leishmania* immunity (*72*). T_H1 immunity to the salivary protein coinjected at the bite site is thought to protect from disease by altering the immune response to parasite antigens (*72*). Recently, immunization of guinea pigs with an mRNA vaccine encoding selected tick salivary proteins induced a skin response that prevented *Borrelia* transmission by ticks in vaccinated animals (*73*). In mosquitoes, vaccination of mice with *Anopheles* salivary protein AgTRIO protects animals from *Plasmodium* infection (*74*), whereas immunization with the *A. aegypti* salivary protein AgBR1 protects mice from Zika (*75*) and West Nile virus infections (*76*). Antibodies to AgBR1 prevent AgBR1-induced neutrophil activation and block saliva-mediated enhancement of virus establishment (*75*). Recently, a mosquito salivary peptide–based vaccine was shown to be safe and to produce specific immunity in a phase 1 clinical trial in humans (*77*).

Arthropod salivary proteins as biomarkers of vector exposure

Humans mount antibody responses to certain salivary proteins that can be used as biomarkers of exposure to vector bites (*78*). Several recombinant vector salivary proteins and synthetic peptides have been developed as biomarkers, including the gSG6-P1 salivary peptide from *A. gambiae* (*79*), Nterm-34kDa salivary peptide from *A. aegypti* (*80*), rLJM17 and rLJM11 from *L. longipalpis* (*81*), rSP03B from *Phlebotomus perniciosus* (*82*), PpSP32 from *Phlebotomus*

papatasi (*83*), Tsgf118-43 from tsetse flies (*84*), rTisP14.6 from *Triatoma infestans* (*85*), and Calreticulin from *I. scapularis* (*86*). These are useful tools to assess risk of disease transmission and the effectiveness of vector control strategies (*87*) in ongoing disease elimination campaigns.

Transgenesis, paratransgenesis, and other vector control strategies

Genetic modifications can be used to reduce natural vector populations or to replace them with transgenic vectors that no longer transmit disease (Fig. 3). Two major obstacles to this approach have been overcome: first, the identification of gene targets to be disrupted or previously undiscovered genes that would interrupt pathogen development, and second, strategies to introduce a new gene or to modify a vector gene. However, once released, transgenic insects will mate with wild-type ones, and the genetic modifications of interest will dilute in every generation (*88*) unless they can spread more effectively through non-Mendelian inheritance that can drive the gene through the population.

Several gene drive mechanisms have been proposed, such as transposable elements (*88*) and other gene insertion methods (*89*), including arboviruses and the homing endonuclease system, with various degrees of success. More recently, the CRISPR-Cas9 system has emerged as a very promising approach. CRISPR-Cas9–directed homologous repair of the germ line cuts the gene in the wild-type chromosome of heterozygous mosquitoes and repairs it by homologous repair with the chromosome containing the effector gene of interest (*90*). A great variety of genes have been proposed as insertion targets, including expression of recombinant antibodies that target the pathogen (*91*) or that affect mosquito reproduction (*92*–*94*). However, a word of caution for constructs affecting fertility is needed. A partial decrease of fertility may ultimately lead to more rather than fewer mosquitoes because it will reduce competition for resources during larval stages. Emerging adults may also be better nourished and live longer, resulting in adults with increased vectorial capacity (*95*). This problem can be circumvented by strategies that are deleterious to adult stages but allow normal larval development (*96*).

An alternative strategy to modify vectors is to introduce commensal microorganisms that reduce vectorial capacity (Fig. 3) (*97*). A *Serratia* strain that quickly colonizes the mosquito gut when fed in a sugar solution was recently identified that, when engineered to secrete anti-*Plasmodium* effector proteins, greatly reduces the ability of mosquitoes to transmit malaria (*97*). *Rhodococcus rhodnii*, a triatomine endosymbiont, has been modified to express an anti-*Trypanosoma* peptide. This microbe rendered *Rhodnius prolixus* resistant to *Trypanosoma cruzi*, the parasite that causes Chagas disease (*98*). In this system, symbionts are transmitted from adults to nymphs by coprophagy. Genetically modified *R. rhodnii* has been used to prepare a mixture that is actively ingested by triatomine nymphs (*99*). Another successful development has been the exploitation of *Wolbachia* that naturally infect insects (*100*). This is an intracellular bacterium that is transmitted vertically and spreads through natural insect populations by inducing cytoplasmic incompatibility (CI). Infected females have viable offspring when they mate with either noninfected or infected males, whereas *Wolbachia*-free females are only fertile if they mate with uninfected males. When *A. aegypti* mosquitoes—the vectors of dengue, Zika, and Chikungunya—are infected with some strains of *Wolbachia*, this greatly reduces viral replication and transmission (*101*). This strategy is already undergoing field trials in several countries to disrupt transmission of arboviruses (*102*, *103*). A *Metarhizium* fungus genetically modified to express an insect toxin was very effective in suppressing natural populations of mosquitoes highly resistant to insecticides (*104*). A different strategy, where the antimalarial atovaquone was applied to surfaces with which mosquitoes came into contact, disrupted *Plasmodium* development, providing an additional tool to prevent malaria transmission (*105*).

Future directions

Most blood-feeding arthropods eliminate the pathogens they ingest and do not transmit disease. However, there are extremely rare, fortuitous encounters in which a pathogen interacts with vector factors that allow it to survive and/or evade elimination by the vector immune system and infect a new host when the vector takes the next blood meal. This ability to jump or fly from one host to another gives these pathogens an enormous advantage, with devastating

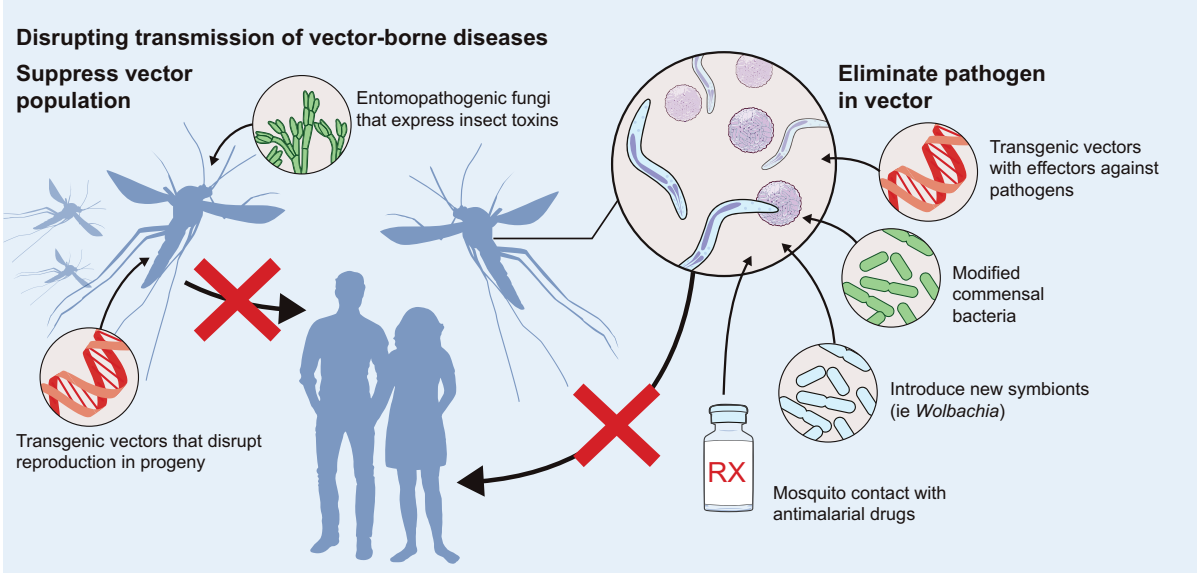


Fig. 3. Next-generation strategies to disrupt pathogen transmission by arthropod vectors include suppression of vector populations or elimination of the pathogens in the vector. Effective entomopathogenic fungi expressing insect toxins or genetic modifications deleterious to specific stages of the vectors have been developed to suppress vector populations. Pathogens can be eliminated by genetically modified arthropods or commensal bacteria expressing effectors against the pathogen; by introducing a commensal, such as *Wolbachia*, that creates a physiological state nonpermissive to the pathogen; or by exposing the vector to drugs that target the pathogen, such as contact of mosquitoes with antimalarial drugs that eliminate *Plasmodium* parasites.

consequences for human and animal health. There is growing consensus that disrupting disease transmission by arthropod vectors is critical for disease eradication. As we continue to harness our growing understanding of the biology of pathogen transmission, we uncover critical interactions that can be targeted to prevent disease. New translational tools are constantly being developed that may allow us to witness the long-awaited eradication of some of the most devastating vector-borne diseases.

REFERENCES AND NOTES

1. S. Kumar, A. Molina-Cruz, L. Gupta, J. Rodrigues, C. Barillas-Mury, A peroxidase/dual oxidase system modulates midgut epithelial immunity in *Anopheles gambiae*. *Science* **327**, 1644–1648 (2010). doi: 10.1126/science.1184008; pmid: 20223948
2. C. Rose *et al*., *Trypanosoma brucei* colonizes the tsetse gut via an immature peritrophic matrix in the proventriculus. *Nat. Microbiol.* **5**, 909–916 (2020). doi: 10.1038/s41564-020-0707-z; pmid: 32313202
3. S. Kamhawi *et al*., A role for insect galectins in parasite survival. *Cell* **119**, 329–341 (2004). doi: 10.1016/j.cell.2004.10.009; pmid: 15543683
4. U. Pal *et al*., TROSPA, an *Ixodes scapularis* receptor for *Borrelia burgdorferi*. *Cell* **119**, 457–468 (2004). doi: 10.1016/j.cell.2004.10.027; pmid: 15537536
5. M. Gendrin *et al*., Antibiotics in ingested human blood affect the mosquito microbiota and capacity to transmit malaria. *Nat. Commun.* **6**, 5921 (2015). doi: 10.1038/ncomms6921; pmid: 25562286
6. P. H. Kelly *et al*., The Gut Microbiome of the Vector *Lutzomyia longipalpis* Is Essential for Survival of *Leishmania infantum*. *mBio* **8**, e01121-16 (2017). doi: 10.1128/mBio.01121-16; pmid: 28096483
7. C. M. Cirimotich *et al*., Natural microbe-mediated refractoriness to *Plasmodium* infection in *Anopheles gambiae*. *Science* **332**, 855–858 (2011). doi: 10.1126/science.1201618; pmid: 21566196
8. J. L. Ramirez *et al*., *Chromobacterium Csp_P* reduces malaria and dengue infection in vector mosquitoes and has entomopathogenic and *in vitro* anti-pathogen activities. *PLOS Pathog.* **10**, e1004398 (2014). doi: 10.1371/journal.ppat.1004398; pmid: 25340821
9. T. D. Serafim *et al*., Sequential blood meals promote *Leishmania* replication and reverse metacyclogenesis augmenting vector infectivity. *Nat. Microbiol.* **3**, 548–555 (2018). doi: 10.1038/s41564-018-0125-7; pmid: 29556108
10. P. M. Armstrong *et al*., Successive blood meals enhance virus dissemination within mosquitoes and increase transmission potential. *Nat. Microbiol.* **5**, 239–247 (2020). doi: 10.1038/s41564-019-0619-y; pmid: 31819213
11. S. Kumar *et al*., The role of reactive oxygen species on *Plasmodium* melanotic encapsulation in *Anopheles gambiae*. *Proc. Natl. Acad. Sci. U.S.A.* **100**, 14139–14144 (2003). doi: 10.1073/pnas.2036262100; pmid: 14623973
12. S. Kumar, L. Gupta, Y. S. Han, C. Barillas-Mury, Inducible peroxidases mediate nitration of *Anopheles* midgut cells undergoing apoptosis in response to *Plasmodium* invasion. *J. Biol. Chem.* **279**, 53475–53482 (2004). doi: 10.1074/jbc.M409905200; pmid: 15456781
13. Y. S. Han, C. Barillas-Mury, Implications of Time Bomb model of ookinete invasion of midgut cells. *Insect Biochem. Mol. Biol.* **32**, 1311–1316 (2002). doi: 10.1016/S0965-1748(02)00093-0; pmid: 12225921
14. Y. S. Han, J. Thompson, F. C. Kafatos, C. Barillas-Mury, Molecular interactions between *Anopheles stephensi* midgut cells and *Plasmodium berghei*: The time bomb theory of ookinete invasion of mosquitoes. *EMBO J.* **19**, 6030–6040 (2000). doi: 10.1093/emboj/19.22.6030; pmid: 11080150
15. G. d. A. Oliveira, J. Lieberman, C. Barillas-Mury, Epithelial nitration by a peroxidase/NOX5 system mediates mosquito antiplasmodial immunity. *Science* **335**, 856–859 (2012). doi: 10.1126/science.1209678; pmid: 22282475
16. A. B. F. Barletta, N. Trisnadi, J. L. Ramirez, C. Barillas-Mury, Mosquito Midgut Prostaglandin Release Establishes Systemic Immune Priming. *iScience* **19**, 54–62 (2019). doi: 10.1016/j.isci.2019.07.012; pmid: 31351392
17. J. C. Castillo, A. B. B. Ferreira, N. Trisnadi, C. Barillas-Mury, Activation of mosquito complement antiplasmodial response requires cellular immunity. *Sci. Immunol.* **2**, eaal1505 (2017). doi: 10.1126/sciimmunol.aal1505; pmid: 28736767
18. S. Blandin *et al*., Complement-like protein TEP1 is a determinant of vectorial capacity in the malaria vector *Anopheles gambiae*. *Cell* **116**, 661–670 (2004). doi: 10.1016/S0092-8674(04)00173-4; pmid: 15006349
19. A. Molina-Cruz *et al*., The human malaria parasite *Pfs47* gene mediates evasion of the mosquito immune system. *Science* **340**, 984–987 (2013). doi: 10.1126/science.1235264; pmid: 23661646
20. A. Molina-Cruz *et al*., Some strains of *Plasmodium falciparum*, a human malaria parasite, evade the complement-like system of *Anopheles gambiae* mosquitoes. *Proc. Natl. Acad. Sci. U.S.A.* **109**, E1957–E1962 (2012). doi: 10.1073/pnas.1121183109; pmid: 22623529
21. A. Molina-Cruz *et al*., *Plasmodium falciparum* evades immunity of anopheline mosquitoes by interacting with a Pfs47 midgut receptor. *Proc. Natl. Acad. Sci. U.S.A.* **117**, 2597–2605 (2020). doi: 10.1073/pnas.1917042117; pmid: 31969456
22. A. Molina-Cruz *et al*., *Plasmodium* evasion of mosquito immunity and global malaria transmission: The lock-and-key theory. *Proc. Natl. Acad. Sci. U.S.A.* **112**, 15178–15183 (2015). doi: 10.1073/pnas.1520426112; pmid: 26598665
23. R. P. van Rij *et al*., The RNA silencing endonuclease Argonaute 2 mediates specific antiviral immunity in *Drosophila melanogaster*. *Genes Dev.* **20**, 2985–2995 (2006). doi: 10.1101/gad.1482006; pmid: 17079687
24. R. W. Carthew, E. J. Sontheimer, Origins and Mechanisms of miRNAs and siRNAs. *Cell* **136**, 642–655 (2009). doi: 10.1016/j.cell.2009.01.035; pmid: 19239886
25. D. Galiana-Arnoux, C. Dostert, A. Schneemann, J. A. Hoffmann, J. L. Imler, Essential function *in vivo* for Dicer-2 in host defense against RNA viruses in drosophila. *Nat. Immunol.* **7**, 590–597 (2006). doi: 10.1038/ni1335; pmid: 16554838
26. I. Sánchez-Vargas *et al*., Dengue virus type 2 infections of *Aedes aegypti* are modulated by the mosquito's RNA interference pathway. *PLOS Pathog.* **5**, e1000299 (2009). doi: 10.1371/journal.ppat.1000299; pmid: 19214215
27. C. L. Campbell *et al*., *Aedes aegypti* uses RNA interference in defense against Sindbis virus infection. *BMC Microbiol.* **8**, 47 (2008). doi: 10.1186/1471-2180-8-47; pmid: 18366655
28. K. M. Keene *et al*., RNA interference acts as a natural antiviral response to O'nyong-nyong virus (*Alphavirus*; Togaviridae) infection of *Anopheles gambiae*. *Proc. Natl. Acad. Sci. U.S.A.* **101**, 17240–17245 (2004). doi: 10.1073/pnas.0406983101; pmid: 15583140
29. J. Brennecke *et al*., An epigenetic role for maternally inherited piRNAs in transposon silencing. *Science* **322**, 1387–1392 (2008). doi: 10.1126/science.1165171; pmid: 19039138
30. V. V. Vagin *et al*., A distinct small RNA pathway silences selfish genetic elements in the germline. *Science* **313**, 320–324 (2006). doi: 10.1126/science.1129333; pmid: 16809489
31. U. Palatini *et al*., Comparative genomics shows that viral integrations are abundant and express piRNAs in the arboviral vectors *Aedes aegypti* and *Aedes albopictus*. *BMC Genomics* **18**, 512 (2017). doi: 10.1186/s12864-017-3903-3; pmid: 28676109
32. Z. J. Whitfield *et al*., The Diversity, Structure, and Function of Heritable Adaptive Immunity Sequences in the *Aedes aegypti* Genome. *Curr. Biol.* **27**, 3511–3519.e7 (2017). doi: 10.1016/j.cub.2017.09.067; pmid: 29129531
33. M. Tassetto *et al*., Control of RNA viruses in mosquito cells through the acquisition of vDNA and endogenous viral elements. *eLife* **8**, e41244 (2019). doi: 10.7554/eLife.41244; pmid: 31621580
34. B. Goic *et al*., Virus-derived DNA drives mosquito vector tolerance to arboviral infection. *Nat. Commun.* **7**, 12410 (2016). doi: 10.1038/ncomms12410; pmid: 27580708
35. J. A. Souza-Neto, S. Sim, G. Dimopoulos, An evolutionary conserved function of the JAK-STAT pathway in anti-dengue defense. *Proc. Natl. Acad. Sci. U.S.A.* **106**, 17841–17846 (2009). doi: 10.1073/pnas.0905006106; pmid: 19805194
36. Z. Xi, J. L. Ramirez, G. Dimopoulos, The *Aedes aegypti* toll pathway controls dengue virus infection. *PLOS Pathog.* **4**, e1000098 (2008). doi: 10.1371/journal.ppat.1000098; pmid: 18604274
37. A. B. Barletta *et al*., Microbiota activates IMD pathway and limits Sindbis infection in *Aedes aegypti*. *Parasit. Vectors* **10**, 103 (2017). doi: 10.1186/s13071-017-2040-9; pmid: 28231846
38. G. Carissimo *et al*., Antiviral immunity of *Anopheles gambiae* is highly compartmentalized, with distinct roles for RNA interference and gut microbiota. *Proc. Natl. Acad. Sci. U.S.A.* **112**, E176–E185 (2015). doi: 10.1073/pnas.1412984112; pmid: 25548172
39. R. P. Olmo *et al*., Control of dengue virus in the midgut of *Aedes aegypti* by ectopic expression of the dsRNA-binding protein Loqs2. *Nat. Microbiol.* **3**, 1385–1393 (2018). doi: 10.1038/s41564-018-0268-6; pmid: 30374169
40. J. Rodrigues, F. A. Brayner, L. C. Alves, R. Dixit, C. Barillas-Mury, Hemocyte differentiation mediates innate immune memory in *Anopheles gambiae* mosquitoes. *Science* **329**, 1353–1355 (2010). doi: 10.1126/science.1190689; pmid: 20829487
41. P. A. Nuttall, Wonders of tick saliva. *Ticks Tick Borne Dis.* **10**, 470–481 (2019). doi: 10.1016/j.ttbdis.2018.11.005; pmid: 30459085
42. J. M. C. Ribeiro, B. Arca, From sialomes to the sialoverse: An insight into the salivary potion of blood feeding insects. *Adv. Insect Physiol.* **37**, 59–118 (2009). doi: 10.1016/S0065-2806(09)37002-2
43. C. Stutzer, B. J. Mans, A. R. Gaspar, A. W. Neitz, C. Maritz-Olivier, *Ornithodoros savignyi*: Soft tick apyrase belongs to the 5′-nucleotidase family. *Exp. Parasitol.* **122**, 318–327 (2009). doi: 10.1016/j.exppara.2009.04.007; pmid: 19393241
44. E. Faudry *et al*., *Triatoma infestans* apyrases belong to the 5′-nucleotidase family. *J. Biol. Chem.* **279**, 19607–19613 (2004). doi: 10.1074/jbc.M401681200; pmid: 14985353
45. D. E. Champagne, C. T. Smartt, J. M. Ribeiro, A. A. James, The salivary gland-specific apyrase of the mosquito *Aedes aegypti* is a member of the 5′-nucleotidase family. *Proc. Natl. Acad. Sci. U.S.A.* **92**, 694–698 (1995). doi: 10.1073/pnas.92.3.694; pmid: 7846038
46. J. F. Andersen *et al*., An insight into the sialome of the oriental rat flea, *Xenopsylla cheopis* (Rots). *BMC Genomics* **8**, 102 (2007). doi: 10.1186/1471-2164-8-102; pmid: 17437641
47. J. G. Valenzuela, Y. Belkaid, E. Rowton, J. M. Ribeiro, The salivary apyrase of the blood-sucking sand fly *Phlebotomus papatasi* belongs to the novel *Cimex* family of apyrases. *J. Exp. Biol.* **204**, 229–237 (2001). doi: 10.1242/jeb.204.2.229; pmid: 11136609
48. J. G. Valenzuela, R. Charlab, M. Y. Galperin, J. M. Ribeiro, Purification, cloning, and expression of an apyrase from the bed bug *Cimex lectularius*. A new type of nucleotide-binding enzyme. *J. Biol. Chem.* **273**, 30583–30590 (1998). doi: 10.1074/jbc.273.46.30583; pmid: 9804829
49. E. A. Lerner, J. M. C. Ribeiro, R. J. Nelson, M. R. Lerner, Isolation of maxadilan, a potent vasodilatory peptide from the salivary glands of the sand fly *Lutzomyia longipalpis*. *J. Biol. Chem.* **266**, 11234–11236 (1991). doi: 10.1016/S0021-9258(18)99153-2; pmid: 2040631
50. J. F. Andersen, J. M. Ribeiro, S. K. S. H. P. E. D. B. Feeding, in *Arthropod Vector: Controller of Disease Transmission*, S. Wikel, S. Aksoy, G. Dimopoulos, Eds. (Elsevier, 2017), pp. 51–63.
51. A. F. Mendes-Sousa *et al*., An inhibitor of the alternative pathway of complement in saliva of New world anopheline mosquitoes. *J. Immunol.* **197**, 599–610 (2016). doi: 10.4049/jimmunol.1600020; pmid: 27307559
52. V. C. Barros *et al*., The role of salivary and intestinal complement system inhibitors in the midgut protection of triatomines and mosquitoes. *PLOS ONE* **4**, e6047 (2009). doi: 10.1371/journal.pone.0006047; pmid: 19557176
53. K. R. Tyson, C. Elkins, A. M. de Silva, A novel mechanism of complement inhibition unmasked by a tick salivary protein that binds to properdin. *J. Immunol.* **180**, 3964–3968 (2008). doi: 10.4049/jimmunol.180.6.3964; pmid: 18322205
54. R. R. Cavalcante, M. H. Pereira, N. F. Gontijo, Anti-complement activity in the saliva of phlebotomine sand flies and other haematophagous insects. *Parasitology* **127**, 87–93 (2003). doi: 10.1017/S0031182003003329; pmid: 12885192
55. J. M. Ribeiro, B. J. Mans, B. Arcà, An insight into the sialome of blood-feeding Nematocera. *Insect Biochem. Mol. Biol.* **40**, 767–784 (2010). doi: 10.1016/j.ibmb.2010.08.002; pmid: 20728537
56. I. M. B. Francischetti, A. Sá-Nunes, B. J. Mans, I. M. Santos, J. M. C. Ribeiro, The role of saliva in tick feeding. *Front. Biosci.* **14**, 2051–2088 (2009). doi: 10.2741/3363; pmid: 19273185
57. S. Karim, J. M. Ribeiro, An Insight into the sialome of the Lone Star tick, *Amblyomma americanum*, with a glimpse on

its time dependent gene expression. *PLOS ONE* **10**, e0131292 (2015). doi: 10.1371/journal.pone.0131292; pmid: 26131772
58. L. M. Styer *et al*., Mosquito saliva causes enhancement of West Nile virus infection in mice. *J. Virol.* **85**, 1517–1527 (2011). doi: 10.1128/JVI.01112-10; pmid: 21147918
59. M. Pingen *et al*., Host Inflammatory Response to Mosquito Bites Enhances the Severity of Arbovirus Infection. *Immunity* **44**, 1455–1469 (2016). doi: 10.1016/j.immuni.2016.06.002; pmid: 27332734
60. R. Dey *et al*., Gut Microbes Egested during Bites of Infected Sand Flies Augment Severity of Leishmaniasis via Inflammasome-Derived IL-1β. *Cell Host Microbe* **23**, 134–143.e6 (2018). doi: 10.1016/j.chom.2017.12.002; pmid: 29290574
61. B. S. Schneider, C. Mathieu, R. Peronet, S. Mécheri, *Anopheles stephensi* saliva enhances progression of cerebral malaria in a murine model. *Vector Borne Zoonotic Dis.* **11**, 423–432 (2011). doi: 10.1089/vbz.2010.0120; pmid: 21395422
62. N. Ramamoorthi *et al*., The Lyme disease agent exploits a tick protein to infect the mammalian host. *Nature* **436**, 573–577 (2005). doi: 10.1038/nature03812; pmid: 16049492
63. A. C. Chagas *et al*., Lundep, a sand fly salivary endonuclease increases *Leishmania* parasite survival in neutrophils and inhibits XIIa contact activation in human plasma. *PLOS Pathog.* **10**, e1003923 (2014). doi: 10.1371/journal.ppat.1003923; pmid: 24516388
64. V. Volfova, J. Hostomska, M. Cerny, J. Votypka, P. Volf, Hyaluronidase of bloodsucking insects and its enhancing effect on leishmania infection in mice. *PLOS Negl. Trop. Dis.* **2**, e294 (2008). doi: 10.1371/journal.pntd.0000294; pmid: 18820742
65. J. M. C. Ribeiro, I. Martin-Martin, F. R. Moreira, K. A. Bernard, E. Calvo, A deep insight into the male and female sialotranscriptome of adult *Culex tarsalis* mosquitoes. *Insect Biochem. Mol. Biol.* **95**, 1–9 (2018). doi: 10.1016/j.ibmb.2018.03.001; pmid: 29526772
66. A. K. Hastings *et al*., *Aedes aegypti* NeSt1 Protein Enhances Zika Virus Pathogenesis by Activating Neutrophils. *J. Virol.* **93**, e00395-19 (2019). doi: 10.1128/JVI.00395-19; pmid: 30971475
67. P. Sun *et al*., A mosquito salivary protein promotes flavivirus transmission by activation of autophagy. *Nat. Commun.* **11**, 260 (2020). doi: 10.1038/s41467-019-14115-z; pmid: 31937766
68. V. D. Atayde *et al*., Exosome Secretion by the Parasitic Protozoan *Leishmania* within the Sand Fly Midgut. *Cell Rep.* **13**, 957–967 (2015). doi: 10.1016/j.celrep.2015.09.058; pmid: 26565909
69. E. Giraud *et al*., *Leishmania* proteophosphoglycans regurgitated from infected sand flies accelerate dermal wound repair and exacerbate leishmaniasis via insulin-like growth factor 1-dependent signalling. *PLOS Pathog.* **14**, e1006794 (2018). doi: 10.1371/journal.ppat.1006794; pmid: 29352310
70. M. Labuda *et al*., An antivector vaccine protects against a lethal vector-borne pathogen. *PLOS Pathog.* **2**, e27 (2006). doi: 10.1371/journal.ppat.0020027; pmid: 16604154
71. J. G. Valenzuela *et al*., Toward a defined anti-*Leishmania* vaccine targeting vector antigens: Characterization of a protective salivary protein. *J. Exp. Med.* **194**, 331–342 (2001). doi: 10.1084/jem.194.3.331; pmid: 11489952
72. F. Oliveira *et al*., A sand fly salivary protein vaccine shows efficacy against vector-transmitted cutaneous leishmaniasis in nonhuman primates. *Sci. Transl. Med.* **7**, 290ra90 (2015). doi: 10.1126/scitranslmed.aaa3043; pmid: 26041707
73. A. Sajid *et al*., mRNA vaccination induces tick resistance and prevents transmission of the Lyme disease agent. *Sci. Transl. Med.* **13**, eabj9827 (2021). doi: 10.1126/scitranslmed.abj9827; pmid: 34788080
74. S. M. Dragovic *et al*., Immunization with AgTRIO, a Protein in Anopheles Saliva, Contributes to Protection against Plasmodium Infection in Mice. *Cell Host Microbe* **23**, 523–535.e5 (2018). doi: 10.1016/j.chom.2018.03.008; pmid: 29649443
75. R. Uraki *et al*., *Aedes aegypti* AgBR1 antibodies modulate early Zika virus infection of mice. *Nat. Microbiol.* **4**, 948–955 (2019). doi: 10.1038/s41564-019-0385-x; pmid: 30858571
76. R. Uraki, A. K. Hastings, D. E. Brackney, P. M. Armstrong, E. Fikrig, AgBR1 antibodies delay lethal *Aedes aegypti*-borne West Nile virus infection in mice. *NPJ Vaccines* **4**, 23 (2019). doi: 10.1038/s41541-019-0120-x; pmid: 31312526
77. J. E. Manning *et al*., Safety and immunogenicity of a mosquito saliva peptide-based vaccine: A randomised, placebo-controlled, double-blind, phase 1 trial. *Lancet* **395**, 1998–2007 (2020). doi: 10.1016/S0140-6736(20)31048-5; pmid: 32534628
78. A. P. Souza *et al*., Using recombinant proteins from *Lutzomyia longipalpis* saliva to estimate human vector exposure in visceral Leishmaniasis endemic areas. *PLOS Negl. Trop. Dis.* **4**, e649 (2010). doi: 10.1371/journal.pntd.0000649; pmid: 20351785
79. C. Rizzo *et al*., Humoral response to the *Anopheles gambiae* salivary protein gSG6: A serological indicator of exposure to Afrotropical malaria vectors. *PLOS ONE* **6**, e17980 (2011). doi: 10.1371/journal.pone.0017980; pmid: 21437289
80. E. Elanga Ndille *et al*., First attempt to validate human IgG antibody response to Nterm-34kDa salivary peptide as biomarker for evaluating exposure to *Aedes aegypti* bites. *PLOS Negl. Trop. Dis.* **6**, e1905 (2012). doi: 10.1371/journal.pntd.0001905; pmid: 23166852
81. C. Teixeira *et al*., Discovery of markers of exposure specific to bites of *Lutzomyia longipalpis*, the vector of *Leishmania infantum chagasi* in Latin America. *PLOS Negl. Trop. Dis.* **4**, e638 (2010). doi: 10.1371/journal.pntd.0000638; pmid: 20351786
82. L. Willen, P. Mertens, P. Volf, Evaluation of the rSP03B sero-strip, a newly proposed rapid test for canine exposure to *Phlebotomus perniciosus*, vector of *Leishmania infantum*. *PLOS Negl. Trop. Dis.* **12**, e0006607 (2018). doi: 10.1371/journal.pntd.0006607; pmid: 30071017
83. S. Marzouki *et al*., Validation of Recombinant Salivary Protein PpSP32 as a Suitable Marker of Human Exposure to *Phlebotomus papatasi*, the Vector of *Leishmania major* in Tunisia. *PLOS Negl. Trop. Dis.* **9**, e0003991 (2015). doi: 10.1371/journal.pntd.0003991; pmid: 26368935
84. E. Dama *et al*., *In silico* identification of a candidate synthetic peptide ($Tsgf_{118–43}$) to monitor human exposure to tsetse flies in West Africa. *PLOS Negl. Trop. Dis.* **7**, e2455 (2013). doi: 10.1371/journal.pntd.0002455; pmid: 24086785
85. A. Schwarz *et al*., Immunogenic salivary proteins of *Triatoma infestans:* Development of a recombinant antigen for the detection of low-level infestation of triatomines. *PLOS Negl. Trop. Dis.* **3**, e532 (2009). doi: 10.1371/journal.pntd.0000532; pmid: 19841746
86. F. Alarcon-Chaidez *et al*., Confirmation of tick bite by detection of antibody to *Ixodes* calreticulin salivary protein. *Clin. Vaccine Immunol.* **13**, 1217–1222 (2006). doi: 10.1128/CVI.00201-06; pmid: 16928887
87. P. M. Drame *et al*., Human antibody response to *Anopheles gambiae* saliva: An immuno-epidemiological biomarker to evaluate the efficacy of insecticide-treated nets in malaria vector control. *Am. J. Trop. Med. Hyg.* **83**, 115–121 (2010). doi: 10.4269/ajtmh.2010.09-0684; pmid: 20595489
88. C. M. A. Carareto *et al*., Testing transposable elements as genetic drive mechanisms using Drosophila P element constructs as a model system. *Genetica* **101**, 13–33 (1997). doi: 10.1023/A:1018339603370; pmid: 9465407
89. M. A. Sperança, M. L. Capurro, Perspectives in the control of infectious diseases by transgenic mosquitoes in the post-genomic era—A review. *Mem. Inst. Oswaldo Cruz* **102**, 425–433 (2007). doi: 10.1590/S0074-02762007005000054; pmid: 17612761
90. L. Alphey, Can CRISPR-Cas9 gene drives curb malaria? *Nat. Biotechnol.* **34**, 149–150 (2016). doi: 10.1038/nbt.3473; pmid: 26849518
91. M. de Lara Capurro *et al*., Virus-expressed, recombinant single-chain antibody blocks sporozoite infection of salivary glands in Plasmodium gallinaceum-infected Aedes aegypti. *Am. J. Trop. Med. Hyg.* **62**, 427–433 (2000). doi: 10.4269/ajtmh.2000.62.427; pmid: 11220756
92. Z. N. Adelman, Z. Tu, Control of mosquito-borne infectious diseases: Sex and gene drive. *Trends Parasitol.* **32**, 219–229 (2016). doi: 10.1016/j.pt.2015.12.003; pmid: 26897660
93. K. Kyrou *et al*., A CRISPR-Cas9 gene drive targeting *doublesex* causes complete population suppression in caged *Anopheles gambiae* mosquitoes. *Nat. Biotechnol.* **36**, 1062–1066 (2018). doi: 10.1038/nbt.4245; pmid: 30247490
94. A. Hammond *et al*., A CRISPR-Cas9 gene drive system targeting female reproduction in the malaria mosquito vector *Anopheles gambiae*. *Nat. Biotechnol.* **34**, 78–83 (2016). doi: 10.1038/nbt.3439; pmid: 26641531
95. L. Yakob, L. Alphey, M. B. Bonsall, *Aedes aegypti* control: The concomitant role of competition, space and transgenic technologies. *J. Appl. Ecol.* **45**, 1258–1265 (2008). doi: 10.1111/j.1365-2664.2008.01498.x
96. L. Alphey, A. McKemey, D. Nimmo, M. N. Oviedo, R. Lacroix, K. Matzen, C. Beech, in *Global Health Impacts of Vector-Borne Diseases: Workshop Summary* (The National Academies Press, 2016), pp. 106–125.
97. S. Wang *et al*., Driving mosquito refractoriness to *Plasmodium falciparum* with engineered symbiotic bacteria. *Science* **357**, 1399–1402 (2017). doi: 10.1126/science.aan5478; pmid: 28963255
98. R. V. Durvasula, R. K. Sundaram, C. Cordon-Rosales, P. Pennington, B. Beard, in *Insect Symbiosis*, K. Bourtzis, T. A. Miller, Eds. (CRC Press, 2003), pp. 83–95.
99. C. B. Beard *et al*., Bacterial symbiosis and paratransgenic control of vector-borne Chagas disease. *Int. J. Parasitol.* **31**, 621–627 (2001). doi: 10.1016/S0020-7519(01)00165-5; pmid: 11334952
100. P. Kittayapong, P. Mongkalangoon, V. Baimai, S. L. O'Neill, Host age effect and expression of cytoplasmic incompatibility in field populations of *Wolbachia*-superinfected *Aedes albopictus*. *Heredity* **88**, 270–274 (2002). doi: 10.1038/sj.hdy.6800039; pmid: 11920134
101. L. A. Moreira *et al*., A *Wolbachia* symbiont in *Aedes aegypti* limits infection with dengue, Chikungunya, and *Plasmodium*. *Cell* **139**, 1268–1278 (2009). doi: 10.1016/j.cell.2009.11.042; pmid: 20064373
102. H. A. Flores, S. L. O'Neill, Controlling vector-borne diseases by releasing modified mosquitoes. *Nat. Rev. Microbiol.* **16**, 508–518 (2018). doi: 10.1038/s41579-018-0025-0; pmid: 29777177
103. E. P. Caragata, H. L. C. Dutra, L. A. Moreira, Exploiting Intimate Relationships: Controlling Mosquito-Transmitted Disease with *Wolbachia*. *Trends Parasitol.* **32**, 207–218 (2016). doi: 10.1016/j.pt.2015.10.011; pmid: 26776329
104. B. Lovett *et al*., Transgenic *Metarhizium* rapidly kills mosquitoes in a malaria-endemic region of Burkina Faso. *Science* **364**, 894–897 (2019). doi: 10.1126/science.aaw8737; pmid: 31147521
105. D. G. Paton *et al*., Exposing *Anopheles* mosquitoes to antimalarials blocks *Plasmodium* parasite transmission. *Nature* **567**, 239–243 (2019). doi: 10.1038/s41586-019-0973-1; pmid: 30814727

ACKNOWLEDGMENTS

We thank J. Andersen, S. Kamhawi, A. Molina-Cruz, F. Oliveira, and A. Costero for critical evaluation of this work; B. Brown (NIH Library Writing Center) for manuscript editing assistance; and R. Kissinger (RTB/RML/NIAID) for figure preparation. **Funding:** The authors were supported by the Intramural Research Program of the National Institute of Allergy and Infectious Diseases. **Competing interests:** The authors have several patents related to this Review, including USPTO nos. 5,397,772; 6,500,420; 6,749,855; 7,078,508; 7,153,947; 7,388,089; 7,485,306; 8,383,589; 8,603,808; 8,980,859; and 8,772,238 and the international application PCT/US2018/019770. The authors declare no other competing interests. **License information:** Copyright © 2022 the authors, some rights reserved; exclusive licensee American Association for the Advancement of Science. No claim to original US government works. https://www.science.org/about/science-licenses-journal-article-reuse

Submitted 1 June 2020; accepted 25 August 2022
10.1126/science.abc2757

RESEARCH ARTICLE SUMMARY

AGING

Sex- and age-dependent genetics of longevity in a heterogeneous mouse population

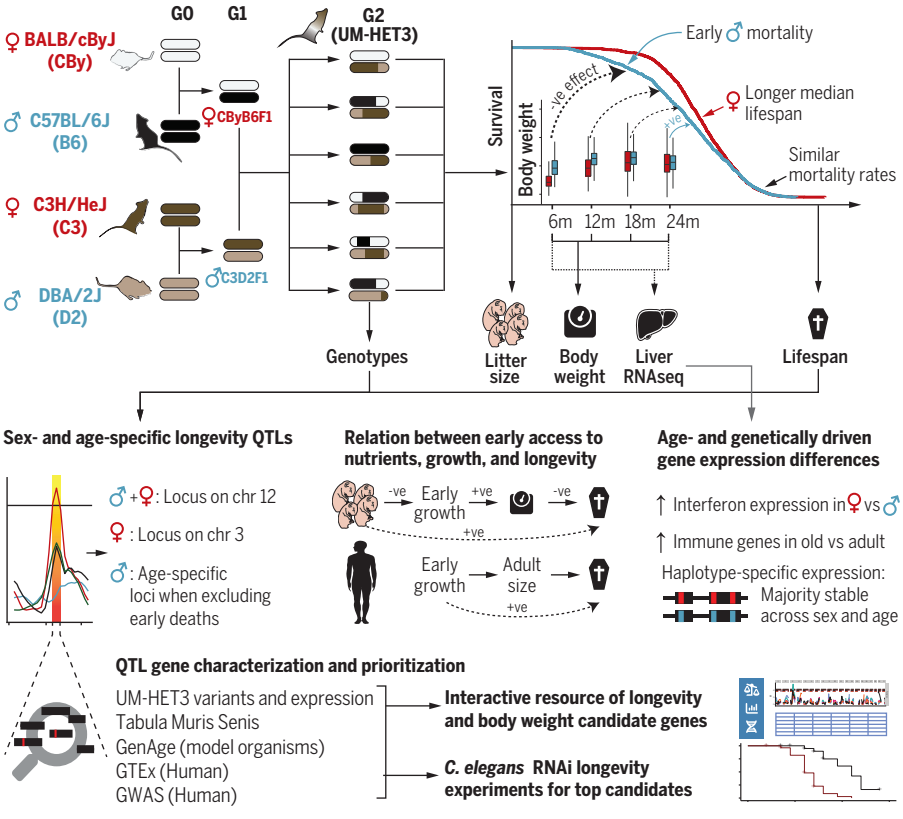
Maroun Bou Sleiman†, Suheeta Roy†, Arwen W. Gao, Marie C. Sadler, Giacomo V. G. von Alvensleben, Hao Li, Saunak Sen, David E. Harrison, James F. Nelson, Randy Strong, Richard A. Miller, Zoltán Kutalik, Robert W. Williams*, Johan Auwerx*

INTRODUCTION: Aging is the progressive decline in physical, mental, and reproductive capacities that is accompanied by multiple morbidities and associated with increased mortality. Despite advances in identifying aging pathways and drugs that extend life span in model systems, an integrative understanding of the interplay between genetics, sex, and environment in aging and life-span determination is largely lacking.

RATIONALE: Although there is no single measure of aging, studies depend on surrogate or related traits such as longevity, life history, age-related disease onset, and physiological markers. Characterizing genetic and nongenetic determinants of longevity at the population level may identify genes and pathways involved in aging, providing avenues for targeted anti-aging therapies and extension of healthy longevity. We set out to query genetic regulators of longevity in a total of 3276 UM-HET3 mice used in longevity studies by the National Institute on Aging's Interventions Testing Program (NIA ITP). We interrogated whether the genetic basis of longevity is sex and age dependent, and whether nongenetic factors such as litter size and the effect of early access to nutrients on growth contribute to longevity determination. We characterized the age- and genotype-dependent changes in liver gene expression in mice from the same genetic cross. Finally, we integrated these results with orthogonal datasets to obtain a resource of prioritized candidate genetic loci and genes for further investigation.

RESULTS: When jointly analyzing males and females, we obtained a single, previously described, longevity locus on chromosome 12. However, when analyzed separately, males and females had distinct genetic determinants of longevity. In females, a single locus on chromosome 3 was uncovered, whereas in males, loci were detected only when early deaths were excluded, suggesting that some genetic variations had an effect on longevity beyond a certain age. Increased body weight associated with earlier death and some of the variation in adult body weight are explained by litter size. Hence, early access to nutrients may affect mouse longevity through its effect on growth. We used Mendelian randomization to replicate the relationships between early growth, adult size, and longevity in humans. To prioritize genes under the longevity loci, we profiled liver gene expression of adult and old mice to look for sex-, age-, and genetically driven differences in expression. Female livers had higher interferon-related gene expression, and older mice had overexpressed immune-related genes. Genetic regulation of gene expression was assessed, with the majority being conserved across sexes and age. We combined our results with data from multiple sources in model organisms and humans to compile an interactive resource for conserved longevity gene prioritization (https://www.systems-genetics.org/itp-longevity). Worm life-span experiments validated some of the most highly scoring genes and identified *Hipk1*, *Ddost*, *Hspg2*, *Fgd6*, and *Pdk1* as candidates.

CONCLUSION: This study provided insights into determinants of longevity, highlighting genetic mediators that can be sex or age specific, and nongenetic effects such as early access to nutrients. The combined body of information assembled from this study and the external data constitute a hypothesis-building resource for future studies on, and therapies for, aging, age-related disease, and longevity. ■



Genetic analyses in UM-HET3 mice used in the Interventions Testing Program highlight sex- and age-specific longevity loci. Body weight associates with longevity, as does litter size, through its effect on body weight. Mendelian randomization in humans recapitulated these relationships between early growth and life span. Gene expression analyses, cross-species integration, and *Caenorhabditis elegans* life-span experiments highlight candidate longevity genes and provide a resource for further investigation.

*Corresponding author. Email: labwilliams@gmail.com (R.W.W.); admin.auwerx@epfl.ch (J.A.)
The list of author affiliations is available in the full article online.
†These authors contributed equally to this work.
Cite this article as M. Bou Sleiman *et al.*, *Science* **377**, eabo3191 (2022). DOI: 10.1126/science.abo3191

READ THE FULL ARTICLE AT
https://doi.org/10.1126/science.abo3191

RESEARCH ARTICLE

AGING

Sex- and age-dependent genetics of longevity in a heterogeneous mouse population

Maroun Bou Sleiman[1]†, Suheeta Roy[2]†, Arwen W. Gao[1], Marie C. Sadler[3,4,5], Giacomo V. G. von Alvensleben[1], Hao Li[1], Saunak Sen[6], David E. Harrison[7], James F. Nelson[8], Randy Strong[8,9], Richard A. Miller[10], Zoltán Kutalik[3,4,5], Robert W. Williams[2]*, Johan Auwerx[1]*

DNA variants that modulate life span provide insight into determinants of health, disease, and aging. Through analyses in the UM-HET3 mice of the Interventions Testing Program (ITP), we detected a sex-independent quantitative trait locus (QTL) on chromosome 12 and identified sex-specific QTLs, some of which we detected only in older mice. Similar relations between life history and longevity were uncovered in mice and humans, underscoring the importance of early access to nutrients and early growth. We identified common age- and sex-specific genetic effects on gene expression that we integrated with model organism and human data to create a hypothesis-building interactive resource of prioritized longevity and body weight genes. Finally, we validated *Hipk1*, *Ddost*, *Hspg2*, *Fgd6*, and *Pdk1* as conserved longevity genes using *Caenorhabditis elegans* life-span experiments.

Aging is a time-dependent functional decline in molecular, cellular, and organismal homeostasis that is affected by multiple environmental and genetic factors (*1*). Genetic studies, such as loss or gain of function or forward genetic screens, have identified many of its conserved genes and mechanisms (*2*, *3*). From the metabolic perspective, nutrient-sensing pathways such as the growth hormone and insulin-like growth factor axis (GH/IGF1), target of rapamycin (TOR), adenosine 5´-monophosphate (AMP)–activated protein kinase (AMPK), and sirtuins control aging or affect longevity (*1*, *3*). In addition to metabolic decline, other features such as loss of proteostasis, increased genome instability, changes in epigenetic marks, and alterations in telomere length have been proposed to promote aging (*1*, *4*, *5*). Here we used an unbiased genetic and molecular cross-species approach to highlight drivers of aging, starting with genetic mapping of loci that modulate variation in life span in a large multicenter and multiyear four-way intercross of male and female untreated control mice from the Interventions Testing Program (ITP).

[1]Laboratory of Integrative Systems Physiology, Institute of Bioengineering, École Polytechnique Fédérale de Lausanne, Lausanne 1015, Switzerland. [2]Department of Genetics, Genomics and Informatics, University of Tennessee Health Science Center (UTHSC), Memphis, TN 38163, USA. [3]Institute of Primary Care and Public Health (Unisante), University of Lausanne, Lausanne 1011, Switzerland. [4]Swiss Institute of Bioinformatics, Lausanne 1015, Switzerland. [5]Department of Computational Biology, University of Lausanne, Lausanne 1015, Switzerland. [6]Department of Preventive Medicine, University of Tennessee Health Science Center, Memphis, TN 38163, USA. [7]The Jackson Laboratory, Bar Harbor, ME 04609, USA. [8]Barshop Center for Longevity Studies at the University of Texas Health Science Center at San Antonio, San Antonio, TX 78229, USA. [9]South Texas Veterans Healthcare System, San Antonio, TX 78229, USA. [10]Department of Pathology, University of Michigan Geriatrics Center, Ann Arbor, MI 48109-2200, USA.
†These authors contributed equally to this work.
*Corresponding author. Email: labwilliams@gmail.com (R.W.W.); admin.auwerx@epfl.ch (J.A.)

Multicenter and multiyear analysis identifies sex- and age-specific longevity loci

The ITP was funded by the National Institute on Aging starting in 2004 to test putative positive effects of dietary and drug interventions on life span (healthy aging) (*6*, *7*). For each intervention, a large and sex-balanced subcohort of control animals was aged until close to natural death along with the treated cases (*8*). All controls and cases were from a four-way intercross made by mating BALB/cByJ × C57BL/6J F_1 females—JAX Stock #100009—to C3H/HeJ × DBA/2J F_1 males—JAX Stock # 100004—the so-called UM-HET3 cross. Animals were bred at three independent testing sites (Jackson Laboratory, University of Michigan, and University of Texas Health Science Center at San Antonio) using F_1 animals from the Jackson Laboratory. The combination of a high level of genetic heterogeneity, very large family sample size, and balanced replication across sites has led to an unprecedented resource of longevity research (*9*). Tail biopsies were systematically collected from almost all mice, thus enabling the genotyping and subsequent genetic analyses presented here (*8*) (Fig. 1A).

We generated genotype data on 3276 mice, including 2356 control and 920 drug-treated mice (fig. S1, A and B, and data S1). The treated cases included animals subjected to 20 different drugs that had no population-level influence on longevity; this complexity renders the statistical inference of genetic and drug effects more challenging, and we therefore used this group in combination with the controls in supplementary quantitative trait locus (QTL) analyses. In addition to being a genetically heterogeneous panel with a wide range of variation in longevity and body weight, the cohort (year of birth) and site have effects on body weight and longevity (most prominently in males) despite all efforts of standardization (*10*) (fig. S1, C and D). To avoid biases due to these nongenetic effects, we accounted for center and year in all analyses.

As previously shown in the UM-HET3 cross (*10*), females have a higher median life span than males (female median = 886 days, 95% confidence interval (CI) [871–897], male median = 836 days, 95% CI [816–851]), with the largest difference in the survival curves attributable to increased early mortality in males between ages of about 300 and 800 days. Between 800 and 1000 days, females have a higher rate of mortality (fig. S1B). As of 1000 days, mortality rates are similar, indicating similar hazard rates at later ages and similar maximum longevity (fig. S1, A to C).

Given such age- and sex-specific hazards, we asked whether segregating loci affect life span in both sexes at all ages or whether sex- and age-specific effects are predominant (fig. S2). To determine whether genetic loci are sex specific, we performed four QTL mapping analyses: for each sex separately, and for the combined dataset with and without sex-by-genotype interaction term. To accommodate the multicenter and multiyear study design, we used mixed-effects Cox models with site and cohort as random effects and sex as fixed effect when appropriate. To assess the statistical significance of the results, we calculated empirical p values for the associations based on permutations (*8*) and characterized QTLs with $p < 0.2$.

A genome scan including both sexes identified a single QTL at chromosome 12, which may be a previously described locus in the UM-HET3 and BXD cohorts (Fig. 1B, data S2, and table S1) (*11*, *12*). We also detect one significant female-specific locus at chromosome 3 ($p = 0.006$) but no significant exclusive male loci. There is no evidence for sex-by-haplotype interaction, which may be related to power limitations due to sample size.

Early male mortality raised the possibility that some early pathologies or behavioral factors, possibly genetically driven, may mask genetic effects on longevity. Previously, this potential confounding was dealt with through removal of data from mice with early deaths, and this strategy has proven to be useful in identifying longevity-associated QTLs (*11*). We therefore performed successive QTL scans by removing increasing proportions of early deaths (Fig. 1C). To define peaks in these scans based on smaller subsets of the mice, we also relaxed the significance thresholds from 0.05 to 0.2. This approach revealed that the female chromosome 3

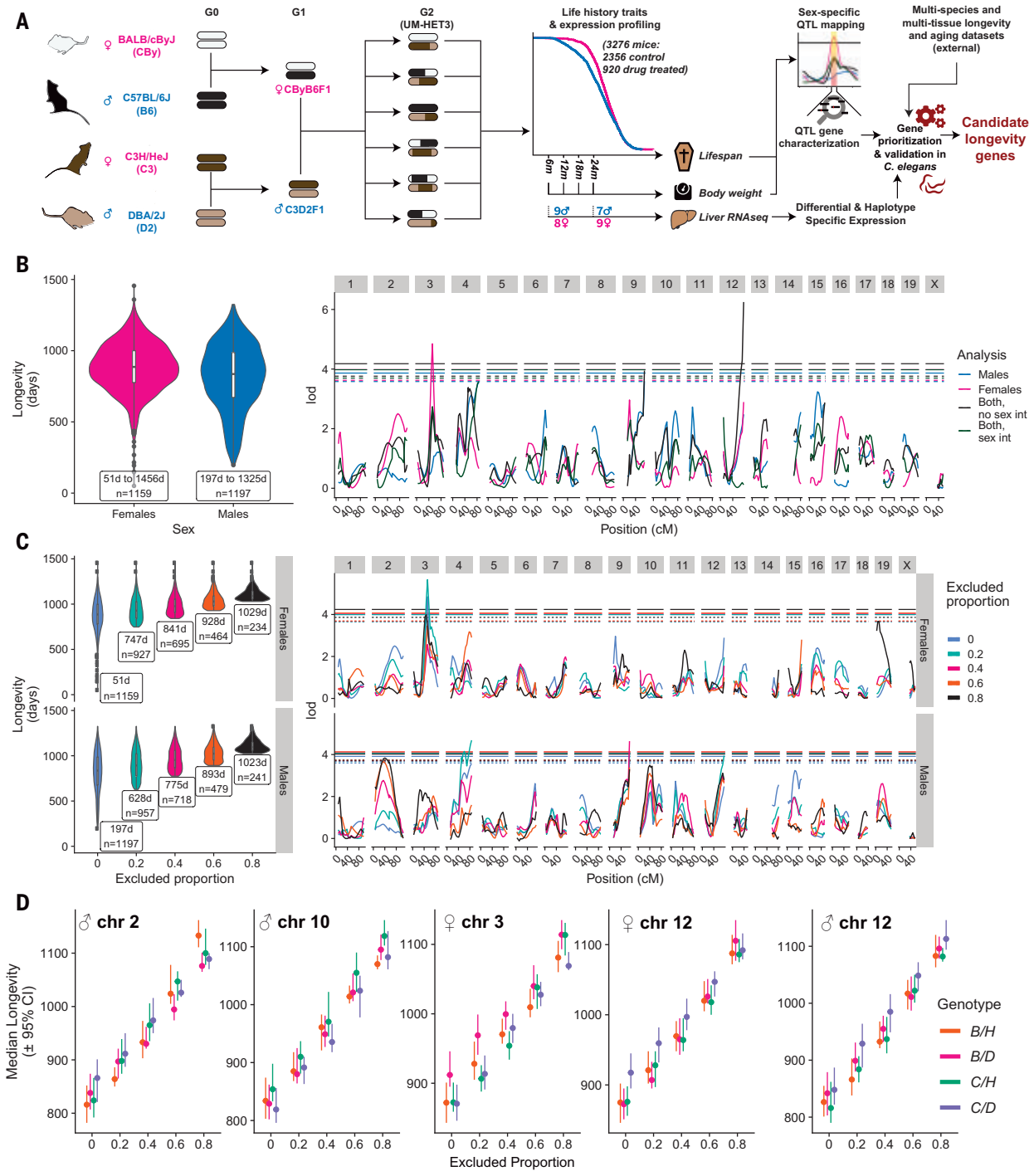


Fig. 1. QTL mapping of longevity identifies sex- and age-specific loci. (**A**) General scheme of the UM-HET3 four-way intercross and the end points examined in this study. The UM-HET3 mice come from a cross of a female (BALB/cByJ × C57BL/6J) F_1 and a male (C3H/HeJ × DBA/2J) F_1. The 3276 mice in this study are either controls (n = 2356) or were treated with 20 drugs that had no population-level effect on longevity (n = 920, data S1), from the NIA ITP conducted at two different sites (UT and UM) and spanning years 2004 to 2011. Natural life span, body weight, and DNA were collected from these mice. A separate UM-HET3 cohort (Glenn Center, UM) was used to obtain livers from young and old males and females for RNA sequencing to study sex- and age-related gene expression changes and haplotype-specific expression. (**B**) (Left) Distribution of female and male life spans. (Right) QTL mapping results for longevity in four analyses. The "Both, no sex int" includes all mice with sex as a fixed effect and site as a random effect and cohort year as a nested random effect within site. The "Both, sex int" tests for sex-by-haplotype interactions. The Male and Female models are restricted to one sex. Solid and dashed horizontal lines indicate permutation-based significance thresholds for α = 0.05 and 0.2, respectively. (**C**) QTL scans for life span performed after excluding different percentiles of mice that die early. (Left) Distribution of life-span values after exclusion of mice. The labels indicate the minimal life span in days and the number of mice. (Right) Overlaid QTL scans, colored by truncation level for females and males. Solid and dashed horizontal lines indicate permutation-based significance thresholds as in (B). (**D**) Median longevity of mice stratified by haplotype at male loci on chromosomes 2 and 10, female loci on chromosomes 3, and male and females at the chromosome 12 locus, after exclusion of different proportions of early deaths. Alleles *B*, *C*, *H*, and *D* correspond to CBy, B6, C3, and D2 strains, respectively.

QTL is robust to removal of early deaths as it only slightly decreased in significance (empirical p value = 0.006 and 0.081 when 0 and 80% of mice are removed, respectively) even upon removal of 80% of early deaths—that is, when only 20% of the longest-lived female mice were retained. One female-specific locus emerged on chromosome 19 only in the 20% of longest-lived females.

In contrast to females, multiple male loci increased in significance upon exclusion of early deaths. Specifically, the most significant locus is on chromosome 4 (at 20% truncation, empirical p value = 0.017) followed by less significant ones on chromosomes 2, 9, 10, and 12 (at 60, 20, 80, and 20% truncation, respectively; $0.05 < p < 0.2$). Upon observing the longevity distribution of mice carrying different allelic combinations at the chromosome 2 locus, we could appreciate how allelic effects become significant when early-death animals were progressively removed (Fig. 1D). Male mice carrying the *B/H* allele combination in the chromosome 2 locus do not differ from the whole male population ($p = 1$, Fig. 1D, left panel), but are the longest lived as we removed earlier deaths ($p = 0.137$ at 80% truncation). The age-specific and male-specific chromosome 10 locus ($p = 1$ and 0.185 at 0 and 80% truncation, respectively) overlaps with another previously described UM-HET3 longevity locus (*11*). The chromosome 12 locus detected in males overlaps with the one that we found in the analysis incorporating males and females and already identified in UM-HET3 (*11*). When examining sex-specific scans, the *C/D* allele combination offers an advantage in males (Fig. 1C, lowest empirical p value = 0.06 at 20% truncation in males) but not in females (Fig. 1C, lowest empirical p value = 0.357, no truncation).

To further explore whether QTLs overlap with known genetic associations, we looked for correspondence with known longevity, growth, and body size QTLs in the Mouse Genome Informatics database (*13*) (table S1). Except for the chromosome 10 and 12 loci in males, there is no overlap with longevity or life-span loci, which is not surprising given the general dearth of longevity QTLs likely due to limited power of existing studies. Instead, we found extensive overlap with known growth or body weight loci, pointing to the importance of genetic determination of growth rates on longevity.

Interplay between early growth, size, and longevity in mice and humans

The relation between growth, body size, and longevity has been extensively studied (*10*, *14*, *15*). This and our observation of overlap between longevity loci and growth QTLs prompted us to explore this relation further. At the phenotypic level, we observed an inverse relationship between early body weight and longevity that is more pronounced in males (Fig. 2, A and B). For instance, the hazard ratio of a 10-g increase at 6 months is ~1.8 and ~1.20 in males and females, respectively (mixed-effects Cox model p values < 0.00001 and 0.0016). This relation progressively decreased in magnitude, yet remained detectable until 18 months. At 24 months, the relation disappeared in females and reversed in males, suggesting that lower body weight at an advanced age (between 18 and 24 months) may be a predictor of earlier mortality in males as they lose weight prior to death. These observations are not only in agreement with studies in UM-HET3 mice (*10*, *14*) but also with findings in humans, in which higher childhood weight is associated with higher morbidity and mortality, especially in males (*16*, *17*), and weight loss at older ages is associated with increased frailty and mortality risk (*18*, *19*).

Before exploring the genetic determinants of body weight variation, we characterized the effects of nongenetic factors on body weight and whether they can contribute to variation in longevity in the UM-HET3 mice. Because the differences in body weight can be attributed to genetic and environmental factors, we wondered whether early access to nutrients as a result of litter size differences could affect growth, and consequently adult body weight and longevity (*20*). We used litter size information of a subset of 1575 control mice aged at the University of Texas, San Antonio. Indeed, a significant negative effect of litter size on male and female body weights at 6, 12, 18, and 24 months of age was observed, indicating long-lasting effects of early growth due to differential access to nutrients ($p < 0.05$ for female 24-month body weight, $p < 0.001$ for the rest; fig. S3, A and B). Furthermore, we observed an effect of litter size on longevity, apparently acting through body weight, as smaller litter size is associated with higher weight, which, in turn, is associated with shorter life span (*8*) (Fig. 2C). We therefore investigated whether including body weight and litter size as covariates in a longevity QTL scan would affect the results. Life span was remapped for males and females separately, without body weight, with body weight at 6 months (an age at which the relation is strongest), and with body weight at 6 months and litter size (fig. S3C). This analysis was performed for a total of 1122 control mice of both sexes, which resulted in similar linkages to the analysis excluding litter size as a covariate, albeit with reduced significance (highest peak in females is at chromosome 3 with empirical p value = 0.399). Logarithm of the odds (LOD) scores and significance are reduced by inclusion of body weight only in males. The inclusion of litter size in addition to body weight has little to no effect, in agreement with the mediation analysis in which the effect of litter size on longevity is mediated by body weight. Although the individual findings and pairwise relationships between litter size-growth and growth-longevity are not novel, here we provided an integrated view in a large and genetically heterogeneous mouse population.

We next asked if these relations are specific to UM-HET3 mice and whether we could establish similar associations in humans. We applied a Mendelian randomization (MR) strategy to large human datasets. Specifically, we assessed whether early and adult body size or height relate to parental longevity (a proxy of the individual's longevity) and indeed, early body weight at 10 years, height at 10 years, adult body mass index (BMI), but not adult height have potential negative effects on longevity (Fig. 2D) (*21*–*23*). An interesting finding is that the early body size effect is completely mediated by adult BMI (Fig. 2E). Height, by contrast, has a more complicated relationship with longevity, likely because it is also associated with higher socioeconomic status, which itself extends life span, and may be affected by population stratification (Fig. 2F) (*24*). Faster early growth may therefore be detrimental, but adult height may have antagonistic effects on longevity as it is jointly affected by growth and socioeconomic status.

To further deconstruct this, we performed an MR analysis for early and late height while excluding shared instrumental variables; that is, we used genetic instruments that are specific to each stage (Fig. 2G). Notably, the opposing effects become larger and more significant, supporting the hypothesis of distinct antagonistic age-specific effects of early and adult height on longevity. Finally, we analyzed whether the early height's effect is mediated by adult BMI in a manner similar to early weight through MR mediation and found that this is not the case, supporting a distinct relationship between early weight and height and longevity (Fig. 2H). An analogous investigation is not possible in our mouse population, as only body weight is available and not length or adiposity. Taken together, the interplay between different life-history traits that is similar between mice and humans shows that determinants of longevity can be decomposed into distinct genetic factors acting on other life-history traits, as well as nongenetic factors such as early growth, which may be controlled by early access and use of nutrients.

Analysis of body weight QTLs in relation to the longevity QTLs

Given the conserved age-dependent relationship between longevity and body weight across sexes and that this is also the case in humans, we explored whether variation in these traits is explained by the same genetic alleles. If that is the case, one explanation would be that the same genes may be universally affecting

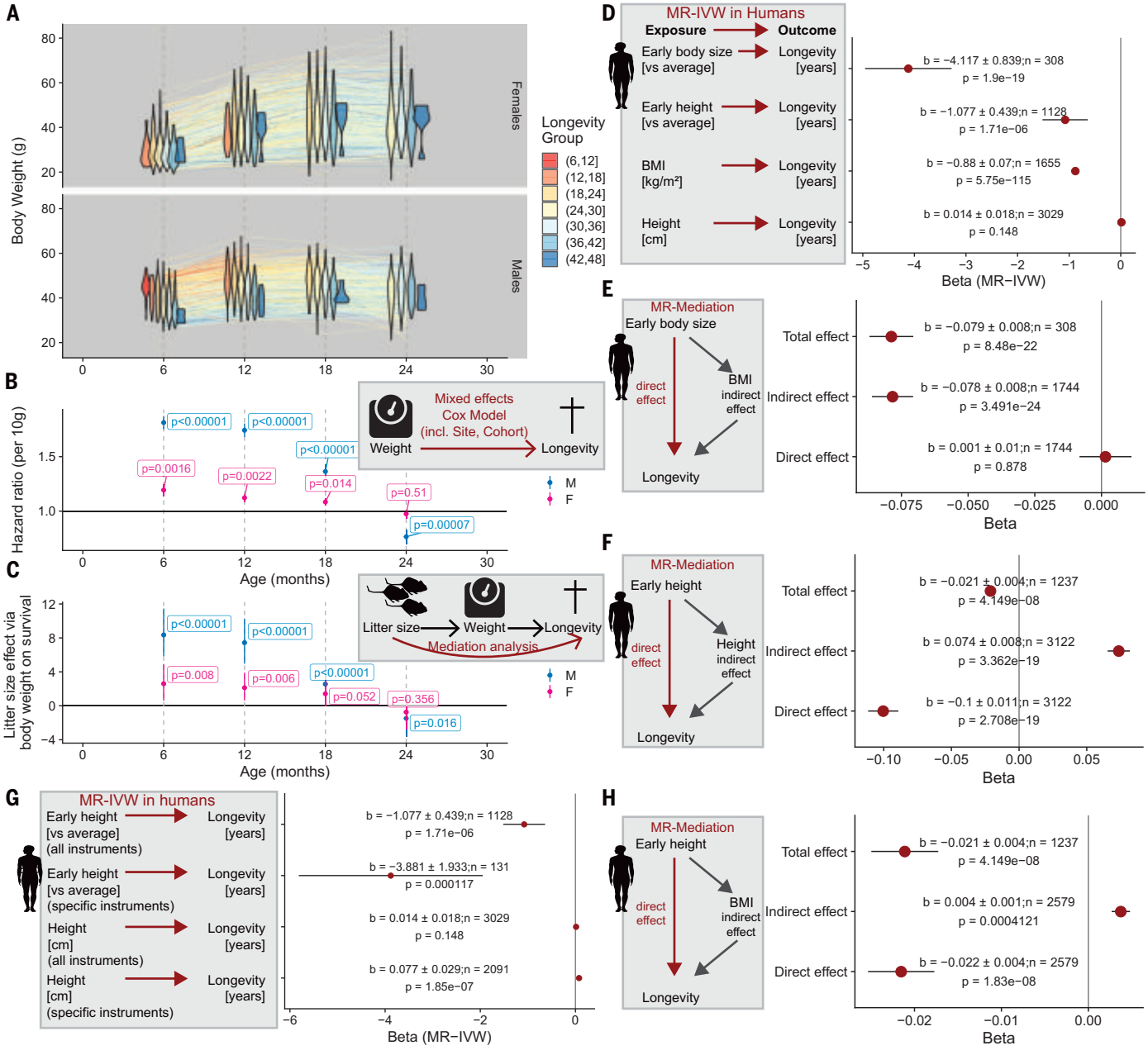


Fig. 2. Interplay between early growth, size, and longevity in mice and humans. (**A**) Inverse relationship between body weight and longevity is stronger in males than in females and at younger ages. Body weight trajectories of UM-HET3 mice, separated by sex. Each line represents body weight evolution of a single mouse. Body weight measurements were performed at 6, 12, 18, and 24 months, which are marked by vertical dashed gray lines. Mice are split into seven groups and colored on the basis of their longevity. Violin plots show the distribution of body weight at the measured ages. (**B**) Mixed-effects Cox model hazard ratio of an increase in 10 g in body weight in males and females, as well as the 95% confidence interval and *p* value (*8*). (**C**) Effect of litter size on survival mediated by body weight at different ages using mediation analysis (b indicates effect size, and n is the number of instruments). (**D**) Inverse variance weighted Mendelian randomization results for body weight and height and parental life span (*22*). Early body size and heights are the comparative body weight and heights at age 10 of ~500,000 individuals from the UK Biobank (data fields 1687 and 1697, respectively). BMI (body mass index) is from ~700,000 individuals (*23*). (**E**) MR-Mediation analysis shows that the effect of early body weight is completely mediated by BMI. (**F**) MR-Mediation shows that the effect of early height is not mediated by height. (**G**) Because adult and early height share genetic associations (or instrumental variables, IVs), MR was performed with the IVs that are specific to each phenotype, excluding the common IVs, further enhancing the opposing effects of early and adult height. (**H**) MR-Mediation shows that the effect of early height is not mediated by BMI.

different facets of aging, for which body weight and longevity act as surrogate traits. For that, we performed QTL mapping in the UM-HET3 mice with a total of four models, as we had done for longevity (Fig. 3A, and fig. S4A).

We detected sex-specific body weight QTLs that are conserved at different ages. For instance, we identified a female body weight QTL at chromosome 7 at all ages, and one at chromosome 6 that is significant until 18 months ($p < 0.05$). Some other QTLs were also conserved in at least two different ages such as those on chromosomes 5,6, and 15 in females and 9 and 17 in males. Indeed, a previous QTL study in UM-HET3 combining two sexes had already

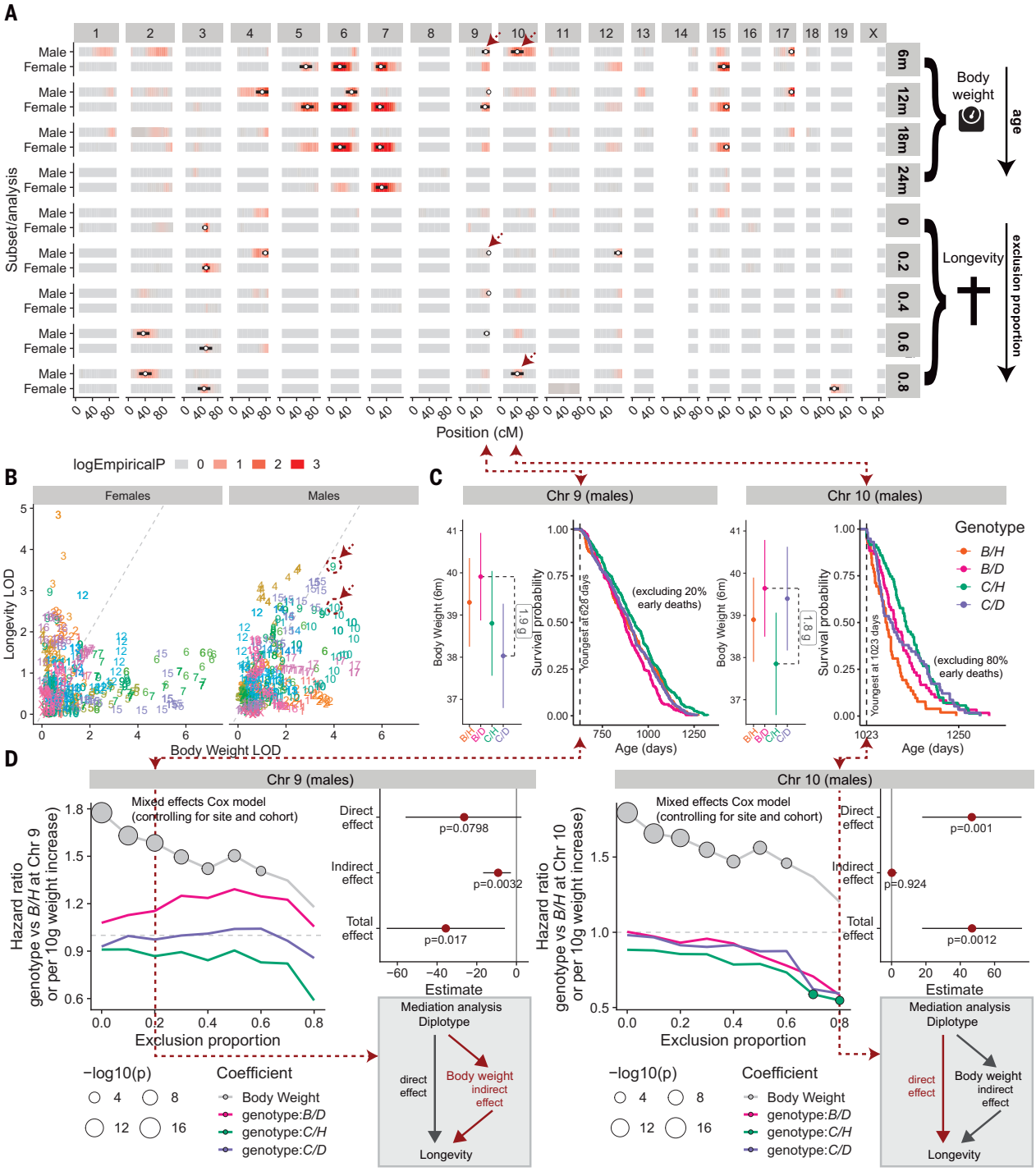


Fig. 3. QTL mapping of body weight identifies sex-specific loci and evidence of shared genetic effects on longevity in males. (**A**) QTL mapping results for sex-specific body weight at different ages and longevity scans at different exclusion levels. Each locus is colored by the −log10(empirical *p* value), and QTL peaks are marked with a black line [see (*8*) for peak definition]. The peak location of each locus is marked by a white dot. Red arrows mark the two loci on chromosomes 9 and 10 where QTL signals for longevity and body weight colocalize. (**B**) Scatterplot of the LOD scores at each marker for longevity and body weight at 6 months on the vertical and horizontal axes, respectively. Each marker is labeled and colored by the chromosome on which it resides. Circles show the markers that were further examined in (C) and (D). (**C**) Effect plots for body weight at 6 months by genotype, as well as survival curves, at the chromosome 9 and 10 loci in males (excluding 20 and 80% of early deaths, respectively). In the effect plot, the mean body weight and standard deviations per genotype are represented, as well as the difference between the highest and lowest averages. The dashed red lines are visual aids to connect the longevity and body weight QTL colocalizations in (A) and the allelic effects in (C). (**D**) Mixed-effects Cox model of the association of genotype and body weight as a function of different truncation proportions (nine truncation levels from 0 to 0.8). Points are drawn when the *p* value is less than the Bonferroni-corrected *p*-value threshold (0.05/9 = 0.0056). B/H is the reference genotype to which all others are compared. The mediation analysis is performed at the indicated truncation levels (0.2 and 0.8 for chromosome 9 and 10 loci, respectively) to match the longevity association results.

identified the loci on chromosomes 6, 7, and 15 (*14*) that also agree with the findings here in terms of directionality and magnitude (Fig. 3B). Notably, these earlier results were performed in one site, whereas the current data are from two sites across many years. With the exception of a locus on distal chromosome 9 for male and female body weight, which also overlaps with the male longevity QTL, there were no instances of the same QTL emerging in both sexes (fig. S4A), indicating that the genetic effects on body weight are predominantly sex specific. In sex-combined QTL scans, some QTLs overlap with existing sex-specific QTLs (chromosomes 10 and 17 for males and 5, 6, 7, and 15 for females), and some additional QTLs are evident on chromosomes 2 and 11. In terms of sex-by-genotype interaction, we identified loci on chromosomes 7 and 15. We also performed QTL scans for body weight change that yielded a single QTL on chromosomes 4 in males and 5, 6, and 7 in females, overlapping with body weight QTLs (fig. S4A). These results do not support the presence of genetic modifiers of rates of body weight changes in adult mice that are distinct from the determinants of body weight.

Although we identified significant QTLs in most analyses, this ensemble of QTL mapping results for longevity, body weight, and body weight change suggests that there is little QTL sharing across sexes and traits (Fig. 3A; fig. S4, A and B; and data S2 and S3). There are no overlaps in females, whereas in males, the chromosome 4 and 9 loci and the age- and male-specific longevity locus at chromosome 10 overlap with body weight loci. Indeed, when we observed the genome-wide relationship between the LOD scores for longevity and body weight QTL scans, we saw that they correlate in males but not in females, paralleling the strong relationship at the phenotypic level (Pearson correlation in males = 0.339, $p = 2.33 \times 10^{-12}$, Fig. 3B). The male-specific colocalization may either be the result of the two traits' correlation or due to genetic effects on longevity being mediated by genetic regulation of body weight. To distinguish between these two possibilities, we examined the effect of each genotype on longevity and body weight and performed mediation analyses.

We found no relationship between the genetic association with body weight and longevity on chromosome 4 (fig. S4C). That is, mice carrying the lightest allele are not the longest-lived or vice versa. This is an indication that body weight modulation and longevity are distinctly affected by genetic variants in this locus. By contrast, male mice with the *B/D* combination on the distal chromosome 9 locus are the heaviest at 6 months and the shortest-lived (Fig. 3C). Similarly, mice carrying the *C/H* at the chromosome 10 longevity locus (when 80% of deaths are excluded) are the lightest at 6 months and the most long-lived (Fig. 3C). These patterns chromosomes 9 and 10 raise the possibility that the effect of genetic variation on longevity is through modulation of body weight or growth.

To further examine these two loci, we tested whether including body weight in a Cox model would extinguish the genetic effect we observe on longevity (Fig. 3D). For chromosome 9, we observed that body weight, and not genotype, is significantly associated with hazard ($p = 6.15 \times 10^{-11}$). In addition, a mediation analysis illustrates that the effect of genotype on longevity is predominantly mediated by body weight. The chromosome 10 male locus, however, shows signs that the genetic effect on longevity is independent on the effect on body weight. The *C/H* genotype combination is significantly associated with male longevity when at least 70% of early deaths are removed even when controlling for body weight ($p = 0.0021$). In addition, the mediation analysis shows that the effect of genotype is direct and not through body weight. Taken together, these results designate the loci on chromosomes 4 and 10 as male-specific longevity modifiers through an unknown mechanism, whereas a locus on chromosome 9 may be modulating longevity through its effect on growth or body weight.

Liver gene expression reveals age- and sex-related differences in gene- and haplotype-specific expression

Having identified several QTLs for longevity and body weight, we next explored the genes under the QTL peaks in an effort to shortlist candidate longevity genes. Because the identified QTLs are large owing to limited recombination in a four-way intercross, there may be dozens of genes under each QTL. Furthermore, genetic variation within or around these genes may affect the gene's function either directly or through regulatory variation (*25*). We devised multiple strategies to home in on candidate causal genes within these loci, none of which provides enough confidence in isolation. For instance, endophenotypes such as gene expression allow a more fine-grained investigation of genetic effects on quantitative traits and typically have a simpler genetic architecture. We performed RNA sequencing (RNA-seq) of 33 livers from adult (6 month) and old (22 month), male and female UM-HET3 mice to identify genes with allele- and haplotype-specific expression (HSE).

Prior to HSE analysis, we characterized the effects of sex and age by performing differential gene expression for age, sex, and age-by-sex interaction, followed by gene set enrichment analysis (*8*) (fig. S5A and data S4). Although most of these age-related changes in gene expression are not expected to be causal (*26*), they provide insights into the footprint of aging (*27*, *28*). Differential expression in livers of UM-HET3 mice has already uncovered genes whose expression is related to life span–extending interventions (*29*). However, it is not clear if differentially expressed genes are more likely to explain interindividual differences in aging or longevity than genes whose expression remains stable with age. There were 444 sex- and 190 age-related differentially expressed genes (absolute $\log_2$ fold change > 1, BH-adjusted $p < 0.05$). The most significant functional enrichment for the sex effect is in the "cellular response to interferon-β" gene ontology term, with genes expressed higher in females (adjusted $p = 0.047$; Fig. 4, A and B). The interferon response is not only sexually dimorphic and higher in female mice (*30*) but also a major determinant in mediating severity of infections, including COVID-19, likely explaining higher mortality in men who have lower type I interferon activity than women (*31*, *32*). It is therefore possible that differences in interferon response may play a contributing role in the sex- and age-specific differences in disease susceptibility.

As for the effect of age on liver expression, we observed very significant enrichment of immune-related terms in genes whose expression increases with age (adjusted $p < 0.05$) and no significant enrichment in those with decreased expression (Fig. 4A). This is in line with previous findings that there are more genes that are consistently expressed with age than are underexpressed and that the overexpressed genes tend to be immune related (*33*). Specifically, the most enriched biological processes relate to leukocyte activation and proliferation, possibly reflecting a change in tissue composition due to increased number or activity of infiltrating or resident immune cells in the aged liver. Indeed, published single-cell RNAseq data indicate that changes in liver cellular composition, as well as an increase in immune signature, occur with age (*34*). Specifically, the relative number of hepatocytes decreases, whereas the number of liver sinusoidal endothelial cells (LSECs) increases. By contrast, Kupffer cells seem to remain stable in numbers, but more of them express *Il1b* in older mice. To corroborate these findings, we performed single-cell deconvolution analysis on the bulk RNA-seq results (*8*) (Fig. 4C). We detected changes in estimated cell type proportions only in males, with significant loss in hepatocyte number (Dirichlet regression p value = 0.00024) and gain in B cells, Kupffer cells, and LSECs ($p = 0.011, 0.013, 9 \times 10^{-4}$, respectively), in line with single-cell analyses (*34*). Taken together, the age-related changes in gene expression in UM-HET3 livers support established functional and compositional changes, an indication of the conservation of major age-related changes across studies.

We also exploited the presence of segregating UM-HET3 variants to detect HSE (*8*) (Fig. 4, D and E; fig. S5, B to E; and data S5). Allelic imbalance is a pervasive phenomenon

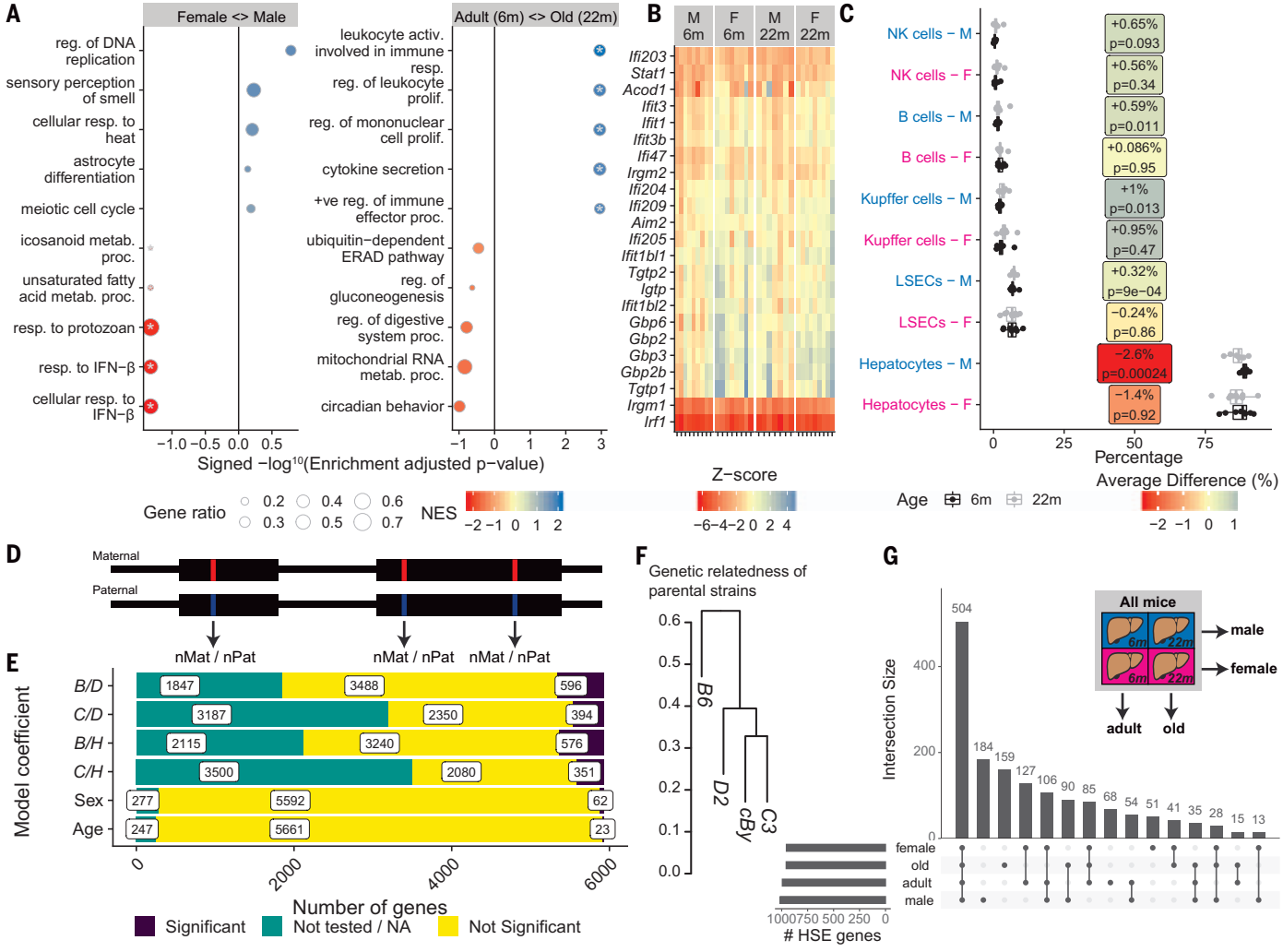


Fig. 4. Liver gene expression reveals age- and sex-related differences in gene and haplotype-specific expression. (**A**) Gene set enrichment analysis of biological processes in sex- and age-related differences in UM-HET3 liver gene expression. A positive value indicates an enrichment of a gene set driven by higher expression of its genes in males (in the left panel) or an expression increase due to age (in the right panel). (**B**) Heatmap illustrating the expression levels of genes contributing to the enrichment of cellular response to IFN-β in females when compared to males. (**C**) Cell type proportions as estimated using single-cell deconvolution analysis. NK, natural killer; LSECs, liver sinusoidal endothelial cells. For each cell type and sex, the mean difference in cell proportions is represented along with the *p* values for the age group effect from Dirichlet regression was applied to each sex separately. (**D**) Workflow and results of haplotype-specific expression (HSE) analysis. Each mouse was first genotyped at every polymorphic locus, then haplotype calling was performed. The numbers of maternal and paternal reads were collected and used in several binomial generalized linear mixed models to test for the effect of haplotype, age, and sex. (**E**) HSE results for the whole dataset. Within each model, genes were divided into whether the parameter's *p* value is significant (at a BH-adjusted $p < 0.05$). "Not tested / NA" indicates that coefficients could not be estimated for a model component for a certain gene. Stacked bar plots indicate the number of genes in each group. Text labels are the number of genes. (**F**) Hierarchical clustering of genetic relatedness of parental strains explains differences in the number of detected HSE genes per genotype. The more distant the strain pair, the more HSE genes are detected (*8*). (**G**) UpSet plot of the number and sharing of genes with significant HSE across different analysis subsets.

in mice that is affected by parent-of-origin effects and regulatory variation, which contributes to complex traits (*35*–*37*). The main rationale is that an allelic imbalance under a QTL of a complex trait may be causal and underlying variation in longevity or body weight. The fact that allele-specific expression is directly implicated in disease or useful in inferring causal mechanism of disease-associated loci provides further support to this approach (*38*). Briefly, we inferred genotypes on the basis of the RNA-seq data and used a binomial generalized linear mixed model to infer whether sex, age, or specific haplotype combinations affect the ratio of maternal to paternal transcripts or allelic imbalance. The data and specific experimental design allowed us to assess HSE in ~6000 genes, using ~70,000 variants (Fig. 4E). Using this strategy, we attributed the measured bias in maternal to paternal reads to age, sex, or one of the genotypes. For example, there are 23 and 62 genes for which a bias in expression can be attributed to sex and age, respectively. As expected, identified HSE is mostly attributed to genotype effects, with *B/D* having the most and *C/H* the fewest HSE events (596 and 351 significant, respectively). It is noteworthy that the UM-HET3 parental strains are not genetically equidistant from each other, with B6 being the most distant from the three other

strains and C3 and cBy being the closest pair (Fig. 4F). This genetic relatedness, coupled with the cross design, implies that some haplotype combinations are more likely to have HSE than others, simply because of differences in the abundance of variants enabling HSE inference (Fig. 4, E and F). Specifically, it is more likely to detect HSE in genes in mice that are carrying the *B* maternal allele, as the B6 strain is genetically the most distant from the three other strains.

We compared the results of HSE separately on different subsets (males of both ages, females of both ages, young adults of both sexes, old of both sexes) by finding overlaps of genes with HSE (Fig. 4G). The largest set of genes (n = 504) is the intersection of all subsets and consists of genes that have HSE independent of sex or age, likely ones with robust determinants in cis. The next largest set (n = 184) is male specific, followed by one that is specific to old mice (male and female), suggesting that some of the observed HSE effects may be mediated by sex- or age-specific factors.

Cross-species search of candidate genes implicated in longevity modulation

Having identified QTLs for body weight and longevity, gene expression differences by sex and age, and HSE for different ages and sexes, we combined all this information to catalog and develop a simple scoring scheme for genes under QTLs (*8*) (table S2, Fig. 5, and data S6). Because genetic variation can affect a protein-coding gene's function, we examined whether genes have high-impact variants (HIVs) that may affect their splicing or coding potential in one of the parental strains. We further determined whether these variants segregate in the UM-HET3 in a way that is consistent with the observed QTL effect. We postulated that genes under the QTL with age-related differential expression (DE) could be of interest in hypothesis building, even if DE may be a result and not a cause of aging, so we investigated whether the gene is differentially expressed in the liver dataset. Finally, to detect regulatory variant effects on gene expression, which could be driving the QTL signal, we asked whether the genes exhibit HSE.

Going beyond UM-HET3, we expanded the search toward other mouse and model organism databases. We examined whether QTL genes are differentially expressed in all the tissues of Tabula Muris Senis (TMS) (*34*) and gave an additional point if they are differentially expressed in multiple tissues. In addition, we extended the search to model organisms and cross-referenced the genes and their orthologs with the GenAge database, which contains a curated list of longevity genes (*39*). Additional points were given if a gene is a known longevity gene in mice or in more than one species.

In addition to analysis of mouse data, we also characterized the genes' human orthologs by mirroring the available mouse data generated in this study that span the genetic, gene expression, and genetically driven gene expression (*8*). First, we checked for age-associated DE in all GTEx tissues (*40*). Additional points were given if the gene is differentially expressed in more than one tissue. Then we looked at whether there is any human genome-wide association study (GWAS) hit for longevity (or BMI for the mouse body weight QTLs). To establish genetic links between gene expression and BMI and longevity, we performed transcriptome-wide Mendelian randomization (TWMR) (*41*). The combination of all these data serves as a hypothesis-building knowledge base for longevity and body weight genes. Figure 5B shows genes with a minimum score of 5 under the longevity QTLs of females, and males with 20% and males with 80% truncation, representing early and late determinants of male longevity (data S6 includes all the annotations and scores). Although the results of this investigation cannot attribute causal roles to these genes in longevity modulation, they provide valuable candidates for in-depth mechanistic studies that capitalize on our system's genetics observations. We illustrate this by performing survival analyses in *C. elegans* to test whether RNA interference (RNAi)–knockdown of the worm orthologs of the top-scoring genes would modulate longevity, therefore highlighting interesting genes for follow-up (Fig. 5C and fig. S6).

In the female longevity locus on chromosome 3, the five highest-scoring genes are *Ctss*, *Ecm1*, *Fcrl1*, *Hipk1*, and *Etv3* (aggregate score ≥ 5; Fig. 5B and data S6). Among those, we could validate the orthologs of *Ctss* (*K02E7.10* and *Y113G7B.15*) and *Hipk1* (*hpk-1*) in the worm and find that *hpk-1* RNAi significantly reduces life span (p < 0.0001; Fig. 5C and fig. S6). Indeed, *hpk-1* is already annotated as a worm pro-longevity gene in GenAge (*42*), and the transcriptional cofactor that it encodes has been shown to maintain proteostasis and extend longevity (*43*). The *ETS Variant Transcription Factor 3* (*Etv3),* which has an HIV with segregation patterns concordant with longevity and is differentially expressed in UM-HET3 and in TMS, has not been implicated in mammalian aging. However, the *Drosophila* ETS family members, *Aop* and *Pnt*, have been found to control longevity (*44*). Similarly, *Ctss* has HIV, HSE, and is differentially expressed in multiple TMS tissues, yet has not been implicated in mammalian aging. More in-depth studies would be required to assess the roles of the top-scoring genes.

For the early male longevity QTLs excluding 20% of deaths, the top-scoring genes are *Alpl*, *Eif4g3*, *Ece1*, *Pafah2*, *Hspg2*, and *Ddost* (aggregate score > 5; Fig. 5B and data S6). The highest-scoring gene is the tissue-nonspecific or liver, bone, kidney-type alkaline phosphatase (*Alpl*) gene that also harbors an HIV, exhibits HSE but has a decreasing expression in the UM-HET3 liver, and is differentially expressed in GTEx adipose tissue. More investigation is required to confirm this gene and establish a mechanistic link with longevity. We tested orthologs of all genes except *Alpl*, which does not have a worm ortholog, and found that *unc-52* (*Hspg2*) and *ostb-1* (*Ddost*) RNAi both significantly shorten life span (p < 0.0001; Fig. 5C and Fig. S6). Although *unc-52* is already known to affect worm life span (*45*, *46*), *ostb-1* or its ortholog (*Ddost*) has not yet been directly linked to longevity. However, Dolichyl-diphosphooligosaccharide–protein glycosyltransferase noncatalytic subunit (DDOST) is implicated in processing advanced glycation end products (AGEs) (*47*), which accumulate with age and exacerbate the aging phenotype (*48*). In the UM-HET3, the gene has HIVs as well as HSE, which may affect rates of AGE processing and ultimately longevity.

In the late male longevity QTLs excluding 80% of deaths, 11 genes have an equal aggregate score of 5: *Ank3*, *Slc25a3*, *Vezt*, *Stab2*, *Gnptab*, *Tdg*, *Fgd6*, *Slc17a8*, *Abcb11*, *Slc25a12*, and *Pdk1* (Fig. 5B and data S6). We tested the orthologs of *Ank3*, *Slc25a3*, *Fgd6*, *Slc17a8*, *Abcb11*, *Slc25a12*, and *Pdk1* in *C. elegans* (Fig. 5C and fig. S6). Of those, *tag-77* (*Fgd6*) and *pdhk-2* (*Pdk1*) shortened and increased life span, respectively (p = 0.0019 and p < 0.0001). Whereas the *tag-77* RNAi life-span reduction is modest compared with the other significant RNAi effects (~14% reduction in median and maximum life span), a locus near human *FGD6* (rs12830425) has been recently found to be associated with health span, life span, and exceptional longevity, rendering it a very interesting cross-species aging and longevity candidate gene (*49*). Pyruvate dehydrogenase kinase 1 (Pdk1) regulates cellular energetics, as its kinase activity inactivates pyruvate dehydrogenase (PDH) activity, thereby shutting down glucose oxidation in the mitochondrion. In agreement with our results, RNAi and mutations in *pdhk-2* have been previously shown to extend worm life span (*50*). As PDH complex has been proposed to be a therapeutic target for age-related diseases, Pdk1 modulation may be appealing as an anti-aging intervention because it is a known target of dichloroacetate (*51*). Some of the top-scoring late male longevity QTL genes encode mitochondrial proteins (*Slc25a3*, *Slc25a12*, *Pdk1*). Mitochondrial dysfunction has been extensively linked to growth and longevity regulation in model organisms (*52*–*54*). In addition to their metabolic role, mitochondria affect other features of aging such as epigenetics and proteostasis, hence acting as a central hub in the aging process (*4*, *5*). As a case in point, mitochondrial health is associated with a 31%

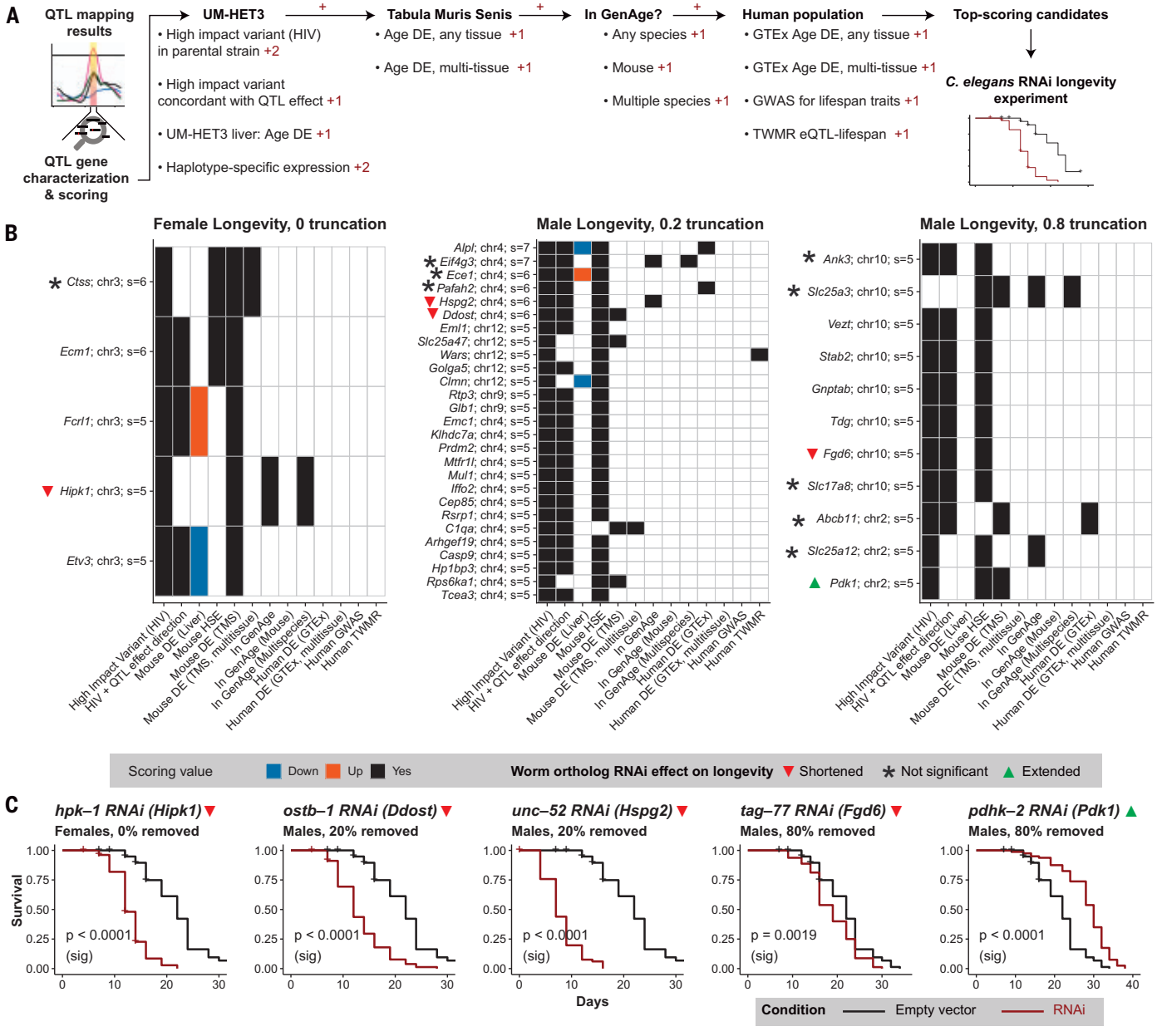


Fig. 5. Annotation, prioritization, and validation of candidate longevity genes. (**A**) Diagram of the gene annotation and scoring pipeline. Scores are indicated in red. Genes under longevity QTL peaks were annotated based on whether they (i) have a high impact variant (HIV) in one of the UM-HET3 parents; (ii) have an HIV whose parental alleles are in line with the direction of the QTL's effect; (iii) are differentially expressed in the UM-HET3 livers; (iv) show haplotype-specific expression in UM-HET3 livers; (v) are differentially expressed in any tissue in the *Tabula Muris Senis* (TMS); (vi) are differentially expressed in more than one TMS tissue; (vii) are or have orthologs that are already in GenAge; (viii) are in GenAge in the mouse; (ix) are in GenAge in multiple species; (x) have a differentially expressed human ortholog in any GTEx tissue; (xi) are differentially expressed in GTEx in multiple tissues; (xii) have been identified in human GWAS for longevity or age-related disease; or (xiii) have a link to longevity through transcriptome-wide Mendelian randomization (TWMR) (*41*). Genes that have a worm ortholog and an available RNAi clone were further validated and marked based on whether there is shortened, extended, or unchanged life span. (**B**) Top-scoring genes under selected longevity QTL genes. (**C**) Significant effects of RNAi-mediated knockdown of worm orthologs of some of the highest-scoring genes. Eighty worms were used per group and the log-rank test was performed. Worms that escaped from the plates or had vulva explosions were censored from the life span measurements. Nominal *p* values are indicated and significance is determined after Bonferroni correction (n = 19 genes tested in total; see fig. S6 for all tested genes).

longer life span in rats selectively bred for higher intrinsic exercise capacity (*55*). It is worth noting, however, that the late male longevity locus on chromosome 10 also contains genes known to affect aging such as *Igf1*, *Sirt1*, and *Sirt6*, yet these genes have not been prioritized on the basis of criteria used in this study (data S6).

As the results here serve for hypothesis generation rather than to establish causal relations, they provide a resource for the community. For that purpose, we developed an interactive web application that is helpful to explore the entirety of the results (https://www.systems-genetics.org/itp-longevity).

Discussion

Our analyses draw a general picture in which the effects of genetic factors are mostly sex, age, and trait specific. One key finding is that many of the QTLs seem to modulate life span only in mice beyond a certain age, especially in males. We find that genetic determinants of longevity and body weight variation are different and sex specific even though the two traits are highly correlated. These two traits are more correlated in males, leading to some overlaps in the identified QTL peaks. Using mediation analysis, we could discern whether overlaps in male-specific longevity and body weight QTL are due to distinct genetic effects on each trait (chromosomes 4 and 10) or genetic effects on body weight affecting longevity (chromosome 9).

Although our work did not document a large number of segregating loci with detectably large effects on life span in both male and female mice, it is possible that life span is instead modulated by a large number of loci with smaller individual effects. It is also possible that life span is modulated by interactions among segregating loci (gene-by-gene interactions). Regulation of insulin-like growth factor 1 (IGF1) levels in UM-HET3 mice, for example, has been shown to be influenced largely by three-gene and four-gene combinations (*56*), so that extreme levels of IGF1 require allele combinations present in only 1/8 or 1/16 of the population. Our methods do not consider gene-by-gene interactions of this kind and may have missed life span loci that have effects only in specific genetic contexts.

The combination of high heterozygosity in any single mouse combined with variability across mice means that the UM-HET3 are more heterogeneous than most mice currently used in research, most of which are inbred. However, we note that all four inbred grandparents of the UM-HET3 population have undergone hundreds of generations of selection for breeding success in laboratory conditions and may well have lost genetic variants, present in natural mouse populations, with major effects on maturation rate, growth rate, body size, IGF1 levels, and life span. There is evidence, for example, that offspring of crosses between wild-trapped mice and laboratory-adapted stocks of mice vary in IGF1 levels, with high life span associated with lower IGF1 levels within these segregating F_2 populations (*57*). Restricting our genetic analysis to alleles present in laboratory-adapted stocks would prevent us from detecting alleles present only in wild mouse populations.

It is also plausible that segregating alleles that do influence life span in UM-HET3 mice are principally effective in one but not both sexes. Genetic analysis of *Drosophila* longevity (*58*) has shown that most life-span loci are indeed sex specific, and studies of drugs that modulate mouse life span have also shown sex specificity for more than half of the effective drugs (*59*–*61*). The apparent near-absence of loci with strong, sex-independent effects on life span does not preclude the possibility that shared processes—such as proteostasis, mitochondrial protection, inflammation, stress-resistance pathways, and many others—could contribute to regulation of aging and longevity in both sexes.

In addition to genetics, nongenetic factors such as very early growth and access to nutrients play a role in determining longevity. Although the relationship between early growth, metabolism, and growth has been established through direct experimentation (*14*, *62*), it is important to shed light on these effects in the ITP UM-HET3 mice. Understanding how genetics affects longevity will thus inevitably require accounting for the different effects of genetics, life history, and environment on processes that affect aging, disease risk, and mortality. Indeed, we show that litter size has a negative association with body weight and a marked indirect effect on longevity.

Not all aspects of mouse physiology are expected to be identical in humans, as has been shown in a study showing that, in contrast to humans, mouse fasting glucose levels increase with age and higher glucose is associated with longer life span (*63*). In the same study, however, the longitudinal trajectories of body weight and fat were shown to be similar between mice and humans. Therefore, there may be sufficient similarities for genetic studies in mouse populations to inform studies on human aging. Here we show that relationships between early growth, body size, and longevity are also conserved in humans. Specifically, the MR and MR-mediation analysis of the UK Biobank data indicate that early growth is likely causal in determining adult longevity, through its effect on adult BMI. BMI is determined by adiposity and size in different ways than body weight in mice; hence exploring similarities between mice and humans will require measurements of body composition and size in mice, data which are not available in the ITP.

In terms of gene expression, the liver profiles reveal a strong increase in immune-related transcripts with age, which is indicative of chronic inflammation or inflammaging (*64*). Another case in point is that females, who are longer-lived than males, have a higher expression of interferon-β (IFN-β)–related genes, consistent with previous observations (*30*). This is reminiscent of the situation in humans where the more vigorous IFN-β response in women has been invoked to explain the attenuated severity of infections, including COVID-19, likely explaining higher mortality in males (*31*). It is therefore possible that differences in interferon response gene activity may play a contributing role in the sex- and age-specific differences in disease susceptibility. We capitalized further on the fact that UM-HET3 mice are heterozygous to detect extensive haplotype-specific expression across two sexes and two ages. This information was used to help prioritize genes under QTL peaks and could also serve as a resource for more in-depth study of the effect of regulatory variation on gene expression.

The characterization of genes under QTLs provides a resource for further investigation of their putative roles in mediating longevity and body weight variation (see interactive application: https://www.systems-genetics.org/itp-longevity). Future studies that include more ITP mice as well as denser genetic maps may yield improved QTL results. Finally, more longitudinal data collection accompanied by extensive phenotyping would be required to shift the focus from longevity to a better understanding of genetics of healthy aging or health span. There is therefore great potential to reach valuable insights into aging by feeding into the virtuous cycle between mouse genetics and human drug discovery, which has already been a successful paradigm in identifying disease genes for drug discovery (*65*).

Materials and methods summary

Phenotype and genotype data of UM-HET3 mice from the ITP

The UM-HET3 mice are genetically heterogeneous progeny of CByB6F1 females and C3D2F1 males, produced at each of three sites—the Jackson Laboratory (JL), the University of Michigan at Ann Arbor (UM), and the University of Texas Health Science Center at San Antonio (UT) (*6*). Experiments at the JL, the UM, and the UT were reviewed and approved annually by the Institutional Animal Care and Use Committees at each site. Life span and weight data for ITP mice were compiled by the laboratories of D. Harrison, R. Miller, and R. Strong, and are available in the Mouse Phenome Database (*66*). Litter size data were provided by J. Nelson. Tail samples were sent to GeneSeek (Neogen Corporation), where genomic DNA was extracted, followed by single-nucleotide polymorphism (SNP) genotyping by matrix-assisted laser desorption/ionization–time-of-flight mass spectrometry (*67*) at a maximum of 270 markers.

QTL mapping

Longevity

To assess the effect of haplotype on longevity, we used the coxme package to fit multiple mixed-effects Cox models. The full model includes the two sexes and has sex as a fixed effect and site as a random effect. The cohort year was included as a random effect that is nested in site. The sex-specific models do not have sex as a fixed effect. To define significance thresholds, we performed 1000 permutations with label swapping. We systematically performed

QTL mapping for longevity by eliminating different percentiles (or quantiles) of the shortest-lived mice.

Body weight

We employed a similar strategy as for longevity but using the lme4 package to fit mixed linear models.

Web application

We developed an application using the R Shiny package to allow researchers to browse the raw data and results of this project: https://www.systems-genetics.org/itp-longevity.

Full materials and methods are available in the supplementary materials (*8*).

REFERENCES AND NOTES

1. C. López-Otín, M. A. Blasco, L. Partridge, M. Serrano, G. Kroemer, The hallmarks of aging. *Cell* **153**, 1194–1217 (2013). doi: 10.1016/j.cell.2013.05.039; pmid: 23746838
2. C. J. Kenyon, The genetics of ageing. *Nature* **464**, 504–512 (2010). doi: 10.1038/nature08980; pmid: 20336132
3. M. Hook *et al*., Genetic cartography of longevity in humans and mice: Current landscape and horizons. *Biochim. Biophys. Acta Mol. Basis Dis.* **1864** (9 Pt A), 2718–2732 (2018). doi: 10.1016/j.bbadis.2018.01.026; pmid: 29410319
4. L. N. Booth, A. Brunet, The aging epigenome. *Mol. Cell* **62**, 728–744 (2016). doi: 10.1016/j.molcel.2016.05.013; pmid: 27259204
5. R. C. Taylor, A. Dillin, Aging as an event of proteostasis collapse. *Cold Spring Harb. Perspect. Biol.* **3**, a004440 (2011). doi: 10.1101/cshperspect.a004440; pmid: 21441594
6. R. A. Miller *et al*., An Aging Interventions Testing Program: Study design and interim report. *Aging Cell* **6**, 565–575 (2007). doi: 10.1111/j.1474-9726.2007.00311.x; pmid: 17578509
7. N. L. Nadon *et al*., Design of aging intervention studies: The NIA interventions testing program. *Age (Dordr.)* **30**, 187–199 (2008). doi: 10.1007/s11357-008-9048-1; pmid: 19424842
8. See supplementary materials.
9. F. Macchiarini, R. A. Miller, R. Strong, N. Rosenthal, D. E. Harrison, "Chapter 10 - NIA Interventions Testing Program: A collaborative approach for investigating interventions to promote healthy aging" in *Handbook of the Biology of Aging (Ninth Edition)*, N. Musi, P. J. Hornsby, Eds. (Academic Press, 2021; https://www.sciencedirect.com/science/article/pii/B978012815962000010X), *Handbooks of Aging*, pp. 219–235.
10. C. J. Cheng, J. A. L. Gelfond, R. Strong, J. F. Nelson, Genetically heterogeneous mice exhibit a female survival advantage that is age- and site-specific: Results from a large multi-site study. *Aging Cell* **18**, e12905 (2019). doi: 10.1111/acel.12905; pmid: 30801953
11. A. U. Jackson, A. T. Galecki, D. T. Burke, R. A. Miller, Mouse loci associated with life span exhibit sex-specific and epistatic effects. *J. Gerontol. A Biol. Sci. Med. Sci.* **57**, B9–B15 (2002). doi: 10.1093/gerona/57.1.B9; pmid: 11773201
12. R. Gelman, A. Watson, R. Bronson, E. Yunis, Murine chromosomal regions correlated with longevity. *Genetics* **118**, 693–704 (1988). doi: 10.1093/genetics/118.4.693; pmid: 3163317
13. C. J. Bult *et al*., Mouse Genome Database (MGD) 2019. *Nucleic Acids Res.* **47**, D801–D806 (2019). doi: 10.1093/nar/gky1056; pmid: 30407599
14. R. A. Miller, J. M. Harper, A. Galecki, D. T. Burke, Big mice die young: Early life body weight predicts longevity in genetically heterogeneous mice. *Aging Cell* **1**, 22–29 (2002). doi: 10.1046/j.1474-9728.2002.00006.x; pmid: 12882350
15. S. Roy *et al*., Gene-by-environment modulation of lifespan and weight gain in the murine BXD family. *Nat. Metab.* **3**, 1217–1227 (2021). doi: 10.1038/s42255-021-00449-w; pmid: 34552269
16. W. H. Dietz, Childhood weight affects adult morbidity and mortality. *J. Nutr.* **128** (Suppl), 411S–414S (1998). doi: 10.1093/jn/128.2.411S; pmid: 9478038
17. C. Maffeis, L. Tatò, Long-term effects of childhood obesity on morbidity and mortality. *Horm. Res.* **55** (Suppl 1), 42–45 (2001). pmid: 11408761
18. M. E. Bowen, The relationship between body weight, frailty, and the disablement process. *J. Gerontol. B Psychol. Sci. Soc. Sci.* **67**, 618–626 (2012). doi: 10.1093/geronb/gbs067; pmid: 22967933
19. D. H. Sullivan, L. Liu, P. K. Roberson, M. M. Bopp, J. C. Rees, Body weight change and mortality in a cohort of elderly patients recently discharged from the hospital. *J. Am. Geriatr. Soc.* **52**, 1696–1701 (2004). doi: 10.1111/j.1532-5415.2004.52463.x; pmid: 15450047
20. L. Sun, A. A. Sadighi Akha, R. A. Miller, J. M. Harper, Life-span extension in mice by preweaning food restriction and by methionine restriction in middle age. *J. Gerontol. A Biol. Sci. Med. Sci.* **64**, 711–722 (2009). doi: 10.1093/gerona/glp051; pmid: 19414512
21. S. Burgess *et al*., Dissecting causal pathways using Mendelian randomization with summarized genetic data: Application to age at menarche and risk of breast cancer. *Genetics* **207**, 481–487 (2017). doi: 10.1534/genetics.117.300191; pmid: 28835472
22. P. R. Timmers *et al*., Genomics of 1 million parent lifespans implicates novel pathways and common diseases and distinguishes survival chances. *eLife* **8**, e39856 (2019). doi: 10.7554/eLife.39856; pmid: 30642433
23. L. Yengo *et al*., Meta-analysis of genome-wide association studies for height and body mass index in ~700000 individuals of European ancestry. *Hum. Mol. Genet.* **27**, 3641–3649 (2018). doi: 10.1093/hmg/ddy271; pmid: 30124842
24. J. Tyrrell *et al*., Height, body mass index, and socioeconomic status: Mendelian randomisation study in UK Biobank. *BMJ* **352**, i582 (2016). doi: 10.1136/bmj.i582; pmid: 26956984
25. F. W. Albert, L. Kruglyak, The role of regulatory variation in complex traits and disease. *Nat. Rev. Genet.* **16**, 197–212 (2015). doi: 10.1038/nrg3891; pmid: 25707927
26. E. Porcu *et al*., Differentially expressed genes reflect disease-induced rather than disease-causing changes in the transcriptome. *Nat. Commun.* **12**, 5647 (2021). doi: 10.1038/s41467-021-25805-y; pmid: 34561431
27. M. Bou Sleiman *et al*., The gene-regulatory footprint of aging highlights conserved central regulators. *Cell Rep.* **32**, 108203 (2020). doi: 10.1016/j.celrep.2020.108203; pmid: 32997995
28. B. A. Benayoun *et al*., Remodeling of epigenome and transcriptome landscapes with aging in mice reveals widespread induction of inflammatory responses. *Genome Res.* **29**, 697–709 (2019). doi: 10.1101/gr.240093.118; pmid: 30858345
29. A. Tyshkovskiy *et al*., Identification and application of gene expression signatures associated with lifespan extension. *Cell Metab.* **30**, 573–593.e8 (2019). doi: 10.1016/j.cmet.2019.06.018; pmid: 31353263
30. S. T. Gal-Oz *et al*., ImmGen report: Sexual dimorphism in the immune system transcriptome. *Nat. Commun.* **10**, 4295 (2019). doi: 10.1038/s41467-019-12348-6; pmid: 31541153
31. P. Bastard *et al*., Autoantibodies against type I IFNs in patients with life-threatening COVID-19. *Science* **370**, eabd4585 (2020). doi: 10.1126/science.abd4585; pmid: 32972996
32. T. Takahashi *et al*., Sex differences in immune responses that underlie COVID-19 disease outcomes. *Nature* **588**, 315–320 (2020). doi: 10.1038/s41586-020-2700-3; pmid: 32846427
33. J. P. de Magalhães, J. Curado, G. M. Church, Meta-analysis of age-related gene expression profiles identifies common signatures of aging. *Bioinformatics* **25**, 875–881 (2009). doi: 10.1093/bioinformatics/btp073; pmid: 19189975
34. N. Almanzar *et al*., A single-cell transcriptomic atlas characterizes ageing tissues in the mouse. *Nature* **583**, 590–595 (2020). doi: 10.1038/s41586-020-2496-1; pmid: 32669714
35. J. J. Crowley *et al*., Analyses of allele-specific gene expression in highly divergent mouse crosses identifies pervasive allelic imbalance. *Nat. Genet.* **47**, 353–360 (2015). doi: 10.1038/ng.3222; pmid: 25730764
36. S. F. Pinter *et al*., Allelic imbalance is a prevalent and tissue-specific feature of the mouse transcriptome. *Genetics* **200**, 537–549 (2015). doi: 10.1534/genetics.115.176263; pmid: 25858912
37. R. Mott *et al*., The architecture of parent-of-origin effects in mice. *Cell* **156**, 332–342 (2014). doi: 10.1016/j.cell.2013.11.043; pmid: 24439386
38. S. Cleary, C. Seoighe, Perspectives on allele-specific expression. *Annu. Rev. Biomed. Data Sci.* **4**, 101–122 (2021). doi: 10.1146/annurev-biodatasci-021621-122219; pmid: 34465174
39. R. Tacutu *et al*., Human ageing genomic resources: New and updated databases. *Nucleic Acids Res.* **46** (D1), D1083–D1090 (2018). doi: 10.1093/nar/gkx1042; pmid: 29121237
40. A. Battle, C. D. Brown, B. E. Engelhardt, S. B. Montgomery; GTEx Consortium; Laboratory, Data Analysis &Coordinating Center (LDACC)—Analysis Working Group; Statistical Methods groups—Analysis Working Group; Enhancing GTEx (eGTEx) groups; NIH Common Fund; NIH/NCI; NIH/NHGRI; NIH/NIMH; NIH/NIDA; Biospecimen Collection Source Site—NDRI; Biospecimen Collection Source Site—RPCI; Biospecimen Core Resource—VARI; Brain Bank Repository—University of Miami Brain Endowment Bank; Leidos Biomedical—Project Management; ELSI Study; Genome Browser Data Integration &Visualization—EBI; Genome Browser Data Integration &Visualization—UCSC Genomics Institute, University of California Santa Cruz; Lead analysts; Laboratory, Data Analysis &Coordinating Center (LDACC); NIH program management; Biospecimen collection; Pathology; eQTL manuscript working group, Genetic effects on gene expression across human tissues. *Nature* **550**, 204–213 (2017). doi: 10.1038/nature24277; pmid: 29022597
41. E. Porcu *et al*., Mendelian randomization integrating GWAS and eQTL data reveals genetic determinants of complex and clinical traits. *Nat. Commun.* **10**, 3300 (2019). doi: 10.1038/s41467-019-10936-0; pmid: 31341166
42. A. V. Samuelson, C. E. Carr, G. Ruvkun, Gene activities that mediate increased life span of *C. elegans* insulin-like signaling mutants. *Genes Dev.* **21**, 2976–2994 (2007). doi: 10.1101/gad.1588907; pmid: 18006689
43. R. Das *et al*., The homeodomain-interacting protein kinase HPK-1 preserves protein homeostasis and longevity through master regulatory control of the HSF-1 chaperone network and TORC1-restricted autophagy in *Caenorhabditis elegans*. *PLOS Genet.* **13**, e1007038 (2017). doi: 10.1371/journal.pgen.1007038; pmid: 29036198
44. A. J. Dobson *et al*., Longevity is determined by ETS transcription factors in multiple tissues and diverse species. *PLOS Genet.* **15**, e1008212 (2019). doi: 10.1371/journal.pgen.1008212; pmid: 31356597
45. S. P. Curran, G. Ruvkun, Lifespan regulation by evolutionarily conserved genes essential for viability. *PLOS Genet.* **3**, e56 (2007). doi: 10.1371/journal.pgen.0030056; pmid: 17411345
46. C. Y. Ewald, J. N. Landis, J. Porter Abate, C. T. Murphy, T. K. Blackwell, Dauer-independent insulin/IGF-1-signalling implicates collagen remodelling in longevity. *Nature* **519**, 97–101 (2015). doi: 10.1038/nature14021; pmid: 25517099
47. T. Yamagata *et al*., Genome organization of human 48-kDa oligosaccharyltransferase (DDOST). *Genomics* **45**, 535–540 (1997). doi: 10.1006/geno.1997.4966; pmid: 9367678
48. R. D. Semba, E. J. Nicklett, L. Ferrucci, Does accumulation of advanced glycation end products contribute to the aging phenotype? *J. Gerontol. A Biol. Sci. Med. Sci.* **65**, 963–975 (2010). doi: 10.1093/gerona/glq074; pmid: 20478906
49. P. R. H. J. Timmers, J. F. Wilson, P. K. Joshi, J. Deelen, Multivariate genomic scan implicates novel loci and haem metabolism in human ageing. *Nat. Commun.* **11**, 3570 (2020). doi: 10.1038/s41467-020-17312-3; pmid: 32678081
50. L. Mouchiroud *et al*., Pyruvate imbalance mediates metabolic reprogramming and mimics lifespan extension by dietary restriction in *Caenorhabditis elegans*. *Aging Cell* **10**, 39–54 (2011). doi: 10.1111/j.1474-9726.2010.00640.x; pmid: 21040400
51. P. W. Stacpoole, The pyruvate dehydrogenase complex as a therapeutic target for age-related diseases. *Aging Cell* **11**, 371–377 (2012). doi: 10.1111/j.1474-9726.2012.00805.x; pmid: 22321732
52. A. Dillin *et al*., Rates of behavior and aging specified by mitochondrial function during development. *Science* **298**, 2398–2401 (2002). doi: 10.1126/science.1077780; pmid: 12471266
53. R. H. Houtkooper *et al*., Mitonuclear protein imbalance as a conserved longevity mechanism. *Nature* **497**, 451–457 (2013). doi: 10.1038/nature12188; pmid: 23698443
54. T. Lima, T. Y. Li, A. Mottis, J. Auwerx, Pleiotropic effects of mitochondria in aging. *Nat Aging* **2**, 199–213 (2022). doi: 10.1038/s43587-022-00191-2
55. M. A. Aon *et al*., Mitochondrial health is enhanced in rats with higher vs. lower intrinsic exercise capacity and extended lifespan. *NPJ Aging Mech. Dis.* **7**, 1–16 (2021). doi: 10.1038/s41514-020-00054-3; pmid: 33398019
56. P. Hanlon *et al*., Three-locus and four-locus QTL interactions influence mouse insulin-like growth factor-I. *Physiol. Genomics* **26**, 46–54 (2006). doi: 10.1152/physiolgenomics.00247.2005; pmid: 16782841
57. J. M. Harper, S. J. Durkee, R. C. Dysko, S. N. Austad, R. A. Miller, Genetic modulation of hormone levels and life span in hybrids between laboratory and wild-derived mice.

J. Gerontol. A Biol. Sci. Med. Sci. **61**, 1019–1029 (2006). doi: 10.1093/gerona/61.10.1019; pmid: 17077194
58. S. V. Nuzhdin, E. G. Pasyukova, C. L. Dilda, Z.-B. Zeng, T. F. C. Mackay, Sex-specific quantitative trait loci affecting longevity in *Drosophila melanogaster*. *Proc. Natl. Acad. Sci. U.S.A.* **94**, 9734–9739 (1997). doi: 10.1073/pnas.94.18.9734; pmid: 9275193
59. M. Sadagurski, G. Cady, R. A. Miller, Anti-aging drugs reduce hypothalamic inflammation in a sex-specific manner. *Aging Cell* **16**, 652–660 (2017). doi: 10.1111/acel.12590; pmid: 28544365
60. M. Garratt, B. Bower, G. G. Garcia, R. A. Miller, Sex differences in lifespan extension with acarbose and 17-α estradiol: Gonadal hormones underlie male-specific improvements in glucose tolerance and mTORC2 signaling. *Aging Cell* **16**, 1256–1266 (2017). doi: 10.1111/acel.12656; pmid: 28834262
61. R. A. Miller *et al*., Rapamycin-mediated lifespan increase in mice is dose and sex dependent and metabolically distinct from dietary restriction. *Aging Cell* **13**, 468–477 (2014). doi: 10.1111/acel.12194; pmid: 24341993
62. M. Parra-Vargas, M. Ramon-Krauel, C. Lerin, J. C. Jimenez-Chillaron, Size does matter: Litter size strongly determines adult metabolism in rodents. *Cell Metab.* **32**, 334–340 (2020). doi: 10.1016/j.cmet.2020.07.014; pmid: 32814016
63. D. L. Palliyaguru *et al*., Fasting blood glucose as a predictor of mortality: Lost in translation. *Cell Metab.* **33**, 2189–2200.e3 (2021). doi: 10.1016/j.cmet.2021.08.013; pmid: 34508697
64. C. Franceschi, J. Campisi, Chronic inflammation (inflammaging) and its potential contribution to age-associated diseases. *J. Gerontol. A Biol. Sci. Med. Sci.* **69** (Suppl 1), S4–S9 (2014). doi: 10.1093/gerona/glu057; pmid: 24833586
65. J. H. Nadeau, J. Auwerx, The virtuous cycle of human genetics and mouse models in drug discovery. *Nat. Rev. Drug Discov.* **18**, 255–272 (2019). doi: 10.1038/s41573-018-0009-9; pmid: 30679805
66. M. A. Bogue *et al*., Mouse Phenome Database: A data repository and analysis suite for curated primary mouse phenotype data. *Nucleic Acids Res.* **48**, D716–D723 (2020). pmid: 31696236
67. S. Gabriel, L. Ziaugra, D. Tabbaa, SNP genotyping using the Sequenom MassARRAY iPLEX platform. *Curr. Protoc. Hum. Genet.* **60**, 2.12.1–2.12.18 (2009). doi: 10.1002/0471142905.hg0212s60; pmid: 19170031
68. M. Bou Sleiman, Sex- and age-dependent genetics of longevity in a heterogeneous mouse population, Zenodo (2022); https://doi.org/10.5281/zenodo.6625242.

ACKNOWLEDGMENTS

We thank all technical and scientific members of the Interventions Testing Program, who have produced and made the data available. We also thank J.-D. Morel, G. Benegiamo, and L. Goeminne for comments on the manuscript. **Funding:** Ecole Polytechnique Fédérale de Lausanne (J.A.); European Research Council grant ERC-AdG-787702 (J.A.); Swiss National Science Foundation grant 31003A-179435 (J.A.); Swiss National Science Foundation grant 310030-189147 (Z.K.); National Institutes of Health grant AG043930 (R.W., J.A.); National Institutes of Health grant AG022303 (R.M.); National Institutes of Health grant AG022308 (D.H.); National Institutes of Health grant AG022307 (R.S.); Glenn Foundation for Medical Research (R.M.); R.S. is supported by a Senior Research Career Scientist Award from the Department of Veterans Affairs Office of Research and Development. **Author contributions:** Conceptualization: J.A., R.W., R.M. Data curation: S.R., M.B.S. Formal Analysis: M.B.S., M.S., G.V.G.vA. Investigation: M.B.S., A.G., M.S. Methodology: M.B.S., S.R., R.W. Resources: R.M., R.S., J.N., D.H., R.W., J.A. Software: M.B.S. Validation: M.B.S., A.G. Visualization: M.B.S. Web application: M.B.S. Writing – original draft: M.B.S., J.A. Writing – review and editing: M.B.S., J.A., R.W., R.M., Z.K. Funding acquisition: J.A., R.W., R.M., J.N., D.H., R.S. Project administration: R.W., J.A. Supervision: J.A., R.W. **Competing interests:** The authors declare that they have no competing interests. **Data and materials availability:** All data and code are available at Zenodo (*68*). Raw RNA-seq data are available on GEO (GSE194321). **License information:** Copyright © 2022 the authors, some rights reserved; exclusive licensee American Association for the Advancement of Science. No claim to original US government works. https://www.science.org/about/science-licenses-journal-article-reuse

SUPPLEMENTARY MATERIALS

science.org/doi/10.1126/science.abo3191
Materials and Methods
Figs. S1 to S6
Tables S1 and S2
References (*69*–*93*)
Data S1 to S6

Submitted 27 January 2022; resubmitted 9 June 2022
Accepted 10 August 2022
10.1126/science.abo3191

RESEARCH ARTICLE SUMMARY

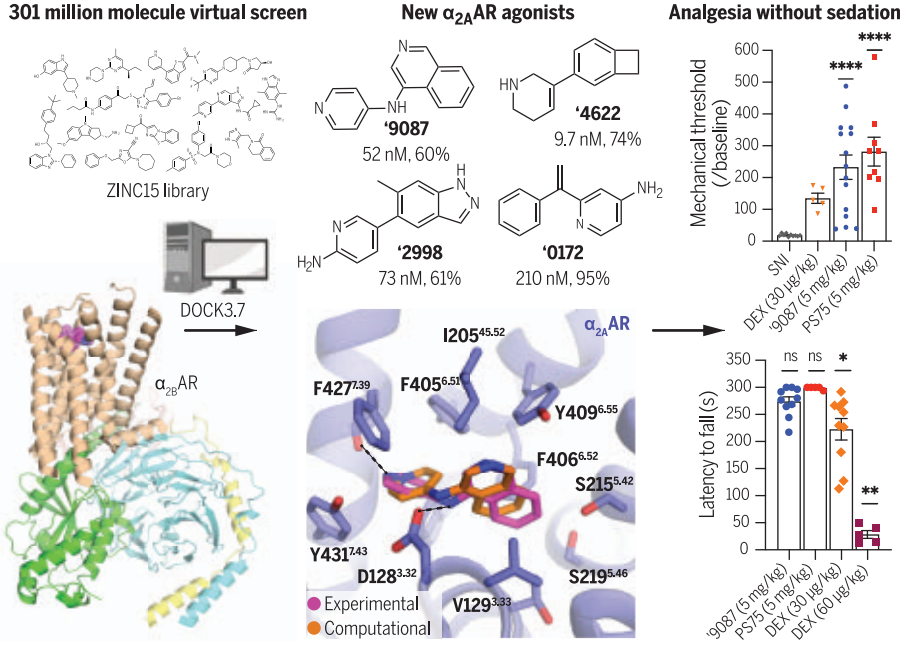
DRUG DESIGN

Structure-based discovery of nonopioid analgesics acting through the α_{2A}-adrenergic receptor

Elissa A. Fink†, Jun Xu†, Harald Hübner†, Joao M. Braz†, Philipp Seemann†, Charlotte Avet, Veronica Craik, Dorothee Weikert, Maximilian F. Schmidt, Chase M. Webb, Nataliya A. Tolmachova, Yurii S. Moroz, Xi-Ping Huang, Chakrapani Kalyanaraman, Stefan Gahbauer, Geng Chen, Zheng Liu, Matthew P. Jacobson, John J. Irwin, Michel Bouvier*, Yang Du*, Brian K. Shoichet*, Allan I. Basbaum*, Peter Gmeiner*

INTRODUCTION: Epidemics of pain and opioid abuse underscore the need for new nonopioid therapeutics to treat pain. Many nonopioid receptors are involved in pain processing (nociception), but only a few have been validated therapeutically. Of particular interest is the α_{2A}-adrenergic receptor (α_{2A}AR), a G protein–coupled receptor (GPCR) whose activation in the central nervous system has pain-relieving effects. The known therapeutics targeting the α_{2A}AR, like clonidine and dexmedetomidine, are known to be analgesic. They are also strongly sedating, which is important for the primary indication of dexmedetomidine. This, however, has restricted the use of these drugs to hospital settings and kept them from being used in broader patient populations.

RATIONALE: Because GPCRs, like α_{2A}AR, can signal into the cell through multiple downstream effectors, we reasoned that agonists that were chemically dissimilar to the highly related dexmedetomidine, clonidine, and brimonidine might have different signaling and might be able to separate sedation from analgesia. We sought these chemotypes among a virtual library of more than 301 million diverse, readily accessible molecules in the ZINC15 library (http://zinc15.docking.org), few of which have been previously synthesized. We computationally docked each virtual molecule into the highly similar α_{2B}AR binding site, prioritizing those that physically fit and that were chemically unrelated to the known drugs.



Newly identified α_{2A}AR agonists are analgesic without sedation. More than 301 million molecules were docked against the activated α_{2B}AR. Experimental testing identified α_{2A}AR agonists with diverse chemical scaffolds. The experimental structure of the '9087-α_{2A}AR complex superposed closely to the computational prediction. The newly discovered agonists had efficacy in an in vivo neuropathic pain model (top right) without sedation, unlike dexmedetomidine (DEX) (bottom right). G_{i1}-activation EC_{50} (nanomolar) and E_{max} (percentage) values are shown. Single-letter abbreviations for the amino acid residues are as follows: D, Asp; F, Phe; I, Ile; S, Ser; V, Val; and Y, Tyr. ns, not significant; *P < 0.05; ****P < 0.0001; SNI, spared nerve injury.

RESULTS: From the high-ranking docked compounds, we selected 48 for de novo synthesis and testing. Against the α_{2B}AR used in the virtual docking screens, 30 molecules bound for a 63% hit rate, among the highest to date for docking campaigns. Seventeen further bound to α_{2A}AR with binding constants in the low-nanomolar to low-micromolar concentration range. Several acted as full or partial agonists of α_{2A}AR, activating the receptor. Among these was '9087 [mean effective concentration (EC_{50}) of 52 nM]. Notably, the docking-derived agonists preferentially activated G_i, G_o, and G_z G protein subtypes, which contrasts with known drugs, like dexmedetomidine and brimonidine, that activate a much broader set of G proteins and recruit β-arrestins. Thus, the new agonists activate a more selective set of cellular pathways than the known α_{2A}AR drugs, something we had hoped for when prioritizing new chemotypes.

The structures of two of these agonists were experimentally determined in complex with the activated state of α_{2A}AR. These experimental ligand geometries closely corresponded to computational predictions. They also templated the optimization of the initial docking hits and led to more potent analogs, including PS75 (EC_{50} 4.8 nM). The physical features of these agonists allowed them to reach high brain concentrations after systemic dosing. In animal behavioral assays, six of these previously uncharacterized agonists relieved pain behaviors in neuropathic, inflammatory, and acute thermal nociception assays. Gene mutation and reversal of receptor binding with an α_2AR antagonist confirmed that analgesia occurred primarily through α_{2A}AR. Crucially, when compared with dexmedetomidine, none of the new compounds caused sedation, even at substantially higher doses than required for pain relief.

CONCLUSION: The separation of analgesic properties from sedation of the new agonists is important for further α_{2A}AR drug development. The newly identified agonists, especially '9087 and PS75, overcome the sedation liability of the previously known drugs, and several are orally bioavailable. This makes them lead molecules for the development of nonopioid pain therapeutics. ■

The list of author affiliations is available in the full article online.
*Corresponding author. Email: peter.gmeiner@fau.de (P.G.); allan.basbaum@ucsf.edu (A.I.B.); bshoichet@gmail.com (B.K.S.); yangdu@cuhk.edu.cn (Y.D.); michel.bouvier@umontreal.ca (M.B.)
†These authors contributed equally to this work.
Cite this article as E. A. Fink *et al.*, *Science* **377**, eabn7065 (2022). DOI: 10.1126/science.abn7065

READ THE FULL ARTICLE AT
https://doi.org/10.1126/science.abn7065

RESEARCH ARTICLE

DRUG DESIGN

Structure-based discovery of nonopioid analgesics acting through the α_{2A}-adrenergic receptor

Elissa A. Fink[1,2]†, Jun Xu[3,4]†, Harald Hübner[5]†, Joao M. Braz[6]†, Philipp Seemann[5]†, Charlotte Avet[7], Veronica Craik[6], Dorothee Weikert[5], Maximilian F. Schmidt[5], Chase M. Webb[1,8], Nataliya A. Tolmachova[9,10], Yurii S. Moroz[11,12], Xi-Ping Huang[13], Chakrapani Kalyanaraman[1], Stefan Gahbauer[1], Geng Chen[3], Zheng Liu[3], Matthew P. Jacobson[1], John J. Irwin[1], Michel Bouvier[7]*, Yang Du[3]*, Brian K. Shoichet[1]*, Allan I. Basbaum[6]*, Peter Gmeiner[5]*

Because nonopioid analgesics are much sought after, we computationally docked more than 301 million virtual molecules against a validated pain target, the α_{2A}-adrenergic receptor (α_{2A}AR), seeking new α_{2A}AR agonists chemotypes that lack the sedation conferred by known α_{2A}AR drugs, such as dexmedetomidine. We identified 17 ligands with potencies as low as 12 nanomolar, many with partial agonism and preferential G_i and G_o signaling. Experimental structures of α_{2A}AR complexed with two of these agonists confirmed the docking predictions and templated further optimization. Several compounds, including the initial docking hit '9087 [mean effective concentration (EC_{50}) of 52 nanomolar] and two analogs, '7075 and PS75 (EC_{50} 4.1 and 4.8 nanomolar), exerted on-target analgesic activity in multiple in vivo pain models without sedation. These newly discovered agonists are interesting as therapeutic leads that lack the liabilities of opioids and the sedation of dexmedetomidine.

Epidemics in pain (*1*) and in opioid-use disorder (*2*, *3*) have inspired a search for nonopioid analgesics (*1*, *4*). The α_{2A}-adrenergic receptor (α_{2A}AR) is a nonopioid receptor targeted by dexmedetomidine, a sedative that also has strong analgesic activity (*5*). Although dexmedetomidine has many advantages in emergency room and intensive care settings, its strong sedative effects (*6*, *7*) and its lack of an oral formulation (*8*) have limited its broad use as an analgesic. These properties are barriers for future therapeutics targeting this receptor.

[1]Department of Pharmaceutical Chemistry, University of California, San Francisco, San Francisco, CA, USA. [2]Graduate Program in Biophysics, University of California, San Francisco, San Francisco, CA, USA. [3]Kobilka Institute of Innovative Drug Discovery, School of Life and Health Sciences, Chinese University of Hong Kong, Shenzhen, Guangdong 518172, China. [4]Department of Molecular and Cellular Physiology, Stanford University School of Medicine, Stanford, CA, USA. [5]Department of Chemistry and Pharmacy, Friedrich-Alexander-Universität Erlangen-Nürnberg, 91058 Erlangen, Germany. [6]Department of Anatomy, University of California, San Francisco, San Francisco, CA, USA. [7]Department of Biochemistry and Molecular Medicine, Institute for Research in Immunology and Cancer, Université de Montréal, Montréal, QC, Canada. [8]Graduate Program in Pharmaceutical Sciences and Pharmacogenomics, University of California, San Francisco, San Francisco, CA, USA. [9]Enamine Ltd., 02094 Kyiv, Ukraine. [10]Institute of Bioorganic Chemistry and Petrochemistry, National Ukrainian Academy of Science, 02660 Kyiv, Ukraine. [11]National Taras Shevchenko University of Kyiv, 01601 Kyiv, Ukraine. [12]Chemspace, Riga LV-1082, Latvia. [13]National Institute of Mental Health Psychoactive Drug Screening Program (NIMH PDSP), School of Medicine, University of North Carolina at Chapel Hill School of Medicine, Chapel Hill, NC, USA.

***Corresponding author. Email: peter.gmeiner@fau.de (P.G.); allan.basbaum@ucsf.edu (A.I.B.); bshoichet@gmail.com (B.K.S.); yangdu@cuhk.edu.cn (Y.D.); michel.bouvier@umontreal.ca (M.B.)**

†These authors contributed equally to this work.

Most α_{2A}AR analgesics are chemically related, and the relationship of their sedative to their analgesic properties is unclear. To find therapeutics with new pharmacology, we sought new α_{2A}AR chemotypes, topologically unrelated to known α_{2A}AR agonists. The α_{2B}-adrenergic receptor (α_{2B}AR) active-state structure (*9*) became available, and its binding site is highly conserved compared with that of α_{2A}AR (fig. S1); therefore, it should be possible to identify new α_{2A}AR agonists by structure-based docking. Meanwhile, the advent of readily accessible make-on-demand ("tangible") molecules (*10*–*12*) ranging from hundreds of millions (*10*, *13*, *14*) to more than a billion molecules (*15*, *16*) has vastly increased the chemotypes available for ligand discovery. Docking these libraries has revealed new chemotypes with 20 to 60% hit rates (*13*, *14*, *17*–*20*) and sometimes nanomolar potencies for a growing range of targets (*10*, *13*, *14*, *18*, *21*–*24*), often with new pharmacology (*10*, *13*, *17*, *25*). Therefore, we targeted the α_{2B}AR with an ultralarge library docking screen.

Docking 301 million molecules versus the α_{2B}AR

The ZINC15 and ZINC20 virtual libraries are composed of millions to billions of tangible molecules, depending on the molecular property range targeted, and are accessed by combining hundreds of thousands of diverse building blocks through hundreds of well-characterized reactions (*10*–*12*). Most of the molecules have not previously been synthesized and range in mass, calculated LogP (cLogP) values (a measure of hydrophobicity), and formal charge. Given the small size of the α_{2B}AR orthosteric site, we docked both the 20 million fragment-like [compounds with smaller masses of <250 atomic mass units (amu)] and 281 million lead-like (compounds with larger masses of 250 to 350 amu) molecules from the ZINC15 library (both sets having cLogP ≤ 3.5) (*11*) (Fig. 1A). More than 233 trillion complexes, an average of 452,000 per molecule, were sampled by DOCK3.7 and scored with its physics-based energy function (*26*) across three separate screens (two fragment screens with different variables and one lead-like screen; see Materials and methods). For each screen, the top 300,000 docking-ranked compounds were clustered for topological similarity and then filtered to identify scaffolds dissimilar to known agonists using an extended connectivity fingerprint (ECFP4). These known agonists were drawn from the International Union of Basic and Clinical Pharmacology (IUPHAR)–British Pharmacological Society (BPS) database (*27*) and from the literature (*28*–*31*). Ligands with internal torsional strain were deprioritized (*32*). An additional novelty filter removed molecules similar to annotated α_{2A}AR compounds in CHEMBL29 (*28*). Of the remaining top-ranked cluster representatives, 5000 from each fragment screen and 20,000 for the lead-like screen were manually evaluated in UCSF Chimera (https://rbvi.ucsf.edu/chimera) for key polar and nonpolar interactions with α_{2B}AR (*9*), including with D92$^{3.32}$, F412$^{7.39}$, F387$^{6.51}$, Y391$^{6.55}$, and F388$^{6.52}$ [residues conserved in α_{2A}AR: D128$^{3.32}$, F427$^{7.39}$, F405$^{6.51}$, Y409$^{6.55}$, and F406$^{6.52}$; superscripts use Ballesteros-Weinstein and the G protein–coupled receptor database (GPCRdb) nomenclature (*33*)]. Most α_{2A}AR agonists, and certainly the clinically used dexmedetomidine and clonidine, are fragments (*27*), and the docking results reflected this. The docked fragment molecules fit in the orthosteric site, making key contacts with the receptor, whereas molecules in the lead-like screen generally did not fit in the small cavity (Fig. 1A). Accordingly, most selected ligands came from the fragment docking screens.

From the 64 high-ranking docked compounds prioritized by visual inspection and purchased for in vitro testing, 48 were successfully synthesized—44 fragments and 4 lead-like molecules. Compounds were first tested for binding to the human α_{2B}AR receptor, the structure used in docking screens. Thirty molecules of the 48 tested had binding constant (K_i) values less than 10 μM (table S1). This 63% hit rate is among the highest for a docking campaign to date (*10*, *14*, *21*, *23*, *34*). In radioligand competition assays, compound ZINC1173879087 (from here on referred to as '9087) had a K_i of 1.7 nM; the remaining 29 had K_i values ranging from 60 nM to 9.4 μM, which is relatively potent for initial docking hits. Ten compounds (21%) had K_i values

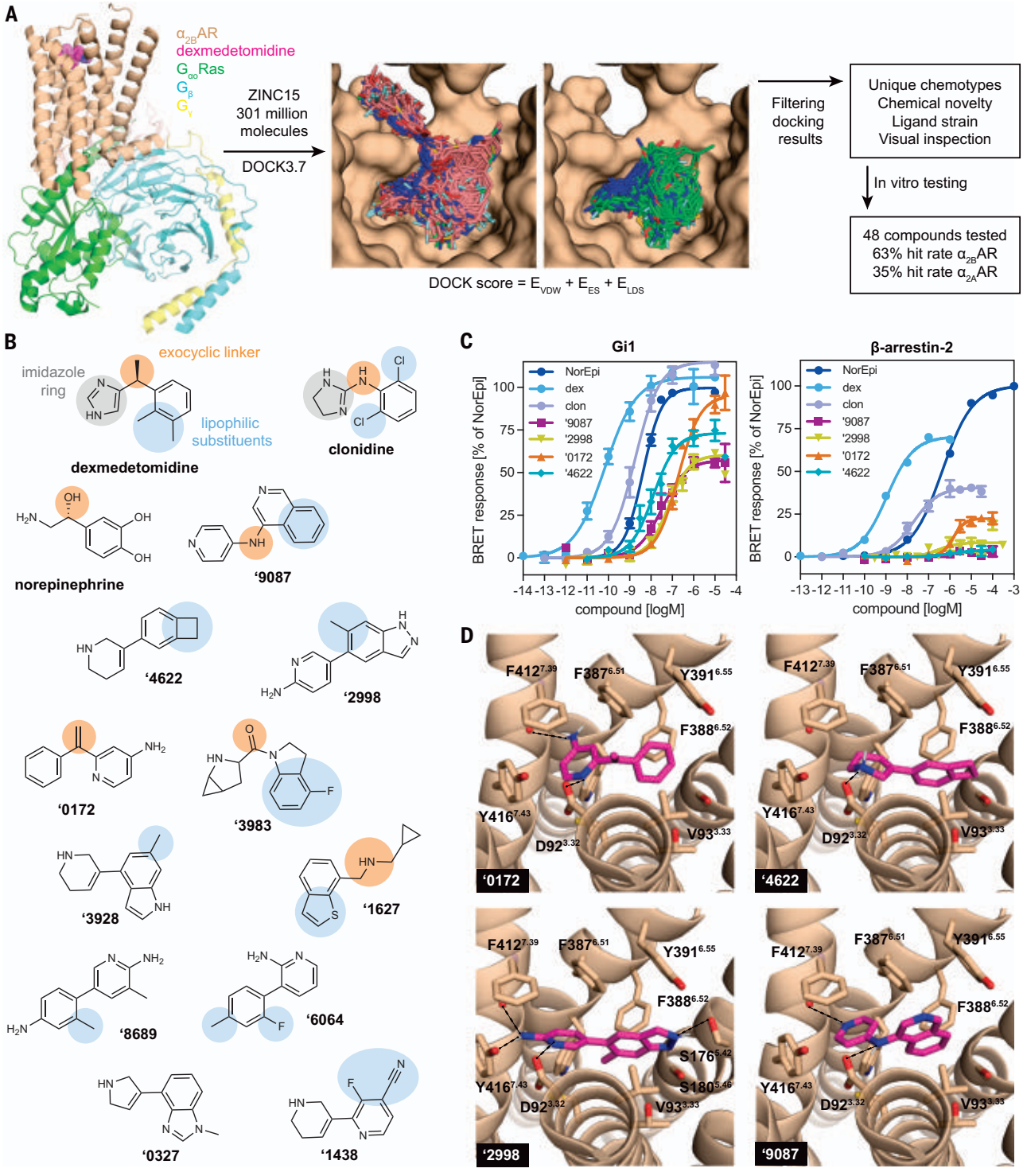


Fig. 1. Newly discovered α_{2A}AR agonists from ultralarge library docking. (**A**) 301 million molecules were docked against the active state of α_{2B}AR (PDB 6K41). Lead-like molecules (pink carbons) often spilled out of the orthosteric site, whereas fragment molecules (green carbons) are well complemented by that site. Hit rates were determined with a K_i cutoff of 10 μM. E_{VDW}, van der Waals; E_{ES}, electrostatic; E_{LDS}, ligand desolvation. (**B**) The αAR pharmacophore model (*9*) overlaid on known α_{2A}AR agonists dexmedetomidine, clonidine, and norepinephrine and new agonists from docking (colors represent the different moieties fulfilling the same role). (**C**) G_i activation and β-arrestin-2 recruitment for norepinephrine (NorEpi), dexmedetomidine (dex), clonidine (clon), and several of the newly discovered docking agonists. (**D**) Docked poses of these new agonists with hydrogen bonds to key recognition residues of α_{2B}AR shown as black dashed lines. For (C), data are means ± SEMs of normalized results (n = 4 to 17 measurements for G_i and n = 3 to 8 measurements for β-arrestin-2). Single-letter abbreviations for the amino acid residues are as follows: A, Ala; C, Cys; D, Asp; E, Glu; F, Phe; G, Gly; H, His; I, Ile; K, Lys; L, Leu; M, Met; N, Asn; P, Pro; Q, Gln; R, Arg; S, Ser; T, Thr; V, Val; W, Trp; and Y, Tyr.

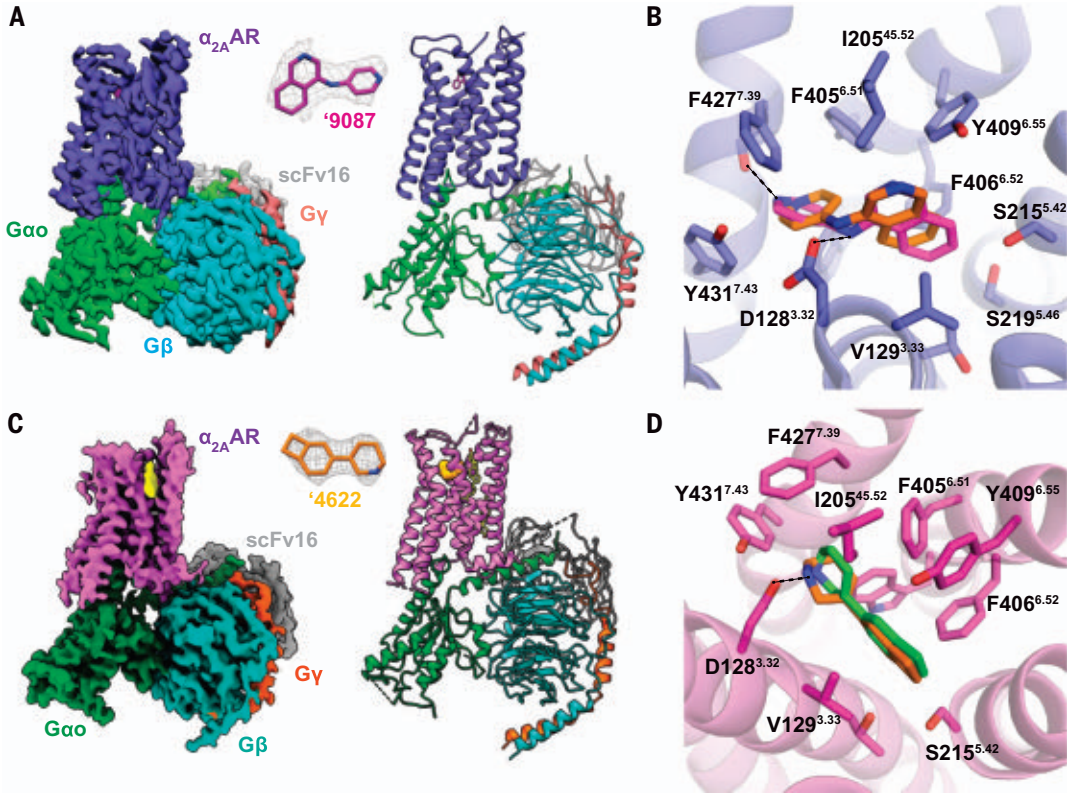


Fig. 2. Docking-predicted poses of '9087 and '4622 superpose well on the cryo-EM structures of the '9087-α_{2A}AR-G_{oA} and '4622-α_{2A}AR-G_{oA} complexes. (**A** and **C**) Cryo-EM structure of the '9087-α_{2A}AR-G_{oA} (A) and '4622-α_{2A}AR-G_{oA} (C) complexes. (**B**) Experimental '9087 structure (pink carbons) superposed on the docked pose (orange carbons) (PDB 7W6P; RMSD 1.14 Å). Hydrogen bonds and ion pairs are shown with dashed black lines to F427$^{7.39}$ and D128$^{3.32}$, respectively. (**D**) Experimental '4622 structure (green carbons) superposed on the docked pose (orange carbons) (PDB 7W7E; RMSD 1.14 Å). Hydrogen bond shown with dashed black lines to D128$^{3.32}$. For (B) and (D), side chains of α_{2A}AR residues within 4 Å of ligands are shown as sticks.

below 1 μM (table S1). The compounds were then tested for binding to the murine α_{2A}AR, again by radioligand competition. Of these, 17 (35%) had a K_i better than 10 μM, with affinities ranging from 72 nM to 9.4 μM; five compounds (10%) had K_i values below 1 μM (table S1). Against human α_{2A}AR, the highest affinity was 12 nM (table S2).

Discovery of new α_{2A}AR, partial G_i and G_o ($G_{i/o}$) agonists

In functional assays, most of the potent binders were partial or full agonists for α_{2A}AR and α_{2B}AR (Fig. 1, B to D; tables S1 and S2; and figs. S2 to S4); few antagonists were found among the more potent docking hits. This reflects the targeting of the activated state of the receptor (*35*, *36*) and was a goal of the screen. The best four agonists from the docking screen include '9087 as well as ZINC1240664622, ZINC1242282998, and ZINC001242890172 (from here on referred to as '4622, '2998, and '0172, respectively), with the α_{2A}AR-mediated G_i activation maximum effect (E_{max}) ranging from 60 to 95% of norepinephrine response and mean effective concentration (EC_{50}) values of 9.7 to 210 nM in $G\alpha_i$ bioluminescence resonance energy transfer (BRET) assays (Fig. 1C and table S2). We tested the effect of receptor expression in cells on the functional properties of the partial agonist, '9087, and ultimately of two optimized analogs, '7075 and PS75; all three remained potent G_i partial agonists, with E_{max} decreasing with receptor expression (fig. S5). In an orthogonal cyclic adenosine monophosphate (cAMP) assay, '9087 was a partial agonist with an EC_{50} of 87 nM and E_{max} of 42%, which is broadly consistent with the BRET assay (from here on, G_i activities are the $G\alpha_i$ BRET assay values, unless otherwise noted) (Fig. 1C, fig. S4, and table S2).

The docking agonists had strong differential activity for G_i activation compared with recruitment of β-arrestin-2. Although this was also true of the known agonists, dexmedetomidine and clonidine, for the new agonists the difference was accentuated so that arrestin recruitment was almost completely eliminated at relevant concentrations. Of the four best docking agonists, only '0172 had a measurable efficacy for β-arrestin-2 recruitment, but only with 22% of the E_{max} of norepinephrine and with weak potency (EC_{50} 1.7 μM); for the other three, β-arrestin-2 recruitment was negligible (Fig. 1C and table S2). We note that this lack of arrestin recruitment could reflect the partial agonism of the new agonists combined with the weaker coupling of the arrestin pathway versus the well-coupled G_i pathway, as indicated by the differences in potency and efficacy of the reference agonists, dexmedetomidine and clonidine.

Agonists of α_{2A}AR, including its endogenous ligand norepinephrine, also activate other G protein pathways (*37*). Accordingly, we used the enhanced bystander BRET (ebBRET)–based effector membrane translocation assay (EMTA) (*38*) to test '9087 and its analogs, '7075 and PS75, against a more expansive panel of G protein and β-arrestin subtypes. The docking compounds preferentially activated G_i, G_o, and G_z ($G_{i/o/z}$) signaling, whereas known agonists norepinephrine, dexmedetomidine, and brimonidine strongly activated multiple additional G proteins and β-arrestins (figs. S6 and S7 and tables S3 and S4). Receptor internalization after treatment with compound was also investigated by monitoring disappearance of α_{2A}ARs from the plasma membrane (α_{2A}AR-RlucII/rGFP-CAAX biosensor) and relocalization of the receptors in endosomes (α_{2A}AR-RlucII/rGFP-FYVE biosensor) (*39*). Known agonists brimonidine and

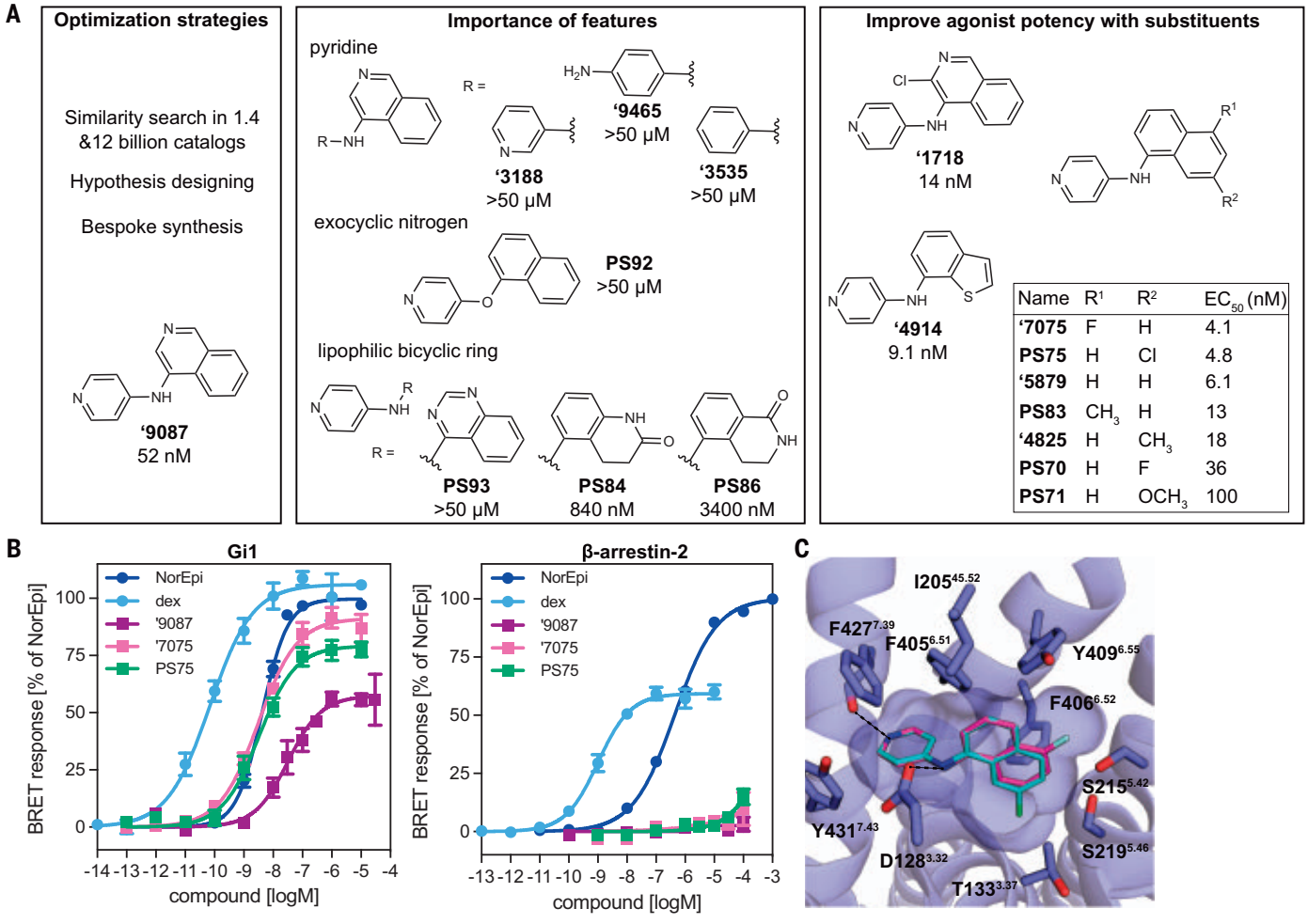


Fig. 3. Structure-based optimization of '9087. (**A**) Strategies for analoging '9087 (left). Analogs of the pyridine, exocyclic nitrogen, and lipophilic nature of the bicyclic ring revealed their importance for '9087 activity (middle). Sampling alternate lipophilic bicyclic rings and modifying their substituents identified eight more potent agonists (right). EC_{50} values are shown for G_i activation. (**B**) G_i and β-arrestin-2 recruitment for '9087 and its two most potent analogs, '7075 and PS75. (**C**) Modeled poses of '7075 (pink carbons) and PS75 (blue carbons) based on the '9087-α_{2A}AR cryo-EM structure with substituents oriented toward open space in the orthosteric site. Hydrogen bonds and ionic interactions are shown with dashed black lines to $F427^{7.39}$ and $D128^{3.32}$, respectively. For (A), G_i and β-arrestin-2 recruitment data for analogs are shown in figs. S14 and S15 and table S8. For (B), data are means ± SEMs of normalized results (n = 7 to 17 measurements for G_i and n = 4 to 8 measurements for β-arrestin-2).

norepinephrine show comparable responses for both biosensors, whereas dexmedetomidine has about half of this response. Consistent with their absence of β-arrestin recruitment, we found no effect of '9087, '7075, and PS75 on disappearance from the plasma membrane and marginal effect at the highest concentrations on endosomal relocalization (fig. S8). Although such functional selectivity was not explicitly modeled in the docking, it likely results from the new chemistry, which was explicitly required (*13*, *14*, *17*).

Comparing the new agonists with dexmedetomidine, clonidine, norepinephrine, and a previously described pharmacophore model for αAR selective agonists (*9*), both similar and distinct features emerge (Fig. 1B). The pharmacophore model for known agonists and the new docking compounds both have basic, nitrogen-containing rings. However, known agonists are dominated by imidazoles (unsaturated or partially saturated), whereas the docking compounds have diverse nonimidazole rings. Both sets of compounds contain additional moieties off of a second aryl ring, typically two substituents for the known agonists; however, for the docking-derived compounds, these vary from bulky hydrophobic rings, to hydrophilic rings, to single substituents, to having no substituents off of the aryl ring at all. Not all of the docking compounds have an exocyclic linker as described in the pharmacophore model. The protonated imidazole of known agonists ion pairs with $D92^{3.32}$ and hydrogen bonds to the backbone of $F412^{7.39}$ of α_{2B}AR (*9*, *40*) (fig. S1). Although several of the docking-derived compounds also interacted with both $D92^{3.32}$ and $F412^{7.39}$, they did so with different heterocyclic rings (Fig. 1D).

To test the docking model and to template structure-based optimization, we determined the structure of the '9087-α_{2A}AR-G_{oA} and '4622-α_{2A}AR-G_{oA} complexes at a nominal resolution of 3.47 and 3.38 Å, respectively, using single-particle cryo–electron microscopy (cryo-EM) (Fig. 2, A to D, and figs. S9 and S10). The predicted docked pose superimposes on the cryo-EM result of '9087 with a 1.14-Å all-atom root mean square deviation (RMSD) of the agonist; the docking-predicted interactions are recapitulated in the experimental structure (Fig. 2B). The interactions between '9087 and α_{2A}AR differ from that of norepinephrine but resemble those of imidazoline-containing agonists (*9*, *40*). '9087 interacts with α_{2A}AR mainly through van der Waals and aromatic interactions to transmembrane helices (TM) 3, 5, 6, and 7 and $I205^{45.52}$ of extracellular loop

2 (ECL2). It also forms an ionic interaction with the conserved D128$^{3.32}$, and although this interaction is relatively distant at 3.6 Å, it is similar to those of norepinephrine (*40*) and dexmedetomidine (*9*) that are 3.0 and 3.7 Å from D128$^{3.32}$, respectively (Fig. 2B). As in the docking prediction, the basic, formally cationic nitrogen of '9087 is not oriented toward D128$^{3.32}$ to form a salt bridge (Fig. 2B and fig. S11), as seen in norepinephrine, but instead hydrogen bonds with the backbone carbonyl of F427$^{7.39}$, as it does in dexmedetomidine (*9*). The bridging exocyclic and formally neutral amine of the '9087 ion pairs with D128$^{3.32}$. Typically for aminergic G protein–coupled receptors (GPCRs), the conserved hydrogen bond with D128$^{3.32}$ would be made by the stronger base (*9*, *17*, *20*, *40*). In fact, the formal charge of '9087 after protonation of the pyridine moiety is almost equally shared between the two nitrogens, as calculated by semiempirical quantum mechanics and as reflected in the docking model (fig. S11). For '4622, the docked pose is also in good agreement with the cryo-EM result with an all-atom RMSD of 1.14 Å; '4622 forms a 3.4-Å hydrogen bond to D128$^{3.32}$ and makes several hydrophobic interactions (Fig. 2D). Both '4622- and '9087-bound structures have similar receptor-$G_{o\alpha}$ interfaces to other ligand-bound α_2AR–G protein complexes (figs. S9 and S10).

The interactions observed in the '9087 and '4622 receptor complexes, and in the modeled pose of analog '7075, were tested by residue substitution for effects on G_i activation and β-arrestin recruitment (figs. S12 and S13 and tables S6 and S7). Consistent with the observed ion pair with D128$^{3.32}$, norepinephrine and dexmedetomidine are highly sensitive to substitutions to D128$^{3.32}$, with an almost complete loss of G_i activation and β-arrestin recruitment. For dexmedetomidine, the G_i EC_{50} is 170,000-fold higher for activation of D128$^{3.32}$A. Although the G_i activity of '9087 and '7075 is also diminished in the D128$^{3.32}$ mutant receptors, potency only falls by ~200- to 1600-fold. By contrast, the G_i activity of '9087, '7075, and '4622 is eliminated in the F427$^{7.39}$A mutant. The backbone carbonyl of F427$^{7.39}$ hydrogen bonds with '9087, whereas its aromatic side chain stacks with the agonist in the cryo-EM structure, perhaps indicating formation of a cation-pi interaction between the pyridine of '9087 and F427$^{7.39}$, as previously suggested for agonist-induced α_2AR activation (*41*). Meanwhile, dexmedetomidine and especially norepinephrine, which lack these interactions, are less affected by this mutant (Fig. 2B). Mutations of Y409$^{6.55}$ greatly affect norepinephrine, increasing (weakening) G_i EC_{50} values 500- to 10,000-fold, likely disrupting a key hydrogen bond (*40*, *41*); the importance of position 6.55 was previously observed in agonist-induced β_2AR activation (*42*–*44*). The potencies of '9087 and dexmedetomidine are only modestly worse in Y409$^{6.55}$ mutants, and for '9087, the G_iE_{max} is even slightly increased. For '4622 and '7075, most substitutions diminished activity, with the exception of S215$^{5.42}$A, which slightly increased the agonist activity of '7075 and '4622 in the G_i activation and β-arrestin recruitment assays and hardly influenced '9087 and dexmedetomidine. By contrast, S215$^{5.42}$A negatively affected norepinephrine-induced receptor activation, consistent with previous studies on direct interactions of full agonists and S215$^{5.42}$ (*40*, *41*). The Y431$^{7.43}$A and F mutations overall influenced β-arrestin recruitment of norepinephrine more than G_i signaling. This has been previously observed, leading to the proposal that direct hydrogen bonding between the agonist and the residue at position 7.43 could more tightly couple TM7 and thereby play a role in β-arrestin signaling (*40*). Taken together, the differential responses to the residue substitutions supports suggestions from the structures that the new agonists, although binding in the same overall site as the canonical agonists, interact in meaningfully different ways, with potential implications for differential receptor signaling.

Optimization of docking hit '9087

To optimize '9087, we adopted two strategies. First, we used classic medicinal chemistry hypothesis-testing and generation of analogs to investigate and improve key recognition features. We looked for possible analogs by similarity-searching among 1.4 billion and 12 billion tangible molecules using the Arthor and SmallWorld programs (*12*) (NextMove Software, UK). From these searches, we docked prioritized subsets, leading to 13 of the 19 '9087 analogs that we ultimately selected (Fig. 3A and table S5). Another six analogs were designed to probe particular protein-ligand interactions. Analogs were also investigated around compounds '2998, '4622, and '0172 (table S5). In the '9087 series, perturbing the pyridine eliminated activity and confirmed the importance of the cationic character and the importance of the hydrogen bond with F427$^{7.39}$ (Fig. 3A, figs. S14 and S15, and table S8).

The most potent analogs emerged from variations of the isoquinoline ring in '9087. Proximal hydrophobic residues F405$^{6.51}$, F406$^{6.52}$, Y409$^{6.55}$, and I205$^{45.52}$ do not make obvious polar interactions with the isoquinoline nitrogen of '9087 (Fig. 2B). Accordingly, we added small nonpolar groups, like the chlorine in '1718, or changed the isoquinoline to a different bicyclic system, like the benzothiophene in '4914 or naphthalene in '5879. A set of analogs also had the isoquinoline-to-naphthalene change but with a single substituent added at two different positions of the naphthalene, as in '4825 and PS83. Overall, this set of analogs resulted in five potent agonists (EC_{50} 4.1 nM to 18 nM) (data supporting the '9087 optimization are summarized in Fig. 3, A and B; figs. S14 and S15; and tables S2, S5, and S8). '7075 was the most potent full agonist in the '9087 series with 13-fold increased potency in the BRET G_i activation (EC_{50} 4.1 nM, E_{max} 93%) and cAMP assays (EC_{50} 18 nM, E_{max} 96%) (Fig. 3B, fig. S4, and table S2). It preferentially activated $G_{i/o}$ signaling over other G protein subtypes and β-arrestins and caused no receptor internalization (figs. S6 to S8 and tables S3 and S4).

Our second strategy for ligand optimization was purely structure based, using the newly determined '9087-α_{2A}AR complex. Molecules were prioritized for their favorable docked pose in a ligand-free version of the α_{2A}AR-'9087 structure or were designed to improve protein-ligand interactions based on the '9087-alpha2a cryo-EM structure, leading us to synthesize eight further analogs. Two derivatives of '9087 (PS84 and PS86) confirm the importance of the lipophilic and aromatic properties of the bicyclic moiety for α_{2A}AR binding and activation, facilitating favorable interactions with the aromatic residues F405$^{6.51}$, F406$^{6.52}$, and Y409$^{6.55}$ (Fig. 2B). Other substitutions confirmed the importance of the ion pair to D128$^{3.32}$ and of the interaction between the protonated pyridine of '9087 and the backbone carbonyl atom of F427$^{7.39}$ (PS92, PS93), as also shown by the mutational analysis (figs. S12 and S13 and tables S6 and S7).

Seeking more potent analogs, we focused on derivatizing the lipophilic substituents of '9087, building off analogs '5879 and '7075. Assuming the same binding mode for the naphthalene derivative '5879 as for '9087 in the cryo-EM structure, unexploited space between the ligand and the receptor in the orthosteric site was revealed in positions 5 and 7 of the bicyclic moiety of '5879 (R^1 and R^2 in Fig. 3A). We first tried to fill available space with substituents of different sizes at the R^1 position of '5879. From largest to smallest, substituents were methoxy (PS71), chlorine (PS75), and fluorine (PS70). The potency of PS75 for G_i activation was similar to that of '5879 (EC_{50} values of 4.8 nM and 6.1 nM, respectively), PS70 (EC_{50} 36 nM) did not improve activity, and PS71 had 16-fold worse activity compared with '5879; for PS71, this may reflect entropic and desolvation penalties and a repulsive interaction for the bulky methoxy substituent that the receptor was unable to accommodate. Similar to '7075 with a substituent at the R^2 position of the bicyclic moiety, addition of a methyl (PS83) had a similar EC_{50} of 13 nM to that of '7075 and '5879 (EC_{50} values of 4.1 nM and 6.1 nM, respectively).

PS75 was the most potent analog to arise from the second round of optimization. The molecule was a full agonist with 11-fold improved potency (EC_{50} 4.8 nM, E_{max} 82%) for G_i

activation compared with '9087, and it more potently activated $G_{i/o/z}$ subtypes than '9087. Meanwhile, PS75 still retained the preferential signaling through the $G_{i/o}$ versus other G protein families and β-arrestins and again led to negligible receptor internalization (figs. S5 to S8 and tables S3 and S4). In the modeled pose of PS75, the chlorine substituent is oriented toward the open space below its naphthalene ring toward $T133^{3.37}$ (Fig. 3C). Its potency and efficacy make PS75 a lead molecule for treatment in pain.

Newly discovered α_{2A}AR agonists are analgesic with reduced side effects

In preparation for in vivo studies, we investigated the selectivity and pharmacokinetic properties of our most potent agonists. '9087 activated only a few of the 320 GPCRs screened (*45*) (fig. S16A). Only the dopamine D_2 receptor (D2R) had weak activity in secondary assays, with EC_{50} values of 4.5 μM and 16 μM in G protein signaling and β-arrestin recruitment, respectively (fig. S16B). '9087 did not measurably activate the μ-opioid receptor (μOR) nor did it inhibit the human ether-à-go-go-related gene (hERG) at concentrations below 10 μM (fig. S16, C and D). In binding experiments to other adrenergic receptors, '9087 bound to the α_{2C}-subtype at mid-nanomolar concentration and to other α_1-subtypes in the 1-to-10-μM range (table S9). The molecule had no measurable binding for β-adrenergic receptors up to 10 μM. Against the imidazoline-2 receptor (I2R), a common off-target of α_{2A}AR agonists, '9087 bound with a K_i of 300 nM, showing a modest sixfold selectivity for the α_{2A}AR, whereas a few docking-derived compounds actually had higher affinities for I2R than for the α_{2A}AR (fig. S16E).

Computational models suggested that '9087, '4622, '7075, and '2998 would all have good physiologic permeability, consistent with their small size, low topological polar surface area, and weakly basic character (table S10). Consistent with this prediction, on 10-mg/kg intraperitoneal (i.p.) injection in mice, the first three compounds, especially, had high brain and cerebrospinal fluid (CSF) exposure, indicating that the compounds are likely to reach centrally acting α_{2A}ARs (table S10). '9087 reached a similar maximum concentration (C_{max}) in the CSF as did '7075, both of which were fourfold greater than the C_{max} of PS75, and '9087 had a 12- to 20-fold higher area under the concentration-time curve (AUC) in the CSF compared with either '7075 or PS75; CSF concentrations are often used as a proxy for fraction unbound in the brain (*46*). Encouragingly, '9087 reached high brain exposure after both intravenous (i.v.) and oral (p.o.) administration, with AUC values of 420,000 ng min mL^{-1} and 2,540,000 ng min mL^{-1} (table S10). The oral bioavailability was higher than 100%, which may reflect metabolic saturation at nonequal i.v. and p.o. doses, or enterohepatic recirculation (table S10); this merits further investigation. PS75 was fully bioavailable, though, as an analog of '9087, the same caveats apply. We also investigated the metabolic stability of '9087, '7075, and PS75 in male rat liver microsomes. All three compounds remain largely unmodified after 1 hour, with '9087 having lower clearance and a higher half-life than its two analogs (fig. S17).

Given their selectivity and high brain exposures, we tested the more potent agonists for pain-relief after systemic dosing (Fig. 4, A to G). Initial doses were chosen to be less than the 10 mg/kg dose used in pharmacokinetics studies owing to favorable CSF and brain properties. We started with '9087, the initial docking hit, and evaluated analogs as they emerged from compound optimization. With naïve (uninjured) mice, '9087 did not increase baseline mechanical withdrawal thresholds, something observed with many antipain medications, which often only have an antinociceptive effect in the presence of pain. We then investigated the activity of '9087 in a mouse model of neuropathic pain, in which partial peripheral nerve injury invokes profound mechanical hypersensitivity (*47*). Systemic subcutaneous (s.c.) injections of '9087 dose-dependently increased the mechanical thresholds of spared nerve injury (SNI) mice, with a sharp increase in activity from 3 mg/kg to 5 mg/kg, at which point the effects plateaued (Fig. 4A). Lower doses were antiallodynic, returning mechanical thresholds to preinjury levels, whereas the higher doses were genuinely analgesic, generating mechanical thresholds substantially higher than baseline, preinjury levels. '9087 also increased thermal latencies in the complete Freund's adjuvant (CFA)–mediated inflammatory pain model, which indicates that the molecule is effective in both tissue and nerve injury–induced pain models (Fig. 4G). '9087 also increased withdrawal latencies in the hot plate (55°C) and tail flick (50°C) assays of acute thermal (heat) pain (Fig. 4, E and F). Consistent with its relatively high exposure on oral dosing, this molecule also conferred a dose-dependent antiallodynic effect when delivered orally in the SNI neuropathic pain model (Fig. 4A). Doses up to 20 mg/kg of '9087 did not reduce the ability of the mice to perform in the rotarod test, which contrasts with the complete sedation of a dexmedetomidine dose of 60 μg/kg (Fig. 4H). This finding is an important differentiator for the new series and indicates that the analgesic effects of '9087 are not the result of motor impairment.

We also investigated the mechanistic bases for the analgesia of the new α_{2A}AR agonists, both pharmacologically and genetically. Pharmacologically, the analgesic effect of '9087 was reversed by a systemic injection of the well-known α_2AR antagonist, atipamezole (2 mg/kg; administered 15 min before '9087) (Fig. 4C). Because atipamezole has broad activity against the α_2AR receptor subtypes and imidazoline receptors (*48*), we also tested '9087 in mice that express an inactive form of the α_{2A}AR (point mutation D79N) (*5*, *49*–*51*). D79N mutant mice were tested in the tail flick (50°C) assays. As previously reported, dexmedetomidine no longer induced analgesia in the mutant mice (*52*), and, as a control, the analgesia conferred by a 10-mg/kg dose of morphine was not significantly altered by the mutation (Fig. 4D). Consistent with activity through α_{2A}AR, the analgesia conferred by '9087 was reduced by >50% back to baseline in the D79N mutant mice (Fig. 4D). Although most of the antinociceptive activity appears to derive from activity at the α_{2A}AR, we cannot discount contributions from other receptors.

Five other of the new, docking-derived α_{2A}AR agonists ('2998, '4622, '0172, '7075, and PS75) also exhibited antiallodynic effects in the SNI mice (Fig. 4, A and B). The '9087 analogs, '7075 and PS75, completely reversed the mechanical hypersensitivity in the neuropathic pain model, with PS75 being more effective than '9087 (Fig. 4A). In contrast to '9087, PS75 did increase the mechanical thresholds of naïve (uninjured) mice (Fig. 4A). The antiallodynic effects of '4622 and '7075 were reversed by atipamezole (*48*); although this antagonist also partially reversed the antiallodynia of PS75, '2998, and '0172, these effects did not reach statistical significance at the small numbers of mice tested (Fig. 4C). PS75 also increased withdrawal latencies in the tail flick (50°C) acute thermal pain assay, and when tested in the D79N mutant mice, its analgesic effect was reduced by >50% (Fig. 4, D and E). Compounds '0172 and '4622 also exhibited antihyperalgesic effects in the CFA inflammatory pain model (Fig. 4G); '2998 did not, which may reflect the reduced brain penetration of this molecule (table S10). Only '4622 caused slight motor impairment at its equianalgesic dose in the rotarod test; however, the effect did not reach the full sedation observed with dexmedetomidine (Fig. 4H). As with '9087, increased dosing up to 20 mg/kg PS75 did not have an effect on the rotarod test (Fig. 4H). Taken together, these pharmacological and chemical-genetic epistasis experiments support a mechanism of action primarily through the α_{2A}AR receptor, though a lesser contribution of other α_2AR subtypes cannot be ruled out.

Some α_{2A}AR agonists can produce changes in feeding, weight gain, and hyperglycemia (*53*, *54*) as side effects. Accordingly, we evaluated the effect of compound treatment on body weight >48 hours after injection while allowing the mice to freely feed. We found no effect on body weight for '9087 dosed at 5 mg/kg, 10 mg/kg, or 20 mg/kg, nor for dexmedetomidine dosed at 30 μg/kg (fig. S18). We also investigated whether '9087 induced constipation, a side

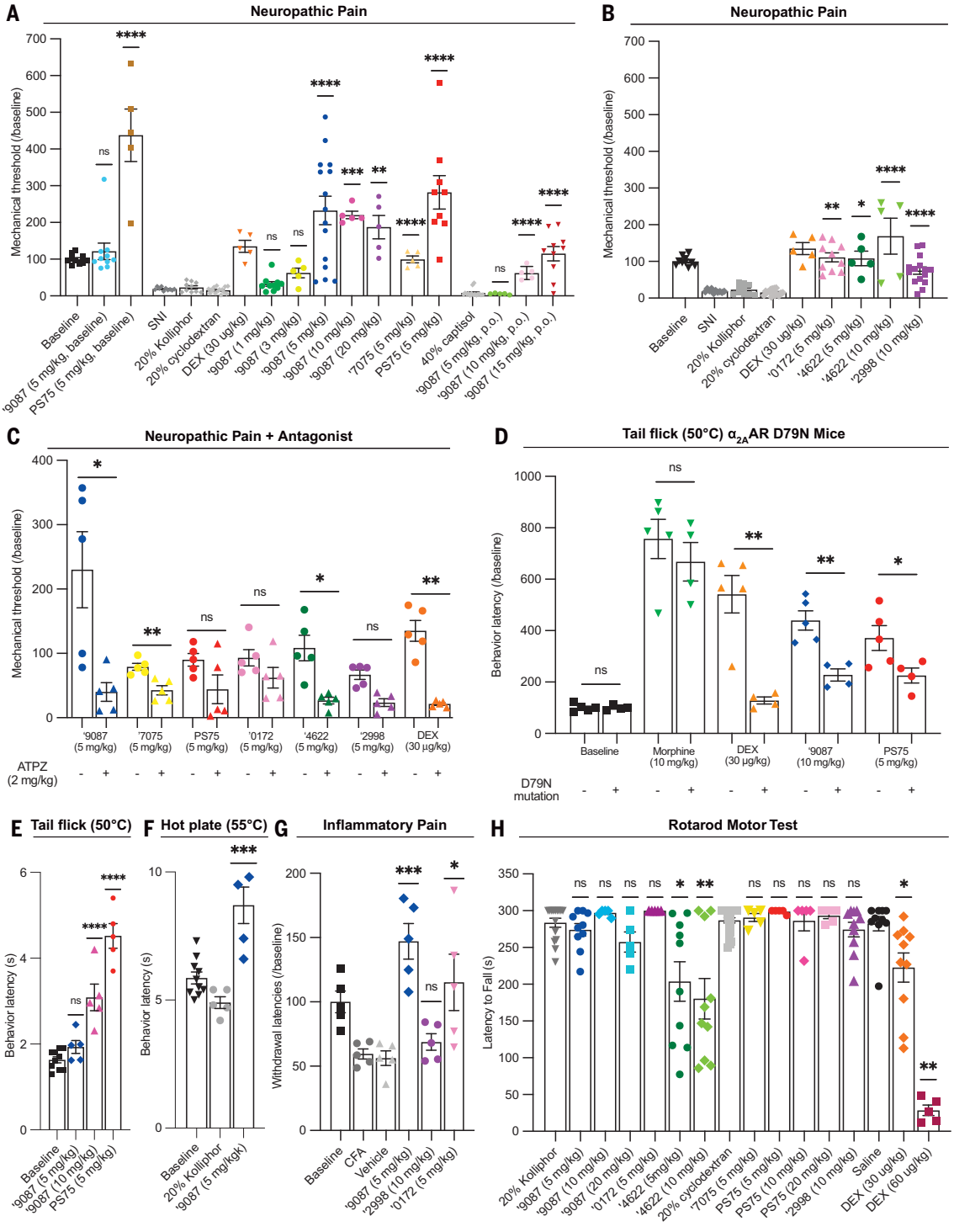


Fig. 4. The docking-derived agonists are antinociceptive in neuropathic, inflammatory, and acute thermal pain through the α_{2A}AR but are not sedating. (A to C) Effect of new α_{2A}AR agonists in neuropathic pain model in mice after SNI with mechanical allodynia. (**A**) The new agonists '9087 and PS75 administered in naïve mice (baseline versus '9087, 5 mg/kg; baseline versus PS75, 5 mg/kg; one-way ANOVA; ns, not significant; ****$P < 0.0001$), dose response of '9087 in SNI mice and analogs '7075 and PS75 compared with their vehicles (20% kolliphor versus all '9087 doses; 20% cyclodextran versus '7075 and PS75; one-way ANOVA; **$P < 0.01$; ***$P < 0.001$; ****$P < 0.0001$) with positive control dexmedetomidine (DEX), and '9087 administered orally (p.o.) compared with its vehicle (40% captisol versus '9087 doses; one-way ANOVA; ****$P < 0.0001$). (**B**) Effect of additional agonists '4622, '0172, and '2998 compared with their vehicles (20% kolliphor versus '4622, 5 mg/kg; '4622, 10 mg/kg; and '0172, 5 mg/kg; one-way ANOVA; 20% cyclodextran versus '2998; two-tailed *t* test; ns = *$P < 0.05$; **$P < 0.01$; ****$P < 0.0001$) and positive control DEX. (**C**) Administration of α_2AR antagonist atipamezole (ATPZ, 2 mg/kg i.p.) to block agonist efficacy in neuropathic pain model ('9087 versus '9087 with ATPZ; '7075 versus '7075 with ATPZ; PS75 versus PS75 with ATPZ; '0172 versus '0172 with ATPZ; '4622 versus '4622 with ATPZ; '2998 versus '2998 with ATPZ; DEX versus DEX with ATPZ; two-tailed *t* test; *$P < 0.05$; **$P < 0.01$). (**D**) Diminished analgesia in α_{2A}AR D79N mice in the 50°C tail flick assay for acute thermal (heat) pain. The mutation does not affect morphine analgesia but substantially decreases the analgesia by DEX, '9087, and PS75 (baseline WT versus D79N; morphine WT versus D79N; DEX WT versus D79N; '9087 WT versus D79N; PS75 WT versus D79N; two-tailed *t* test; *$P < 0.05$; **$P < 0.01$). (**E**) Analgesia of '9087 and PS75 in 50°C tail flick assay for acute thermal (heat) pain compared with its vehicle (20% Kolliphor versus '9087 and PS75; one-way ANOVA; ****$P < 0.0001$). (**F**) Analgesia of '9087 in 55°C hot plate assay for acute thermal (heat) pain compared with its vehicle (20% Kolliphor versus '9087; two-tailed *t* test; ***$P < 0.001$). (**G**) Efficacy of newly characterized agonists in CFA-induced hyperalgesia compared with the vehicle (vehicle versus '9087, '2998, and '0172; one-way ANOVA; *$P < 0.05$; ***$P < 0.001$). (**H**) Evaluating motor impairment and sedation of newly characterized agonists in the rotarod motor test. Only '4622 causes slight motor impairment, whereas other agonists do not. DEX causes significant impairment and complete sedation at higher doses. All compounds compared with their vehicles (20% Kolliphor versus '9087, '0172, and '4622; 20% cyclodextran versus '2298, '7075, and PS75; saline versus DEX; one-way ANOVA; *$P < 0.05$; **$P < 0.01$; ****$P < 0.0001$). For (A) to (G), all compounds were administered s.c., unless otherwise indicated. Data are shown as individual data points and means ± SEMs (n = 4 to 25).

effect well-known for opioids and other classes of analgesics, comparing it with dexmedetomidine and with morphine tested at analgesic doses (30 μg/kg and 10 mg/kg, respectively). The number of accumulated pellets over 6 hours after vehicle or compound injection was measured. As expected, morphine induced constipation when compared with vehicle at the 1-, 2-, and 3-hour marks. By contrast, although pellet number did decrease modestly with '9087 and dexmedetomidine, neither effect differed significantly from vehicle (fig. S18). We recognize that other possible side effects remain untested in this study; we return to these in the Discussion section.

Discussion

Three key observations emerge from this study. First, multiple chemotypes, unrelated to known agonists, discovered directly from large-library docking are efficacious in neuropathic, inflammatory, and acute pain models through α_{2A}AR agonism (Fig. 4, A to F). In docking, as in other target-based screens, the initial goal is to identify molecules with in vitro activity; these are then optimized for in vivo activity through extensive structure-activity optimization (*13*, *14*, *17*, *20*). Although it may be rare that direct hits from a docking screen are themselves in vivo active, such activity of the direct docking hits in this study does speak to the strengths of interrogating vast virtual libraries (*11*, *12*). Second, functional assays reveal preferential $G_{i/o/z}$ activation versus other G protein subtypes, no β-arrestin activity, and no receptor internalization for '9087 and its analogs, '7075 and PS75, compared with the established therapeutic α_{2A}AR agonists, like dexmedetomidine and brimonidine, that also activate multiple other G protein and β-arrestin signaling pathways (Fig. 1C, Fig. 3B, table S2, and figs. S6 to S8). Although the high rate of agonist discovery was an intended outcome of docking against the activated state of the α_{2B}AR, the functional selectivity was not designed and can be attributed to the chemotypes they explore and, by extension, their use of both canonical and noncanonical receptor interactions (Fig. 2 and figs. S12 and S13). There is no logical requirement that new chemotypes lead to new signaling pharmacology, though this has often been observed for other receptors (*10*, *13*, *17*, *25*). Third, unlike dexmedetomidine and clonidine (*6*, *7*, *55*), '9087 and its analogs, PS75 and '7075, do not cause sedation or motor impairment at analgesic doses, potentially enabling broader applications to pain treatment and attesting to the ability to differentiate these two effects with α_{2A}AR agonists (Fig. 4H).

The new α_{2A}AR chemotypes explored (Fig. 1B) reflect the size and diversity of the docked libraries. Most of the actives emerged from the fragment-like library in ZINC, which covers a much greater portion of the chemical universe in its size range than do the lead-like or drug-like libraries. This is akin to physical fragment libraries, which typically might include ~1500 molecules (*56*) but are thought to cover more chemotypes than high-throughput screening libraries that are 1000-fold larger. Meanwhile, the virtual fragment library in ZINC enumerates more than 20 million molecules (*11*, *12*), ~10,000-fold more than in most physical fragment libraries. With more than 800,000 Bemis-Murcko scaffolds (*18*), there are 500-fold more fragment scaffolds in the docked library than there are molecules in most physical fragment libraries. From this great chemotype diversity springs opportunities for ligands with distinct pharmacology.

How the new chemotypes confer new pharmacology is uncertain. From the cryo-EM co-complex with '9087 and substitution of binding site residues, '9087 and '7075 appear to make weaker interactions with $D128^{3.32}$ and an apparently stronger interaction with $F427^{7.39}$ compared with the canonical agonists (Fig. 2B and figs. S12 and S13). These structural differences may contribute to the unusual functional $G_{i/o/z}$ selectivity over other G protein subtypes and β-arrestins as compared with known agonists, and to the lack of receptor internalization (Fig. 3B and figs. S6 to S8). In turn, this unusual signaling may play a role in conferring analgesia without sedation (Fig. 4). Admittedly, as the engagement of transducing G proteins and β-arrestins occurs 35 Å away from the orthosteric site, other mechanisms may be involved (*57*). Moreover, the physiological impact of the selective signaling will be entangled with the pharmacokinetics of the molecules. Regardless, what should be clear is that the analgesic potential of α_{2A}AR agonists may be disentangled from their sedative effect, which is important for future drug development.

Several cautions merit re-emphasis. '9087 and its analogs are not as potent as dexmedetomidine. The action of '9087 in vivo is blocked by the α_2AR antagonist atipamezole (*48*) and much reduced in D79N α_{2A}AR mice, which indicates that the α_{2A}AR is the primary receptor mediating activity in vivo (Fig. 4, C and D). However, especially for the mutant mice, we note that although most efficacy above baseline was reduced, it was not fully reversed (Fig. 4, C and D), and other targets may also play a role, including the I2R and other α_2AR subtypes. We also have not extensively evaluated side effects common for α_{2A}AR agonists, especially cardiovascular effects mediated by α_{2A}AR and α_{2B}AR activation (*6*). Finally, we do not anticipate that the ability to translate directly from docking hits to in vivo activity, as we saw in this study, will be common. In this case, it was helped by the small size of the α_{2B}AR and α_{2A}AR orthosteric sites and correspondingly the high potencies and good physical properties of the docking hits (fig. S1 and tables S2 and S10).

These caveats should not obscure the key observations of this study. From an ultralarge library docking screen emerged low-nanomolar α_{2A}AR partial agonists, topologically unrelated to previously known ligands, making previously unobserved interactions with the receptor that appear to confer new pharmacology (Fig. 1; Fig. 2B; table S2; and figs. S6 to S8, S12, and S13). Several of the new α_{2A}AR agonists were antiallodynic and analgesic in neuropathic and inflammatory pain models and against acute nociception in naïve animals (Fig. 4, A to G). Among the most promising are '9087 and PS75, both of which are strongly analgesic without the sedative effects of dexmedetomidine (Fig. 4) and are orally bioavailable (table S10). These properties make the compounds plausible therapeutic leads for new nonopioid pain therapeutics without the sedation of classic α_{2A}AR drugs.

Materials and methods

Molecular docking

The α_{2B}AR receptor with dexmedetomidine and G_{oA} [Protein Data Bank (PDB) ID: 6K41] (*9*) was used for docking calculations before the determination of the α_{2B}AR dexmedetomidine-bound structure (PDB 7EJA; comparison shown in fig. S1). Three screens of the ZINC15 database were run, two for fragment molecules (<250 amu, cLogP ≤ 3.5) and one for lead-like (250 to 350 amu, cLogP ≤ 3.5). Docking was performed with DOCK3.7 (*26*). For the first screen, 45 matching spheres (*26*) were used, 15 from the docked pose of dexmedetomidine and 30 from SPHGEN-generated spheres (*58*). The receptor structure was protonated using REDUCE (*59*), and AMBER united atom charges were assigned (*60*). In control calculations (*61*) with 15 known agonists from the IUPHAR-BPS database (*27*) and from the literature (*29*–*31*), balanced against 1800 property matched decoys (*62*), docking parameters were optimized based on adjusted logAUC (*61*) and based on recapitulation of ligand interactions with residues α_{2B}AR $D92^{3.32}$, $F412^{7.39}$, $F387^{6.51}$, $Y391^{6.55}$, and $F388^{6.52}$ (residues conserved in α_{2A}AR: $D128^{3.32}$, $F427^{7.39}$, $F405^{6.51}$, $Y409^{6.55}$, and $F406^{6.52}$). An "extrema" set was used to evaluate cationic charge preference, as described (*18*, *62*). The protein low dielectric and desolvation regions, defined by pseudoatoms calculated with SPHGEN (*58*), were extended as previously described (*63*), based on the control calculations, by a radius of 1 and 0.3 Å, respectively (*10*, *64*). Energy potential grids were calculated using CHEMGRID for AMBER-based van der Waals potential, QNIFFT (*65*) for Poisson-Boltzmann–based electrostatic potentials, and SOLVMAP (*66*) for context-dependent

ligand desolvation. In the second and third docking screens, differences included modified matching spheres (added rigid fragments of xylazine docked-pose, only used 40 matching spheres) and extension of the desolvation pseudoatoms by a radius of 0.2 A.

For the first screen, 20 million molecules from the ZINC15 (https://zinc15.docking.org/) fragments subset were docked in 3008 core hours or ~6 wall-clock hours on a 500-core cluster. Almost 5 trillion complexes were sampled, on average each molecule sampled 2405 orientations and 202 conformations. Only ~8 of 20 million could be sterically accommodated in the orthosteric site, reflecting its small size. For the second screen, the same 20 million fragments were docked in 3830 core hours or 7.7 hours on 500-core cluster, sampling more than 6 trillion complexes; on average, each molecule sampled 3122 orientations and 203 conformations. About 9 million molecules were accommodated in the site. For the third screen, 281 million molecules from ZINC15 lead-like subset were screened in 71,625 core hours or ~1 week on 500 cores. More than 222 trillion complexes were sampled with an average of 4553 orientations and 469 conformations per molecule, though ultimately only 13.5 million could sterically fit in the site.

For the first and second screens, the top 161,055 scored compounds were clustered by ECFP4-based Tanimoto coefficient (Tc) of 0.5 to identify distinct chemotypes, resulting in 37,150 and 33,378 clusters. For the third screen, the top 300,000 scored compounds were clustered in the same manner, resulting in 57,168 clusters. Molecules were filtered for novelty, removing those with Tc > 0.35 to 15 α_{2A}AR agonists used in control calculations. The top 5000 ranked molecules remaining were visually filtered for interactions at α_{2B}AR residues D92$^{3.32}$, F412$^{7.39}$, F387$^{6.51}$, Y391$^{6.55}$, and F388$^{6.52}$for the first and second screens; for the third screen, the top 20,000 molecules were examined by the same criteria. Lastly, prioritized molecules were also filtered for internal torsional strain; this was done visually for the first screen, whereas the second and third screens used a method drawing on CSD torsion populations cutting off at a total energy of 2 torsion energy units (*32*). An additional novelty filter was performed removing molecules with TC > 0.35 to CHEMBL29 (*28*) α_{2A}AR compounds. Sixty-four molecules were selected for purchasing: 33, 26, and 5 from the first, second, and third screens, respectively. Ten were sourced from WuXi and another 54 from Enamine, of which 8 and 40 were successfully synthesized, respectively. Most of these compounds have not previously been synthesized before, to the best of our knowledge, except for some of the smaller fragments, which have been previously used as building blocks (table S5).

Synthesis of tangible molecules

Forty-eight molecules prioritized for purchasing were synthesized by Enamine and Wuxi for a total fulfilment rate of 75%. Compounds were sourced from the Enamine REAL database (https://enamine.net/compound-collections/real-compounds) or the WuXi GalaXi virtual library. The purities of active molecules synthesized by Enamine and WuXi were at least 90% and typically above 95%. For bespoke compound synthesized in house purities were at least 96% and typically above 99%. The purity of compounds tested in vivo were >95% and typically above 98% (table S5 and figs. S19 and S20).

Ligand optimization

Analogs for four docking hits ('9087, '2998, '0172, and '4622) were queried in Arthor and SmallWorld 1.4 and 12 Billion tangible libraries (https://sw.docking.org/, https://arthor.docking.org), the latter primarily containing Enamine REAL Space compounds (https://enamine.net/compound-collections/real-compounds/real-space-navigator). Results from SmallWorld, Bemis-Murcko framework, and substructure queries were pooled, docked into the α_{2B}AR site before '9087-α_{2A}AR structure being determined. Compounds with favorable interactions in the orthosteric site were prioritized, leading to 13 analogs for '9087 (table S5). Also, for the four docking hits, analogs were designed by modifying the two-dimensional (2D) chemical structure to test specific hypotheses, adding another six analogs for '9087 (table S5). The second round of analogs for '9087 were designed and prioritized for bespoke synthesis. Some were docked to a preliminary cryo-EM model of the '9087-α_{2A}AR structure, whereas several were designed and synthesized regardless of docked pose to test specific hypotheses; in total, eight of these were synthesized and tested (table S5). Calculation of the contact areas was performed by means of UCSF Chimera (https://rbvi.ucsf.edu/chimera).

Bespoke synthesis

'7075 was designed for hypothesis testing and was bespoke synthesized by Enamine (fig. S19).

Molecular modeling of '7075 and PS75

Maestro (version 2019-4, Schrödinger, Inc.) was used to manually change the chemical structure of '9087 to '7075 or PS75 in a preliminary model of the '9087-α_{2A}AR complex cryo-EM structure. The isoquinoline nitrogen was changed to a carbon and the fluorine or chlorine substituent was added to the naphthalene ring for '7075 and PS75, respectively. The resulting complex of '7075 or PS75 and α_{2A}AR coupled to the G protein but without scFv16 was energy minimized following the Protein Preparation Wizard protocol using the OPLS3e force field. The maximum heavy atom deviation from the initial model was 0.3 Å.

Passive membrane permeability prediction

Ligand structures were converted from SMILES strings to 3D structures using LigPrep (version 53013, Schrödinger, Inc.). For the passive membrane permeability prediction (*67*, *68*), we retained only neutral form for each ligand. Passive membrane permeability of a ligand is predicted from the free-energy of insertion (ΔG_I), i.e., from the energy difference between a conformer in low and high dielectric media. Therefore, we generated conformations of each ligand using ConfGen software (version 5.1, Schrödinger, Inc.). We minimized each conformer in a low dielectric medium (chloroform) to mimic the membrane dielectric using Protein Local Optimization Program (PLOP) (*69*). After finding the lowest energy conformer in the low dielectric medium, we calculated the energy of that energy-minimized conformer in water. We subtracted the energy of the ligand in the high-dielectric water from the low-dielectric medium. We further added a deionization penalty term to account for transforming ionized form of the ligand in water to its neutral form in membrane. We computed the deionization penalty energy using the empirical pK_a (where K_a is the acid dissociation constant) prediction software Epik (version 5.1013, Schrödinger, Inc.). We rank-ordered the ligands based on their free-energy of insertion.

Radioligand binding experiments

Receptor binding affinities for the α_{2A}AR receptor and to α_{2B}AR as well as the related adrenergic subtypes α_{1A}, α_{1B}, α_{2C}, β_1, and β_2 were determined as described previously (*44*, *70*). In brief, membranes were prepared from HEK293T cells transiently transfected with the cDNA for human α_{2A}AR, murine α_{2A}AR (provided by D. Calebiro, Birmingham, UK), human α_{2B}AR (obtained from the cDNA resource center, www.cdna.org), or with the cDNAs for the human α_{1A}, α_{1B}, α_{2C}, β_2 (all from cDNA resource center), and β_1 (provided by R. Sunahara, UCSD). Receptor densities (B_{max} value) and specific binding affinities (K_d value) for the radioligand [^{3}H]RX82,1002 (specific activity 52 Ci/mmol, Novandi, Södertälje, Sweden) were determined as 1400 ± 210 fmol/mg protein and 0.54 ± 0.024 nM for human α_{2A}AR, 4000 ± 720 fmol/mg protein and 1.8 ± 0.61 nM for murine α_{2A}AR, and 3400 ± 580 fmol/mg protein and 2.3 ± 0.52 nM for α_{2B}AR, respectively. Further values are 3200 ± 1900 fmol/mg protein and 0.58 ± 0.11 nM for α_{2C}, 2000 ± 950 fmol/mg protein and 0.70 ± 0.13 nM for α_{1A}, and 4000 fmol/mg protein and 0.11 nM for α_{1B}, both determined with [^{3}H]prazosin (51 Ci/mmol, PerkinElmer, Rodgau, Germany), respectively, and 1400 ± 360 fmol/mg protein and 0.070 ± 0.006 nM for β_1 and 1300 ± 230 fmol/mg protein and 0.074 ± 0.012 nM for β_2, both determined with [^{3}H]CGP12,188 (52 Ci/mmol, PerkinElmer).

Competition binding with α_2AR subtypes were performed by incubating membranes in buffer A (50 mM TRIS at pH 7.4) at final protein concentrations of 3 to 10 μg per well with the radioligand (final concentration 0.5 to 2.0 nM according to the appropriate K_d and B_{max}) and varying concentrations of the competing ligands for 60 min at 37°C. Binding to α_{1A} and α_{1B} was measured with buffer B (50 mM TRIS, 5 mM $MgCl_2$, 1 mM EDTA, 100 μg/mL bacitracin and 5 μg/mL soybean trypsin inhibitor at pH 7.4) at 2 to 6 μg per well (radioligand at 0.2 to 0.3 nM) and binding to β_1 and β_2 was measured with buffer C (25 mM HEPES, 5 mM $MgCl_2$, 1 mM EDTA, and 0.006% bovine serum albumin at pH 7.4) at 4 to 8 μg per well (radioligand 0.2 nM). Nonspecific binding was determined in the presence of unlabeled ligand at 10 μM. Protein concentration was measured using the method of Lowry (*71*).

The resulting competition curves were analyzed by nonlinear regression using the algorithms implemented in Prism 8.0 (GraphPad Software, San Diego, CA) to provide mean inhibitory concentration (IC_{50}) values, which were subsequently transformed into a K_i values applying the equation of Cheng and Prusoff (*72*). Mean K_i values (±SEM for $n \geq 3$ or ±SD for $n = 2$) were derived from two to seven experiments each performed in triplicates.

Functional assays

Plasmids

The human wild-type (WT) α_{2A}AR, its respective receptor mutants (*73*) and the murine α_{2A}AR, all carrying an N-terminal HA-signal sequence and a FLAG-tag, as well as the human adrenergic receptor subtypes α_{1A}, α_{1B}, α_{2C}, β_1, and β_2 and the dopamine receptor D_{2long} were cloned to pCDNA3.1 for G protein activation assays [BRET, inositol phosphate (IP) accumulation]. Human α_{2A}AR and α_{2B}AR were fused to the ARMS2-PK2 sequence and cloned to pCMV (DiscoverX, Eurofins) for β-arrestin-2 recruitment assays, respectively, using polymerase chain reaction (PCR) and Gibson Assembly (New England Biolabs) (*70*). Sequence integrity was verified by DNA sequencing (Eurofins Genomics).

Bioluminescence resonance energy transfer

G protein activation by human α_{2A}AR and D_{2long} was monitored with $G\alpha_{i1}$-RLucII (*74*, *75*) together with $G\beta_1$ and $G\gamma_2$-GFP_{10}. Assessment of arrestin recruitment was performed by enhanced bystander BRET using CAAX-rGFP and β-arrestin-2–RLucII as biosensors (*39*, *74*) in the presence of GRK2, as described (*44*, *76*). In brief, HEK293T cells (gift from the Chair of Physiology, FAU Erlangen-Nürnberg) were transfected with 200 ng receptor plasmid for G protein activation (receptor:Gα:Gβ:Gγ ratio 2:0.5:1:4) or 100 ng receptor plasmid for β-arrestin recruitment (receptor:β-arrestin:GRK2:CAAX ratio 1:0.2:1:3) using linear polyethyleneimine (PEI, Polysciences, 3:1 PEI:DNA ratio). The DNA was complemented to a total amount of 1 μg DNA per 3×10^5 cells with single-stranded DNA (ssDNA) (Sigma Aldrich) and 10,000 cells per well were transferred into 96-well half-area plates (Greiner, Frickenhausen, Germany). Additional experiments were performed using the same amount of G protein plasmids as described above but 50 ng or 10 ng α_{2A}AR plasmid instead. 48 hours after transfection, the cell medium was exchanged with PBS (phosphate buffered saline), and cells were stimulated with ligands at 37°C for 10 min. Coelenterazine 400a (abcr GmbH, Karlsruhe, Germany) at a final concentration of 2.5 μM was added 5 min before measurement. BRET was monitored on a Clariostar plate reader (BMG, Ortenberg, Germany) with the appropriate filter sets (donor 410/80 nm, acceptor 515/30 nm) and was calculated as the ratio of acceptor emission to donor emission. BRET ratio was normalized to the effect of buffer (0%) and the maximum effect of norepinephrine (100%) for adrenergic receptors and quinpirole (100%) for D_{2long}. For each compound, 3 to 17 individual experiments were performed, each done in duplicates.

Surface expression of the α_{2A}AR in the G protein activation assays was monitored applying an enzyme-linked immunosorbent assay (ELISA) directed against the N-terminal FLAG tag. HEK293T cells were transfected with the cDNAs encoding α_{2A}AR, $G\alpha_{i1}$-RLucII, $G\beta_1$, $G\gamma_2$-GFP_{10}, and ssDNA, as described above. As a control, cells transfected with only α_{2A}AR or mock pcDNA3.1 plasmid and ssDNA were used. Immediately after transfection, 50,000 cells per well were transferred to a 48-well plate (Greiner) pretreated with poly-D-lysine (Sigma Aldrich) and incubated at 37°C and 5% CO_2 for 48h. The medium was removed, cells were treated with 4% paraformaldehyde for 10 min, washed once (wash buffer, 150 mM NaCl, 25 mM Tris, pH 7.5), and blocked for 60 min (30 g/liter skim milk powder in wash buffer, all steps carried out at room temperature). After incubation with anti-FLAG M2 mouse IgG (F3165, Sigma Aldrich, 1:4000 in blocking solution) for 60 min, cells were washed twice, blocked again for 60 min and incubated with anti-mouse rabbit IgG-HPR (A9044, Sigma Aldrich, 1:20,000 in blocking solution) for 60 min. Cells were washed thrice, before 200 μL substrate buffer was added (2.8 mM o-phenylenediamine, 35 mM citric acid, 66 mM Na_2HPO_4, pH 5.0). Reactions were kept in the dark for 5 to 15 min and stopped by addition of 1 M H_2SO_4 (200 μL). Resulting mixtures were transferred to a 96-well plate and absorption was determined with the Clariostar microplate reader at 492 nm. Data were normalized using cells transfected with only α_{2A}AR (100%) and mock pcDNA3.1 (0%), respectively. $n = 4$ independent experiments were performed with each condition in triplicate.

The sensitivity of selected ligands to the receptor mutants α_{2A}AR-D128$^{3.32}$A, α_{2A}AR-D128$^{3.32}$T, α_{2A}AR-D128$^{3.32}$L, α_{2A}AR-S215$^{5.42}$A, α_{2A}AR-Y409$^{6.55}$A, α_{2A}AR-Y409$^{6.55}$T, α_{2A}AR-Y409$^{6.55}$F, α_{2A}AR-F427$^{7.39}$F, α_{2A}AR-Y431$^{7.43}$A, and α_{2A}AR-Y431$^{7.43}$F was monitored by G protein activation as described above, transfecting the appropriate receptor together with $G\alpha_{i1}$-RLucII and $G\beta_1/G\gamma_2$-GFP_{10}. Data were analyzed as ligand-induced changes in BRET compared with vehicle (deltaBRET), and normalization was done according to the effect of buffer (0%) and norepinephrine (100%) with the exception of α_{2A}AR-D128$^{3.32}$A (dexmedetomidine = 100%), α_{2A}AR-D128$^{3.32}$T, and α_{2A}AR-D128$^{3.32}$L (“7075 = 100%). Similarly, the effect of the α_{2A}AR-D128$^{3.32}$A, α_{2A}AR-S215$^{5.42}$A, α_{2A}AR-Y409$^{6.55}$A, α_{2A}AR-Y409$^{6.55}$F, α_{2A}AR-F427$^{7.39}$F, α_{2A}AR-Y431$^{7.43}$A, and α_{2A}AR-Y431$^{7.43}$F mutations on arrestin recruitment was evaluated as described above, transfecting the appropriate receptor together with CAAX-rGFP, GRK2, and β-arrestin-2–RLucII. Data were analyzed as ligand-induced changes in BRET compared with vehicle (deltaBRET). Three to seven experiments were done in duplicate.

IP accumulation assay

Determination of G protein–mediated signaling by human α_{2A}AR, murine α_{2A}AR, and human α_{2B}AR was performed applying an IP accumulation assay (IP-One HTRF, Cisbio, Codolet, France) according to the manufacturer’s protocol and in analogy to previously described protocols (*77*, *78*). In brief, HEK 293T cells were cotransfected with the cDNA for a receptor and the hybrid G protein $G\alpha_{qi}$ ($G\alpha_q$ protein with the last five amino acids at the C terminus replaced by the corresponding sequence of $G\alpha_i$) (gift from The J. David Gladstone Institutes, San Francisco, CA), respectively, in a ratio of 1:2. After 1 day, cells were transferred into 384-well microplates (Greiner) and incubated for further 24 hours. On the day of the experiment, cells were incubated with test compounds for 90 min (α_{2A}AR) or 120 min (α_{2B}AR), and accumulation of second messenger was stopped by adding detection reagents (IP1-d2 conjugate and Anti-IP1cryptate TB conjugate). After 60 min, TR-FRET was monitored with a Clariostar plate reader. FRET-signals were normalized to buffer (0%) and the maximum effect of norepinephrine (100%). Three to nine (murine α_{2A}AR, α_{2B}AR) or 4 to 11 repeats (human α_{2A}AR), respectively, were performed for each test compound all done in duplicate.

PathHunter arrestin recruitment assay

Investigation of α_{2A}AR and α_{2B}AR stimulated β-arrestin-2 recruitment was performed applying an assay which is based on fragment

complementation of β-galactosidase (PathHunter assay, DiscoverX, Birmingham, UK) as described (*79*). In detail, HEK293T cells stably expressing the enzyme acceptor (EA) tagged β-arrestin-2 were cotransfected with human α_{2A}AR or α_{2B}AR each fused to the ProLink-ARMS2-PKS2 fragment for enzyme complementation and GRK2 (cDNA Resource Center) at equal amounts and subsequently transferred into 384 well microplates (Greiner) after 1 day. After incubation for further 24 hours cells were incubated with test compounds for 60 min (α_{2A}AR) or 90 min (α_{2B}AR), arrestin recruitment was stopped by adding detection regent and the resulting chemoluminescence was monitored with a Clariostar plate microreader. Data were normalized relative to buffer (0%) and the maximum effect of norepinephrine (100%). Three to nine repeats for α_{2A}AR (three to six for α_{2B}AR) in duplicate were measured.

DiscoverX HitHunter cAMP G protein activation assay

Dexmedetomidine, brimonidine, '9087, and '7075 were tested by DiscoverX (catalog item 86-0007P-2270AG; Eurofins; CA, USA) in their HitHunter XS+ assay. Freezer stock cAMP Hunter cell lines were expanded, then seeded in a total volume of 20 μL into white walled, 384-well microplates and incubated at 37°C before testing. For agonist determination, cells were incubated with compound samples in the presence of EC_{80} forskolin to induce response. Media was aspirated from cells and replaced with 15 μL 2:1 HBSS/10 mM Hepes: cAMP XS+ Ab reagent. Intermediate dilution of sample stocks was performed to generate 4X sample in assay buffer containing 4X EC_{80} forskolin. 5 μL of 4X sample was added to cells and incubated at 37°C or room temperature for 30 to 60 min. Finally assay vehicle concentration was 1%. After sample incubation assay signal was generated through incubation with 20 μL cAMP XS+ ED/CL lysis cocktail for one hour followed by incubation with 20 μL cAMP XS+ EA reagent for three hours at room temperature. Microplates were read after signal generation with a PerkinElmer Envision Instrument for chemiluminescent signal detection. Compound activity was analyzed using CBIS data analysis suite. For G_i agonist mode, percentage activity is calculated using the following formula: percentage activity = 100% × [1 – (mean RLU of test sample – mean RLU of MAX control) / (mean RLU of vehicle control – mean RLU of MAX control)]. Brimonidine was used as the control agonist. Each measurement was done in duplicate.

EMTA coupling panel for α_{2A}AR

The ebBRET-based effector membrane translocation assay (EMTA) allows detection of each Gα protein subunit activation. Upon receptor activation, G protein–effector proteins fused at their C terminus to Renilla luciferase (RlucII) translocate from cytoplasm to the plasma membrane to selectively bind activated Gα proteins (p63-RhoGEF-RlucII with $G_{q/11}$ family, Rap1-GAP-RlucII with $G_{i/o}$ family and PDZ-RhoGEF-RlucII with $G_{12/13}$ family), thus leading to an increase in ebBRET by becoming in close proximity to the plasma membrane targeted energy acceptor, Renilla green fluorescent protein (rGFP-CAAX). The heterologous coexpression of each Gα subunits allow to identify which specific members of each G protein families (i.e.: G_{i1}, G_{i2}, G_{i3}, G_{oA}, G_{oB}, G_z, G_q, G_{11}, G_{14}, G_{15}, G_{12}, and G_{13}) is activated by a receptor. The assay is also sensitive enough to detect responses elicited by endogenous $G_{i/o}$ protein families in the absence of heterologously expressed G protein. The same plasma membrane translocation principle is used to measure β-arrestin-1 or -2 recruitment (*39*) using β-arrestin–RlucII/rGFP-CAAX biosensors.

Cell culture

HEK293 clonal cell line (HEK293SL cells), hereafter referred to as HEK293 cells, were a gift from S. Laporte (McGill University, Montreal, Quebec, Canada) and previously described (*39*). Cells were cultured in DMEM medium (Wisent; St-Jean-Baptiste, QC, Canada) supplemented with 10% newborn calf serum iron fortified (NCS) (Wisent). Cells were passaged weekly and incubated at 37°C in a humidified atmosphere with 5% CO_2 and checked for mycoplasma contamination.

Transfection

HEK293 cells (1.2 mL at 3.5×10^5 cells per mL) were transfected with a fixed final amount of premixed biosensor-encoding DNA (0.57 μg, adjusted with salmon sperm DNA; Invitrogen) and human α_{2A}AR DNA for G_s, $G_{i/o}$, $G_{q/11}$ and β-arrestins experiments. For $G_{12/13}$ experiments, cells were transfected with 1 μg of total DNA (adjusted with salmon sperm DNA; Invitrogen), including empty pCDNA3.1 vector or human α_{2A}AR DNA. Transfections were performed using linear polyethylenimine (PEI, 1 mg/mL; Polysciences) diluted in NaCl (150 mM, pH 7.0) as a transfecting agent (3:1 PEI/DNA ratio). Cells were immediately seeded (3.5×10^4 cells per well) into 96-well white microplates (PerkinElmer), maintained in culture for the next 48 hours and BRET experiments carried out. ebBRET (*38*) was used to monitor the activation of each Gα protein, as well as β-arrestin-1 and -2 recruitment to the plasma membrane. $G\alpha_s$ protein engagement was measured between the plasma membrane marker rGFP-CAAX and human $G\alpha_s$-RlucII in presence of human $G\beta_1$, $G\gamma_9$, and α_{2A}AR. $G\alpha_{12}$ or $G\alpha_{13}$ protein family activation was assessed using the selective-$G_{12/13}$ effector PDZ-RhoGEF-RlucII and rGFP-CAAX coexpressed with $G\beta_1$, $G\gamma_1$, and either $G\alpha_{12}$ or $G\alpha_{13}$, in presence of α_{2A}AR. $G\alpha_{i/o}$ protein family activation was followed using the selective-$G_{i/o}$ effector Rap1GAP-RlucII and rGFP-CAAX along with the human $G\alpha_{i1}$, $G\alpha_{i2}$, $G\alpha_{oA}$, $G\alpha_{oB}$, or $G\alpha_z$ subunits and α_{2A}AR. $G\alpha_{q/11}$ protein family activation was determined using the selective-$G_{q/11}$ effector p63-RhoGEF-RlucII and rGFP-CAAX along with the human $G\alpha_q$, $G\alpha_{11}$, $G\alpha_{14}$, or $G\alpha_{15}$ subunits and α_{2A}AR. β-arrestin recruitment to the plasma membrane was determined using DNA mix containing rGFP-CAAX and β-arrestin-1–RlucII or β-arrestin-2–RlucII in presence of α_{2A}AR.

Bioluminescence resonance energy transfer measurement

The day of the experiment, cells were washed with phosphate-buffered saline (PBS) and incubated in Tyrode Hepes buffer (137 mM NaCl, 0.9 mM KCl, 1 mM $MgCl_2$, 11.9 mM $NaHCO_3$, 3.6 mM NaH_2PO_4, 25 mM HEPES, 5.5 mM D-Glucose and 1 mM $CaCl_2$, pH 7.4) for 1 hour at 37°C. Cells were then treated with increasing concentrations of compounds for 10 min at 37°C. The luciferase substrate Prolume purple (1 μM, NanoLight Technologies) was added during the last 6 min before the reading. Plates were read on the TriStar^2 LB 942 Multimode Microplate Reader (Berthold Technologies) with the energy donor filter (410 ± 80 nm; RlucII) and energy acceptor filter (515 ± 40 nm; GFP10 and rGFP CAAX). BRET signal (BRET^2) was determined by calculating the ratio of the light intensity emitted by the acceptor (515 nm) over the light intensity emitted by the donor (410 nm) and data were normalized in percentage of the maximal response elicited by the reference compound norepinephrine. The data were analyzed in GraphPad Prism 9.1 using "dose–response-stimulation log(agonist) versus response (four parameters)" and data were presented as means ± SEMs of at least three different experiments each done in simplicate. E_{max} and EC_{50} values were determined from dose-response curves to calculate the log (E_{max}/EC_{50}) value for each pathway and each compound. To determine the relative efficacy of the compounds to activate the different signaling pathways, the difference between the log(E_{max}/EC_{50}) values was calculated using the following equation

$$\Delta\log\left(\frac{E_{max}}{EC_{50}}\right) = \log\left(\frac{E_{max}}{EC_{50}}\right)_{compound} - \log\left(\frac{E_{max}}{EC_{50}}\right)_{norepinephrine} \quad (1)$$

The compounds' efficacy toward each pathway, relative to norepinephrine, were calculated as the inverse logarithm of the Δlog

(E_{max}/EC_{50}) using the following equation

$$\text{relative efficacy (RE)} = 10^{\Delta\log\left(\frac{E_{max}}{EC_{50}}\right)} \quad (2)$$

The SEM was calculated for the $\log(E_{max}/EC_{50})$ ratios using the following equation

$$SEM = \frac{\sigma}{\sqrt{n}} \quad (3)$$

where σ is the standard deviation, and n is the number of experiments.

The SEM was calculated for the $\Delta\log(E_{max}/EC_{50})$ ratios using the following equation

$$SEM_{\left[\Delta\log\left(\frac{E_{max}}{EC_{50}}\right)\right]} = \sqrt{(SEM_{compound})^2 + (SEM_{norepinephrine})^2} \quad (4)$$

Statistical analysis was performed using a two-tailed unpaired t test on the $\Delta\log(E_{max}/EC_{50})$ ratios to make pairwise comparisons between tested compounds and norepinephrine for a given pathway, where $P < 0.05$ was considered statistically significant.

Internalization assay with rGFP-CAAX and rGFP-FYVE biosensors

Plasmids

Human α_{2A}AR sequence was fused to RlucII by cloning between the NheI and BamHI sites of pCDNA3.1/Zeo(+)-RlucII vector, using PCR (Q5 Hot Start High-Fidelity DNA Polymerase from NEB), enzymatic digestion (NEB) and ligation (Anza T4 DNA Ligase Master Mix; Invitrogen).

Transfection

The protocol used for transfection is the same as for $G_{12/13}$ EMTA experiments [i.e., cells were transfected with 1 μg of total DNA (adjusted with salmon sperm DNA; Invitrogen)]. Transfections were performed using linear polyethylenimine (PEI, 1 mg/mL; Polysciences) diluted in NaCl (150 mM, pH 7.0) as a transfecting agent (3:1 PEI/DNA ratio). Cells were immediately seeded (3.5×10^4 cells per well) into 96-well white microplates (PerkinElmer), maintained in culture for the next 48 hours and BRET experiments carried out. Human α_{2A}AR internalization was evaluated by measuring the disappearance of hα_{2A}AR-RlucII from the plasma membrane labeled with rGFP-CAAX and its relocalization in endosome labeled with rGFP-FYVE (*39*).

Bioluminescence resonance energy transfer measurement

The day of the experiment, cells were washed with phosphate-buffered saline (PBS) and incubated in Tyrode Hepes buffer for 1 hour at 37°C. Cells were incubated during 6 min with the luciferase substrate Prolume purple (1 μM, NanoLight Technologies) before addition of the indicated compound (0 or 100 μM) and kinetics were recorded during 30 min. For concentration-response curves, BRET signal was measured after 30 min incubation. Plates were read on a Spark microplate reader (Tecan; Männedorf, Switzerland) using the BRET2 manufacturer settings. BRET signal ($BRET^2$) was determined by calculating the ratio of the light intensity emitted by the acceptor (515 nm) over the light intensity emitted by the donor (410 nm) and for concentration-response curves, data were normalized in percentage of the maximal response elicited by the reference compound norepinephrine. The data were analyzed in GraphPad Prism 9.1 using "log(agonist) versus response–Variable slope (four parameters)" and data were presented as means ± SEMs of three experiments performed in triplicate for kinetics or in simplicate for concentration-response curves.

Cryo-EM sample preparation and structure determination

Preparation of the '9087-α_{2A}AR-G_{oA}-scFv16 and '4622-α_{2A}AR-G_{oA}-scFv16 complexes

The human WT α_{2A}AR was cloned to pFastBac vector with a N-terminal FLAG tag and a C-terminal histidine Tag. This construct was expressed in Sf9 insect cells using the pfastBac baculovirus system (Expression Systems). Cells were infected at a density of 4×10^6 cells per ml and then incubated for 48 hours at 27°C. Receptor was extracted and purified following the protocol described previously for α_{2B}AR (*9*). Briefly, receptor was purified by Ni-NTA chromatography, Flag affinity chromatography and size exclusion chromatography in the presence of 100 μM '9087 or '4622. The monomeric peak fractions of receptor were collected and concentrated to ~20 mg/mL. The freshly purified '9087-bound or '4622-bound α_{2A}AR was used for complex formation with the G protein. G_{oA} heterotrimers were expressed and purified as previously described with minor modifications (*78*). Briefly, Hi5 cells were grown to a density of 3 million per mL and then infected with $G\alpha_o$ and $G\beta_1\gamma_2$ baculovirus at a ratio of 10 to 20 mL/L and 1 to 2 mL/L, respectively, and then incubated for 48 hours at 27°C. Cells were solubilized with 1% (w/v) sodium cholate and 0.05% (w/v) DDM. After centrifugation, the supernatant was loaded onto Ni-NTA column and then exchanged to 0.05% DDM. The eluted G_{oA} heterotrimer was dephosphorylated by lambda phosphatase (homemade) and further purified through ion exchange using a Mono Q 10/100 GL column (GE Healthcare) and the peak fractions were collected and flash frozen in liquid nitrogen until use. The scFv16 (*80*) protein was expressed in insect Sf9 cells and purified with Ni-NTA column followed by the Superdex 200 Increase 10/300 GL column (GE Healthcare) with a buffer composed of 20 mM HEPEs, pH 7.5 and 100 mM NaCl. The monomeric peak fractions of receptor were collected and concentrated and stored at −80°C until use. The complex formation process is same as described. Briefly, the complex of α_{2A}AR with heterotrimeric G_{oA} was formed in a buffer containing 20 mM HEPEs pH 7.5, 100 mM NaCl, 0.1% DDM, 1 mM $MgCl_2$, 10 μM GDP, and 100 μM '9087 or '4622. The α_{2A}AR-G_{oA} complex was then treated with 50 units of apyrase (NEB) on ice overnight, and exchanged on an anti-Flag M1 column into a buffer containing 20 mM HEPES, pH 7.5, 100 mM NaCl, 0.0075% lauryl maltose neopentyl glycol (MNG, NG310 Anatrace), 0.0025% GDN (GDN101, Anatrace), and 0.001% CHS, 100 μM '9087 or '4622, and 2 mM $CaCl_2$ in a stepwise manner. After elution by adding 5 mM EDTA and 0.2 mg/mL Flag peptide, the complex was concentrated and incubated with 1.5x molar excess scFv16 for 1 hour on ice, then further purified using Superdex 200 Increase 10/300 GL column (GE Healthcare) with a running buffer of 20 mM HEPES, pH 7.5, 100 mM NaCl, 0.00075% MNG, 0.00025% GDN and 0.0001% CHS, 100 μM '9087 or '4622. The monomeric peak fraction of α_{2A}AR-G_{oA} complex was collected and concentrated to ~5 mg/mL for cryo-EM.

Cryo-EM data collection, processing, and model building

3 μL of purified complex sample was applied onto the grid (CryoMatrix nickel titanium alloy film, R1.2/1.3, Zhenjiang Lehua Electronic Technology Co., Ltd.) (*81*) glow discharged at Tergeo-EM plasma cleaner and then blotted for 3 s with blotting force of 0 and quickly plunged into liquid ethane cooled by liquid nitrogen using Vitrobot Mark IV (Thermo Fisher Scientific, USA) at 10°C and with 95% humidity. Cryo-EM data were collected on a 300 kV Titan Krios Gi3 microscope. The raw movies were recorded by Gatan K3 BioQuantum Camera at the magnification of 105,000 and the corresponding pixel size is 0.85 Å. Inelastically scattered electrons were excluded by a GIF Quantum energy filter (Gatan, USA) using a slit width of 20 eV. The movie stacks were acquired with the defocus range of −1.0 to −1.6 μm with total exposure time 2.5 s fragmented into 50 frames (0.05 s per frame) with the dose rate of 22.0 e per pixel per second. The imaging mode is super resolution with 2-time hardware binning. The semiautomatic data acquisition was performed using SerialEM (*82*).

For the '9087-α_{2A}AR-G_{oA}-scFv16 complex, raw movie frames were aligned with MotionCor2 (*83*) using a 9 × 7 patch and the contrast transfer function (CTF) parameters were estimated using Gctf and ctf in JSPR (*84*). Micrographs with consistent CTF values including defocus and astigmatism parameter were kept for the following

image processing, which kept 3768 micrographs from 4217 raw movies. Templates for particle auto-picking were generated by projecting the 3D volume of norepinephrine-bound α_{2A}AR-G_{oA} complex (*40*). The 2,137,146 particles picked from template picking was subjected 2D classification in cryoSPARC (*85*) and 3D classication in Relion3.1 (*86*). The sorted 321,762 particles were then subjected to homogeneous reconstruction in cryoSPARC, yielding a 3.57-Å map. Further 3D ab initio reconstruction reduced the particles number to 287,431, which was subjected to CTF refinement and nonuniform refinement after extracting with larger particle box size, and finally yield the 3.47-Å map.

For the '4622-α_{2A}AR-G_{oA}-scFv16 complex, 6983 raw movies were collected and subjected for motion correction using MotionCor2 (*83*). Contrast transfer function parameters were estimated by CTFFIND4, implemented in Relion3.1 (*86*). 2,593,747 particles were auto-picked using the templates in RELION3.1 and then subjected to 2D classification using cryoSPARC. Selected particles with appropriate 2D average from 2D classification were further subjected to ab initio reconstruction. Particles with appropriate initial model were selected from ab initio followed by heterogeneous refinement in cryoSPARC. The particles kept to 563,506 particles were subjected to nonuniform refinement and local refinement and yield a 3.38-Å reconstruction determined by gold standard Fourier shell correlation using the 0.143 criterion.

The norepinephrine-α_{2A}AR-G_{oA} complex structure (PDB 7EJ0) (*40*) was used as the initial template for model building. The model was docked into the cryo-EM density map using UCSF Chimera (https://rbvi.ucsf.edu/chimera), followed by iterative manual building in Coot (*87*) and real space refinement in Phenix. The statistics of the final models were validated by Molprobity. Cryo-EM data collection, refinement, and validation statistics are summarized in table S11. The ligand symmetry accounted RMSDs between the docked pose and cryo-EM pose of '9087 and '4622 were calculated by the Hungarian algorithm in DOCK6 (*88*).

pK_a determination for '9087

The pK_a of '9087 (2.90 mg, 0.013 mmol) was determined by potentiometric titration using a Metrohm pH Meter 632 equipped with a glass electrode (Metrohm 6.0259.100). The compound was dissolved in 15 mL of 10% methanol aqueous solution, at an ionic strength of I = 0.15 M using KCl. The resulting solution was stirred throughout the experiment using a magnetic stir bar and a magnetic agitator. The compound was titrated with 0.01 M HCl (Titrisol) using an automatic burette (Metrohm Dosimat Plus 876). The titrant was added to the analyte stepwise (0.024 to 2.87 mL). The resulting graph for pK_a determination is presented in dependence of τ and pH(τ). The pK_a value was then determined using a simplified Henderson-Hasselbalch equation. The data from the titration experiment were evaluated with Origin 9.60.

Off-target activity

GPCRome

10 μM '9087 was tested for off-target activity at a panel of 320 nonolfactory GPCRs using PRESTO-Tango GPCRome arrestin-recruitment assay as described (*45*). Receptors with at least threefold increased relative luminescence over corresponding basal activity are potential positive hits. Screening was performed by the National Institutes of Mental Health Psychoactive Drug Screen Program (PDSP). Detailed experimental protocols are available on the NIMH PDSP website at https://pdsp.unc.edu/pdspweb/content/PDSP%20Protocols%20II%202013-03-28.pdf.

D2R activation

D2R was selected after the GPCRome panel, and '9087 was retested for full dose-response to determine G protein and arrestin recruitment (see above).

I2R binding

Top docking compounds ('9087, '2998, '4622, and '0172) were tested for I2R binding, performed by Eurofins Cerep (France; catalog no. 81) as described (*78*). For compound '2998, no binding was seen in a single point radioligand competition experiment tested at 500 nM and the compound is not shown.

μOR competition binding

Equilibrium [3H] Diprenorphine competition and saturation binding were carried out in membranes prepared from Chinese Hamster Ovary (CHO-K1) cells stably expressing human μ-opioid receptor, as previously described (*89*–*91*). Briefly, binding was performed at 25°C for 90 min in the dark. Binding in μOR/CHO-K1 cells was carried out in a buffer consisting of 50 mM HEPES-base pH 7.4 (pH adjusted with KOH), 10 mM MgCl2, 0.1 mM EDTA, and 0.1% (w/v) bovine serum albumin with membranes containing ~40 μg/mL protein. After incubation with radioligand (1 pM to 10 nM for saturation, 500 pM for competition), drugs (33 μM to 3.3 pM) and/or 20 μM cold competitor naloxone, the reaction was rapidly filtered onto GF/B (PerkinElmer no. 1450-521) glass fiber filtermats which were equilibrated for 1 hour in binding buffer supplemented with 0.3% (v/v) polyethyleneimine. The filtermats were washed five times in ice-cold 50 mM HEPES-base pH 7.4 using a PerkinElmer semiautomated cell harvester (PerkinElmer FilterMate Harvester). The filtermats were dried and Meltilex solid scintillant (PerkinElmer no. 1450-442) was melted onto the mats for 10 min at 60°C. The scintillant was allowed to resolidify before disintegrations were quantified with a Wallac MicroBeta Scintillation counter using an integration time of 1 min. Nonspecific binding, total binding, the number of receptor binding sites, and the K_d of the radiotracer were determined from saturation binding experiments. Protein concentrations were determined using the microBCA method with BSA as the standard. K_i values were calculated by nonlinear regression analysis and application of the Cheng-Prusoff correction in GraphPad Prism 9.0.

hERG inhibition assays

'9087 was tested for hERG inhibition in the FluxOR assay as described (*92*). hERG experiments used the National Institutes of Mental Health (NIMH) Psychoactive Drug Screening Program (PDSP). Experimental protocols are available on the NIMH PDSP website at https://pdsp.unc.edu/pdspweb/content/PDSP%20Protocols%20II%202013-03-28.pdf.

Metabolic stability studies

Metabolic stability of the test compounds was assessed using male pooled rat liver microsomes (Sprague Dawley, Sigma Aldrich) as previously described (*93*, *94*). The reactions were carried out in 2 mL polyethylene tubes on a rotator carousel (Stuart SB3) in an incubator at 37°C. The incubation mixture contained '9087, '7075, PS75, or the positive controls rotigotine or imipramine (final concentration 20 μM), and pooled rat liver microsomes (0.25 mg protein per tube) in Tris-$MgCl_2$ buffer (50 mM Tris, 5 mM $MgCl_2$, pH 7.4, final volume 500 μL). Transformation reactions were initiated by the addition of 50 μL of cofactor solution (NADPH, Carl Roth, final concentration 1 mM). After time intervals of 0, 30, and 60 min for '9087, '7075, and PS75 or 0, 15, 30, and 60 min for rotigotine and imipramine, respectively, 100 μL aliquots of the reaction mixtures were added to 100 μL ice-cold acetonitrile (containing 10 μM chlorpromazine as internal standard) to terminate enzymatic reactions. Precipitated protein was removed by centrifugation (1 min, 16,000 relative centrifugal force) and the supernatants were analyzed by high-performance liquid chromatography–mass spectrometry (HPLC/MS) on a Thermo Scientific Dionex Ultimate 3000 HPLC system equipped with a Zorbax Eclipse XDB-C8 column (4.6 × 150 mm, 5 μm), a DAD detector (210 nm, 230 nm, 254 nm, 310 nm), and a BRUKER amaZon SL mass spectrometer with ESI source. The following binary eluent system (methanol in water + 0.1% (v/v) formic acid) was used: 10% for 1 min, 10 to 100% in 20 min, 100% for 5 min, 100 to 10% in 2 min, 10% for 2 min, flow 0.4 mL/min. Per compound, four (rotigotine, imipramine) or five ('9087, '7075, PS75) independent experiments were performed.

Control experiments were conducted in the absence of cofactor solution to determine nonspecific binding to matrix. The integral (AUC) of the extracted ion chromatograms (EIC) was used to analyze the concentration of the remaining substrates. Concentrations were plotted in their logarithmic form as a function of the incubation time (in minutes) to calculate the elimination rate constant (k) and to determine the half-life ($T_{1/2}$) and intrinsic hepatic clearance (CL_{int}) for each compound with the following equations (*95*)

$$T_{1/2}[\text{min}] = \frac{\ln(2)}{k} \quad (5)$$

$$CL_{int}\left[\frac{\mu L}{\text{min} \times \text{mg(protein)}}\right] = \frac{\ln(2)}{T_{1/2}} \times \frac{V(\text{of incubation in } \mu L)}{m(\text{of protein in incubation in mg})} \quad (6)$$

In vivo methods

Animals and ethical compliance

Animal experiments were approved by the UCSF Institutional Animal Care and Use Committee and were conducted in accordance with the NIH Guide for the Care and Use of Laboratory animals (protocol no. AN181214). Adult (8 to 10 weeks old) male C56BL/6 mice (strain no. 664) were purchased from the Jackson Laboratory. Mice were housed in cages on a standard 12:12 hour light-dark cycle with food and water ad libitum. The α_{2A}AR D79N mutant mice were purchased from Jackson (stock no. 2777), and 7- to 8-week-old females were used. Sample sizes were modeled on our previous studies and on studies using a similar approach, which were able to detect significant changes (*96*, *97*). The animals were randomly assigned to treatment and control groups. Animals were initially placed into one cage and allowed to freely run for a few minutes. Then each animal was randomly picked up, injected with compound treatment or vehicle, and placed into a separate cylinder before the behavioral test.

In vivo compound preparation

All ligands were synthesized by Enamine ('2998 and '7075) or WuXi ('9087, '4622, and '0172) or in-house (PS75) and dissolved 30 min before testing. Available salt forms were used to aid solubility: HCl for '9087 and '7075, TFA for '4622, '0172, and PS75. '9087, '4622, and '0172 were resuspended in 20% Kolliphor (Sigma-Aldrich; cat. no. C5135) for s.c. and i.p. injections. '2998, '7075, and PS75 were resuspended in 20% cyclodextran (Sigma-Aldrich; cat. no. H107) for s.c. and i.p. injections. Atipamezole (Cayman Chemical Company; cat. no. 9001181) and Dexmedetomidine (Cayman Chemical Company; cat. no. 15581) were resuspended with NaCl 0.9% (Teknova; cat. no. S5819) for s.c. and i.p. injections. '9087 was formulated with 40% Captisol (Carbosynth; cat. no. OC15979) for p.o. dosing.

Behavioral analyses

For all behavioral tests, the experimenter was always blind to treatment. Animals were first habituated for 1 hour in Plexiglas cylinders and then tested 30 min after s.c. injection of the α_{2A}AR compounds. The α_{2A}AR antagonist atipamezole (2 mg/kg, i.p.) was injected 15 min before s.c. injection of the α_{2A}AR agonists. The mechanical (von Frey), thermal (Hargreaves, hot plate, and tail flick) and ambulatory (rotarod) tests were conducted as described previously (*98*). Hindpaw mechanical thresholds were determined with von Frey filaments using the up-down method (*99*). Hindpaw thermal sensitivity was measured with a radiant heat source (Hargreaves) or a 55°C hot plate. For the tail flick assay, sensitivity was measured by immersing the tail into a 50°C water bath for both WT and D79N mutant mice. For the ambulatory (rotarod) test, mice were first trained on an accelerating rotating rod, three times for 5 min, before testing with any compound.

SNI model of neuropathic pain

Under isoflurane anesthesia, two of the three branches of the sciatic nerve were ligated and transected distally, leaving the sural nerve intact. Behavior was tested 7 to 14 days after injury.

CFA

The CFA model of chronic inflammation was induced as described previously (*100*). Briefly, CFA (Sigma) was diluted 1:1 with saline and vortexed for 30 min. When fully suspended, we injected 20 μL of CFA into one hindpaw. Heat thresholds were measured before the injection (baseline) and 3 days after using the Hargreaves test.

Constipation assay

Mice had access to food and water ad libitum before the test. On the test day, mice received an i.p. injection of a solution (100 μL) containing saline, 10 mg/kg morphine, 30 μg/kg dexmedetomidine, or 5 mg/kg '9087 and then individually placed in a clean cage, with no access to food or water. Fecal pellets were collected and counted every hour, up to 6 hours.

Body weight measurement

The body weights were measured before, 24 hours after, and 48 hours after mice received an i.p. injection of a solution (100 μL) containing dexmedetomidine (30 μg/kg) or '9087 (5, 10, or 20 mg/kg).

Pharmacokinetics

Pharmacokinetic experiments were performed by Bienta (Enamine Biology Services) in accordance with Enamine pharmacokinetic study protocols and Institutional Animal Care and Use Guidelines (protocol number 1-2/2020). Plasma pharmacokinetics and brain distribution for '9087, '2998, '4622, '7075, PS75, and CSF distribution for '7075, PS75, '9087, and '4622, were measured after a 10-mg/kg (i.p.) dose. Plasma and brain samples were also collected for '9087 after a 10-mg/kg i.v. and 30-mg/kg p.o. (oral) dose to determine oral bioavailability. In each compound study, nine time points (5, 15, 30, 60, 120, 240, 360, 480, and 1440 min) were collected, each of the time point treatment group included three animals. There was also a control group of one animal. In the '9087, '7075, and '4622 studies, male C57BL/6N mice were used, for PS75 CD-1 mice, and for '2998 male Balb/cAnN mice. For all compound studies the animals were randomly assigned to the treatment groups before the pharmacokinetic study; all animals were fasted for 4 hours before dosing. For injections, '9087 was dissolved in Captisol – water (40%:60%, w/v), '4622 was dissolved in a 20% Kolliphor HS – physiological saline solution, and '7075, PS75, and '2998 were dissolved in a 20% 2-HPBCD–aqueous solution. The batches of working formulations were prepared 10 min before the in vivo study.

Mice were injected i.p. with 2,2,2- tribromoethanol at 150 mg/kg before drawing CSF and blood. CSF was collected under a stereomicroscope from cisterna magna using 1-mL syringes. Blood collection was performed from the orbital sinus in microtainers containing K3EDTA. Animals were euthanized by cervical dislocation after the blood samples collection. Blood samples were centrifuged 10 min at 3000 rpm. Brain samples (right lobe) were weighed and transferred into 1.5 mL tubes. All samples were immediately processed, flash-frozen and stored at −70°C until subsequent analysis.

Plasma samples (40 μL) were mixed with 200 μL of internal standard (IS) solution. After mixing by pipetting and centrifuging for 4 min at 6000 rpm, 4 μL of each supernatant was injected into the liquid chromatography–tandem mass spectrometry (LC-MS/MS) system. Solutions of internal standards were used to quantify compounds in the plasma samples. Brain samples (weight 200 ± 1 mg) were homogenized with 800 μL of an internal stock solution using zirconium oxide beads (115 ± 5 mg) in a Bullet Blender homogenizer for 30 s at speed 8. After this, the samples were centrifuged for 4 min at 14,000 rpm, and supernatant was injected into LC-MS/MS system. CSF samples (2 μL) were mixed with 40 μL of an internal stock solution. After mixing by pipetting and centrifuging for 4 min at 6000 rpm, 5 μL of each supernatant was injected into LC-MS/MS system.

Analyses of plasma, brain, and CSF samples were conducted at Enamine/Bienta. The concentrations of compounds in plasma and brain

samples were determined using HPLC-MS/MS. Data acquisition and system control were performed using Analyst 1.5.2 software (AB Sciex, Canada). The concentrations of the test compound below the lower limit of quantitation (LLOQ = 10 ng/mL for plasma, 20 ng/g for brain, and 5 ng/mL for CSF samples) were designated as zero. Pharmacokinetic data analysis was performed using noncompartmental, bolus injection or extravascular input analysis models in WinNonlin 5.2 (PharSight). Data below LLOQ were presented as missing to improve validity of $T_{1/2}$ calculations.

Additional pharmacokinetic experiments were performed by Sai Life Sciences (Hyderabad, India) in accordance with the Sai Study Protocol SAIDMPK/PK-22-04-0340. Brain distribution of dexmedetomidine was measured after a 30-μg/kg i.p. dose, using normal saline 0.9% as its vehicle. Plasma distributions were also collected for PS75 after 10-mg/kg i.v. and 30-mg/kg p.o. (oral) dosing to determine oral bioavailability; both doses were formulated in 20% v/v HβCD in saline. Testing was done in C57BL/6 mice. For PS75, 24 mice were divided into four groups: nine mice for i.v. dosing of the compound, three mice for i.v. dosing of the vehicle, nine mice for p.o. dosing with the compound, and three mice for p.o. vehicle dosing; sparse sampling of three mice per time point for compound-treated groups and one mouse per time point for vehicle groups was performed. For dexmedetomidine, 36 mice were included and split into two groups: three mice per time point for compound dosing, and one mouse per time point for vehicle-only dosing. For PS75, blood samples (60 μL) were collected under light isoflurane anesthesia (Surgivet) from retro orbital plexus from a set of three mice at 0.083, 0.25, 0.5, 1, 2, 4, 6, 8, and 24 hours. Immediately after blood collection, plasma was harvested by centrifugation at 4000 rpm, 10 min at 4°C. For dexmedetomidine, brain samples were collected at the same time points indicated above. Animals were euthanized at respective time points and brain samples were isolated and homogenized in ice-cold phosphate buffer saline (pH 7.4). Total homogenate volume was three times the tissue weight. Samples were stored at −70°C until bioanalysis. All samples were processed for analysis by protein precipitation method and analyzed with fit-for-purpose LC-MS/MS method (LLOQ = 3.61 ng/mL for plasma for PS75, LLOQ = 0.86 ng/mL for brain for dexmedetomidine). The pharmacokinetic parameters were estimated using the noncompartmental analysis tool of Phoenix WinNonlin software (version 8.0).

Statistical analyses

Data from functional experiments of adrenergic and D_{2long} receptors were analyzed applying the algorithms for four-parameter nonlinear regression implemented in Prism 8.0 (GraphPad, San Diego, CA) to get dose-response curves representing EC_{50} and E_{max} values. Mean values were derived by summarizing the results from each individual experiment to provide EC_{50} ± SEM and E_{max} ± SEM (or SD where indicated). Additional statistical analyses for Fig. 4; fig. S4; fig. S16, A and C to E; and fig. S18 were performed with GraphPad Prism 9.0 (GraphPad Software Inc., San Diego). Data reported are means ± SEMs or, in Fig. 4 and fig. S18, single data points with means ± SEMs. Experiments of the compounds in the in vivo neuropathic, inflammatory, hot plate, tail flick, and rotarod models were evaluated using unpaired two-tailed Student's *t* test or one-way analysis of variance (ANOVA) with Dunnett's multiple comparison post hoc test to determine differences between groups. Experiments for body weight and constipation were analyzed with a two-way ANOVA. Details of the analyses, including groups compared in statistical sets, number of animals per group, and *P* values, can be found in the figure legends.

REFERENCES AND NOTES

1. A. S. Yekkirala, D. P. Roberson, B. P. Bean, C. J. Woolf, Breaking barriers to novel analgesic drug development. *Nat. Rev. Drug Discov.* **16**, 545–564 (2017). doi: 10.1038/nrd.2017.87; pmid: 28596533
2. L. Manchikanti *et al*., Opioid epidemic in the United States. *Pain Physician* **15**, ES9–ES38 (2012). doi: 10.36076/ppj.2012/15/ES9; pmid: 22786464
3. J. Strang *et al*., Opioid use disorder. *Nat. Rev. Dis. Primers* **6**, 3 (2020). doi: 10.1038/s41572-019-0137-5; pmid: 31919349
4. K. Rasmussen, D. A. White, J. B. Acri, NIDA's medication development priorities in response to the Opioid Crisis: Ten most wanted. *Neuropsychopharmacology* **44**, 657–659 (2019). doi: 10.1038/s41386-018-0292-5; pmid: 30538289
5. A. B. Malmberg, L. R. Hedley, J. R. Jasper, J. C. Hunter, A. I. Basbaum, Contribution of α_2 receptor subtypes to nerve injury-induced pain and its regulation by dexmedetomidine. *Br. J. Pharmacol.* **132**, 1827–1836 (2001). doi: 10.1038/sj.bjp.0704032; pmid: 11309255
6. P. P. Lakhlani *et al*., Substitution of a mutant α_{2a}-adrenergic receptor via "hit and run" gene targeting reveals the role of this subtype in sedative, analgesic, and anesthetic-sparing responses *in vivo*. *Proc. Natl. Acad. Sci. U.S.A.* **94**, 9950–9955 (1997). doi: 10.1073/pnas.94.18.9950; pmid: 9275232
7. H. Buerkle, T. L. Yaksh, Pharmacological evidence for different alpha$_2$-adrenergic receptor sites mediating analgesia and sedation in the rat. *Br. J. Anaesth.* **81**, 208–215 (1998). doi: 10.1093/bja/81.2.208; pmid: 9813525
8. M. Anttila, J. Penttilä, A. Helminen, L. Vuorilehto, H. Scheinin, Bioavailability of dexmedetomidine after extravascular doses in healthy subjects. *Br. J. Clin. Pharmacol.* **56**, 691–693 (2003). doi: 10.1046/j.1365-2125.2003.01944.x; pmid: 14616431
9. D. Yuan *et al*., Activation of the α_{2B} adrenoceptor by the sedative sympatholytic dexmedetomidine. *Nat. Chem. Biol.* **16**, 507–512 (2020). doi: 10.1038/s41589-020-0492-2; pmid: 32152538
10. J. Lyu *et al*., Ultra-large library docking for discovering new chemotypes. *Nature* **566**, 224–229 (2019). doi: 10.1038/s41586-019-0917-9; pmid: 30728502
11. T. Sterling, J. J. Irwin, ZINC 15 – Ligand discovery for everyone. *J. Chem. Inf. Model.* **55**, 2324–2337 (2015). doi: 10.1021/acs.jcim.5b00559; pmid: 26479676
12. J. J. Irwin *et al*., ZINC20—A free ultralarge-scale chemical database for ligand discovery. *J. Chem. Inf. Model.* **60**, 6065–6073 (2020). doi: 10.1021/acs.jcim.0c00675; pmid: 33118813
13. R. M. Stein *et al*., Virtual discovery of melatonin receptor ligands to modulate circadian rhythms. *Nature* **579**, 609–614 (2020). doi: 10.1038/s41586-020-2027-0; pmid: 32040955
14. A. Alon *et al*., Structures of the σ_2 receptor enable docking for bioactive ligand discovery. *Nature* **600**, 759–764 (2021). doi: 10.1038/s41586-021-04175-x; pmid: 34880501
15. C. Gorgulla *et al*., An open-source drug discovery platform enables ultra-large virtual screens. *Nature* **580**, 663–668 (2020). doi: 10.1038/s41586-020-2117-z; pmid: 32152607
16. A. A. Sadybekov *et al*., Synthon-based ligand discovery in virtual libraries of over 11 billion compounds. *Nature* **601**, 452–459 (2022). doi: 10.1038/s41586-021-04220-9; pmid: 34912117
17. A. Manglik *et al*., Structure-based discovery of opioid analgesics with reduced side effects. *Nature* **537**, 185–190 (2016). doi: 10.1038/nature19112; pmid: 27533032
18. M. Schuller *et al*., Fragment binding to the Nsp3 macrodomain of SARS-CoV-2 identified through crystallographic screening and computational docking. *Sci. Adv.* **7**, eabf8711 (2021). doi: 10.1126/sciadv.abf8711; pmid: 33853786
19. A. Rudling *et al*., Fragment-based discovery and optimization of enzyme inhibitors by docking of commercial chemical space. *J. Med. Chem.* **60**, 8160–8169 (2017). doi: 10.1021/acs.jmedchem.7b01006; pmid: 28929756
20. A. Levit Kaplan *et al*., Structure-based design of a chemical probe set for the 5-HT$_{5A}$ Serotonin Receptor. *J. Med. Chem.* **65**, 4201–4217 (2022). doi: 10.1021/acs.jmedchem.1c02031; pmid: 35195401
21. C. de Graaf *et al*., Crystal structure-based virtual screening for fragment-like ligands of the human histamine H_1 receptor. *J. Med. Chem.* **54**, 8195–8206 (2011). doi: 10.1021/jm2011589; pmid: 22007643
22. R. Kiss *et al*., Discovery of novel human histamine H4 receptor ligands by large-scale structure-based virtual screening. *J. Med. Chem.* **51**, 3145–3153 (2008). doi: 10.1021/jm7014777; pmid: 18459760
23. N. Patel *et al*., Structure-based discovery of potent and selective melatonin receptor agonists. *eLife* **9**, e53779 (2020). doi: 10.7554/eLife.53779; pmid: 32118583
24. C. J. Langmead *et al*., Identification of novel adenosine A_{2A} receptor antagonists by virtual screening. *J. Med. Chem.* **55**, 1904–1909 (2012). doi: 10.1021/jm201455y; pmid: 22250781
25. S. Wang *et al*., D_4 dopamine receptor high-resolution structures enable the discovery of selective agonists. *Science* **358**, 381–386 (2017). doi: 10.1126/science.aan5468; pmid: 29051383
26. R. G. Coleman, M. Carchia, T. Sterling, J. J. Irwin, B. K. Shoichet, Ligand pose and orientational sampling in molecular docking. *PLOS ONE* **8**, e75992 (2013). doi: 10.1371/journal.pone.0075992; pmid: 24098414
27. K. Altosaar *et al*., Adrenoceptors (version 2019.4) in the IUPHAR/BPS Guide to Pharmacology Database (IUPHAR/BPS Guide to Pharmacology, 2019); doi: 10.2218/gtopdb/F4/2019.4
28. A. Gaulton *et al*., ChEMBL: A large-scale bioactivity database for drug discovery. *Nucleic Acids Res.* **40**, D1100–D1107 (2012). doi: 10.1093/nar/gkr777; pmid: 21948594
29. H. S. Blaxall, T. J. Murphy, J. C. Baker, C. Ray, D. B. Bylund, Characterization of the *Alpha*-2C adrenergic receptor subtype in the opossum kidney and in the OK cell line. *J. Pharmacol. Exp. Ther.* **259**, 323–329 (1991). pmid: 1656026
30. P. B. M. W. M. Timmermans, P. A. van Zwieten, α_2 adrenoceptors: Classification, localization, mechanisms, and targets for drugs. *J. Med. Chem.* **25**, 1389–1401 (1982). doi: 10.1021/jm00354a001; pmid: 6296387
31. B. V. Clineschmidt, L. M. Flataker, E. P. Faison, D. R. Haubrich, alpha-methyldopa reduces locomotor activity in rats via its metabolite, alpha-methylnorepinephrine, acting on alpha 2-adrenoceptors. *Arch. Int. Pharmacodyn. Ther.* **244**, 231–243 (1980). pmid: 6250499
32. S. Gu, M. S. Smith, Y. Yang, J. J. Irwin, B. K. Shoichet, Ligand strain energy in large library docking. *J. Chem. Inf. Model.* **61**, 4331–4341 (2021). doi: 10.1021/acs.jcim.1c00368; pmid: 34467754
33. V. Isberg *et al*., Generic GPCR residue numbers - aligning topology maps while minding the gaps. *Trends Pharmacol. Sci.* **36**, 22–31 (2015). doi: 10.1016/j.tips.2014.11.001; pmid: 25541108
34. M. Congreve *et al*., Discovery of 1,2,4-triazine derivatives as adenosine A_{2A} antagonists using structure based drug

design. *J. Med. Chem.* **55**, 1898–1903 (2012). doi: 10.1021/jm201376w; pmid: 22220592

35. S. Bhattacharya, S. E. Hall, H. Li, N. Vaidehi, Ligand-stabilized conformational states of human β_2 adrenergic receptor: Insight into G-protein-coupled receptor activation. *Biophys. J.* **94**, 2027–2042 (2008). doi: 10.1529/biophysj.107.117648; pmid: 18065472
36. D. R. Weiss *et al*., Conformation guides molecular efficacy in docking screens of activated β-2 adrenergic G protein coupled receptor. *ACS Chem. Biol.* **8**, 1018–1026 (2013). doi: 10.1021/cb400103f; pmid: 23485065
37. M. G. Eason, H. Kurose, B. D. Holt, J. R. Raymond, S. B. Liggett, Simultaneous coupling of α_2-adrenergic receptors to two G-proteins with opposing effects: Subtype-selective coupling of α_2C10, α_2C4, and α_2C2 adrenergic receptors to G_i and G_s. *J. Biol. Chem.* **267**, 15795–15801 (1992). doi: 10.1016/S0021-9258(19)49605-1; pmid: 1322406
38. C. Avet *et al*., Effector membrane translocation biosensors reveal G protein and βarrestin coupling profiles of 100 therapeutically relevant GPCRs. *eLife* **11**, e74101 (2022). doi: 10.7554/eLife.74101; pmid: 35302493
39. Y. Namkung *et al*., Monitoring G protein-coupled receptor and β-arrestin trafficking in live cells using enhanced bystander BRET. *Nat. Commun.* **7**, 12178 (2016). doi: 10.1038/ncomms12178; pmid: 27397672
40. J. Xu *et al*., Structural insights into ligand recognition, activation, and signaling of the α_{2A} adrenergic receptor. *Sci. Adv.* **8**, eabj5347 (2022). doi: 10.1126/sciadv.abj5347; pmid: 35245122
41. L. Qu *et al*., Structural basis of the diversity of adrenergic receptors. *Cell Rep.* **29**, 2929–2935.e4 (2019). doi: 10.1016/j.celrep.2019.10.088; pmid: 31801060
42. F. M. Heydenreich *et al*., Dissecting the allosteric networks governing agonist efficacy and potency in G protein-coupled receptors. *bioRxiv*2021.09.14.460253 [Preprint] (2021). doi: 10.1101/2021.09.14.460253
43. M. Masureel *et al*., Structural insights into binding specificity, efficacy and bias of a β_2AR partial agonist. *Nat. Chem. Biol.* **14**, 1059–1066 (2018). doi: 10.1038/s41589-018-0145-x; pmid: 30327561
44. M. Stanek *et al*., Hybridization of β-Adrenergic agonists and antagonists confers G protein bias. *J. Med. Chem.* **62**, 5111–5131 (2019). doi: 10.1021/acs.jmedchem.9b00349; pmid: 31042379
45. W. K. Kroeze *et al*., PRESTO-Tango as an open-source resource for interrogation of the druggable human GPCRome. *Nat. Struct. Mol. Biol.* **22**, 362–369 (2015). doi: 10.1038/nsmb.3014; pmid: 25895059
46. H. Kodaira *et al*., Quantitative evaluation of the impact of active efflux by p-glycoprotein and breast cancer resistance protein at the blood-brain barrier on the predictability of the unbound concentrations of drugs in the brain using cerebrospinal fluid concentration as a surrogate. *J. Pharmacol. Exp. Ther.* **339**, 935–944 (2011). doi: 10.1124/jpet.111.180398; pmid: 21934030
47. S. D. Shields, W. A. Eckert 3rd, A. I. Basbaum, Spared nerve injury model of neuropathic pain in the mouse: A behavioral and anatomic analysis. *J. Pain* **4**, 465–470 (2003). doi: 10.1067/S1526-5900(03)00781-8; pmid: 14622667
48. R. Virtanen, J. M. Savola, V. Saano, Highly selective and specific antagonism of central and peripheral alpha 2-adrenoceptors by atipamezole. *Arch. Int. Pharmacodyn. Ther.* **297**, 190–204 (1989). pmid: 2567152
49. L. B. MacMillan, L. Hein, M. S. Smith, M. T. Piascik, L. E. Limbird, Central hypotensive effects of the α_{2a}-adrenergic receptor subtype. *Science* **273**, 801–803 (1996). doi: 10.1126/science.273.5276.801; pmid: 8670421
50. P. P. Lakhlani, D. M. Lovinger, L. E. Limbird, Genetic evidence for involvement of multiple effector systems in alpha 2A-adrenergic receptor inhibition of stimulus-secretion coupling. *Mol. Pharmacol.* **50**, 96–103 (1996). pmid: 8700125
51. B. P. Ceresa, L. E. Limbird, Mutation of an aspartate residue highly conserved among G-protein-coupled receptors results in nonreciprocal disruption of α_2-adrenergic receptor-G-protein interactions: A negative charge at amino acid residue 79 forecasts α_{2A}-adrenergic receptor sensitivity to allosteric modulation by monovalent cations and fully effective receptor/G-protein coupling. *J. Biol. Chem.* **269**, 29557–29564 (1994). doi: 10.1016/S0021-9258(18)43916-6; pmid: 7961941
52. J. C. Hunter *et al*., Assessment of the role of α_2-adrenoceptor subtypes in the antinociceptive, sedative and hypothermic action of dexmedetomidine in transgenic mice. *Br. J. Pharmacol.* **122**, 1339–1344 (1997). doi: 10.1038/sj.bjp.0701520; pmid: 9421280
53. S. A. Metz, J. B. Halter, R. P. Robertson, Induction of defective insulin secretion and impaired glucose tolerance by clonidine. Selective stimulation of metabolic alpha-adrenergic pathways. *Diabetes* **27**, 554–562 (1978). doi: 10.2337/diab.27.5.554; pmid: 648745
54. S. S. Lichtenstein, C. Marinescu, S. F. Leibowitz, Chronic infusion of norepinephrine and clonidine into the hypothalamic paraventricular nucleus. *Brain Res. Bull.* **13**, 591–595 (1984). doi: 10.1016/0361-9230(84)90042-X; pmid: 6525531
55. L. S. Stone, J. P. German, K. F. Kitto, C. A. Fairbanks, G. L. Wilcox, Morphine and clonidine combination therapy improves therapeutic window in mice: Synergy in antinociceptive but not in sedative or cardiovascular effects. *PLOS ONE* **9**, e109903 (2014). doi: 10.1371/journal.pone.0109903; pmid: 25299457
56. D. A. Erlanson, S. W. Fesik, R. E. Hubbard, W. Jahnke, H. Jhoti, Twenty years on: The impact of fragments on drug discovery. *Nat. Rev. Drug Discov.* **15**, 605–619 (2016). doi: 10.1038/nrd.2016.109; pmid: 27417849
57. E. Von Moo *et al*., Ligand-directed bias of G protein signaling at the dopamine D_2 receptor. *Cell Chem. Biol.* **29**, 226–238.e4 (2022). doi: 10.1016/j.chembiol.2021.07.004; pmid: 34302750
58. I. D. Kuntz, J. M. Blaney, S. J. Oatley, R. Langridge, T. E. Ferrin, A geometric approach to macromolecule-ligand interactions. *J. Mol. Biol.* **161**, 269–288 (1982). doi: 10.1016/0022-2836(82)90153-X; pmid: 7154081
59. J. M. Word, S. C. Lovell, J. S. Richardson, D. C. Richardson, Asparagine and glutamine: Using hydrogen atom contacts in the choice of side-chain amide orientation. *J. Mol. Biol.* **285**, 1735–1747 (1999). doi: 10.1006/jmbi.1998.2401; pmid: 9917408
60. S. J. Weiner *et al*., A new force field for molecular mechanical simulation of nucleic acids and proteins. *J. Am. Chem. Soc.* **106**, 765–784 (1984). doi: 10.1021/ja00315a051
61. B. J. Bender *et al*., A practical guide to large-scale docking. *Nat. Protoc.* **16**, 4799–4832 (2021). doi: 10.1038/s41596-021-00597-z; pmid: 34561691
62. R. M. Stein *et al*., Property-unmatched decoys in docking benchmarks. *J. Chem. Inf. Model.* **61**, 699–714 (2021). doi: 10.1021/acs.jcim.0c00598; pmid: 33494610
63. M. M. Mysinger *et al*., Structure-based ligand discovery for the protein-protein interface of chemokine receptor CXCR4. *Proc. Natl. Acad. Sci. U.S.A.* **109**, 5517–5522 (2012). doi: 10.1073/pnas.1120431109; pmid: 22431600
64. B. K. Shoichet, A. R. Leach, I. D. Kuntz, Ligand solvation in molecular docking. *Proteins* **34**, 4–16 (1999). doi: 10.1002/(SICI)1097-0134(19990101)34:1<4::AID-PROT2>3.0.CO;2-6; pmid: 10336382
65. K. Gallagher, K. Sharp, Electrostatic contributions to heat capacity changes of DNA-ligand binding. *Biophys. J.* **75**, 769–776 (1998). doi: 10.1016/S0006-3495(98)77566-6; pmid: 9675178
66. M. M. Mysinger, B. K. Shoichet, Rapid context-dependent ligand desolvation in molecular docking. *J. Chem. Inf. Model.* **50**, 1561–1573 (2010). doi: 10.1021/ci100214a; pmid: 20735049
67. T. Rezai *et al*., Conformational flexibility, internal hydrogen bonding, and passive membrane permeability: Successful in silico prediction of the relative permeabilities of cyclic peptides. *J. Am. Chem. Soc.* **128**, 14073–14080 (2006). doi: 10.1021/ja063076p; pmid: 17061890
68. S. S. F. Leung, J. Mijalkovic, K. Borrelli, M. P. Jacobson, Testing physical models of passive membrane permeation. *J. Chem. Inf. Model.* **52**, 1621–1636 (2012). doi: 10.1021/ci200583t; pmid: 22621168
69. M. P. Jacobson, G. A. Kaminski, R. A. Friesner, C. S. Rapp, Force field validation using protein side chain prediction. *J. Phys. Chem. B* **106**, 11673–11680 (2002). doi: 10.1021/jp021564n
70. D. G. Gibson *et al*., Enzymatic assembly of DNA molecules up to several hundred kilobases. *Nat. Methods* **6**, 343–345 (2009). doi: 10.1038/nmeth.1318; pmid: 19363495
71. O. H. Lowry, N. J. Rosebrough, A. L. Farr, R. J. Randall, Protein measurement with the Folin phenol reagent. *J. Biol. Chem.* **193**, 265–275 (1951). doi: 10.1016/S0021-9258(19)52451-6; pmid: 14907713
72. Y.-C. Cheng, W. H. Prusoff, Relationship between the inhibition constant (K_I) and the concentration of inhibitor which causes 50 per cent inhibition (I_{50}) of an enzymatic reaction. *Biochem. Pharmacol.* **22**, 3099–3108 (1973). doi: 10.1016/0006-2952(73)90196-2; pmid: 4202581
73. X. M. Guan, T. S. Kobilka, B. K. Kobilka, Enhancement of membrane insertion and function in a type IIIb membrane protein following introduction of a cleavable signal peptide. *J. Biol. Chem.* **267**, 21995–21998 (1992). doi: 10.1016/S0021-9258(18)41623-7; pmid: 1331042
74. J. Quoyer *et al*., Pepducin targeting the C-X-C chemokine receptor type 4 acts as a biased agonist favoring activation of the inhibitory G protein. *Proc. Natl. Acad. Sci. U.S.A.* **110**, E5088–E5097 (2013). doi: 10.1073/pnas.1312515110; pmid: 24309376
75. C. Galés *et al*., Probing the activation-promoted structural rearrangements in preassembled receptor-G protein complexes. *Nat. Struct. Mol. Biol.* **13**, 778–786 (2006). doi: 10.1038/nsmb1134; pmid: 16906158
76. D. Möller *et al*., Discovery of G protein-biased dopaminergics with a pyrazolo[1,5-a]pyridine substructure. *J. Med. Chem.* **60**, 2908–2929 (2017). doi: 10.1021/acs.jmedchem.6b01857; pmid: 28248104
77. H. Liu *et al*., Structure-guided development of selective M3 muscarinic acetylcholine receptor antagonists. *Proc. Natl. Acad. Sci. U.S.A.* **115**, 12046–12050 (2018). doi: 10.1073/pnas.1813988115; pmid: 30404914
78. J. Xu *et al*., Conformational complexity and dynamics in a muscarinic receptor revealed by NMR spectroscopy. *Mol. Cell* **75**, 53–65.e7 (2019). doi: 10.1016/j.molcel.2019.04.028; pmid: 31103421
79. X. Liu *et al*., An allosteric modulator binds to a conformational hub in the β_2 adrenergic receptor. *Nat. Chem. Biol.* **16**, 749–755 (2020). doi: 10.1038/s41589-020-0549-2; pmid: 32483378
80. S. Maeda *et al*., Development of an antibody fragment that stabilizes GPCR/G-protein complexes. *Nat. Commun.* **9**, 3712 (2018). doi: 10.1038/s41467-018-06002-w; pmid: 30213947
81. X. Huang *et al*., Amorphous nickel titanium alloy film: A new choice for cryo electron microscopy sample preparation. *Prog. Biophys. Mol. Biol.* **156**, 3–13 (2020). doi: 10.1016/j.pbiomolbio.2020.07.009; pmid: 32758492
82. D. N. Mastronarde, Automated electron microscope tomography using robust prediction of specimen movements. *J. Struct. Biol.* **152**, 36–51 (2005). doi: 10.1016/j.jsb.2005.07.007; pmid: 16182563
83. S. Q. Zheng *et al*., MotionCor2: Anisotropic correction of beam-induced motion for improved cryo-electron microscopy. *Nat. Methods* **14**, 331–332 (2017). doi: 10.1038/nmeth.4193; pmid: 28250466
84. W. Jiang, F. Guo, Z. Liu, A graph theory method for determination of cryo-EM image focuses. *J. Struct. Biol.* **180**, 343–351 (2012). doi: 10.1016/j.jsb.2012.07.005; pmid: 22842112
85. A. Punjani, J. L. Rubinstein, D. J. Fleet, M. A. Brubaker, cryoSPARC: Algorithms for rapid unsupervised cryo-EM structure determination. *Nat. Methods* **14**, 290–296 (2017). doi: 10.1038/nmeth.4169; pmid: 28165473
86. S. H. W. Scheres, RELION: Implementation of a Bayesian approach to cryo-EM structure determination. *J. Struct. Biol.* **180**, 519–530 (2012). doi: 10.1016/j.jsb.2012.09.006; pmid: 23000701
87. P. Emsley, B. Lohkamp, W. G. Scott, K. Cowtan, Features and development of *Coot*. *Acta Cryst.* **D66**, 486–501 (2010). doi: 10.1107/S0907444910007493; pmid: 20383002
88. W. J. Allen, R. C. Rizzo, Implementation of the Hungarian algorithm to account for ligand symmetry and similarity in structure-based design. *J. Chem. Inf. Model.* **54**, 518–529 (2014). doi: 10.1021/ci400534h; pmid: 24410429
89. C. A. Flanagan, in *Methods in Cell Biology*, A. K. Shukla, Ed. (Academic Press, 2016), pp. 191–215.
90. R. N. DeHaven, D. L. DeHaven-Hudkins, Characterization of opioid receptors. *Curr. Protocols Pharmacol.* **8**, 1.4.1–1.4.12 (2000). doi: 10.1002/0471141755.ph0104s08
91. E. C. Hulme, M. A. Trevethick, Ligand binding assays at equilibrium: Validation and interpretation. *Br. J. Pharmacol.* **161**, 1219–1237 (2010). doi: 10.1111/j.1476-5381.2009.00604.x; pmid: 20132208
92. X.-P. Huang, T. Mangano, S. Hufeisen, V. Setola, B. L. Roth, Identification of human *Ether-à-go-go* related gene modulators by three screening platforms in an academic drug-discovery setting. *Assay Drug Dev. Technol.* **8**, 727–742 (2010). doi: 10.1089/adt.2010.0331; pmid: 21158687
93. C. Hiller *et al*., Functionally selective dopamine D_2/D_3 receptor agonists comprising an enyne moiety. *J. Med. Chem.*

56, 5130–5141 (2013). doi: 10.1021/jm400520c; pmid: 23730937
94. J. Hellmann *et al*., Structure-based development of a subtype-selective orexin 1 receptor antagonist. *Proc. Natl. Acad. Sci. U.S.A.* **117**, 18059–18067 (2020). doi: 10.1073/pnas.2002704117; pmid: 32669442
95. L. Di *et al*., Mechanistic insights from comparing intrinsic clearance values between human liver microsomes and hepatocytes to guide drug design. *Eur. J. Med. Chem.* **57**, 441–448 (2012). doi: 10.1016/j.ejmech.2012.06.043; pmid: 22840492
96. G. Scherrer *et al*., Dissociation of the opioid receptor mechanisms that control mechanical and heat pain. *Cell* **137**, 1148–1159 (2009). doi: 10.1016/j.cell.2009.04.019; pmid: 19524516
97. A. Muralidharan *et al*., Identification and characterization of novel candidate compounds targeting 6- and 7-transmembrane μ-opioid receptor isoforms. *Br. J. Pharmacol.* **178**, 2709–2726 (2021). doi: 10.1111/bph.15463; pmid: 33782947
98. C. G. Alvaro *et al*., Hippocalcin-like 4, a neural calcium sensor, has a limited contribution to pain and itch processing. *PLOS ONE* **15**, e0226289 (2020). doi: 10.1371/journal.pone.0226289; pmid: 32015563
99. S. R. Chaplan, F. W. Bach, J. W. Pogrel, J. M. Chung, T. L. Yaksh, Quantitative assessment of tactile allodynia in the rat paw. *J. Neurosci. Methods* **53**, 55–63 (1994). doi: 10.1016/0165-0270(94)90144-9; pmid: 7990513
100. Y. Q. Cao *et al*., Primary afferent tachykinins are required to experience moderate to intense pain. *Nature* **392**, 390–394 (1998). doi: 10.1038/32897; pmid: 9537322

ACKNOWLEDGMENTS

We thank B. Kobilka for sharing the structure of PDB 6K41 before publication. We thank T. Tummino and J. Lyu for reading this manuscript. We also thank WuXi AppTec for providing information on compounds sourced from the WuXi GalaXi virtual library. We gratefully acknowledge OpenEye Software for Omega and related tools and Schrödinger, Inc. for the Maestro package. **Funding:** This work is supported by DARPA grant HR0011-19-2-0020 (B.K.S., A.I.B., J.J.I., and M.P.J.), DFG grant GRK 1910 (P.G.), US NIH grant R35GM122481 (B.K.S.), US NIH grant R01GM133836 (J.J.I.), US R35 NS097306 (A.I.B.), Open Philanthropy (A.I.B.), the Facial Pain Research Foundation (A.I.B.), and CIHR Foundation grant FN-148431 (M.B.). C.M.W. is supported by an NSF Graduate Research Fellowship. Y.D. is supported by a grant from the Science, Technology and Innovation Commission of Shenzhen Municipality (project JCYJ20200109150019113) and in part by the Kobilka Institute of Innovative Drug Discovery and Shenzhen Key Lab (ZDSYS20190902093417963). X.-P.H. is supported by NIMH PDSP (HHSN-271-2018-00023-C), directed by B. Roth. M.B. holds the Canada Research Chair in Signal Transduction and Molecular Pharmacology. **Author contributions:** E.A.F. conducted the docking screens with input from B.K.S. Ligand optimization was performed by E.A.F. and P.S. with input from M.F.S., H.H., B.K.S., and P.G. H.H. performed all binding and functional assays and analyses for adrenergic and dopamine receptors with input from D.W. J.X. determined the '9087-α_{2A}AR-G_{oA} and '4622-α_{2A}AR-G_{oA} structures and made α_{2A}AR mutations assisted by G.C. and Z.L., with supervision from Y.D. J.M.B. performed and analyzed the in vivo pharmacology experiments assisted by V.C., supervised and coanalyzed by A.I.B. C.A. tested select compounds in the panel of G protein and β-arrestin subtypes and receptor internalization with supervision from M.B. S.G. modeled compound '7075 and PS75. X.-P.H. tested compounds in GPCRome and hERG assays. M.F.S. performed contact area calculation. P.S. synthesized bespoke compounds and performed pK_a and analytical testing with supervision of P.G. D.W. performed ELISA experiments. C.M.W. tested compounds for μOR activity. C.K. performed permeability calculations with supervision of M.P.J. Y.S.M. supervised compound synthesis of Enamine compounds purchased from the ZINC15 database and 12 billion catalog, assisted by N.A.T. J.J.I. built the ZINC15 ultralarge libraries. B.K.S., P.G., A.I.B., and Y.D. supervised the project. E.A.F. wrote the paper with contributions from J.M.B. and J.X., input from all other authors, and primary editing from B.K.S. and P.G. B.K.S., P.G., and A.I.B. conceived the project. **Competing interests:** B.K.S. and P.G. are founders of Epiodyne. B.K.S. is a founder of BlueDolphin and of Deep Apple Therapeutics and consults in docking and in the GPCR space. J.J.I. is a cofounder of BlueDolphin and Deep Apple Therapeutics. M.P.J. is a consultant to Deep Apple Therapeutics and to Schrödinger, Inc. M.B. is the chair of the scientific advisory board of Domain Therapeutics, to which some of the BRET-based biosensors used are licensed for commercial use. Y.S.M. is a CEO of Chemspace LLC and a scientific advisor at Enamine, Ltd. B.K.S., E.A.F., P.G., H.H., P.S., A.I.B., J.M.B., Y.D., and J.X. are authors of patents on the discovery of new pain modulators acting through the α_{2A}AR. The authors declare no other competing interests. **Data and materials availability:** All data are available in the main text, the supplementary materials, the listed Protein Data Bank (PDB) files, the Electron Microscopy Data Bank (EMDB) files, or at https://github.com/efink14/ADRA2AR_docking_results. The 3D cryo-EM density maps of 9087-α_{2A}AR-G_{oA} and '4622-α_{2A}AR-G_{oA} generated in this study have been deposited with accession codes EMD-32331 and EMD-32342, respectively. The coordinates of '9087-α_{2A}AR-G_{oA} and '4622-α_{2A}AR-G_{oA} have been deposited with PDB accession codes 7W6P and 7W7E, respectively. The identities of compounds docked in this study are freely available from the ZINC15 and ZINC20 databases (https://zinc15.docking.org/ and https://zinc20.docking.org/), and active compounds may be purchased from Enamine and WuXi AppTec or are available from the authors. The docking results, including ZINC number, SMILES, and docking score, are located at https://github.com/efink14/ADRA2AR_docking_results. DOCK3.7 is freely available for noncommercial research (https://dock.compbio.ucsf.edu/DOCK3.7/). A web-based version is freely available to all (https://blaster.docking.org/). The biosensors used for generating the data in tables S3 and S4 and figures S6 to S8 are protected by a patent but are available from M.B. for noncommercial research without restrictions under a regular academic Material Transfer Agreement with the Université de Montréal. **License information:** Copyright © 2022 the authors, some rights reserved; exclusive licensee American Association for the Advancement of Science. No claim to original US government works. https://www.science.org/about/science-licenses-journal-article-reuse

SUPPLEMENTARY MATERIALS

science.org/doi/10.1126/science.abn7065
Figs. S1 to S20
Tables S1 to S11
MDAR Reproducibility Checklist

Submitted 14 December 2021; accepted 30 August 2022
10.1126/science.abn7065



AAAS.ORG/COMMUNITY







AAAS' Member Community is a one-stop destination for scientists and STEM enthusiasts alike. It's "Where Science Gets Social": a community where facts matter, ideas are big and there's always a reason to come hang out, share, discuss and explore.

Member COMMUNITY
AAAS

AMERICAN ASSOCIATION FOR THE ADVANCEMENT OF SCIENCE

RESEARCH ARTICLE SUMMARY

IMMUNE SIGNALING

Cyclic ADP ribose isomers: Production, chemical structures, and immune signaling

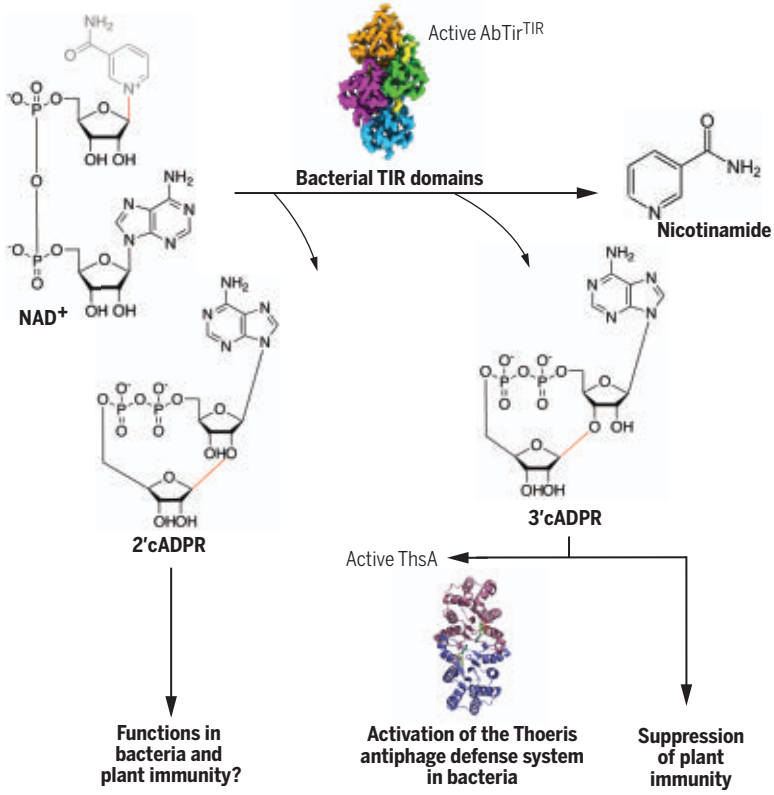
Mohammad K. Manik†, Yun Shi†, Sulin Li†, Mark A. Zaydman, Neha Damaraju, Samuel Eastman, Thomas G. Smith, Weixi Gu, Veronika Masic, Tamim Mosaiab, James S. Weagley, Steven J. Hancock, Eduardo Vasquez, Lauren Hartley-Tassell, Nestoras Kargios, Natsumi Maruta, Bryan Y. J. Lim, Hayden Burdett, Michael J. Landsberg, Mark A. Schembri, Ivan Prokes, Lijiang Song, Murray Grant, Aaron DiAntonio, Jeffrey D. Nanson, Ming Guo, Jeffrey Milbrandt, Thomas Ve*, Bostjan Kobe*

INTRODUCTION: Organisms from bacteria to animals and plants must defend themselves against pathogens. Homologous protein motifs exist in immune pathways of all organisms. One such motif is the TIR domain, named after the mammalian immune receptors—Toll-like receptors and interleukin-1 receptors—where it was first identified. Two properties are shared among most TIR domains from all organisms: the ability to self-associate and enzymatic activity involving the cleavage of nicotinamide adenine dinucleotide (oxidized form) (NAD^+). NAD^+ is a metabolite with redox properties that has roles in many cellular processes. In some cases, cleavage of NAD^+ leads to the production of cyclic adenosine monophosphate (ADP)–ribose (cADPR) isomers.

RATIONALE: In bacteria, NAD^+-cleavage activity by TIR domain–containing proteins plays a role in defense signaling, as well as suppression of host immunity. One corresponding pathway is termed the Thoeris defense system. This signaling pathway protects bacteria against phage infection and involves the *thsA* and *thsB* genes. Upon phage infection, ThsB (a TIR-domain protein) cleaves NAD^+ and produces a cADPR isomer, which activates ThsA-mediated killing of the infected cell, thus protecting the bacterial population. Another bacterial protein that produces a cADPR isomer is HopAM1, the TIR-domain effector protein from *Pseudomonas syringae* DC3000, which is involved in suppressing plant immunity. The chemical structures and mechanisms of action of the responsible cADPR isomers were unknown before this work. Our aim was to determine the chemical structures of cADPR isomers, the structural basis of their production by bacterial TIR domains, and their mechanism of action in Thoeris defense signaling and suppression of plant immunity.

RESULTS: Using a combination of methods, including nuclear magnetic resonance (NMR), mass spectrometry, and crystallography, we show that the cADPR isomers are cyclized by O-glycosidic bond formation between the ribose moieties in ADPR. Structures of TIR domains that produce cADPR isomers, as determined by crystallography and cryo–electron microscopy, reveal conformational changes that lead to an active assembly that resembles those of Toll-like receptor adaptor TIR domains. Mutagenesis reveals a conserved tryptophan that is essential for cyclization. Using crystallography and biophysical approaches, we show that one of the cADPR isomers (3′cADPR) is an activator of Thoeris ThsA proteins responsible for antiphage defense, by inducing a change in its tetrameric state. We also show that the same cADPR isomer is a suppressor of plant immunity when produced by the effector HopAM1.

CONCLUSION: Collectively, our results reveal the molecular basis of cADPR isomer production. The 2′cADPR and 3′cADPR differ only in the location of the O-glycosidic bond between the ribose moieties in ADPR. These compounds add to the growing list of signaling molecules identified in immune pathways that involve proteins containing TIR domains and may represent intermediates in their synthesis or signaling molecules with their own distinctive activities. Our results establish the 3′cADPR isomer produced by bacterial TIR domain–containing proteins as an antiviral and plant immunity–suppressing signaling molecule. ■



Diverse immune roles of bacterial cADPR isomers. Bacteria have TIR domain–containing proteins that cleave NAD to produce cyclic ADPR isomers with different cyclic linkages. One of these molecules, 3′cADPR, has roles in diverse immunity pathways. It acts as an activator of the Thoeris antiphage defense system by binding to the protein ThsA. When produced by the effector HopAM1 from the plant pathogen *P. syringae*, it suppresses plant immunity.

The list of author affiliations is available in the full article online.
*Corresponding author. Email: b.kobe@uq.edu.au (B.K.); t.ve@griffith.edu.au (T.V.)
†These authors contributed equally to this work.
Cite this article as M. K. Manik *et al.*, *Science* 377, eadc8969 (2022). DOI: 10.1126/science.adc8969

READ THE FULL ARTICLE AT
https://doi.org/10.1126/science.adc8969

RESEARCH ARTICLE

IMMUNE SIGNALING

Cyclic ADP ribose isomers: Production, chemical structures, and immune signaling

Mohammad K. Manik[1,2]†‡§, Yun Shi[3]†, Sulin Li[1,2]†, Mark A. Zaydman[4], Neha Damaraju[5,6], Samuel Eastman[7], Thomas G. Smith[8]¶, Weixi Gu[1,2], Veronika Masic[3], Tamim Mosaiab[3], James S. Weagley[9], Steven J. Hancock[1,2]#, Eduardo Vasquez[3], Lauren Hartley-Tassell[3], Nestoras Kargios[10], Natsumi Maruta[1,2], Bryan Y. J. Lim[1,2], Hayden Burdett[1,2]**, Michael J. Landsberg[1,2], Mark A. Schembri[1,2], Ivan Prokes[11], Lijiang Song[11], Murray Grant[10], Aaron DiAntonio[4,5], Jeffrey D. Nanson[1,2], Ming Guo[12], Jeffrey Milbrandt[4], Thomas Ve[3]*, Bostjan Kobe[1,2,13]*

Cyclic adenosine diphosphate (ADP)–ribose (cADPR) isomers are signaling molecules produced by bacterial and plant Toll/interleukin-1 receptor (TIR) domains via nicotinamide adenine dinucleotide (oxidized form) (NAD^+) hydrolysis. We show that v-cADPR (2′cADPR) and v2-cADPR (3′cADPR) isomers are cyclized by O-glycosidic bond formation between the ribose moieties in ADPR. Structures of 2′cADPR-producing TIR domains reveal conformational changes that lead to an active assembly that resembles those of Toll-like receptor adaptor TIR domains. Mutagenesis reveals a conserved tryptophan that is essential for cyclization. We show that 3′cADPR is an activator of ThsA effector proteins from the bacterial antiphage defense system termed Thoeris and a suppressor of plant immunity when produced by the effector HopAM1. Collectively, our results reveal the molecular basis of cADPR isomer production and establish 3′cADPR in bacteria as an antiviral and plant immunity–suppressing signaling molecule.

The ~150-residue Toll/interleukin-1 receptor (TIR) domains are widely distributed in animals, plants, and bacteria and function through self-association and homotypic interactions with other TIR domains (*1*). In plants and animals, these domains are predominantly found in proteins with immune functions [Toll-like receptors (TLRs), interleukin-1 receptors (IL-1Rs), and their adaptor proteins] (*2*) and plant nucleotide-binding, leucine-rich repeat receptors (NLRs) (*3*, *4*). TIR domains form higher-order oligomers and orchestrate signal amplification by a mechanism called signaling by cooperative assembly formation (SCAF) (*3*, *5*–*7*).

In bacteria, initial studies suggested that TIR domain–containing proteins, such as TcpB, TcpC, TirS, PumA, and TcpS, serve as virulence factors that inhibit host innate immune signaling by molecular mimicry, although it is not clear how they enter the cell (*8*). Bacterial TIR domain–containing proteins are further implicated in antiphage defense systems (*9*–*12*).

Many TIR domains have been found to cleave nicotinamide adenine dinucleotide (oxidized form) (NAD^+) (*13*–*16*). In animals, SARM1 (sterile alpha and Toll/interleukin-1 receptor motif-containing 1) is a metabolic sensor of axonal nicotinamide mononucleotide (NMN) and NAD^+ levels, and its TIR domain executes programmed axon death by cleaving NAD^+ into nicotinamide and either adenosine diphosphate (ADP)–ribose (ADPR) or cyclic ADPR (cADPR) (*13*, *16*, *17*). The TIR domains of plant NLRs (TNLs) similarly cleave NAD^+ into nicotinamide and either ADPR or a cADPR isomer known as variant cADPR (v-cADPR) (*14*), which has a different but unknown cyclization site compared with canonical cADPR (*18*). A conserved catalytic glutamate is required for NAD^+ hydrolysis by SARM1 and plant TIR domains, and the same glutamate is required for SARM1 to trigger axon degeneration and plant TNLs to trigger a localized cell death in response to infections (*13*, *14*, *16*). v-cADPR is a biomarker of plant TNL enzymatic activity but may not be sufficient in and of itself to trigger a cell-death response (*19*).

Bacterial TIR domains can also cleave NAD^+ (*10*, *15*, *20*–*22*), again producing nicotinamide and ADPR or the distinct cADPR isomers v-cADPR or v2-cADPR. In bacteria, NAD nucleosidase (NADase) activity by TIR domains is a critical component of STING cyclic dinucleotide sensing (*10*) and the Thoeris defense system (*9*). The Thoeris system protects bacteria against phage infection and consists of two genes: *thsA* and *thsB* (the latter can be present in one or multiple copies). The *thsA* gene encodes a protein that contains either an N-terminal SIR2-like (silent information regulator 2) domain and a C-terminal SLOG-like domain (from the superfamily of ribonuclease like proteins named after SMF/DprA and LOG proteins) or a multitransmembrane N-terminal domain with a C-terminal macro domain. SIR2 domains hydrolyze NAD^+, whereas SLOG domains can bind to NAD^+-derived metabolites and have been suggested as sensors for nucleotide-related ligands (*9*, *23*). The *thsB* gene encodes a TIR domain–containing protein (ThsB) (*9*, *22*–*24*). Upon phage infection, ThsB cleaves NAD^+ and produces a cADPR isomer, which activates ThsA (*22*), causing further NAD^+ depletion and cell death. HopAM1, a bacterial TIR-domain effector protein from *Pseudomonas syringae* DC3000, suppresses plant immunity by producing v2-cADPR (*21*).

TIR domain self-association is required for the NADase activity of SARM1 as well as plant TNLs (*13*, *16*). Crystal and cryo–electron microscopy (cryo-EM) structures of SARM1 in its active conformation revealed the active site spanning two TIR-domain molecules, explaining the requirement for self-association (*25*). The architectures of oligomeric assemblies formed by plant and SARM1 TIR domains are similar ("enzyme assemblies") but are distinct from those formed by animal TIR domains involved in TLR signaling ("scaffold assemblies") [reviewed in (*3*)]. Both types of assemblies feature open-ended complexes with two strands of TIR domains in a head-to-tail arrangement but differ in the orientation of the two strands (antiparallel in enzyme assemblies, parallel in scaffold assemblies). Some plant TIR domains have also been shown to act as 2′,3′-cAMP and 2′,3′-cGMP synthetases, by hydrolyzing RNA and DNA, which requires a different TIR-domain oligomeric architecture

[1]School of Chemistry and Molecular Biosciences, The University of Queensland, Brisbane, QLD 4072, Australia. [2]Australian Infectious Diseases Research Centre, The University of Queensland, Brisbane, QLD 4072, Australia. [3]Institute for Glycomics, Griffith University, Southport, QLD 4222, Australia. [4]Department of Pathology and Immunology, Washington University School of Medicine in St. Louis, St. Louis, MO 63100, USA. [5]Department of Developmental Biology, Washington University School of Medicine in St. Louis, St. Louis, MO 63100, USA. [6]Department of Genetics, Washington University School of Medicine in St. Louis, St. Louis, MO 63100, USA. [7]Department of Plant Pathology, University of Nebraska–Lincoln, Lincoln, NE 68583, USA. [8]Department of Chemistry, University of Nebraska–Lincoln, Lincoln, NE 68588, USA. [9]Edison Family Center for Genome Sciences and Systems Biology, Washington University School of Medicine in St. Louis, St. Louis, MO 63110, USA. [10]School of Life Sciences, University of Warwick, Coventry CV4 7AL, UK. [11]Department of Chemistry, University of Warwick, Coventry CV4 7AL, UK. [12]Department of Agronomy and Horticulture, University of Nebraska–Lincoln, Lincoln, NE 68583, USA. [13]The University of Queensland, Institute for Molecular Bioscience, Brisbane, QLD 4072, Australia.
*Corresponding author. Email: b.kobe@uq.edu.au (B.K.); t.ve@griffith.edu.au (T.V.)
†These authors contributed equally to this work.
‡Present address: Department of Biological Chemistry and Molecular Pharmacology, Harvard Medical School, Boston, MA 02115, USA.
§Present address: Program in Cellular and Molecular Medicine, Boston Children's Hospital, Boston, MA 02115, USA.
¶Present address: Department of Chemistry, University of Minnesota, Minneapolis, MN 55455, USA.
#Present address: Wellcome Wolfson Institute for Experimental Medicine, School of Medicine, Dentistry and Biomedical Sciences, Queen's University Belfast, Belfast BT12 6BA, UK.
**Present address: Wellcome Centre for Cell Biology, University of Edinburgh, Edinburgh EH9 3BF, UK.

(*26*) (cAMP, cyclic adenosine monophosphate; cGMP, cyclic guanosine monophosphate). A limited number of bacterial TIR domains have been characterized structurally and functionally (*23*, *27*–*30*). In this study, we characterized the cyclization site of cADPR isomers, the molecular basis of their production by TIR domains, and their functions in immunity pathways in bacteria and plants.

O-glycosidic linkage between ribose sugars in cADPR isomers

To identify the sites of cyclization in cADPR isomers, we expressed and purified the TIR domains of AbTir (from *Acinetobacter baumannii*; AbTir^{TIR}) and a protein from *Aquimarina amphilecti* (AaTir^{TIR}; fig. S1A and table S1), which produce v- and v2-cADPR, respectively (*15*, *31*). Comparative genomics analyses suggest that AbTir has functions distinct from the Thoeris defense system (fig. S1B).

Real-time nuclear magnetic resonance (NMR)–based and fluorescence-based NADase assays confirmed that purified AbTir^{TIR} and AaTir^{TIR} are enzymatically active and produce cADPR isomers (Fig. 1A and fig. S1, C and D). AbTir^{TIR}-produced v-cADPR is identical to the cADPR isomer produced by TIR domains of the plant immune receptors L6 and ROQ1 (Fig. 1A). Both AbTir^{TIR} and AaTir^{TIR} can catalyze base-exchange reactions with 8-amino-isoquinoline (fig. S2A). They can also use nicotinamide adenine dinucleotide phosphate (NADP$^+$) as a substrate, but its cleavage only yields nicotinamide and adenosine diphosphate ribose 2′-phosphate (ADPPR), indicating that cADPR-isomer production is specific to NAD$^+$ cleavage (fig. S2B). We also tested the activities in the presence of NAD$^+$, adenosine triphosphate (ATP), and Mg^{2+} and observed no formation of metabolites reported for plant TIR domains (*32*, *33*) (fig. S1F).

We purified v-cADPR and v2-cADPR from the reaction mixture, using high-performance liquid chromatography (HPLC), and determined their chemical structures using NMR (Fig. 1B; figs. S1E and S2, C to D; and tables S2 and S3). The heteronuclear multiple bond correlation (HMBC) NMR spectrum of AbTir^{TIR}-produced v-cADPR shows both H1″-C2′ and H2′-C1″ cross-peaks, revealing that AbTir^{TIR} catalyzes the formation of a ribose(1″→2′)ribose O-glycosidic linkage in ADPR (Fig. 1B). By contrast, the HMBC spectrum of v2-cADPR, produced by AaTir^{TIR}, shows both H1″-C3′ and H3′-C1″ cross-peaks, indicating that AaTir^{TIR} catalyzes the formation of a ribose(1″→3′)ribose O-glycosidic linkage in ADPR (Fig. 1, B and C). Because the β configuration of the anomeric carbon in NAD$^+$ is retained in AbTir^{TIR} and

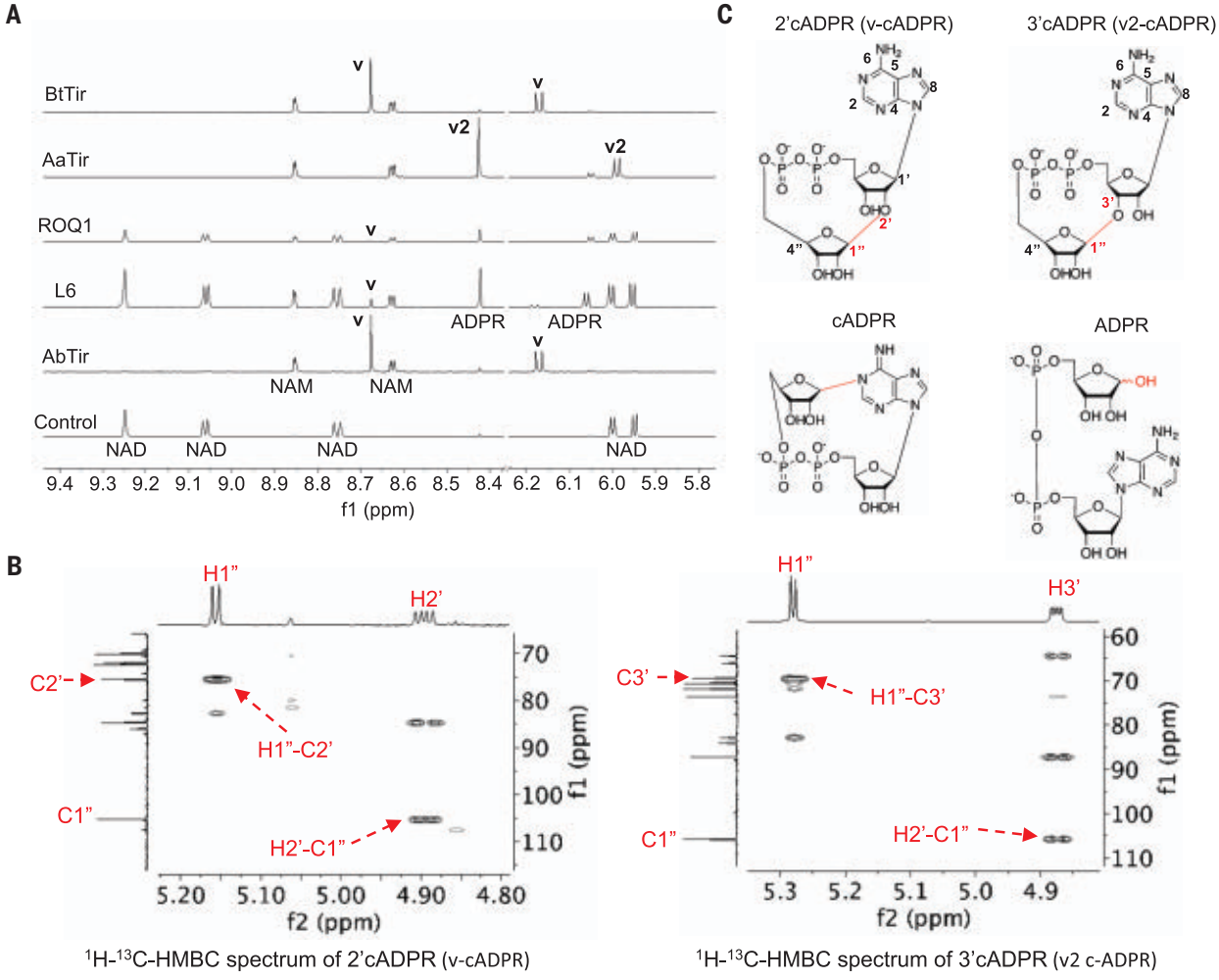


Fig. 1. Chemical structures of v- and v2-cADPR. (**A**) Expansions of ^{1}H NMR spectra showing NADase reactions by 0.1 μM AbTir^{TIR} (*A. baumannii*), 100 μM L6^{TIR} (flax), 26 μM ROQ1^{TIR} (*N. benthamiana*), 0.5 μM AaTir^{TIR} (*A. amphilecti*), and 2.5 μM BtTir^{TIR} (*B. thetaiotaomicron*; table S1). The initial concentration for NAD$^+$ was 500 μM, except for L6 (1 mM). Spectra correspond to 16 hours of incubation time, except for ROQ1 (incubation time of 64 hours). Selected peaks are labeled, showing the formation v-cADPR (v) and v2-cADPR (v2). (**B**) Expansions of HMBC spectra showing correlations through glycosidic linkages for 2′cADPR (v-cADPR) and 3′cADPR (v2-cADPR). ppm, parts per million. (**C**) Chemical structures of 2′cADPR, 3′cADPR, cADPR, and ADPR. Important NMR peaks (B) and their correlated positions in the chemical structure (C) are labeled, showing a 1″-2′ linkage for v-cADPR and a 1″-3′ linkage for v2-cADPR.

AaTir^{TIR}-catalyzed base-exchange reactions (fig. S2A) and the coupling constants of the anomeric protons of v-cADPR (J1″,2″ ~ 5.0 Hz) and v2-cADPR (J1″,3″ ~ 4.4 Hz) are similar to those of NAD$^+$ (5 to 6 Hz), both cADPR isomers are likely to retain the same β configuration. v2-cADPR purified from *Nicotiana benthamiana* leaves expressing HopAM1 showed an identical chemical structure to that of AaTir^{TIR} (table S4). Based on these chemical structures, we term these molecules 2′cADPR and 3′cADPR, highlighting the linkages between ribose rings of v-cADPR and v2-cADPR, respectively.

Ligand-free structures and self-association of bacterial TIR domains

SARM1 and plant TIR domains require self-association for their NADase activity (*13*, *25*, *34*, *35*). The NADase activity of AbTir^{TIR} increases disproportionally with increasing protein concentrations and increases in the presence of molecular crowding agents (fig. S3, A and B). Size-exclusion chromatography coupled with multiangle light scattering (SEC-MALS) experiments show that AbTir self-associates in a concentration-dependent manner (fig. S3, C and D), which requires both the TIR domain and the N-terminal coiled coil (CC) domain (AbTir^{CC}). AbTir$^{full\text{-}length}$ shows an initially suppressed enzymatic activity, suggesting that conformational rearrangements are required for efficient NAD$^+$ cleavage (fig. S1C). Taken together, these results suggest that cADPR isomer–producing bacterial TIR domains also require self-association for their NADase activity.

To provide insight into the molecular basis of cADPR isomer production by TIR domains, we determined the crystal structures of AbTir^{TIR} and a closely related v-cADPR (2′cADPR)–producing TIR domain protein (47% sequence identity) from *Bacteroides thetaiotaomicron* (residues 156 to 287; BtTir^{TIR}; Fig. 1, figs. S1A and S2A, and table S1), at 2.16- and 1.42-Å resolution, respectively (fig. S4, A and B, and table S5). The structure of AbTir^{TIR} closely resembles the structures of BtTir^{TIR}, PdTir^{TIR} [Protein Data Bank (PDB) ID 3H16], and the v-cADPR (2′cADPR)–producing TcpB^{TIR} (PDB ID 4C7M) (*27*–*30*), with Cα root mean square distance (RMSD) values of 1.2, 1.8, and 1.9 Å, respectively (fig. S4, B and C). Both AbTir^{TIR} and BtTir^{TIR} show less similarity to the cADPR isomer–producing ThsB TIR domain of the *Bacillus cereus* MSX-D12 Thoeris defense system (BcThsB; PDB ID 6LHY; Cα RMSD values of 4.4 and 2.5 Å for AbTir^{TIR} and BtTir^{TIR}, respectively).

In TIR domains with NADase activity (from SARM1; plant TNLs RPP1, ROQ1, and RUN1; and oyster TIR-STING; table S1), the conserved glutamate residue essential for NADase activity is localized in a pocket consisting of residues from the βA strand, the AA and BB loops, and the αB and αC helices (*10*, *13*, *25*, *34*). In AbTir^{TIR} and BtTir^{TIR}, the αB and αC helices adopt different conformations and the equivalent glutamate residue (E208 in AbTir; E230 in BtTir) is surface exposed (fig. S4D). Comparing the different chains in the asymmetric unit of the AbTir^{TIR} crystal, the region around E208 is highly flexible. Crystal packing of AbTir^{TIR} and BtTir^{TIR} reveals a common symmetric interface (figs. S4C and S5A), with a large buried surface area (BSA) (AbTir^{TIR}, 1875 Å^2; BtTir^{TIR}, 1332 Å^2), which is also observed in the crystals of PdTir^{TIR} and TcpB^{TIR} (fig. S5A and table S1). The structures suggest that they represent an inactive conformation, possibly stabilized by the symmetric dimeric arrangement.

Cryo-EM structure of AbTir^{TIR} bound to NAD$^+$ mimic

We reasoned that we could capture the active state of AbTir by using base-exchange products of NAD$^+$ hydrolysis, which are more biochemically stable than NAD$^+$ itself and could resist cleavage at high concentrations of the enzyme (*25*). Indeed, in the presence of 8-amino-isoquinoline adenine dinucleotide (3AD), we could visualize filamentous structures of AbTir^{TIR} by negative-stain electron microscopy (Fig. 2A). Filaments could be observed in the presence of NAD$^+$, but too few to support structure determination (fig. S6A). We determined the cryo-EM structure of AbTir^{TIR}:3AD filaments at 2.74-Å resolution (fig. S6 and table S6), which shows the presence of 3AD molecules between monomers of AbTir^{TIR} and an arrangement of TIR domains different from the enzyme assemblies of SARM1 and plant TIR domains but analogous to the scaffold assemblies of the TLR adaptor proteins MAL and MyD88, each of which contains two parallel strands of TIR domains arranged head to tail (Fig. 2, B and D, and fig. S5B) (*3*). The intrastrand "BE" interface (BSA of 710 Å^2) involves the BB-loop, whereas the interstrand "BCD" interface involves one molecule interacting with two molecules in the parallel strand (BSAs of 1340 and 1410 Å^2, respectively). Assembly formation is accompanied by conformational changes involving the BB-loop and the αB and αC helices (RMSD of 1.8 Å for 101 Cα atoms; Fig. 2C and movie S1). The BB-loop and αB helix have tilted outward by ~50° to 55°, whereas the αC helix has refolded and includes residues from both the CC and CD loops. Because it is arranged through the analogous BE interface, the AbTir^{TIR} active site is very similar to that of SARM1^{TIR}, including the conformation of the 3AD molecule (Fig. 2E). Using site-directed mutagenesis, we verified the importance of residues in both the active-site region and in the inter- and intrastrand interfaces for NADase activity of AbTir^{TIR} (Fig. 3A, fig. S7, and table S7).

Tryptophan affects ADPR cyclization

The products of the NADase reaction were also assessed for the AbTir mutants (table S7). The analysis revealed that only the W204A (Trp^{204}→Ala) mutant has reduced production of v-cADPR (2′cADPR) compared with wild-type AbTir, demonstrating its importance for ADPR cyclization (Fig. 3B, fig. S8A, and table S7). We tested whether the mutation of the equivalent tryptophan residue has a similar effect on ADPR cyclization by other bacterial TIR domain–containing proteins. We analyzed the conservation of W204 in a multiple sequence alignment of 122 TIR domains (*15*, *16*, *31*). We observed conservation of aromatic residues at this position among all TIR domains that produced a cyclic ADPR product [cADPR, v-cADPR (2′cADPR), or v2-cADPR (3′cADPR)] in vitro, with a strong preference for tryptophan—W (9 of 12), Y (Tyr) (2 of 12), and F (Phe) (1 of 12) (fig. S8B). This conservation is weaker among TIR domains that either produce noncyclic products (nicotinamide and ADPR) or lack activity altogether in vitro. These observations suggest that a large aromatic residue at this position facilitates the production of a cyclic ADPR product.

To further identify positions important for determining the product specificity of TIR-domain NADases, we analyzed 278 TIR-domain sequences and confirmed that the position corresponding to the tryptophan differs between cyclase and noncyclase TIR domains, although not among cyclase TIR domains that produce different forms of cADPR (data S1 to S4). All cyclase TIR domains contain an aromatic residue at this position (fig. S9, A to E).

We tested the functional importance of the conserved aromatic residue by performing site-directed mutagenesis on TIR domains known to produce different products (fig. S8, C and D), with conservative (W, Y, or F) or disruptive (A) mutations. Reaction products were analyzed by HPLC (fig. S8, C and D). For all TIR domains that produce a cyclic product, the mutants exhibited a decrease in cyclic product formation and an increase in ADPR when compared with the wild-type proteins (Fig. 3, C to F). The nonconservative alanine mutations typically exhibited the greatest impact on the relative production of a cyclic product versus ADPR; however, this trend was not universally true. Mutations in the background of an ADPR-producing template had variable impacts on NADase activity (fig. S8E), but ADPR always remained the only catabolite produced. These results are consistent with the conclusion that the position equivalent to W204 in AbTir is critical for the production of cyclic ADPR products.

3′cADPR (v2-cADPR) activates Thoeris ThsA

Bacterial lysates containing cADPR isomers produced by bacterial ThsB or plant TIR domains have been shown to activate the ThsA NADase (Fig. 4A) of the *B. cereus* MSX-D12 Thoeris antiphage defense system (*22*). To test

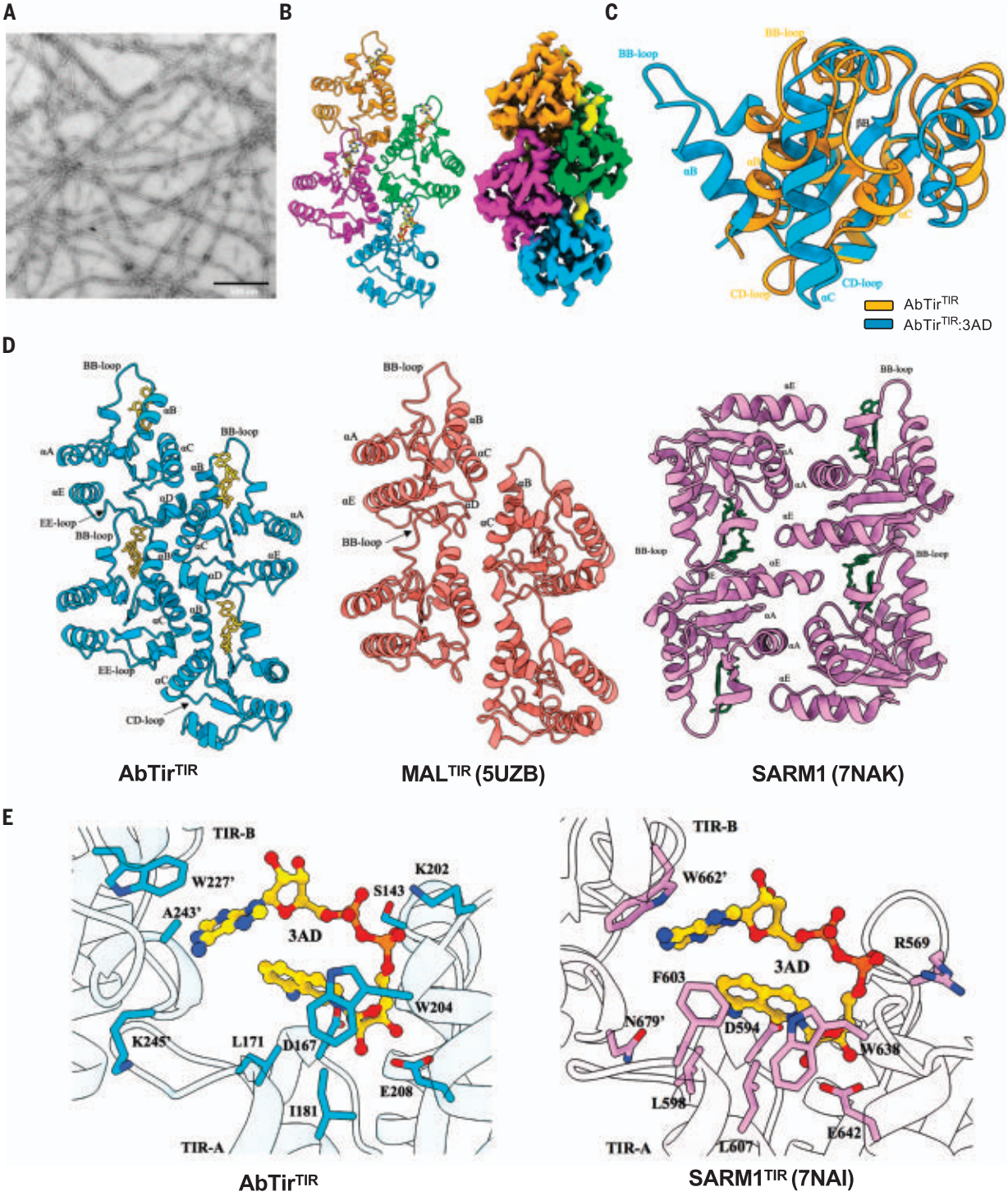


Fig. 2. Cryo-EM structure of the AbTir^{TIR}:3AD filament. (**A**) Negative-stain electron micrograph of AbTir^{TIR}:3AD filaments. (**B**) Cartoon representation and electrostatic potential density map of the AbTir^{TIR}:3AD filament. TIR domain subunits are shown in blue, green, magenta, and orange. 3AD is shown in yellow. (**C**) Structural superposition of ligand-free (crystal structure, orange) and 3AD-bound AbTir^{TIR} (cryo-EM structure, cyan) molecules reveal conformational changes in the BB-loop and αB and αC helices upon substrate binding. (**D**) Comparison of AbTir^{TIR}:3AD, MAL^{TIR} (PDB ID 5UZB) and SARM1^{TIR}:1AD (PDB ID 7NAK) assemblies. (**E**) Comparison of the active sites in AbTir^{TIR} and SARM1^{TIR} (PDB ID 7NAI) reveals similar substrate-binding modes.

if our purified cADPR isomers can directly activate ThsA, we produced and purified four different ThsA proteins (37 to 46% sequence identity) from *B. cereus* MSX-D12 (BcThsA), *A. baumannii* (AbThsA), *Enterococcus faecium* (EfThsA), and *Streptococcus equi* (SeThsA) and monitored the NAD^+-cleavage activity of each in the absence and presence of ADPR, cADPR, v-cADPR (2′cADPR), and v2-cADPR (3′cADPR) using our NMR-based NADase assay (Fig. 4, B and C, and fig. S10, A and B). AbThsA, BcThsA, and a SIR2 domain–only construct of BcThsA (BcThsA^{SIR2}) cleave NAD^+ (fig. S10, A to C), whereas EfThsA, SeThsA, and SeThsA^{SIR2} (Fig. 4, B and C, and fig. S10C) are almost inactive under

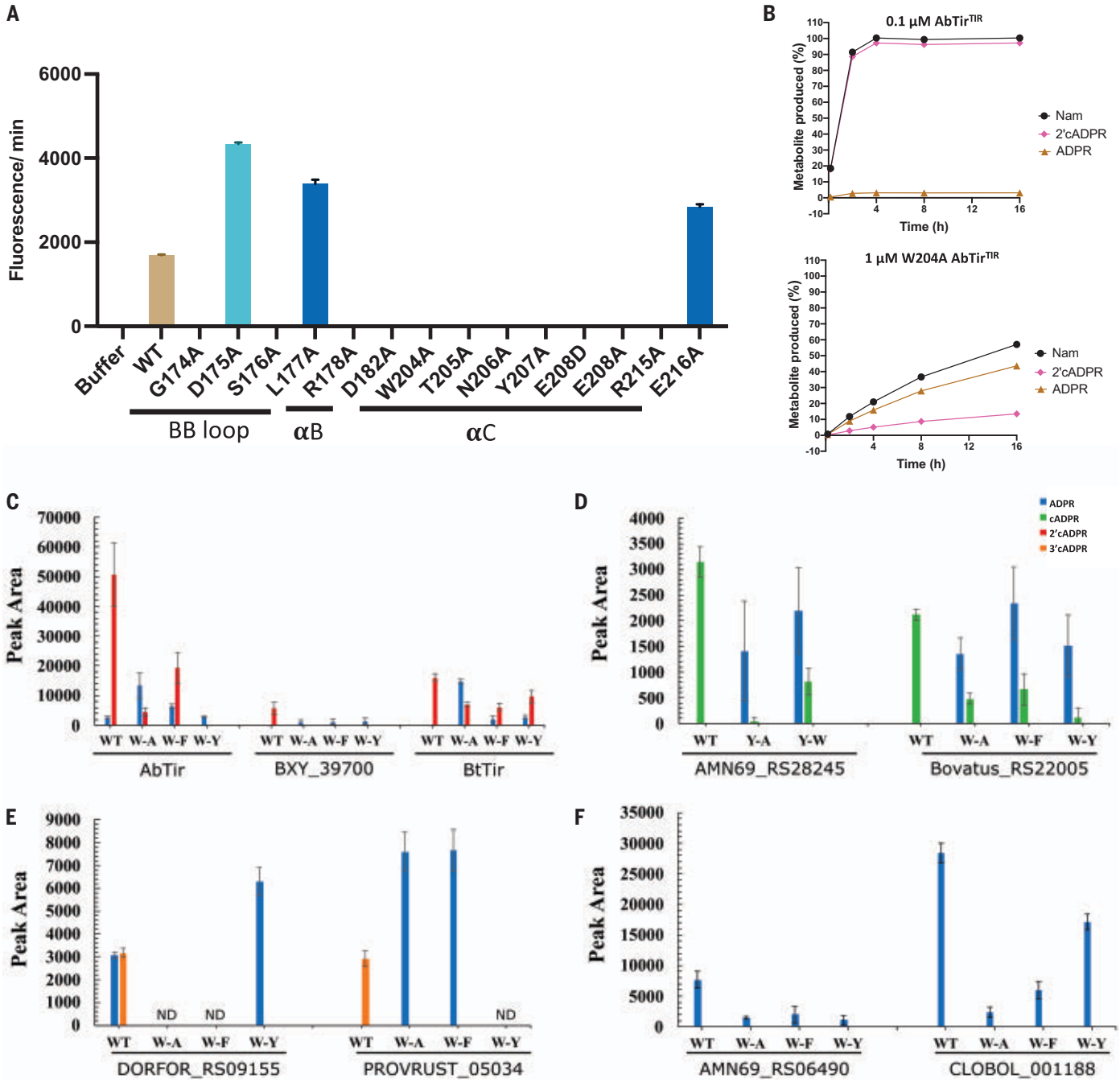


Fig. 3. Mutagenesis of bacterial TIR domains. (**A**) NADase activity of AbTir^{TIR} mutants, using the fluorescence-based assay, with 100 μM εNAD and 100 μM protein. Data are presented as means ± SD (n = 3). (**B**) Production of 2′cADPR and ADPR by wild-type AbTir^{TIR} and its W204A mutant, monitored by ^{1}H NMR, using an initial NAD^{+} concentration of 500 μM. (**C** to **F**) Mutations of the position equivalent to AbTir W204 affect the production of cyclic NAD^{+} catabolites by TIR domains (table S1). The NAD^{+} catabolite peak areas for wild-type and mutant TIR domain reactions after 1 hour are shown. TIR domain grouping is based on the primary product of the wild-type protein [n = 3 for all groups except where no data (ND) could be collected; data are presented as means ± SD].

the same conditions (less than 10% of NAD^{+} consumed after 40 hours). Neither BcThsA nor AbThsA are further activated by ADPR, cADPR, v-cADPR (2′cADPR), or v2-cADPR (3′cADPR) (fig. S10B), suggesting that they have been produced in a fully activated state. Both autoactive and inactive versions of ligand-free BcThsA have previously been reported (*22*, *23*), suggesting that the inactive states of some ThsA variants are sensitive to the choice of purification method or tag. EfThsA and SeThsA cleave NAD^{+} in the presence of 500 μM v-cADPR (2′cADPR) or v2-cADPR (3′cADPR) (Fig. 4, B and C). A dose-response is observed with v2-cADPR (3′cADPR) treatment, and both proteins are activated by v2-cADPR (3′cADPR) concentrations as low as 5 μM (Fig. 4C). In comparison, v-cADPR (2′cADPR) only activates these proteins at the highest concentration tested (500 μM). ADPR and cADPR have no effect on the NADase activity of EfThsA and SeThsA (Fig. 4B).

Isothermal titration calorimetry (ITC) measurements showed that v2-cADPR (3′cADPR) binds directly to inactive (EfThsA) and autoactive (AbThsA) forms of ThsA at a ~1:1 molar ratio, with dissociation constant (K_d)

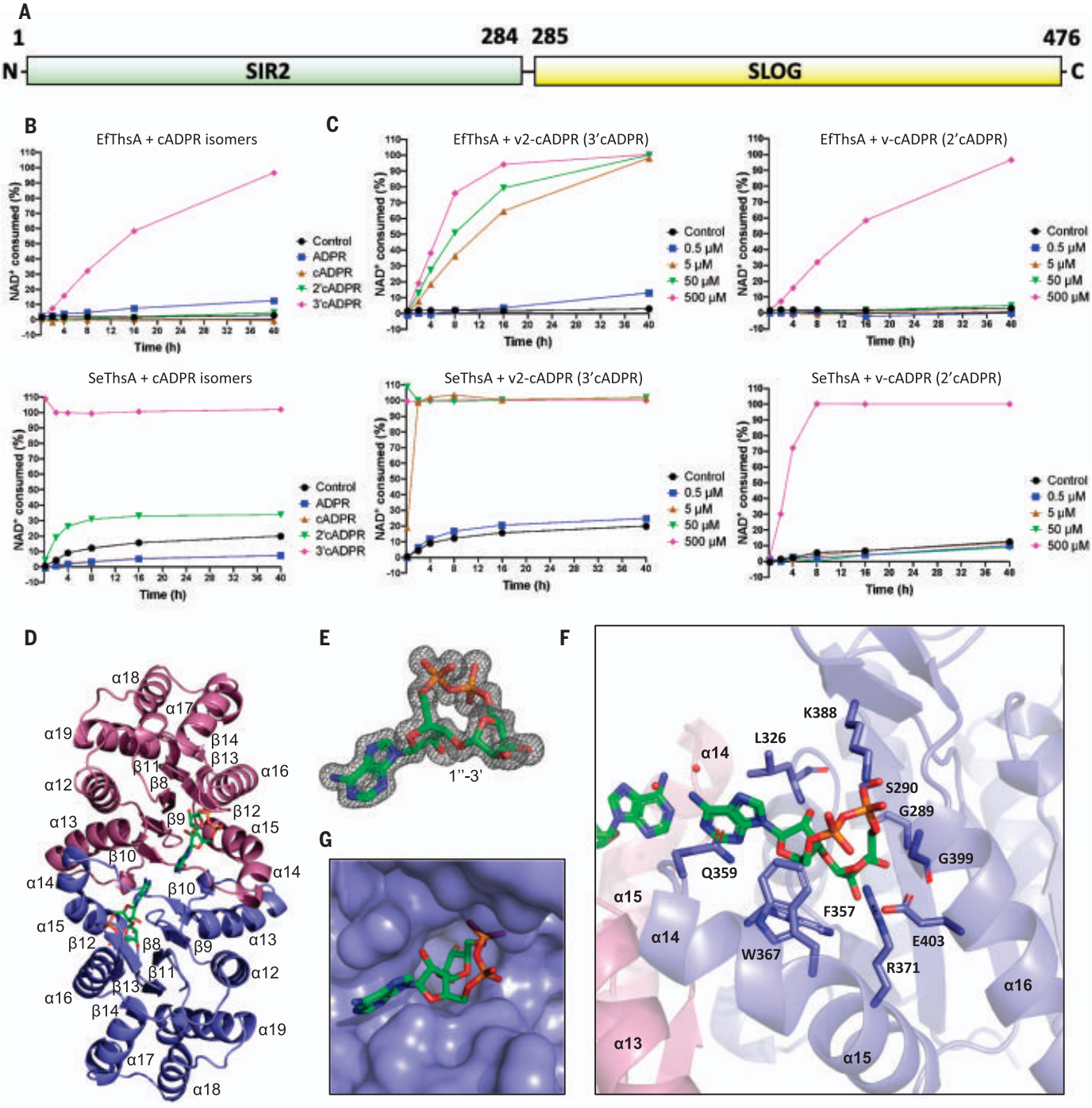


Fig. 4. Binding of v2-cADPR (3′cADPR) to ThsA^{SLOG}. (**A**) Schematic diagram of ThsA domain organization. Residue numbering corresponds to BcThsA (domain boundaries: BcThsA-SIR2, 1 to 283; SLOG, 284 to 476). AbThsA, EfThsA, and SeThsA have identical domain organizations. (**B**) Activation of EfThsA (0.5 μM) and SeThsA (10 μM) NADase activity by 500 μM ADPR, cADPR, v-cADPR (2′cADPR), and v2-cADPR (3′cADPR). The initial NAD^+ concentration was 500 μM. (**C**) Activation of EfThsA (0.5 μM) and SeThsA (10 μM) NADase activity by 0.5, 5, 50, and 500 μM v-cADPR (2′cADPR) and v2-cADPR (3′cADPR). The initial NAD^+ concentration was 500 μM. (**D**) Crystal structure of BcThsA^{SLOG} dimer (cartoon; chains colored in slate and magenta) in complex with v2-cADPR (3′cADPR) (green stick representation). (**E**) Standard omit mFo-DFc map of v2-cADPR (3′cADPR), contoured at 3.0 σ. (**F**) Enlarged cutaway of the v2-cADPR (3′cADPR) binding pocket in the BcThsA^{SLOG} structure. (**G**) Surface representation of the v2-cADPR (3′cADPR) binding pocket.

values of 59.1 ± 15.8 and 189 ± 1.6 nM, respectively (fig. S10, D and E). No binding was detected for v-cADPR (2′cADPR) using ITC (fig. S10, D and E), and the weaker binding affinity of v-cADPR (2′cADPR) was also corroborated by competition binding assays through saturation-transfer difference (STD) NMR, because v2-cADPR (3′cADPR) reduced v-cADPR (2′cADPR) binding to EfThsA, SeThsA, BcThsA, and AbThsA at an equal concentration (fig. S10F). Taken together, these findings support the model that ThsA is activated by TIR domain–produced cADPR isomers, with a preference for v2-cADPR (3′cADPR) over v-cADPR (2′cADPR).

3′cADPR (v2-cADPR) binds to the ThsA SLOG domain

To provide structural insights into cADPR isomer selectivity by ThsA, we determined the crystal structure of the SLOG domain of BcThsA ($BcThsA^{SLOG}$) in complex with v2-cADPR (3′cADPR) at 1.6-Å resolution (Fig. 4D and table S5). Continuous electron density for a cADPR isomer with a ribose(1″→3′)ribose O-glycosidic linkage was observed, confirming the structural configuration assigned by our NMR assays (Fig. 4E). $BcThsA^{SLOG}$ exists as a stable dimer in solution (fig. S11 and table S8) and forms a symmetric dimer (SLOG dimer) in the crystal, with an identical interface to the dimer observed in the ligand-free BcThsA structure (Fig. 4D and fig. S12A; PDB ID 6LHX) (*23*). Binding of v2-cADPR (3′cADPR) does not lead to substantial structural rearrangements in either the SLOG domain or the dimer interface (fig. S12A). 3′cADPR (v2-cADPR) binds to a highly conserved pocket adjacent to the symmetric dimer interface, and the adenine bases of the two v2-cADPR (3′cADPR) molecules in the dimer are only separated by 4.5 Å and are bridged by two water molecules (Fig. 4F, fig. S12B, and table S9). The C-2 and C-3 hydroxyls of the distal ribose interact with E403, whereas the diphosphate group is involved in hydrogen-bonding interactions with S290, R371, K388, and the backbone amide and carbonyl of G289 and G399, respectively (S, Ser; R, Arg; K, Lys; G, Gly). The adenine base stacks against the side chains of L326 and Q359, whereas the C-2 hydroxyl of the adenine-linked ribose forms a hydrogen bond with the backbone amide of L326 (Q, Gln). 2′cADPR (v-cADPR), which has a ribose(1″→2′)ribose O-glycosidic linkage, cannot form this latter hydrogen bond, and the adenosine moiety of this cADPR isomer is also likely to encounter steric hindrance with binding-pocket residues (Fig. 4G), explaining the preference for 3′cADPR. Mutational analysis confirmed the role of the structure-defined binding-pocket residues in ThsA activation (fig. S10G).

3′cADPR (v2-cADPR) changes ThsA tetramer organization

AbThsA, BcThsA, EfThsA, and SeThsA exist as tetramers in solution, and activation of SeThsA by v2-cADPR (3′cADPR) does not lead to a change in its oligomeric state (fig. S11 and table S8). However, the inactive $SeThsA^{SIR2}$ exists as a dimer in solution, whereas the fully active $BcThsA^{SIR2}$ exists as a monomer, suggesting that destabilization of SIR2:SIR2 domain interactions within the tetramer may be required for triggering the ThsA NADase activity (figs. S10C and S11 and table S8). To provide more detailed insight into how ThsA is activated by v2-cADPR (3′cADPR), we determined the ligand-free crystal structure of inactive SeThsA at 3.4-Å resolution (table S5) and compared it with the crystal structures of autoactive BcThsA (PDB ID 6LHX) (*23*) and our $BcThsA^{SLOG}$:v2-cADPR (3′cADPR) complex. Crystal-packing analyses reveal a D2 symmetric tetramer with a core consisting of two SIR2 dimers flanked by SLOG dimers at both sides (Fig. 5A). Both SIR2 dimer interfaces involve residues from the α3, α7, α9, and α10 helices. The crystal structure of autoactive BcThsA (PDB ID 6LHX) (*23*) has a tetramer with an identical architecture to SeThsA, but there are differences in the SIR2:SIR2 interfaces (Fig. 5, A and B). One of the molecules in the BcThsA SIR2 dimers has undergone a rotation of ~27° and translation of ~14 Å, compared with the SeThsA SIR2 dimers (Fig. 5C), resulting in a decrease of the interface area (2901.8 $Å^2$ in SeThsA; 1334.8 $Å^2$ in BcThsA). The α3 helix, which is involved in SIR2 dimerization but also covers a part of the predicted active site region in SeThsA (Fig. 5, B and D), adopts a different conformation ($SIR2^A$ and $SIR2^D$) or is disordered ($SIR2^B$ and $SIR2^C$) in BcThsA, enabling better access to catalytic residues (N113 and H153 in SeThsA, and N112 and H152 in BcThsA; N, Asn; H, His) (Fig. 5, B and D) (*23*). Comparison of the SLOG dimers in the inactive SeThsA structure with the dimer in the $BcThsA^{SLOG}$:v2-cADPR (3′cADPR) complex reveals that v2-cADPR (3′cADPR) binding is likely to induce changes in the orientation and position of the two SLOG domains (Fig. 5, E and F, and movie S2). In the SeThsA tetramer, this change will most likely cause the $SIR2^A$ and $SIR2^B$ domains and the $SIR2^C$ and $SIR2^D$ domains to move in opposite directions, bringing the α10 helices into closer proximity (Fig. 5G and movie S3), adopting a similar configuration to the SIR2 dimer interface observed in the crystal structure of autoactive BcThsA (Fig. 5B). We predict that this movement of the SIR2 domains is sufficient to destabilize the α3 helix conformation, enabling NAD^+ to access the active sites. SeThsA double mutants with reverse-charge substitutions of highly conserved residues in the SIR2 dimer interface (fig. S12C) are either autoactive (E170R, D251R; D, Asp) or not activated by v2-cADPR (3′cADPR) (R166E, R254E), confirming the role of the SIR2 dimer interface in regulating ThsA NADase activity (Fig. 5H). In summary, these findings reveal the structural basis of cADPR isomer selectivity by ThsA and demonstrate that v2-cADPR (3′cADPR) activates the NADase function of ThsA by changing its tetramer organization.

Immunity suppression by HopAM1 requires v2-cADPR (3′cADPR) production

3′cADPR (v2-cADPR) is also produced by the *P. syringae* DC3000 effector HopAM1 (*21*). To examine HopAM1's ability to suppress immunity, we generated transgenic *Arabidopsis* plants that express HopAM1 and the catalytically null mutant $HopAM1^{E191A}$. The transgenic plants were challenged with the immunity-inducing peptide flg22, and the production of reactive oxygen species (ROS), a hallmark of plant immunity, was quantified. Plants induced to express HopAM1 with estradiol, but not $HopAM1^{E191A}$ or the uninduced plants, showed suppressed ROS production (Fig. 6A). The immunity suppression of HopAM1 correlates with v2-cADPR (3′cADPR) production but not NAD^+ depletion (Fig. 6B).

Arabidopsis FRK1 (flg22-induced receptor-like kinase 1) is rapidly induced by multiple microbe-associated molecular patterns, and *FRK1* promoter luciferase reporter (*FRK1-LUC*) lines provide a dynamic readout of pathogen suppression of pattern-triggered immunity (*36*). Real-time imaging of DC3000 or DC3000Δ*hopAM1-1/1-2* challenged *FRK1-LUC* plants shows faster suppression of luciferase activity in DC3000 compared with the HopAM1 mutant (Fig. 6C). Fv/Fm, the maximum (dark-adapted) quantum efficiency of photosystem II, is a chlorophyll fluorescence parameter that allows nondestructive quantitative and spatial measurements of plant health. Fv/Fm has been shown to be strongly suppressed by virulent DC3000 (*36*), the extent of which is modulated by effective pattern-triggered immunity (*37*). Consistent with the reduced suppression of FRK1-LUC luciferase activity in *FRK1-LUC* plants, suppression of Fv/Fm was reduced after infection with the DC3000Δ*hopAM1-1/1-2* mutant (Fig. 6, D and E), and these immunity suppression phenotypes are directly linked to the production of v2-cADPR (3′cADPR; Fig. 6, F to I). These results indicate that v2-cADPR (3′cADPR) is responsible for HopAM1's suppression of plant immunity (a speculative model is shown in fig. S13).

Because HopAM1 acts in plant cells, we also tested its 2′,3′-cAMP and 2′,3′-cGMP synthetase activity, either as a recombinant protein with DNA as a substrate or in *Arabidopsis* challenged with DC3000 or DC3000Δ*hopAM1-1/1-2* (fig. S14). In neither case could we detect any production of 2′,3′-cAMP, cGMP, cyclic cytidine triphosphate (cCTP), or cyclic uridine triphosphate (cUTP).

Discussion

Bacterial and plant TIR domains produce cyclic signaling nucleotides with immune and virulence functions using NAD^+ or nucleic acids as substrates (*14*, *15*, *21*, *22*, *26*, *32*, *33*, *38*–*40*). Here, we report the chemical structures of two TIR domain–produced cADPR isomers, v-cADPR and v2-cADPR, which reveal that TIR domains can catalyze O-glycosidic bond formation between the ribose sugars in ADPR and that cyclization occurs at the 2′ (v-cADPR; 2′cADPR) and 3′ (v2-cADPR; 3′cADPR) positions of the adenosine ribose. These linkages differ from the canonical cADPR (produced by glycohydrolases such as CD38, *Aplysia californica* ADP-ribosyl cyclase, and the SARM1 TIR domain),

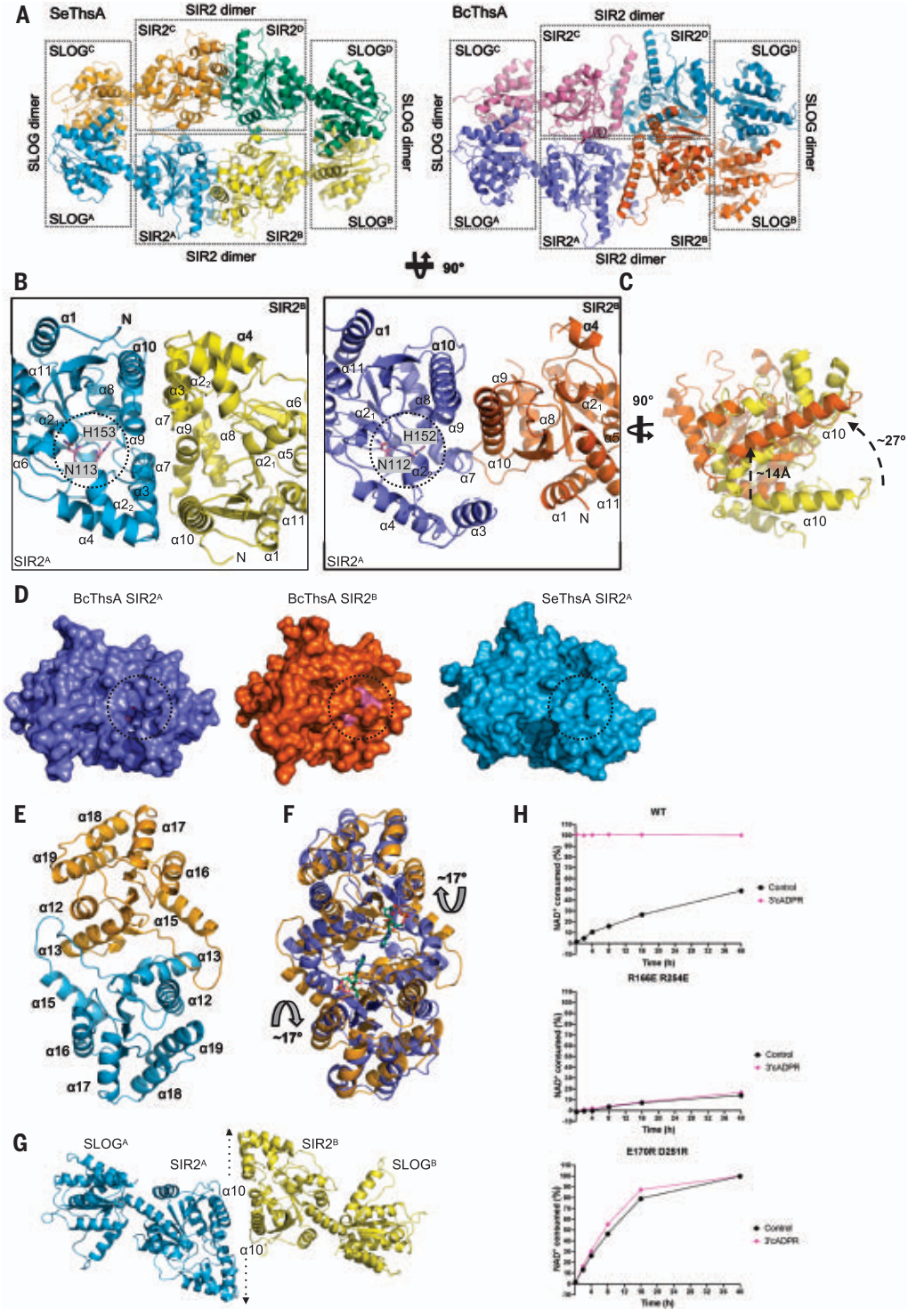


Fig. 5. 3′cADPR (v2-cADPR) changes ThsA tetramer organization. (**A**) Structure of SeThsA (left; chains colored in sky blue, yellow, orange, and green) and BcThsA (right; chains colored in slate, red, magenta, and blue) tetramers. SLOG and SIR2 dimers are highlighted by dashed black boxes. (**B**) Enlarged cutaways of SeThsA (left) and BcThsA (right) SIR2 dimers. Dashed circles represent active site regions with catalytically important residues (N113 and H153 in SeThsA; N112 and H152 in BcThsA) displayed in stick representation (magenta). SIR2 dimers were superimposed using $SIR2^A$ of SeThsA and BcThsA. (**C**) Comparison of $SIR2^B$ in superimposed SeThsA and BcThsA SIR2 dimers. Movement of BcThsA $SIR2^B$ (salmon) with respect to the SeThsA $SIR2^B$ (yellow) is indicated by the black dashed arrows. (**D**) Surface representation of ThsA SIR2 domains. The dashed circles indicate the catalytic residues (magenta). (**E**) SeThsA SLOG dimer. (**F**) Structural superposition of SeThsA (orange) and BcThsA (slate) SLOG dimers. Movements of BcThsA SLOG domains with respect to the SeThsA SLOG domains are indicated by gray arrows. (**G**) Predicted model of SeThsA after 3′cADPR binding. Dashed arrows indicate the direction of SeThsA SIR2 domain movements induced by v2-cADPR (3′cADPR) binding to the SLOG domains. (**H**) NADase activities of 50 μM SeThsA mutants ± 50 μM 3′cADPR. Initial NAD^+ concentration was 500 μM.

which is cyclized via the N1 position of the adenine ring (*16*, *18*, *41*) and do not involve the alternative N positions (N6 and N7) of the adenine ring (*15*, *21*). NAD^+-dependent O-glycosidic bond formation between ribose sugars is a new enzymatic activity of TIR domains, but it has been reported for the ADP-ribosyl transferase (ART) domain of poly(ADP-ribose) polymerases (PARPs), which catalyze 2′–1″ and 2″–1″ ribose-ribose bonds between ADPR molecules using NAD^+ as a substrate (*42*, *43*).

NADase activity of SARM1 and plant TIR domains requires self-association (*13*, *14*, *25*), and our biochemical studies with AbTir suggest that this is also the case for cADPR isomer–producing bacterial TIR domains. The CC domains of both AbTir and TcpB (*27*) self-associate in solution and may therefore have a similar role to SARM1 SAM domains, plant TNL NB-ARC domains, and bacterial SAVED (*44*) and STING (*45*) domains in facilitating TIR-domain clustering.

Crystal structures of cADPR isomer–producing bacterial TIR domains $AbTir^{TIR}$, $BtTir^{TIR}$, $TcpB^{TIR}$ (*27*, *29*, *30*), and BcThsB (*23*) do not display interfaces analogous to enzyme and scaffold TIR-domain assemblies (*3*). Our cryo-EM structure of

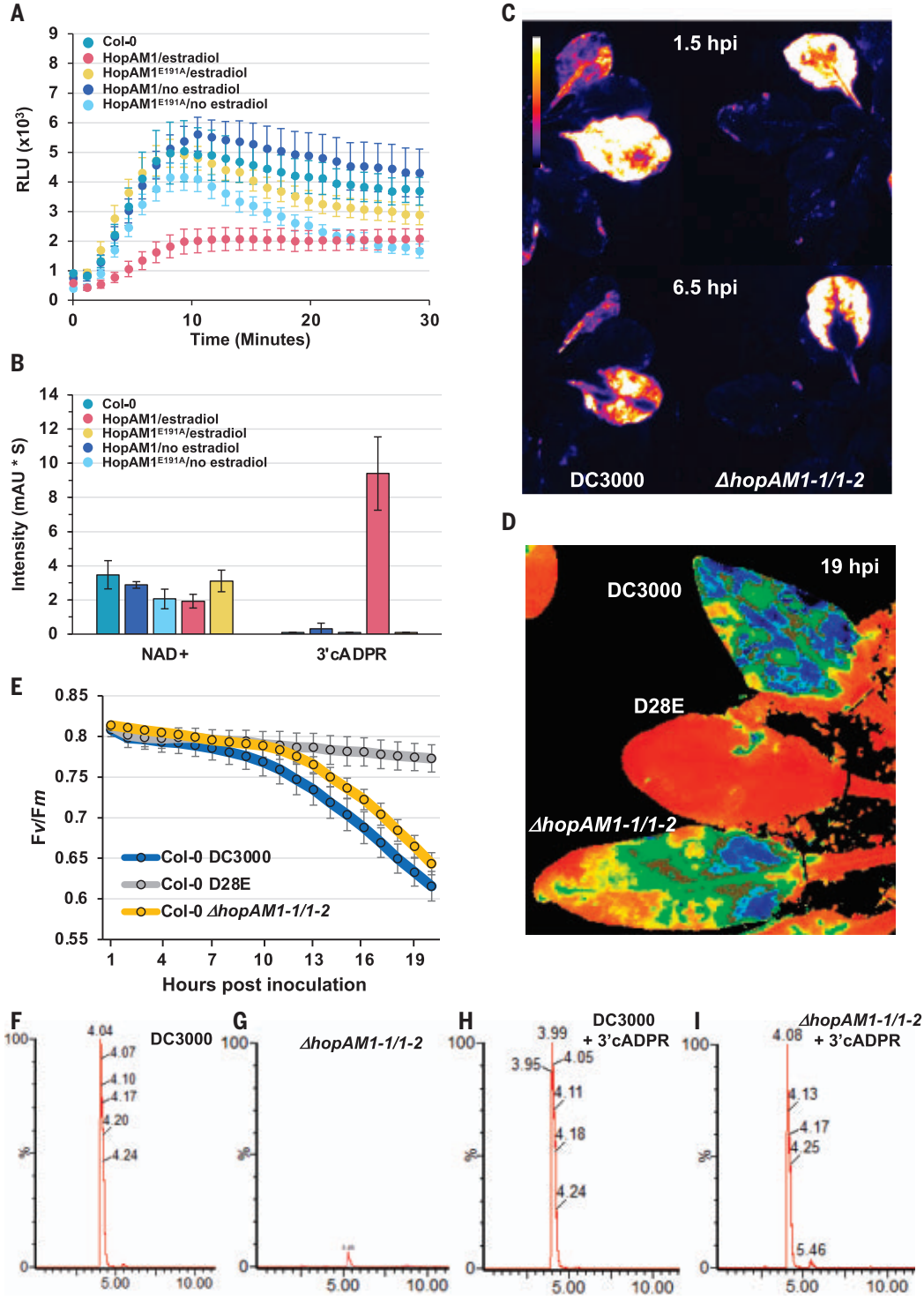


Fig. 6. 3′cADPR (v2-cADPR) production and immunity suppression by HopAM1. (**A**) ROS production of *Arabidopsis* transgenic plants expressing the *P. syringae* DC3000 effector HopAM1 or HopAM1^{E191A}, induced with 10 μM estradiol. ROS production was induced with 1 μM flg22. Data are presented as means ± SE (n = 12; Student's t test, $p < 0.01$). RLU, luminescence unit. (**B**) Quantification of NAD$^+$ and 3′cADPR from transgenic leaf samples in (A). Data are presented as means ± SE (n = 3). Transgenic plants expressing HopAM1 (estradiol-induced) produce significantly lower levels of ROS and significantly higher amounts of 3′cADPR, whereas the differences in NAD$^+$ levels are not significant (Student's t test; $p < 0.01$). mAU, milli–absorbance unit. (**C**) Suppression of pattern-triggered immunity measured by *FRK1-LUC* activity after challenge with DC3000 or the DC3000*ΔhopAM1-1/1-2* mutant. hpi, hours postinoculation. (**D**) Representative chlorophyll fluorescence images of Fv/Fm, a nondestructive measurement related to photosynthetic activity that relates to plant health, after challenge with DC3000, the *ΔhopAM1-1/1-2* mutant, or the effector-deficient mutant DC3000 D28E (reporting pattern triggered immunity). (**E**) The respective quantitative Fv/Fm measurements over the infection time course in (D). Error bars represent SE between three biological replicates of the same challenge, with the *ΔhopAM1-1/1-2* mutant being significantly different from DC3000 (Student's t test, $p < 0.05$ from 18 hpi). The graph is representative of four independent experiments. (**F** to **I**) LC-MS/MS analysis at 18 hpi of v2-cADPR (3′cADPR) production in *A. thaliana* Col-0 challenged with virulent DC3000 (F) or the *ΔhopAM1-1/1-2* mutant (G) and the respective spectra when co-injected with v2-cADPR (3′cADPR) standard from AaTir^{TIR} [(H) and (I)]. The retention time (x axis) is reported in minutes; the y axis reports the relative count per second (with 100% corresponding to the most intense peak). All leaves were challenged with an inoculum of OD_{600nm} (optical density at 600 nm) of 0.15.

the filamentous assembly of AbTir^{TIR}:3AD reveals a scaffold assembly arrangement analogous to MAL and MyD88 (*5*, *7*). Our mutagenesis data confirm that the observed arrangement is important for its catalytic function and that an intact BB loop is required. The active site is similar to the one in SARM1 (*25*), consistent with it being formed though the analogous BE interface–mediated association. Conformational changes in AbTir^{TIR} monomers are required to form the filamentous assembly. Future studies will define how additional domains in bacterial TIR proteins facilitate the active configuration and what size active complexes form in bacterial cells. The symmetric interface—found in crystal structures of all bacterial TIR domain-containing proteins with known structure, except for BcThsB (*23*, *27*–*30*), and shown to facilitate TcpB self-association and modulation of Toll-like receptor signaling (*27*, *46*)—may play a regulatory role in the transition to the active state.

A highly conserved tryptophan residue in the αC helical region, part of the previously

defined WXXXE motif (*47*) (where X is any residue), plays a role in the cyclization of ADPR by bacterial TIR domains. The equivalent tryptophan also plays a role in the catalytic activity by SARM1 and plant TIR domains. In SARM1, this tryptophan (W638) mediates aromatic stacking interactions with NAD^+ mimetics and the W638A mutation reduces NADase activity (*13*, *25*). In the flax L6 TNL protein, alanine mutation of the equivalent tryptophan (W131) abrogates cell-death signaling, and, in the cryo-EM structure of the related flax L7 TIR domain in complex with DNA, it is involved in interaction with the product 2′,3′-cAMP (*26*, *48*). In the *A. californica* ADP ribose cyclase, related to CD38 and similar to AbTir and AaTir in that it produces a cyclic ADPR (canonical cADPR) as the major product of NAD^+ hydrolysis, a phenylalanine residue (F174) directs the folding of the substrate during the cyclization reaction by interacting with the adenine base of ADPR after nicotinamide cleavage (*49*, *50*). Cyclization of 1″-2′ and 1″-3′ ribose O-glycosidic bonds in ADPR by TIR domains will require the two ribose sugars to come into proximity after nicotinamide cleavage and a possible role for the conserved tryptophan residue is to facilitate such substrate folding through interaction with the adenine base.

Although multiple plant TNL proteins and bacterial TIR proteins produce cADPR isomers, their mechanism of action and targets are only starting to be resolved. We speculate that the ThsB-produced cADPR isomer of the Thoeris defense system (*22*) corresponds to v2-cADPR (3′cADPR) because this isomer is a strong activator of ThsA NADase activity and has nanomolar affinity for ThsA proteins from different bacteria (Fig. 4). 2′cADPR (v-cADPR) can also trigger the NADase activity of ThsA [Fig. 4B and (*22*)], but a higher concentration is needed to activate ThsA because it shows weaker binding than v2-cADPR (3′cADPR). Consistent with our biochemical data, the $BcThsA^{SLOG}$:v2-cADPR (3′cADPR) complex structure reveals that the binding pocket is selective for v2-cADPR (3′ cADPR), which induces a reorganization of the ThsA tetramer to allosterically promote binding to its substrate NAD^+. This mode of action is reminiscent of the NMN-induced activation of SARM1, which is only able to bind and cleave the substrate NAD^+ after a change to its octamer organization triggered by NMN binding to its ARM domain (*25*). 2′cADPR (v-cADPR) produced by the protein BdTIR from the plant *Brachipodium distachyon* has been found to bind to the protein Thoeris anti-defense 1 (Tad1) that inhibits Thoeris immunity (*51*), but there is no data showing that this is the isomer produced by ThsB proteins. Future studies will determine the identity of ThsB-produced cADPR isomers, the structural basis for how they activate ThsA, and whether SLOG domains in cytokinin-activating proteins in plants (*52*, *53*) are also receptors for cADPR isomers.

The nucleotides pRib-AMP and pRib-ADP [2′-(5″-phosphoribosyl)-5′-adenosine monophosphate and 2′-(5″-phosphoribosyl)-5′-adenosine diphosphate] were shown to trigger immune signaling in plants by allosterically promoting the EDS1 (enhanced disease susceptibility 1)–PAD4 (phytoalexin deficient 4) complex to bind to the plant NLR protein ADR1-L1; the production requires TIR proteins (*32*). Plant TIR domains can also generate ADP-ribosylated ATP (ADPr-ATP) and di-ADPR, which in turn promote the association of EDS1 and SAG101 (senescence-associated gene 101) with the helper NLR NRG1A (N requirement gene 1A) (*33*). Multiple TIR domains produce cADPR isomers in plants, but the EDS1-binding molecules have not yet been detected in planta and their biosynthetic pathways are not defined. The authors of (*32*, *33*) proposed a pathway for the production of pRib-AMP and pRib-ADP as well as ADPr-ATP and di-ADPR that does not involve cADPR isomers. Our cADPR isomer structures show that pRib-AMP can be derived directly from v-cADPR (2′cADPR) by cleavage of its pyrophosphate bond, suggesting that NAD^+ could be the substrate in this case. The cleavage of the pyrophosphate bond could indicate the involvement of plant NUDIX hydrolases like NUDX6 and 7, which regulate plant immunity by degrading 2′,3′-cAMP and 2′,3′-cGMP, the other nucleotides putatively produced by TIR domains (*26*).

3′-*O*-β-D-ribofuranosyladenosine, which has an identical 1″-3′ O-glycosidic linkage to v2-cADPR (3′cADPR) but lacks the phosphate groups, has been shown to accumulate in leaves infected with the HopAM1-producing bacterium *P. syringae* DC3000 (*54*), suggesting that cADPR isomers can be further modified in plants. Pyrophosphate bond cleavage of HopAM1-produced v2-cADPR (3′cADPR), followed by removal of the two ribose-5-phosphate groups, is a possible synthetic path for this nucleotide product, which suggests that cADPR isomers perhaps not only serve as signaling molecules but are also important intermediates in the synthesis of additional previously uncharacterized nucleosides associated with plant immunity. In conclusion, our study unravels the cyclization site of cADPR isomers and informs on their production by TIR domains and their signaling in immunity pathways in bacteria and plants.

Methods summary

A comprehensive description of materials and methods is presented in the supplementary materials. These descriptions include the details of cloning of expression plasmids and side-directed mutagenesis, protein expression and purification, different assays of NAD^+ cleavage and characterization of its products (fluorescence, NMR, HPLC, and mass spectrometry-based approaches), and bioinformatic analysis. For the determination of chemical structures of cADPR isomers, the compounds were produced by AbTir, AaTir, and HopAM1 and the structures were determined using NMR (assignments are provided in tables S2 to S4) and liquid chromatography–tandem mass spectrometry (LC-MS/MS). Protein:ligand and protein:protein interactions were characterized by STD NMR, ITC, and SEC-MALS. Three-dimensional structures were determined using x-ray crystallography (crystallographic parameters are provided in table S5) and cryo-EM (structure determination details are provided in fig. S5 and table S6). Also described are phytobacterial challenge and ROS assays in HopAM1-expressing *Arabidopsis* plants.

REFERENCES AND NOTES

1. T. Ve, S. J. Williams, B. Kobe, Structure and function of Toll/interleukin-1 receptor/resistance protein (TIR) domains. *Apoptosis* **20**, 250–261 (2015). doi: 10.1007/s10495-014-1064-2; pmid: 25451009
2. S. Nimma, T. Ve, S. J. Williams, B. Kobe, Towards the structure of the TIR-domain signalosome. *Curr. Opin. Struct. Biol.* **43**, 122–130 (2017). doi: 10.1016/j.sbi.2016.12.014; pmid: 28092811
3. S. Nimma *et al*., Structural evolution of TIR-domain signalosomes. *Front. Immunol.* **12**, 784484 (2021). doi: 10.3389/fimmu.2021.784484; pmid: 34868065
4. N. Maruta *et al*., Structural basis of NLR activation and innate immune signalling in plants. *Immunogenetics* **74**, 5–26 (2022). doi: 10.1007/s00251-021-01242-5; pmid: 34981187
5. M. T. B. Clabbers *et al*., MyD88 TIR domain higher-order assembly interactions revealed by microcrystal electron diffraction and serial femtosecond crystallography. *Nat. Commun.* **12**, 2578 (2021). doi: 10.1038/s41467-021-22590-6; pmid: 33972532
6. P. R. Vajjhala, T. Ve, A. Bentham, K. J. Stacey, B. Kobe, The molecular mechanisms of signaling by cooperative assembly formation in innate immunity pathways. *Mol. Immunol.* **86**, 23–37 (2017). doi: 10.1016/j.molimm.2017.02.012; pmid: 28249680
7. T. Ve *et al*., Structural basis of TIR-domain-assembly formation in MAL- and MyD88-dependent TLR4 signaling. *Nat. Struct. Mol. Biol.* **24**, 743–751 (2017). doi: 10.1038/nsmb.3444; pmid: 28759049
8. R. R. Rana, M. Zhang, A. M. Spear, H. S. Atkins, B. Byrne, Bacterial TIR-containing proteins and host innate immune system evasion. *Med. Microbiol. Immunol. (Berl.)* **202**, 1–10 (2013). doi: 10.1007/s00430-012-0253-2; pmid: 22772799
9. S. Doron *et al*., Systematic discovery of antiphage defense systems in the microbial pangenome. *Science* **359**, eaar4120 (2018). doi: 10.1126/science.aar4120; pmid: 29371424
10. B. R. Morehouse *et al*., STING cyclic dinucleotide sensing originated in bacteria. *Nature* **586**, 429–433 (2020). doi: 10.1038/s41586-020-2719-5; pmid: 32877915
11. N. Tal *et al*., Cyclic CMP and cyclic UMP mediate bacterial immunity against phages. *Cell* **184**, 5728–5739.e16 (2021). doi: 10.1016/j.cell.2021.09.031; pmid: 34644530
12. B. Koopal *et al*., Short prokaryotic Argonaute systems trigger cell death upon detection of invading DNA. *Cell* **185**, 1471–1486.e19 (2022). doi: 10.1016/j.cell.2022.03.012; pmid: 35381200
13. S. Horsefield *et al*., NAD^+ cleavage activity by animal and plant TIR domains in cell death pathways. *Science* **365**, 793–799 (2019). doi: 10.1126/science.aax1911; pmid: 31439792
14. L. Wan *et al*., TIR domains of plant immune receptors are NAD^+-cleaving enzymes that promote cell death. *Science* **365**, 799–803 (2019). doi: 10.1126/science.aax1771; pmid: 31439793
15. K. Essuman *et al*., TIR domain proteins are an ancient family of NAD^+-consuming enzymes. *Curr. Biol.* **28**, 421–430.e4 (2018). doi: 10.1016/j.cub.2017.12.024; pmid: 29395922
16. K. Essuman *et al*., The SARM1 Toll/interleukin-1 receptor domain possesses intrinsic NAD^+ cleavage activity that promotes pathological axonal degeneration. *Neuron* **93**,

1334–1343.e5 (2017). doi: 10.1016/j.neuron.2017.02.022; pmid: 28334607
17. M. D. Figley *et al*., SARM1 is a metabolic sensor activated by an increased NMN/NAD^+ ratio to trigger axon degeneration. *Neuron* **109**, 1118–1136.e11 (2021). doi: 10.1016/j.neuron.2021.02.009; pmid: 33657413
18. H. C. Lee, R. Aarhus, D. Levitt, The crystal structure of cyclic ADP-ribose. *Nat. Struct. Biol.* **1**, 143–144 (1994). doi: 10.1038/nsb0394-143; pmid: 7656029
19. Z. Duxbury *et al*., Induced proximity of a TIR signaling domain on a plant-mammalian NLR chimera activates defense in plants. *Proc. Natl. Acad. Sci. U.S.A.* **117**, 18832–18839 (2020). doi: 10.1073/pnas.2001185117; pmid: 32709746
20. J. M. Coronas-Serna *et al*., The TIR-domain containing effectors BtpA and BtpB from *Brucella abortus* impact NAD metabolism. *PLOS Pathog.* **16**, e1007979 (2020). doi: 10.1371/journal.ppat.1007979; pmid: 32298382
21. S. Eastman *et al*., A phytobacterial TIR domain effector manipulates NAD^+ to promote virulence. *New Phytol.* **233**, 890–904 (2022). doi: 10.1111/nph.17805; pmid: 34657283
22. G. Ofir *et al*., Antiviral activity of bacterial TIR domains via immune signalling molecules. *Nature* **600**, 116–120 (2021). doi: 10.1038/s41586-021-04098-7; pmid: 34853457
23. D. Ka, H. Oh, E. Park, J. H. Kim, E. Bae, Structural and functional evidence of bacterial antiphage protection by Thoeris defense system via NAD^+ degradation. *Nat. Commun.* **11**, 2816 (2020). doi: 10.1038/s41467-020-16703-w; pmid: 32499527
24. A. M. Burroughs, L. Aravind, Identification of uncharacterized components of prokaryotic immune systems and their diverse eukaryotic reformulations. *J. Bacteriol.* **202**, e00365–e00320 (2020). doi: 10.1128/JB.00365-20; pmid: 32868406
25. Y. Shi *et al*., Structural basis of SARM1 activation, substrate recognition, and inhibition by small molecules. *Mol. Cell* **82**, 1643–1659.e10 (2022). doi: 10.1016/j.molcel.2022.03.007; pmid: 35334231
26. D. Yu *et al*., TIR domains of plant immune receptors are 2′,3′-cAMP/cGMP synthetases mediating cell death. *Cell* **185**, 2370–2386.e18 (2022). doi: 10.1016/j.cell.2022.04.032; pmid: 35597242
27. M. Alaidarous *et al*., Mechanism of bacterial interference with TLR4 signaling by *Brucella* Toll/interleukin-1 receptor domain-containing protein TcpB. *J. Biol. Chem.* **289**, 654–668 (2014). doi: 10.1074/jbc.M113.523274; pmid: 24265315
28. S. L. Chan *et al*., Molecular mimicry in innate immunity: Crystal structure of a bacterial TIR domain. *J. Biol. Chem.* **284**, 21386–21392 (2009). doi: 10.1074/jbc.C109.007591; pmid: 19535337
29. B. Kaplan-Türköz *et al*., Structure of the Toll/interleukin 1 receptor (TIR) domain of the immunosuppressive *Brucella* effector BtpA/Btp1/TcpB. *FEBS Lett.* **587**, 3412–3416 (2013). doi: 10.1016/j.febslet.2013.09.007; pmid: 24076024
30. G. A. Snyder *et al*., Crystal structures of the Toll/Interleukin-1 receptor (TIR) domains from the *Brucella* protein TcpB and host adaptor TIRAP reveal mechanisms of molecular mimicry. *J. Biol. Chem.* **289**, 669–679 (2014). doi: 10.1074/jbc.M113.523407; pmid: 24275656
31. J. S. Weagley *et al*., Products of gut microbial Toll/interleukin-1 receptor domain NADase activities in gnotobiotic mice and Bangladeshi children with malnutrition. *Cell Rep.* **39**, 110738 (2022). doi: 10.1016/j.celrep.2022.110738; pmid: 35476981
32. A. Jia *et al*., TIR-catalyzed ADP-ribosylation reactions produce signaling molecules for plant immunity. *Science* **377**, eabq8180 (2022). doi: 10.1126/science.abq8180; pmid: 35857644
33. S. Huang *et al*., Identification and receptor mechanism of TIR-catalyzed small molecules in plant immunity. *Science* **377**, eabq3297 (2022). doi: 10.1126/science.abq3297; pmid: 35857645
34. S. Ma *et al*., Direct pathogen-induced assembly of an NLR immune receptor complex to form a holoenzyme. *Science* **370**, eabe3069 (2020). doi: 10.1126/science.abe3069; pmid: 33273071
35. R. Martin *et al*., Structure of the activated ROQ1 resistosome directly recognizing the pathogen effector XopQ. *Science* **370**, eabd9993 (2020). doi: 10.1126/science.abd9993; pmid: 33273074
36. M. de Torres Zabala *et al*., Chloroplasts play a central role in plant defence and are targeted by pathogen effectors. *Nat. Plants* **1**, 15074 (2015). doi: 10.1038/nplants.2015.74; pmid: 27250009
37. S. Breen *et al*., Chloroplasts play a central role in facilitating MAMP-triggered immunity, pathogen suppression of immunity and crosstalk with abiotic stress. *Plant Cell Environ.*pce.14408 (2022). doi: 10.1111/pce.14408; pmid: 35892221
38. M. T. Hulin, W. Ma, Pangenomics facilitated with structural analysis reveals host NAD^+ manipulation as a major virulence activity of bacterial effectors. bioRxiv 2022.2006.2007.495176 [Preprint] (2022); doi: 10.1101/2022.06.07.495176
39. S. Eastman, A. Bayless, M. Guo, The nucleotide revolution: Immunity at the intersection of TIR-domains, nucleotides, and Ca^2. *Mol. Plant Microbe Interact.*MPMI-06-22-0132-CR (2022). doi: 10.1094/MPMI-06-22-0132-CR; pmid: 35881867
40. K. Essuman, J. Milbrandt, J. L. Dangl, M. T. Nishimura, Shared TIR enzymatic functions regulate cell death and immunity across the tree of life. *Science* **377**, eabo0001 (2022). doi: 10.1126/science.abo0001; pmid: 35857622
41. M. Howard *et al*., Formation and hydrolysis of cyclic ADP-ribose catalyzed by lymphocyte antigen CD38. *Science* **262**, 1056–1059 (1993). doi: 10.1126/science.8235624; pmid: 8235624
42. L. Aravind, D. Zhang, R. F. de Souza, S. Anand, L. M. Iyer, The natural history of ADP-ribosyltransferases and the ADP-ribosylation system. *Curr. Top. Microbiol. Immunol.* **384**, 3–32 (2015). doi: 10.1007/82_2014_414; pmid: 25027823
43. K. Ueda, O. Hayaishi, ADP-ribosylation. *Annu. Rev. Biochem.* **54**, 73–100 (1985). doi: 10.1146/annurev.bi.54.070185.000445; pmid: 3927821
44. G. Hogrel *et al*., Cyclic nucleotide-induced helical structure activates a TIR immune effector. *Nature* **608**, 808–812 (2022). doi: 10.1146/annurev.bi.54.070185.000445; pmid: 3927821
45. B. R. Morehouse *et al*., Cryo-EM structure of an active bacterial TIR-STING filament complex. *Nature* **608**, 803–807 (2022). doi: 10.1038/s41586-022-04999-1; pmid: 35859168
46. A. Chaudhary *et al*., The *Brucella* TIR-like protein TcpB interacts with the death domain of MyD88. *Biochem. Biophys. Res. Commun.* **417**, 299–304 (2012). doi: 10.1016/j.bbrc.2011.11.104; pmid: 22155231
47. C. Felix *et al*., The *Brucella* TIR domain containing proteins BtpA and BtpB have a structural WxxxE motif important for protection against microtubule depolymerisation. *Cell Commun. Signal.* **12**, 53 (2014). doi: 10.1186/s12964-014-0053-y; pmid: 25304327
48. M. Bernoux *et al*., Structural and functional analysis of a plant resistance protein TIR domain reveals interfaces for self-association, signaling, and autoregulation. *Cell Host Microbe* **9**, 200–211 (2011). doi: 10.1016/j.chom.2011.02.009; pmid: 21402359
49. Q. Liu *et al*., Structural basis for enzymatic evolution from a dedicated ADP-ribosyl cyclase to a multifunctional NAD hydrolase. *J. Biol. Chem.* **284**, 27637–27645 (2009). doi: 10.1074/jbc.M109.031005; pmid: 19640846
50. R. Graeff *et al*., Mechanism of cyclizing NAD to cyclic ADP-ribose by ADP-ribosyl cyclase and CD38. *J. Biol. Chem.* **284**, 27629–27636 (2009). doi: 10.1074/jbc.M109.030965; pmid: 19640843
51. A. Leavitt *et al*., Viruses inhibit TIR gcADPR signaling to overcome bacterial defense. bioRxiv 2022.2005.2003.490397 [Preprint] (2022); https://doi.org/10.1101/2022.05.03.490397.
52. A. M. Burroughs, D. Zhang, D. E. Schäffer, L. M. Iyer, L. Aravind, Comparative genomic analyses reveal a vast, novel network of nucleotide-centric systems in biological conflicts, immunity and signaling. *Nucleic Acids Res.* **43**, 10633–10654 (2015). doi: 10.1093/nar/gkv1267; pmid: 26590262
53. T. Kuroha *et al*., Functional analyses of *LONELY GUY* cytokinin-activating enzymes reveal the importance of the direct activation pathway in *Arabidopsis*. *Plant Cell* **21**, 3152–3169 (2009). doi: 10.1105/tpc.109.068676; pmid: 19837870
54. M. S. Drenichev *et al*., A role for 3′-O-β-D-ribofuranosyladenosine in altering plant immunity. *Phytochemistry* **157**, 128–134 (2019). doi: 10.1016/j.phytochem.2018.10.016; pmid: 30399495

ACKNOWLEDGMENTS

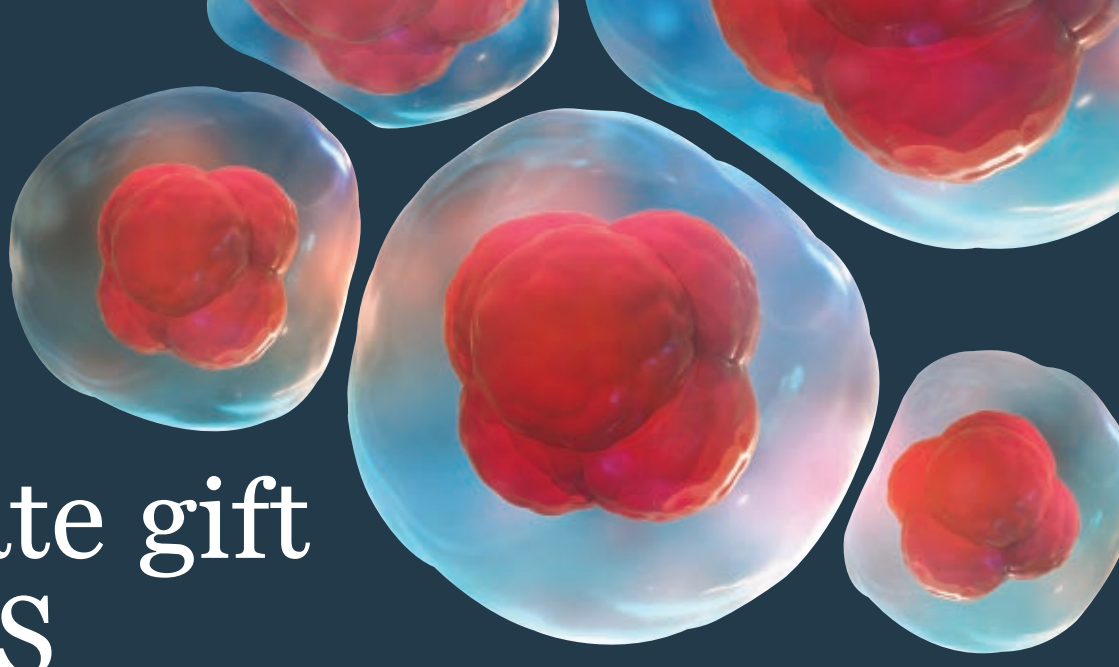
We acknowledge use of the Australian Synchrotron MX facility and thank the staff for their support. We acknowledge the Centre for Microscopy and Microanalysis, University of Queensland (UQ), and staff (L. Brillault, M. Floetenmeyer, R. Webb, and R. Wepf). We thank F. Makino (JEOL) for help with cryo-EM data collection; K. Arachchige and J. Clegg (UQ) for help with crystallization; F. Rose (Griffith University) for help with HPLC purification of 2′cADPR and 3′cADPR; and M. Mobli (UQ) for advice on NMR. **Funding:** The work was supported by the National Health and Medical Research Council (NHMRC) (grants 1196590 to T.V., 1107804 and 1160570 to B.K. and T.V., 1071659 to B.K., and 1108859 to T.V.); an Australian Research Council (ARC) Future Fellowship (FT200100572 to T.V.); an ARC Laureate Fellowship (FL180100109 to B.K.); an ARC Discovery Early Career Researcher Award (DE170100783 to T.V.); the National Institutes of Health (R01NS087632 to J.M. and A.D.); and the Biotechnology and Biological Sciences Research Council (BB/V00400X/1 to M.Gr. and L.S.). Y.S. was a recipient of a Griffith University Postdoctoral Fellowship Scheme. Nebraska Soybean Board project no. 1734 funded the research assistantship for S.E. **Author contributions:** Conceptualization: M.K.M., Y.S., M.A.Z., M.Gr., M.Gu., J.M., A.D., T.V., B.K.; Investigation: M.K.M., Y.S., S.L., M.A.Z., N.D., S.E., T.G.S., W.G., V.M., T.M., J.S.W., S.J.H., E.V., L.H.-T., N.M., B.Y.J.L., H.B., M.J.L., I.P., N.K., L.S., M.Gr., J.D.N., M.Gu., T.V.; Writing – original draft: M.K.M., Y.S., S.L., T.V., B.K.; Writing – review and editing: All authors; Funding acquisition: T.V., B.K., M.Gu., M.Gr., L.S., J.M., A.D.; Resources: T.V., B.K., J.M., A.D.; Supervision: T.V., B.K., J.D.N., J.M., A.D., M.A.S., M.Gr., M.Gu. **Competing interests:** The authors have no competing interests. **Data and materials availability:** Coordinates and structure factors for the $AbTir^{TIR}$, $BtTir^{TIR}$, $BcThsA^{SLOG}$:v2-cADPR (3′cADPR), and SeThsA crystal structures have been deposited in the Protein Data Bank with IDs 7UWG, 7UXR, 7UXS, and 7UXT, respectively. Maps and coordinates for the $AbTir^{TIR}$:3AD cryo-EM structure have been deposited to the Electron Microscopy Data Bank (EMD-26862) and Protein Data Bank (7UXU), respectively. All other data are in the main paper or supplementary materials. Some specific reagents such as 2′cADPR and 3′cADPR may be available from the corresponding authors with a completed materials transfer agreement; restrictions may apply because of limited availability and prioritization for internal use. **License information:** Copyright © 2022 the authors, some rights reserved; exclusive licensee American Association for the Advancement of Science. No claim to original US government works. https://www.science.org/about/science-licenses-journal-article-reuse

SUPPLEMENTARY MATERIALS

science.org/doi/10.1126/science.adc8969
Materials and Methods
Figs. S1 to S14
Tables S1 to S9
References (*55*–*85*)
MDAR Reproducibility Checklist
Movies S1 to S3
Data S1 to S4

Submitted 8 May 2022; accepted 23 August 2022
Published online 1 September 2022
10.1126/science.adc8969

1848 SOCIETY
AAAS



An estate gift to AAAS

Going all the way back to 1848, our founding year, the American Association for the Advancement of Science (AAAS) has been deeply committed to advancing science, engineering and innovation around the world for the benefit of all people.

Today, we are dedicated to advocating for science and scientific evidence to be fully and positively integrated into public policy and for the community to speak with one voice to advance science and engineering in the United States and around the world.

By making AAAS a beneficiary of your will, trust, retirement plan or life insurance policy, you will become a member of our 1848 Society and will help fuel our work on behalf of science and society – including publishing the world's most promising, innovative research in the *Science* family of journals and engaging in the issues that matter locally, nationally and around the world.

"As a teacher and instructor, I bear responsibility for the younger generations. If you have extra resources, concentrate them on organizations, like AAAS, that are doing work for all."

—Prof. Elisabeth Ervin-Blankenheim, 1848 Society member

If you intend to include AAAS in your estate plans, provide this information to your lawyer or financial adviser:

Legal Name: American Association for the Advancement of Science
Federal Tax ID Number: 53-0196568
Address: 1200 New York Avenue, NW, Washington, DC 20005

If you would like more information on making an estate gift to AAAS, cut out and return the form below or send an email to philanthropy@aaas.org. Additional details are also available online at **www.aaas.org/1848Society**.

AMERICAN ASSOCIATION FOR THE ADVANCEMENT OF SCIENCE

cut here

Yes, I would like more information about joining the AAAS 1848 Society.

1848 SOCIETY
AAAS

PLEASE CONTACT ME AT:

Name: _____

Address: _____

City: _____ State: _____ Zip code: _____ Country: _____

Email: _____ Phone: _____

RETURN THIS FORM TO:
AAAS Office of Philanthropy and Strategic Partnerships • 1200 New York Avenue, NW • Washington, DC 20005 USA

RESEARCH ARTICLE SUMMARY

NEUROEVOLUTION

Molecular and cellular evolution of the primate dorsolateral prefrontal cortex

Shaojie Ma†, Mario Skarica†, Qian Li, Chuan Xu, Ryan D. Risgaard, Andrew T. N. Tebbenkamp, Xoel Mato-Blanco, Rothem Kovner, Željka Krsnik, Xabier de Martin, Victor Luria, Xavier Martí-Pérez, Dan Liang, Amir Karger, Danielle K. Schmidt, Zachary Gomez-Sanchez, Cai Qi, Kevin T. Gobeske, Sirisha Pochareddy, Ashwin Debnath, Cade J. Hottman, Joshua Spurrier, Leon Teo, Anthony G. Boghdadi, Jihane Homman-Ludiye, John J. Ely, Etienne W. Daadi, Da Mi, Marcel Daadi, Oscar Marín, Patrick R. Hof, Mladen-Roko Rasin, James Bourne, Chet C. Sherwood, Gabriel Santpere, Matthew J. Girgenti, Stephen M. Strittmatter*, André M. M. Sousa*, Nenad Sestan*

INTRODUCTION: The dorsolateral prefrontal cortex (dlPFC) lies at the center of high-order cognition and complex social behaviors, which are highly derived traits in anthropoid primates—particularly in humans.

RATIONALE: The granular dlPFC represents an evolutionary specialization found only in anthropoid primates, and alterations in the molecular and cellular mechanisms underlying its intricate circuitry have been implicated in myriad neuropsychiatric diseases. However, little is known about the full repertoire of cell types in the primate dlPFC and how conserved these cell types are between human and other primate species.

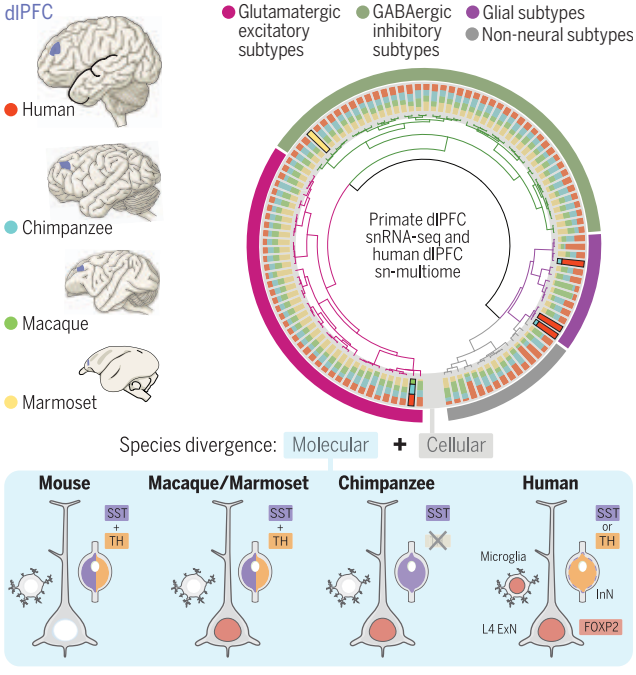
RESULTS: We generated single-nucleus transcriptome data profiling more than 600,000 nuclei from the dlPFC of adult humans, chimpanzees, rhesus macaques, and common marmosets, thus spanning major primate phylogenetic groups. To study regulatory mechanisms underlying human-specific divergence, we generated single-nucleus multiome data (snATAC-seq and snRNA-seq) profiling the human dlPFC. Through cell clustering, marker gene expression, and integration with published multimodal and multispecies data we defined three levels of hierarchically organized taxonomy of transcriptomically defined neuronal, glial, and non-neural cell types in the four species, including four major cell classes, 29 subclasses and 114 subtypes.

Most cell subtypes were conserved across the four species but we unraveled prominent species differences both at the molecular and cellular levels. We identified five cell subtypes detected in only a subset of species, including a layer (L) 2-3 intratelencephalic subtype absent in marmosets, an inhibitory neuron subtype exclusive to marmosets, and a microglial subtype detected only in humans. Cross-species comparisons of cell type proportions showed that L2-3 intratelencephalic neurons underwent substantial expansion in humans compared with other species as well as in Catarrhini as compared with marmosets. Gene expression entropy analysis revealed more transcriptomic heterogeneity among L2-3 intratelencephalic neurons in Catarrhini compared to marmosets. These results confirm and extend theories of primate cortical expansion.

Within homologous cell subtypes across species, we identified prominent molecular changes. These are characterized by loss of expression of tyrosine hydroxylase (TH), the rate-limiting enzyme in catecholamine (including dopamine) biosynthesis, in the inhibitory neurons of chimpanzees that are homologous to TH-expressing inhibitory neurons in the other species studied. Among TH-expressing homologous cell subtypes in humans, macaques, and marmosets, we identified a human-specific posttranscriptional switch between the neuropeptide SST and TH, and the human-specific expression of genes involved in dopaminergic function.

Through transcriptomic comparisons across the four primate species and immunohistochemistry across 51 mammal species, we found that the neuropsychiatric risk gene *FOXP2* exhibited human-specific expression in microglia and primate-specific expression in L4 excitatory neurons. By integrating chromatin accessibility and gene coexpression, we identified cis-regulatory elements regulating *FOXP2* expression and constructed *FOXP2* regulatory networks including downstream targets mirroring the cell type- and species-specific *FOXP2* expression patterns.

CONCLUSION: We produced a transcriptomic catalog of the primate dlPFC cell types, complemented with epigenomic characterization in the human dlPFC. Our analyses delineated cell type homology and transcriptomic conservation across species and identified species divergence at the molecular and cellular levels, as well as potential epigenomic mechanisms underlying these differences. Shared and species-divergent features were implicated in biological pathways and neuropsychiatric diseases. Our data may serve as a resource for future studies on prefrontal cortex function and disease. ■



Transcriptomic taxonomy of the dlPFC in four anthropoid primates. (Top left) Homologous regions of the dlPFC dissected for snRNA-seq and sn-multiome analyses. (Top right) 114 hierarchically organized (dendrogram) transcriptomically defined cell subtypes distributed across the four species (bar plots; same color code as in the top left panel), with species-specific variations highlighted. (Bottom) Notable molecular changes across species featured by species-specific FOXP2 expression and the human-specific posttranscriptional switching between SST and TH.

The list of author affiliations is available in the full article online.
***Corresponding author. Email: stephen.strittmatter@yale.edu (S.M.S.); andre.sousa@wisc.edu (A.M.M.S.); nenad.sestan@yale.edu (N.S.)**
†These authors contributed equally to this work.
Cite this article as S. Ma *et al.*, *Science* 377, eabo7257 (2022). DOI: 10.1126/science.abo7257

READ THE FULL ARTICLE AT
https://doi.org/10.1126/science.abo7257

RESEARCH ARTICLE

NEUROEVOLUTION

Molecular and cellular evolution of the primate dorsolateral prefrontal cortex

Shaojie Ma[1]†, Mario Skarica[1]†, Qian Li[1], Chuan Xu[1], Ryan D. Risgaard[2,3], Andrew T. N. Tebbenkamp[1], Xoel Mato-Blanco[4], Rothem Kovner[1], Željka Krsnik[1,5], Xabier de Martin[4], Victor Luria[1], Xavier Martí-Pérez[4], Dan Liang[1], Amir Karger[6], Danielle K. Schmidt[2], Zachary Gomez-Sanchez[2], Cai Qi[1], Kevin T. Gobeske[7], Sirisha Pochareddy[1], Ashwin Debnath[2], Cade J. Hottman[2], Joshua Spurrier[8], Leon Teo[9], Anthony G. Boghdadi[9], Jihane Homman-Ludiye[9], John J. Ely[10,11], Etienne W. Daadi[12], Da Mi[13], Marcel Daadi[12,14,15], Oscar Marín[16,17], Patrick R. Hof[18], Mladen-Roko Rasin[19], James Bourne[9], Chet C. Sherwood[11], Gabriel Santpere[1,4], Matthew J. Girgenti[20,21], Stephen M. Strittmatter[1,8,22]*, André M. M. Sousa[2,23]*, Nenad Sestan[1,20,22,24]*

The granular dorsolateral prefrontal cortex (dlPFC) is an evolutionary specialization of primates that is centrally involved in cognition. We assessed more than 600,000 single-nucleus transcriptomes from adult human, chimpanzee, macaque, and marmoset dlPFC. Although most cell subtypes defined transcriptomically are conserved, we detected several that exist only in a subset of species as well as substantial species-specific molecular differences across homologous neuronal, glial, and non-neural subtypes. The latter are exemplified by human-specific switching between expression of the neuropeptide somatostatin and tyrosine hydroxylase, the rate-limiting enzyme in dopamine production in certain interneurons. The above molecular differences are also illustrated by expression of the neuropsychiatric risk gene *FOXP2*, which is human-specific in microglia and primate-specific in layer 4 granular neurons. We generated a comprehensive survey of the dlPFC cellular repertoire and its shared and divergent features in anthropoid primates.

The expansion and evolutionary specializations of the cerebral cortex—especially the prefrontal cortex (PFC)—are thought to underlie the rich and complex nature of cognition in humans and other primates (*1*, *2*). The PFC is larger and anatomically more complex in anthropoid primates (i.e., monkeys and apes) compared with that of other analyzed mammals, covering the entire dorsolateral two-thirds of the frontal lobe and having a well-defined granular layer (L) 4 (*1*–*6*). The granular dorsolateral PFC (dlPFC) exhibits broad connectivity with other brain regions (*1*, *2*). Dysfunction of the dlPFC has been implicated in the etiology of many neuropsychiatric disorders (*7*, *8*). Accordingly, nonhuman primates have been used as model species as their complex cognition, expanded PFC, and genetic makeup best approximate that of humans (*9*). Single-cell genomics has emerged as a central tool in understanding cell taxonomy and evolution of the brain, but previous efforts to characterize human PFC were not extensive in the scope of cell type classification and nonhuman primate species selected for comparison (*10*–*15*).

To better understand the cellular repertoire of the dlPFC and its conserved and divergent features, we performed single-nucleus RNA sequencing (snRNA-seq) of the dlPFC in adult humans (*Homo sapiens*), chimpanzees (*Pan troglodytes*), rhesus macaques (*Macaca mulatta*), and common marmosets (*Callithrix jacchus*), representing major anthropoid phylogenetic groups: Hominini (here represented by humans and chimpanzees), Catarrhini (humans, chimpanzees, and macaques) and Platyrrhini (marmosets). The inclusion of chimpanzees—one of the closest living relatives of humans—as well as two outgroup species enabled robust identification of human-specific features. The computational analysis of snRNA-seq data revealed diverse neuronal, glial, and non-neural transcriptomically defined cell types (hereafter referred to as subtypes) and uncovered multiple conserved and divergent features, including those found exclusively in humans. To delineate regulatory mechanisms underlying human-specific changes, we conducted single-nucleus multiome (sn-multiome) characterizing chromatin accessibility [ATAC sequencing (ATAC-seq)] and gene expression (RNA-seq) simultaneously on adult human dlPFC. This resource is interactively accessible at http://resources.sestanlab.org/PFC/.

Transcriptomic classification of dlPFC cells in anthropoid primates

We performed snRNA-seq on histologically validated adult postmortem dlPFC samples from neurotypical male and female humans, chimpanzees, rhesus macaques, and common marmosets (Fig. 1A, fig. S1A, and table S1). Each species group included four donors with four technical replicates per donor, which substantially increased analytic power (fig. S1, B to D). Analysis with the consensus genome annotation (fig. S2; materials and methods), followed by stringent quality control, yielded transcriptomic data from 610,719 high-quality nuclei comparably distributed across the four species (fig. S1E).

Based on unsupervised clustering, expression profiling of marker genes, and transcriptomic integration with published human and mouse single-cell and spatial transcriptomic datasets (*16*–*24*) (materials and methods), we defined three levels of hierarchically related taxonomy of neuronal, glial, and non-neural subtypes (Fig. 1B and fig. S3A). Level 1 included four major classes with 209,824 glutamatergic excitatory neurons, 101,845 GABAergic inhibitory neurons, 247,660 glial cells, and 51,390 non-neural cells. Level 2 included 29 subclasses identified as 10 excitatory neuron subclasses characterized by their layer and axon

[1]Department of Neuroscience, Yale School of Medicine, New Haven, CT 06510, USA. [2]Waisman Center, School of Medicine and Public Health, University of Wisconsin-Madison, Madison, WI 53705, USA. [3]Medical Scientist Training Program, School of Medicine and Public Health, University of Wisconsin-Madison, Madison, WI 53705, USA. [4]Neurogenomics Group, Research Programme on Biomedical Informatics (GRIB), Hospital del Mar Medical Research Institute (IMIM), MELIS, Universitat Pompeu Fabra, 08003 Barcelona, Catalonia, Spain. [5]Croatian Institute for Brain Research, School of Medicine, University of Zagreb, 10000 Zagreb, Croatia. [6]IT-Research Computing, Harvard Medical School, Boston, MA, USA. [7]Division of Neurocritical Care and Emergency Neurology, Department of Neurology, Yale School of Medicine, New Haven, CT 06510, USA. [8]Program in Cellular Neuroscience, Neurodegeneration and Repair, Department of Neurology, Yale School of Medicine, New Haven, CT 06536, USA. [9]Australian Regenerative Medicine Institute, 15 Innovation Walk, Monash University, Clayton, VIC 3800, Australia. [10]MAEBIOS, Alamogordo, NM 88310, USA. [11]Department of Anthropology and Center for the Advanced Study of Human Paleobiology, The George Washington University, Washington, DC, USA. [12]Southwest National Primate Research Center, Texas Biomedical Research Institute, San Antonio, TX, USA. [13]Tsinghua-Peking Center for Life Sciences, IDG/McGovern Institute for Brain Research, School of Life Sciences, Tsinghua University, Beijing 100084, China. [14]Department of Cell Systems and Anatomy, Radiology, Long School of Medicine, UT Health, San Antonio, TX, USA. [15]NeoNeuron LLC, Palo Alto, CA 94306, USA. [16]Centre for Developmental Neurobiology, Institute of Psychiatry, Psychology and Neuroscience, King's College London, London SE1 1UL, UK. [17]MRC Centre for Neurodevelopmental Disorders, King's College London, London SE1 1UL, UK. [18]Nash Family Department of Neuroscience and Friedman Brain Institute, Icahn School of Medicine at Mount Sinai, New York, NY 10029, USA. [19]Department of Neuroscience and Cell Biology, Robert Wood Johnson Medical School, Rutgers University, Piscataway, NJ 08854, USA. [20]Department of Psychiatry, Yale School of Medicine, New Haven, CT 06510, USA. [21]National Center for PTSD, US Department of Veterans Affairs, White River Junction, VT, USA. [22]Kavli Institute for Neuroscience, Yale School of Medicine, New Haven, CT 06510, USA. [23]Department of Neuroscience, School of Medicine and Public Health, University of Wisconsin-Madison, Madison, WI 53705, USA. [24]Departments of Genetics and Comparative Medicine, Program in Cellular Neuroscience, Neurodegeneration and Repair, and Yale Child Study Center, Yale School of Medicine, New Haven, CT 06510, USA.
***Corresponding author. Email: stephen.strittmatter@yale.edu (S.M.S.); andre.sousa@wisc.edu (A.M.M.S.); nenad.sestan@yale.edu (N.S.)**
†These authors contributed equally to this work.

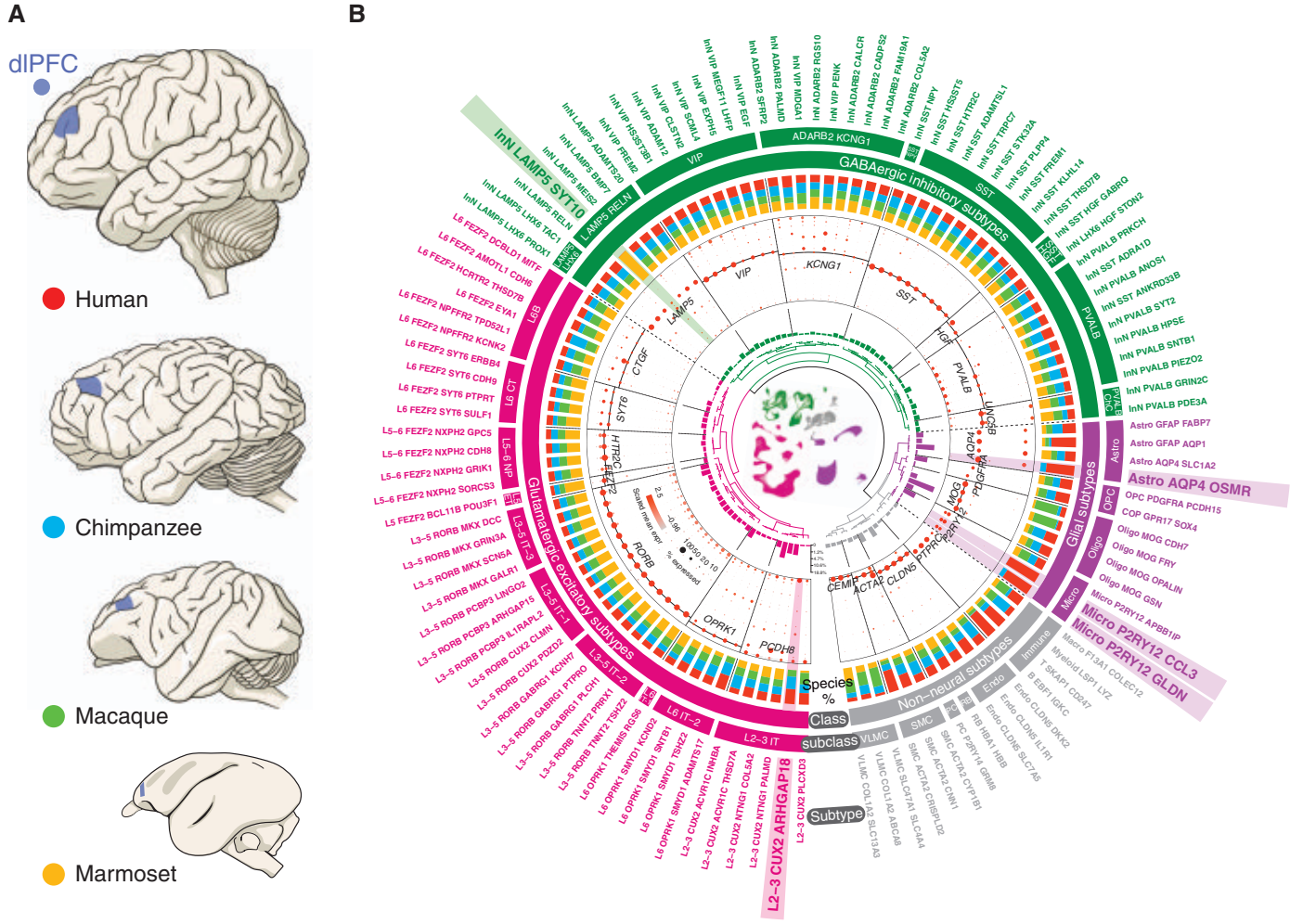


Fig. 1. Transcriptomically defined cell taxonomy of anthropoid primate dlPFC. (**A**) Species (red, human; blue, chimpanzee; green, macaque; yellow, marmoset) and homologous dlPFC areas (blue) analyzed using snRNA-seq. (**B**) Overview of the snRNA-seq dataset, depicting information from inner- to outermost as follows: UMAP of all nuclei; dendrogram of hierarchically related subtypes; subtype proportions; marker gene expression; species representation in each subtype (color conforming to panel A); 4 classes; 29 subclasses; and 114 refined subtypes. The subtypes detected only in some species are highlighted. See fig. S3A for a more detailed description of the cell taxonomy. IT, intratelencephalic; ET, extratelencephalic; NP, near-projecting; CT, corticothalamic; ChC, chandelier cells; Astro, astrocyte; Micro, microglia; Oligo, oligodendrocytes; OPC: oligodendrocyte precursor cells; Endo, endothelial cells; RB, red blood lineage cells; PC, pericyte; SMC, smooth muscle cells; VLMC, vascular leptomeningeal cells.

projection properties (intratelencephalic, extratelencephalic, near projecting, corticothalamic, and L6B); nine inhibitory neuron subclasses characterized by established marker genes; four glial cell subclasses (astrocytes, oligodendrocyte precursor cells, oligodendrocytes, and microglia); and six non-neural cell subclasses (immune cells, endothelial cells, red blood lineage cells, pericytes, smooth muscle cells, and vascular leptomeningeal cells). Level 3 included 114 further refined subtypes within each of the subclasses. These subtypes have a balanced contribution from donors in each species and their transcriptomic stability is generally not affected after randomly removing one donor in a given species (fig. S3, A and B).

All 29 subclasses and most of the 114 subtypes were detected in all four primate species (Fig. 1B). Cell homologies were unaffected when integrating data using different methods (fig. S3C) or clustering nuclei within each species separately (figs. S11A, S13A, and S16A). However, five subtypes were detected only in some species (hereafter referred to as species-specific subtypes), with minimal bias being introduced by donors of that given species (fig. S4, A to D). The five subtypes included the excitatory neuron subtype L2-3 *CUX2 ARHGAP18* absent in marmosets, the inhibitory neuron subtype InN *LAMP5 SYT10* detected only in marmosets, the astroglial subtype Astro *AQP4 OSMR* detected only in humans and chimpanzees, the microglial subtype Micro *P2RY12 CCL3* detected only in humans, and the microglial subtype Micro *P2RY12 GLDN* detected only in humans and chimpanzees.

Cellular and transcriptomic changes across anthropoid primate dlPFC subtypes

The multifaceted functions of the dlPFC require the orchestration of diverse cell types that have undergone substantial specialization, which could include the emergence of new cell subtypes, changes in the abundance of a shared or conserved cell type, variation in intercell heterogeneity, or reorganization of molecular features in conserved cell types (Fig. 2A).

We first assessed whether the five species-specific subtypes (Fig. 2B) were transcriptomically unique for those species. For this, we calculated the markers for each species-specific subtype and visualized their expression enrichment across species on the uniform manifold approximation and projection (UMAP)

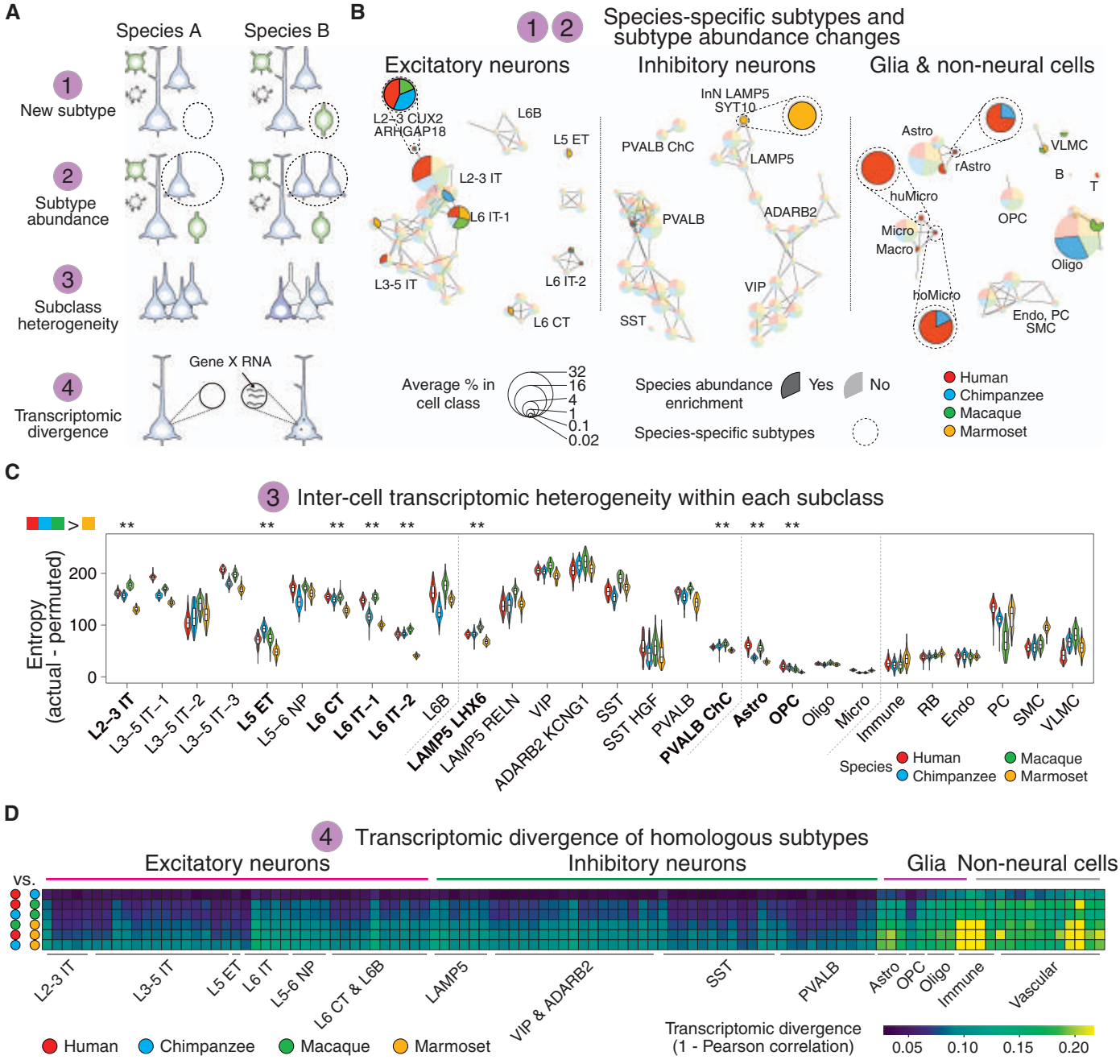


Fig. 2. Shared and divergent features of dlPFC subtypes across anthropoid primates. (**A**) Diagram illustrating possible models of species cellular and transcriptomic differences. (**B**) Subtype abundance comparisons across species. Each pie represents a subtype with size indicating the average subtype proportions across the four species (materials and methods). Links represent the expression correlation among subtypes. Subtypes showing species-enrichment in abundance are opaque in color whereas semitransparent or muted colors indicate no enrichment in abundance. Species-specific subtypes are highlighted by dashed circles. (**C**) Transcriptomic heterogeneity among cells of the same subclasses. Significance was tested with a pairwise Wilcoxon Rank Sum test with Bonferroni correction (**, adjusted $P < 0.01$). (**D**) Raw transcriptomic divergence across subtypes (columns) in all species pairs (rows). IT, intratelencephalic; ET, extratelencephalic; NP, near-projecting; CT, corticothalamic; ChC, chandelier cells; Astro, astrocyte; Micro, microglia; Oligo, oligodendrocytes; OPC, oligodendrocyte precursor cells; Endo, endothelial cells; RB, red blood lineage cells; PC, pericyte; SMC, smooth muscle cells; VLMC, vascular leptomeningeal cells; huMicro, human-specific microglia (Micro *P2RY12 CCL3*); hoMicro, Hominini-specific microglia (Micro *P2RY12 GLDN*). rAstro: reactive astrocyte (Astro *AQP4 OSMR*).

layout (fig. S4, A to D). The homologous cells of each species-specific subtype, if present in one species, were found to be marked by high enrichment scores and clustered together on the UMAP layout (fig. S4, A to D). By contrast, no cells or only a scarce number of cells sparsely distributed on the UMAP were labeled by high enrichment scores in the species in which the species-specific subtypes were absent. By leveraging available cross-species snRNA-seq data (*22*, *25*), we confirmed the species-specific presence of subtypes L2-3 *CUX2 ARHGAP18* and InN *LAMP5 SYT10* and Micro *P2RY12 CCL3* and demonstrated that the detection of species-specific subtypes is not limited to the donors analyzed in this study (figs. S4E and S17F). To further corroborate these results, we conducted single-molecule fluorescence in situ

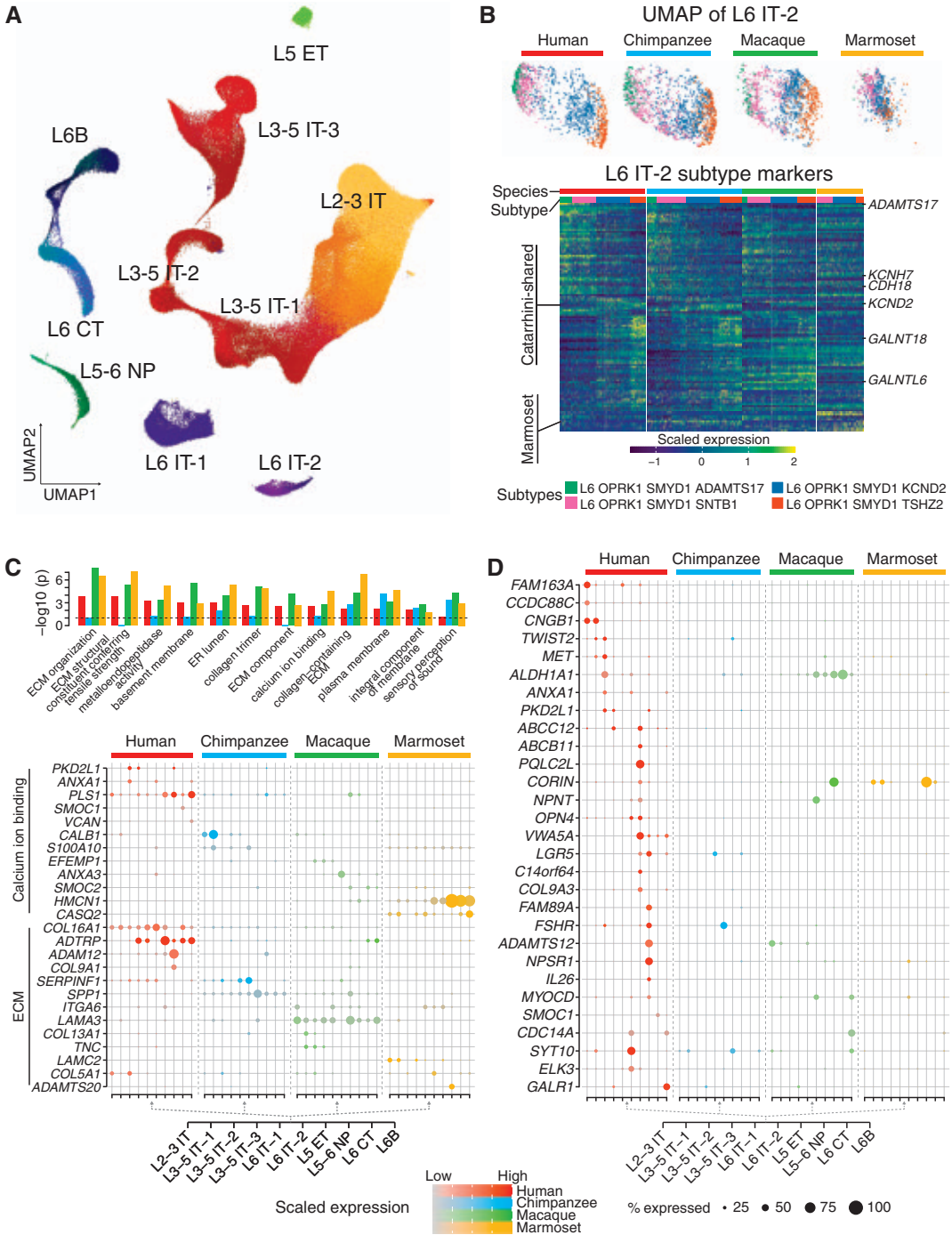


Fig. 3. Taxonomy and divergent features of dlPFC excitatory neuron subtypes. (**A**) UMAP visualization of all glutamatergic excitatory neuron subtypes with subclasses labeled. (**B**) (Top) UMAP showing all L6 IT-2 subtypes. (Bottom) Expression of subtype markers shared in Catarrhini (≥2 species) or specific to marmosets. (**C**) (Top) Enrichment of Gene Ontology (GO) terms in the species-enriched genes from each species, with colors indicating the species. Only the GO terms enriched in at least three species are displayed. (Bottom) Expression of the selected species-enriched genes involved in the calcium ion binding and extracellular matrix (ECM). ER, endoplasmic reticulum. (**D**) Expression of genes with high subclass and human specificity. IT, intratelencephalic; ET, extratelencephalic; NP, near-projecting; CT, corticothalamic.

hybridization for representative marker genes and validated the species-specificity of the Catarrihini-specific upper layer intratelencephalic subtype L2-3 *CUX2 ARHGAP18*, the marmoset-specific inhibitory neuron subtype InN *LAMP5 SYT10*, and the Hominini-specific enrichment in astroglial subtype Astro *AQP4 OSMR* (figs. S5 to S7). Similar to the observation in the snRNA-seq data (fig. S4), we observed only a limited number of cells labeled by in situ hybridization in the species lacking the species-specific subtypes.

Although most subtypes are shared across the four analyzed primates, changes in their relative abundance can contribute to distinct cellular networks. An L2-3 intratelencephalic subtype (L2-3 *CUX2 ACVR1C THSD7A*)—the most abundant subtype among all L2-3 intratelencephalic subtypes—was found to be enriched in humans compared with other species and enriched in Catarrhini compared with marmosets (Fig. 2B and fig. S8). By contrast, we observed notable reduction of the L5 extratelencephalic subtype and an L6 corticothalamic subtype in Catarrhini compared with marmosets (Fig. 2B).

Differences in cellular diversity across species can also arise when cell subpopulations within a subclass become transcriptomically more diversified or more homogenous within a given species. To delineate transcriptomic heterogeneity among cells within a given subclass, we adopted the concept of entropy, a measurement of uncertainty, in analyzing gene expression variability (fig. S9A; materials and methods). Larger entropy values associate with

higher gene expression variability and vice versa. By subtracting the entropy in permutated data from that in the actual data we were able to reveal the overall transcriptomic heterogeneity among cells within each homologous subclass across species (Fig. 2C). We found a considerable heterogeneity increase in Catarrhini compared with marmosets in multiple neuronal and glial subclasses such as L2-3 intratelencephalic, *PVALB* chandelier cells, and astrocyte subclasses (Fig. 2C). Such heterogeneity arising in Catarrhini L2-3 intratelencephalic excitatory neurons confirms previous reports (*16*, *26*) and extends our observations of expanded diversity and abundance in upper layer neurons in Catarrhini (Fig. 2B). Patterns of increased heterogeneity in Catarrhini were further supported by the augmented cell separation in principal component dimensions and the expansion of marker expression profiles distinguishing subtypes in Catarrhini (fig. S9, B and C). Although many of these subtype markers shared across Catarrhini were also expressed broadly in marmosets, their expression was not distinguishable among the same subtypes (fig. S9, D and E). This result suggests a possible mechanism underlying cell type heterogeneity whereby genes originally shared among different subtypes become variable, resulting in greater intersubtype transcriptomic differences.

Species differences can also arise from divergent gene expression in homologous types. We defined transcriptomic divergence based upon expression correlation of highly variable genes between homologous subtypes for each species-wise pair (materials and methods). Observed patterns of transcriptomic divergence mirrored evolutionary distances between the four species with the human-chimpanzee and chimpanzee-marmoset pairs showing the smallest and largest transcriptomic divergence, respectively (Fig. 2D). This analysis also showed that glia cell and non-neural cell subtypes were the most divergent in all species pairs (Fig. 2D), consistent with studies comparing primate species at the level of bulk tissue and cell-sorted populations (*27*, *28*). We confirmed that these observations were not influenced by unequal cell numbers across subtypes or using a different highly variable gene set (fig. S10, A and B) and were commensurate with species differences measured by the proportion of differentially expressed genes (fig. S10C). Together, this revealed that multiple sources of variation contributed to neuronal, glial, and non-neural cell type differences across anthropoids.

Conserved and divergent features of excitatory neuron subtypes

We next investigated each major cell class to better delineate conserved and divergent features among subtypes. Excitatory neurons in each species were comprised by a multitude of subtypes predicted to have distinct properties (Fig. 3A and fig. S11A). Imputation of layer distribution and long-range projection types by integrating our data with published snRNA-seq data from human middle temporal gyrus (MTG) (*16*), spatial transcriptomic data from human PFC (*18*), and data from mouse primary visual cortex including projection identity (*17*) showed that excitatory neuron subtypes can be classified into 10 subclasses. These subclasses are characterized according to their predicted L2 to L6 layer localization and projection types (Fig. 1B and fig. S11, B to D). The intratelencephalic subclass that accounted for more than 80% of the excitatory neurons was predicted to span layers L2 to L6 and was marked by layer-specific markers (L2-3, *PCDH8*; L3-5, *RORB*; L6, *OPRK1*; Fig. 1B). The extratelencephalic, corticothalamic, and other subclasses were predicted to be localized in deep layers and were transcriptomically distinct (L5 extratelencephalic, *FEZF2*, *BCL11B*, and *POU3F1*; L6 corticothalamic, *SYT6*; L5-6 near-projecting, *HTR2C*; L6B, *CTGF*; Fig. 1B).

Assessment of subclass heterogeneity across species revealed one L6 intratelencephalic subclass (L6 IT-2) having the greatest increase of intercell transcriptomic differences in Catarrhini compared with marmosets (Fig. 2C). In line with this observation marmoset subtypes of this subclass were less separated on the UMAP and expressed fewer genes distinguishing them when compared with humans, chimpanzees, and macaques (Fig. 3B). Genes delineating the subtypes of this subclass in Catarrhini also mapped onto important biological pathways including extracellular matrix and cell-cell interaction (*ADAMTS17*, *CDH18*), calcium ion binding proteins (*KCNH7*, *KCND2*), and protein glycosylation (*GALNT18*, *GALNTL6*), suggesting more diversified cellular functions.

We next identified transcriptomic changes restricted to each excitatory neuron subtype (fig. S12A). Within each species, we identified more species-enriched genes than species-depleted genes. As expected, marmosets had both more up- and downregulated genes compared to humans, chimpanzees, and macaques. Gene ontology enrichment of the exclusively enriched genes for each species converged upon processes related to extracellular matrix and calcium ion binding functions involved in synaptic transmission (Fig. 3C). For instance, genes within the annexin family, which play a critical role in calcium ion binding, were used differentially across primate brains: humans selectively expressed *ANXA1* in upper-layer intratelencephalic neurons whereas macaques specifically expressed *ANXA3* in deep-layer intratelencephalic neurons. This analysis also highlighted human L3-5 intratelencephalic subclass enrichment of *PKD2L1*, which encodes a calcium-regulated cation channel. These results suggest that the components of the same biological pathways are differentially recruited across species, resulting in divergent molecular and cellular functions.

We further filtered genes with species- and subclass-restricted expression patterns using more stringent criteria (materials and methods), resulting in 20 to 51 genes in each species with potentially higher functional relevance (Fig. 3D and fig. S12B). The 29 genes detected in the human lineage included genes encoding transcription factors (*TWIST2* and *ELK3*), genes associated with autism spectrum disorder (ASD) in the SFARI gene list (https://gene.sfari.org/; *CCDC88C*, *MET*, *ANXA1*) as well as genes encoding critical retinoic acid signaling components (*ALDH1A1*; Fig. 3D and fig. S12, C and D), which have recently been shown to regulate gene expression, spinogenesis, and connectivity in PFC (*29*). We also found other retinoic acid signaling–associated genes exhibiting divergent expression across species: *CYP26B1*, enriched in Hominini L5-6 near-projecting and L6 corticothalamic subclasses, and *CBLN2*, globally upregulated in multiple Hominini excitatory neuron subclasses. These findings validate recently reported Hominini-specific changes in the retinoic acid-responsive enhancer predicted to upregulate *CBLN2* expression in PFC excitatory neurons (*30*).

Conserved and divergent features of interneuron subtypes

Based on marker gene expression and transcriptomic integration with other human and mouse single-cell RNA-seq data (*12*, *16*, *17*, *19*, *20*) (Fig. 4A, fig. S13, B to D, and fig. S14, A to C), we classified inhibitory neurons into nine subclasses predicted as follows: long-range projecting neurons (*SST NPY*), Martinotti and non-Martinotti cells (*SST*), basket cells (*PVALB*), chandelier cells (*PVALB* ChC), Ivy cells (*LAMP5 LHX6*), *LAMP5* neurogliaform cells (*LAMP5 RELN*), *VIP* inhibitory neurons (*VIP*), homologs of human tyrosine hydroxylase (TH)-expressing inhibitory neurons (*SST HGF*), and homologs of mouse *Sncg* inhibitory neurons (*ADARB2 KCNG1*). We detected two *PVALB* chandelier subtypes marked by distinct expression profiles, showing specific enrichment of NMDA glutamate receptors regulating excitatory synaptic communication as well as nonclustered protocadherins mediating cell adhesion (fig. S14, D to E). This pattern was observed in all four primates analyzed (fig. S14, D to E), suggesting conserved functional diversification between the two *PVALB* chandelier subtypes.

These inhibitory neuron subtypes were predicted to have different developmental origins based on lineage-related marker expression: medial ganglionic eminence (MGE), *LHX6*; caudal ganglionic eminence (CGE), *ADARB2*, *NR2F2*, and *PROX1*, figs. S13D and S14, A and B). We found that the *LAMP5 LHX6* subclass consisted of two subtypes marked by *LHX6* expression, among which one subtype also

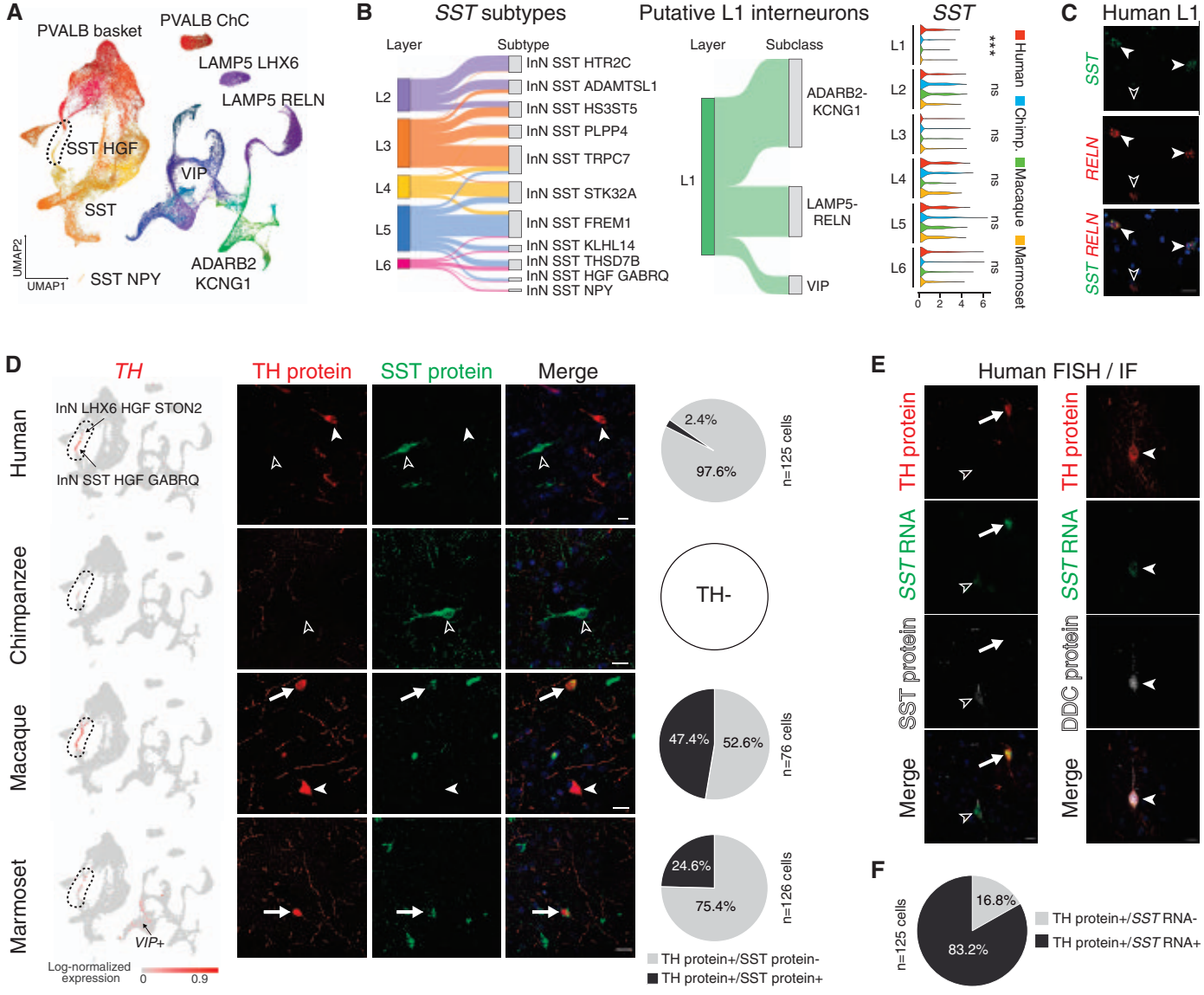


Fig. 4. Taxonomy and divergent features of dlPFC inhibitory neuron subtypes. (**A**) UMAP layout of all GABAergic inhibitory neuron subtypes with subclasses labeled. ChC, chandelier cells. (**B**) (Left) Sankey plots showing correspondence between predicted laminar organization and subtypes and/or subclasses. (Right) *SST* expression across putative cortical layers. Significance was tested with a one-sided Wilcoxon Rank Sum test (***, $P < 0.001$; ns, not significant). (**C**) colocalization of *SST* and *RELN* (arrowhead) in human dlPFC L1 revealed by double RNA in situ hybridization. Scale bar, 20 μm. (**D**) (Left) log-normalized expression of *TH*. (Middle) Double immunostaining for SST and TH. (Right) Proportion of SST+ and SST- cells within TH+ neurons. Scale bars, 20 μm in all species. (**E**) Immunofluorescence staining for TH and SST (left) or DDC (right), combined with *SST* RNA in situ hybridization. Scale bars, 20 μm. (**F**) Proportion of *SST*+ and *SST*− cells in human TH+ neurons.

expressed *PROX1* (*LHX6*+/*PROX1*+; fig. S13D). The *LAMP5 LHX6* subclass was previously reported to be enriched in primates (*12*, *16*) and was considered to be derived from MGE (*31*). We found that the markers of the *LHX6*+/*PROX1*+ subtype showed expression enrichment in CGE-derived inhibitory neurons whereas the markers of the *LHX6*+/*PROX1*− subtype showed enrichment in MGE-derived inhibitory neurons (fig. S14F). This pattern was conserved across all four studied primates (fig. S14F), suggesting a potential overlap of *PROX1* and *LHX6* molecular mechanisms commonly present in all primates analyzed.

Imputation of layer distribution by transcriptomic integration with human MTG inhibitory neurons (fig. S14G) (*16*) showed that *SST* and *PVALB* inhibitory neuron subtypes were preferentially located from L2 to L6 whereas L1 inhibitory neurons included only *ADARB2 KCNG1*, *VIP*, and *LAMP5* subtypes (Fig. 4B). Some putative L1 inhibitory neuron subtypes in humans also expressed *SST* (Fig. 4B and fig. S14G) but they lacked expression of other MGE-related genes including *LHX6* and *PVALB*. However, few putative L1 inhibitory neurons from other species expressed *SST* (Fig. 4B). We confirmed the presence of these inhibitory neurons by performing in situ hybridization in human tissue against *SST* and *RELN*, a gene marking human L1 *SST*–expressing inhibitory neurons in the snRNA-seq data (Fig. 4C). These results suggest the presence of *SST*–expressing inhibitory neurons in human L1.

Within homologous inhibitory neuron subtypes we detected pronounced transcriptomic

changes across species that followed patterns similar to those of excitatory neurons, with marmosets having the most distinct expression profiles, commensurate with phylogenetic relationships of the four primates (fig. S14H). *MELTF*—which encodes melanotransferrin and is involved in cellular iron uptake—was specifically upregulated in *PVALB* chandelier subtypes in humans (fig. S14H), suggesting novel roles for iron homeostasis in fast-spiking inhibitory neurons. Analysis of gene families (https://www.genenames.org/; materials and methods) overrepresented in species-enriched genes highlighted collagens in almost all species (fig. S14I), a pattern also observed in excitatory neurons (Fig. 3C). This analysis also revealed genes encoding neuropeptides (e.g., *NMU* and *PENK*) and carbonic anhydrases overrepresented in human-enriched genes; the former is a critical component orchestrating cell-cell communications, and the latter can regulate neuronal signaling through modulation of pH transients (fig. S14I). Cumulatively, these results suggested possible reorganization of synaptic communication across primate inhibitory neurons.

Human-specific switching between expression of SST and TH in interneurons

We have previously found that inhibitory neurons expressing TH—the rate-limiting enzyme in the biosynthesis of catecholamine neurotransmitters such as dopamine—are absent from the neocortex of nonhuman African apes (i.e., chimpanzees, bonobos, and gorillas) (*32*, *33*). Given the functional significance of dopamine in PFC function (*7*), we further profiled these inhibitory neurons using our dataset. We found *TH* expression in a small subset of dlPFC inhibitory neurons in humans and macaques. Expression was notably less in marmosets and absent in chimpanzees. Human and macaque *TH*-expressing inhibitory neurons coexpressed *SST* and were transcriptomically classified as the *SST HGF* subclass that was hierarchically split into two subtypes: InN *LHX6 HGF STON2* subtype (low *TH* expression) and InN *SST HGF GABRQ* subtype (high *TH* expression) (Fig. 4D). Homologous subtypes were also found in chimpanzees (Fig. 4D), indicating that these inhibitory neurons are not absent in chimpanzees but simply do not express *TH*. Expression of *TH* was also detected in the two homologous subtypes in marmosets and some *VIP*-expressing inhibitory neurons but generally showed much lower expression compared with humans and macaques (Fig. 4D), indicating a more complex pattern of species-specific regulation of *TH* expression in these inhibitory neurons.

Since these two subtypes are readily distinguishable by levels of *SST* expression (high in subtype InN *SST HGF GABRQ* and extremely low in subtype InN *LHX6 HGF STON2*; fig. S15A), we characterized these two subtypes by immunofluorescence staining for TH and SST. TH-immunopositive inhibitory neurons were found in deep layers and the adjacent white matter of dlPFC in humans, macaques, and marmosets—but not in chimpanzees (Fig. 4D). Many TH-immunopositive inhibitory neurons were also co-immunolabeled for SST in macaques (47.4%) and marmosets (24.6%; Fig. 4D). The two populations or states of TH-immunopositive inhibitory neurons distinguished by SST immunolabeling in macaques likely represent the two *TH*-expressing subtypes detected in our snRNA-seq data (fig. S15A). Furthermore, the lower proportion of TH-immunopositive inhibitory neurons co-immunolabeled for SST in marmosets may be due to the *TH* expression in marmoset *VIP* inhibitory neurons (Fig. 4D). Consistent with this, a subset of marmoset TH-immunopositive inhibitory neurons also expressed VIP in upper layers (28.1%; fig. S15C).

By contrast, only a few TH-immunopositive inhibitory neurons were co-immunolabeled for SST in humans (2.4%; Fig. 4D). Even with tyramide signal amplification we could only detect trace SST-immunolabeling signals in human TH-immunopositive inhibitory neurons (fig. S15, D to E). Such low SST-immunopositivity among human TH-immunopositive inhibitory neurons was inconsistent with our snRNA-seq data as one human *TH*-expressing subtype (InN *SST HGF GABRQ*) exhibited prominent *SST* RNA expression comparable to the homolog subtype in macaques and marmosets (fig. S15A). Such inconsistency prompted us to investigate *SST* RNA expression in TH-immunopositive inhibitory neurons using additional tissue samples and methods. We complemented the immunofluorescence findings with in situ hybridization-based detection of *SST* RNA in human dlPFC tissue samples and found that most human TH-immunopositive cells expressed *SST* RNA transcripts (83.2%; Fig. 4, E and F), as predicted by our snRNA-seq data. This proportion is notably greater than the proportion of inhibitory neurons co-immunolabeled for both TH and SST (2.4%), suggesting that certain post-transcriptional mechanisms exist in humans to downregulate SST protein expression. Additionally, we profiled SST and TH immunohistochemistry in the mouse frontal cortex, which revealed a proportion of inhibitory neurons co-immunolabeled for both SST and TH (57.9%; fig. S15F), similar to macaques (47.4%) but not humans (2.4%). Together, these results indicate that the switching between expression of SST and TH protein, a pattern reminiscent of populations of interneurons in the adult rat hypothalamus with switch between SST and TH expression—and subsequent dopamine production (*34*)—is also present in certain dlPFC interneurons in a human-specific manner, at least in the context of the primates that we analyzed.

Because TH expression itself does not necessarily effectuate active dopamine production or signaling, this prompted us to profile other dopamine signaling pathway components in our dlPFC dataset (fig. S15, A to B). We found that many genes orchestrating key dopamine signaling pathway processes, including dopamine synthesis (*TH*, *GCH1*), transport (*SLC18A2*), and binding to presynaptic receptors (*DRD2*) (*7*), were expressed in the human subtype InN *SST HGF GABRQ*. However, these genes exhibited either low or no expression in the other subtype InN *LHX6 HGF STON2* or in other analyzed species (fig. S15A). *DDC* was not detected in the human InN *SST HGF GABRQ* subtype likely because of its low expression, which we could detect in the matched inhibitory neuron subtype in the human MTG data (*Inh L5-6 SST TH*; fig. S15A), which has higher sequencing depth using SMART-seq (*16*). In situ hybridization also confirmed the presence of RNA transcripts for both *TH* and *DDC* in the same human dlPFC cells that exhibited typical interneuronal morphology (fig. S15K). We further validated the protein expression of DDC in TH+/*SST*+ inhibitory neurons by performing double immunofluorescent staining for TH and DDC combined with in situ hybridization for *SST* in human dlPFC tissue samples (Fig. 4E). By contrast, in mice, DDC immunolabeling was detected in putative dopaminergic neurons in the substantia nigra and ventral tegmental area but not in neocortical TH-immunopositive inhibitory neurons (fig. S15L). Although expression of *SLC6A3* was not detected in either our dlPFC or published MTG single cell dataset, *SLC47A1*, which encodes a noncanonical dopamine transporter (*35*), was exclusively expressed in both *TH*-expressing inhibitory neuron subtypes in humans (fig. S15A). These results suggest the emergence of key dopamine signaling pathway components in a subset of TH-expressing inhibitory neurons in humans.

Conserved and divergent features of glial and non-neural subtypes

Within glia cells and non-neural cells, the observed taxonomy of oligodendroglial, astroglial, microglial, immune, and vascular cells corresponded to 28 subtypes in humans, 27 subtypes in chimpanzees, 25 subtypes in macaques, and 25 subtypes in marmosets (Fig. 5A and fig. S16A). Although these subtypes were labeled by conserved subclass markers (fig. S16B), prominent species-specific expression profiles were detected in each subtype with a pattern consistent with that of the phylogenetic relationship among the four primates (Fig. 5B).

Subtypes related to the oligodendrocyte lineage represented a cellular differentiation and maturation trajectory spanning from oligodendrocyte precursor cells to mature oligodendrocytes (fig. S16C). This trajectory was shaped by

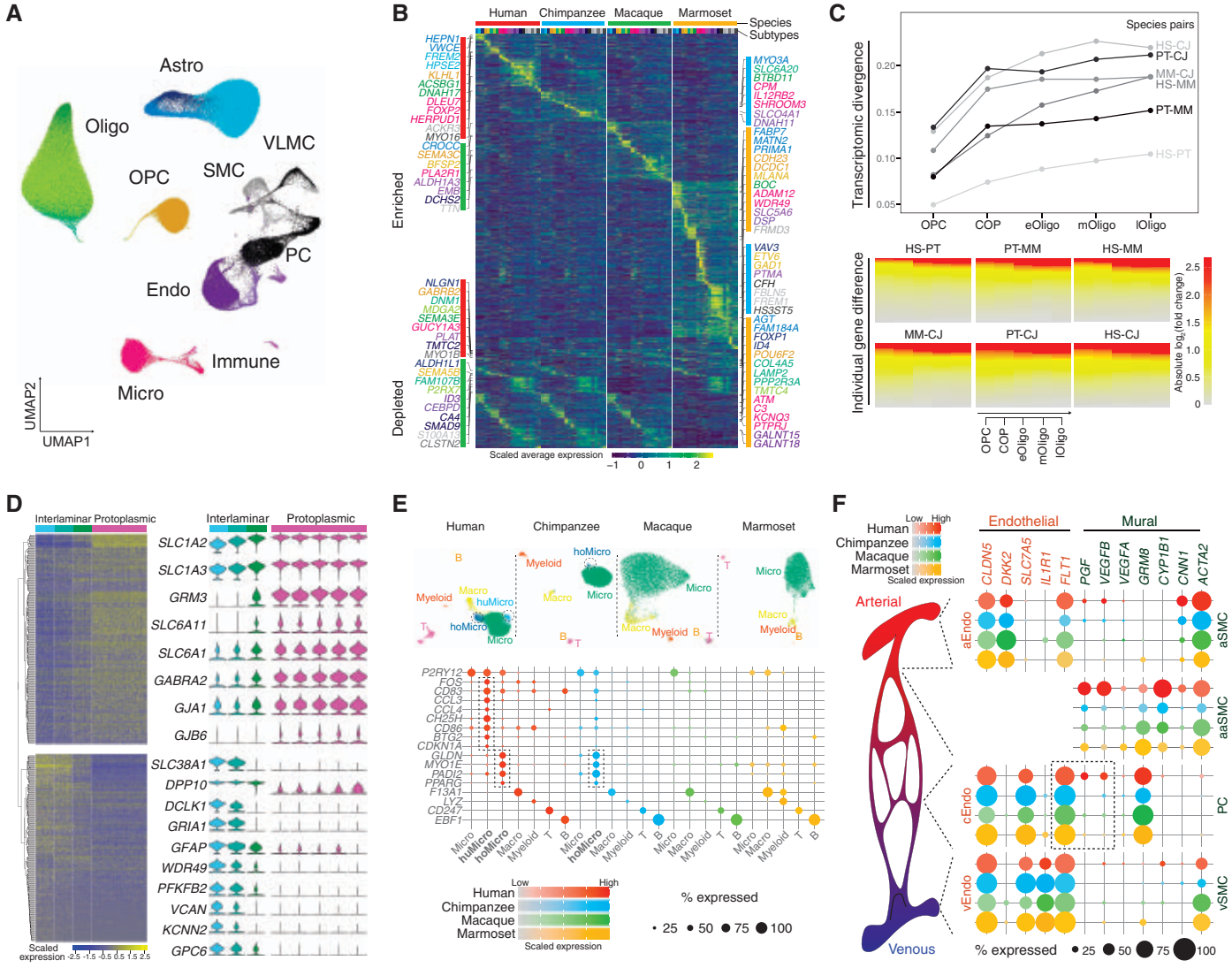


Fig. 5. Taxonomy and divergent features of dlPFC glia cell and non-neural cell subtypes. (**A**) UMAP showing all glia cell and non-neural cell subtypes in the four primates with subclasses labeled. (**B**) Standardized average expression of genes (rows) which are species-enriched (top) or species-depleted (bottom) across subtypes (columns). Subtypes are color-barcoded on the top with color scheme conforming to panel A. Genes were colored according to the subtypes where they show enrichment or depletion. (**C**) Transcriptomic divergence (top) and gene expression differences (bottom) of subtypes in the oligodendrocyte lineage between each pair of species. HS, human; PT, chimpanzee; MM, macaque; CJ, marmoset. (**D**) (Left) the two gene modules differentially expressed among the three interlaminar astrocyte subclusters. (Right) Expression of the selected genes across the interlaminar and protoplasmic astrocyte subclusters. (**E**) (Top) UMAP plots illustrating microglia and immune subtypes detected in the four primates. (Bottom) expression of manually selected subtype marker genes. Marker expression labeling species-specific subtypes are highlighted by dashed rectangles. (**F**) (Left) Illustration of the brain vascular architecture from arteries (red), arterioles, and capillaries to veins (blue). (Right) Vascular subtypes divided into endothelial (left) and mural cells (pericytes and smooth muscle cells) (right) located along the arterial-venous axis. Dot plots show expression of marker genes and *FLT1* signaling genes. Astro, astrocyte; Micro, microglia; Oligo, oligodendrocytes; OPC, oligodendrocyte precursor cells; Endo, endothelial cells; PC, pericyte; SMC, smooth muscle cells; VLMC, vascular leptomeningeal cells; huMicro, human-specific microglia subtype (Micro *P2RY12 CCL3*); hoMicro, Hominini-specific microglia subtype (Micro *P2RY12 GLDN*).

conserved gene expression cascades across the four primates and transcriptomically resembled that described in mice (*21*) (fig. S16, C and D). However, prominent species differences were also observed, with transcriptomic divergence and individual gene expression differences among the four primates increasing along the trajectory (Fig. 5C). Evolutionarily divergent genes along the trajectory were particularly enriched for ligand and receptor binding features such as semaphorins and their neuropilin and plexin receptors (fig. S17, A and B), which highlights the role of semaphorin signaling in regulating oligodendrocyte precursor cell recruitment and differentiation as well as oligodendrocyte myelination.

Based on marker gene expression and imputation of layer distribution by integration of our data with human MTG and motor cortex data (*16*, *22*), astrocytic subtypes were characteristic of known astrocyte subpopulations, including interlaminar astrocytes localizing in L1, protoplasmic astrocytes populating the gray matter, fibrous astrocytes residing in the white matter, and reactive astrocytes (fig. S16, E and H) (*36*). Because there is limited characterization of interlaminar astrocytes we further subclustered these cells to probe their transcriptomic heterogeneity in greater detail. The resulting three subclusters displayed substantial expression

differences in 612 genes organized into two coexpression modules (Fig. 5D). Module 1 included many genes encoding the major effectors for astrocyte-mediated clearance of glutamate and GABA from the extracellular space, such as glutamate transporters (*SLC1A2* and *SLC1A3*) and GABA transporters (*SLC6A11* and *SLC6A1*; Fig. 5D). Preferential expression of these genes in a subset of interlaminar astrocytes—juxtaposed to their broad expression in protoplasmic astrocytes—suggests a role in the clearance of neurotransmitters in cortical L1 by a subset of interlaminar astrocytes cells that adopted machineries similar to those of protoplasmic astrocytes.

Subtypes of Microglia, macrophages, myeloid cells, and T and B cells formed the immune populations in these data (fig. S16A) (*37*). Although we found broad conservation of immune subtypes across species we highlighted one microglia subtype specific to humans (Micro *P2RY12 CCL3*) and one microglia subtype specific to Hominini (Micro *P2RY12 GLDN*, Fig. 5E). The human-specific microglial subtype expressed signatures of preactivation (*FOS*, *CD83*), chemokine secretion (*CCL3*, *CCL4*), antiviral defense (*CH25H*), costimulation (*CD86*), and proliferation (*BTG2*, *CDKN1A*; Fig. 5E) and was very similar to a previously reported preactive immune-sensing subpopulation, which emerges as early as the 10th gestational week and expands to midgestation in the absence of inflammation (*38*). We show that this cell type likely persists into adulthood in the human cerebral cortex (fig. S17, E and F) (*25*). Its presence was also unrelated to sample age (table S1 and fig. S4H). The early developmental rise and persistence of this cell type, independent of different pathological states, may suggest a specific and essential immune homeostatic and/or senescence-associated role in contrast to specifically induced disease-associated microglial subtypes (*25*, *37*). The Hominini-specific microglial type showed high expression of *GLDN*, *MYO1E*, *PADI2*, and *PPARG* (Fig. 5E).

In addition to microglia, we identified 1416 putative T cells, with most (885 or 62.5%) from human samples (fig. S16I), the abundance of which is consistent across the human donors analyzed (8.24% ± 1.66% among all immune cells; fig. S4I). This number greatly exceeded those of myeloid and B cells (81 and 53 cells, respectively), surpassing proportions in peripheral circulation that would be expected for contaminants rather than a brain-resident T cell population. Such cells likewise had expression of multiple genes not detected during T cell development in the human thymus (fig. S16K).

Through combinatorial marker gene expression and transcriptomic integration with mouse snRNA-seq data (*23*, *24*), we found that vascular subtypes were predicted to locate along the arterial-arteriolar-capillary-venous axis including three endothelial subtypes (arterial, capillary, and venous endothelial cells), four mural subtypes (pericytes, arterial, arteriolar, and venous smooth muscle cells), three vascular leptomeningeal-like cell subtypes, and one putative red blood cell lineage subtype (fig. S16L; materials and methods). Some genes involved in key biological pathways displayed species-specific profiles along this vascular axis. This is exemplified by *FLT1*, which encodes the vascular endothelial growth factor receptor, with conserved expression marking the capillary endothelial subtype. Among the three genes encoding its signaling molecules, *VEGFA* was sparsely expressed in pericytes of all species whereas *VEGFB* and *PGF* were enriched in human pericytes (Fig. 5F), suggesting the presence of human-specific signaling shaping vascular cell identity and communication.

Primate- and human-specific expression patterns of *FOXP2*

By assessing the intersection of genes showing human-enriched expression in microglia and those showing microglia-enriched expression compared with macrophages, we found 19 genes. *FOXP2* was of particular interest among those genes given that it encodes a transcription factor mutated in developmental verbal dyspraxia (*39*, *40*), and is implicated in a number of neuropsychiatric disorders. Although previous studies have shown that *FOXP2* is expressed in neurons of the basal ganglia and neocortical layers 6 and 5 (*40*), its expression in microglia is unexpected. Some *FOXP2*-related disorders have been linked to alterations in microglia and neuroinflammation (*37*), highlighting the potential functional importance of human-specific *FOXP2* expression in the context of microglia. We next performed in situ hybridization for *FOXP2* RNA, combined with immunofluorescent staining against IBA1, and validated *FOXP2* expression in human microglia (Fig. 6B). Similarly, we confirmed its protein expression in human microglia by performing triple-labeling immunofluorescence for RBFOX3 (NeuN), IBA1, and FOXP2 in human tissue, which revealed FOXP2 expression in both RBFOX3-positive neurons and IBA1-positive microglia (fig. S18A). Using multiple published datasets, we independently validated human specificity of *FOXP2* expression in microglia and found that it was a common feature shared by multiple brain regions (fig. S18, B to E); these datasets included bulk tissue RNA-seq data of sorted microglia from the cerebral cortices of eight species (human, macaque, marmoset, sheep, mouse, rat, hamster, and chicken; fig. S18B) (*25*), snRNA-seq data from mouse primary visual cortex (Fig. 6A) (*17*), cross-species snRNA-seq data of motor cortex (human, marmoset, and mouse; fig. S18C) (*22*), and cross-species snRNA-seq data of hippocampus (human, macaque, pig, and mouse; fig. S18D) (*41*). By contrast, *FOXP2* expression was not detected in macrophages in brain or other tissues (fig. S18F) nor in fetal microglia (fig. S18, G and H).

We found that *FOXP2* is highly expressed in several major L5 and L6 excitatory neuron subclasses across primates in our data (Fig. 6A), which matches previous studies in mice (*40*). However, we also observed previously unknown enrichment of *FOXP2* expression in L3-5 intratelencephalic excitatory neurons across primates, which was not detected in mice (Fig. 6A). The L3-5 intratelencephalic excitatory neurons likely encompass small neurons that give the primate dlPFC L4 its characteristic granular appearance (with a high density of small excitatory neurons). To test whether FOXP2 is expressed in neurons of the granular L4, we conducted immunohistochemistry in the four primates analyzed in this study (Fig. 6C and table S3). We found that the majority of neuronal nuclei in granular L4 of the dlPFC were immunolabeled for FOXP2. To test whether this expression pattern is specific to primates—the only mammals with granular dlPFC—we extended our immunohistochemical study of FOXP2 expression to 21 primates and 30 nonprimate mammals. This represented a total of 19 orders, including monotremes (represented by echidna)—the lineage with the most ancient divergence from other mammals (table S3)—and allowed us to identify the evolutionary conservation of this expression profile. We found that the pattern of prominent L4 FOXP2 expression was only observed in primates (Fig. 6D and figs. S19 and S20A) and was notable in granular PFC and other analyzed granular association areas involved in higher integrative functions (table S3). Overall, this indicates that broad expression of FOXP2 in L4 excitatory neurons is an evolutionary specialization of primates.

To assess temporal expression patterns that might inform developmental regulation of primate FOXP2 specificity in L4, we performed immunohistochemistry on frontal cortices from fetal, perinatal, and adult humans, and observed FOXP2-immunopositive nuclei in L5 and L6 (fig. S20B) across all analyzed developmental periods. However, human L4 FOXP2 immunoreactivity did not emerge until after 10 days postnatal (fig. S20B), suggesting that FOXP2 is expressed well after L4 neurons have reached their laminar position and myelination and synaptogenesis are at their peaks (*42*). This suggests that FOXP2 is likely controlled by transcriptional programs that differ from those controlling *FOXP2* expression in L5 and L6 excitatory neurons.

Shared and cell type–specific *FOXP2* regulatory mechanisms

To identify possible regulatory mechanisms and the functional significance underlying the cell type- and species-specific *FOXP2* expression patterns, we next performed sn-multiome

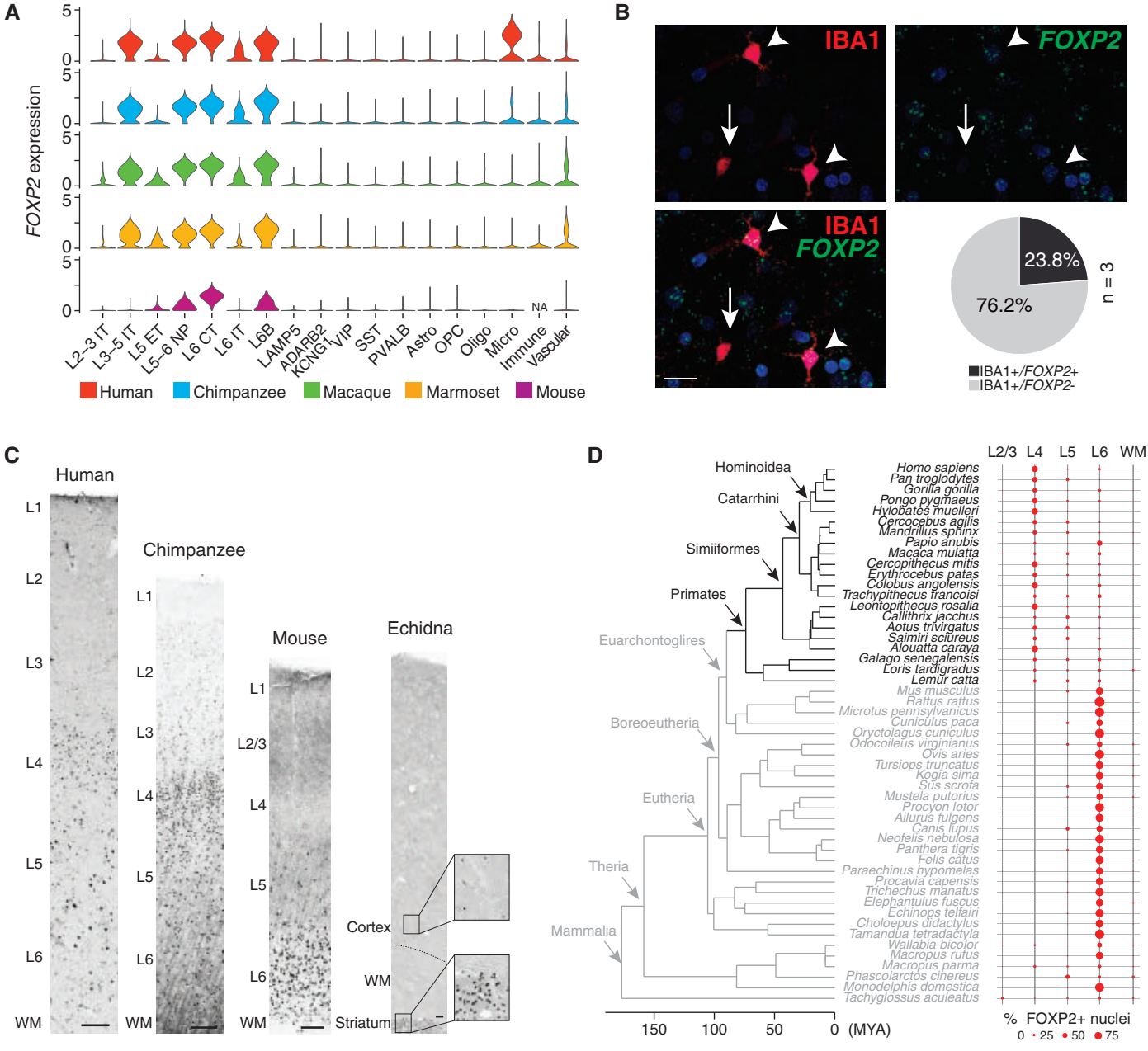


Fig. 6. Species- and cell type-specific expression of FOXP2. (**A**) Violin plots of *FOXP2* expression across all subclasses in the four primates and mouse neocortex (*17*). (**B**) Immunofluorescent staining against IBA1 (red) combined with RNA in situ hybridization for *FOXP2* RNA (green) in L6 of human dlPFC. Arrowheads indicate *FOXP2*+/IBA1+ microglia, whereas the arrow indicates *FOXP2*-/IBA1+ microglia. The pie chart summarizes the proportion of *FOXP2*-expressing cells among IBA1-immunopositive cells. Nuclei are stained with 4′,6-diamidino-2-phenylindole (DAPI) (blue). Scale bar, 20 μm. (**C**) Representative images of FOXP2 immunohistochemistry throughout cortical columns in human, chimpanzee, mouse, and echidna. The position of layers and white matter (WM) are indicated. Insets for echidna highlight numerous FOXP2-immunopositive nuclei in the striatum and scarce FOXP2-immunopositive nuclei in the deep neocortical layers. Scale bars, 100 μm for all species. (**D**) Phylogeny dendrogram of the 51 mammals and their corresponding laminar distribution of FOXP2-immunopositive nuclei.

(snATAC-seq and snRNA-seq), profiling chromatin accessibility and gene expression simultaneously on the dlPFC of five additional neurotypical male and female adult human donors (table S1). Following stringent quality control we obtained transcriptome data from 56,938 nuclei and chromatin accessibility data from 41,591 nuclei (fig. S21, A and B). With the human snRNA-seq data as the reference we were able to define the same cell subclasses that were similarly distributed across donors (fig. S21B).

Through investigation of chromatin accessibility and physical contacts (*43*) in microglia from the sn-multiome data and multiple independent studies, we found that one cis-regulatory element topologically interacted with *FOXP2* and was exclusive to microglia (fig. S21, C to D). Similarly, using the sn-multiome data we identified several cis-regulatory elements proximal to *FOXP2* selectively enriched in L3-5 intratelencephalic excitatory neurons (fig. S21D and table S4).

By integrating the DNA coaccessibility and gene coexpression, we constructed gene regulatory networks connecting upstream regulators that positively regulate *FOXP2* as well

as downstream targets that are either positively or negatively regulated by *FOXP2*, in each of the *FOXP2*-expressing subclasses (fig. S22A and table S5). Whereas the upstream regulators scarcely overlap between subclasses, the downstream targets are substantially shared among excitatory neuron subclasses (fig. S22, B and C). This analysis highlighted *NFIA*, a previously reported *FOXP2* cofactor (*44*) having both upstream and downstream regulatory roles in L5-6 non-intratelencephalic excitatory neurons (fig. S22C). Furthermore, *DSCAM*, which is implicated in Down syndrome, was predicted to be positively regulated by *FOXP2* in microglia and exhibited human-specific expression in microglia as well (fig. S22, C and D). Several genes (*PHLDB2*, *PLCH1*, and *IL1RAPL2*), which are positively regulated by *FOXP2* in L3-5 intratelencephalic excitatory neurons, also displayed primate-specific expression in these neurons compared to mice (fig. S22, C and D). Among these targets, *IL1RAPL2* has been reported to play a key role in dendritic spine formation (*45*). Using an independent algorithm identifying the *FOXP2*-related regulon (a module consisting of a transcription factor and its targets) across all cell subclasses rather than in a subclass–wise manner, we found that the *FOXP2*-regulon ranked as the top regulon of those specific to L3-5 intratelencephalic neurons (fig. S22, E and F). This suggests a central role for *FOXP2* in the transcriptional regulation in L3-5 intratelencephalic excitatory neurons (fig. S22G).

To validate the downstream targets in excitatory neurons independently, we electroporated either *GFP* or *FOXP2* (human or mouse sequence) into the ventricular walls of fetal mice (embryonic day 14.5), followed by RNA-seq analysis of neocortices at postnatal day 7. From this we were able to validate several targets positively regulated by FOXP2, including *PHLDB2*, *CALCRL*, *CNR1*, and *CALD1* as well as *SHISA6*, which is negatively regulated by FOXP2 (fig. S22C and table S7). Taken together, our results highlight cellular, phylogenetic, and developmental features in the cortical expression pattern of FOXP2 as well as potential regulatory mechanisms that might underlie its functional relevance to speech, language, and multiple neuropsychiatric disorders.

Certain brain disorder risk genes exhibit cell type- and species-specific expression

The species-divergent expression of the neuropsychiatric disease risk gene *FOXP2* prompted us to characterize the expression of 906 genes previously associated with 12 major brain disorders systematically in this setting (materials and methods). By calculating the coefficients of variation of gene expression across species we found that the risk genes of many disorders such as ASD, developmental delay disorder, and epilepsy are more conserved than background genes (fig. S23A). Based on gene expression conservation these genes were parcellated into conserved (320 genes, 35%) or divergent (586 genes, 65%) categories (fig. S23B), followed by coexpression network analysis within each category to group these genes into different modules. In the divergent category, we identified multiple modules exhibiting phylogenetic group- or species-specific (including human-specific) patterns (fig. S23C and table S8). For example, two Parkinson's disease risk genes (*GBA* and *GOSR2*, module 22) that regulate the degradation and secretion of alpha-synuclein displayed Hominini-enriched expression in a subset of excitatory neuron and inhibitory neuron subclasses (fig. S23D).

To gain a more detailed view into the cell type-specific expression of the 586 genes with species-divergent expressions we performed differential expression analysis across subclasses. Of those genes, 157 (27%) exhibited subclass- and species-specific expression patterns (table S9). These are exemplified by the multiple sclerosis risk gene *MERTK*, enriched in human L3-5 IT excitatory neurons, and the ASD risk gene *CACNA1D*, enriched in human microglia. *MERTK* showed conserved expression in microglia, consistent with its known function in myelination equilibrium regulation by modulating microglia activities (fig. S23F). However, its human-specific expression in L3-5 intratelencephalic neurons suggests an uncharacterized role in human excitatory neurons. Similarly, the ASD risk gene *NR4A2*, which encodes a transcription factor, exhibited human-specific expression in smooth muscle cells (fig. S23, E and F), suggesting possible reorganization of transcriptional regulation in anthropoids.

Conclusions

We generated a comprehensive transcriptomic survey of dlPFC neuronal, glial, and non-neural cells in the most commonly studied anthropoid primates. We also revealed and characterized species differences in transcriptomic profiles, composition, and diversity of cell types, including those associated with evolutionary specializations and functionality of dlPFC.

Although most cell subtypes are shared across the four species studied we identified 5 species-specific subtypes. These subtypes showed balanced proportions in all donors of a given species and some were detected in independent studies, corroborating the robustness of identifying cellular differences across species. Nevertheless, detection of a subtype in a subset of species does not necessarily implicates species-specificity but alternatively could represent potential differences in cell type abundance or individual variability across species. To address this we performed marker gene enrichment and in situ hybridization (figs. S4 to S7) and revealed that even in species where we did not detect a cell subtype, rare cells expressing markers of those subtypes may exist. Although such results still substantiated species differences, species-specificity can be better resolved by profiling more cells and donors. Alternatively, species specificity might represent different cell states of homologous subtypes, and their species-specific presence could be associated with differences in living environments and lifestyles between these species. This might associate with baseline inflammation differences across species, which is particularly important for immune populations such as microglia and astrocytes.

Furthermore, we found that certain genes associated with key biological pathways exhibited cell type- and species-specific expression differences, featured by the switch of SST and TH expression in a subset of human inhibitory neurons. A possible mechanism underlying the posttranscriptional regulation of *SST* expression is that mRNA sequence changes lead to gain or loss of regulation from ribosome-binding proteins. Consistent with this, SST protein sequence changes are highly conserved in primates and the mRNA sequences included one nonsynonymous mutation specific to humans and multiple other synonymous mutations specific to apes (fig. S15, G to J).

These putative dopaminergic interneurons have been previously described (*32*) but their molecular characterization and developmental origin have remained unknown. Our study demonstrated that these interneurons express *SST* as well as other key genes that are essential for dopaminergic function and likely originate in the medial ganglionic eminence. Notably, it has been reported that humans—as well as other great apes—have an enrichment of dopaminergic afferents in the prefrontal cortex (*33*) and our results suggest that humans have an extra population of dopaminergic interneurons in these cortical areas. This potential increase in dopamine levels might have functional relevance for the evolution of human cognitive abilities and behavior (*46*).

In addition, notable molecular differences across species were unveiled in many neuropsychiatric disease risk genes, exemplified by human-specific *FOXP2* expression in microglia and primate-specific *FOXP2* expression in L4 excitatory neurons. Although such expression patterns are associated with cell type-specific cis-regulatory elements, future studies are needed to determine their species specificity. As a transcription factor, the species-specific expression of FOXP2 also leads to species-specific transcriptional changes in the L4 excitatory neurons or microglia (fig. S22), including upregulation of *IL1RAPL2* involved in dendritic spine formation and *DSCAM* implicated in Down syndrome. Together, our results demonstrated this data as a resource for future studies in selecting primate models or

developing human-specific platforms to model diseases.

Materials and methods summary

In the snRNA-seq experiment, the brain cell nuclei were isolated according to our previous protocol (*10*, *13*, *41*) and the following nuclei capture and library preparation were conducted using Chromium Single Cell 3, Solution v3. The snRNA-seq reads were preprocessed with CellRanger using the consensus genome built in this study based on reciprocal exon liftOver. Doublet removal was carried out using scrublet (*47*) and custom AUCell-based (*48*) doublet detection scripts. Downstream batch correction, dimension reduction and cell clustering were performed via Seurat (*49*). Cell subtype separability was measured based on AUROC scores evaluating cell type identity prediction in downsampled data where one donor was randomly removed. Detection of cell type markers and species-specific genes were realized using Wilcoxon Rank Sum test. Cell cluster identity annotation was based on marker gene expression and transcriptomic comparisons with multiple published data sets (*16*–*24*).

In assessing the global cellular and transcriptomic changes across species, AUCell-based (*48*) cell type marker enrichment was used to evaluate species-specificity of the detected species-specific subtypes. Cell subtype abundance comparisons were carried out using the scCODA algorithm (*50*), transcriptomic heterogeneity assessment was calculated via custom scripts based on Shannon entropy, and transcriptomic divergence was defined as the Pearson correlation coefficients subtracted from 1.

In the sn-multiome experiment, the brain cell nuclei isolation is a comparable modification of our previous protocol (*10*, *13*, *41*) followed by library construction using Chromium Single Cell Multiome ATAC + Gene Expression (10x Genomics PN 1000283). The sn-multiome data was preprocessed with CellRanger and MACS2 (*51*) followed by downstream filtering and dimension reduction using Seurat and Signac (*49*, *52*). Cell type annotation was achieved via the label transfer algorithms in Seurat using the human snRNA-seq data as the reference. Detection of differentially accessible peaks was performed using the logistic regression implemented in Seurat. *FOXP2* regulatory networks were constructed via scanpy (*53*), cicero (*54*), CellOracle (*55*) and pySCENIC (*56*) by integrating the DNA coaccessibility and gene coexpression information.

In the mouse in utero electroporation experiment, either FOXP2 or GFP was electroporated into embryonic day 14.5 mice ventricular walls and RNA-seq was performed on neocortices at postnatal day 7. Analysis of the RNA-seq data included reads alignment via STAR (*57*), reads counting via HTSeq (*58*) and differential gene expression via DESeq2 (*59*).

In analysis of FOXP2 cortical expression across species, immunohistochemistry for FOXP2 was conducted in 21 primate and 30 nonprimate mammals with subsequent quantification of FOXP2 laminar distribution.

In the validation of species-specific subtypes, RNA in situ hybridization was performed with RNAscope on human, chimpanzee, and marmoset dorsolateral prefrontal cortices with probes targeting *LAMP5* and *CD8A*, *CUX2* and *PRLR*, or *AQP4* and *CHI3L1*.

In characterization of SST expression in TH-expressing interneurons across species, immunohistochemistry of TH and SST was performed in human, chimpanzee, macaque, and marmoset dorsolateral prefrontal cortices and the percentage of SST+/TH+ interneurons was quantified. RNA in situ hybridization with *SST* probe was combined with immunohistochemistry of TH and SST protein in human dorsolateral prefrontal cortices utilizing RNAscope codetection.

REFERENCES AND NOTES

1. H. Barbas, General cortical and special prefrontal connections: Principles from structure to function. *Annu. Rev. Neurosci.* **38**, 269–289 (2015). doi: 10.1146/annurev-neuro-071714-033936; pmid: 25897871
2. T. M. Preuss, S. P. Wise, Evolution of prefrontal cortex. *Neuropsychopharmacology* **47**, 3–19 (2022). doi: 10.1038/s41386-021-01076-5; pmid: 34363014
3. K. Semendeferi, A. Lu, N. Schenker, H. Damasio, Humans and great apes share a large frontal cortex. *Nat. Neurosci.* **5**, 272–276 (2002). doi: 10.1038/nn814; pmid: 11850633
4. P. T. Schoenemann, M. J. Sheehan, L. D. Glotzer, Prefrontal white matter volume is disproportionately larger in humans than in other primates. *Nat. Neurosci.* **8**, 242–252 (2005). doi: 10.1038/nn1394; pmid: 15665874
5. J. B. Smaers, A. Gómez-Robles, A. N. Parks, C. C. Sherwood, Exceptional Evolutionary Expansion of Prefrontal Cortex in Great Apes and Humans. *Curr. Biol.* **27**, 714–720 (2017). doi: 10.1016/j.cub.2017.01.020; pmid: 28162899
6. C. J. Donahue, M. F. Glasser, T. M. Preuss, J. K. Rilling, D. C. Van Essen, Quantitative assessment of prefrontal cortex in humans relative to nonhuman primates. *Proc. Natl. Acad. Sci. U.S.A.* **115**, E5183–E5192 (2018). doi: 10.1073/pnas.1721653115; pmid: 29739891
7. R. Cools, A. F. T. Arnsten, Neuromodulation of prefrontal cortex cognitive function in primates: The powerful roles of monoamines and acetylcholine. *Neuropsychopharmacology* **47**, 309–328 (2022). doi: 10.1038/s41386-021-01100-8; pmid: 34312496
8. D. A. Lewis, K. Mirnics, Transcriptome alterations in schizophrenia: Disturbing the functional architecture of the dorsolateral prefrontal cortex. *Prog. Brain Res.* **158**, 141–152 (2006). doi: 10.1016/S0079-6123(06)58007-0; pmid: 17027695
9. J. C. Izpisua Belmonte *et al.*, Brains, genes, and primates. *Neuron* **86**, 617–631 (2015). doi: 10.1016/j.neuron.2015.03.021; pmid: 25950631
10. M. Li *et al.*, Integrative functional genomic analysis of human brain development and neuropsychiatric risks. *Science* **362**, eaat7615 (2018). doi: 10.1126/science.aat7615; pmid: 30545854
11. H. Mathys *et al.*, Single-cell transcriptomic analysis of Alzheimer's disease. *Nature* **570**, 332–337 (2019). doi: 10.1038/s41586-019-1195-2; pmid: 31042697
12. F. M. Krienen *et al.*, Innovations present in the primate interneuron repertoire. *Nature* **586**, 262–269 (2020). doi: 10.1038/s41586-020-2781-z; pmid: 32999462
13. Y. Zhu *et al.*, Spatiotemporal transcriptomic divergence across human and macaque brain development. *Science* **362**, eaat8077 (2018). doi: 10.1126/science.aat8077; pmid: 30545855
14. S. Kanton *et al.*, Organoid single-cell genomic atlas uncovers human-specific features of brain development. *Nature* **574**, 418–422 (2019). doi: 10.1038/s41586-019-1654-9; pmid: 31619793
15. B. B. Lake *et al.*, Neuronal subtypes and diversity revealed by single-nucleus RNA sequencing of the human brain. *Science* **352**, 1586–1590 (2016). doi: 10.1126/science.aaf1204; pmid: 27339989
16. R. D. Hodge *et al.*, Conserved cell types with divergent features in human versus mouse cortex. *Nature* **573**, 61–68 (2019). doi: 10.1038/s41586-019-1506-7; pmid: 31435019
17. B. Tasic *et al.*, Shared and distinct transcriptomic cell types across neocortical areas. *Nature* **563**, 72–78 (2018). doi: 10.1038/s41586-018-0654-5; pmid: 30382198
18. K. R. Maynard *et al.*, Transcriptome-scale spatial gene expression in the human dorsolateral prefrontal cortex. *Nat. Neurosci.* **24**, 425–436 (2021). doi: 10.1038/s41593-020-00787-0; pmid: 33558695
19. D. Mi *et al.*, Early emergence of cortical interneuron diversity in the mouse embryo. *Science* **360**, 81–85 (2018). doi: 10.1126/science.aar6821; pmid: 29472441
20. C. Mayer *et al.*, Developmental diversification of cortical inhibitory interneurons. *Nature* **555**, 457–462 (2018). doi: 10.1038/nature25999; pmid: 29513653
21. S. Marques *et al.*, Oligodendrocyte heterogeneity in the mouse juvenile and adult central nervous system. *Science* **352**, 1326–1329 (2016). doi: 10.1126/science.aaf6463; pmid: 27284195
22. T. E. Bakken *et al.*, Comparative cellular analysis of motor cortex in human, marmoset and mouse. *Nature* **598**, 111–119 (2021). doi: 10.1038/s41586-021-03465-8; pmid: 34616062
23. J. Kalucka *et al.*, Single-Cell Transcriptome Atlas of Murine Endothelial Cells. *Cell* **180**, 764–779.e20 (2020). doi: 10.1016/j.cell.2020.01.015; pmid: 32059779
24. M. Vanlandewijck *et al.*, A molecular atlas of cell types and zonation in the brain vasculature. *Nature* **554**, 475–480 (2018). doi: 10.1038/nature25739; pmid: 29443965
25. L. Geirsdottir *et al.*, Cross-Species Single-Cell Analysis Reveals Divergence of the Primate Microglia Program. *Cell* **179**, 1609–1622.e1616 (2019). doi: 10.1038/nature25739; pmid: 29443965
26. J. J. Hutsler, D. G. Lee, K. K. Porter, Comparative analysis of cortical layering and supragranular layer enlargement in rodent carnivore and primate species. *Brain Res.* **1052**, 71–81 (2005). doi: 10.1016/j.brainres.2005.06.015; pmid: 16018988
27. W. G. Pembroke, C. L. Hartl, D. H. Geschwind, Evolutionary conservation and divergence of the human brain transcriptome. *Genome Biol.* **22**, 52 (2021). doi: 10.1186/s13059-020-02257-z; pmid: 33514394
28. S. Berto *et al.*, Accelerated evolution of oligodendrocytes in the human brain. *Proc. Natl. Acad. Sci. U.S.A.* **116**, 24334–24342 (2019). doi: 10.1073/pnas.1907982116; pmid: 31712436
29. M. Shibata *et al.*, Regulation of prefrontal patterning and connectivity by retinoic acid. *Nature* **598**, 483–488 (2021). doi: 10.1038/s41586-021-03953-x; pmid: 34599305
30. M. Shibata *et al.*, Hominini-specific regulation of CBLN2 increases prefrontal spinogenesis. *Nature* **598**, 489–494 (2021). doi: 10.1038/s41586-021-03952-y; pmid: 34599306
31. Y. Shi *et al.*, Mouse and human share conserved transcriptional programs for interneuron development. *Science* **374**, eabj6641 (2021). doi: 10.1126/science.abj6641; pmid: 34882453
32. A. M. M. Sousa *et al.*, Molecular and cellular reorganization of neural circuits in the human lineage. *Science* **358**, 1027–1032 (2017). doi: 10.1126/science.aan3456; pmid: 29170230
33. M. A. Raghanti *et al.*, Species-specific distributions of tyrosine hydroxylase-immunoreactive neurons in the prefrontal cortex of anthropoid primates. *Neuroscience* **158**, 1551–1559 (2009). doi: 10.1016/j.neuroscience.2008.10.058; pmid: 19041377
34. D. Dulcis, P. Jamshidi, S. Leutgeb, N. C. Spitzer, Neurotransmitter switching in the adult brain regulates behavior. *Science* **340**, 449–453 (2013). doi: 10.1126/science.1234152; pmid: 23620046
35. M. Kajiwara, T. Ban, K. Matsubara, Y. Nakanishi, S. Masuda, Urinary Dopamine as a Potential Index of the Transport Activity of Multidrug and Toxin Extrusion in the Kidney. *Int. J. Mol. Sci.* **17**, 1228 (2016). doi: 10.3390/ijms17081228; pmid: 27483254
36. L. Ben Haim, D. H. Rowitch, Functional diversity of astrocytes in neural circuit regulation. *Nat. Rev. Neurosci.* **18**, 31–41 (2017). doi: 10.1038/nrn.2016.159; pmid: 27904142
37. M. W. Salter, B. Stevens, Microglia emerge as central players in brain disease. *Nat. Med.* **23**, 1018–1027 (2017). doi: 10.1038/nm.4397; pmid: 28886007
38. L. Kracht *et al.*, Human fetal microglia acquire homeostatic immune-sensing properties early in development. *Science* **369**, 530–537 (2020). doi: 10.1126/science.aba5906; pmid: 32732419

39. C. S. Lai, S. E. Fisher, J. A. Hurst, F. Vargha-Khadem, A. P. Monaco, A forkhead-domain gene is mutated in a severe speech and language disorder. *Nature* **413**, 519–523 (2001). doi: 10.1038/35097076; pmid: 11586359
40. R. J. Ferland, T. J. Cherry, P. O. Preware, E. E. Morrisey, C. A. Walsh, Characterization of Foxp2 and Foxp1 mRNA and protein in the developing and mature brain. *J. Comp. Neurol.* **460**, 266–279 (2003). doi: 10.1002/cne.10654; pmid: 12687690
41. D. Franjic *et al*., Transcriptomic taxonomy and neurogenic trajectories of adult human, macaque, and pig hippocampal and entorhinal cells. *Neuron* **110**, 452–469.e14 (2022). doi: 10.1016/j.neuron.2021.10.036; pmid: 34798047
42. J. C. Silbereis, S. Pochareddy, Y. Zhu, M. Li, N. Sestan, The Cellular and Molecular Landscapes of the Developing Human Central Nervous System. *Neuron* **89**, 248–268 (2016). doi: 10.1016/j.neuron.2015.12.008; pmid: 26796689
43. A. Nott *et al*., Brain cell type-specific enhancer-promoter interactome maps and disease-risk association. *Science* **366**, 1134–1139 (2019). doi: 10.1126/science.aay0793; pmid: 31727856
44. S. L. Hickey, S. Berto, G. Konopka, Chromatin Decondensation by FOXP2 Promotes Human Neuron Maturation and Expression of Neurodevelopmental Disease Genes. *Cell Rep* **27**, 1699–1711. e1699 (2019). doi: 10.1016/j.celrep.2019.04.044
45. P. Valnegri *et al*., The X-linked intellectual disability protein IL1RAPL1 regulates excitatory synapse formation by binding PTPδ and RhoGAP2. *Hum. Mol. Genet.* **20**, 4797–4809 (2011). doi: 10.1093/hmg/ddr418; pmid: 21926414
46. M. A. Raghanti *et al*., A neurochemical hypothesis for the origin of hominids. *Proc. Natl. Acad. Sci. U.S.A.* **115**, E1108–E1116 (2018). doi: 10.1073/pnas.1719666115; pmid: 29358369
47. S. L. Wolock, R. Lopez, A. M. Klein, Scrublet: Computational Identification of Cell Doublets in Single-Cell Transcriptomic Data. *Cell Syst.* **8**, 281–291.e9 (2019). doi: 10.1016/j.cels.2018.11.005; pmid: 30954476
48. S. Aibar *et al*., SCENIC: Single-cell regulatory network inference and clustering. *Nat. Methods* **14**, 1083–1086 (2017). doi: 10.1038/nmeth.4463; pmid: 28991892
49. T. Stuart *et al*., Comprehensive Integration of Single-Cell Data. *Cell* **177**, 1888–1902.e1821 (2019). doi: 10.1038/nmeth.4463; pmid: 28991892
50. M. Büttner, J. Ostner, C. L. Müller, F. J. Theis, B. Schubert, scCODA is a Bayesian model for compositional single-cell data analysis. *Nat. Commun.* **12**, 6876 (2021). doi: 10.1038/s41467-021-27150-6; pmid: 34824236
51. Y. Zhang *et al*., Model-based analysis of ChIP-Seq (MACS). *Genome Biol.* **9**, R137 (2008). doi: 10.1186/gb-2008-9-9-r137; pmid: 18798982
52. T. Stuart, A. Srivastava, S. Madad, C. A. Lareau, R. Satija, Single-cell chromatin state analysis with Signac. *Nat. Methods* **18**, 1333–1341 (2021). doi: 10.1038/s41592-021-01282-5; pmid: 34725479
53. F. A. Wolf, P. Angerer, F. J. Theis, SCANPY: Large-scale single-cell gene expression data analysis. *Genome Biol.* **19**, 15 (2018). doi: 10.1186/s13059-017-1382-0; pmid: 29409532
54. H. A. Pliner *et al*., Cicero Predicts cis-Regulatory DNA Interactions from Single-Cell Chromatin Accessibility Data. *Mol. Cell* **71**, 858–871.e8 (2018). doi: 10.1016/j.molcel.2018.06.044; pmid: 30078726
55. K. Kamimoto, C. M. Hoffmann, S. A. Morris, CellOracle: Dissecting cell identity via network inference and in silico gene perturbation. bioRxiv 2020.2002.2017.947416 [Preprint] (2020); doi: 10.1101/2020.02.17.947416
56. B. Van de Sande *et al*., A scalable SCENIC workflow for single-cell gene regulatory network analysis. *Nat. Protoc.* **15**, 2247–2276 (2020). doi: 10.1038/s41596-020-0336-2; pmid: 32561888
57. A. Dobin *et al*., STAR: Ultrafast universal RNA-seq aligner. *Bioinformatics* **29**, 15–21 (2013). doi: 10.1093/bioinformatics/bts635; pmid: 23104886
58. S. Anders, P. T. Pyl, W. Huber, HTSeq—A Python framework to work with high-throughput sequencing data. *Bioinformatics* **31**, 166–169 (2015). doi: 10.1093/bioinformatics/btu638; pmid: 25260700
59. M. I. Love, W. Huber, S. Anders, Moderated estimation of fold change and dispersion for RNA-seq data with DESeq2. *Genome Biol.* **15**, 550 (2014). doi: 10.1186/s13059-014-0550-8; pmid: 25516281
60. S. Ma *et al*., Molecular and cellular changes underlying evolutionary specializations of the primate dorsolateral prefrontal cortex, Version 1, Zenodo (2022); doi: 10.5281/zenodo.6824097

ACKNOWLEDGMENTS

We thank S. Wilson for assistance with tissue acquisition and processing, R. Chen and M. Shibata for assistance with immunostaining, and A. Cherskov and lab colleagues for comments. We also thank the Traumatic Stress Brain Research Group for tissue acquisition. **Funding:** This work was funded by the following: Medical Scientist Training Program grant T32 GM140935 (to R.D.R.); NINDS Ruth L. Kirschstein National Research Service Award: F32NS117780 (to R.K.); Agencia Estatal de Investigación (AEI) Spain grant PRE2020-093064 (to X.D.M.); Institutional Ruth L. Kirschstein National Research Service Award: T32 GM141013 (to Z.G.-S.); National Institute on Aging R56 AG059284 (to M.D.); National Primate Research Centers P51 OD011133 (to M.D.); National Institutes of Health grants NS092988 and HG011641 (to C.C.S.); National Science Foundation EF-2021785 (to C.C.S.); Instituto de Salud Carlos III Spain and European Social Fund grant MS20/00064 (to G.S.); Agencia Estatal de Investigación (AEI) Spain grant PID2019-104700GA-I00 (to G.S.); National Institutes of Health grant R01HG010898-01 (to G.S. and N.S.); National Institutes of Health grant U01AG058608, R01AG066165 and P30 AG066508 (to S.M.S.); NARSAD Young Investigator Grant from the Brain and Behavior Research Foundation 28721 (to A.M.M.S.); National Institute of Child Health and Human Development core grant P50HD105353 (Waisman Center); National Institutes of Health grant U01MH124619, U01MH116488, and U01 DA053628 (to N.S.)
Author contributions: S.M., M.S., A.M.M.S., and N.S. conceived and designed the study. M.S., A.M.M.S., L.T., A.G.B., J.H.-L., M.D., J.B., P.R.H., C.C.S., and N.S. collected and processed the tissue specimens and dissected the samples for analyses. M.S. performed the snRNA-seq and sn-multiome experiments. S.M., Q.L., and C.X. analyzed the snRNA-seq data. S.M. and D.L. analyzed the sn-multiome data. R.D.R., D.K.S., Z.G.-S., A.D., and C.J.H. performed RNA in situ hybridization validating species-specific subtypes. Z.K., M.R., A.T.N.T., R.K., R.D.R., Z.G.-S., A.D. and C.Q. conducted *FOXP2* immunohistochemistry and in situ hybridization. A.T.N.T. generated the mouse in utero electroporation RNA-seq data and S.M. and Q.L. analyzed the data. X.M.-B., S.M., X.D.M., X. M.-P., and G.S. performed additional *FOXP2* analysis. R.D.R., D.K.S., A.D., and A.M.M.S. conducted *SST* and *TH* experiments. V.L., A.K., and S.M. analyzed *SST* sequence evolution. S.M., M.S., A.M.M.S., Q.L., C.X., R.K., D.K.S., Z.G.-S., K.T.G., S.P., J.S., L.T., A.G.B., J.H.-L., J.J.E., E.W.D., D.M., M.D., O.M., P.R.H., J.B., C.C.S., G.S., M.J.G., and S.M.S. contributed to additional data collection and interpretation. S.M., M.S., A.M.M.S., and N.S. wrote the manuscript. All authors edited the manuscript.
Competing interests: The authors declare that they have no competing interests. **Data and materials availability:** The PFC snRNA-seq data were deposited in the NEMO Archive (RRID: SCR_002001) under identifier nemo:dat-zkgd0it accessible at https://assets.nemoarchive.org/dat-zkgd0it. The data can also be interactively visualized at http://resources.sestanlab.org/PFC. The human PFC sn-multiome data were deposited at NCBI GEO under the accession number: GSE207334. The mouse in utero electroporation RNA-seq data were deposited at NCBI GEO under the accession number: GSE206994. Scripts used in this study are available at Github repository: https://github.com/sestanlab/Cross-species-PFC-snRNA-seq and at Zenodo (*60*). All other data are available in the main paper or supplement.
License information: Copyright © 2022 the authors, some rights reserved; exclusive licensee American Association for the Advancement of Science. No claim to original US government works. https://www.sciencemag.org/about/science-licenses-journal-article-reuse

SUPPLEMENTARY MATERIALS

science.org/doi/10.1126/science.abo7257
Materials and Methods
Figs. S1 to S23
Tables S1 to S10
MDAR Reproducibility Checklist
References (*61*–*124*)

Submitted 22 February 2022; accepted 9 August 2022
Published online 25 August 2022
10.1126/science.abo7257

Your Legacy to Science

AN ESTATE GIFT TO THE
AMERICAN ASSOCIATION FOR THE ADVANCEMENT OF SCIENCE





Since 1848, our founding year, the American Association for the Advancement of Science (AAAS) has been deeply committed to advancing science, engineering and innovation around the world for the benefit of all people.

By making AAAS a beneficiary of your will, trust, retirement plan or life insurance policy, you become a member of our 1848 Society, joining Thomas Edison, Alexander Graham Bell and the many distinguished individuals whose vision led to the creation of AAAS and our world-renowned journal, *Science*, so many years ago.

Unlike many of its peers, *Science* is not for-profit. Your estate gift would provide long-term financial stability and durable annual income that will support operations and competitive innovation for years to come. **This support is vital.**

"As a teacher and instructor, I bear responsibility for the younger generations. If you have extra resources, concentrate them on organizations, like AAAS, that are doing work for all."

—Prof. Elisabeth Ervin-Blankenheim, 1848 Society member

If you intend to include AAAS in your estate plans, provide this information to your lawyer or financial adviser:

Legal Name: American Association for the Advancement of Science
Federal Tax ID Number: 53-0196568
Address: 1200 New York Avenue, NW, Washington, DC 20005

If you would like more information on making an estate gift to AAAS, cut out and return the form below or send an email to philanthropy@aaas.org. Additional details are also available online at **www.aaas.org/1848Society**.

1848 SOCIETY AAAS

cut here

Yes, I would like more information about joining the AAAS 1848 Society.

PLEASE CONTACT ME AT:

Name: _____

Address: _____

City: _____ State: _____ Zip code: _____ Country: _____

Email: _____ Phone: _____

RETURN THIS FORM TO:
AAAS Office of Philanthropy and Strategic Partnerships • 1200 New York Avenue, NW • Washington, DC 20005 USA

RESEARCH ARTICLE SUMMARY

MARTIAN GEOLOGY

Aqueously altered igneous rocks sampled on the floor of Jezero crater, Mars

K. A. Farley *et al.*

INTRODUCTION: The Perseverance rover landed in Jezero crater on Mars on 18 February 2021 with three scientific objectives: to explore the geologic setting of the crater, to identify ancient habitable environments and assess the possibility of past martian life, and to collect samples for potential transport to Earth for analysis in laboratories. In the 290 martian days (sols) after landing, Perseverance explored rocks of the Jezero crater floor.

RATIONALE: Jezero, a 45-km-diameter crater, was selected for investigation by Perseverance because orbital observations had shown that it previously contained an open-system lake, prior to ~3.5 billion years ago. Major climate change then left Mars in its current cold and dry state. On Earth, broadly similar environments of similar age to Jezero contain evidence of microbial life. Jezero crater contains a well-preserved delta, identified as a target for astrobiological investigation by the rover. Perseverance landed ~2 km away from the delta, on rocks of the crater floor. Previously proposed origins for these rocks have ranged from lake (or river) sediments to lava flows. Olivine-rich rocks identified on the crater floor, as well as in the area surrounding Jezero, have previously been attributed to a widely distributed impact melt or volcanic deposit, variably altered to carbonate. We used Perseverance to investigate the origin of the crater floor rocks and to acquire samples of them.

RESULTS: The Jezero crater floor consists of two geologic units: the informally named Máaz formation covers much of the crater floor and surrounds the other unit, which is informally named the Séítah formation. Máaz rocks display a range of morphologies: structureless boulders, flagstone-like outcrops, and ridges that are several meters high. The ridges expose prominent layers, ranging in thickness from a few centimeters to a few tens of centimeters. Rocks of Séítah are often tabular and strongly layered, with layer thicknesses ranging from centimeters to meters. Máaz and Séítah rocks display no outcrop or grain-scale evidence for transport by wind or water.

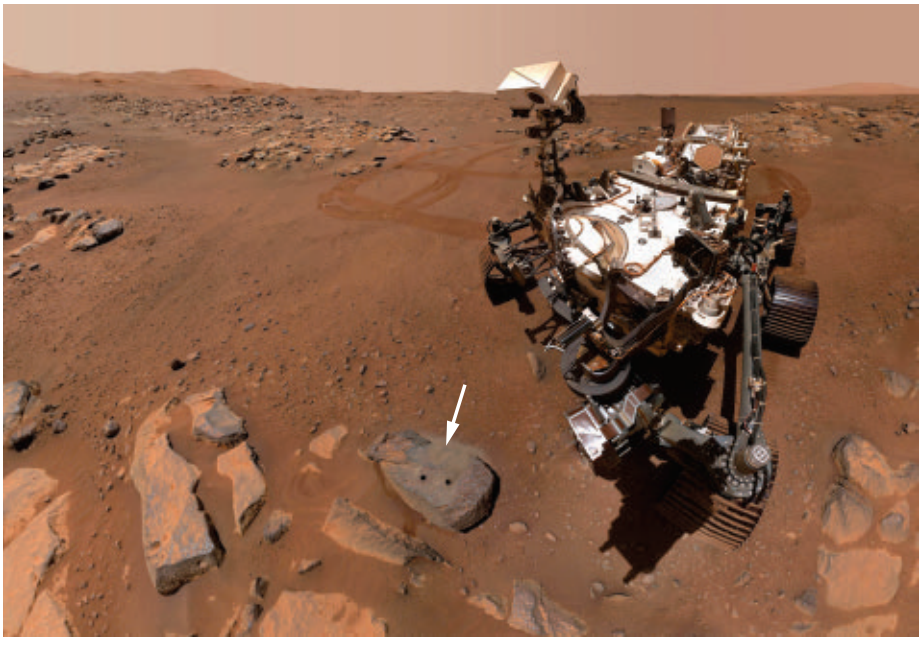
Perseverance observations show that the Máaz rocks consist of 0.5- to 1-mm interlocking crystals of pyroxene and plagioclase. Combined with bulk chemical composition measurements, this suggests Máaz is an igneous unit that cooled slowly. In contrast, most Séítah rocks are very rich in magnesium and are dominated by densely packed 2- to 3-mm-diameter crystals of olivine, surrounded by pyroxene. These properties indicate settling and accumulation of olivine near the base of a thick magma body, such as an intrusion, lava lake, or thick lava flow. Ground-penetrating radar indicates that Séítah rocks dip beneath the Máaz formation. We hypothesize that Máaz could be the magmatic complement to the Séítah olivine-rich rocks or, alternatively, Máaz could be a series of basaltic lavas that flowed over and around the older Séítah formation.

The olivines in the Séítah formation are rimmed with magnesium-iron carbonate, likely produced by interaction with CO_2-rich water. Máaz formation rocks contain an aqueously deposited iron oxide or iron silicate alteration product. Both units commonly contain patches of bright-white salts, including sodium perchlorate and various sulfate minerals. Although both rock units have been altered by water, preservation of the original igneous minerals and the absence of aluminous clay minerals indicate that the alteration occurred under low water/rock ratio and that there was little loss of soluble species to the surroundings. It remains unclear when these aqueous processes occurred and whether they relate to the lake that once filled Jezero.

The exposure of the olivine-rich Séítah rocks at the surface, the absence of lake or river sediment in the exploration area, and several nearby erosional remnant hills of delta sediment indicate that substantial crater floor erosion occurred after formation of these igneous units.

Samples of both of these geologic units were collected as drill cores. The drill cores were stored in ultraclean sample tubes, for potential transport to Earth by future missions in the early 2030s.

CONCLUSION: The floor of Jezero crater explored by Perseverance consists of two distinct igneous units that have both experienced reactions with liquid water. Multiple rock cores were collected from these units for potential transport to Earth and analysis in terrestrial laboratories. ■



Sample collection by Perseverance on Mars. This image mosaic was acquired by the WATSON camera on the rover's robot arm. Rock cores were drilled from the two holes (arrow) in an igneous rock of the Máaz formation. The 6-cm-long, 1.3-cm-diameter cores were sealed into individual sample tubes and are now stored inside the rover.

All authors and affiliations appear in the full article online.
Corresponding author. Email: kenneth.a.farley@jpl.nasa.gov
Cite this article as K. A. Farley *et al.*, *Science* 377, eabo2196 (2022). DOI: 10.1126/science.abo2196

READ THE FULL ARTICLE AT
https://doi.org/10.1126/science.abo2196

RESEARCH ARTICLE

MARTIAN GEOLOGY

Aqueously altered igneous rocks sampled on the floor of Jezero crater, Mars

K. A. Farley[1]*, K. M. Stack[2], D. L. Shuster[3], B. H. N. Horgan[4], J. A. Hurowitz[5], J. D. Tarnas[2], J. I. Simon[6], V. Z. Sun[2], E. L. Scheller[1], K. R. Moore[1], S. M. McLennan[5], P. M. Vasconcelos[7], R. C. Wiens[8]†, A. H. Treiman[9], L. E. Mayhew[10], O. Beyssac[11], T. V. Kizovski[12], N. J. Tosca[13], K. H. Williford[14], L. S. Crumpler[15], L. W. Beegle[2], J. F. Bell III[16], B. L. Ehlmann[1], Y. Liu[2], J. N. Maki[2], M. E. Schmidt[12], A. C. Allwood[2], H. E. F. Amundsen[17], R. Bhartia[18], T. Bosak[19], A. J. Brown[20], B. C. Clark[21], A. Cousin[22], O. Forni[22], T. S. J. Gabriel[23], Y. Goreva[2], S. Gupta[24], S.-E. Hamran[17], C. D. K. Herd[25], K. Hickman-Lewis[26,27], J. R. Johnson[28], L. C. Kah[29], P. B. Kelemen[30], K. B. Kinch[31], L. Mandon[32], N. Mangold[33], C. Quantin-Nataf[34], M. S. Rice[35], P. S. Russell[36], S. Sharma[2], S. Siljeström[37], A. Steele[38], R. Sullivan[39], M. Wadhwa[16], B. P. Weiss[19,2], A. J. Williams[40], B. V. Wogsland[29], P. A. Willis[2], T. A. Acosta-Maeda[41], P. Beck[42], K. Benzerara[11], S. Bernard[11], A. S. Burton[43], E. L. Cardarelli[2], B. Chide[8], E. Clavé[44], E. A. Cloutis[45], B. A. Cohen[46], A. D. Czaja[47], V. Debaille[48], E. Dehouck[34], A. G. Fairén[49,50], D. T. Flannery[51], S. Z. Fleron[52], T. Fouchet[32], J. Frydenvang[53], B. J. Garczynski[4], E. F. Gibbons[54], E. M. Hausrath[55], A. G. Hayes[50], J. Henneke[56], J. L. Jørgensen[56], E. M. Kelly[41], J. Lasue[22], S. Le Mouélic[33], J. M. Madariaga[57], S. Maurice[22], M. Merusi[31], P.-Y. Meslin[22], S. M. Milkovich[2], C. C. Million[58], R. C. Moeller[2], J. I. Núñez[28], A. M. Ollila[59], G. Paar[60], D. A. Paige[36], D. A. K. Pedersen[56], P. Pilleri[22], C. Pilorget[61,62], P. C. Pinet[22], J. W. Rice Jr.[16], C. Royer[11], V. Sautter[11], M. Schulte[63], M. A. Sephton[24], S. K. Sharma[41], S. F. Sholes[2], N. Spanovich[2], M. St. Clair[58], C. D. Tate[50], K. Uckert[2], S. J. VanBommel[64], A. G. Yanchilina[65], M.-P. Zorzano[50]

The Perseverance rover landed in Jezero crater, Mars, to investigate ancient lake and river deposits. We report observations of the crater floor, below the crater's sedimentary delta, finding that the floor consists of igneous rocks altered by water. The lowest exposed unit, informally named Séítah, is a coarsely crystalline olivine-rich rock, which accumulated at the base of a magma body. Magnesium-iron carbonates along grain boundaries indicate reactions with carbon dioxide–rich water under water-poor conditions. Overlying Séítah is a unit informally named Máaz, which we interpret as lava flows or the chemical complement to Séítah in a layered igneous body. Voids in these rocks contain sulfates and perchlorates, likely introduced by later near-surface brine evaporation. Core samples of these rocks have been stored aboard Perseverance for potential return to Earth.

The Perseverance rover, part of the Mars 2020 mission, landed on the floor of Jezero crater on 18 February 2021. Perseverance was designed to characterize the geology, investigate records of past climate, and seek evidence of possible ancient life contained in rocks laid down when martian surface conditions were more habitable than they are today (*1*). The multiyear mission is intended to select, collect, and document ~35 rock and soil samples for potential transport to Earth by future missions for laboratory analysis (*1*). We report results from the science campaign that ran until mission sol (martian day) 290, exploring the geology and geochemistry of geological units on the Jezero crater floor. These rocks, which form part of a regional stratigraphy, record an ancient period when impact cratering, volcanism, and water were actively shaping the surface of the planet.

Jezero crater, with a diameter of 45 km, lies on the western flank of Isidis, a giant impact basin of Noachian age [~4.0 billion years ago (Ga)] (*2*) and northeast of Syrtis Major, a younger shield volcano (*3*). Jezero was formed by an impact onto an early Noachian basement unit that includes Isidis impact deposits (*3*–*6*). The crater later hosted an open-basin lake, fed by a large system of river valleys that were active in the late Noachian (~3.6 to 3.8 Ga) (*7*) to early Hesperian (>3.2 Ga) (*8*). Sediments delivered by those rivers into the crater lake produced a clay and carbonate–bearing delta, which appears to be well preserved (*4*, *8*–*10*). The valleys that fed Jezero pass through a regional stratigraphy that includes an olivine-bearing unit, partially altered to carbonate (*11*, *12*), that overlies the Noachian basement. The olivine unit is in turn overlain by a low-albedo crater-retaining unit, with spectral signatures of pyroxene (*5*, *13*). Mars' three largest impact basins are each surrounded by such olivine-bearing rocks (*14*). The olivine unit on the southern and western margins of the Isidis basin is the largest contiguous olivine-rich unit on Mars, with several hypothesized origins: impact melt (*3*, *5*), extrusive or intrusive magmatism (*15*–*17*), volcanic ash fall (*18*), pyroclastic surge deposition (*19*), and detrital sedimentation (*20*).

Rock units potentially equivalent to this regional stratigraphy occur on the floor of Jezero crater (*9*, *21*). Orbital mapping of the Jezero crater interior (*21*) before landing delineated a pyroxene-bearing unit, with a high density of superposed impact craters, named Crater Floor Fractured Rough (hereafter Cf-fr), and an olivine-bearing unit named Crater Floor Fractured 1 (Cf-f-1). Perseverance directly accessed these two geologic units (Fig. 1B). The rocks of Cf-fr, informally named the Máaz formation (see supplementary text in the supplementary materials), have been interpreted to be lava flows (*9*, *22*) or sandstones deposited by flowing water or wind (*21*, *23*). Crater counting on this unit constrains the ages of Jezero crater floor rocks, but studies have yielded inconsistent age estimates ranging from 1.4 to 3.45 Ga (*9*, *22*, *24*). The spatially heterogeneous crater density on this unit (Fig. 1B) is likely the source of this age discrepancy and indicates that the Máaz formation experienced a complex history of surface exposure. Olivine-bearing rocks occur outside Jezero crater, draping across the rim, and within the crater (*9*). The olivine-bearing rocks of the Cf-f-1 unit, informally named the Séítah formation, have previously been proposed to share an origin with the regional olivine-bearing unit (*9*, *21*, *25*), possibly reworked or chemically modified by water within Jezero crater (*21*, *23*). Although the Séítah formation has been interpreted as older than the delta and its associated lake (*21*, *23*, *26*), the age of the Máaz formation relative to the delta is debated. The Máaz formation has been interpreted as one of the youngest units in the crater, postdating all delta deposition (*27*), or as substantially older, predating the delta (*21*, *23*, *28*). Much of the Séítah formation is topographically higher than the Máaz formation, but previous studies agree that it is nonetheless older (*23*, *28*).

During atmospheric entry, the Mars 2020 spacecraft's Terrain Relative Navigation system (*27*) autonomously selected the highest-probability safe landing site available, which was at 18.4447°N, 77.4508°E, between the heavily cratered Máaz terrain to the east and the abundant aeolian bedforms of the Séítah terrain to the west (Fig. 1). This location has been informally named the Octavia E. Butler landing site (OEB); it lies on a narrow strip of smooth topography, ~2 km southeast of the delta scarp and within tens of meters of the Séítah-Máaz geologic contact. Neither the cratered terrain of the Máaz formation nor the rugged sandy terrain of the Séítah formation is suitable for rover operations, but a narrow smooth strip of Máaz rocks near their contact provided a traversable pathway for the mission's first science campaign. In June 2021, after completion of hardware commissioning and demonstration flights of the

Ingenuity helicopter, the rover embarked on an out-and-back-again journey to the south and then west, with the goal of documenting the two formations. This route provided access to abundant surface exposure of Máaz rocks and more-limited exposures of Séítah bedrock, along with a scarp informally named Artuby ridge, which delimits the two units (Fig. 1C).

Rover observations

We used Perseverance to acquire colocated textural, compositional, and mineralogical maps, at both the microscopic and outcrop scale, along a 2.4-km traverse of the Jezero crater floor. Subsurface structure was imaged with a ground-penetrating radar (*29*). We characterized the natural surfaces of rock outcrops along the rover traverse using the Mastcam-Z multispectral stereo camera (*30*), the WATSON [Wide Angle Topographic Sensor for Operations and eNgineering (*31*)] microscopic camera, and the SuperCam laser-induced breakdown and visual-infrared spectrometers (*32*). These instruments are most effective when there is minimal coating of rock surfaces by dust and other materials. Removal of dust is also required for the proximity science instruments

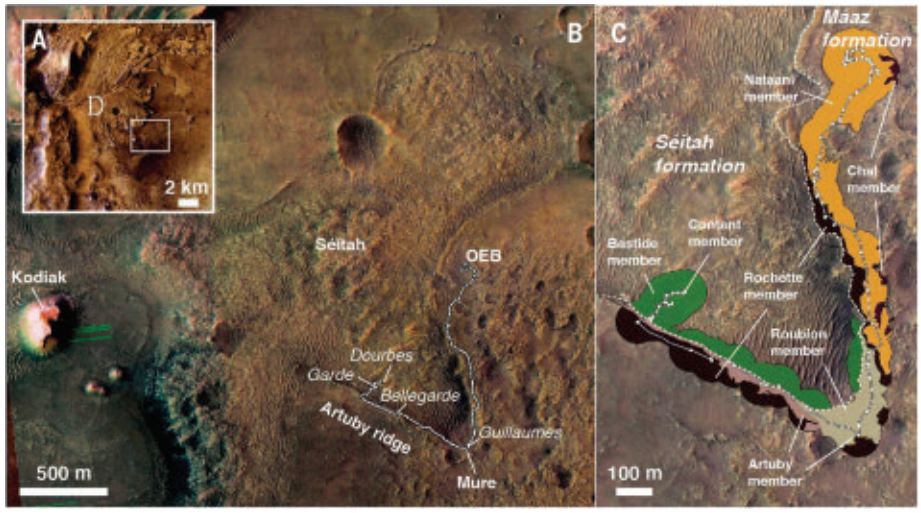


Fig. 1. Orbital images of the Jezero crater floor study area. (**A**) Mars Reconnaissance Orbiter (MRO) Context Camera (CTX) base map overlain by Mars Express High Resolution Stereo Camera color images. The study area is on the western side of Jezero crater, a few kilometers east of the delta (indicated by the letter D). (**B**) High Resolution Imaging Science Experiment (HiRISE) color image of the rover's landing site at the Octavia E. Butler landing site (OEB), and its traverse up to sol 290 (white path; each circle on the path is the end of a sol). The locations of the four abrasion patches are labeled in italics, and four landforms, Séítah, Artuby ridge, the Kodiak delta remnant (*60*), and the Mure outcrop, are labeled in roman. Séítah is characterized by abundant aeolian bedforms and northeast-southwest striking ridges. The region east and southeast of OEB is part of the Máaz formation, which exhibits high but variable impact crater density. (**C**) Enlarged portion of (B), overlain with a geologic map showing our interpreted distribution of the Séítah and Máaz formations. Colors indicate mapped distribution of formation members (labeled), and the formation contact is indicated by the dashed white line. The Content member is only visible at the point indicated. Figure S5 shows stratigraphic columns associated with this map.

[1]Division of Geological and Planetary Sciences, California Institute of Technology, Pasadena, CA 91125, USA. [2]Jet Propulsion Laboratory, California Institute of Technology, Pasadena, CA 91109, USA. [3]Department of Earth and Planetary Science, University of California, Berkeley, Berkeley, CA 94720, USA. [4]Department of Earth, Atmospheric, and Planetary Sciences, Purdue University, West Lafayette, IN 47907, USA. [5]Department of Geosciences, Stony Brook University, Stony Brook, NY 11794, USA. [6]Center for Isotope Cosmochemistry and Geochronology, Astromaterials Research and Exploration Science Division, NASA Johnson Space Center, Houston, TX 77058, USA. [7]School of Earth and Environmental Sciences, University of Queensland, Brisbane, QLD 4072, Australia. [8]Planetary Exploration Team, Los Alamos National Laboratory, Los Alamos, NM 87545, USA. [9]Lunar and Planetary Institute, Universities Space Research Association, Houston, TX 77058, USA. [10]Department of Geological Sciences, University of Colorado, Boulder, Boulder, CO 80309, USA. [11]Institut de Minéralogie, de Physique des Matériaux et de Cosmochimie, Centre National de la Recherche Scientifique, Sorbonne Université, Muséum National d'Histoire Naturelle, 75005 Paris, France. [12]Department of Earth Sciences, Brock University, St. Catharines, ON L2S 3A1, Canada. [13]Department of Earth Sciences, University of Cambridge, Cambridge CB2 3EQ, UK. [14]Blue Marble Space Institute of Science, Seattle, WA 98104, USA. [15]New Mexico Museum of Natural History and Science, Albuquerque, NM 8710, USA. [16]School of Earth and Space Exploration, Arizona State University, Tempe, AZ 85287, USA. [17]Center for Space Sensors and Systems, University of Oslo, 2007 Kjeller, Norway. [18]Photon Systems Inc., Covina, CA 91725, USA. [19]Department of Earth, Atmospheric and Planetary Sciences, Massachusetts Institute of Technology, Cambridge, MA 02139, USA. [20]Plancius Research, Severna Park, MD 21146, USA. [21]Space Science Institute, Boulder, CO 80301, USA. [22]Institut de Recherche en Astrophysique et Planétologie, Université de Toulouse 3 Paul Sabatier, Centre National de la Recherche Scientifique, Centre National d'Etude Spatiale, 31400 Toulouse, France. [23]Astrogeology Science Center, US Geological Survey, Flagstaff, AZ 86001, USA. [24]Department of Earth Sciences and Engineering, Imperial College London, London SW7 2AZ, UK. [25]Department of Earth and Atmospheric Sciences, University of Alberta, Edmonton, AB T6G 2E3, Canada. [26]Department of Earth Sciences, The Natural History Museum, London SW7 5BD, UK. [27]Dipartimento di Scienze Biologiche, Geologiche e Ambientali, Università di Bologna, 40126 Bologna, Italy. [28]Johns Hopkins University Applied Physics Laboratory, Laurel, MD 20723, USA. [29]Department of Earth and Planetary Sciences, University of Tennessee, Knoxville, TN 37996, USA. [30]Department of Earth and Environmental Sciences, Lamont Doherty Earth Observatory of Columbia University, Palisades, NY 10964, USA. [31]Niels Bohr Institute, University of Copenhagen, 1350 Copenhagen, Denmark. [32]Laboratoire d'Etudes Spatiales et d'Instrumentation en Astrophysique, Observatoire de Paris, Centre National de la Recherche Scientifique, Sorbonne Université, Université Paris Diderot, 92195 Meudon, France. [33]Laboratoire de Planétologie et Géosciences, Centre National de la Recherche Scientifique, Nantes Université, Université Angers, 44000 Nantes, France. [34]Laboratoire de Géologie de Lyon: Terre, Université de Lyon, Université Claude Bernard Lyon1, Ecole Normale Supérieure de Lyon, Université Jean Monnet Saint Etienne, Centre National de la Recherche Scientifique, 69622 Villeurbanne, France. [35]Department of Geology, Western Washington University, Bellingham, WA 98225, USA. [36]Department of Earth, Planetary, and Space Sciences, University of California, Los Angeles, Los Angeles, CA 90095, USA. [37]Department of Metrology, Textiles and Medical Technology, Research Institutes of Sweden, 11486 Stockholm, Sweden. [38]Earth and Planetary Laboratory, Carnegie Science, Washington, DC 20015, USA. [39]Cornell Center for Astrophysics and Planetary Science, Cornell University, Ithaca, NY 14853, USA. [40]Department of Geological Sciences, University of Florida, Gainesville, FL 32611, USA. [41]Hawai'i Institute of Geophysics and Planetology, University of Hawai'i at Mānoa, Honolulu, HI 96822, USA. [42]Institut de Planétologie et Astrophysique de Grenoble, Centre National de la Recherche Scientifique, Université Grenoble Alpes, 38000 Grenoble, France. [43]NASA Johnson Space Center, Houston, TX 77058, USA. [44]Centre Lasers Intenses et Applications, Centre National de la Recherche Scientifique, Commissariat à l'Energie Atomique, Université de Bordeaux, 33400 Bordeaux, France. [45]Centre for Terrestrial and Planetary Exploration, University of Winnipeg, Winnipeg, MB R3B 2E9, Canada. [46]NASA Goddard Space Flight Center, Greenbelt, MD 20771, USA. [47]Department of Geology, University of Cincinnati, Cincinnati, OH 45221, USA. [48]Laboratoire G-Time, Université Libre de Bruxelles, 1050 Brussels, Belgium. [49]Centro de Astrobiología, Consejo Superior de Investigaciones Científicas–Instituto Nacional de Técnica Aeroespacial, 28850 Madrid, Spain. [50]Department of Astronomy, Cornell University, Ithaca, NY 14853, USA. [51]School of Earth and Atmospheric Sciences, Queensland University of Technology, Brisbane, QLD 4001, Australia. [52]Department of Geosciences and Natural Resource Management, University of Copenhagen, 1350 Copenhagen, Denmark. [53]Globe Institute, University of Copenhagen, 1350 Copenhagen, Denmark. [54]Department of Earth and Planetary Sciences, McGill University, Montreal, QC H3A 0E8, Canada. [55]Department of Geoscience, University of Nevada, Las Vegas, Las Vegas, NV 89154, USA. [56]National Space Institute, Technical University of Denmark, 2800 Kongens Lyngby, Denmark. [57]Department of Analytical Chemistry, University of the Basque Country, 48940 Leioa, Spain. [58]Million Concepts, Louisville, KY 40204, USA. [59]Los Alamos National Laboratory, Los Alamos, NM 87545, USA. [60]Institute for Information and Communication Technologies, Joanneum Research, 8010 Graz, Austria. [61]Institut d'Astrophysique Spatiale, Université Paris-Saclay, 91405 Orsay, France. [62]Institut Universitaire de France, Paris, France. [63]Mars Exploration Program, Planetary Science Division, NASA Headquarters, Washington, DC 20546, USA. [64]McDonnell Center for the Space Sciences and Department of Earth and Planetary Sciences, Washington University in St. Louis, St. Louis, MO 63130, USA. [65]Impossible Sensing LLC, St. Louis, MO 63118, USA.

***Corresponding author. Email: kenneth.a.farley@jpl.nasa.gov**

†Present address: Department of Earth, Atmospheric, and Planetary Sciences, Purdue University, West Lafayette, IN 47907, USA.

SHERLOC (Scanning Habitable Environments with Raman & Luminescence for Organics & Chemicals), a Raman and fluorescence spectrometer (*31*), and PIXL (Planetary Instrument for X-ray Lithochemistry), an x-ray fluorescence spectrometer (*33*). To remove the dust coating, rocks were studied after abrading a circular pit of ~5 cm diameter and ~1 cm depth into each target. Debris was removed from the resulting abrasion patch using compressed N_2 gas (*34*). Proximity observations were taken at four abrasion sites (informally named Guillaumes, Bellegarde, Garde, and Dourbes; Fig. 1B); sample collection was attempted at each of these sites except Garde.

Descriptions of Máaz and Séítah formations

Máaz

The Máaz formation consists of blocky, massive, and layered bedrock (Fig. 2 and fig. S1). Natural surfaces of Máaz formation rocks contain occasional millimeter-sized grains and millimeter-to-centimeter–sized voids or pits. Many Máaz formation outcrops appear polished and grooved by aeolian abrasion. Others appear to be failing along concentric fractures, consistent with spheroidal weathering (fig. S1C). Máaz rocks are often partially covered by regolith, dust, and sometimes a discontinuous purple coating or rind (Fig. 3A); rock textures are more clearly observed on mechanically abraded surfaces. Sedimentary structures formed by grain transport, such as migrating ripples and dunes, were not observed within this formation.

The Roubion member is exposed at the lowest elevation along the traverse, and we therefore infer it to be the oldest interval of the Máaz sequence (fig. S5). This member is composed of meter-scale low-lying (<5 cm of relief) rock surfaces, which are polygonally fractured. The Guillaumes abrasion patch was performed on such an outcrop of the Roubion member; it reveals light and dark grains with a pervasive but heterogeneously distributed brown tint (Fig. 3A). In the least-brownish regions, we observed millimeter-sized interlocking dark gray or green and light-toned prismatic grains, with no evidence of intergranular porosity or visible cement. Although sometimes elongated, grains show no preferred orientation. If this rock is igneous, the coarse grains suggest a moderately slow cooling rate (i.e., it is a holocrystalline or microgabbroic rock). Irregularly shaped voids or pits, up to 5 mm in diameter, are present within the abrasion patch, which also contains elongated crevices. The edges of these features, and several other areas on the abrasion surface, appear to be coated by a smooth red-brown or black mantle that partially or completely obscures the underlying grains. Many of the lighter-toned grains are variably stained reddish brown. Millimeter-sized irregularly shaped patches of bright-white material, some also stained brown, occur between grains

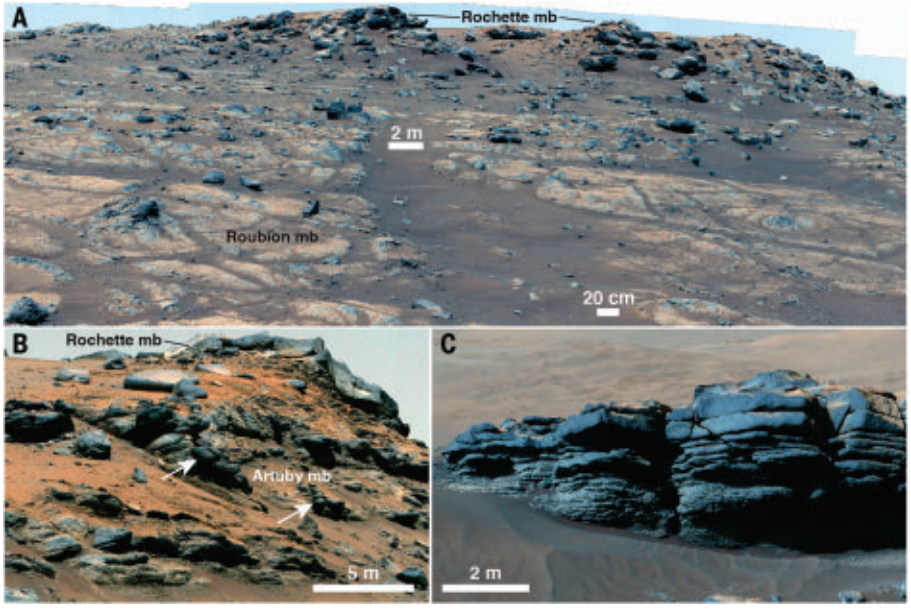


Fig. 2. Rover images of igneous rocks of the Máaz formation. All panels show enhanced-color Mastcam-Z images. (**A**) Image acquired on sol 138, showing low-relief, friable outcrops of the Roubion member (mb; foreground) overlain upslope by resistant caprocks of the Rochette member. (**B**) Image acquired on sol 175, showing layered rocks of the Artuby member, which are capped by the resistant rocks of the Rochette member. Artuby member layers range in thickness from <1 cm up to several decimeters and are generally planar. White arrows point to rounded outcrop protrusions. (**C**) Image acquired on sol 282, showing layered caprock of the Rochette member. Layers range in thickness from several centimeters to several decimeters and show an apparent thickening-upward trend. Layers are planar and dip ~10° to the south (into the page). Source images (*39*) in this figure and shown below have been white-balanced, contrast-stretched, and gamma-corrected to improve viewability and contrast.

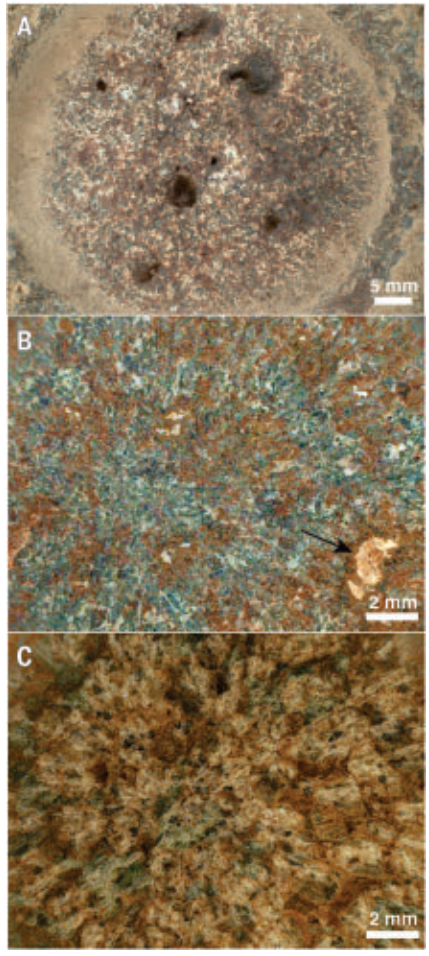


Fig. 3. Microscope images of abrasion patches. (**A**) WATSON image of the Guillaumes abrasion patch, on the Roubion member of the Máaz formation, acquired on sol 160. Millimeter-sized light- and dark-toned minerals interlock, bright-white and brown-to-black material coats surfaces and fills interstices, and several holes and crevices penetrate into the rock. (**B**) Combined SHERLOC and WATSON images of the Bellegarde abrasion patch, on the Rochette member of the Máaz formation, acquired on sol 186. Light and dark minerals ranging from 0.5 to 1 mm in size are present, coated or stained with brown material, but less extensively than in Guillaumes. The black arrow points to bright-white material, also stained brown, likely filling a void in the rock. (**C**) Combined SHERLOC and WATSON images of the Dourbes abrasion patch, on the Bastide member of the Séítah formation, acquired on sol 257. Light-toned grains ranging from 2 to 3 mm in size are surrounded by a dark-green mineral. Brown material occurs on most grain boundaries, sometimes coating the lighter-toned grains.

(likely in filled voids) and as a surface coating on some of the prismatic grains. Collectively, these observations are consistent with an igneous rock that has experienced aqueous alteration (i.e., modification by reactions with water).

Up-section and westward along Artuby ridge, an ~1-km-long linear scarp that reveals 2 to 3 m of southwest-dipping stratigraphy on its northeastern side (Fig. 2B), the Roubion member transitions into the Artuby member, distinguished by the presence of distinct layering. The Artuby member is composed of decimeter-thick layers with rounded protrusions and an apparently coarse granular surface texture, although this is sometimes obscured by regolith (Fig. 2 and fig. S1). The thick layers are separated by, and sometimes transition laterally into, thin recessive subcentimeter-scale layers. The layered rocks of the Artuby member are typically overlain by a resistant caprock, the Rochette member, that can be traced laterally over hundreds of meters along the crest of Artuby ridge. This caprock also appears to extend southward from the ridge as fragmented blocky flat-lying exposures partially covered by regolith (Fig. 1B). The Rochette member is ~30 to 50 cm thick and sometimes appears structureless but more commonly exhibits centimeter-scale layering. At an outcrop informally named Mure (fig. S1, D and E), the Rochette caprock exhibits thin layers that pinch out below more-massive layers and an ~2-cm-wide chain of pits (possibly vesicles) that for ~75 cm traces the curvature of the layer in which it is enclosed. A second abrasion patch, Bellegarde, was performed on a tabular boulder of the Rochette member, on the crest of Artuby ridge. Bellegarde is characterized by smaller crystals (~0.5 mm) of similar appearance to Guillaumes (Fig. 3). These crystals are occasionally stained by a reddish-brown material that is less pervasive than in Guillaumes but appears otherwise similar. Irregular white patches are also present, but there are no large pits or thick dark coatings in Bellegarde.

Resistant, blocky caprocks, like those of the Rochette member, are also observed in several ~1- to 2-m-high scarps along the eastern edge of Séítah (west and southwest of OEB). Here, the Rochette member appears to be overlain by disaggregating low-relief polygonal outcrops of the Nataani member. Rocks of the Nataani member appear morphologically and lithologically similar to those of the underlying Roubion member but are distinct in their geographic extent, elevation, and inferred local stratigraphic relationships (Fig. 1B and fig. S5). The low-relief Nataani member transitions eastward and up-section into the boulder-forming hills of the Chal member. East of OEB and the southbound rover traverse, massive submeter-to-meter-scale boulders of the Chal member erode from hilly outcrops, with no signs of internal layering. This rough terrain extends to cover most of the crater floor and is associated with the highest crater densities observed within Jezero (Fig. 1B).

Séítah

Bedrock exposure of the Séítah formation is mostly limited to ~1- to 10-m-tall ridges trending northeast-southwest, with the remainder of the region covered by sand ripples, loose rocks, and boulders (Fig. 4 and fig. S2). The Séítah formation comprises the strongly layered Bastide member and the overlying Content member, which is structureless and characterized by abundant millimeter-to-centimeter–sized pits (fig. S2A). Long-distance imaging shows that the Bastide member is widespread and exposed in outcrops throughout the several square kilometers of observed Séítah formation. Most layers of the Bastide member are 1 to 3 cm thick, but the thickest layers are apparently structureless over thicknesses of 10 to 40 cm. Thinner layers sometimes transition laterally into massive outcrops. There is an apparent thickening-upward trend within the Bastide member, in which thinly layered rocks transition up-section into thicker-layered rocks that cap ridges (fig. S2C). Most layers are generally tabular and even in thickness, with planar layer-bounding surfaces, although some exhibit centimeter-scale undulations. Individual layers can sometimes be traced laterally over distances of several meters within an individual outcrop, but individual layers and distinctive sets of layers usually cannot be correlated between outcrops. We identified no indicators of transport by wind or water, such as planar lamination and ripple or dune-cross stratification. The pitted rocks of the overlying Content member do not exhibit layering, and they lack olivine (as discussed in the section on Séítah mineralogy). The Content member is observed only locally, exposed over lateral distances no greater than several meters. Its contact relationship with the Bastide member is unknown.

Natural surfaces of Bastide member outcrops show densely packed, clast-supported, homogeneous 2- to 3-mm-diameter dark-gray or green grains (or crystals) with indistinct, lighter-toned material between grains (Fig. 4C). The grain-size distributions do not vary across multiple outcrops, nor did we visually detect grain-scale sorting or grading at apparent layer boundaries. The millimeter-sized grains, when observed in abraded surfaces of Bastide (the Dourbes and Garde abrasion patches), are light toned and mostly equant, but some elongated grains are also present (Fig. 3C) (*35*); we observed no gradation in grain size in the abrasion patches. Less common than the light-toned grains are slightly

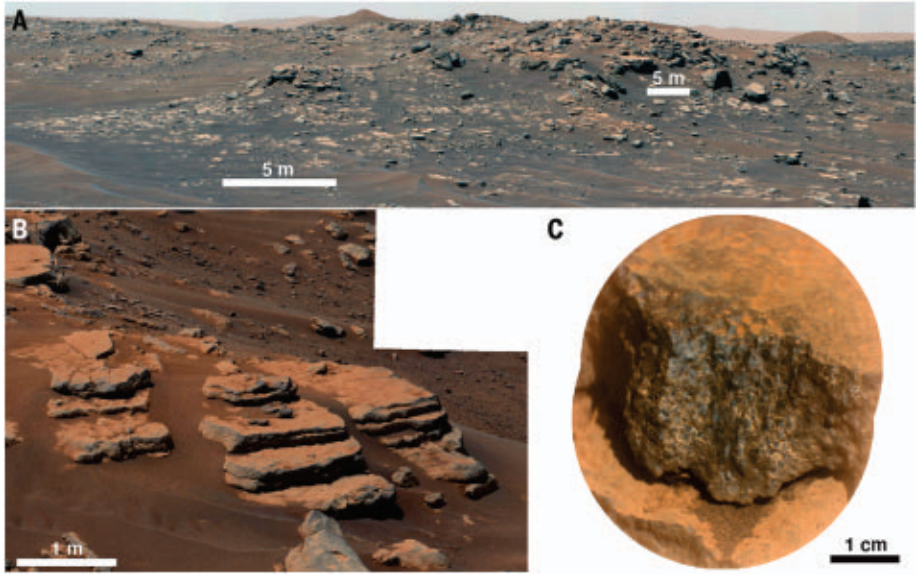


Fig. 4. Layered and coarse-grained appearance of the Bastide member of the Séítah formation. (**A**) Enhanced-color Mastcam-Z mosaic of Bastide, acquired on sol 201, showing bedrock exposures eroding into tabular boulders, which occur mostly on ridges. Bastide member bedrock varies from thinly layered to structureless, and individual layers cannot typically be traced more than a few meters. The platy and tabular appearance of the Séítah formation contrasts strongly with the more-rounded boulders of Máaz (Fig. 2A). (**B**) Enhanced-color Mastcam-Z mosaic, acquired on sol 204, of the Bastide outcrop where the Garde abrasion was performed. Centimeter-scale layering is accentuated by differential erosion. (**C**) SuperCam mosaic of the Cine abrasion target on the Bastide formation, acquired on sol 206. On surfaces with little dust or coating, the Bastide member rocks reveal abundant 2- to 3-mm angular to rounded gray-green grains, separated by lighter-toned material.

smaller dark-gray or green grains that are sometimes angular but more often appear to fill the space between lighter grains. Light-brown material stains the light-toned grains and is concentrated between grains, in some cases encircling or rimming them. A few submillimeter-scale bright-white patches are also present. Although a few natural surfaces of Bastide member rocks contain millimeter-scale pits, the occasional voids in the two abraded surfaces are much smaller.

Near the base of Artuby ridge, at the transition between the Máaz and Séítah formations, Séítah layering is observed both in outcrop and in the subsurface with ground-penetrating radar. The layering typically dips ~10° to 15° to the southwest (fig. S3). These dips are consistent with those of Máaz formation rocks exposed along Artuby ridge. This indicates that Séítah formation bedrock lies stratigraphically below Máaz formation rocks, even though the Máaz formation is topographically lower than some Séítah exposures, confirming a pre-landing hypothesis (*23*). Thus, the Séítah formation is the lowest exposed stratigraphic unit on the Jezero crater floor, which is overlain by the Máaz formation. The boundary between the Séítah and Máaz formations is obscured by regolith, so it is unknown whether the units are separated by an unconformity. The inferred contact between the two units varies in elevation, by ~10 m along Artuby ridge and up to ~30 m around the entire Séítah exposure.

Máaz formation geochemistry and mineralogy

Mastcam-Z multispectral observations (*30*) of Máaz formation rocks along the traverse show broad absorption bands centered near 0.88 to 0.90 μm, consistent with pyroxene or Fe^{+3}-bearing alteration minerals (fig. S4). These are similar to the weak pyroxene bands observed from orbit across the eastern portion of the crater floor (*9*, *36*). Seventy-seven Máaz formation targets were analyzed with SuperCam infrared (IR) spectroscopy (*32*); these spectra frequently show a band at 1.92 to 1.93 μm, which we attribute to hydrated iron oxides, ferric smectites, or hydrated salts (fig. S6) (*37*). Weaker absorption features observed at 1.42 and 2.28 μm are consistent with Fe-OH bands in hydrated silicates (*37*).

SuperCam laser-induced breakdown spectroscopy (LIBS) (*32*) was used to characterize the elemental composition of 67 Máaz formation targets. At its typical operating distance of 2.7 m from the rover, the laser beam interrogates a region ~350 μm in diameter at each of the 5 to 10 observation points investigated on each rock target. In some cases, individual points had elemental abundances consistent with specific minerals rather than mixtures. From these points we infer the presence of common igneous minerals (augite, plagioclase, ilmenite, ferrosilite, and unidentified iron oxides), at least some of which are moderately coarse grained (>350 μm). No IR spectra or LIBS compositions consistent with olivine were observed in Máaz formation bedrock. Figure S8 shows the average composition of each analyzed rock target, which indicates that the Máaz formation is fairly homogeneous and dominated by varying proportions of plagioclase and augite. The average LIBS-based composition of Máaz (table S1) is broadly basaltic, with 48% SiO_2, low MgO (3 wt %), and high (20 wt %) FeO_T (defined as total iron as Fe^{+2}).

PIXL x-ray fluorescence mapping (*33*) shows (Fig. 5) that the Guillaumes (Roubion member) and Bellegarde (Rochette member) abrasion patches are dominated by two distinct 0.5- to 1-mm-scale common igneous phases. The blocky to prismatic white grains (Fig. 3) are chemically consistent with plagioclase (Al-rich regions in Fig. 5A), whereas the darker grains have the composition of pyroxene (specifically augite, Ca-rich regions). Also present are 100-μm-scale regions indicative of FeTi oxides and Ca phosphates. The red-brown to black material consists mostly of Fe and Si, with molar Fe/Si ratios ranging from ~0.7 to 1.5 and MgO and Al_2O_3 both <4%. This composition overlaps with some igneous Fe silicate minerals, such as Fe-bearing pyroxene and olivine, but is also consistent with several secondary Al-free Fe silicates, such as greenalite, hisingerite, and cronstedtite. Alternatively, this material may be a mixture of iron oxide and silicates; Mastcam-Z multispectral data indicate the presence of hematite and/or goethite in both Máaz abrasion patches (fig. S4). Coupled with its elemental composition, the color and textural properties of this material (Fig. 3) suggest in situ aqueous alteration of one or more primary igneous minerals.

Raman spectroscopy indicates that the bright-white void-filling material in the Máaz formation abrasion patches is at least partially composed of hydrous Ca sulfate and Na perchlorate, sometimes colocated with each other (fig. S7, A and B). Elemental abundances support these identifications; a phase with molar Na/Cl ratio of ~1 is consistent with Na perchlorate, halite, or both.

In the average bulk composition of the Máaz abrasion patches (table S2), the abundances of SO_3 (~3.0 wt %) and Cl (~2.6 wt %) are both far higher than typical unaltered martian igneous rocks (*38*). If Máaz consists of igneous rocks, they have experienced addition of S- and Cl-bearing materials. To estimate the primary chemical compositions of Guillaumes and Bellegarde, we computed a subset average of PIXL data by excluding salt-rich bright-white areas (Fig. 3) (*39*). This alteration-free compositional average (table S2) indicates, on the basis of total alkali metals and silica, that the primary Máaz formation rocks were basaltic in composition. Compared with Earth basalts, Máaz rocks are enriched in FeO_T (22 wt %) and P_2O_5 (2.2 wt %). Compositions estimated by x-ray fluorescence, which represent the analysis of just a few square millimeters of rock, are similar to the average composition of all Máaz formation rocks obtained by LIBS (fig. S8).

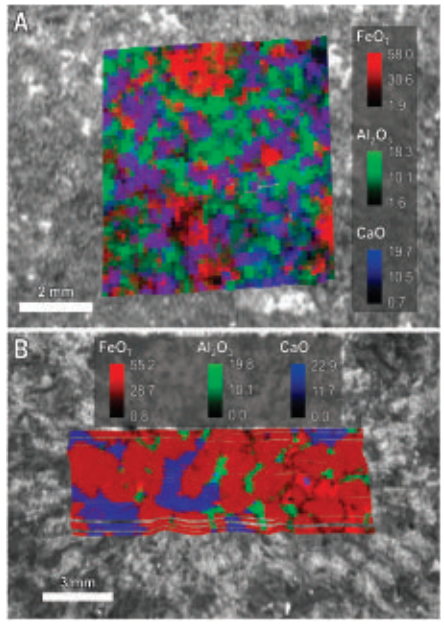


Fig. 5. Compositional maps of Guillaumes and Dourbes abrasion patches. PIXL x-ray fluorescence maps indicating composition are shown in color (as indicated in the legends), with concentrations in weight %. These are overlain on grayscale visual images indicating rock texture. (**A**) Guillaumes is dominated by grains with compositions consistent with plagioclase (high Al, corresponding to the light grains visible in Fig. 3A) and augite (high Ca and Fe, corresponding to dark grains in Fig. 3A). Fe-rich material appears brown in Fig. 3A; it could be primary or secondary Fe silicates, iron oxides, both, or FeTi oxides and sulfates, as these are indistinguishable in this representation. (**B**) Dourbes is dominated by euhedral to subhedral olivine of ~Fo_{55} composition (Fe-rich, corresponding to light-toned grains in Fig. 3C). Augite (high Ca, corresponding to dark-green grains in Fig. 3C) engulfs olivine, which a companion paper interprets as poikilitic igneous texture indicating an igneous olivine cumulate rock (*35*). High-Al regions indicate plagioclase. Sulfates and carbonates appear as small areas with the highest Fe. Figure S9 provides individual maps of Ca, Fe, and Al concentrations to aid interpretation of colors in this figure. FeO_T is total iron as Fe^{+2}.

Séítah formation geochemistry and mineralogy

Mastcam-Z multispectral images and SuperCam IR spectra of Bastide member rocks of the Séítah formation are dominated by a broad

1-μm absorption feature, indicating olivine (fig. S4). IR spectroscopy also shows a 1.9-μm feature similar to, but weaker than, that observed in Máaz formation rocks, which we attribute to mineral hydration (fig. S6) (*37*). Individual LIBS points on the prominent 2- to 3-mm gray-green grains observed on natural surfaces (Fig. 3C) commonly have compositions approaching those of pure olivine. The target-averaged LIBS compositions of 25 Bastide member rocks extend from olivine toward mixtures of augite and plagioclase (fig. S8). The Bastide member compositions have only minor overlap with the dominantly plagioclase-augite Máaz formation rocks. The overall mean composition of all Bastide member targets is listed in table S1.

Raman spectra of the Bastide member abrasion patches (Dourbes and Garde) confirm the abundant presence of olivine (fig. S7C). X-ray fluorescence elemental mapping (performed on Dourbes only; Fig. 5B) indicates that 65% of the analyzed surface, associated with the light-toned grains (Fig. 3), is chemically consistent with approximately Fo_{55} olivine (i.e., 55% Mg and 45% Fe on an atom basis) (*35*). The olivine is partially surrounded with, and sometimes enclosed by, dark-green augite (13% of the analyzed surface). A companion paper (*35*) interprets this relationship as consistent with poikilitic igneous texture in which late-forming augite grows around density-segregated olivine. Al-rich areas making up 10% of the analyzed surface likely include feldspars; 0.1-mm-scale phosphates and Cr- and Ti-bearing Fe oxides are also present. The reddish-brown material that occurs between grains (Fig. 3C) is chemically complex. It often has Raman peaks consistent with carbonate, frequently associated with olivine peaks (fig. S7). In other instances, Raman spectra consistent with hydrated sulfate (fig. S7) yield Mg/S ratios that indicate the presence of $MgSO_4$. In elemental composition maps, the brown areas sometimes contain low SiO_2, elevated abundances of Fe and Mg, and low analytical oxide totals, consistent with carbonate with an approximate composition of $Fe_{0.5}Mg_{0.5}CO_3$. Raman signatures of the rare white patches indicate the presence of hydrated Ca and Mg sulfates and perchlorate (fig. S7). A broad Raman signature at ~1020 cm^{-1}, widely distributed in the abrasion patch, is potentially amorphous silicate (fig. S7G).

Séítah formation rocks, like those of Máaz, appear to consist of primary igneous minerals (e.g., olivine, augite, plagioclase) and secondary aqueous alteration phases (carbonate, sulfates). Excluding material that has likely been transported from elsewhere (*39*), the mean primary composition obtained by PIXL on Dourbes is ultramafic, with 20 wt % MgO and 40 wt % SiO_2 (table S2). Compared with the Bastide member LIBS average, this composition has lower SiO_2 and higher FeO but is otherwise similar.

In contrast to the Bastide member targets, LIBS measurements of the Content member appear to be dominated by augite and feldspar, with no olivine. This is consistent with the appearance of this rock, which lacks the coarse gray-green olivine grains characteristic of the Bastide member. Only limited data on this member were acquired.

Interpretations and hypotheses

Origins of Máaz and Séítah formations

We interpret the Bastide member of the Séítah formation as igneous. The grain size and high modal abundance of olivine, coupled with the poikilitic texture, indicate an olivine cumulate in which pyroxene, plagioclase, and primary Fe-Ti-Cr oxides crystallized from residual melt (*35*). These characteristics indicate slow cooling, differentiation, and crystal settling (*40*). Therefore, Bastide member rocks likely crystallized in a thick lava flow, a lava lake or impact melt sheet, or an intrusion. On Earth, variations in crystal size or modal mineralogy define layers that often give cumulate rocks a sedimentary appearance in outcrop (*40*, *41*). Imaging, spectroscopic, and LIBS observations revealed no evidence for such differences among Bastide layers or at their interface. The prominently layered appearance of the Séítah formation (Fig. 4) could arise from layer-parallel cooling joints, differential aqueous alteration, or subtle variations in rock composition or texture that enhance near-horizontal fracturing. Such features are likely to have been accentuated by erosional processes, especially wind abrasion. This interpretation implies that the layering in Séítah corresponds to magmatic layering.

Given their mineralogy, texture, and bulk composition, rocks of the Máaz formation are also most consistent with a primary igneous, rather than sedimentary, origin. We exclude the possibility that Máaz consists of basaltic sandstones owing to the lack of sorting among grains of different size and specific gravity, the interlocking grain texture, the lack of evidence for pervasive intergranular porosity or cements in the Guillaumes and Bellegarde abrasion patches, and the apparent absence of subaqueous or aeolian transport features.

On Earth, the high abundance of olivine in olivine cumulate rocks is usually complemented by less-mafic (i.e., less Fe and Mg) materials, commonly overlying the cumulate, that, when combined, constitute the parental melt composition (*40*). Rover observations within Jezero crater, and more spatially extensive orbital spectroscopy (*36*), indicate that the high olivine abundances characteristic of the Bastide formation are also found throughout Séítah, with olivine-poor rocks (such as the Content member) being rare. If a less-mafic complement to the Bastide member previously existed in this region, it must have been at least partially removed by erosion. The Máaz formation could be the remnant of such a complement—it has abundant pyroxene and plagioclase and little magnesium, is moderately coarsely crystalline, and lies stratigraphically above the Bastide member, all of which would be expected if the two units originated from a single differentiated igneous melt. The various members of the Máaz formation could be equivalent to layers in the igneous body.

Alternatively, the Máaz formation could be a sequence of younger basaltic lavas that flowed up against, and at least partially overtopped, the Séítah formation after erosional removal of the putative less-mafic complement. The morphologically distinct Máaz members could then be cogenetic lava flows, with variable properties related to composition and/or eruption temperature. An extrusive igneous origin for Máaz would account for some of its morphologies and textures, for example, the lobate structures in the Artuby member (Fig. 2B), possible vesicles in Guillaumes (Fig. 3A), and in the chain of pits in the Rochette member (Fig. 2). Variations in elevation of the Máaz–Séítah contact could reflect underlying topography of the Séítah formation on which the Máaz lavas were erupted. However, other features are less characteristic of lava flows, such as the centimeter-scale layers observed in the Rochette and Artuby members and the lack of flow orientation of elongated grains in the Máaz abrasion patches (Fig. 3).

The limited data on the Content member of the Séítah formation make it difficult to define its origin. It could also be a remnant of a once more-expansive less-mafic complement to Bastide; a remnant of Máaz formation lava flows that overtopped the Bastide member; or remnant sedimentary rocks deposited atop the Bastide member.

Multiple sources of melting are possible for the igneous crater floor units within Jezero; present data are insufficient to discriminate between the possibilities. The impact that produced Jezero could have generated a sufficiently deep melt sheet to differentiate into an olivine cumulate, but we have found no evidence of associated impact breccias on the crater floor, and crater-scaling relationships suggest that the original Jezero floor is buried by ~1 km of postimpact basin-filling materials (*4*, *22*). Although Jezero is close to the Isidis impact basin, and Bastide member petrology is similar to hypothesized olivine-rich cumulates in a melt sheet potentially created by the Isidis impact (*3*, *5*), Isidis cannot be the source because Jezero postdates Isidis. There are no other impact basins of appropriate age, size, and proximity to Jezero to be plausible sources. Alternatively, melting could have occurred without an impact, especially in the early

Hesperian, when the martian mantle was substantially hotter than at present—this is thought to be the origin of the nearby Syrtis Major shield volcano (*42*).

Magmas could have been introduced into Jezero crater over its rim or from below. Although the Jezero crater rim has been extensively eroded, materials like those in the Bastide member have been interpreted as draping its western side (*9*), and we suggest that hills on the southeast rim of Jezero could be of volcanic construction. However, these features are not contiguous with the Séítah formation. We consider the most likely scenario to be fissure-fed eruptions occurring both within Jezero and in the surrounding region. By analogy to some volcanically filled craters on the Moon (*43*) and other craters on Mars (*44*), magma injection could have occurred directly into the low-density materials of the crater floor at any time after Jezero formation. This process could lead to intrusive and/or extrusive igneous activity (*43*).

Séítah formation rocks were previously proposed to be part of an ~70,000-km^2 olivine-rich region associated with the Isidis basin (*15*, *18*, *45*, *46*). The widespread distribution of this olivine-rich material, apparent draping across topography, poor crater retention, and limited regolith cover have been interpreted as indicating a clastic origin (*5*, *18*–*20*). That interpretation is difficult to reconcile with our conclusion that the Séítah formation is a slowly cooled magmatic differentiate. Despite their similarities, the regional olivine unit could have an origin distinct from that of Séítah. Alternatively, widespread injection and differentiation of compositionally similar magmas might have occurred throughout the region.

Aqueous processes

After emplacement of the igneous rocks on the crater floor, multiple forms of aqueous interaction modified—but did not destroy—their igneous mineralogy, composition, and texture. Evidence for alteration includes the presence of carbonate in the Séítah abrasion patches, the iron oxides in the Máaz formation abrasion patches (which we presume are due to iron mobilization and precipitation), and the deposition of salts, including sulfates and perchlorate. More broadly, the appearance of possible spheroidal weathering textures (fig. S1C) suggests that aqueous alteration played a role in rock disintegration (*47*).

The similarity of Fe/Mg ratios in the carbonates and olivine within the Dourbes abrasion patch, rimming of olivine by carbonate, and their possible association with likely amorphous silicate are all consistent with in situ olivine carbonation, in which olivine reacts with CO_2-rich water to produce this phase assemblage in close physical proximity (*48*–*50*). Olivine carbonation often occurs together with conversion of olivine to serpentine group minerals (serpentinization), but in the Séítah formation we have found no evidence for such minerals. The similarity of olivine and carbonate cation compositions, and the survival of substantial abundances of olivine, indicate aqueous alteration under rock-dominated conditions, possibly occurring over a short duration. Olivine carbonation can occur over a wide range of temperatures, from hydrothermal or metamorphic conditions to low-temperature weathering (*11*). The presence of carbonate places a lower bound on fluid pH that depends on the concentrations of cations and dissolved inorganic carbon (*51*, *52*). For example, if Mg and Fe concentrations ranged from 10^{-4} to 10^{-2} mol kg^{-1} and the initial dissolved inorganic carbon equilibrated with 0.1 to 10 bar CO_2(g), the pH would have a lower limit of between 5.5 and 7.5 (at 25°C).

Although we have found no evidence for carbonate in the Máaz formation abrasion patches, the abundant dark mantling material (Fig. 3A) could be a secondary serpentine group mineral produced by aqueous alteration of Fe-rich pyroxene or olivine (*53*). The presence of secondary Fe silicate without high abundances of carbonate in Máaz formation rocks could indicate a fluid with lower dissolved inorganic carbon concentrations than we inferred for the Séítah formation. These Fe silicates can also form across a wide range of temperatures, from ambient to hydrothermal; we cannot constrain the emplacement conditions without knowing the precise mineral composition. Alternatively, the Fe-rich materials could represent films of Fe oxides or oxyhydroxides coating and penetrating primary silicates, such that our elemental measurements include both phases. On Earth, iron staining of rocks is common when reduced Fe is released from aqueously altered igneous phases and then precipitated under oxidizing conditions. For example, sulfide dissolution by oxidizing solutions commonly yields hematite or goethite, while simultaneously mobilizing sulfate (*54*).

Sulfate minerals, sodium perchlorate, and possibly other salts (e.g., halite) indicate that other styles of aqueous activity also occurred in the crater-floor igneous formations. These salts fill pore spaces, voids, and cracks that themselves might have resulted from aqueous alteration, for example, from volume expansion accompanying carbonation and serpentinization (*55*), dissolution of phases such as sulfides, or by chemical and physical erosion processes producing open space (such as the pits in Guillaumes). We have not observed sulfides, but if they were once present, their alteration could have contributed to the production of Ca, Mg, or Fe sulfates or mixtures of them in situ. However, the high sulfate concentrations observed in Guillaumes and Bellegarde suggest an external source for at least some of the sulfates. As has been proposed for rocks at Gale crater investigated by the Curiosity rover (*56*), perchlorate can be introduced into near-surface rocks by downward percolation and evaporation of brines, possibly associated with ephemeral wetting events extending into the Amazonian (<3 Ga). The co-occurrence of perchlorate and sulfate minerals indicates that at least some of the sulfate could have been similarly sourced. The diversity of salt compositions in the analyzed white patches (e.g., their variety of S/Cl and Ca/Mg/Fe ratios) indicates that several different fluids could have been involved, possibly at different times and possibly repeatedly. The extreme solubility of perchlorate salts indicates that they are the youngest alteration materials in these rocks. Salt hydration and dehydration can cause substantial volume expansion (*57*), weakening the rock and contributing to the mechanical erosion and disaggregation of outcrop by aeolian processes across the floor of Jezero crater.

Although there is evidence for rock-dominated aqueous alteration and a diversity of secondary phases, there is no geochemical or mineralogical indication of extensive open-system aqueous alteration, in which soluble cations (Ca, Na, K) are entirely removed, resulting in enrichments in aluminous phases (i.e., Al-rich clays) (*58*). The bulk compositions of both the Máaz and Séítah formations are consistent with near-pristine igneous rocks (except in S and Cl; see tables S1 and S2); hydrated aluminosilicates are rare or absent; and there is no textural or chemical evidence for extensive plagioclase alteration or olivine and pyroxene dissolution (*59*).

Geologic models

We propose two scenarios for the history of the Jezero crater floor, given our inability to distinguish whether the Máaz formation consists of lava flows (hereafter model 1) or an igneous complement to the olivine cumulate of the Séítah formation (model 2).

During or after the formation of Jezero crater, a thick magma body or melt sheet (*35*) existed within the crater. This could have been emplaced on, or intruded into, a preexisting crater fill. Differentiation and crystal settling formed the olivine cumulate (*35*) while also producing a less-mafic complement (Fig. 6A). In model 1, erosion removed most (or all) of this less-mafic material, leaving at least tens of meters of topography on the residual olivine cumulate deposit (Fig. 6B), after which lava flows of the Máaz formation flowed around, and at least partially overtopped, the underlying topography (Fig. 6C). Deformation of unknown origin then tilted the originally flat-lying layers of both formations, at least locally, by ~10° to the southwest (Fig. 6D), as observed

along Artuby ridge. In model 2, both Máaz and Séítah were produced by magmatic differentiation similar to a layered igneous body (Fig. 6E). Deformation of unknown origin then uplifted Séítah relative to Máaz, tilting both (Fig. 6F).

In both models, the Máaz and Séítah formations later experienced further erosion that removed overlying Máaz formation rocks from above the Séítah formation (Fig. 6G). We adopt the interpretation (*21*, *28*) that the crater-floor units were then at least partially buried by the delta and associated Jezero lake deposits (Fig. 6H). The late Noachian age (3.6 to 3.8 Ga) (*7*) of the largest river valley networks feeding Jezero and the assumed Hesperian age of the exposed delta (*8*) provide a possibly long period of aqueous activity during which lacustrine and igneous processes both occurred, possibly driving hydrothermal interactions. However, we have found no evidence for remnant sedimentary units along Perseverance's traverse up to sol 290. If delta or lake sediments once covered both the Máaz and Séítah formations (Fig. 6H), they appear to have largely eroded away (Fig. 6I), except for delta remnant mounds such as Kodiak (*60*).

A variety of concurrent and subsequent processes, including rock-dominated alteration and salt deposition, modified the chemistry and mineralogy of these rocks as they interacted with aqueous solutions. Spatially and chemically distinct materials (carbonate, likely amorphous silicate, Fe oxides, perchlorate, sulfates, and possibly Fe silicates) could be the product of multiple distinct aqueous events, differing in chemistry and possibly separated in time. Both hydrothermal waters and groundwater could have played a role.

Habitability and preservation potential

One proposed definition of a habitable environment is one in which liquid water, available energy, nutrients, and other physicochemical conditions are adequate for supporting known forms of life (*61*). On Earth, reactions of igneous rocks with water produce diverse habitats for microbial life (*62*, *63*). The oxidation and partitioning of iron into secondary phases during alteration processes, such as carbonation and serpentinization, can yield H_2—a potential energy source—along with methane and other hydrocarbons, which can form raw materials for the synthesis of more-complex organic molecules (*62*, *63*). The chemical reduction of nitrate, sulfate, and metal ions, along with hydrocarbon degradation, is thought to power microbial metabolisms in Earth's deep subsurface (*64*). Rocks of the Jezero crater floor appear to share the compositional components of these habitable environments. The soluble salts and vein-filling minerals we observe, such as iron oxides, perchlorate, and sulfate salts, could have formed under habitable low-temperature conditions but could also have formed under nonhabitable conditions (*65*–*67*).

The potential for secondary aqueous phases to preserve evidence of life depends on how they formed. On Earth, studies of evaporitic and desert environments demonstrate the presence and preservation of microbial life in association with salts (*65*, *66*, *68*, *69*). Carbonate veins on Earth, produced through serpentinization and carbonation, can preserve biomarkers such as lipids (*70*–*72*) and/or organic structures interpreted as fossilized microbial communities (*71*). By analogy, we propose that the secondary phases in the altered igneous rocks of the Jezero crater floor might have the potential to record biosignatures, if ancient habitable environments existed.

Sample collection

Laboratories on Earth have measurement capabilities superior to instruments that can

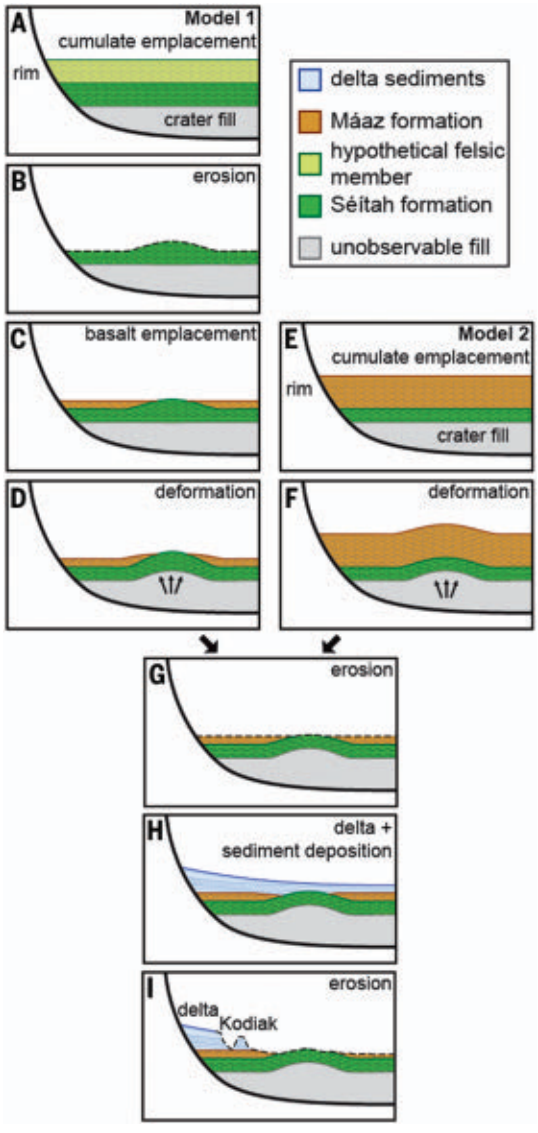


Fig. 6. Two possible models for the evolution of the Jezero crater floor. Proposed geological formations are indicated by the legend. (**A**) In model 1, the differentiated magma body experienced (**B**) erosion that removed a less-mafic complement, producing topography on the Séítah formation olivine cumulate. (**C**) Máaz formation lavas surrounded this underlying topography. (**D**) Deformation of unknown cause tilted both Séítah and Máaz, as observed along Artuby ridge. (**E**) In model 2, flat-lying layers of a differentiated magma body (**F**) deformed in a way that tilted both the olivine cumulate (Séítah formation) and the less-mafic complement (Máaz formation) and also uplifted Séítah relative to Máaz. In (**G**) and (**H**), common to both models, erosion occurred and delta and lacustrine sediments were deposited in the lake that filled Jezero. (**I**) Later, these rock units were eroded to their current surface exposure distribution. Aqueous alteration processes could have occurred during any of these steps.

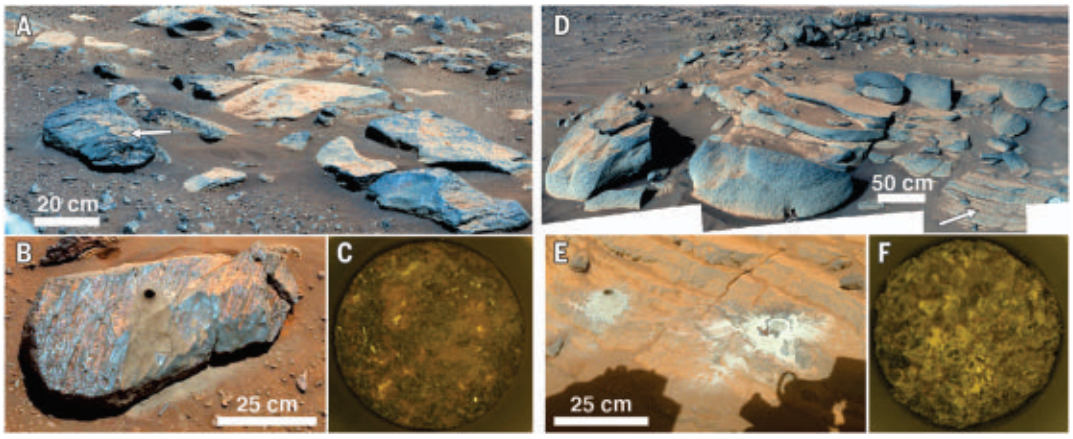


Fig. 7. Core samples collected for potential return to Earth. (**A**) Máaz formation Rochette member outcrop. The white arrow indicates the sampled rock, part of an apparent degrading layer on the crest of Artuby ridge. Enhanced-color Mastcam-Z mosaic acquired on sol 180. (**B**) Close-up of the sampled rock, showing the core hole. The Bellegarde abrasion patch is located directly below the hole, partly buried by tailings. Perseverance Navigation Camera (Navcam) (*75*) image acquired on sol 190, white-balanced with slight color saturation applied. (**C**) White-balanced Cache Camera (CacheCam) (*75*) image of the bottom of the core named Montdenier associated with the Bellegarde abrasion patch, contained in its sample tube, acquired on sol 194. The sample is 1.3 cm in diameter and ~5.5 cm long. (**D**) The white arrow indicates the sampling site on the thinly layered Séítah formation Bastide member outcrop. Enhanced-color mosaic acquired by Mastcam-Z on sol 240. (**E**) Core hole and Dourbes abrasion patch imaged by the front Hazard Camera (Hazcam) (*75*) on sol 263. This image has been white-balanced with a slight color saturation applied. (**F**) White-balanced CacheCam image of the bottom of the core named Salette associated with the Dourbes abrasion patch, acquired on sol 262.

be mounted on a Mars rover. An objective of the Mars 2020 mission is therefore to collect samples, in the form of drilled rock cores, for potential transport to Earth by another spacecraft in the 2030s (supplementary text). We attempted core acquisition on three different rock targets: two in the Máaz formation and one in the Séítah formation. The first coring attempt occurred near Guillaumes (Fig. 1B), in the low-lying, polygonal pavement of the Roubion member of the Máaz formation. Although the sample collection process appeared to execute as expected, the sample tube was subsequently found to contain no rock or rock fragments. A likely explanation is that this rock disintegrated during drilling, probably as a result of the rock's aqueous alteration (Fig. 3A). The sample tube was sealed and instead provides a sample of ambient martian atmosphere. A second sample acquisition attempt was performed on the Rochette member on the crest of Artuby ridge near Bellegarde, and a third on the Séítah formation Bastide member near Dourbes; these were both successful (Fig. 7).

Aqueously altered igneous rocks have advantages as samples for return to Earth. The formations these samples were taken from likely date from the late Noachian to early Hesperian; only a small fraction of martian meteorites are this old (*73*). Their crystallization ages, along with the pressures and temperatures during igneous rock formation, could potentially be determined with current laboratory equipment. Because both the Máaz and Séítah formations are thought to extend beneath the delta in Jezero (*21*, *28*), igneous crystallization ages would provide upper bounds on the age of the lake and the fluvial processes that deposited the delta (*60*), a lower bound on the age of the Jezero impact, and an upper bound on the age of the smaller craters on the Máaz formation. The igneous lithologies of the samples might be suitable for paleomagnetic analysis of the ancient martian magnetic field (*74*).

REFERENCES AND NOTES

1. K. A. Farley *et al*., Mars 2020 mission overview. *Space Sci. Rev.* **216**, 142 (2020). doi: 10.1007/s11214-020-00762-y
2. S. C. Werner, The early martian evolution—Constraints from basin formation ages. *Icarus* **195**, 45–60 (2008). doi: 10.1016/j.icarus.2007.12.008
3. J. F. Mustard *et al*., Mineralogy of the Nili Fossae region with OMEGA/Mars Express data: 1. Ancient impact melt in the Isidis Basin and implications for the transition from the Noachian to Hesperian. *J. Geophys. Res.* **112**, E08S03 (2007). doi: 10.1029/2006JE002834
4. B. L. Ehlmann *et al*., Clay minerals in delta deposits and organic preservation potential on Mars. *Nat. Geosci.* **1**, 355–358 (2008). doi: 10.1038/ngeo207
5. J. F. Mustard *et al*., Composition, morphology, and stratigraphy of Noachian crust around the Isidis basin. *J. Geophys. Res.* **114**, E00D12 (2009). doi: 10.1029/2009JE003349
6. N. Mangold *et al*., Mineralogy of the Nili Fossae region with OMEGA/Mars Express data: 2. Aqueous alteration of the crust. *J. Geophys. Res.* **112**, E08S04 (2007). doi: 10.1029/2006JE002835
7. C. I. Fassett, J. W. HeadIII, Valley network-fed, open-basin lakes on Mars: Distribution and implications for Noachian surface and subsurface hydrology. *Icarus* **198**, 37–56 (2008). doi: 10.1016/j.icarus.2008.06.016
8. N. Mangold *et al*., Fluvial regimes, morphometry, and age of Jezero crater paleolake inlet valleys and their exobiological significance for the 2020 Rover Mission landing site. *Astrobiology* **20**, 994–1013 (2020). doi: 10.1089/ast.2019.2132; pmid: 32466668
9. T. A. Goudge, J. F. Mustard, J. W. Head, C. I. Fassett, S. M. Wiseman, Assessing the mineralogy of the watershed and fan deposits of the Jezero crater paleolake system, Mars. *J. Geophys. Res. Planets* **120**, 775–808 (2015). doi: 10.1002/2014JE004782
10. C. I. Fassett, J. W. HeadIII, Fluvial sedimentary deposits on Mars: Ancient deltas in a crater lake in the Nili Fossae region. *Geophys. Res. Lett.* **32**, L14201 (2005). doi: 10.1029/2005GL023456
11. B. L. Ehlmann *et al*., Orbital identification of carbonate-bearing rocks on Mars. *Science* **322**, 1828–1832 (2008). doi: 10.1126/science.1164759; pmid: 19095939
12. A. J. Brown, C. E. Viviano, T. A. Goudge, Olivine-carbonate mineralogy of the Jezero crater region. *J. Geophys. Res. Planets* **125**, JE006011 (2020). doi: 10.1029/2019JE006011; pmid: 33123452
13. B. L. Ehlmann *et al*., Identification of hydrated silicate minerals on Mars using MRO-CRISM: Geologic context near Nili Fossae and implications for aqueous alteration. *J. Geophys. Res.* **114**, E00D08 (2009). doi: 10.1029/2009JE003339
14. A. Ody *et al*., Global investigation of olivine on Mars: Insights into crust and mantle compositions. *J. Geophys. Res. Planets* **118**, 234–262 (2013). doi: 10.1029/2012JE004149
15. T. M. Hoefen *et al*., Discovery of olivine in the Nili Fossae region of Mars. *Science* **302**, 627–630 (2003). doi: 10.1126/science.1089647; pmid: 14576430
16. V. E. Hamilton, P. R. Christensen, Evidence for extensive, olivine-rich bedrock on Mars. *Geology* **33**, 433–436 (2005). doi: 10.1130/G21258.1
17. L. L. Tornabene *et al*., Surface and crater-exposed lithologic units of the Isidis Basin as mapped by coanalysis of THEMIS and TES derived data products. *J. Geophys. Res.* **113**, E10001 (2008). doi: 10.1029/2007JE002988
18. C. H. Kremer, J. F. Mustard, M. S. Bramble, A widespread olivine-rich ash deposit on Mars. *Geology* **47**, 677–681 (2019). doi: 10.1130/G45563.1
19. L. Mandon *et al*., Refining the age, emplacement and alteration scenarios of the olivine-rich unit in the Nili Fossae region, Mars. *Icarus* **336**, 113436 (2020). doi: 10.1016/j.icarus.2019.113436
20. A. D. Rogers, N. H. Warner, M. P. Golombek, J. W. Head3rd, J. C. Cowart, Areally extensive surface bedrock exposures on Mars: Many are clastic rocks, not lavas. *Geophys. Res. Lett.* **45**, 1767–1777 (2018). doi: 10.1002/2018GL077030; pmid: 30598561
21. V. Z. Sun, K. M. Stack, Geologic map of Jezero crater and the Nili Planum region, Mars: US Geological Survey Scientific Investigations Map 3464 (US Geological Survey, 2020); https://doi.org/10.3133/sim3464.
22. S. C. Schon, J. W. Head, C. I. Fassett, An overfilled lacustrine system and progradational delta in Jezero crater, Mars: Implications for Noachian climate. *Planet. Space Sci.* **67**, 28–45 (2012). doi: 10.1016/j.pss.2012.02.003
23. K. M. Stack *et al*., Photogeologic map of the Perseverance rover field site in Jezero crater constructed by the Mars 2020 Science Team. *Space Sci. Rev.* **216**, 127 (2020). doi: 10.1007/s11214-020-00739-x; pmid: 33568875

24. S. Shahrzad *et al*., Crater statistics on the dark-toned, mafic floor unit in Jezero crater, Mars. *Geophys. Res. Lett.* **46**, 2408–2416 (2019). doi: 10.1029/2018GL081402
25. J. D. Tarnas *et al*., Characteristics, origins, and biosignature preservation potential of carbonate-bearing rocks within and outside of Jezero crater. *J. Geophys. Res. Planets* **126**, JE006898 (2021). doi: 10.1029/2021JE006898; pmid: 34824965
26. T. A. Goudge, K. L. Aureli, J. W. Head, C. I. Fassett, J. F. Mustard, Classification and analysis of candidate impact crater-hosted closed-basin lakes on Mars. *Icarus* **260**, 346–367 (2015). doi: 10.1016/j.icarus.2015.07.026
27. A. Nelessen, C. Sackier, I. Clark, P. Brugarolas, G. Villar, A. Chen, A. Stehura, R. Otero, E. Stilley, D. Way, K. Edquist, S. Mohan, C. Giovingo, M. Lefland, "Mars 2020 Entry, Descent, and Landing System overview," 2019 IEEE Aerospace Conference, Big Sky, MT, 2 to 9 March 2019.
28. S. Holm-Alwmark *et al*., Stratigraphic relationships in Jezero crater, Mars: Constraints on the timing of fluvial-lacustrine activity from orbital observations. *J. Geophys. Res. Planets* **126**, (2021). doi: 10.1029/2021JE006840
29. S.-E. Hamran *et al*., Radar Imager for Mars' Subsurface Experiment—RIMFAX. *Space Sci. Rev.* **216**, 128 (2020). doi: 10.1007/s11214-020-00740-4
30. J. F. Bell 3rd *et al*., The Mars 2020 Perseverance rover Mast Camera Zoom (Mastcam-Z) multispectral, stereoscopic imaging investigation. *Space Sci. Rev.* **217**, 24 (2021). doi: 10.1007/s11214-020-00755-x; pmid: 33612866
31. R. Bhartia *et al*., Perseverance's Scanning Habitable Environments with Raman and Luminescence for Organics and Chemicals (SHERLOC) Investigation. *Space Sci. Rev.* **217**, 58 (2021). doi: 10.1007/s11214-021-00812-z
32. R. C. Wiens *et al*., The SuperCam Instrument Suite on the NASA Mars 2020 Rover: Body unit and combined system tests. *Space Sci. Rev.* **217**, 4 (2021). doi: 10.1007/s11214-020-00777-5; pmid: 33380752
33. A. C. Allwood *et al*., PIXL: Planetary Instrument for X-Ray Lithochemistry. *Space Sci. Rev.* **216**, 134 (2020). doi: 10.1007/s11214-020-00767-7
34. R. C. Moeller *et al*., The Sampling and Caching Subsystem (SCS) for the scientific exploration of Jezero crater by the Mars 2020 Perseverance rover. *Space Sci. Rev.* **217**, 5 (2020). doi: 10.1007/s11214-020-00783-7
35. Y. Liu *et al*., An olivine cumulate outcrop on the floor of Jezero crater, Mars. *Science* **377**, eabo2756 (2022). doi: 10.1126/science.abo2756
36. B. H. N. Horgan, R. B. Anderson, G. Dromart, E. S. Amador, M. S. Rice, The mineral diversity of Jezero crater: Evidence for possible lacustrine carbonates on Mars. *Icarus* **339**, 113526 (2020). doi: 10.1016/j.icarus.2019.113526
37. J. L. Bishop, J. F. Bell III, J. E. Moersch, Eds., *Remote Compositional Analysis: Techniques for Understanding Spectroscopy, Mineralogy, and Geochemistry of Planetary Surfaces* (Cambridge Univ. Press, 2019).
38. J. Filiberto *et al*., A review of volatiles in the Martian interior. *Meteorit. Planet. Sci.* **51**, 1935–1958 (2016). doi: 10.1111/maps.12680
39. See supplementary materials.
40. L. R. Wager, G. M. Brown, *Layered Igneous Rocks* (W. H. Freeman & Co., 1967).
41. O. Namur, B. Abily, A. E. Boudreau, F. Blanchette, J. W. M. Bush, G. Ceuleneer, B. Charlier, C. H. Donaldson, J.-C. Duchesne, M. D. Higgins, D. Morata, T. F. D. Nielsen, B. O'Driscoll, K. N. Pang, T. Peacock, C. J. Spandler, A. Toramaru, I. V. Veksler, "Igneous layering in basaltic magma chambers" in *Layered Intrusions*, B. Charlier, O. Namur, R. Latypov, C. Tegner, Eds. (Springer Geology, Springer Dordrecht, 2015), pp. 75–152.
42. H. Hiesinger, J. W. HeadIII, The Syrtis Major volcanic province, Mars: Synthesis from Mars Global Surveyor data. *J. Geophys. Res.* **109**, E01004 (2004). doi: 10.1029/2003JE002143
43. L. M. Jozwiak, J. W. Head, L. Wilson, Lunar floor-fractured craters as magmatic intrusions: Geometry, modes of emplacement, associated tectonic and volcanic features, and implications for gravity anomalies. *Icarus* **248**, 424–447 (2015). doi: 10.1016/j.icarus.2014.10.052
44. C. S. Edwards, J. L. Bandfield, P. R. Christensen, A. D. Rogers, The formation of infilled craters on Mars: Evidence for widespread impact induced decompression of the early martian mantle? *Icarus* **228**, 149–166 (2014). doi: 10.1016/j.icarus.2013.10.005
45. B. L. Ehlmann, J. F. Mustard, An in-situ record of major environmental transitions on early Mars at Northeast Syrtis Major. *Geophys. Res. Lett.* **39**, L11202 (2012). doi: 10.1029/2012GL051594
46. M. S. Bramble, J. F. Mustard, M. R. Salvatore, The geological history of Northeast Syrtis Major, Mars. *Icarus* **293**, 66–93 (2017). doi: 10.1016/j.icarus.2017.03.030
47. E. El-Hinnawi, S. D. Abayazeed, A. S. Khalil, Spheroidal weathering of basalt from Gebel Qatrani, Fayum Depression, Egypt. *Bull. Natl. Res. Cent.* **45**, 1 (2021). doi: 10.1186/s42269-020-00453-2
48. P. B. Kelemen *et al*., Rates and mechanisms of mineral carbonation in peridotite: Natural processes and recipes for enhanced, in situ CO_2 capture and storage. *Annu. Rev. Earth Planet. Sci.* **39**, 545–576 (2011). doi: 10.1146/annurev-earth-092010-152509
49. F. Wang, D. Dreisinger, M. Jarvis, T. Hitchins, Kinetics and mechanism of mineral carbonation of olivine for CO_2 sequestration. *Miner. Eng.* **131**, 185–197 (2019). doi: 10.1016/j.mineng.2018.11.024
50. F. Dufaud, I. Martinez, S. Shilobreeva, Experimental study of Mg-rich silicates: Carbonation at 400 and 500 C and 1 kbar. *Chem. Geol.* **265**, 79–87 (2009). doi: 10.1016/j.chemgeo.2009.01.026
51. S. He, J. W. Morse, The carbonic acid system and calcite solubility in aqueous Na-K-Ca-Mg-Cl-SO4 solutions from 0 to 90°C. *Geochim. Cosmochim. Acta* **57**, 3533–3554 (1993). doi: 10.1016/0016-7037(93)90137-L
52. L. Chai, A. Navrotsky, Synthesis, characterization, and enthalpy of mixing of the (Fe,Mg)CO_3 solid solution. *Geochim. Cosmochim. Acta* **60**, 4377–4383 (1996). doi: 10.1016/S0016-7037(96)00261-X
53. B. M. Tutolo, B. W. Evans, S. M. Kuehner, Serpentine–hisingerite solid solution in altered ferroan peridotite and olivine gabbro. *Minerals (Basel)* **9**, 47 (2019). doi: 10.3390/min9010047
54. K. Bladh, The formation of goethite, jarosite, and alunite during the weathering of sulfide-bearing felsic rocks. *Econ. Geol.* **77**, 176–184 (1982). doi: 10.2113/gsecongeo.77.1.176
55. P. B. Kelemen, G. Hirth, Reaction-driven cracking during retrograde metamorphism: Olivine hydration and carbonation. *Earth Planet. Sci. Lett.* **345–348**, 81–89 (2012). doi: 10.1016/j.epsl.2012.06.018
56. P. E. Martin *et al*., Reevaluation of perchlorate in Gale Crater rocks suggests geologically recent perchlorate addition. *J. Geophys. Res. Planets* **125**, (2020). doi: 10.1029/2019JE006156
57. A. S. Goudie, H. A. Viles, *Salt Weathering Hazard* (Wiley, 1997).
58. H. W. Nesbitt, R. E. Wilson, Recent chemical weathering of basalts. *Am. J. Sci.* **292**, 740–777 (1992). doi: 10.2475/ajs.292.10.740
59. M. A. Velbel, "Aqueous alteration in martian meteorites: Comparing mineral relations in igneous-rock weathering of martian meteorites and in the sedimentary cycle of Mars" in *Sedimentary Geology of Mars*, J. P. Grotzinger, R. E. Milliken, Eds. (Society for Sedimentary Geology, 2012).
60. N. Mangold *et al*., Perseverance rover reveals an ancient delta-lake system and flood deposits at Jezero crater, Mars. *Science* **374**, 711–717 (2021). doi: 10.1126/science.abl4051; pmid: 34618548
61. C. S. Cockell *et al*., Habitability: A review. *Astrobiology* **16**, 89–117 (2016). doi: 10.1089/ast.2015.1295; pmid: 26741054
62. T. O. Stevens, J. P. McKinley, Lithoautotrophic microbial ecosystems in deep basalt aquifers. *Science* **270**, 450–455 (1995). doi: 10.1126/science.270.5235.450
63. K. H. Nealson, F. Inagaki, K. Takai, Hydrogen-driven subsurface lithoautotrophic microbial ecosystems (SLiMEs): Do they exist and why should we care? *Trends Microbiol.* **13**, 405–410 (2005). doi: 10.1016/j.tim.2005.07.010; pmid: 16054814
64. O. U. Mason *et al*., First investigation of the microbiology of the deepest layer of ocean crust. *PLOS ONE* **5**, e15399 (2010). doi: 10.1371/journal.pone.0015399; pmid: 21079766
65. N. Stivaletta, R. Barbieri, D. Billi, Microbial colonization of the salt deposits in the driest place of the Atacama Desert (Chile). *Orig. Life Evol. Biosph.* **42**, 187–200 (2012). doi: 10.1007/s11084-012-9289-y; pmid: 22661023
66. K. C. Benison, How to search for life in Martian chemical sediments and their fluid and solid inclusions using petrographic and spectroscopic methods. *Front. Environ. Sci.* **7**, 108 (2019). doi: 10.3389/fenvs.2019.00108
67. S. McMahon *et al*., A field guide to finding fossils on Mars. *J. Geophys. Res. Planets* **123**, 1012–1040 (2018). doi: 10.1029/2017JE005478; pmid: 30034979
68. M. R. Mormile *et al*., Isolation of *Halobacterium salinarum* retrieved directly from halite brine inclusions. *Environ. Microbiol.* **5**, 1094–1102 (2003). doi: 10.1046/j.1462-2920.2003.00509.x; pmid: 14641589
69. B. A. Schubert, T. K. Lowenstein, M. N. Timofeeff, M. A. Parker, Halophilic Archaea cultured from ancient halite, Death Valley, California. *Environ. Microbiol.* **12**, 440–454 (2010). doi: 10.1111/j.1462-2920.2009.02086.x; pmid: 19840101
70. S. A. Newman *et al*., Lipid biomarker record of the serpentinite-hosted ecosystem of the Samail Ophiolite, Oman and implications for the search for biosignatures on Mars. *Astrobiology* **20**, 830–845 (2020). doi: 10.1089/ast.2019.2066; pmid: 32648829
71. F. Klein *et al*., Fluid mixing and the deep biosphere of a fossil Lost City-type hydrothermal system at the Iberia Margin. *Proc. Natl. Acad. Sci. U.S.A.* **112**, 12036–12041 (2015). doi: 10.1073/pnas.1504674112; pmid: 26324888
72. A. S. Templeton *et al*., Accessing the subsurface biosphere within rocks undergoing active low-temperature serpentinization in the Samail Ophiolite (Oman Drilling Project). *J. Geophys. Res. Biogeosci.* **126**, (2021). doi: 10.1029/2021JG006315
73. A. Udry *et al*., What Martian meteorites reveal about the interior and surface of Mars. *J. Geophys. Res. Planets* **125**, (2020). doi: 10.1029/2020JE006523
74. A. Mittelholz *et al*., The Mars 2020 candidate landing sites: A magnetic field perspective. *Earth Space Sci.* **5**, 410–424 (2018). doi: 10.1029/2018EA000420
75. J. N. Maki *et al*., The Mars 2020 engineering cameras and microphone on the Perseverance rover: A next-generation imaging system for Mars exploration. *Space Sci. Rev.* **216**, 137 (2020). doi: 10.1007/s11214-020-00765-9; pmid: 33268910
76. A. C. Allwood, J. A. Hurowitz, Mars 2020 PIXL Raw and Processed Data Bundle, Planetary Data System (2021); https://doi.org/10.17189/1522645.
77. S.-E. Hamran, D. A. Paige, Mars 2020 RIMFAX Bundle, Planetary Data System (2021); https://doi.org/10.17189/1522644.
78. L. W. Beegle, R. Bhartia, Mars 2020 SHERLOC Bundle, Planetary Data System (2021); https://doi.org/10.17189/1522643.
79. R. C. Wiens, S. A. Maurice, Mars 2020 SuperCam Bundle, Planetary Data System (2021); https://doi.org/10.17189/1522646.
80. J. F. Bell, J. N. Maki, Mars 2020 Mast Camera Zoom Data Bundle, from Operations Team, calibrated products, Planetary Data System (2021); https://doi.org/10.17189/bs6b-4782.
81. J. N. Maki, Mars 2020 Engineering Camera (ECAM) Bundles, Planetary Data System (2021); https://doi.org/10.17189/1522847.

ACKNOWLEDGMENTS

The authors thank three anonymous reviewers for helpful suggestions that improved this manuscript. This work was enabled by a large and dedicated team of engineers that designed, built, and operate the Mars 2020 spacecraft. We thank J. Arballo for drafting many of the figures in this paper. **Funding:** This effort was carried out in part at the Jet Propulsion Laboratory, California Institute of Technology, under a contract with the National Aeronautics and Space Administration (80NM0018D0004). K.A.F., K.M.S., J.D.T., V.Z.S., Y.L., J.N.M., A.C.A., Y.G., P.A.W., E.L.C., S.M.Mi., R.C.M., S.F.S., N.S., and K.U. were supported by NASA grant 80NM0018D0004 through JPL. D.T.F. was supported by Australian Research Council grant DE210100205. E.F.G. was supported by Canadian Space Agency grant 21EXPCOI1. E.A.C. was supported by Canadian Space Agency grant 19PACOI0 and Natural Sciences and Engineering Research Council of Canada grant RGPIN-2021-02995. C.D.K.H., T.V.K., and M.E.S. were supported by Canadian Space Agency M2020 Participating Scientist grants. M.M. was supported by the EU's Horizon 2020 research and innovation program under the Marie Skłodowska Curie grant 801199. G.P. was supported by ESA PRODEX Experiment Arrangement PEA 4000117520. V.D. was supported by Fonds pour la Recherche Scientifique. A.J.W., S.J.V., D.L.S., J.I.S., L.E.M., T.B., and E.M.H. were supported by NASA Mars 2020 Participating Scientist grants. T.B. was supported by the Simons Foundation Collaboration on the Origins of Life grant 327126. R.C.W. was supported by NASA Mars 2020 contracts NNH15AZ24I and NNH13ZDA018O for SuperCam and a LANL internal LDRD grant. S.K.S. was supported by JPL subcontract 1654163. S.G. was supported by the Royal Society Leverhulme Trust Senior Research Fellowship (SRF\R1\21000106) and the UK Space Agency Aurora program. M.-P.Z. was supported by the Spanish Ministry of Science and Innovation under grant PID2019-104205GB-C21. S.Si.

was supported by the Swedish National Space Agency under contracts 137/19 and 2021-00092. K.B.K. was supported by the Carlsberg Foundation, grant CF19-0023. S.-E.H. was supported by the Research Council of Norway under grants 301238 and 309835. The work of O.B., A.C., O.F., L.M., N.M., C.Q.-N., P.B., K.B., B.C., E.C., E.D., T.F., J.L., S.L.M., S.M., P.-Y.M., P.P., C.P., P.C.P., C.R., and V.S. on Mars 2020 was supported by CNES. K.H.-L. was supported by a UK Space Agency Aurora Research Fellowship. M.A.S. was supported by UK Space Agency grants ST/V002732/1 and ST/V006134/1. J.F.B. was supported by NASA-JPL subcontract number 1511125. A.G.F. was supported by the European Research Council, Consolidator Grant 818602. **Author contributions:** Conceptualization: K.A.F., R.C.W., J.A.H., J.I.S., K.M.S., and D.L.S. Methodology: K.A.F., K.M.S., E.L.S., J.N.M., J.D.T., A.G.H., P.-Y.M., G.P., D.A.K.P., C.D.T., K.U., R.C.W., T.V.K., M.E.S., J.A.H., J.F.B., B.H.N.H., Y.L., R.B., S.-E.H., L.M., C.Q.-N., and C.C.M. Investigation: K.A.F., K.M.S., B.H.N.H., J.D.T., J.I.S., V.Z.S., E.L.S., K.R.M., S.M.Mc., R.C.W., A.H.T., L.E.M., O.B., T.V.K., N.J.T., J.A.H., K.H.W., L.S.C., J.F.B., Y.L., J.N.M., M.E.S., R.B., T.B., A.J.B., B.C.C., A.C., O.F., T.S.J.G., Y.G., S.G., S.-E.H., C.D.K.H., K.H.-L., J.R.J., L.C.K., P.B.K., K.B.K., L.M., N.M., C.Q.-N., M.S.R., P.S.R., S.Sh., S.Si., A.S., M.W., B.P.W., A.J.W., B.V.W., P.A.W., T.A.A.-M., P.B., K.B., S.B., A.S.B., E.L.C., B.C., E.C., E.A.C., B.A.C., V.D., E.D., A.G.F., D.T.F., S.Z.F., T.F., J.F., B.J.G., E.F.G., E.M.H., A.G.H., J.H., J.L.J., E.M.K., J.L., S.L.M., J.M.M., S.M., M.M., P.-Y.M., S.M.Mi., C.C.M., R.C.M., J.I.N., A.M.O., G.P., D.A.P., P.P., C.P., P.C.P., C.R., V.S., M.S., M.A.S., S.K.S., S.F.S., M.S.C., C.D.T., K.U., S.J.V., M.-P.Z., J.W.R., A.D.C., A.G.Y., A.C.A., H.E.F.A., M.S.C., and R.S. Visualization: K.A.F., K.M.S., D.L.S., E.L.S., J.N.M., L.W.B., R.B., J.H., S.Sh., L.S.C., B.H.N.H., J.D.T., J.F.B., S.-E.H., and P.S.R. Funding acquisition: K.A.F., K.M.S., K.H.W., M.S., A.J.B., N.S., A.C.A., S.-E.H., R.C.W., L.W.B., and J.F.B. Project administration: K.A.F., K.M.S., K.H.W., R.C.W., J.A.H., L.W.B., J.F.B., J.N.M., R.B., T.B., A.J.B., S.-E.H., C.D.K.H., S.M., D.A.P., M.S., N.S., S.M.Mi., and A.C.A. Supervision: K.A.F., K.M.S., K.H.W., D.L.S., B.H.N.H., J.D.T., J.I.S., V.Z.S., L.E.M., Y.G., S.G., K.H.-L., J.R.J., L.C.K., N.M., M.S.R., B.P.W., A.J.W., P.A.W., E.L.C., B.A.C., D.T.F., and J.F. Writing: K.A.F., K.M.S., D.L.S., B.H.N.H., J.D.T., V.Z.S., J.I.S., E.L.S., K.R.M., J.H., R.C.W., K.H.W., N.J.T., J.A.H., B.L.E., L.E.M., P.M.V., and S.M.Mc. Writing – review & editing: K.A.F., K.M.S, D.L.S., B.L.E., and S.G. **Competing interests:** The authors declare that they have no competing interests. **Data and materials availability:** All data used in this paper are archived in the NASA Planetary Data System (*76–81*). Details of which files were used for each figure are provided in the supplementary text section of the supplementary materials. **License information:** Copyright © 2022 the authors, some rights reserved; exclusive licensee American Association for the Advancement of Science. No claim to original US government works. https://www.science.org/about/science-licenses-journal-article-reuse

SUPPLEMENTARY MATERIALS

science.org/doi/10.1126/science.abo2196
Materials and Methods
Supplementary Text
Figs. S1 to S9
Tables S1 and S2
Data Sources
References (*82–92*)

Submitted 21 January 2022; accepted 25 July 2022
Published online 25 August 2022
10.1126/science.abo2196



Pushing the Boundaries of Knowledge

As AAAS's first multidisciplinary, open access journal, *Science Advances* publishes research that reflects the selectivity of high impact, innovative research you expect from the *Science* family of journals, published in an open access format to serve a vast and growing global audience. Check out the latest findings or learn how to submit your research: **ScienceAdvances.org**

Science Advances
AAAS

GOLD OPEN ACCESS, DIGITAL, AND FREE TO ALL READERS

RESEARCH ARTICLES

MARTIAN GEOLOGY

An olivine cumulate outcrop on the floor of Jezero crater, Mars

Y. Liu[1]*, M. M. Tice[2], M. E. Schmidt[3], A. H. Treiman[4], T. V. Kizovski[3], J. A. Hurowitz[5], A. C. Allwood[1], J. Henneke[6], D. A. K. Pedersen[6], S. J. VanBommel[7], M. W. M. Jones[8,9], A. L. Knight[7], B. J. Orenstein[10], B. C. Clark[11], W. T. Elam[12], C. M. Heirwegh[1], T. Barber[1], L. W. Beegle[1], K. Benzerara[13], S. Bernard[13], O. Beyssac[13], T. Bosak[14], A. J. Brown[15], E. L. Cardarelli[1], D. C. Catling[16], J. R. Christian[7], E. A. Cloutis[17], B. A. Cohen[18], S. Davidoff[1], A. G. Fairén[19,20], K. A. Farley[21], D. T. Flannery[10], A. Galvin[1], J. P. Grotzinger[21], S. Gupta[22], J. Hall[14], C. D. K. Herd[23], K. Hickman-Lewis[24,25], R. P. Hodyss[1], B. H. N. Horgan[26], J. R. Johnson[27], J. L. Jørgensen[6], L. C. Kah[28], J. N. Maki[1], L. Mandon[29], N. Mangold[30], F. M. McCubbin[31], S. M. McLennan[5], K. Moore[21], M. Nachon[2], P. Nemere[10], L. D. Nothdurft[10], J. I. Núñez[27], L. O'Neil[12], C. M. Quantin-Nataf[32], V. Sautter[13], D. L. Shuster[33], K. L. Siebach[34], J. I. Simon[31], K. P. Sinclair[12], K. M. Stack[1], A. Steele[35], J. D. Tarnas[1], N. J. Tosca[36], K. Uckert[1], A. Udry[37], L. A. Wade[1], B. P. Weiss[14], R. C. Wiens[38]†, K. H. Williford[1,39], M.-P. Zorzano[19]

The geological units on the floor of Jezero crater, Mars, are part of a wider regional stratigraphy of olivine-rich rocks, which extends well beyond the crater. We investigated the petrology of olivine and carbonate-bearing rocks of the Séítah formation in the floor of Jezero. Using multispectral images and x-ray fluorescence data, acquired by the Perseverance rover, we performed a petrographic analysis of the Bastide and Brac outcrops within this unit. We found that these outcrops are composed of igneous rock, moderately altered by aqueous fluid. The igneous rocks are mainly made of coarse-grained olivine, similar to some martian meteorites. We interpret them as an olivine cumulate, formed by settling and enrichment of olivine through multistage cooling of a thick magma body.

Jezero crater, the landing site of the Perseverance rover, is located at the western edge of Isidis Planitia on Mars (Fig. 1A). Orbital data have constrained the crater's age to between 3.82 billion and 3.96 billion years (*1*, *2*). A light-toned, olivine- and carbonate-bearing rock unit exposed on the floor of Jezero has been informally named the Séítah formation (Fig. 1C) (*3*–*5*). Rocks similar to Séítah in morphology and mineralogy extend beyond the rim of Jezero; they span >70,000 km^2 from inside Isidis Planitia (*6*), to the neighboring regions of Northeast Syrtis (*7*), Nili Fossae (*8*), and Libya Montes (Fig. 1B) (*9*, *10*). Orbital observations have shown that this regional unit has high abundances of olivine (*11*)—an early crystallizing, rock-formimg mineral—with large inferred grain sizes (several millimeters) and moderate magnesium contents of $Fo_{44–66}$ [where Fo is forsterite (Mg_2SiO_4) and the subscript numbers indicate its molar percentage in olivine] (*4*, *11*). Hypotheses for the unit's origin include an impact melt or intrusive igneous rocks (*6*), basaltic lava flows (*9*, *12*), volcanic ash (*2*, *13*), or clastic material (fragmental deposits formed by transport and deposition from volcanic eruptions, impacts, water, or wind) (*14*).

Images of Séítah formation rocks taken by the Perseverance rover have shown centimeter- to decimeter-scale layering and abundant dark, millimeter-scale angular grains, reported in a companion paper (*5*). These observations were consistent with any of the above hypotheses for the regional unit's origin. We sought to distinguish between these possibilities using the rover's arm-mounted Planetary Instrument for X-ray Lithochemistry (PIXL) (*15*).

PIXL observations

To remove any modified surface materials, two 50-mm-diameter patches (informally named Garde and Dourbes) were abraded into two rock outcrops (informally named Bastide and Brac, respectively). Both outcrops are part of the Bastide member (informal name) of the Séítah formation (Fig. 1C). Reflectance optical images of both patches—illuminated with ultraviolet (UV; 385 nm), blue (B; 450 nm), green (G; 530 nm), and near-infrared (NIR; 735 nm) light-emitting diodes (LEDs)—were acquired by using PIXL's micro context camera (MCC). The Dourbes patch was subsequently analyzed to produce two x-ray fluorescence (XRF) raster maps with areas of 4 by 12.5 mm and 5 by 7 mm, at a step size of 0.125 mm (Fig. 2) (*16*).

We used these data to produce color and color ratio images of both patches and estimated volume percentages of phases in each (Fig. 2A, fig. S1, and table S1). For the Dourbes patch where XRF maps were acquired, we produced diffraction maps of crystallinity and crystal orientation (Fig. 2C and fig. S2), composite maps of elemental abundances (Fig. 2D and figs. S3 and S4), and chemical analyses of individual minerals and the bulk rock (tables S2 to S5) (*16*). The reconstructed color images show that both patches display a similar texture, with beige equant grains of sizes ranging from 1 to 3.5 mm, greenish-gray irregularly

[1]Jet Propulsion Laboratory, California Institute of Technology, Pasadena, CA 91109, USA. [2]Department of Geology and Geophysics, Texas A&M University, College Station, TX 77843, USA. [3]Department of Earth Sciences, Brock University, St. Catharines, ON L2S 3A1, Canada. [4]Lunar and Planetary Institute, Universities Space Research Association, Houston, TX 77058, USA. [5]Department of Geosciences, Stony Brook University, Stony Brook, NY 11794, USA. [6]Department of Space, Measurement and Instrumentation, Technical University of Denmark, Lyngby, Denmark. [7]McDonnell Center for the Space Sciences, Department of Earth and Planetary Sciences, Washington University in St. Louis, St. Louis, MO 63130, USA. [8]Central Analytical Research Facility, Queensland University of Technology, Brisbane, QLD 4000, Australia. [9]School of Chemistry and Physics, Queensland University of Technology, Brisbane, QLD 4000, Australia. [10]School of Earth and Atmospheric Sciences, Queensland University of Technology, Brisbane, QLD 4000, Australia. [11]Space Science Institute, Boulder, CO 80301, USA. [12]Applied Physics Lab and Department of Earth and Space Sciences, University of Washington, Seattle, WA 98052, USA. [13]Institut de Minéralogie, Physique des Matériaux et Cosmochimie, Centre National de la Recherche Scientifique (CNRS), Muséum National d'Histoire Naturelle, Sorbonne Université, 75005 Paris, France. [14]Department of Earth, Atmospheric and Planetary Sciences, Massachusetts Institute of Technology, Cambridge, MA 02139, USA. [15]Plancius Research, Severna Park, MD 21146, USA. [16]Department of Earth and Space Sciences, University of Washington, Seattle WA 98195, USA. [17]Department of Geography, University of Winnipeg, Winnipeg, MB R3B 2E9, Canada. [18]NASA Goddard Space Flight Center, Greenbelt, MD 20771, USA. [19]Centro de Astrobiología, Consejo Superior de Investigaciones Cientificas–Instituto Nacional de Tecnica Aeroespacial, 28850 Madrid, Spain. [20]Department of Astronomy, Cornell University, Ithaca, NY 14853, USA. [21]Division of Geological and Planetary Sciences, California Institute of Technology, Pasadena, CA 91125, USA. [22]Department of Earth Science and Engineering, Imperial College London, London SW7 2AZ, UK. [23]Department of Earth and Atmospheric Sciences, University of Alberta, Edmonton, AB T6G 2E3, Canada. [24]Department of Earth Sciences, The Natural History Museum, South Kensington, London, SW7 5BD UK. [25]Dipartimento di Scienze Biologiche, Geologiche e Ambientali, Università di Bologna, I-40126 Bologna, Italy. [26]Department of Earth, Atmospheric, and Planetary Sciences, Purdue University, West Lafayette, IN 47907, USA. [27]Applied Physics Laboratory, Johns Hopkins University, Laurel, MD 20723, USA. [28]Department of Earth and Planetary Sciences, University of Tennessee, Knoxville, TN 37996, USA. [29]Laboratoire d'Etudes Spatiales et d'Instrumentation en Astrophysique, Observatoire de Paris-Université Paris Sciences et Lettres, CNRS, Sorbonne Université, Université de Paris Cité, 92190 Meudon, France. [30]Laboratoire Planetologie et Geosciences, Centre National de Recherches Scientifiques, Universite Nantes, Universite Angers, Unite Mixte de Recherche 6112, 44322 Nantes, France. [31]NASA Johnson Space Center, Houston, TX 77058, USA. [32]Laboratoire de Geologie de Lyon-Terre Planetes Environnement, Université Lyon, Université Claude Bernard Lyon 1, Ecole Normale Superieure Lyon, Centre National de Recherches Scientifiques, 69622 Villeurbanne, France. [33]Department of Earth and Planetary Science, University of California, Berkeley, Berkeley, CA 94720, USA. [34]Department of Earth, Environmental, and Planetary Sciences, Rice University, Houston, TX 77005, USA. [35]Earth and Planets Laboratory, Carnegie Institution for Science, Washington, DC 20015, USA. [36]Department of Earth Sciences, University of Cambridge, Cambridge CB2 3EQ, UK. [37]Department of Geosciences, University of Nevada, Las Vegas, Las Vegas, NV 89154, USA. [38]Los Alamos National Laboratory, Los Alamos, NM 87545, USA. [39]Blue Marble Space Institute of Science, Seattle, WA 98104, USA.

***Corresponding author. Email: yang.liu@jpl.nasa.gov**

†Present address: Department of Earth, Atmospheric, and Planetary Sciences, Purdue University, West Lafayette, IN 47907, USA.

shaped grains, and reddish-brown materials rimming these grains or occupying irregular areas between them (fig. S1, A and E). These features are discernable in color ratio plots (Fig. 2A and fig. S1). Elemental maps show intergrain areas that contain distinct chemical variations, and additional irregular regions with high aluminum (Al) (Fig. 2D) and non-uniform distribution of sodium (Na), potassium (K), and phosphorus (P) (figs. S3 and S4).

Our identifications of olivine and pyroxene minerals are supported by stoichiometric analysis of the PIXL data and are consistent with observations by other Perseverance instruments (*5*). We found that the beige equant grains have molar (Mg+Fe)/Si ≈ 2 and total cations of 2.995 to 3.025 per four oxygens (table S2), which is consistent with olivine's chemical formula, $(FeMg)_2SiO_4$. The greenish-gray grains have molar (Ca+Mg+Fe)/Si ≈ 1 and total cations of 4.032 to 4.042 per six oxygens (table S3), which is consistent with pyroxene's formula $(CaFeMg)_2Si_2O_6$. The molar Ca/(Ca+Mg+Fe) ratios of the pyroxene (0.35 to 0.37) show that it is the mineral augite (Fig. 3A) (*17*). Back-reflected diffracted x-rays from some noncontiguous augite regions show that they have identical crystal orientations, indicating that these regions are likely to be part of the same three-dimensional grain (a single augite crystal) (Fig. 2C and fig. S2). This texture, in which a large single pyroxene grain encloses smaller olivine grains (poikilitic texture), is characteristic of igneous cumulate rocks (Fig. 2B). The irregular intergrain Al-rich areas contain intergrown grains of Na-rich feldspar (<1 mm), Fe–Cr–Ti oxide (≤0.25 mm), K-rich feldspar (<0.125 mm), and Ca-phosphate (<0.125 mm), which are typical features of mesostasis—the last formed materials in the intergranular space—in igneous rocks (figs. S3 and S4). Olivine, augite, and mesostasis are the primary minerals in the prealteration bedrocks in the Séítah formation. The intergrain reddish-brown materials contain silicates, Fe–Mg carbonate, and Fe–Mg–Ca sulfate, which are secondary materials from alteration. The presence of carbonates was also indicated by other instruments on Perseverance (*5*) and consistent with orbital observations. We focused our analysis on the primary minerals.

Olivine is the dominant primary mineral, making up 65 ± 5 vol % of the Dourbes and Garde rocks (fig. S1 and table S1). The remainder of the analyzed area is made of augite at ~13 vol %, mesostasis at ~10 vol %, and secondary materials at ~12 vol %. The relative mineral proportions of olivine, augite, and feldspar (Fig. 3C) indicate that Dourbes is an olivine-rich wehrlite, a type of ultramafic igneous rock (*18*).

The chemical compositions of the olivine grains ($Fo_{55\pm1}$) are uniform, both within and between grains (Fig. 3B and table S2). Olivine grains contain more Fe than that would be in equilibrium with a melt of the rock's bulk composition (fig. S5 and tables S2 and S5). The augite composition is $Wo_{35-38}En_{43-44}Fs_{20-21}$, expressed as molar percentages of wollastonite (Wo; $Ca_2Si_2O_6$), enstatite (En; $Mg_2Si_2O_6$), and ferrosilite (Fs; $Fe_2Si_2O_6$) (Fig. 3A). Some regions in the single large poikilitic augite grain we investigated have small variations in Ca (<0.7 wt % Ca), Fe (<0.6 wt %), Mg (<0.6 wt %), and Cl (~0.3 wt %) (table S3). These could indicate the presence of inclusions, thin lamellae of pyroxene of different compositions, and/or minor alteration products that are smaller than PIXL's x-ray beam size.

Fe/Mn ratios of olivine and pyroxene in meteorites have been used to determine their planetary parentage (*19*). The molar Fe/Mn ratios in martian meteorites are 47 ± 3 for olivine and 32 ± 6 for pyroxene (uncertainties are 1 standard deviation) (*19*). The Dourbes minerals have ranges of molar Fe/Mn ratios

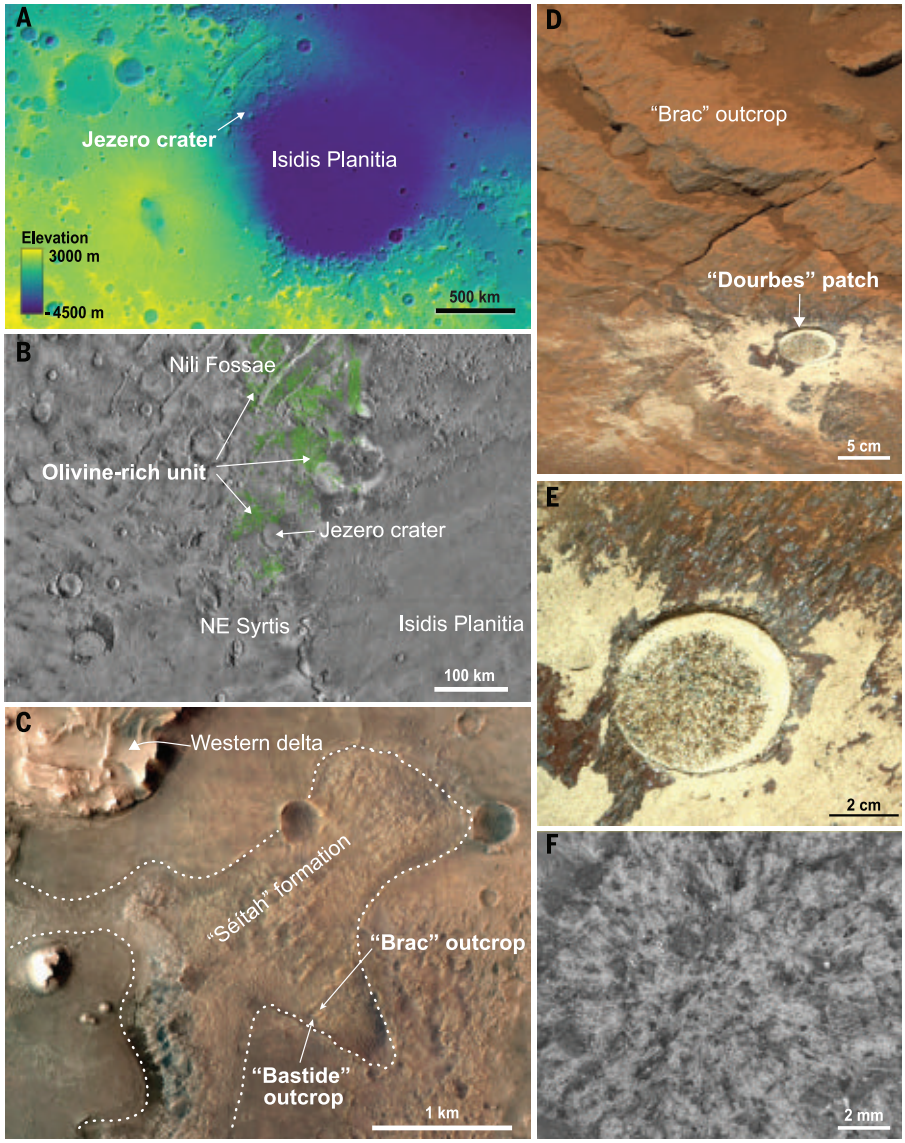


Fig. 1. The Dourbes patch in context from outcrop to regional scale. (**A**) Colorized terrain topography map showing location of Jezero crater on west edge of Isidis Planitia. Color scale bar shows altitude in meters. (**B**) Distribution of the regional olivine-bearing unit (green) on an orbital image. Data are from (*2*). (**C**) Color orbital image showing the location of Brac and the Bastide outcrops in the Séítah formation. The dotted white line demarcates the boundary of the Séítah formation outcrops. (**D**) Mast Camera Zoom (Mastcam-Z) image of the Brac outcrop, showing 5- to 10-cm-thick layers and the location of Dourbes patch (5 cm diameter). (**E**) Mastcam-Z image showing more detail of the Dourbes patch. (**F**) A portion of the abraded patch shown by the autofocus and context imager (ACI) of the Scanning Habitable Environments with Raman and Luminescence for Organics and Chemicals (SHERLOC) instrument on Perseverance rover (*5*). Image sources are listed in table S7.

of 55 ± 8 to 67 ± 9 for olivine and 38 ± 13 to 42 ± 3 for augite. The lower ends of these ranges are consistent with the values found for meteorites; we speculate that the higher Fe/Mn values could be due to a small amount of Fe-bearing minerals formed from aqueous alteration of olivine and augite.

Mesostasis areas show few signs of secondary salts; they have low abundances of SO_3 and Cl, and all analyzed element abundances sum to ~94.0 to 99.5 wt % (table S4), indicating the presence of little to no additional material enriched in C or H, which PIXL cannot detect directly. Compositions of the Fe–Cr–Ti oxide grains in Dourbes vary, depending on their petrographic setting. Those embedded in olivine have high molar Cr/Ti (~10), those at olivine-pyroxene boundaries have moderate Cr/Ti (~3.6), and those in mesostasis have low Cr/Ti (1 to 1.9) (fig. S6), leading to the variations in their estimated chemistry (table S4). Calcium phosphate occurs only in the mesostasis and has molar Ca/P ratios most consistent with merrillite (9:7) (fig. S7).

Interpretation as an igneous cumulate

We used our observations to evaluate the hypotheses mentioned above for the origin of olivine-carbonate unit exposed in Séítah.

Volcaniclastic (for example, pyroclastic deposits) or impact clastic (for example, rock fragments cemented by quenched impact melt) origins typically produce heterogeneous mixtures of mineral grains and rock fragments, embedded in a fine-grained matrix of (or altered from) ash particles (<50 μm). For Brac and Bastide outcrops in the Séítah formation, there is no evidence of rock fragments or a zoned fine-grained texture (Fig. 1). Observations of other outcrops also reveal no evidence of heterogeneous mixtures (*5*). We therefore exclude this possibility.

Sedimentary deposition of detrital olivine grains with cements is unlikely. The observed assemblage of coarse-grain augite and mesostasis with feldspar and Fe–Cr–Ti oxides has not previously been observed as a sedimentary cement and would not precipitate from fluids at near-surface temperatures and pressures. These grains are also too coarsely crystalline to be a detrital matrix. It is also not likely that the entire abrasion patch sits within one rock fragment in an extremely coarse-grained water-transported clastic rock (a conglomerate) because there is no evidence in images of the host rock for pebble-sized or larger grain boundaries, cements or fine-grained matrix, hydraulic sorting, sedimentary structures, erosion, or channel forms, as would be expected for such a deposit (*5*).

Instead, we conclude that the olivine and augite formed by cooling of a magma body. The magma could have arisen from volcanism or an impact because impact melting can fully homogenize the target rock, which would then solidify and crystallize very similarly to a magma originating from the martian mantle. We interpret Brac to be a cumulate igneous rock formed by settling and accumulation of olivine crystals from a molten mafic magma. The observed poikilitic texture is common in cumulate rocks on Earth (*20*) and in several martian meteorites (*21*). The compositional trend in Cr/Ti ratios we observed in the Fe–Cr–Ti oxide grains is also consistent with oxides crystallizing from a cooling magma (fig. S6). The similarity in mineralogy (*5*), textures, color, and reflectance spectral properties between Brac and Bastide outcrops within the Séítah formation indicates that our cumulate lithology interpretation can be extrapolated beyond the Dourbes abraded patch.

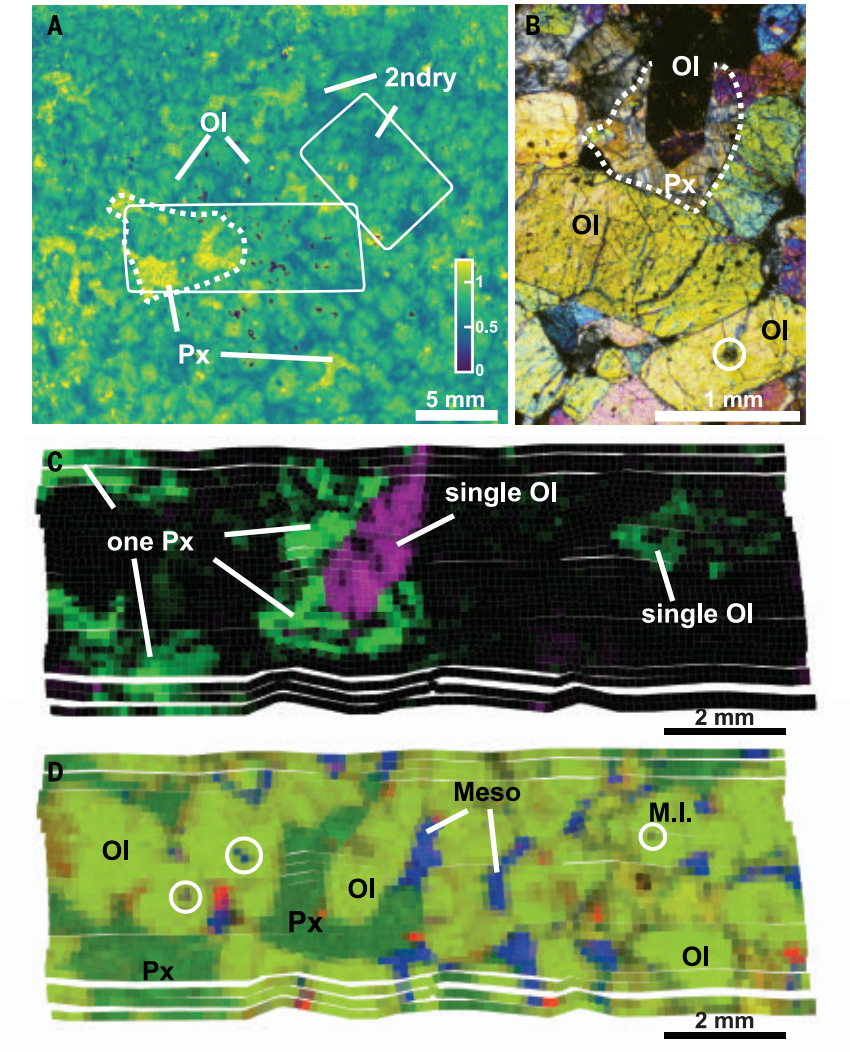


Fig. 2. Cumulate texture of Dourbes. (**A**) Ratio image taken with the PIXL MCC, showing the G/NIR ratios (color bar). Dourbes has a cumulate texture with olivine grains (Ol) and a poikilitic texture (region within the white dotted line) with pyroxene (Px). Secondary minerals are labeled "2ndry." White boxes indicate the areas used for x-ray fluorescence scans (figs. S3 and S4), the larger of which is shown in (C) and (D). (**B**) Cross-polarized light image of the Chassigny meteorite for comparison, showing poikilitic texture. Labels are the same as in (A). The white circle indicates a melt inclusion (M.I.) in Ol. (**C**) Mineral domain clustering map of the same region shown in (D). Green and magenta are used for two different diffraction peaks (7.28 to 7.72 keV and 5.67 to 6.17 keV, respectively). Points with the same diffraction peak are shown in the same color. All three regions of Px chemistry display the same diffraction peak (all green), suggesting that these regions are from a single pyroxene crystal. Ol grains inside the Px grains display different orientations, although all points inside one grain display the same diffraction peak (magenta) (*16*). (**D**) Chemical map derived from x-ray fluorescence, showing FeO (red), MgO (green), and Al_2O_3 (blue) concentrations (grayscale images of each element are provided in fig. S3). Labels indicate olivine, pyroxenes, and mesostasis (Meso). White circles indicate M.I.s. This composition map is shown in context with other optical images in movie S1.

Petrogenetic history

We next considered the magmatic crystallization and cooling history of the olivine cumulate outcrops in the Séítah formation. Using the chemistry of the olivine (fig. S5), we inferred that the magma was more iron rich, with Mg# = 27 to 30 [where Mg# is the molar Mg/(Mg+Fe) × 100] (*16*), than previously found (Mg# = 52 to 67) for Martian meteorites (*22*, *23*). We suggest that Séítah cumulate rocks formed from a parent magma that had previously lost Mg-rich minerals. Brac is different in both mineralogy and bulk chemistry from olivine-rich cumulates in Martian meteorites, and also from olivine-rich rocks at Gusev crater investigated by the Spirit rover (Figs. 3 and 4A) (*16*). The olivine grain size distribution and uniform composition in Brac, as well as the lack of larger olivine crystals observed in any Séítah outcrops, indicates an initially crystal-free melt (Fig. 5B). The presence of similarly sized olivine grains indicates an early stage of rapid homogeneous olivine nucleation, due to oversaturation, possibly induced by rapid cooling (Fig. 5C). Additionally, the presence of melt inclusions (typically 100 to 300 μm, with one up to ~600 μm) in the Dourbes olivine grains (Fig. 2D and fig. S4) suggests early rapid growth of olivine, forming crystals with open space between their outside faces (hopper or skeletal shaped crystals), typical morphology under rapid cooling (*24*). Later, olivine crystal of euhedral shapes formed through additional olivine growth filling in the open space, before or during gravitational settling (Fig. 5C). The gravitational settling forms a framework of olivine grains of mostly point contact with open space between grains (Fig. 5D). There is little textural or chemical evidence for later olivine growth filling in the open space between olivine grains, indicating that the cumulate was unaffected by subsequent magma infiltration or exchange after the olivine crystals had formed and accumulated. The proportion (~35 vol %) of other minerals among the olivine is consistent with the expected porosity of an olivine cumulate unaffected by compaction (*25*). The chemical equilibrium of olivine and augite and the coarse grains of augite imply extended cooling at a temperature (~1085°C) below that at which olivine starts to crystallize (*16*).

Emplacement history

Olivine cumulates can form in different geological settings, including large layered mafic intrusions (LLMIs), thick lava flows and ponds, shallow intrusive bodies as sills or laccoliths (lens-shaped igneous formations), or thick melt sheets from large impacts or their melt ejecta (Fig. 5A). The emplacement environment of cumulate rocks as observed in the Séítah formation can be assessed by using Earth analogs, after considering the difference in gravity (*16*). Unlike similar rocks in Earth LLMIs (*20*), Séítah olivine grains host large melt inclusions and show negligible additional growth after the olivine framework formed, indicating that Brac formed at depths of no more than a few kilometers. Thick (100 to 150 m) mafic or ultramafic lava flows or ponds on Earth form uncompacted frameworks of euhedral to subhedral olivine, similar to those observed in the Séítah formation. However, among Earth examples, olivine grains are typically smaller and the mesostasis is more fine-grained (or glassy) than in Séítah rocks (*16*). This indicates that these martian cumulates experienced later cooling at a lower rate than those of Earth analogs. We suggest potential explanations of a thicker lava than on Earth, or emplacement into hot surroundings (such as a crystal-laden lava injecting into a still-hot flow), or an intrusive environment such as a sill or a laccolith. Alternatively, similar features could have formed in a superheated impact melt sheet.

In those environments, olivine cumulates represent only the lower portion of the petrogenetic sequence. On Earth, pyroxene-rich cumulates commonly occur stratigraphically above olivine-rich layers, with a trend of minerals increasing in Fe, Na, and K higher in the sequence (Fig. 5D). Similar petrogenetic sequences have been hypothesized for cumulate

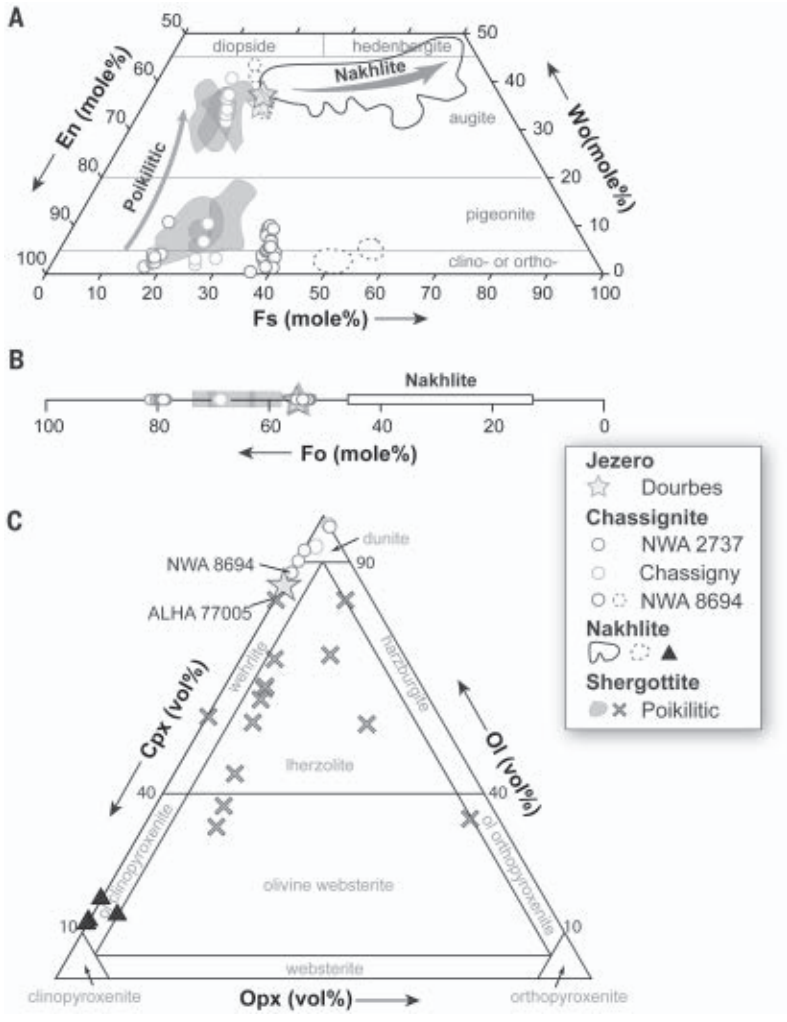


Fig. 3. Mineralogy of Dourbes. (**A**) Classification of pyroxene by using the percentage compositions of wollastonite (Wo), enstatite (En), and ferrosilite (Fs) (*17*). The average compositions of Dourbes pyroxene grains in table S3 are indicated with star symbols. Symbols or fields with solid lines indicate volumetrically major pyroxene species, and those with dotted lines are minor pyroxene species. Arrows indicate the direction of crystallization. (**B**) Binary diagram showing mole percentage of forsterite (Fo) in the olivine (Ol). The average compositions of Dourbes olivines (table S2) are indicated with star symbols. Dourbes olivine and pyroxene differ from martian meteorites. (**C**) Classification of ultramafic rocks by using volume percentages of olivine (Ol), clinopyroxene (Cpx), and orthopyroxene (Opx) (*18*). Symbols are defined in the legend. Source data for meteorites are listed in table S7.

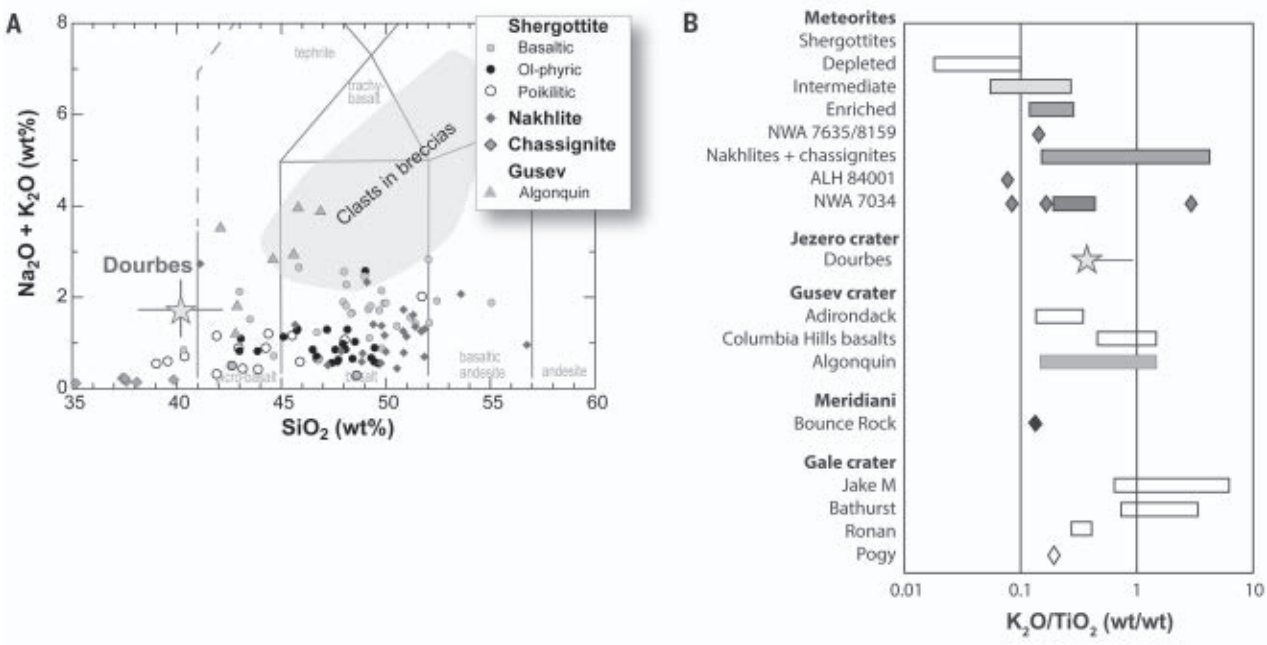


Fig. 4. Bulk chemistry of Dourbes compared with meteorites and igneous rocks elsewhere on Mars. (**A**) Plot of total alkali oxides as a function of SiO_2 abundance. Fields defined by vertical gray lines indicate the classification of volcanic rocks (*37*). The gray field indicates igneous clasts in breccia meteorite NWA 7034 (*38*). Dourbes contains less SiO_2 and higher alkali oxides than other martian igneous rocks. (**B**) Weight percentage ratios of K_2O/TiO_2 for Dourbes and other martian igneous rocks. Horizontal bars indicate the range of values from different samples of the listed targets. Solid diamonds indicate individual samples. Dourbes is most similar to K-enriched meteorites, such as chassignite and nakhlite, and the Algonquin rock in Gusev crater. Dourbes data are plotted as star symbols, with the error bar indicating the estimated 1σ uncertainty. Dourbes data are listed in table S5, and data sources for meteorites and rover data are listed in table S7.

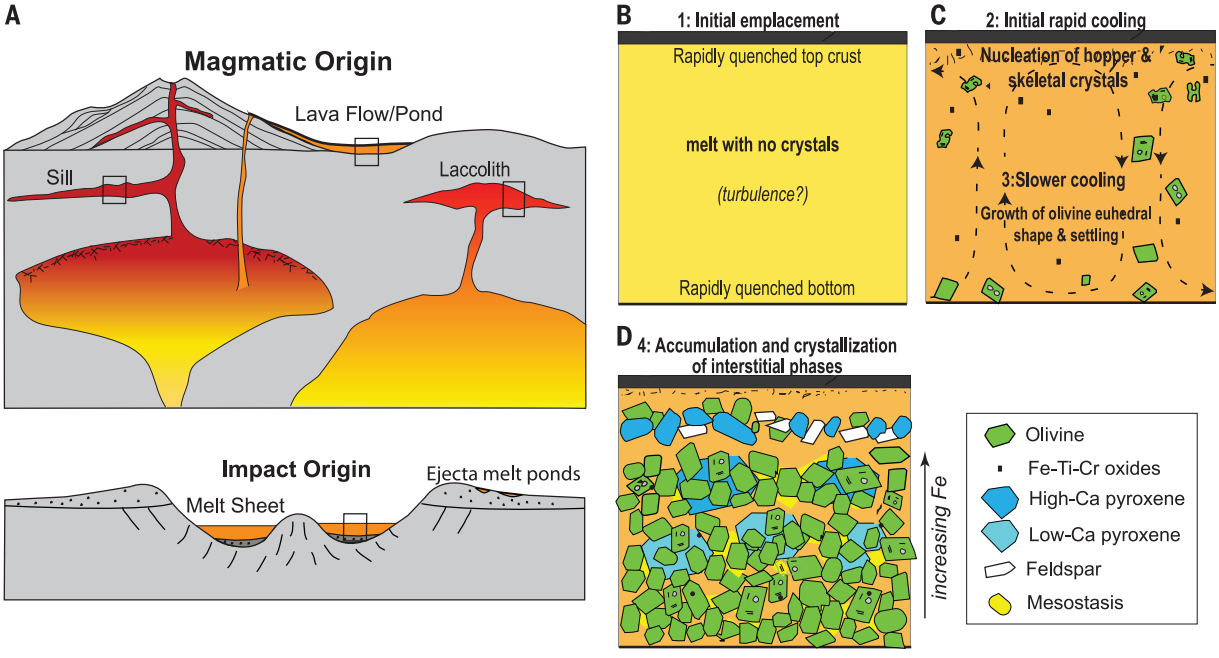


Fig. 5. Schematic diagram of potential emplacement models. (**A**) Potential emplacement models for the Bastide member, which hosts the Brac and Bastide outcrops. Color hue schematically indicates the temperature of the melt, with darker being cooler. Possible scenarios are an extrusive lava flow or pond, an intrusive sill or a small laccolith, or an impact melt sheet or ejecta melt ponds. All models provide the range of cooling rates as we infer for the Brac outcrop. (**B** to **D**) The petrology of our model (not to scale). (B) Initial emplacement of melt without any crystals, forming a rapidly quenched top crust and bottom. (C) Rapid cooling after emplacement causes nucleation and growth of hopper or skeletal olivine grains near the top surface. Convection of olivine into the (more slowly cooling) interior promotes olivine growth. Once each crystal reaches a critical size, it sinks to the bottom. (D) Continued cooling, crystallization, and sinking concentrates olivine at the base. Further crystallization of low-Ca pyroxene, high-Ca pyroxene, and other minerals (indicated in the legend) forms stratified layers, with increasing Fe contents higher in the melt body.

martian meteorites (*26*–*28*). The overlying Máaz formation could consist of such rocks (*5*); however, the contact between the Séítah and Máaz formations is obscured along the rover traverse, preventing a definitive determination of their relationship (*5*). Alternatively, the originally overlying strata might not have been explored by the rover or could have been eroded, or there is no petrographic link between the Séítah and Máaz formations.

Regional and planetary context

The presence of olivine cumulates in Jezero crater constrains the origin of the more widespread olivine-bearing regional units in and around Isidis Planitia. On petrologic evidence alone, it is most plausible that emplacement of the Séítah olivine cumulate was through magma injection into an environment that permitted slow cooling, such as a shallow igneous intrusion in the martian crust or into existing lava flows (*6*). However, this interpretation does not necessarily extend to the regional scale. A single large shallow intrusion seems unlikely to explain a regional unit over such a wide area (>70,000 km^2) with diverse local topographical influences. Similarly, the cumulate rock does not support the hypothesis that the regional unit is formed by a single deposit of clastic material (volcanic ash, impact ash, or sediments). We suggest that the regional exposure represents a series of related intrusive (sills and laccoliths) and extrusive magma bodies (lava flows and pyroclastic deposits). It could also contain some reworked sedimentary derivatives of the igneous rocks.

Abundances of incompatible elements [those that preferentially partition into the melt, such as Na, K, rubidium (Rb), strontium (Sr), lanthanum (La), samarium (Sm), neodymium (Nd), ytterbium (Yb), uranium (U), and thorium (Th)] in igneous rocks constrain the mantle source compositions. Ratios of rare earth elements (for example, La/Yb) are often used. However, these elements are of low abundances (typically at parts per million or parts per billion by weight) that are below PIXL's detection limit. The abundance ratio of K_2O/TiO_2 can be used instead to constrain source characteristics, provided that the magma has not experienced crystallization and removal of K- or Ti-bearing minerals (*29*). We compared our results with meteorites and igneous rocks studied by other rovers. The weight K_2O/TiO_2 ratio (0.38 ± 0.48) of the unaltered portion of Dourbes falls in the range found in martian meteorites containing olivine cumulates (chassignite) or augite cumulates (nakhlite), as well as mafic rocks investigated by other Mars rovers and landers (Fig. 4B). All of these samples are enriched in highly incompatible elements (such as K, U, and Th) compared with Ti (*30*). Measurements of Sm–Nd and Rb–Sr isotopes in nakhlites and chassignites have indicated that their mantle sources were depleted in highly incompatible elements; this suggests enrichment of highly incompatible elements in these cumulate meteorites during melt separation from the mantle sources (*26*, *28*). A process that enriches highly incompatible elements—possibly driven by interaction with high-temperature aqueous fluids after rock formation (metasomatic processes)—has previously been suggested for the mantle source regions of meteorites (*31*), alkali-rich basalts in Gusev crater (*32*) and Gale crater (*33*, *34*). Alternatively, geophysical data and models have been interpreted as indicating that Mars' mantle is depleted overall in radioactive heat-producing (K, U, and Th) and other highly incompatible elements, implying that those elements are instead concentrated in the planet's crust or upper mantle (*35*). Elevated abundances of highly incompatible elements in the mantle source regions at Gusev, Gale, and Jezero craters, as well as those for chassignites and nakhlites, could indicate a general enrichment of such elements in Mars' upper mantle, possibly caused by metasomatic processes and/or plume activity. These different samples range from a formation age of >3.9 billion to 1.34 billion years (*3*, *36*). This wide range of ages and geographic locations of igneous rocks with these properties indicates a long-lived process that has been operating on Mars for billions of years and has affected a large fraction of Mars's crust and upper mantle (*16*).

REFERENCES AND NOTES

1. S. C. Werner, *Icarus* **195**, 45–60 (2008).
2. L. Mandon *et al*., *Icarus* **336**, 113436 (2020).
3. B. L. Ehlmann *et al*., *Science* **322**, 1828–1832 (2008).
4. A. J. Brown, C. E. Viviano, T. A. Goudge, *J. Geophys. Res. Planets* **125**, JE006011 (2020).
5. K. A. Farley *et al*., *Science* **377**, eabo2196 (2022).
6. T. M. Hoefen *et al*., *Science* **302**, 627–630 (2003).
7. M. S. Bramble, J. F. Mustard, M. R. Salvatore, *Icarus* **293**, 66–93 (2017).
8. B. L. Ehlmann, J. F. Mustard, *Geophys. Res. Lett.* **39**, 1–7 (2012).
9. L. L. Tornabene *et al*., *J. Geophys. Res.* **113** (E10), E10001 (2008).
10. J. L. Bishop *et al*., *J. Geophys. Res. Planets* **118**, 487–513 (2013).
11. A. Ody *et al*., *J. Geophys. Res. Planets* **118**, 234–262 (2013).
12. V. E. Hamilton, P. R. Christensen, *Geology* **33**, 433–436 (2005).
13. C. H. Kremer, J. F. Mustard, M. S. Bramble, *Geology* **47**, 677–681 (2019).
14. A. D. Rogers, N. H. Warner, M. P. Golombek, J. W. Head 3rd, J. C. Cowart, *Geophys. Res. Lett.* **45**, 1767–1777 (2018).
15. A. C. Allwood *et al*., *Space Sci. Rev.* **216**, 134 (2020).
16. Materials and methods are available as supplementary materials.
17. N. Morimoto *et al*., *Am. Mineral.* **73**, 1123–1133 (1988).
18. R. W. Le Maitre *et al*., *Igneous Rocks: A Classification and Glossary of Terms* (Cambridge Univ. Press, ed. 2, 2002).
19. J. J. Papike, J. M. Karner, J. M. Shearer, *Am. Mineral.* **88**, 469–472 (2003).
20. L. R. Wager, *J. Petrol.* **1**, 364–398 (1960).
21. R. R. Rahib *et al*., *Geochim. Cosmochim. Acta* **266**, 463–496 (2019).
22. D. S. Musselwhite, H. A. Dalton, W. S. Kiefer, A. H. Treiman, *Meteorit. Planet. Sci. Arch.* **41**, 1271–1290 (2005).
23. J. B. Balta, H. Y. McSween, *Geology* **41**, 1115–1118 (2013).
24. F. Faure, P. Schiano, G. Trolliard, C. Nicollet, B. Soulestin, *Contrib. Mineral. Petrol.* **153**, 405–416 (2007).
25. M. W. Schmidt, M. Forien, G. Solferino, N. Bagdassarov, *Contrib. Mineral. Petrol.* **164**, 959–976 (2012).
26. A. H. Treiman, *Chem. Erde* **65**, 203–270 (2005).
27. F. M. McCubbin *et al*., *Meteorit. Planet. Sci.* **48**, 819–853 (2013).
28. A. Udry, J. M. D. Day, *Geochim. Cosmochim. Acta* **238**, 292–315 (2018).
29. M. E. Schmidt, C. M. Schrader, T. J. McCoy, *Earth Planet. Sci. Lett.* **384**, 198–208 (2013).
30. A. H. Treiman, *Meteorit. Planet. Sci.* **38**, 1849–1864 (2003).
31. J. M. D. Day *et al*., *Nat. Commun.* **9**, 4799 (2018).
32. M. E. Schmidt, T. J. McCoy, *Earth Planet. Sci. Lett.* **296**, 67–77 (2010).
33. E. M. Stolper *et al*., *Science* **341**, 1239463 (2013).
34. M. E. Schmidt *et al*., *J. Geophys. Res. Planets* **119**, 64–81 (2014).
35. G. J. Taylor *et al*., *J. Geophys. Res.* **112**, E03S10 (2006).
36. L. E. Nyquist *et al*., *Space Sci. Rev.* **96**, 105–164 (2001).
37. M. J. Le Bas, R. W. Le Maitre, A. Streckeisen, B. Zanettin, *J. Petrol.* **27**, 745–750 (1986).
38. A. R. Santos *et al*., *Geochim. Cosmochim. Acta* **157**, 56–85 (2015).
39. A. C. Allwood, J. A. Hurowitz, Mars 2020 PIXL raw and processed data bundle. *Planetary Data System* (2021).
40. L. Beegle, Mars 2020 SHERLOC bundle. *Planetary Data System* (2021).
41. J. F. Bell, J. N. Maki, Mars 2020 Mast Camera zoom bundle, from operations team, calibrated products. *Planetary Data System* (2021).
42. T. Barbaer, S. Davidoff, pixlise/piquant: 3.2.11 Open Source. *Zenodo* (2022).
43. T. Barber, pixlise/core: 2.0 open source migration release. *Zenodo* (2022).
44. S. Davidoff, pixlise/pixlise-ui: 2.0 open source migration release. *Zenodo* (2022).
45. T. Barber, pixlise/diffraction-peak-detection: 2.0 open source migration release. *Zenodo* (2022).
46. T. Barber, pixlise/data-formats: 2.0 open source migration release. *Zenodo* (2022).

ACKNOWLEDGMENTS

We are grateful to the Mars 2020 team members who participated in tactical and strategic science operations. Detailed comments by K. Edgett are greatly appreciated. Y.L. thanks L. P. Keszthelyi for the discussion about Earth and Mars lava flows; N. Williams for providing the base maps used in Fig. 1, A and C; and J. Bell for providing the image used in Fig. 1D. **Funding:** The work described in this paper was partially carried out at the Jet Propulsion Laboratory (JPL), California Institute of Technology, under a prime contract with the National Aeronautics and Space Administration (80NM0018D0004). Y.L., M.M.T., A.C.A., J.A.H., C.M.H., S.D., R.P.H., J.H., D.A.K.P., J.L.J., K.A.F., K.M.S., J.D.T., B.C.C., E.L.C., K.M., L.W.B., L.A.W., J.P.G., A.H.T., B.H.N.H., J.R.J., W.T.E., S.M.M., A.G., R.C.W., and K.U. were supported by NASA grant 80NM0018D0004 through JPL. J.R.J. was also supported by ASU subcontract 15-707. R.C.W. was also supported by NASA grant NNH13ZDA018O for Supercam to LANL. D.T.F. was supported by Australian Research Council grant DE210100205. E.A.C. was supported by Canadian Space Agency grant 19PACOI0 and Natural Sciences and Engineering Research Council of Canada grant RGPIN-2021-02995. C.D.K.H., T.V.K., and M.E.S. were supported by Canadian Space Agency M2020 Participating Scientist grants. A.U., S.J.V., B.A.C., M.N., D.L.S., J.I.S., K.L.S., T.Bo., and B.P.W. were supported by NASA Mars 2020 Participating Scientist grants. The work of K.B., S.B., O.B., L.M., N.M., C.M.Q.-N., and V.S. on Mars 2020 was supported by CNES. K.H.-L. was supported by a UK Space Agency Aurora Research Fellowship. T.Bo. was supported by the Simons Foundation Collaboration on the Origins of Life. S.G. was supported by the UK Space Agency and the Royal Society (grant SRF\R1\21000106). A.G.F. was supported by the European Research Council CoG #818602. **Author contributions:** Y.L. led the writing of the manuscript. Y.L., M.E.S., A.H.T., M.M.T., J.A.H., A.C.A., and T.V.K. prepared the original draft, with input from C.D.K.H., A.U., N.M., S.G., K.H.-L., L.M., D.L.S., D.C.C., F.M.M., A.J.B., J.I.S., S.M.M., D.T.F., C.M.Q.-N., and B.H.N.H. All authors provided input to the manuscript through discussion, editing, or reviewing. Y.L., M.M.T., M.W.M.J., D.A.K.P., J.A.H., T.V.K., S.V.B., A.L.K., B.C.C., and B.J.O. performed methods and data processing. Y.L., D.A.K.P., and J.H. prepared visualization, with contributions from A.C.A., M.E.S., M.W.M.J., M.M.T., C.M.Q.-N., T.V.K., and A.H.T.; K.U. and Y.L. made movie S1. W.T.E. and C.M.H. developed the PIQUANT software; S.D. led development of the PIXLISE software, with P.N., A.G., and T.Ba. Project management of PIXL investigation

was by A.C.A. as the PIXL principal investigator, J.A.H. as the deputy principal investigator, W.T.E. as the chief spectroscopist, and L.A.W. as the instrument chief engineer. **Competing interests:** The authors declare that they have no competing interests. **Data and materials availability:** All data used in this paper are archived in the NASA Planetary Data System (*39*–*41*). Image numbers and data sources for the meteorites and other rovers used for comparison are listed in table S7. The source codes for the PIXLISE and PIQUANT software are available at (*42*–*46*). Our derived elemental abundances are listed in tables S2 to S5.

License information: Copyright © 2022 the authors, some rights reserved; exclusive licensee American Association for the Advancement of Science. No claim to original US government works. https://www.science.org/about/science-licenses-journal-article-reuse

SUPPLEMENTARY MATERIALS

science.org/doi/10.1126/science.abo2756

Materials and Methods
Supplementary Text
Figs. S1 to S10
Tables S1 to S7
References (*47*–*109*)
Movie S1

Submitted 24 January 2022; accepted 8 August 2022
10.1126/science.abo2756

CANCER

Oncometabolite D-2HG alters T cell metabolism to impair CD8$^+$ T cell function

Giulia Notarangelo[1], Jessica B. Spinelli[1]†, Elizabeth M. Perez[2,3,4], Gregory J. Baker[5,6], Kiran Kurmi[1], Ilaria Elia[1]‡, Sylwia A. Stopka[7,8], Gerard Baquer[7,9], Jia-Ren Lin[5], Alexandra J. Golby[7], Shakchhi Joshi[1], Heide F. Baron[10,11], Jefte M. Drijvers[1,12]§, Peter Georgiev[1,12], Alison E. Ringel[1]¶, Elma Zaganjor[1]#, Samuel K. McBrayer[13], Peter K. Sorger[5], Arlene H. Sharpe[2,12], Kai W. Wucherpfennig[2,12,14,15], Sandro Santagata[5,6,16], Nathalie Y. R. Agar[7,8,17], Mario L. Suvà[2,3], Marcia C. Haigis[1]*

Gain-of-function mutations in isocitrate dehydrogenase (IDH) in human cancers result in the production of D-2-hydroxyglutarate (D-2HG), an oncometabolite that promotes tumorigenesis through epigenetic alterations. The cancer cell–intrinsic effects of D-2HG are well understood, but its tumor cell–nonautonomous roles remain poorly explored. We compared the oncometabolite D-2HG with its enantiomer, L-2HG, and found that tumor-derived D-2HG was taken up by CD8$^+$ T cells and altered their metabolism and antitumor functions in an acute and reversible fashion. We identified the glycolytic enzyme lactate dehydrogenase (LDH) as a molecular target of D-2HG. D-2HG and inhibition of LDH drive a metabolic program and immune CD8$^+$ T cell signature marked by decreased cytotoxicity and impaired interferon-γ signaling that was recapitulated in clinical samples from human patients with *IDH1* mutant gliomas.

The discovery of mutations in genes encoding key metabolic enzymes has highlighted a direct link between altered metabolism and disease. In particular, the discovery of mutations in fumarate hydratase, succinate dehydrogenase, and isocitrate dehydrogenase (*IDH*), all enzymes of the tricarboxylic acid cycle, has uncovered how mitochondrial metabolites can accumulate and act as disease-driving signaling molecules, becoming bona fide oncometabolites (*1*). Beyond their established intracellular functions, oncometabolites have tumor cell–nonautonomous roles and mediate intercellular cross talk in the tumor microenvironment (TME).

The oncometabolite D-2-hydroxyglutarate (D-2HG) is produced by cancers with gain-of-function mutations in *IDH1* and *IDH2* and accumulates to levels up to ~30 mM in the surrounding TME (*2*–*8*). D-2HG is an inhibitor of many alpha ketoglutarate (αKG)–dependent dioxygenases, leading to slow accumulating alterations in the epigenetic landscape of cells that result in oncogenic transformation (*9*–*12*). Despite our understanding of the cancer cell–intrinsic regulation of epigenetics by D-2HG, the tumor cell–nonautonomous effects of D-2HG in the TME still remain poorly understood. *IDH*-mutant gliomas have fewer tumor-infiltrating lymphocytes, including T cells, compared with their wild-type (WT) counterparts, suggesting that D-2HG promotes the establishment of an immunosuppressive TME (*7*, *13*–*16*). However, the mechanisms by which D-2HG alters antitumor immunity remain unknown.

We focused on CD8$^+$ T cells, which are a major component of the adaptive immune response and specialize in the direct killing of malignant cells, to investigate the impact of tumor-derived D-2HG on antitumor immunity.

Results

Acute and reversible inhibition of CD8$^+$ T cell proliferation, cytotoxicity, and interferon-γ signaling by D-2HG

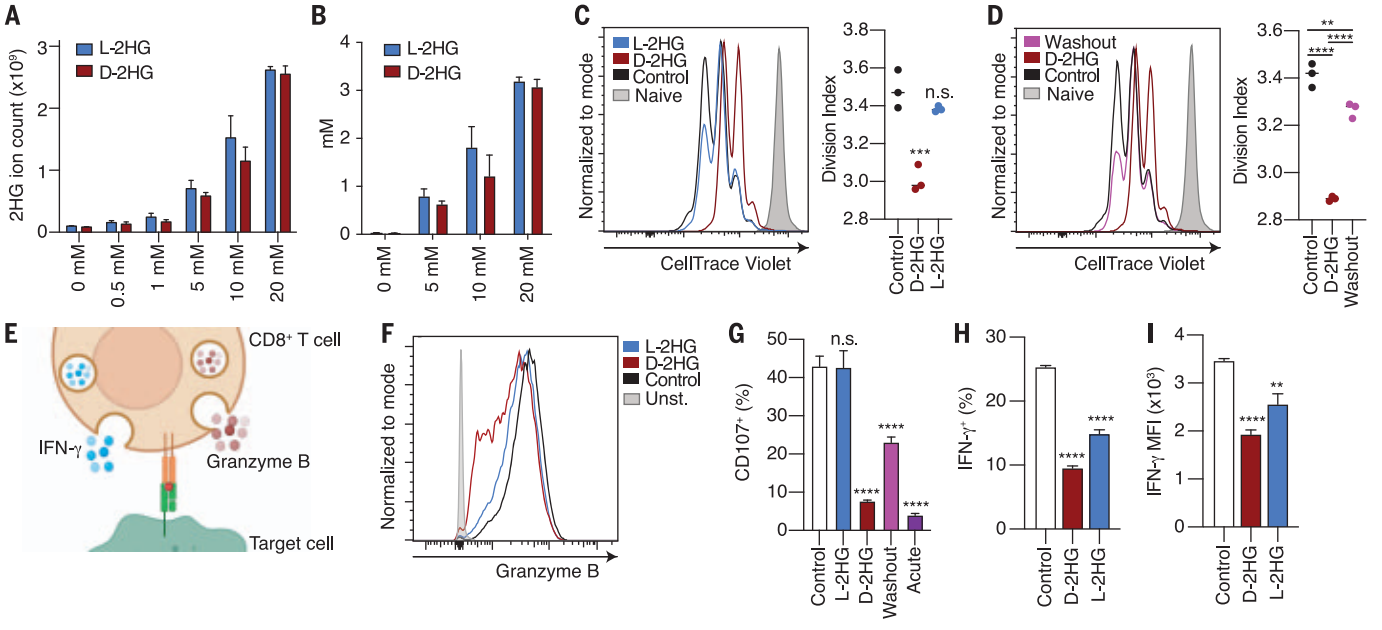
To evaluate the tumor cell–nonautonomous mechanisms by which D-2HG influences antitumor immunity, we examined the effects of the oncometabolite on the function of murine CD8$^+$ T cells. We compared D-2HG with its enantiomer, L-2HG, a metabolic by-product of enzyme promiscuity that supports T cell survival and function (*17*, *18*). To determine whether pathophysiological concentrations of D-2HG in the TME of *IDH*-mutant tumors (*2*–*8*) permit cellular uptake by CD8$^+$ T cells, we treated activated CD8$^+$ T cells with various doses of non-cell-permeable D-2HG and L-2HG and monitored uptake by liquid chromatography–mass spectrometry. Both enantiomers were taken up rapidly and in similar quantities when supplied in millimolar concentrations (Fig. 1A and fig. S1A). Next, we quantified the intracellular levels of each enantiomer. When 20 mM D-2HG or L-2HG was added, we estimated that the intracellular concentration of 2HG reached low millimolar levels (Fig. 1B). At this concentration, neither enantiomer had a detrimental effect on cell viability over a 6-day time course (fig. S1B).

Upon entering the TME of *IDH*-mutant tumors, infiltrating CD8$^+$ T cells undergo local expansion and reactivation in the presence of high amounts of D-2HG. Therefore, we evaluated the effects of D-2HG or L-2HG on the activation and proliferation of CD8$^+$ T cells.

[1]Department of Cell Biology, Blavatnik Institute, Harvard Medical School, Boston, MA, USA. [2]Broad Institute of MIT and Harvard, Cambridge, MA, USA. [3]Department of Pathology and Center for Cancer Research, Massachusetts General Hospital, Boston, MA, USA. [4]Department of Systems Biology, Blavatnik Institute, Harvard Medical School, Boston, MA, USA. [5]Laboratory of Systems Pharmacology, Harvard Medical School, Boston, MA, USA. [6]Ludwig Center at Harvard, Harvard Medical School, Boston, MA, USA. [7]Department of Neurosurgery, Brigham and Women's Hospital, Harvard Medical School, Boston, MA, USA. [8]Department of Radiology, Brigham and Women's Hospital, Harvard Medical School, Boston, MA, USA. [9]Department of Electronic Engineering, Rovira i Virgili University, Tarragona, Spain. [10]Chemical Neurobiology Laboratory, Center for Genomic Medicine, Massachusetts General Hospital, Boston, MA, USA. [11]Departments of Psychiatry and Neurology, Harvard Medical School, Boston, MA, USA. [12]Department of Immunology, Blavatnik Institute, Harvard Medical School, Boston, MA, USA. [13]Children's Medical Center Research Institute and Department of Pediatrics, University of Texas Southwestern Medical Center, Dallas, TX, USA. [14]Department of Cancer Immunology and Virology, Dana-Farber Cancer Institute, Boston, MA, USA. [15]Department of Neurology, Brigham and Women's Hospital, Boston, MA, USA. [16]Department of Pathology, Brigham and Women's Hospital, Harvard Medical School, Boston, MA, USA. [17]Department of Cancer Biology, Dana-Farber Cancer Institute, Boston, MA, USA.
***Corresponding author. Email: Marcia_haigis@hms.harvard.edu**
†Present address: Whitehead Institute for Biomedical Research, Massachusetts Institute of Technology, Cambridge, MA, USA. ‡Present address: Department of Cellular and Molecular Medicine, KU Leuven, 3000 Leuven, Belgium. §Present address: Abata Therapeutics, Cambridge, MA, USA. ¶Present address: Department of Biology, Massachusetts Institute of Technology, Cambridge, MA, USA, and Ragon Institute of MGH, MIT and Harvard, Cambridge, MA, USA. #Present address: Department of Molecular Physiology and Biophysics, Vanderbilt University School of Medicine, Nashville, TN, USA.

After stimulation with anti-CD3/CD28 antibodies, $CD8^+$ T cells fully activated in the presence of either enantiomer, as assessed by cell surface expression of the activating markers CD69 and CD25 (fig. S1C). Although both enantiomers achieved similar intracellular concentrations, D-2HG was a more potent inhibitor of T cell proliferation than L-2HG (Fig. 1C). The inhibitory effects of D-2HG on proliferation were dose dependent and observed only at concentrations sufficient for cellular uptake (fig. S1D). Removing D-2HG from the culture medium alleviated this proliferative block (Fig. 1D and fig. S1E), demonstrating that the effects of D-2HG on proliferation are reversible.

$CD8^+$ T cells can eliminate target cells through exocytosis of preformed lysosomes containing cytotoxic proteins such as granzyme B (Fig. 1E) (*19*). After T cell activation, intracellular granzyme B levels were decreased in the presence of D-2HG (Fig. 1F). During the process of degranulation, the membrane of granzyme-containing lysosomes fuses with the plasma membrane of activated $CD8^+$ T lymphocytes to allow for cargo release (*20*). To evaluate degranulation, we assessed the cycling of lysosomal-associated membrane protein 1 and 2 (LAMP-1 and LAMP-2, also known as CD107a and CD107b) to the cell surface in response to T cell receptor signaling (*21*). $CD8^+$ T cells activated in the presence of



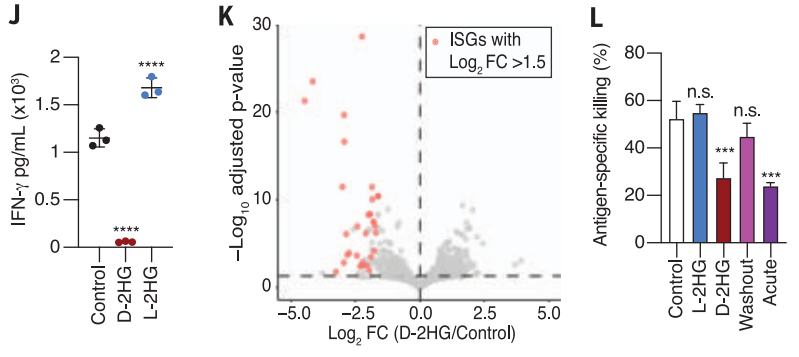


Fig. 1. D-2HG impairs $CD8^+$ T cell proliferation, cytotoxicity, and IFN-γ signaling in an acute and reversible fashion. (**A**) Total 2HG levels in activated $CD8^+$ T cells after 24-hour treatment with increasing concentrations of D-2HG or L-2HG. Total ion count was normalized to cell number (n = 3). (**B**) Intracellular 2HG concentration determined by assuming a T cell volume of 500 fl (n = 3). (**C**) Left: CellTrace Violet dilution assay at day 3 of $CD8^+$ T cells activated by CD3/CD28 mAbs in the presence of 20 mM D-2HG, 20 mM L-2HG, or left untreated. Stained, naive cells (shaded gray) that did not proliferate are shown. Right: Division index corresponds to the average number of cell divisions that a cell in the total cell population has undergone (n = 3). (**D**) CellTrace Violet dilution assay according to experimental design described in fig. S1E to assess reversibility of proliferation phenotype. (**E**) Schematic of a cytotoxic $CD8^+$ T cell releasing granzyme B and IFN-γ. (**F**) Intracellular granzyme B levels of $CD8^+$ T cells activated by CD3/CD28 mAbs in the presence of 20 mM D-2HG, 20 mM L-2HG, or left untreated for 3 days. (**G**) Percentage degranulation as assessed by CD107a/b staining of $CD8^+$ T cells activated by CD3/CD28 mAbs and restimulated by CD3 mAb in the presence of 20 mM D-2HG, 20 mM L-2HG, or left untreated. In the washout condition, $CD8^+$ T cells were activated in the presence of 20 mM D-2HG, and the oncometabolite was subsequently washed out before restimulation. In the acute condition, D-2HG was added solely at the time of restimulation. In all other conditions, the metabolites were kept for the entirety of the assay (n = 3). (**H**) Percentage of IFN-γ^+ $CD8^+$ T cells after intracellular cytokine staining of $CD8^+$ T cells activated with phorbol myristate acetate (PMA) and ionomycin for 4 hours in the presence of 20 mM D-2HG, 20 mM L-2HG, or left untreated (n = 3). (**I**) Mean fluorescent intensity for IFN-γ after intracellular cytokine staining of $CD8^+$ T cells activated with PMA and ionomycin for 4 hours in the presence of 20 mM D-2HG, 20 mM L-2HG, or left untreated (n = 3). (**J**) IFN-γ levels in the medium of $CD8^+$ T cells activated with 20 mM D-2HG, 20 mM L-2HG, or left untreated for 24 hours (n = 3). (**K**) Volcano plot showing distribution of the top down-regulated and up-regulated genes in $CD8^+$ T cells activated in the presence of 20 mM D-2HG or left untreated. Statistically significant ISGs with a fold change >1.5 are marked in pink (n = 3). (**L**) Antigen-specific killing of B16 ovalbumin-positive tumor cells by OT1 $CD8^+$ T cells that were activated in the presence of 20 mM D-2HG, 20 mM L-2HG, or left untreated. In the washout condition, D-2HG was removed before co-culture seeding of tumor cells and T cells. In the acute condition, D-2HG was added at the time of tumor cell and T cell co-culture. In all other conditions, the metabolites were kept for the entirety of the assay (n = 3). *P < 0.05, **P < 0.01, ***P < 0.001, ****P < 0.0001 (one-way and two-way ANOVA). Data are representative of at least two independent experiments.

D-2HG failed to degranulate upon antigen restimulation in a dose-dependent manner (fig. S1, F, G, and I, and Fig. 1G). The total amounts of intracellular LAMP-1 were not affected by D-2HG treatment (fig. S1H). Given these observations, we then investigated whether the loss of LAMP-1/2 surface expression could be attributed to an impairment in granule formation at the time of ex vivo activation (day 0) or a defect in degranulation at the time of restimulation (day 6). To test this, $CD8^+$ T cells were activated in the presence of D-2HG for 6 days, and then D-2HG was removed at the time of restimulation. Washing away D-2HG at the time of restimulation partially restored the ability of $CD8^+$ T cells to degranulate (fig. S1, F and I, and Fig. 1G, washout condition). Conversely, $CD8^+$ T cells that were activated for 6 days and subsequently exposed to D-2HG only at the time of restimulation failed to degranulate (fig. S1, F and I, and Fig. 1G, acute condition). These data indicate that D-2HG leads to acute defects in $CD8^+$ T cell degranulation by affecting processes involved in the formation of lytic effectors and the release of lytic contents.

Together with granzyme B, $CD8^+$ T cells also secrete interferon-γ (IFN-γ), a cytokine that sensitizes tumor cells to killing by T cells (Fig. 1E) (*22*). After stimulation, D-2HG–treated $CD8^+$ T cells exhibited a dose-dependent defect in IFN-γ production, as determined by decreased IFN-γ intracellular staining and reduced release of the cytokine into the medium (Fig. 1, H to J, and fig. S1J). IFN-γ controls specific gene expression programs of hundreds of genes (*23*). Therefore, we performed gene expression profiling by RNA sequencing of $CD8^+$ T cells activated in the presence of D-2HG or L-2HG or left untreated. Gene Ontology (GO) analysis showed that most of the down-regulated genes upon D-2HG treatment belonged to the class of IFN-γ–stimulated genes (ISGs) (Fig. IK and fig. S1, K and L). Thus, $CD8^+$ T cells exhibit a decrease in the IFN-γ–induced signature, reflecting a decrease in IFN-γ production and secretion after D-2HG treatment.

To assess whether the decreased production of cytotoxic proteins and effector cytokines had functional consequences, we probed the antigen-specific antitumor killing capacities of D-2HG– or L-2HG–treated cells in an in vitro killing assay. D-2HG–treated $CD8^+$ T cells exhibited poor killing of cancer cells both when D-2HG was provided starting at the time of their activation and when it was administered to activated $CD8^+$ T cells only at the time of co-culture with cancer cells (Fig. 1L and fig. S1, M to O). Thus, the effects of D-2HG on cytotoxicity are rapid and independent of upstream events involving T cell activation. Removal of D-2HG at the time of co-culture from $CD8^+$ T cells that had been activated in the presence of D-2HG restored their antitumor killing capacities (Fig. 1L and fig. S1M, washout condition), indicating that D-2HG must be present at the time of tumor cell recognition to impair their killing. Thus, we conclude that D-2HG acutely impairs the antitumor killing properties on $CD8^+$ T cells.

D-2HG alters glycolysis in CD8⁺ T cells

Because of their acute and reversible nature, the effects of D-2HG on $CD8^+$ T cell proliferation, cytokine production, and cytotoxicity appear to be independent of its established role as an epigenetic regulator. In support of this, acute treatment with D-2HG did not

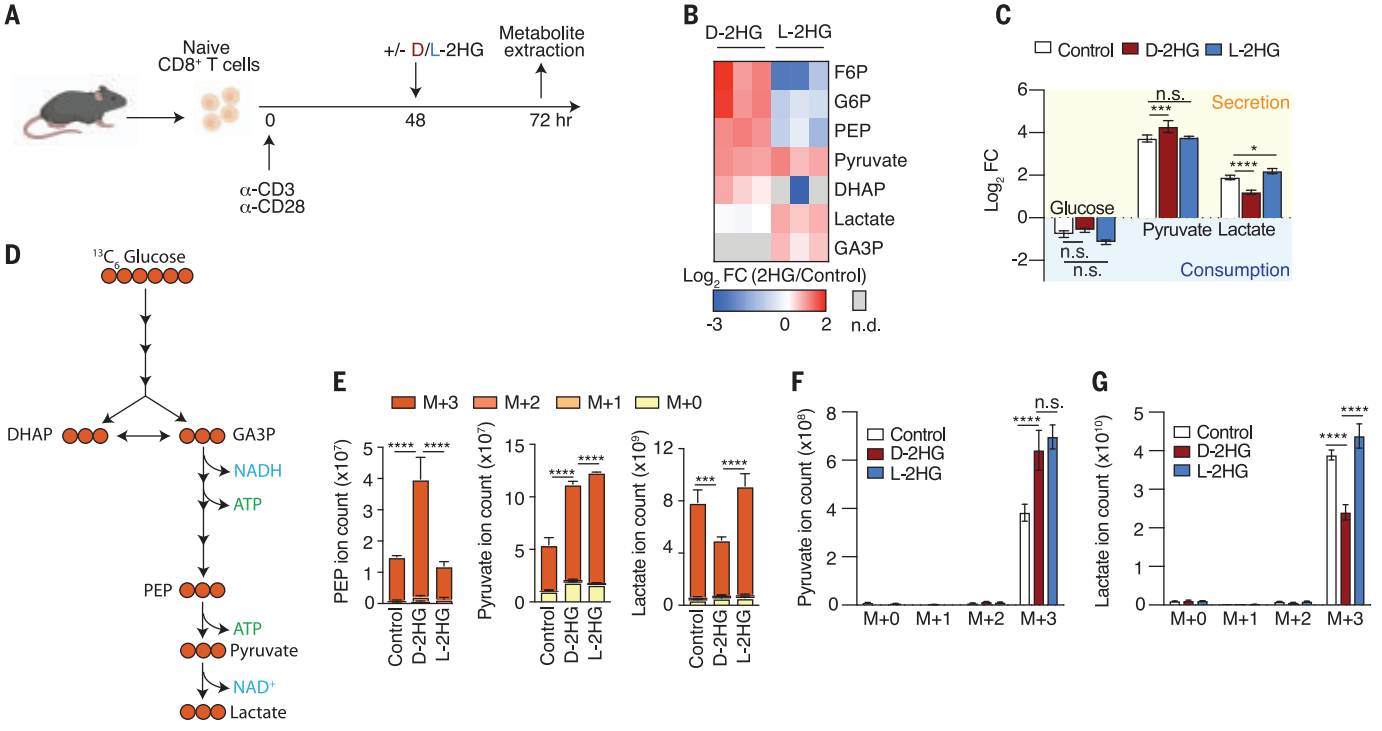


Fig. 2. D-2HG alters glycolysis in $CD8^+$ T cells. (**A**) Schematic of experimental design to assess the acute (24 hours) effects of 20 mM D-2HG and 20 mM L-2HG on steady-state metabolite levels in activated $CD8^+$ T cells. (**B**) Log_2 fold changes of glycolytic intermediates in 20 mM D-2HG–treated versus 20 mM L-2HG–treated $CD8^+$ T cells relative to control. F6P, fructose 6-phosphate; G6P, glucose 6-phosphate; DHAP, dihydroxyacetone phosphate; GA3P, glyceraldehyde 3-phosphate; PEP, phosphoenolpyruvic acid ($n = 3$). (**C**) Log_2 fold changes of key glycolytic metabolites that are secreted into or consumed from the medium of D-2HG–treated, L-2HG–treated, or untreated $CD8^+$ T cells ($n = 3$). (**D**) Schematic of expected incorporation of heavy carbons into glycolytic intermediates after $^{13}C_6$ glucose is provided for 24 hours. (**E**) Ion intensities of glycolytic intermediates and their respective ^{13}C-isotopologs after 24-hour cotreatment of $^{13}C_6$ glucose with 20 mM D-2HG, 20 mM L-2HG, or control ($n = 3$). (**F**) Levels of secreted pyruvate isotopologs in the medium of 20 mM D-2HG–treated, 20 mM L-2HG–treated, and untreated $CD8^+$ T cells after providing $^{13}C_6$ glucose for 24 hours ($n = 3$). (**G**) Levels of secreted lactate isotopologs in the medium of 20 mM D-2HG–treated, 20 mM L-2HG–treated, and untreated $CD8^+$ T cells after providing $^{3}C_6$ glucose for 24 hours ($n = 3$). $^*P < 0.05$, $^{**}P < 0.01$, $^{***}P < 0.001$, $^{****}P < 0.0001$ (two-way ANOVA). Data are representative of at least two independent experiments.

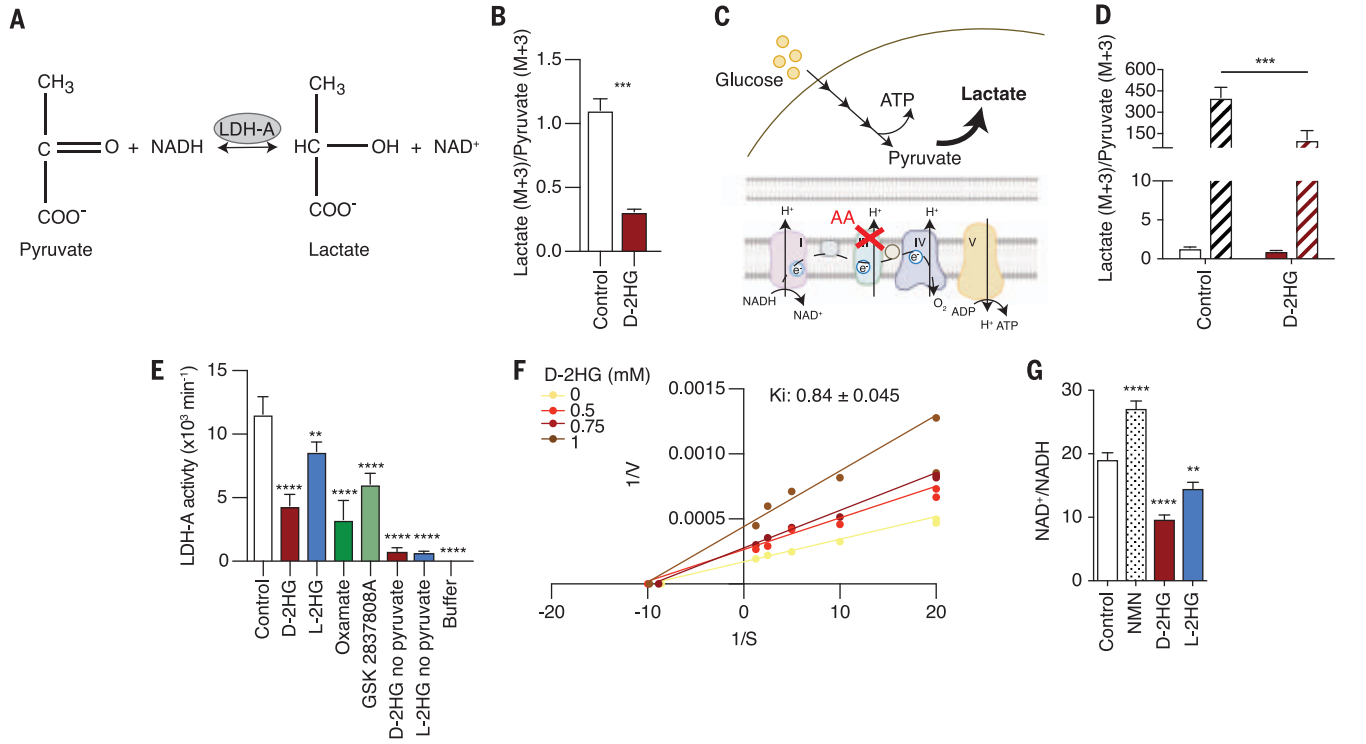


Fig. 3. D-2HG inhibits LDH-A activity in vitro and in CD8⁺ T cells. (**A**) Schematic of LDH reaction. (**B**) Intracellular lactate (M+3)/pyruvate (M+3) ratio of CD8⁺ T cells after 24-hour cotreatment of $^{13}C_6$ glucose with 20 mM D-2HG or control (n = 3). (**C**) Schematic of the metabolic consequences of antimycin A (AA) treatment on glucose catabolism. (**D**) Intracellular lactate (M+3)/pyruvate (M+3) ratio after brief 20 mM D-2HG pretreatment, followed by AA and $^{13}C_6$ glucose cotreatment (n = 3). Solid bars, −AA; striped bars, +AA. (**E**) In vitro enzymatic assessment of 3 mM L-2HG, 3 mM D-2HG, 80 μM oxamate, and 10 nM GSK2837808A on LDH-A activity. Oxamate and GSK2837808A are known LDH inhibitors and were used as a control (n = 3). (**F**) Lineweaver-Burk plot for D-2HG. (**G**) NAD⁺/NADH ratio of CD8⁺ T cells treated for 24 hours with control, 1 mM nicotinamide mononucleotide (NMN), 20 mM D-2HG, or 20 mM L-2HG. NMN raises intracellular NAD⁺ levels and was therefore used as a positive control (n = 3). *P < 0.05, **P < 0.01, ***P < 0.001, ****P < 0.0001 (Student's t test, one-way and two-way ANOVA). Data are representative of at least two independent experiments.

result in epigenetic reprogramming of T cells (fig. S2A). We therefore investigated whether D-2HG had an effect on metabolism. First, we tested whether either enantiomer could be metabolized. The chiral-specific reduction of 2HG to αKG is mediated by D-2HG and L-2HG dehydrogenase (D-2HGDH and L-2HGDH, respectively) (*24*). In agreement with the literature (*25*), Western blot analysis demonstrated undetectable amounts of D-2HGDH and L-2HGDH in CD8⁺ T cells (fig. S2B). Furthermore, stable isotope tracing of $^{13}C_5$ D-2HG or L-2HG did not show evidence of L-2HG and D-2HG metabolism over a 48-hour time course, despite achieving steady-state isotopic enrichment (fig. S2, C to E). We conclude that D-2HG and L-2HG are not readily metabolized in CD8⁺ T cells.

Given that D-2HG and L-2HG led to distinct functional effects on CD8⁺ T cells, we performed steady-state metabolomics of intracellular metabolites and metabolites from cell culture medium after acute 2HG treatment with the goal of identifying metabolic pathways that were differentially altered by the two enantiomers (Fig. 2A). The metabolic pathway most altered upon D-2HG treatment was glycolysis. D-2HG, but not L-2HG, promoted the accumulation of many glycolytic intermediates (Fig. 2B and fig. S2F). Consistent with altered glucose utilization, we also observed increased pyruvate and decreased lactate in the medium of D-2HG–treated CD8⁺ T cells (Fig. 2C and fig. S2G). L-2HG stabilizes hypoxia-inducible factor-1α (HIF-1α), which is a master transcriptional regulator of glycolysis (*17*, *26*, *27*). Therefore, we assessed whether the reported changes in glucose catabolism could be attributed to D-2HG–mediated HIF-1α regulation. We found that D-2HG, unlike its enantiomer L-2HG (*28*), did not promote HIF-1α stability in T cells (fig. S2H). This result was further confirmed by quantitative polymerase chain reaction analysis, showing no major changes in the expression of genes involved in glucose utilization upon D-2HG treatment (fig. S2I). Thus, we conclude that D-2HG alters glucose catabolism through an HIF-1α–independent mechanism.

To further investigate how glycolytic flux is altered in the presence of D-2HG and L-2HG, we performed tracing experiments with $^{13}C_6$ glucose (Fig. 2D). Consistent with our steady-state metabolomic profiles, we observed increased labeling in glycolytic intermediates preceding lactate and a decrease in labeling of lactate (Fig. 2E). These results were confirmed by metabolite analysis in the cell culture medium. We detected increased pyruvate (M+3) accumulation and decreased lactate (M+3) secretion upon D-2HG treatment (Fig. 2, F and G). Collectively, these findings demonstrate that D-2HG, and not L-2HG, strongly inhibits glycolysis in CD8⁺ T cells.

D-2HG inhibits LDH activity in CD8⁺ T cells and lowers the NAD⁺/NADH ratio

Pyruvate to lactate interconversion is catalyzed by the enzyme LDH (Fig. 3A) (*29*). The dose-dependent decrease in pyruvate to lactate conversion, as measured by the ratio of lactate (M+3) to pyruvate (M+3) upon $^{13}C_6$ glucose tracing (Fig. 3B and fig. S3A), led us to test whether LDH activity is impaired in the presence of D-2HG. We treated CD8⁺ T cells with antimycin A, an inhibitor of the electron transport chain (ETC) that limits mitochondria's ability to generate ATP and increases reliance on glycolysis to support the bioenergetic needs of a cell (Fig. 3C) (*30*). In response to antimycin A, activated CD8⁺ T cells induced pyruvate to lactate conversion, as indicated by an increase

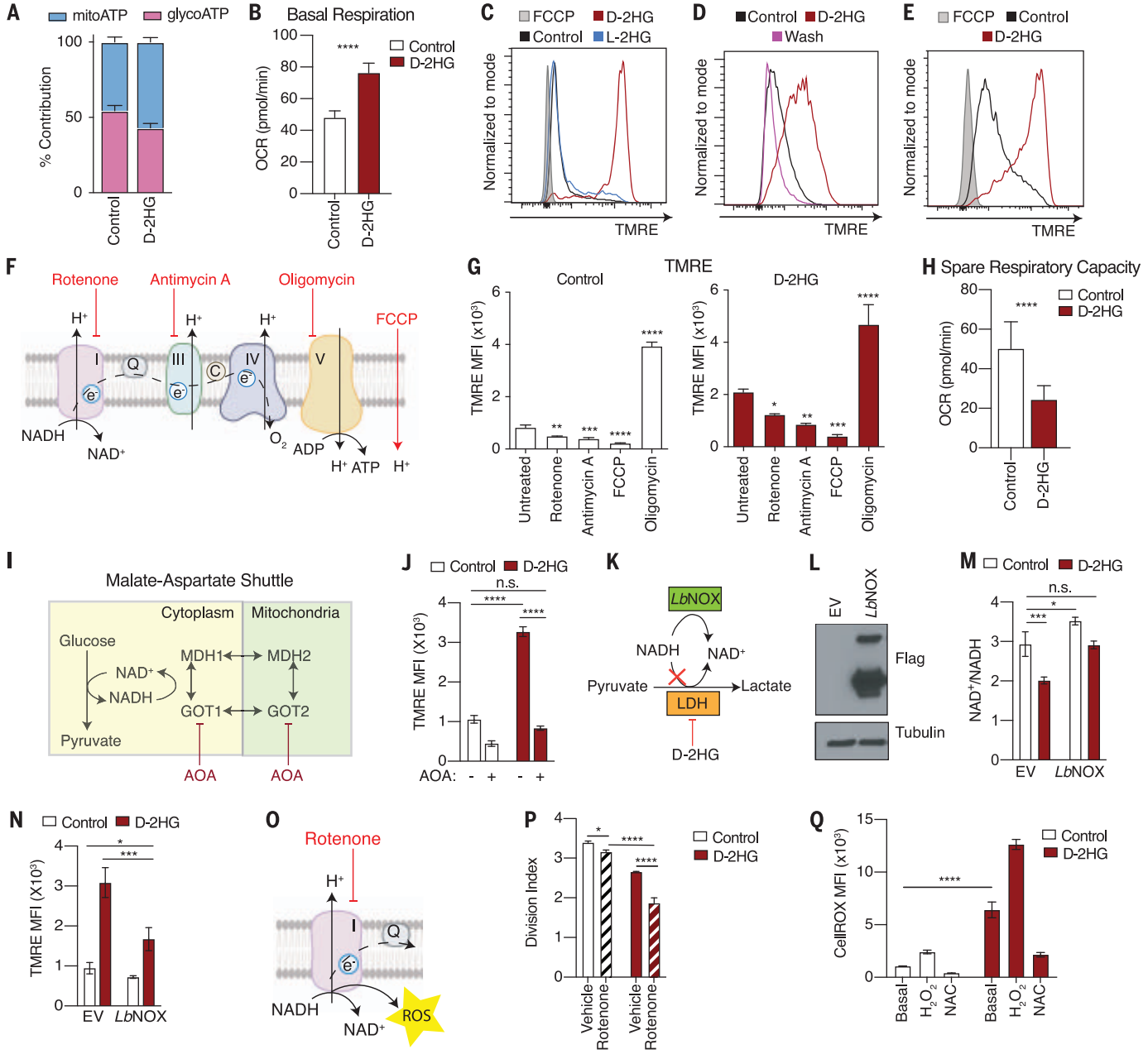


Fig. 4. Cytosolic NAD(H) imbalance drives mitochondrial membrane hyperpolarization in D-2HG–treated CD8⁺ T cells. (**A**) Relative contribution of mitochondrial oxidative phosphorylation and glycolysis to ATP production in response to D-2HG after 24 hours of treatment (n = 10). (**B**) Quantification of basal respiration in response to 20 mM D-2HG after 24 hours of treatment (n = 10). (**C**) Mitochondrial membrane potential as assessed by tetramethylrhodamine ethyl ester (TMRE) fluorescence in CD8⁺ T cells treated with 20 mM D-2HG, 20 mM L-2HG, or control for 3 days. (**D**) TMRE assay according to experimental design described in fig. S4F. (**E**) Mitochondrial membrane potential as assessed by TMRE fluorescence in CD8⁺ T cells treated with 20 mM D-2HG, 20 mM L-2HG, or control for 2 hours. (**F**) Schematic of targets of rotenone, AA, oligomycin, and FCCP. (**G**) Effects of inhibition of ETC complexes on mitochondrial membrane potential in control and D-2HG–treated CD8⁺ T cells (n = 3). (**H**) Quantification of spare respiratory capacity in response to 20 mM D-2HG after 24 hours of treatment (n = 10). (**I**) Schematic of targets of AOA. (**J**) Mitochondrial membrane potential as assessed by TMRE fluorescence in CD8⁺ T cells treated with 20 mM D-2HG or control for 24 hours in the presence or absence of 1 mM AOA (n = 3). (**K**) Schematic of *Lb*NOX mechanism of action. (**L**) Western blot of CD8⁺ T cells overexpressing empty vector (EV) or FLAG-tagged cytosolic *Lb*NOX. (**M**) NAD⁺/NADH ratio of CD8⁺ T cells overexpressing EV or cytosolic *Lb*NOX after a 24-hour-long treatment with 20 mM D-2HG or control (n = 3). (**N**) TMRE staining of EV or *Lb*NOX-overexpressing CD8⁺ T cells treated with 20 mM D-2HG or left untreated for 24 hours (n = 3). (**O**) Schematic of the target of rotenone. (**P**) Quantification of division index of CD8⁺ T cells activated in the presence or absence of 20 mM D-2HG for 3 days and cotreated with 1 nM rotenone (n = 3). (**Q**) Quantification of intracellular ROS levels as assessed by CellROX staining in CD8⁺ T cells treated with 20 mM D-2HG or left untreated for 1 day. Hydrogen peroxide (H_2O_2, 100 mM) and 10 mM NAC were used as positive and negative controls, respectively (n = 3). *P < 0.05, **P < 0.01, ***P < 0.001, ****P < 0.0001 (Student's t test, one-way and two-way ANOVA). Data are representative of at least two independent experiments.

in the lactate/pyruvate ratio. By contrast, this induction was significantly suppressed in D-2HG–treated CD8$^+$ T cells (Fig. 3D), supporting the model that LDH function is compromised in the presence of D-2HG.

To determine whether D-2HG is a direct inhibitor of LDH activity, we used purified recombinant LDH-A protein, the LDH isozyme expressed by T cells, and measured its activity in the presence or absence of D-2HG or L-2HG. Using the intracellular 2HG concentration previously determined (3 mM; Fig. 1B), we observed that D-2HG strongly inhibited LDH-A activity in vitro (Fig. 3E and fig. S3, B and C). LDH-B was also inhibited by D-2HG, suggesting that the inhibitory properties of D-2HG are not isozyme specific (fig. S3D). Although our tracing studies did not provide strong evidence for L-2HG–mediated inhibition of LDH, our in vitro kinetic assay revealed that L-2HG also inhibits, albeit less effectively,

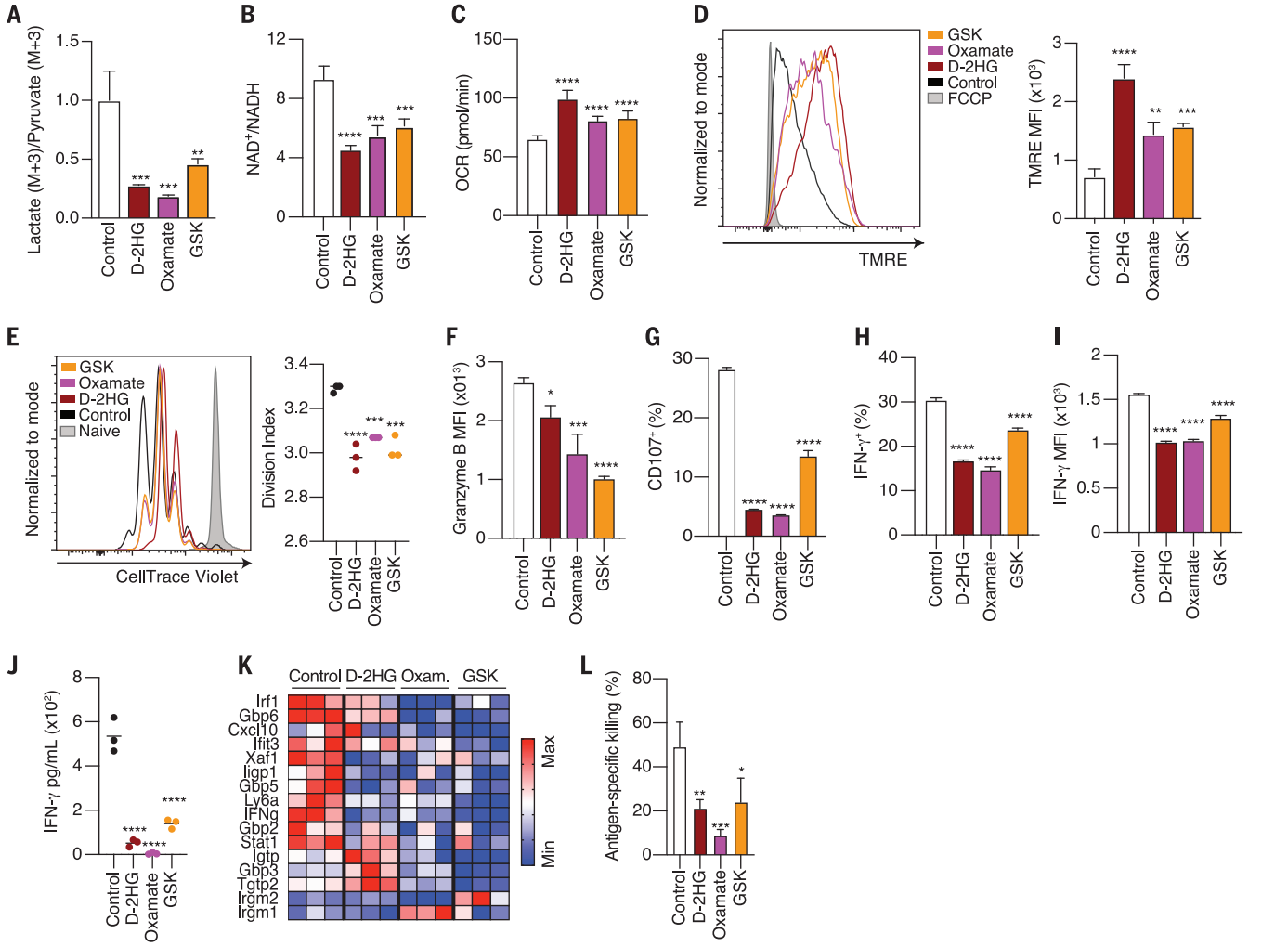


Fig. 5. LDH inhibition recapitulates the effects of D-2HG on CD8$^+$ T cell metabolism, proliferation, cytotoxicity, and IFN-γ signaling. (**A**) Lactate (M+3)/pyruvate (M+3) ratio in CD8$^+$ T cells treated with 20 mM D-2HG, 20 mM oxamate, 10 μM GSK2837808A, or left untreated for 24 hours (n = 3). (**B**) NAD$^+$/NADH ratio of CD8$^+$ T cells after a 24-hour-long treatment with 20 mM D-2HG, 20 mM oxamate, 10 μM GSK2837808A, or control (n = 3). (**C**) Quantification of basal respiration in response to 20 mM D-2HG, 20 mM oxamate, 10 μM GSK2837808A, or control after 24 hours of treatment (n = 10). (**D**) Left: Mitochondrial membrane potential as assessed by TMRE fluorescence in CD8$^+$ T cells treated with 20 mM D-2HG, 20 mM oxamate, 10 μM GSK2837808A, or control for 24 hours. Right: quantification of mean fluorescence intensity for TMRE (n = 3). (**E**) Left: CellTrace Violet dilution assay at day 3 of CD8$^+$ T cells activated in the presence of 20 mM D-2HG, 20 mM oxamate, 10 μM GSK2837808A, or left untreated. Right: quantification of division index (n = 3). (**F**) Quantification of intracellular granzyme B expression in CD8$^+$ T cells activated in the presence of 20 mM D-2HG, 20 mM oxamate, 10 μM GSK2837808A, or control for 3 days (n = 3). (**G**) Percentage degranulation assessed by CD107a/b staining in CD8$^+$ T cells activated in the presence of 20 mM D-2HG, 20 mM oxamate, 10 μM GSK2837808A, or left untreated (n = 3). (**H**) Percentage of IFN-γ$^+$ CD8$^+$ T cells after intracellular cytokine staining of CD8$^+$ T cells activated with PMA and ionomycin for 4 hours in the presence of 20 mM D-2HG, 20 mM oxamate, 10 μM GSK2837808A, or left untreated (n = 3). (**I**) Mean fluorescent intensity for IFN-γ after intracellular cytokine staining of CD8$^+$ T cells activated with PMA and ionomycin for 4 hours in the presence of 20 mM D-2HG, 20 mM oxamate, 10 μM GSK2837808A, or left untreated (n = 3). (**J**) Cell number–normalized levels of IFN-γ in the cell culture medium of CD8$^+$ T cells activated in the presence of 20 mM D-2HG, 20 mM oxamate, 10 μM GSK2837808A, or control for 2 days (n = 3). (**K**) Relative mRNA expression of ISGs in CD8$^+$ T cells activated in the presence of 20 mM D-2HG, 20 mM oxamate, 10 μM GSK2837808A, or control for 24 hours (n = 3). (**L**) Specific killing of B16 ovalbumin-positive tumor cells by OT1 CD8$^+$ T cells activated in the presence of 20 mM D-2HG, 20 mM oxamate, 10 μM GSK2837808A, or control (n = 3). *P < 0.05, **P < 0.01, ***P < 0.001, ****P < 0.0001 (one-way ANOVA). Data are representative of at least two independent experiments.

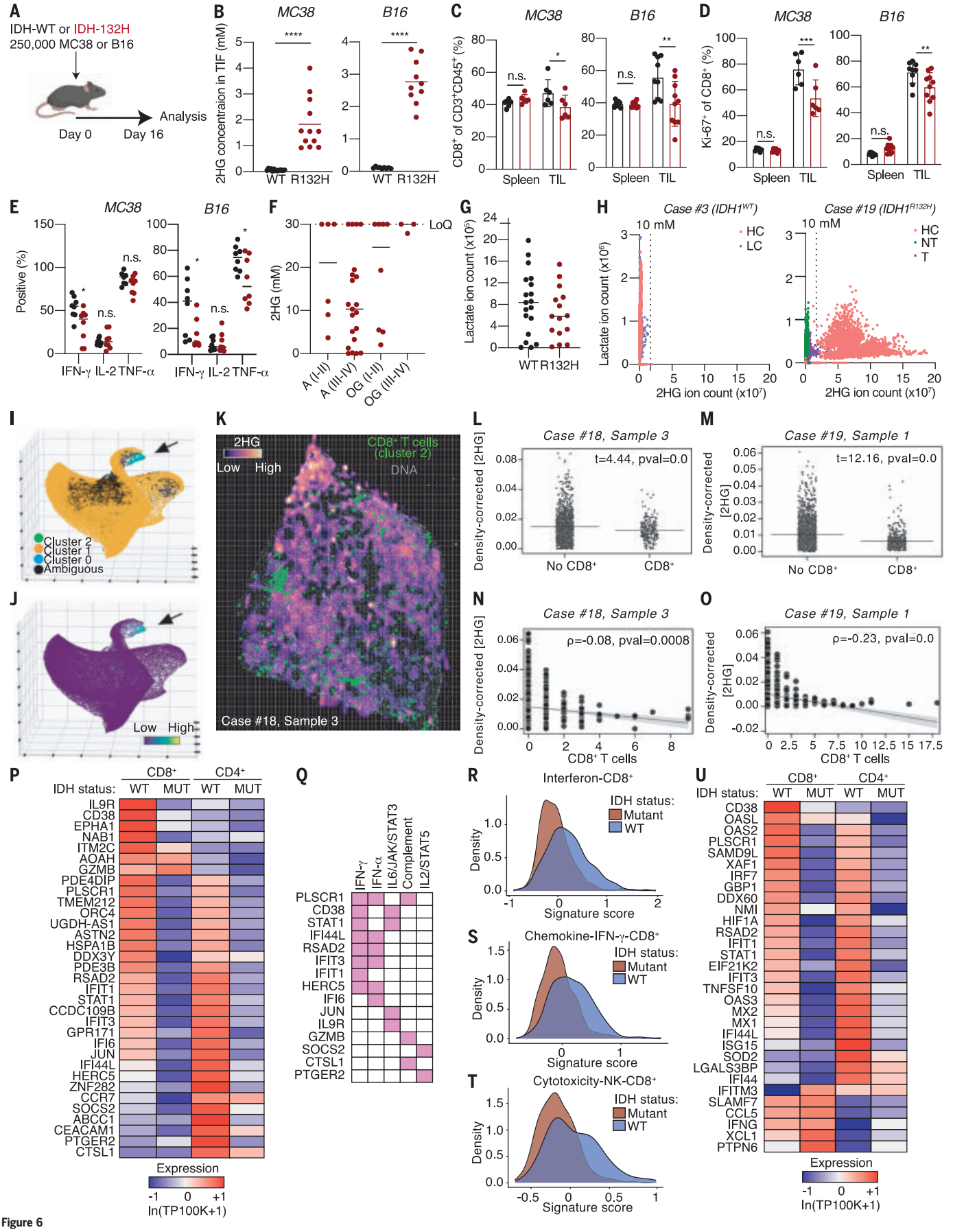

A
IDH-WT or IDH-132H
250,000 MC38 or B16
Analysis
Day 0
Day 16
B
MC38
B16
2HG concentraion in TIF (mM)
WT R132H
C
MC38
B16
CD8+ of CD3+CD45+ (%)
n.s.
Spleen
TIL
D
MC38
B16
Ki-67+ of CD8+ (%)
E
MC38
B16
Positive (%)
IFN-γ IL-2 TNF-α
F
2HG (mM)
LoQ
A (I-II)
A (III-IV)
OG (I-II)
OG (III-IV)
G
Lactate ion count (x10^6)
H
Case #3 (IDH1WT)
Case #19 (IDH1R132H)
10 mM
HC
LC
NT
T
Lactate ion count (x10^6)
2HG ion count (x10^7)
I
Cluster 2
Cluster 1
Cluster 0
Ambiguous
J
Low High
K
2HG
Low High
CD8+ T cells (cluster 2)
DNA
Case #18, Sample 3
L
Case #18, Sample 3
t=4.44, pval=0.0
Density-corrected [2HG]
No CD8+
CD8+
M
Case #19, Sample 1
t=12.16, pval=0.0
N
Case #18, Sample 3
ρ=-0.08, pval=0.0008
CD8+ T cells
O
Case #19, Sample 1
ρ=-0.23, pval=0.0
P
CD8+
CD4+
IDH status:
WT MUT WT MUT
IL9R
CD38
EPHA1
NAB1
ITM2C
AOAH
GZMB
PDE4DIP
PLSCR1
TMEM212
ORC4
UGDH-AS1
ASTN2
HSPA1B
DDX3Y
PDE3B
RSAD2
IFIT1
STAT1
CCDC109B
IFIT3
GPR171
IFI6
JUN
IFI44L
HERC5
ZNF282
CCR7
SOCS2
ABCC1
CEACAM1
PTGER2
CTSL1
Expression
-1 0 +1
ln(TP100K+1)
Q
IFN-γ
IFN-α
IL6/JAK/STAT3
Complement
IL2/STAT5
PLSCR1
CD38
STAT1
IFI44L
RSAD2
IFIT3
IFIT1
HERC5
IFI6
JUN
IL9R
GZMB
SOCS2
CTSL1
PTGER2
R
Interferon-CD8+
IDH status:
Mutant
WT
Density
Signature score
S
Chemokine-IFN-γ-CD8+
T
Cytotoxicity-NK-CD8+
U
CD8+
CD4+
IDH status:
WT MUT WT MUT
CD38
OASL
OAS2
PLSCR1
SAMD9L
XAF1
IRF7
GBP1
DDX60
NMI
HIF1A
RSAD2
IFIT1
STAT1
EIF21K2
IFIT3
TNFSF10
OAS3
MX2
MX1
IFI44L
ISG15
SOD2
LGALS3BP
IFI44
IFITM3
SLAMF7
CCL5
IFNG
XCL1
PTPN6
Expression
-1 0 +1
ln(TP100K+1)

Figure 6

Fig. 6. Altered metabolic and cytotoxicity signatures in *IDH1*-mutant relative to *IDH1*^{WT} cancers. (**A**) Schematic depicting experimental setup. (**B**) Quantification of 2HG levels by liquid chromatography–mass spectrometry in the tumor interstitial fluid (TIF) from *IDH1*^{WT} and *IDH1*^{R132H} MC38 and B16 tumors (n = 10 to 12). (**C**) Quantification of the percentage of CD8$^+$ T cells (of CD3$^+$CD45$^+$ cells) in spleen and tumor of *IDH1*^{WT} and *IDH1*^{R132H} MC38 and B16 syngeneic tumor mouse models (n = 6 to 10). (**D**) Quantification of the percentage of Ki67$^+$ CD8$^+$ T cells in spleen and tumor of *IDH1*^{WT} and *IDH1*^{R132H} MC38 and B16 syngeneic tumor mouse models (n = 6 to 10). (**E**) Quantification of the percentage of IFN-γ^+, IL-2$^+$, and TNF-α^+CD8$^+$ T cells isolated from *IDH1*^{WT} or *IDH1*^{R132H} MC38 or B16 tumors on day 16 after inoculation and after ex vivo restimulation with PMA and ionomycin for 4 hours in the presence of 0 or 2.5 mM D-2HG to recapitulate the 2HG levels measured in the TIF (n = 8). (**F**) MSI-based quantification of 2HG levels in tissue sections of human *IDH1*^{R132H} gliomas subdivided by grade. The upper limit of 2HG quantification based on the calibration curve was 30 mM; therefore, any value beyond that was collapsed to 30 mM. A, astrocytoma; OD, oligodendroglioma; I-II, low-grade; III-IV, high-grade. (**G**) Per-section average lactate ion counts across *IDH1*^{WT} GBM (n = 5) and *IDH1*^{R132H} (n = 4) astrocytoma, grade IV patients. (**H**) Per-pixel lactate and 2HG ion counts across all sections from case #3, an *IDH1*^{WT} GBM patient, and case #19, an *IDH1*^{R132H} glioma patient. Sections were annotated based on high cellularity (HC), low cellularity (LC), nontumor (NT), and transition (T). (**I**) Three-dimensional (3D) UMAP embedding of single-cell CyCIF data derived from human brain tumor sections colored by HDBSCAN cluster identifying a population of CD8$^+$ T cells (cluster 2, black arrow). (**J**) 3D UMAP embedding color mapped according to CD8 signal intensity showing that cluster 2 cells (black arrow) are characterized by high levels of CD8 expression. (**K**) Overlay of matched MSI and CyCIF images from case #18, sample 3 of an *IDH1*^{R132H} astrocytoma. Spatial positions of cluster 2 cells are shown in green; Hoechst nuclear dye (DNA) is shown in gray. Grid superimposed on the image shows equal-sized microregions of tissue with x and y intervals corresponding to the pixel size of the original MSI image used to compute statistics in (L) and (M). (**L**) Welch's t tests comparing mean tissue density–corrected D-2HG levels in microregions of tissue with and without CD8$^+$ T cells in case #18, sample 3. (**M**) Welch's t tests comparing mean tissue density–corrected D-2HG levels in microregions of tissue with and without CD8$^+$ T cells in case #19, sample 1. (**N**) Spearman's rank-order correlation showing anticorrelation between mean tissue density-corrected D-2HG levels and CD8$^+$ T cell counts in microregions of tissue in case #18, sample 3. (**O**) Spearman's rank-order correlation showing anticorrelation between mean tissue density–corrected D-2HG levels and CD8$^+$ T cell counts in microregions of tissue in case #19, sample 1. (**P**) Heatmap showing expression of top DE up-regulated genes in CD8$^+$ and CD4$^+$ T cells in *IDH*^{WT} GBM relative to *IDH*-mutant gliomas. Gene expression is zero-centered and given in units of ln(TP100K+1). (**Q**) Grouping of the top up-regulated genes into hallmark gene sets. (**R**) Density plot of expression of top DE up-regulated genes in the IFN subcluster for CD8$^+$ T cells in *IDH*^{WT} and *IDH*-mutant samples. (**S**) Density plot of expression of the top DE up-regulated CD8$^+$ *IDH*^{WT} genes in the chemokine–IFN-γ subcluster for T cells in and *IDH*-mutant samples. (**T**) Density plot of expression of the top DE up-regulated genes in cytotoxicity-NK subcluster for CD8$^+$ T cells in *IDH*^{WT} and *IDH*-mutant samples. (**U**) Overlay of the top DE ISGs from mouse RNA sequencing onto the top 400 DE up-regulated genes in the CD4$^+$ and CD8$^+$ T cell populations of *IDH*-mutant and *IDH*^{WT} tumors showing the relative expression of genes in common between the two datasets. *P < 0.05, **P < 0.01, ***P < 0.001, ****P < 0.0001 (Student's t test and two-way ANOVA). Data are representative of at least two independent experiments.

LDH-A activity (Fig. 3E and fig. S3, E and F). We determined D-2HG and L-2HG to be noncompetitive inhibitors of LDH-mediated pyruvate reduction, with inhibition constant (K_i) values of 840 ± 0.045 μM and 3.58 ± 0.206 mM, respectively (Fig. 3F and fig. S3G). Given that the reported K_i value for D-2HG is below the estimated intracellular D-2HG concentration, we inhibit LDH activity in CD8$^+$ T cells.

A critical function of the LDH reaction is the regeneration of cytosolic NAD$^+$ to support the continued functioning of glycolysis (*31*). D-2HG treatment lowered the NAD$^+$/NADH ratio of the cell (Fig. 3G). Thus, our data indicate that D-2HG inhibits LDH activity in CD8$^+$ T cells, resulting in altered glycolytic flux and NAD(H) balance.

D-2HG treatment induces CD8$^+$ T cells to maximize mitochondrial respiration

Upon activation, T cells undergo a switch from oxidative phosphorylation to glycolysis to support their proliferative and effector functions (*32*). We sought to investigate how D-2HG affects this metabolic switch. We tested the source (mitochondrial or glycolytic) of cellular ATP in D-2HG–treated CD8$^+$ T cells using the Seahorse XF Real-Time ATP rate assay. Consistent with our model of D-2HG–mediated LDH inhibition, D-2HG–treated CD8$^+$ T cells relied less on glycolysis and more on oxidative phosphorylation for ATP production than untreated cells (Fig. 4A). Furthermore, we observed an increased oxygen consumption rate and decreased extracellular acidification rate upon D-2HG treatment (Fig. 4B and fig. S4, A to C).

To study how D-2HG increases reliance on mitochondrial function in response to D-2HG, we assessed mitochondrial function by measuring changes in the mitochondrial membrane potential (MMP). D-2HG caused hyperpolarization of the MMP in a dose-dependent manner (Fig. 4C and fig. S4D). Kinetics studies revealed that the membrane of D-2HG–treated mitochondria remained hyperpolarized over several days after T cell activation (fig. S4E). To determine whether the increase in MMP by D-2HG was reversible, we provided D-2HG to CD8$^+$ T cells for 2 days and then removed it (fig. S4F). Removing D-2HG for as little as 1 hour was sufficient to completely restore the MMP (Fig. 4D). Conversely, a 2-hour exposure to D-2HG was sufficient to promote mitochondrial membrane hyperpolarization (Fig. 4E). The increase in MMP did not result from an increase in mitochondrial number, because D-2HG treatment did not alter the mitochondrial to nuclear DNA ratio or the expression of subunits of the ETC (fig. S4, G and H). Thus, D-2HG hyperpolarizes the mitochondrial membrane and increases mitochondrial respiration in an acute and reversible manner.

The MMP is maintained by the activity of the proton-pumping complexes (I, III, and IV) of the ETC (*33*). To determine whether the increase in MMP upon D-2HG treatment was due to increased complex activity, we used a series of inhibitors against various ETC complexes (Fig. 4F). In both untreated and D-2HG–treated T cells, inhibition of complexes I and III by rotenone and antimycin A, respectively, lowered the MMP. Similarly, treatment with carbonyl cyanide ptrifluoromethoxyphenylhydrazone (FCCP), an uncoupling agent that collapses the proton gradient, decreased the MMP. Conversely, inhibition of complex V by oligomycin, which prevents proton reentry into the matrix, further increased the MMP (Fig. 4G). Despite respiring at a higher rate, the mitochondria of D-2HG–treated CD8$^+$ T cells exhibited decreased maximal respiration and thus a decreased spare respiratory capacity, a measure of the cells' ability to respond to increased energy demand or stress (Fig. 4H and fig. S4, I and J). These data indicate that the mitochondria of CD8$^+$ T cells maximize mitochondrial respiration in response to D-2HG.

Cytosolic NAD(H) imbalance supports mitochondrial function in D-2HG–treated CD8$^+$ T cells

LDH inhibition results in cytosolic accumulation of NADH, which can enter mitochondria and provide reducing equivalents for the ETC (*34*). We tested whether cytosolic NADH might be diverted to the mitochondria for oxidation in response to D-2HG. Because mitochondria are impermeable to NADH, cytosolic NADH transfer is facilitated by a variety of shuttles,

one being the malate-aspartate shuttle (*35*). To prevent shuttling of cytosolic NADH to the mitochondria, we used aminooxyacetate (AOA), which blocks cytosolic and mitochondrial aspartate aminotransferase reactions (Fig. 4I), and measured the state of the MMP. Although D-2HG treatment promoted mitochondrial membrane hyperpolarization, simultaneous treatment with AOA prevented this effect (Fig. 4J).

To test the contribution of cytosolic NAD(H) imbalance to driving the increase in MMP, we overexpressed a cytosol-localized NADH oxidase from *Lactobacillus brevis*, *Lb*NOX, which generates NAD^+ from NADH independently of LDH activity (Fig. 4, K and L) (*36*). In the presence of *Lb*NOX, the NAD^+/NADH ratio of D-2HG–treated $CD8^+$ T cells was increased (Fig. 4M). Cytosolic *Lb*NOX overexpression lowered the MMP in the presence of D-2HG (Fig. 4N and fig. S4, K and L), indicating that cytosolic NAD^+/NADH imbalance partially drives the MMP of the cell.

Because NADH is oxidized by complex I of the ETC, we tested whether interventions that limit NAD^+ recycling in the mitochondria might exacerbate the effect of D-2HG treatment. We exposed D-2HG–treated $CD8^+$ T cells to rotenone, a complex I inhibitor, and monitored the cells' ability to proliferate (Fig. 4O). Although rotenone alone had a small effect on proliferation, the combination of rotenone and D-2HG impaired cell proliferation more strongly than D-2HG alone (Fig. 4P). Thus, NADH oxidation by complex I of the ETC appears to be important to sustain the proliferative potential of $CD8^+$ T cells in the presence of D-2HG. Because complex I is the main source of reactive oxygen species (ROS) in the mitochondria (*33*, *37*), we measured ROS and oxidative stress levels in response to D-2HG. D-2HG significantly increased intracellular ROS levels, which were decreased in cells exposed to the antioxidant *N*-acetyl-cysteine (Fig. 4Q and fig. S4M). Accordingly, D-2HG treatment was accompanied by a significant increase in total glutathione (GSSG) levels, resulting in a lower $GSH_{reduced}$/$GSSG_{oxidized}$ ratio, which is indicative of cellular redox stress (fig. S4, N to P). Overall, these data support the idea that D-2HG increases dependency on mitochondrial complex I activity, resulting in higher ROS production.

LDH inhibition is sufficient to recapitulate the effects of D-2HG on $CD8^+$ T cell metabolism and proliferation and IFN-γ signaling and cytotoxicity

To assess the contribution of LDH inhibition to the metabolic phenotypes caused by D-2HG, we tested whether LDH inhibition alone was sufficient to phenocopy treatment of cells with D-2HG using two well-established LDH inhibitors, oxamate and GSK-2837808A (abbreviated as GSK). $^{13}C_6$ glucose tracing in the presence of either LDH inhibitor recapitulated the effects of D-2HG on glucose catabolism. The LDH inhibitors each promoted the accumulation of glycolytic intermediates up to pyruvate, with concomitant loss of lactate labeling (fig. S5, A and B), resulting in a lower lactate (M+3)/pyruvate (M+3) ratio (Fig. 5A). Inhibition of LDH activity by the inhibitors was further validated by metabolite analysis in cell culture medium, in which we observed increased pyruvate and decreased lactate secretion relative to that from untreated cells (fig. S5, C and D). Consistent with LDH inhibition, the NAD^+/NADH ratio of the cell was also decreased in response to either of the inhibitors (Fig. 5B). Thus, oxamate and GSK recapitulate the effects of D-2HG on glucose catabolism.

Impairment of LDH activity by D-2HG caused $CD8^+$ T cells to undergo a metabolic transition toward oxidative phosphorylation. Therefore, we tested whether LDH inhibition was sufficient to cause this effect. LDH inhibition by oxamate or GSK recapitulated the increase in oxygen consumption rate, the decrease in extracellular acidification rate, and the hyperpolarization of the mitochondrial membrane observed in cells treated with D-2HG (Fig. 5, C and D, and fig. S5, E to G). No change in the mitochondrial/nuclear DNA ratio of the cell was detected after LDH inhibition (fig. S5H). Therefore, LDH inhibition is sufficient to cause increased reliance on mitochondrial respiration and hyperpolarization of the mitochondrial membrane in $CD8^+$ T cells.

To test whether LDH inhibition is sufficient to cause the immune phenotypes promoted by D-2HG accumulation, we tested the effects of LDH inhibition alone on viability, antigen-driven proliferation, IFN-γ production, and cytotoxicity. Each of the LDH inhibitors impaired T cell proliferation despite having no effect on cell viability (Fig. 5E and fig. S5I). A D-2HG–mediated decrease in cytotoxicity was also observed in response to each of the LDH inhibitors. Upon LDH inhibition, $CD8^+$ T cells exhibited lower expression of granzyme B and failed to degranulate upon antigen restimulation (Fig. 5, F and G, and fig. S5J). IFN-γ production was also decreased in response to LDH inhibition, resulting in a lower percentage of IFN-γ^+ $CD8^+$ T cells, decreased IFN-γ accumulation in the media, and a subsequent decrease in the induction of ISGs (Fig. 5, H to K, and fig. S5K). Ultimately, these cytotoxic defects culminated in impaired killing of tumor cells upon LDH inhibition (Fig. 5L and fig. S5L). Thus, LDH inhibition alone phenocopies the effects of D-2HG on $CD8^+$ T cell proliferation, activation, IFN-γ signaling, and cytotoxicity.

IDH-mutant glioma-infiltrating $CD8^+$ T cells exhibit altered metabolic and cytotoxic programs in patient samples

To determine whether D-2HG impairs antitumor immunity, we used two different syngeneic mouse tumor models. We injected B16 melanoma and MC38 colorectal adenocarcinoma cells overexpressing $IDH1^{WT}$ or $IDH1^{R132H}$ into the flanks of C57BL/6J mice (Fig. 6A). On day 16, when the tumors were comparable in weight, we isolated tumor interstitial fluid and detected low-millimolar levels of D-2HG in tumors harboring the *IDH1* mutation (Fig. 6B and fig. S6A). Flow cytometry profiling of cells in the immune infiltrate of these tumors revealed changes in lymphocytes (fig. S6, B and C), including reduced infiltration, proliferation, and cytokine levels of $CD8^+$ T cells in $IDH1^{R132H}$ tumors in both models (Fig. 6, C to E). These results suggest that tumor-derived D-2HG impairs T cell responses in the TME of $IDH1^{R132H}$ tumors.

Mouse models of *IDH* do not fully recapitulate the developmental and morphological features of human *IDH*-mutant cancers, arguing for characterization of human specimens. Moreover, the reversible and acute nature of the metabolic phenotypes caused by D-2HG makes it important to study these properties in an intact TME. Thus, we leveraged mass spectrometry imaging (MSI) to study the tumor metabolic landscape of five patients with *IDH*-WT and 17 patients with *IDH*-mutant gliomas (table S1). Quantification of 2HG levels in tissue sections revealed a range of high-millimolar concentrations of 2HG across all *IDH*-mutant gliomas regardless of grade (Fig. 6F and fig. S6D). The 2HG signal was restricted to the tumor area and was absent in surrounding healthy tissue, indicating that 2HG levels accumulate at the tumor site (fig. S6E). Comparison of $IDH1^{R132H}$ grade IV astrocytomas with $IDH1^{WT}$ glioblastoma (GBM) revealed trending lower lactate levels in $IDH1^{R132H}$ relative to $IDH1^{WT}$ gliomas (Fig. 6, G and H, and fig. S6, F to H).

Because of the immunosuppressive properties of D-2HG, we hypothesized that tumor regions characterized by high levels of the oncometabolite would contain fewer $CD8^+$ T cells compared with those with lower expression. To test this hypothesis, we coupled cyclic immunofluorescence (CyCIF) of $IDH1^{R132H}$ grade IV astrocytomas with MSI rasters of D-2HG collected on the same tissue sections to study the location of $CD8^+$ T cells with respect to D-2HG expression. Dimensionality reduction [uniform manifold approximation and projection (UMAP)] and clustering [hierarchical density-based clustering (HDBSCAN)] algorithms applied to CyCIF-derived single-cell data identified a population of $CD8^+$ T cells that coexpressed CD8α and CD45RB (Fig. 6, I and J, and fig. S6I). Mapping the coordinates of these cells onto D-2HG MSI rasters, we observed a tendency for these cells to be less present in regions of tissue high in the oncometabolite (Fig. 6K). To quantify this effect, tissues were divided into microregions the size of pixels in the original MSI rasters before computing mean tissue density-corrected

D-2HG expression per region. Independent, two-way Welch's *t* tests were then used to compare microregions with and without at least one $CD8^+$ T cell (Fig. 6, L and M). Across multiple tissue samples from different patients, this analysis revealed that D-2HG expression was significantly lower in regions of tissue containing $CD8^+$ T cells compared with those that did not. Correlation analysis comparing D-2HG levels and $CD8^+$ T cell numbers using Spearman's rank-order method established a significant anticorrelation between these variables that was not explained by concurrent anticorrelation between $CD8^+$ T cells and tissue density (Fig. 6, N and O, and fig. S6, K, L, N, and O), suggesting that the avoidance of regions of tissue high in D-2HG by $CD8^+$ T cells was not due to their failure to infiltrate tumor tissue. Together, these studies reveal a dose-dependent relationship between D-2HG and $CD8^+$ T cell density in human gliomas and support the hypothesis that D-2HG may regulate $CD8^+$ T cell proliferation in this context.

To better understand the physiological role of D-2HG accumulation in the microenvironment of *IDH*-mutant tumors on $CD8^+$ T cell function, we analyzed single-cell RNA-sequencing data from a different set of IDH^{WT} GBM patients ($n = 16$) and *IDH*-mutant glioma patients ($n = 15$) (*38*) and profiled the gene expression signature of tumor-infiltrating T cells. We identified the top differentially up-regulated genes in $CD8^+$ and $CD4^+$ T cell subpopulations and grouped these into hallmark gene signatures (Fig. 6P and fig. S6P). This showed that several of the top down-regulated genes in $CD8^+$ T cells from *IDH*-mutant samples fall under the IFN signaling signature (Fig. 6Q).

Previous analysis of this single-cell RNA-sequencing dataset revealed six subclusters for $CD8^+$ T cell subsets [cytotoxicity–natural killer (NK), IFN, effector memory, chemokine–IFN-γ, not determined, and stress cells] and $CD4^+$ T cell subsets (cytotoxicity-chemokine, IFN, effector memory, Treg, memory, and stress cells) (*38*). Thus, we assessed the gene expression signature of the top 20 up-regulated genes in IDH^{WT} GBM within each of the previously identified subclusters. The top 20 up-regulated genes gave a weaker signature score in the cytotoxic, IFN, and IFN-γ subclusters for $CD8^+$ T cells from *IDH*-mutant gliomas compared with IDH^{WT} GBM (Fig. 6, R to T). The expression of the top up-regulated genes was not affected in the Tregs and cytotoxicity subclusters for $CD4^+$ T cells, but it was elevated in the $CD4^+$ IFN subcluster for IDH^{WT} compared with *IDH*-mutant (fig. S6Q). Thus, we concluded that the cytotoxic and IFN programs of effector T cells, in particular effector $CD8^+$ T cells, are lower in *IDH*-mutant samples compared with IDH^{WT}.

Finally, we validated the relevance of the ex vivo–derived IFN-γ signature from D-2HG–treated mouse $CD8^+$ T cells (fig. S1G) using the human single-cell RNA-sequencing data. We generated a gene list containing the top differentially expressed (DE) ISGs upon D-2HG treatment from the mouse RNA-sequencing experiment and used this gene list to filter the top 400 DE genes in $CD4^+$ and $CD8^+$ T cell populations from *IDH*-mutant and IDH^{WT} tumors. Overall, both $CD8^+$ and $CD4^+$ T cell populations from *IDH*-mutant tumors showed decreased expression of the IFN-induced mouse gene signature (Fig. 6U), demonstrating that the human IFN-γ signature of $CD8^+$ T cells derived from *IDH*-mutant tumors is similar to that of D-2HG–treated mouse $CD8^+$ T cells.

Discussion

Our results suggest that D-2HG may not only affect tumor initiation and growth through tumor cell-intrinsic mechanisms but also by directly affecting the cells in the surrounding TME. In the context of antitumor immunity, *IDH*-mutant tumors are surveyed by immune cells, which, upon infiltrating, face a newly D-2HG–rich microenvironment. *IDH*-mutant tumors have fewer tumor-infiltrating T cells compared with IDH^{WT} tumors (*7*, *13*–*16*), but the factors that mediate the immunosuppressive functions of D-2HG have remained elusive. We propose that D-2HG acts directly on $CD8^+$ T cells in the TME of *IDH*-mutant tumors by altering their metabolic and cytotoxic signatures.

Glucose metabolism has a central role in regulating cytotoxic T cell responses. As effector $CD8^+$ T cells undergo extensive proliferation in response to antigen stimulation, maintaining a high glycolytic flux is needed to support the bioenergetic needs, as well as to provide the building blocks for cellular biomass (*32*). Furthermore, glucose metabolism has also been tightly linked to IFN-γ signaling and T cell cytotoxicity (*30*, *39*–*46*). Our findings show that D-2HG alters glucose metabolism in $CD8^+$ T cells, resulting in impaired proliferation, cytokine production, and cytotoxicity. Specifically, we show that decreased IFN-γ production in D-2HG–treated $CD8^+$ T cells results in a suppressed autocrine IFN-γ gene expression signature, which has been shown to be important for effector function (*47*). Moreover, although a link between glucose metabolism and the expression of lytic molecules has previously been made (*40*), our work has uncovered a previously unknown role for LDH and D-2HG in regulating the process of degranulation. Thus, our studies expand upon previous work demonstrating the role of glycolytic metabolism in regulating T cell effector function and proliferation.

Analysis of the metabolic landscape of human gliomas has revealed altered lactate levels and decreased IFN-γ signatures in glioma samples from *IDH*-mutant patients. Mechanistically, we propose that D-2HG alters $CD8^+$ T cell metabolism through direct LDH inhibition. Decreased LDH-A activity caused by epigenetic silencing in *IDH*-mutant tumors had previously been reported (*48*–*51*), but our work shows that D-2HG can additionally have a new, direct and immediate effect on LDH enzymatic activity in $CD8^+$ T cells. Future studies are required to investigate the in vivo immunotherapeutic relevance of the proposed mechanism and determine whether D-2HG inhibition of LDH activity expands beyond $CD8^+$ T cells in vivo, affecting other cells within the TME.

Finally, we found that many of the effects caused by D-2HG are reversible upon D-2HG removal. In the future, it will be interesting to determine whether therapeutic interventions involving US Food & Drug Administration–approved, mutation-specific IDH inhibitors potentiate immune responses by removing immunosuppressive D-2HG from the TME, in addition to having a direct role in the inhibition of tumor growth. In support of this idea, recent studies have shown that $CD8^+$ T cell infiltration is restored in the presence of inhibitors of mutant IDH (*52*).

REFERENCES AND NOTES

1. D. G. Ryan *et al.*, *Nat. Metab.* **1**, 16–33 (2019).
2. C. Choi *et al.*, *Nat. Med.* **18**, 624–629 (2012).
3. L. Dang *et al.*, *Nature* **462**, 739–744 (2009).
4. J. A. Losman, W. G. KaelinJr.., *Genes Dev.* **27**, 836–852 (2013).
5. O. C. Andronesi *et al.*, *Sci. Transl. Med.* **4**, 116ra4 (2012).
6. O. C. Andronesi *et al.*, *J. Clin. Invest.* **123**, 3659–3663 (2013).
7. L. Bunse *et al.*, *Nat. Med.* **24**, 1192–1203 (2018).
8. A. Linninger *et al.*, *Neuro Oncol.* **20**, 1197–1206 (2018).
9. R. Chowdhury *et al.*, *EMBO Rep.* **12**, 463–469 (2011).
10. M. E. Figueroa *et al.*, *Cancer Cell* **18**, 553–567 (2010).
11. S. Turcan *et al.*, *Nature* **483**, 479–483 (2012).
12. W. Xu *et al.*, *Cancer Cell* **19**, 17–30 (2011).
13. A. S. Berghoff *et al.*, *Neuro Oncol.* **19**, 1460–1468 (2017).
14. F. Klemm *et al.*, *Cell* **181**, 1643–1660.e17 (2020).
15. G. Kohanbash *et al.*, *J. Clin. Invest.* **127**, 1425–1437 (2017).
16. B. Weenink *et al.*, *Sci. Rep.* **9**, 14643 (2019).
17. P. A. Tyrakis *et al.*, *Nature* **540**, 236–241 (2016).
18. A. M. Intlekofer *et al.*, *Nat. Chem. Biol.* **13**, 494–500 (2017).
19. S. I. Tsukumo, K. Yasutomo, *Front. Immunol.* **9**, 101 (2018).
20. M. Barry, R. C. Bleackley, *Nat. Rev. Immunol.* **2**, 401–409 (2002).
21. M. R. Betts *et al.*, *J. Immunol. Methods* **281**, 65–78 (2003).
22. M. D. McKenzie *et al.*, *Int. Immunol.* **18**, 837–846 (2006).
23. S. J. Waddell *et al.*, *PLOS ONE* **5**, e9753 (2010).
24. M. K. Engqvist, C. Eßer, A. Maier, M. J. Lercher, V. G. Maurino, *Mitochondrion* **19**, 275–281 (2014).
25. E. A. Struys *et al.*, *J. Inherit. Metab. Dis.* **28**, 921–930 (2005).
26. S. P. Burr *et al.*, *Cell Metab.* **24**, 740–752 (2016).
27. S. M. Nadtochiy *et al.*, *J. Biol. Chem.* **291**, 20188–20197 (2016).
28. P. Koivunen *et al.*, *Nature* **483**, 484–488 (2012).
29. A. Farhana, S. L. Lappin, "Biochemistry, lactate dehydrogenase," in StatPearls [Internet]. Treasure Island, FL: StatPearls Publishing (2022).
30. C. H. Chang *et al.*, *Cell* **153**, 1239–1251 (2013).
31. S. Y. Lunt, M. G. Vander Heiden, *Annu. Rev. Cell Dev. Biol.* **27**, 441–464 (2011).
32. G. J. W. van der Windt, E. L. Pearce, *Immunol. Rev.* **249**, 27–42 (2012).
33. L. D. Zorova *et al.*, *Anal. Biochem.* **552**, 50–59 (2018).
34. S. C. Lu, *Biochim. Biophys. Acta* **1830**, 3143–3153 (2013).
35. J. B. Spinelli, M. C. Haigis, *Nat. Cell Biol.* **20**, 745–754 (2018).
36. D. V. Titov *et al.*, *Science* **352**, 231–235 (2016).
37. S. E. Weinberg, N. S. Chandel, *Nat. Chem. Biol.* **11**, 9–15 (2015).
38. N. D. Mathewson *et al.*, *Cell* **184**, 1281–1298.e26 (2021).
39. Y. Cao, J. C. Rathmell, A. N. Macintyre, *PLOS ONE* **9**, e104104 (2014).
40. C. M. Cham, G. Driessens, J. P. O'Keefe, T. F. Gajewski, *Eur. J. Immunol.* **38**, 2438–2450 (2008).

41. C. M. Cham, T. F. Gajewski, *J. Immunol.* **174**, 4670–4677 (2005).
42. L. F. Gemta *et al*., *Sci. Immunol.* **4**, eaap9520 (2019).
43. P. J. Siska *et al*., *JCI Insight* **2**, e93411 (2017).
44. P. C. Ho *et al*., *Cell* **162**, 1217–1228 (2015).
45. W. J. Quinn 3rd *et al*., *Cell Rep.* **33**, 108500 (2020).
46. M. Peng *et al*., *Science* **354**, 481–484 (2016).
47. J. M. Curtsinger, P. Agarwal, D. C. Lins, M. F. Mescher, *J. Immunol.* **189**, 659–668 (2012).
48. C. Chesnelong *et al*., *Neuro Oncol.* **16**, 686–695 (2014).
49. L. J. M. Dekker *et al*., *FASEB J.* **34**, 3646–3657 (2020).
50. M. M. Chaumeil *et al*., *Neuroimage Clin.* **12**, 180–189 (2016).
51. J. Balss *et al*., *Leukemia* **30**, 782–788 (2016).
52. M. Lu *et al*., *Cancer Res.* **80** (Supplement), 2046–2046 (2020).

ACKNOWLEDGMENTS

We thank Agios Pharmaceuticals, Inc., for providing $^{13}C_5$ D-2HG and L-2HG; members of the Haigis laboratory for productive discussions; C. Park and lab mates A. Ringel and J. van der Reest for helping with enzyme biochemistry; J. van der Reest for feedback on the manuscript; C. Benoist for facilitating the mouse RNA-sequencing experiment and providing feedback on the manuscript; W. Kaelin Jr. for providing reagents and feedback on the manuscript; and the HMS System Biology FACS facility, HMS Immunology Flow Core, and the Broad Genetic Platform for access to equipment. Schematics were generated in Adobe Illustrator with the support of ChemDraw (PerkinElmer Informatics) and Biorender (https://biorender.com). **Funding:** G.N. was supported by the National Science Foundation (NSF) Graduate Research Fellowship Program (grant DGE1745303). I.E. was supported by the European Molecular Biology Organization (grant ALTF-107802017). K.K. was supported by the Life Sciences Research Foundation. M.H. was supported by National Institutes of Health (NIH) grant R01CA213062. M.H. and P.S. were supported by the Ludwig Center at Harvard Medical School. M.H., P.S., and A.H.S. were supported by NIH grant U54-CA225088. K.W.W., M.L.S., and A.H.S. were supported by NIH grant 1P01CA236749. E.M.P. was supported by the NSF Graduate Research Fellowship Program (fellowship DGE1745303). N.Y.R.A. was supported by NIH grants U54-CA210180 and P41-EB028741 and by a Capital Award from the Massachusetts Life Sciences Center. S.A.S. was supported by NIH grant T32EB025823. G.B. was supported by Marie Skłodowska-Curie grant 713679, by European Union's Horizon 2020, and by Universitat Rovira i Virgili. **Author contributions:** G.N., J.B.S., and M.C.H. conceived the project. G.N. performed most of the experiments. I.E., J.M.D., S.J., H.F.B., P.G., E.Z., A.E.R., A.H.S., S.K.M., and K.K. provided research assistance. K.K. performed RNA-sequencing analyses. E.M.P., K.W.W., and M.L.S. generated and analyzed single-cell RNA-sequencing datasets. A.J.G. obtained human glioma tissue samples and oversaw human subject research. G.J.B., G.B., S.A.S., J.L., P.K.S., S.S., and N.Y.R.A. oversaw, performed, and analyzed the MSI and CyCIF studies. G.N. and M.H. analyzed and interpreted the data. G.N. and M.H. wrote the manuscript with input from all authors. **Competing interests:** M.H. received research funding from Agilent Technologies and Roche Pharmaceuticals and is on advisory boards for Alixia and Minovia. M.L.S. and K.W.W. are equity holders, scientific cofounders, and advisory board members of Immunitas Therapeutics. K.W.W. serves on the scientific advisory board of TCR2 Therapeutics, T-Scan Therapeutics, SQZ Biotech, and Nextechinvest and receives sponsored research funding from Novartis. N.Y.R.A. is key opinion leader for Bruker Daltonics, scientific adviser to Invicro, and receives support from Thermo Finnegan and EMD Serono. A.H.S. has patents and/or pending royalties on the PD-1 pathway from Roche and Novartis. A.H.S. is on advisory boards for Surface Oncology, SQZ Biotechnologies, Elpiscience, Selecta, Bicara, Monopteros, Fibrogen, Alixia, GlaxoSmithKline, and Janssen. A.H.S. has received research funding from Merck, Vertex, Moderna, Quark/Iome, and AbbVie unrelated to this project. The remaining authors declare no competing interests. **Data and materials availability:** Bulk mouse RNA-sequencing datasets have been deposited to the Gene Expression Omnibus (GEO) website with identifier GSE209757. All other data are available in the main manuscript or supplementary materials. **License information:** Copyright © 2022 the authors, some rights reserved; exclusive licensee American Association for the Advancement of Science. No claim to original US government works. https://www.science.org/about/science-licenses-journal-article-reuse

SUPPLEMENTARY MATERIALS

science.org/doi/10.1126/science.abj5104
Materials and Methods
Table S1
Figs. S1 to S6
References (*53*–*57*)
MDAR Reproducibility Checklist

Submitted 17 May 2021; accepted 9 August 2022
10.1126/science.abj5104

REPORTS

GEOCHEMISTRY

Earth's composition was modified by collisional erosion

Paul Frossard[1,2]*, Claudine Israel[1]†, Audrey Bouvier[3,4], Maud Boyet[1]

The samarium-146 (^{146}Sm)–neodymium-142 (^{142}Nd) short-lived decay system (half-life of 103 million years) is a powerful tracer of the early mantle-crust evolution of planetary bodies. However, an increased ^{142}Nd/^{144}Nd in modern terrestrial rocks relative to chondrite meteorites has been proposed to be caused by nucleosynthetic anomalies, obscuring early Earth's differentiation history. We use stepwise dissolution of primitive chondrites to quantify nucleosynthetic contributions on the composition of chondrites. After correction for nucleosynthetic anomalies, Earth and the silicate parts of differentiated planetesimals contain resolved excesses of ^{142}Nd relative to chondrites. We conclude that only collisional erosion of primordial crusts can explain such compositions. This process associated with planetary accretion must have produced substantial loss of incompatible elements, including long-term heat-producing elements such as uranium, thorium, and potassium.

Short-lived radioactive systems are used as high-resolution chronometers of early Solar System events. Notably, the ^{146}Sm-^{142}Nd pair provides important constraints on mantle-crust evolution of early Earth and its modern composition. In 2005, Boyet and Carlson (*1*) were the first to find evidence for an offset of 20 parts per million (ppm) in the ^{142}Nd /^{144}Nd ratio between terrestrial samples and chondrites that are usually considered to be building blocks of planets. They interpreted the excess of ^{142}Nd in Earth as the result of an early differentiation event and subsequent burial and isolation of this early-formed crust, which left the mantle depleted in incompatible elements and, over time, enriched in ^{142}Nd. Alternative scenarios such as collisional erosion of the early crust or accretion of Earth from material with a non-chondritic Sm/Nd ratio have been invoked to explain the observed excess (*1*–*3*).

Chronological information from short-lived radioactive systems is complicated by nucleosynthetic anomalies, which are mass-independent stable isotope variations that are inherited from incomplete mixing of the solar nebula [e.g., (*4*)]. Neodymium and Sm isotopes are produced by a mixture of *s*-, *r*-, and *p*-nucleosynthetic processes, which correspond to slow and rapid neutron capture and proton capture or photodisintegration of large nuclei, respectively. The contribution of the *p*-process to ^{142}Nd is particularly ill-constrained because it cannot be identified by measuring the Nd isotope composition alone. Estimates range from 1 to 20% according to astrophysical models and cosmochemical constraints (*5*–*11*). *p*-Process variation is determined by combining Sm and Nd isotope measurements because ^{144}Sm is a pure *p*-process nuclide (*4*, *8*).

A radiogenic origin for the excess of ^{142}Nd in Earth was recently argued against on the basis of evidence that Earth lies on the ^{146}Sm-^{142}Nd isochron of the first solids formed in the Solar System, the Ca-Al–rich inclusions (CAIs) (*5*), as well as on *s*-process mixing lines with chondrites (*6*). Earth shares closest affinities with the subgroup of EL*3* enstatite chondrites (*12*). Nevertheless, the potential contribution of the *p*-process on ^{142}Nd is poorly constrained [e.g., (*7*)]. Nucleosynthetic compositions identified in meteorites deviate from the astrophysical models of nucleosynthesis and may not be similar in all chondrite groups (*8*, *13*).

In this work, we report a comprehensive set of coupled Nd and Sm isotope compositions of bulk rocks and of components of unequilibrated chondrites from both the noncarbonaceous (NC) (enstatite and ordinary chondrites) and the carbonaceous (CC) groups. Our objective was to identify the sources and variability of nucleosynthetic anomalies, including the *p*-process, that potentially affect the ^{142}Nd/^{144}Nd ratio in bulk meteorites. Mass-independent Nd and Sm isotope compositions, which were

[1]Université Clermont Auvergne, CNRS, IRD, OPGC, Laboratoire Magmas et Volcans, F-63000 Clermont-Ferrand, France. [2]Institute of Geochemistry and Petrology, ETH Zürich, Zürich, Switzerland. [3]Bayerisches Geoinstitut, Universität Bayreuth, 95447 Bayreuth, Germany. [4]Department of Earth Sciences, University of Western Ontario, London, ON N6A 5B7, Canada.
***Corresponding author. Email: paul.frossard@erdw.ethz.ch**
†Present address: Université Paris Cité, Institut de Physique du Globe de Paris, CNRS, F-75005 Paris, France.

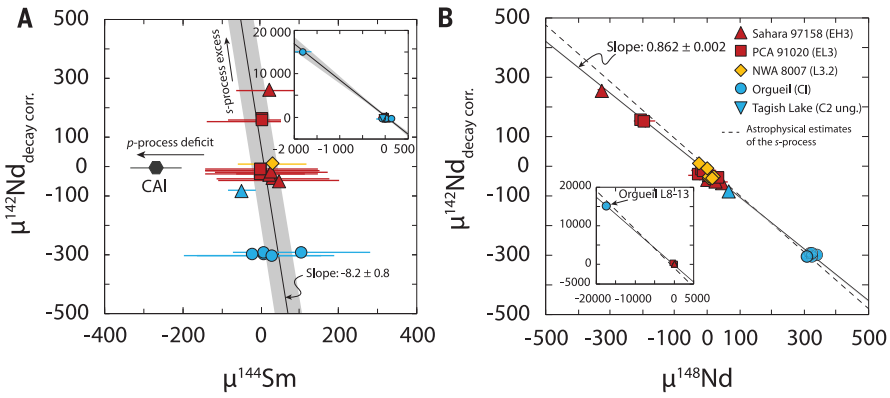


Fig. 1. Coupled μ^{142}Nd and μ^{144}Sm and coupled μ^{142}Nd and μ^{148}Nd composition of leachates. (**A**) The regression line is calculated by using solely leachates from NC chondrites and leachates L8 to L13 of Orgueil to avoid the contribution of CAIs. μ^{142}Nd compositions of leachates are corrected (corr.) for the decay of ^{146}Sm (*16*). Leachates of NC chondrites do not deviate from the leachate regression line that represents the *s*-process, which evidences the homogeneous *p*-process contribution to Nd and the lack of pure *p*-process carriers in NC chondrites. CAI compositions are from (*5*, *6*, *17*, *18*), which are compiled in (*25*). (**B**) Leachates are used to calculate a regression line that models the *s*-process trend in meteorites, which accurately relates the nucleosynthetic compositions of μ^{148}Nd and μ^{142}Nd. The dashed line represents the mixing line between Earth and the *s*-process estimates from astrophysical models (*11*). Errors are twice the standard error of a single measurement or twice the standard deviation of the standard processed with similar contents in the same analysis session, whichever is larger. Errors on the regression are 95% confidence intervals that were calculated by using IsoplotR (*21*).

normalized to fixed ^{146}Nd/^{144}Nd or ^{147}Sm/^{152}Sm ratios, are hereafter expressed as deviations from a synthetic terrestrial standard in ppm $\{\mu^{i}X = [(^{i}X/^{j}X)_{sample}/(^{i}X/^{j}X)_{standard} - 1] \times 10^{6}$, where i and j are isotopes of the element X$\}$. We used a recently improved mass spectrometric method (*14*) for Nd isotope analyses of eight bulk chondrites and some of the separated components of chondrites. Pooled chondrules and a single large chondrule (~200 mg) from the ordinary chondrite NWA 8007 (L3) and magnetically separated and sorted fragments of the EH3 chondrite Sahara 97158 were analyzed only for their Nd isotope compositions. Enstatite (Sahara 97158-EH3, PCA 91020-EL3), ordinary (NWA 8007-L3.2), and carbonaceous (Orgueil-CI) chondrites were sequentially dissolved with increasingly aggressive acids and analyzed for their Nd and Sm isotope compositions. This procedure produced several fractions (named L1 to L13), thereby isolating the most refractory minerals that include presolar grains with the most extreme isotopic compositions (*8*, *13*, *15*).

Leachates from enstatite and carbonaceous chondrites display much larger nucleosynthetic anomalies than bulk chondrites in the range of tens to hundreds of ppm in magnitude (fig. S1 and table S1). The first leachates have positive $\mu^{145,148,150}$Nd anomalies, whereas those produced by the last and most aggressive dissolution steps (L6 and L7 for EH and EL and L8 to L13 pooled together for CI chondrites) have negative $\mu^{145,148,150}$Nd anomalies. Leachates L8 to L13 of the Orgueil CI chondrite reach extreme compositions, down to μ^{150}Nd of −20,336 ± 47 (twice the standard error). By contrast, the leachates and chondrules of ordinary chondrites (OCs) and separates of the EH3 chondrite exhibit only small variations. Corrections for radiogenic contributions of ^{146}Sm are needed to interpret nucleosynthetic anomalies on μ^{142}Nd. Because sequential dissolution may fractionate Sm and Nd (*8*), we calculated the corresponding ^{147}Sm/^{144}Nd ratios using the ^{143}Nd/^{144}Nd ratio of each sample (*12*) after correction for nucleosynthetic anomalies on the ^{143}Nd/^{144}Nd ratio (*16*).

Most leachates of NC chondrites display Sm isotope compositions that are indistinguishable from the terrestrial standard. Small deviations in all Sm isotope ratios are observed for leachates of CC chondrites. Variations in μ^{149}Sm and μ^{150}Sm reflect neutron capture reactions, but this effect is negligible for other Nd and Sm isotope ratios (up to 1.9 ppm on μ^{145}Nd; fig. S2) (*16*). The largest variations are obtained in L8 to L13 of the Orgueil meteorite, with a μ^{144}Sm of −1797 ± 176 and a μ^{148}Sm of 8176 ± 48 (twice the standard error) (fig. S2 and table S2).

Nucleosynthetic *p*-process contributions on μ^{142}Nd are constrained by using μ^{144}Sm in leachates (Fig. 1A). Deviations from the trend modeled by NC leachates and L8 to L13 of Orgueil are solely observed for leachates of CC chondrites and are related to signatures of CAIs that display large deficits in *p*-process ^{144}Sm and small deficits in ^{142}Nd (*5*, *6*, *17*, *18*). However, no other *p*-process endmember is identified in leachates from all chondrite groups. *s*-Process excesses are indistinguishable from *r*-process deficits with Nd and Sm isotope compositions. We constrain endmembers using a mass balance calculation on leachates by using presolar SiC that is the only *s*-process–rich carrier of rare earth elements identified so far [e.g., (*13*, *16*)] (fig. S3). Small amounts of presolar SiC are therefore enough to produce the range of Nd isotope compositions measured in leachates, without invoking an *r*-process carrier. The CAIs that bear fractionated and unknown nuclear isotope compositions (FUN CAIs) display large anomalies (*19*). They have, however, a negligible effect on the Nd and Sm isotope compositions of leachates and bulk rocks of CC chondrites because of their very rare occurrence in CV chondrites. We also confirm that Nd and Sm *s*-process compositions estimated by astrophysical models are substantially different compared to leachates (figs. S4 and S5), as pointed out by Saji *et al.* (*20*).

Given that Nd isotope composition in chondrites is solely related to *s*-process variations induced by variable amounts of presolar SiC, leachates can be used to define the nucleosynthetic trend by comparing a stable isotope ratio with μ^{142}Nd (Fig. 1B). For consistency and after comparison with previous studies (*8*, *13*, *20*) (figs. S5 and S6), we use only leachates from this study to construct regression lines that define the nucleosynthetic variability in chondrites. We obtain slopes by total least squares regression of μ^{145}Nd or μ^{148}Nd on μ^{142}Nd of −1.599 ± 0.007 and −0.862 ± 0.002 [95% confidence interval; (*21*)], respectively. However, the intercepts of the regression lines (theoretical Earth's μ^{142}Nd) are poorly constrained, owing to the low precision for many leachates with Nd isotope compositions close to the terrestrial value (fig. S7).

Bulk chondrites provide the best samples to define accurately the Nd isotope compositions of Earth because of their much higher precision compared to leachates and their unfractionated Sm/Nd ratio. We critically assessed data from the literature to offer an up-to-date compilation of the highest precision measurements on meteorites (table S1) (*6*, *9*, *22*–*25*). The compilation gives weighted averages with two standard errors of μ^{142}Nd = −9.9 ± 2.5, μ^{145}Nd = 0.5 ± 1.5, μ^{148}Nd = 2.2 ± 1.4, and μ^{150}Nd = 8.0 ± 5.1 for enstatite chondrites (ECs) and μ^{142}Nd = −13.9 ± 1.8, μ^{145}Nd = 4.4 ± 1.7, μ^{148}Nd = 7.6 ± 1.3, and μ^{150}Nd = 14.9 ± 3.3 for OCs.

We used slopes defined by leachate regression lines linking a stable isotope ratio to μ^{142}Nd to calculate the μ^{142}Nd composition of chondrites without nucleosynthetic anomalies relative to Earth. The theoretical composition of Earth, assuming NC chondrites are its main building blocks, is calculated in this manner. We corrected EC and OC ^{142}Nd isotope compositions for nucleosynthetic anomalies using

their measured μ^{145}Nd and μ^{148}Nd. We find very similar results, with an average of μ^{142}Nd = −7.9 ± 1.9 (twice the standard deviation, n = 4) (Fig. 2A). This negative value of μ^{142}Nd relative to Earth contrasts with μ^{145}Nd and μ^{148}Nd, which lie on the leachate regression line that passes through the NC chondrites (Fig. 2B). We did not consider CC chondrites because of their depletion in μ^{144}Sm, which suggests the presence of *p*-process–depleted material, likely related to the presence of CAIs that can substantially alter the theoretical μ^{142}Nd composition of Earth (Fig. 1A and fig. S8). After correcting μ^{142}Nd for nucleosynthetic anomalies, the corrected data for NC chondrites are resolved from Earth's μ^{142}Nd composition by using Student's t tests, with p values [significance level (α) of 0.05] between 6.7×10^{-7} and 4.8×10^{-4}. Recent studies (*9*, *24*, *25*) reported high-precision Nd isotope compositions of achondrites by sampling early planetesimals. When corrected for nucleosynthetic anomalies, their μ^{142}Nd values are between those of Earth and NC chondrites, and more specifically, angrites and eucrites are resolved from NC chondrites ($p < 0.007$).

The cause of the excess in μ^{142}Nd in Earth and achondrites may be related to several factors: (i) a *p*-process excess, (ii) accretion of material with a nonchondritic composition, or (iii) early silicate differentiation and isolation of the enriched reservoir. We did not identify any *p*-process–rich carriers in leachates of chondrites, and such a carrier is unlikely to be present only in Earth and achondrites. The lack of precision in μ^{144}Sm of bulk chondrites does not allow for the elimination of this possibility entirely, but current datasets imply that a contribution of *p*-process of this magnitude is nevertheless unlikely. Chondrites, despite having been formed 2 million to 3 million years after the first planetesimals [e.g., (*26*)], are representative of the early Solar System composition before differentiation of planet-size objects. The most likely hypothesis is that the excess of ^{142}Nd in Earth and achondrites reflects an early silicate differentiation of planets and planetesimals that produced mantles with superchondritic Sm/Nd ratios. Achondrite parent bodies accreted within 1.5 million years after the crystallization of CAI [e.g., (*26*)] and experienced global magma ocean stages. Early crustal material may have been buried and isolated in the mantle of large bodies during the overturn of high-density cumulates during the evolution of magma oceans [e.g., (*27*)]. However, the presence of hidden crustal reservoirs in the mantle of planetesimals is very unlikely because it would imply overturn mechanisms that are difficult to produce on planetesimals (*27*). The absence of achondrites displaying subchondritic Sm/Nd and Hf/Sm ratio variation (*28*), for instance, also corroborates this interpretation.

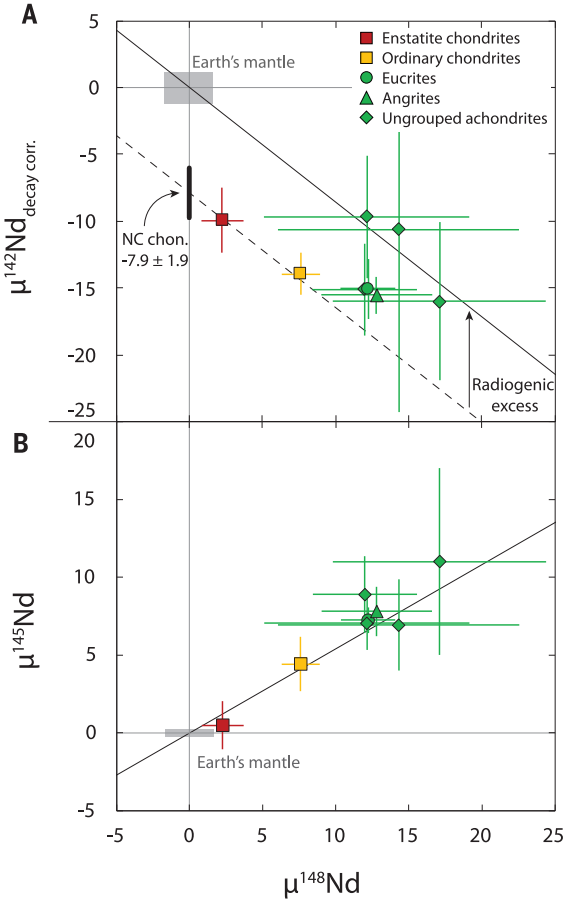


Fig. 2. *s*-Process nucleosynthetic contributions on Nd isotope compositions of bulk NC meteorites. Nd isotope compositions of meteorites have been compiled to include only the most precise and accurate data (table S3). Averages of meteorite groups are plotted, except for the three ungrouped achondrites. (**A**) The μ^{142}Nd-μ^{148}Nd space shows the radiogenic excess of ^{142}Nd in Earth and NC achondrites. The two lines represent the *s*-process nucleosynthetic trend with the slope determined with leachates of this study with a terrestrial origin (μ^{142}Nd = 0; black line) and an origin corresponding to the mean of μ^{142}Nd corrected from nucleosynthetic anomalies in NC chondrites (μ^{142}Nd = 7.9 ± 1.9; dashed line). chon., chondrite. (**B**) Earth, NC chondrites, and achondrites are all aligned on the nucleosynthetic trend with a terrestrial origin (black line). Earth's mantle composition corresponds to the largest series of JNdi-1 standards measured by using the four-lines dynamic method (twice the standard error, n = 18) (table S5). Errors on averages are twice the standard error when $n > 4$ or twice the standard deviation otherwise, all in ppm.

Destruction of the primordial crust through collisions or explosive volcanism (*29*) are the more suitable processes to explain the ubiquitous excess in ^{142}Nd in both Earth and planetesimal samples (Fig. 3). We favor collisional erosion in light of the overwhelming evidence of common collisions in the early Solar System that led to the accretion of planets and the quantification of this process by numerical models [e.g., (*30*, *31*)].

We estimate the amount of crust lost during collisional erosion using mass balance calculations. Given the antiquity of the early planetesimals, silicate differentiation events most likely occurred very early (<1 million years ago for achondrite parent bodies). We assume that collisional erosion for both Earth and planetesimals occurred 4.567 billion years ago (*32*). Given Earth's excess in ^{142}Nd of 7.9 ppm compared with that of NC chondrites, we infer a ^{147}Sm/^{144}Nd ratio of 0.2012 ± 0.0051 (ε^{143}Nd = 3.3 ± 4.4) for Earth's modern mantle or early depleted reservoir, which is higher than the chondritic reference of 0.1960 ± 0.0004 (*33*). We estimate the mass of crustal material that was removed during collisional erosion events for various crustal compositions (Fig. 4). Considering crusts with a low Sm/Nd ratio and high Nd contents [lunar KREEP (potassium rare earth elements and phosphorus), Earth's continental crust, and martian crust, (*34*–*36*), respectively], the mass balance suggests that up to 5% of the total initial accreted mass needs to be removed. About 4 to 20% of the total initial mass is required to be eroded by using a crust with lower Sm/Nd ratio and Nd contents such as those of the lunar Mg suite (*37*) and of the achondrite GRA 06128/9 (*38*). The accretion of differentiated planetesimals as building blocks of Earth is supported by models of collisional erosion that estimate the mass eroded during accretion from ~10 to 20% of the total initial mass of all planetesimals [e.g., (*31*, *39*)].

The ubiquity of collisional erosion recorded by Nd isotope compositions suggests substantial consequences for the highly incompatible elemental compositions of Earth and planetesimals. In this regard, K, Th, and U are critical as radioactive heat-producing elements [e.g., (*40*)]. We are limited in estimating the depletion in K, Th, and U in primordial crusts owing to the lack of complete meteorite igneous suites from various parent bodies. K, Th, and U are more incompatible than rare earth elements, and the amount lost during collisional erosion is estimated to be greater than 30%.

Chondrites have long been considered to be the building blocks of Earth. However, growing

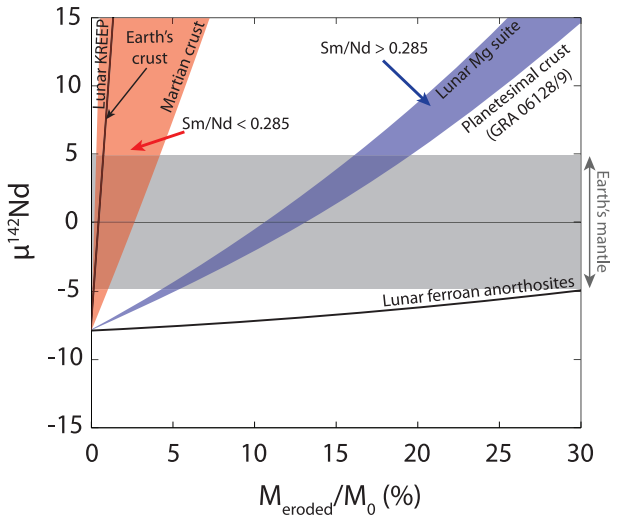


Fig. 3. Mass proportion of crust eroded by collisions to produce Earth's μ^{142}Nd. The composition of a hypothetical crust is calculated by mass balance by using a starting composition at −7.9 ppm (NC chondrites) and various types of crustal materials. The red area corresponds to compositions with a low Sm/Nd ratio (<0.285) and high Nd content represented by lunar KREEP (*34*), Earth's continental crust (*35*), and the martian crust from the basaltic breccia NWA 7034 (*36*). The blue area corresponds to more mafic compositions with a higher Sm/Nd ratio (>0.285) and lower Nd content, which is represented by the lunar Mg suite (*37*) and the alkali- and silica-rich crust of a planetesimal with GRA 06128/9 (*38*). Lunar ferroan anorthosites (*42*) are also represented as a black line. M_{eroded}/M_0, the mass proportion of crust eroded from the total accreted mass.

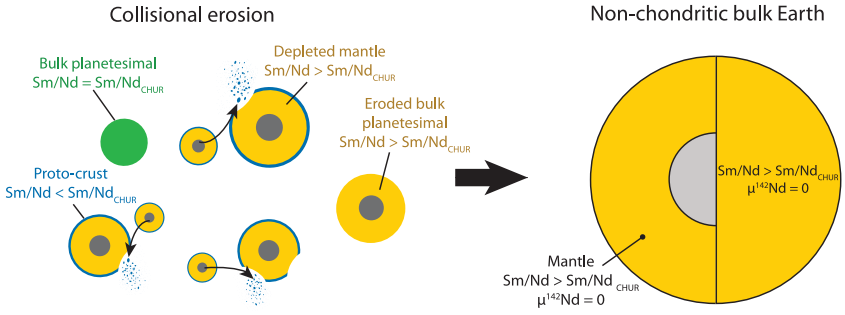


Fig. 4. Sketch of the collisional erosion scenario on planetesimals and Earth. Collisions between differentiated planetesimals strip off protocrusts, which leaves bodies with a mantle that is enriched in Sm over Nd compared with undifferentiated chondrites [Sm/Nd_{CHUR} = 0.311, where CHUR stands for chondritic uniform reservoir; (*33*)]. Earth accreted from collisionally eroded planetesimals is depleted in incompatible elements and displays a superchondritic Sm/Nd ratio.

evidence suggests that Earth accreted substantial parts of unknown material with *s*-process excesses compared with both known meteorites and differentiated planetesimals [e.g., (*6*, *24*, *25*, *41*)]. Although our data are inconclusive in this regard, excesses in ^{142}Nd in both Earth and achondrites support the accretion of differentiated planetesimals as Earth's building blocks. Resolving this puzzle may require integrating differentiated planetesimals in accretion models of planets and the impact of preferential incorporation of core and mantle versus crustal materials. Considering this history of collisional erosion may help refining estimates of the bulk composition of planets and their evolution.

REFERENCES AND NOTES

1. M. Boyet, R. W. Carlson, *Science* **309**, 576–581 (2005).
2. G. Caro, B. Bourdon, A. N. Halliday, G. Quitté, *Nature* **452**, 336–339 (2008).
3. H. S. C. O'Neill, H. Palme, *Philos. Trans.- Royal Soc., Math. Phys. Eng. Sci.* **366**, 4205–4238 (2008).
4. R. Andreasen, M. Sharma, *Science* **314**, 806–809 (2006).
5. A. Bouvier, M. Boyet, *Nature* **537**, 399–402 (2016).
6. C. Burkhardt *et al.*, *Nature* **537**, 394–398 (2016).
7. A. Gannoun, M. Boyet, H. Rizo, A. El Goresy, *Proc. Natl. Acad. Sci. U.S.A.* **108**, 7693–7697 (2011).
8. L. Qin, R. W. Carlson, C. M. D. Alexander, *Geochim. Cosmochim. Acta* **75**, 7806–7828 (2011).
9. N. S. Saji, D. Wielandt, J. C. Holst, M. Bizzarro, *Geochim. Cosmochim. Acta* **281**, 135–148 (2020).
10. C. Arlandini *et al.*, *Astrophys. J.* **525**, 886–900 (1999).
11. S. Bisterzo, C. Travaglio, R. Gallino, M. Wiescher, F. Käppeler, *Astrophys. J.* **787**, 10 (2014).
12. M. Boyet *et al.*, *Earth Planet. Sci. Lett.* **488**, 68–78 (2018).
13. M. Boyet, A. Gannoun, *Geochim. Cosmochim. Acta* **121**, 652–666 (2013).
14. M. Garçon *et al.*, *Chem. Geol.* **476**, 493–514 (2018).
15. E. Zinner, S. Amari, R. S. Lewis, *Astrophys. J.* **382**, L47–L50 (1991).
16. Materials and methods are available as supplementary materials.
17. G. A. Brennecka, L. E. Borg, M. Wadhwa, *Proc. Natl. Acad. Sci. U.S.A.* **110**, 17241–17246 (2013).
18. Q. R. Shollenberger *et al.*, *Geochim. Cosmochim. Acta* **228**, 62–80 (2018).
19. M. T. McCulloch, G. J. Wasserburg, *Astrophys. J.* **220**, L15–L19 (1978).
20. N. S. Saji, M. Schiller, J. C. Holst, M. Bizzarro, *Astrophys. J. Lett.* **919**, L8 (2021).
21. P. Vermeesch, R. Isoplot, *Geoscience Frontiers* **9**, 1479–1493 (2018).
22. R. Fukai, T. Yokoyama, *Earth Planet. Sci. Lett.* **474**, 206–214 (2017).
23. R. Fukai, T. Yokoyama, *Astrophys. J.* **879**, 79 (2019).
24. J. Render, G. A. Brennecka, *Earth Planet. Sci. Lett.* **555**, 116705 (2021).
25. P. Frossard, Z. Guo, M. Spencer, M. Boyet, A. Bouvier, *Earth Planet. Sci. Lett.* **566**, 116968 (2021).
26. N. Sugiura, W. Fujiya, *Meteorit. Planet. Sci.* **49**, 772–787 (2014).
27. L. T. Elkins-Tanton, *Annu. Rev. Earth Planet. Sci.* **40**, 113–139 (2012).
28. A. Bouvier, J. Blichert-Toft, M. Boyet, F. Albarède, *Meteorit. Planet. Sci.* **50**, 1896–1911 (2015).
29. P. H. Warren, *Geochim. Cosmochim. Acta* **72**, 2217–2235 (2008).
30. G. W. Wetherill, *Annu. Rev. Earth Planet. Sci.* **18**, 205–256 (1990).
31. S. T. Stewart, Z. M. Leinhardt, *Astrophys. J.* **751**, 32 (2012).
32. J. N. Connelly *et al.*, *Science* **338**, 651–655 (2012).
33. A. Bouvier, J. D. Vervoort, P. J. Patchett, *Earth Planet. Sci. Lett.* **273**, 48–57 (2008).
34. G. W. Lugmair, R. W. Carlson, in *Lunar and Planetary Science Conference Proceedings*, vol. 9 (Lunar and Planetary Institute, 1978), pp. 689–704.
35. R. L. Rudnick, S. Gao, in *Treatise on Geochemistry*, vol. 3, H. D. Holland, K. K. Turekian, Eds. (Elsevier, 2003), pp. 1–64.
36. R. M. Armytage, V. Debaille, A. D. Brandon, C. B. Agee, *Earth Planet. Sci. Lett.* **502**, 274–283 (2018).
37. R. W. Carlson, L. E. Borg, A. M. Gaffney, M. Boyet, *Philos. Trans. R. Soc. London Ser. A* **372**, 20130246 (2014).
38. J. M. Day *et al.*, *Geochim. Cosmochim. Acta* **81**, 94–128 (2012).
39. L. Allibert, S. Charnoz, J. Siebert, S. A. Jacobson, S. N. Raymond, *Icarus* **363**, 114412 (2021).
40. J. Sclater, C. Jaupart, D. Galson, *Rev. Geophys.* **18**, 269–311 (1980).
41. M. Fischer-Gödde *et al.*, *Nature* **579**, 240–244 (2020).

ACKNOWLEDGMENTS

We are grateful to R. Carlson and two other anonymous reviewers for insightful reviews that helped improve the manuscript. We thank D. Auclair for her help and assistance with the thermal ionization mass spectrometer and the use of the 10^{13} Ω amplifiers, J.-L. Piro for his assistance with the quadrupole inductively coupled plasma mass spectrometer, and C. Bosq for her management of the clean lab facilities. We thank P. Bonnand for his help with analytical development and for discussions and A. Withers for his help in improving the English of the manuscript. P.F. acknowledges discussions with M. Garçon, P. Faure, A. Hunt, M. Ek, and B. Peters and particularly thanks M. Schönbächler for allowing him to finalize this study while at ETH Zürich. We thank institutions and people for providing us meteorite samples used in this study: M. Gounelle and E. Jacquet of the Muséum National d'Histoire Naturelle, the National Museum of Natural History of the Smithsonian Institution, M. Isakar of the Tartu Ülikool Loodsmuuseum, the University of Western Ontario, and the Antarctic Meteorite Collection. US Antarctic meteorite samples were recovered by the Antarctic Search for Meteorites (ANSMET) program, which has been funded by NSF and NASA, and characterized and curated by the Department of Mineral Sciences of the Smithsonian Institution and Astromaterials Curation Office at the NASA Johnson Space Center. **Funding:** This project has received funding from the European Research Council (ERC) under the European Union's Horizon 2020 research and innovation program (grant agreement no. 6822778 to M.B.), the Canada Foundation for Innovation (33353 to A.B.), a Natural Sciences and Engineering Research Council of Canada (NSERC) Discovery Grant (06310-2014 to A.B.), and the Canada Research Chairs programs (950-229061 to A.B.). This is Laboratory of Excellence ClerVolc contribution n°562. **Author contributions:** Conceptualization: P.F., M.B., A.B.; Formal analysis: P.F., C.I., M.B.; Investigation: P.F., M.B., A.B.; Writing–original draft: P.F., M.B., A.B., C.I. **Competing interests:** The authors declare that they have no competing interests. **Data and materials availability:** All data are available in the main text or the supplementary materials. **License information:** Copyright © 2022 the authors, some rights reserved; exclusive licensee American Association for the Advancement of Science. No claim to original US government works. https://www.science.org/about/science-licenses-journal-article-reuse

SUPPLEMENTARY MATERIALS

science.org/doi/10.1126/science.abq7351
Materials and Methods
Supplementary Text
Figs. S1 to S9
Tables S1 to S7
References (*42*–*64*)

Submitted 27 April 2022; accepted 6 August 2022
10.1126/science.abq7351

CYTOSKELETON

Actin maturation requires the ACTMAP/C19orf54 protease

Peter Haahr[1,2], Ricardo A. Galli[3], Lisa G. van den Hengel[1,4], Onno B. Bleijerveld[5], Justina Kazokaitė-Adomaitienė[6], Ji-Ying Song[7], Lona J. Kroese[8], Paul Krimpenfort[8], Marijke P. Baltissen[9], Michiel Vermeulen[9], Coen A. C. Ottenheijm[3], Thijn R. Brummelkamp[1,4]*

Protein synthesis generally starts with a methionine that is removed during translation. However, cytoplasmic actin defies this rule because its synthesis involves noncanonical excision of the acetylated methionine by an unidentified enzyme after translation. Here, we identified C19orf54, named ACTMAP (actin maturation protease), as this enzyme. Its ablation resulted in viable mice in which the cytoskeleton was composed of immature actin molecules across all tissues. However, in skeletal muscle, the lengths of sarcomeric actin filaments were shorter, muscle function was decreased, and centralized nuclei, a common hallmark of myopathies, progressively accumulated. Thus, ACTMAP encodes the missing factor required for the synthesis of mature actin and regulates specific actin-dependent traits in vivo.

The actin cytoskeleton organizes cellular architecture, force generation, and cell migration (*1*). Humans express six highly abundant actin isoforms: two cytoplasmic actins and four muscle actins. The biosynthesis of all actin molecules requires N-terminal processing referred to as actin maturation (*2*–*6*). For cytoplasmic β- and γ-actin molecules, the initiating acetyl methionine is removed after translation by an unknown enzyme (Fig. 1A). For muscle actin, the initiator methionine is canonically removed, and the exposed cysteine is acetylated and then trimmed by an unknown enzyme (fig. S1) (*5*, *6*). The trimmed N terminus is then reacetylated by NAA80, generating mature actin (*7*–*9*). However, 40 years after the observation of N-terminal actin processing (*3*), we still lack a clear understanding of this pathway.

To study actin maturation, we generated an antibody that recognizes the immature N terminus of β-actin (Fig. 1B). In the absence of a specific antibody for mature β-actin, an antibody for mature γ-actin was used (Fig. 1B). Having previously applied haploid genetics to study posttranslational modifications (*10*–*12*), we performed two complementary haploid screens to find regulators of actin maturation. Mutagenized cells were stained with actin antibodies, and cell populations with relatively high or low antibody staining were isolated (Fig. 1C) (*10*). We looked for genes that were enriched for disruptive gene-trap mutations in the cell population with high immature actin staining (negative regulators; data S1) and genes that were enriched for mutations in the cells displaying low levels of mature actin (positive regulators; data S2). *C19orf54* fulfilled these parameters and scored as the top hit (Fig. 1, D to F, and fig. S2A). In contrast to other hits, *C19orf54* has never been identified in screens unrelated to actin processing, suggesting specificity for this process (fig. S2B) (*10*–*12*). We renamed this factor ACTMAP (actin maturation protease) for reasons described below.

Ablation of *ACTMAP* resulted in undetectable actin maturation and accumulation of immature actin (Fig. 1, G to I). Moreover, we observed no effect on the total levels of actin using a pan-actin antibody raised against the C-terminal region of actin (Fig. 1, H and I). Additionally, no overt changes were detected in cytoskeletal organization (fig. S3), G-actin/F-actin ratios (fig. S4, A and B), F-actin staining intensities (figs. S4C and S5, A to E), filopodia formation (fig. S6, A to F), cell size (figs. S5, C to E, and S7, A and B), or cell motility (figs. S8, A and B, and S9, A to F). As an independent approach to antibody detection, we used bottom-up proteomics to study the actin N terminus. We found that N-terminal actin peptides in HAP1 cells were almost exclusively detected in the mature state (Fig. 1, J and K, and fig. S10), as has been reported previously (*13*, *14*). Conversely, loss of *ACTMAP* resulted in actin molecules exclusively detected in their immature acetylated and methionated state (Fig. 1, J and K, and fig. S10). As expected, *NAA80*-knockout cells exclusively contained the nonacetylated form of mature actin (Fig. 1, J and K, and fig. S10). Thus, ACTMAP is critical for actin maturation and stimulates the excision step of acetylated methionine from cytoplasmic actin.

Because ACTMAP was an uncharacterized protein, we analyzed the structure predicted in the AlphaFold Protein Structure Database (*15*). Its C-terminal domain (UPF0692, domain of unknown protein function) and proline-rich N-terminal region were predicted to have a globular fold and to be disordered, respectively (Fig. 2, A and B, and fig. S11A). Furthermore, protein structure comparisons (*16*) against experimentally determined structures in the Protein Data Bank (PDB) found that the UPF0692 domain was similar in structure to bacterial cysteine proteases such as the putative C39-like peptidase (PDB identifier: 3ERV; Dali z score: 15.5; root mean square deviation: 2.3Å) despite only sharing 12% sequence identity (fig. S11, B and C). A conserved cysteine (Cys^{132}) and histidine (His^{234}) in ACTMAP were positioned in a potential catalytic dyad, as observed in cysteine peptidases (Fig. 2, A and B, and fig. S11B). To determine whether ACTMAP is indeed a cysteine protease, we complemented *ACTMAP*-knockout cells with wild-type (WT) and mutant *ACTMAP* transgenes. WT ACTMAP fully restored actin processing, whereas a point mutation affecting the cysteine in the predicted catalytic site (C132A) prevented this (Fig. 2C and fig. S12, A and B). Thus, ACTMAP cysteine protease activity is essential for actin maturation.

Next, we generated recombinant, full-length ACTMAP WT and C132A protein to test the enzymatic activity in vitro (Fig. 2D and fig. S13, A and B). Recombinant ACTMAP efficiently catalyzed N-terminal cleavage of immature actin in cellular extracts (Fig. 2E and fig. S14A). Purified green fluorescent protein–tagged β-actin was also processed by recombinant ACTMAP, albeit less efficiently (fig. S14, B and C). This activity required the catalytic site of ACTMAP, because C132A ACTMAP was inactive (Fig. 2E and fig. S14, A and C). The structural model of ACTMAP showed that Cys^{132} was accessible through a pocket lined with conserved, positively charged residues that, in contrast to METAP1/2 (*17*), could accommodate negatively charged N termini such as actin (fig. S15A). Moreover, a Colabfold model (*18*) of the plausible ACTMAP:β-actin complex placed the methionated β-actin N terminus within the positively charged catalytic pocket of ACTMAP (fig. S15B). On the basis of this prediction, we could validate binding between actin and ACTMAP in vitro (fig. S15C).

To address the specificity of ACTMAP cleavage activity for actin, we analyzed our whole-cell proteomics dataset of WT and *ACTMAP*-knockout cells. *ACTMAP* loss selectively affected

[1]Division of Biochemistry, Netherlands Cancer Institute, 1066CX Amsterdam, Netherlands. [2]Novo Nordisk Foundation Center for Protein Research (NNF-CPR), Faculty of Health and Medical Sciences, University of Copenhagen, 2200 Copenhagen, Denmark. [3]Department of Physiology, Amsterdam UMC (VUmc), 1081HV Amsterdam, Netherlands. [4]Oncode Institute, Division of Biochemistry, Netherlands Cancer Institute, 1066CX Amsterdam, Netherlands. [5]Proteomics Facility, Netherlands Cancer Institute, 1066CX Amsterdam, Netherlands. [6]Protein Facility, Division of Biochemistry, Netherlands Cancer Institute, 1066CX Amsterdam, Netherlands. [7]Animal Pathology, Netherlands Cancer Institute, 1066CX Amsterdam, Netherlands. [8]Animal Modeling Facility, Netherlands Cancer Institute, 1066CX Amsterdam, Netherlands. [9]Department of Molecular Biology, Faculty of Science, Radboud Institute for Molecular Life Sciences, Oncode Institute, Radboud University Nijmegen, 6525GA Nijmegen, Netherlands.
*Corresponding author. Email: t.brummelkamp@nki.nl

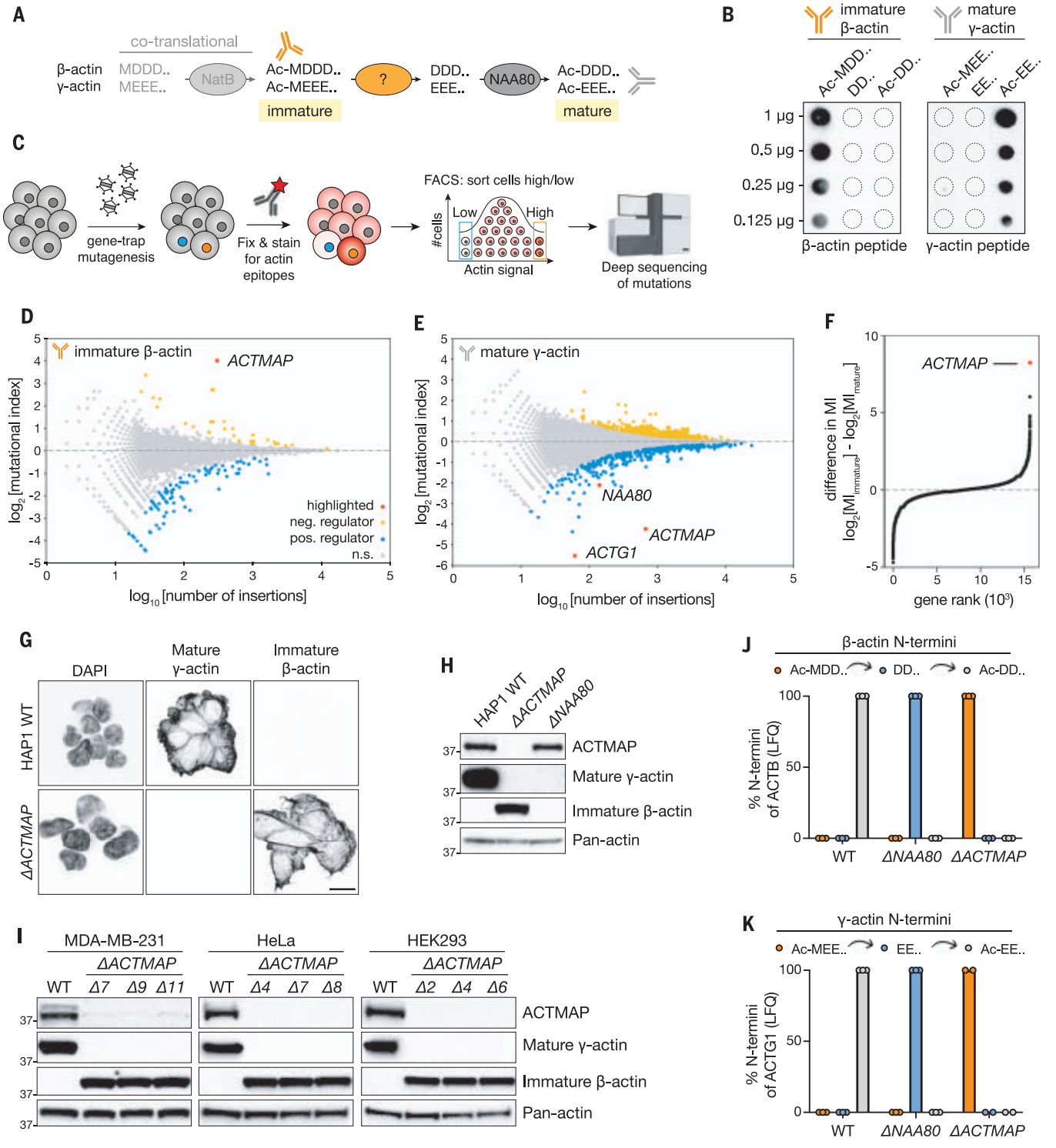


Fig. 1. A haploid genetic screen identifies ACTMAP as a regulator of actin maturation. (**A**) Schematic of N-terminal actin processing. (**B**) β- and γ-actin N-terminal peptides were subjected to dot blot analysis using actin antibodies. (**C**) Workflow of haploid genetic screens. (**D** and **E**) Screens for immature β-actin (D) and mature γ-actin (E) presented as fishtail plots in which genes are plotted according to their mutational index (*y* axis) and the total number of gene-trap insertions in the gene (*x* axis). Positive and negative regulators are labeled blue and yellow, respectively [two-sided Fisher's exact test, false discovery rate (FDR) corrected $P \leq 0.05$; nonsignificant genes are shown in gray]. (**F**) Gene-rank plot of a combined mutational index (MI) score from (D) and (E). Combined MI was calculated as $MI_{immature} - MI_{mature}$. (**G**) Confocal laser scanning images of HAP1 and *ACTMAP*-knockout cells stained with actin antibodies and DAPI. Scale bar, 10 µm. (**H**) HAP1, *ACTMAP*-knockout, and *NAA80*-knockout (Δ) cells were subjected to immunoblot analysis to monitor actin processing. (**I**) Parental cell lines and three independent *ACTMAP*-knockout clones were analyzed as in (H). (**J** and **K**) The abundance of indicated N-terminal peptides of β-actin (J) and γ-actin (K) in HAP1 cells and independent knockouts of *NAA80* and *ACTMAP* were determined by quantitative label-free mass spectrometry (LFQ) and plotted as a percentage of the total abundance of the three quantified N-terminal actin peptides.

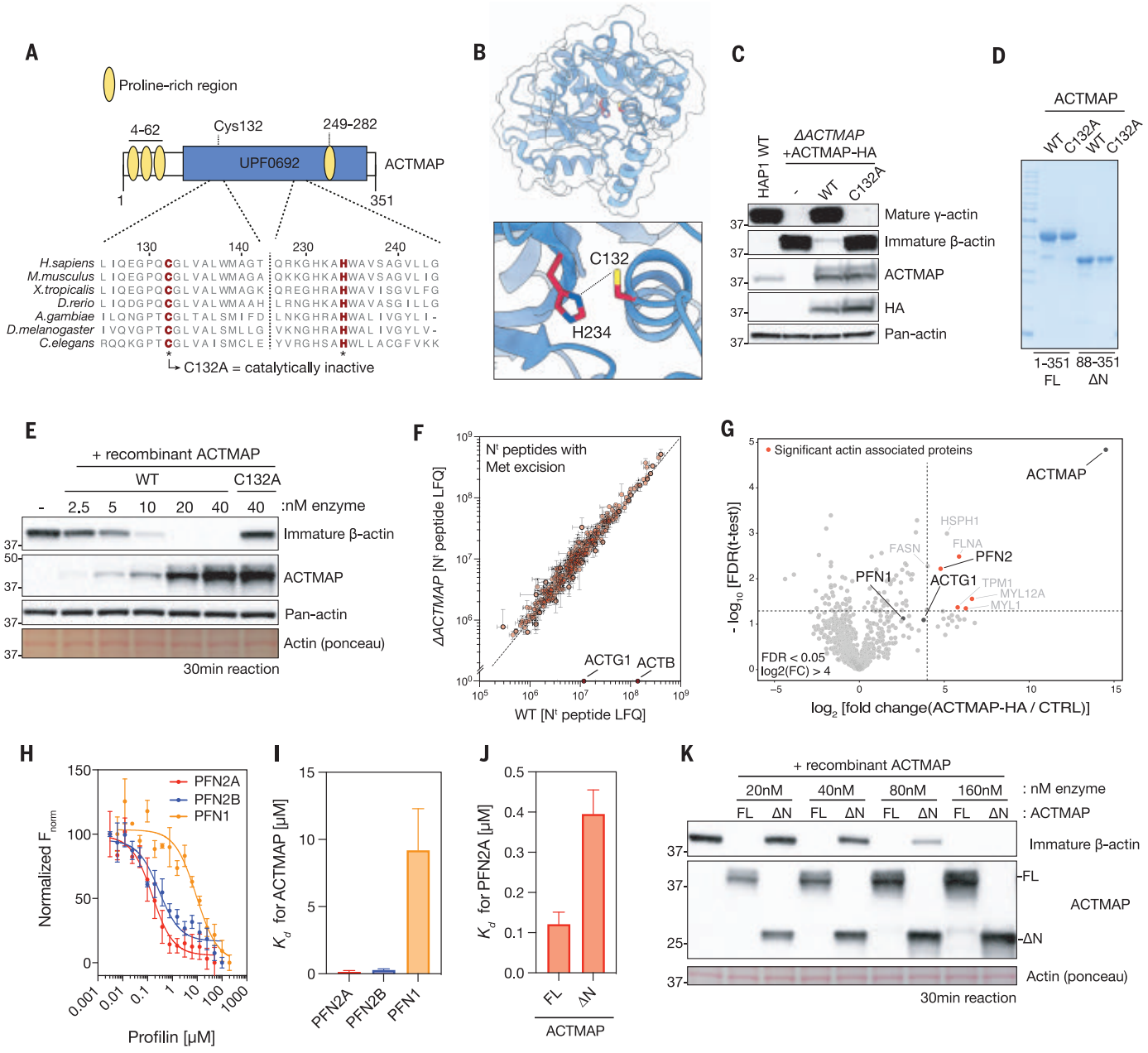


Fig. 2. ACTMAP cysteine protease activity specifically cleaves actin N termini. (**A**) Predicted catalytic residues Cys^{132} and His^{234} (red) in human ACTMAP. (**B**) Alphafold model (ACTMAP residues 71 to 351) with predicted catalytic dyad (bottom) in red. (**C**) Actin processing in *ACTMAP*-knockout cells expressing hemagglutinin (HA)–tagged WT or C132A ACTMAP. (**D**) Coomassie gel of recombinant ACTMAP. (**E**) Actin processing in *ACTMAP*-knockout lysates incubated with recombinant WT or C132A ACTMAP for 30 min. (**F**) Abundance of robustly detected N termini without initiator methionine in WT cells (317 proteins, *x* axis) and *ACTMAP*-knockout cells (*y* axis) quantified by label-free mass spectrometry (LFQ) (data are shown as mean ± SD; *n* = 3 clones). (**G**) HAP1 (CTRL) and *ACTMAP* knockouts expressing HA-tagged ACTMAP subjected to HA pulldown and analyzed by mass spectrometry. Plot shows mean log_2-fold change (FC) from triplicates plotted against the $-log_{10}$(FDR) permutation-based *t* test. Dashed lines represent FDR *t* test $P < 0.05$ and $log_2(FC) > 4$. Significantly enriched proteins are labeled in addition to ACTG1 and PFN1. (**H**) Affinity of PFNs (*x* axis) for fluorescent ACTMAP. F_{norm} (*y* axis) denotes change in fluorescence measured by microscale thermophoresis. (**I**) Mean dissociation constant (K_d) from (H). PFN2A, K_d = 0.12 ± 0.03 μM; PFN2B, K_d = 0.28 ± 0.09 μM; PFN1, K_d = 9.2 ± 3.10 μM. (**J**) Mean K_d values as in (I) to (H) comparing PFN2A binding with ACTMAP FL (K_d = 0.12 ± 0.03 μM) and ΔN (K_d = 0.39 ± 0.06 μM). (**K**) As in (E) comparing ACTMAP FL with residues 88 to 351 (ΔN).

actin across all robustly detected protein N termini with methionine removal (Fig. 2F and data S3). This specificity for actin was not solely determined by the N-terminal sequence, because other proteins with N-terminal sequences similar to that of actin (M-[DE]-[DE]-[DE]) retained their initiator methionine in cells (fig. S15D) and thus are not ACTMAP substrates.

The interactome of ACTMAP was enriched for actin and actin-associated proteins, supporting the idea that ACTMAP specifically targets actin (Fig. 2G and data S4). The monomeric actin-binding protein profilin-2 (PFN2) was about fivefold enriched compared with its paralog PFN1, which is ~10-fold more

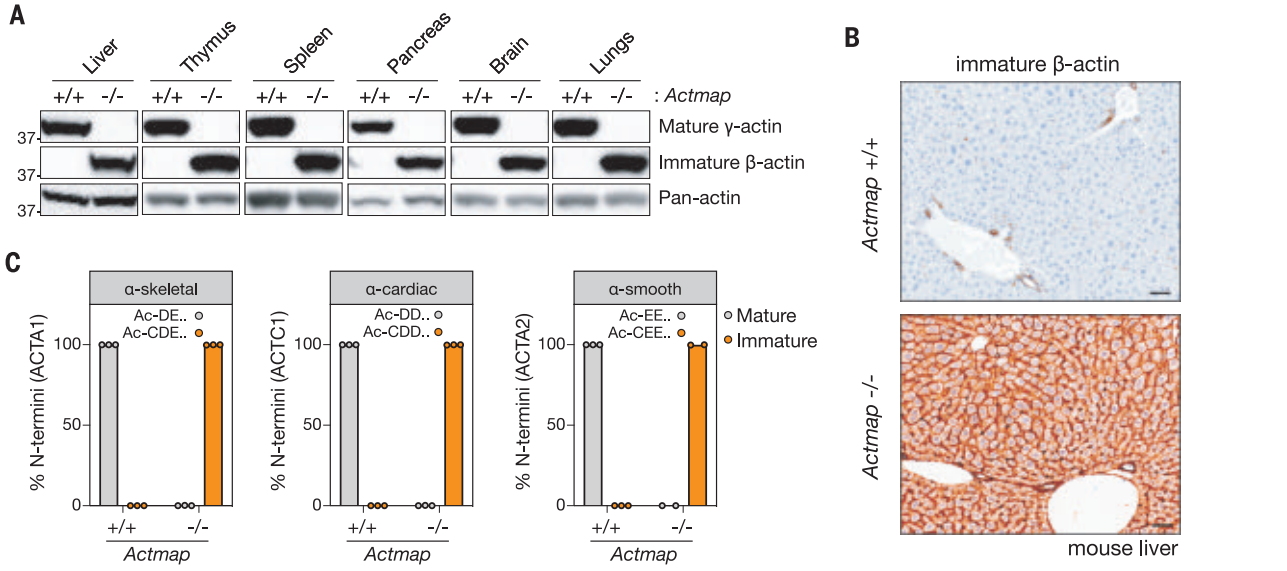


Fig. 3. ACTMAP is required for cytoplasmic and muscle actin maturation in mice. (**A**) Indicated tissues and organs collected from WT (+/+) or *Actmap*-deficient (−/−) mice were subjected to immunoblot analysis to monitor actin processing. (**B**) Immunohistochemistry of immature β-actin staining in liver sections of the indicated genotypes. Scale bar, 50 μm. (**C**) Abundance of mature and immature muscle actin N termini (percentage of total) from mouse muscle tissue analyzed by LFQ. Data are shown as means ± SEM (*n* = 3 mice).

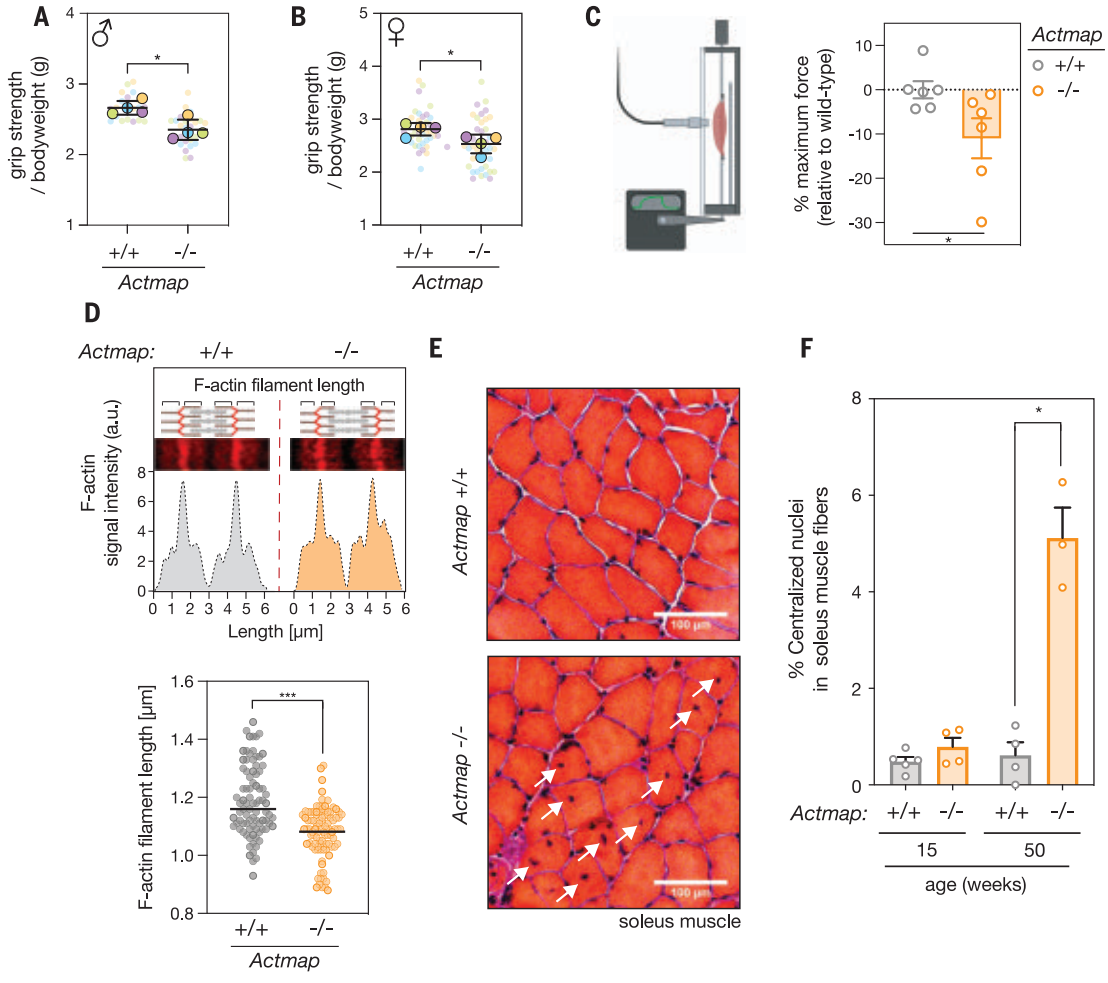


Fig. 4. ACTMAP is required for muscle strength. (**A** and **B**) Grip strength of male (A) and female (B) mice normalized to their bodyweight. *n* = 4 independent experiments (color coded) with ≥6 mice per condition. Data are shown as means ± SEM. **P* ≤ 0.05, unpaired *t* test. (**C**) Schematic diagram of ex vivo muscle force measurement (left) and quantification (right) presented as percentage force loss. Data are shown as means ± SEM (*n* = 6 mice). **P* ≤ 0.05, unpaired *t* test. (**D**) Isolated stretched soleus muscles were cryopreserved, longitudinal sections were stained with phalloidin, and the length of sarcomeric F-actin filaments was analyzed by stimulated emission depletion microscopy. Shown are examples of phalloidin staining (top) and quantification of F-actin filament length (bottom). Black bar indicates mean (*n* > 85 sarcomeres and *n* = 3 or 4 mice per condition; ****P* ≤ 0.001, Welch's unpaired *t* test). (**E**) Hematoxylin and eosin stain of soleus muscle in 50-week-old mice. White arrows point to centralized nuclei. Scale bar, 100 μm. (**F**) Quantification of centralized nuclei in 15- and 50-week-old mice. Data are shown as means ± SEM (*n* = 3 to 5 mice). **P* ≤ 0.05, two-way ANOVA.

abundant in HAP1 cells (*19*). NAA80 also preferentially associates with PFN2 over PFN1. This interaction stimulates N-terminal acetylation of actin by NAA80 in vitro, although loss of PFN2 did not affect steady-state actin maturation in HAP1 cells (fig. S16A) (*7*, *19*).

To study ACTMAP-PFN interactions, we purified recombinant PFN2A, PFN2B, and PFN1 (fig. S16, B and C). Binding affinities measured in solution by microscale thermophoresis revealed that ACTMAP bound all PFNs but preferred PFN2 isoforms, with a 50- to 100-fold lower dissociation constant (K_d) compared with PFN1 (Fig. 2, H and I). The disordered N-terminal part of ACTMAP contains polyproline regions (Fig. 2A), which is a common PFN-binding motif (*20*). Deletion of the proline-rich ACTMAP N-terminal region (ΔN, amino acid residues 88 to 351) decreased binding to PFN2A and PFN2B by ~70% (Fig. 2J and fig. S16D). Recombinant ACTMAP ΔN protein also processed immature actin about sixfold less efficiently than full-length ACTMAP in protein extracts of *ACTMAP*-knockout cells (Fig. 2K). Consistently, inducible reconstitution of exogenous ACTMAP in *ACTMAP*-deficient cells confirmed that ΔN was less efficient in processing immature actin compared with full-length ACTMAP (fig. S16, E and F). Thus, the proline-rich ACTMAP N terminus enhances PFN2 binding and facilitates efficient actin processing.

To address the physiological role of ACTMAP, we disrupted *Actmap* (*Mus musculus* gene *BC024978*) in mice (fig. S17A). Homozygous *Actmap*-knockout mice were viable and born at the expected Mendelian ratio (fig. S17B; P = 0.97, chi-square test; n = 200 mice) and displayed no obvious genotype-specific morbidity during their first year of life despite the absence of cytoplasmic actin processing across all inspected tissues (Fig. 3, A and B, and fig. S17C). Processing of muscle actin involves a different route that requires excision of an N-terminal acetylated cysteine, likewise by an unknown enzyme (fig. S1). To determine whether ACTMAP is also required for muscle actin maturation, we performed quantitative mass spectrometry on mouse muscle tissue. We found that the N termini of α-skeletal (ACTA1), α-cardiac (ACTC1), and α-smooth (ACTA2) actin completely retained their (immature) acetyl cysteine in an *Actmap*-deficient background (Fig. 3C). Thus, in vivo, ACTMAP is the sole enzyme responsible for removing the acetylated methionine and cysteine of cytoplasmic and muscle actin, respectively, and mice are viable despite a cytoskeleton composed of immature actin molecules.

We found that loss of *Actmap* was associated with decreased muscle strength by ~12% and ~11% in male and female mice, respectively, as measured by grip strength (Fig. 4, A and B). To directly investigate single-muscle mechanics, we measured the ex vivo contractile parameters of isolated intact soleus muscles (*21*). Soleus muscles from *Actmap*-knockout mice generated ~11% lower absolute maximal force compared with those of WT littermates (Fig. 4C). Actin, the main protein in sarcomeric thin filaments in muscle, is important for generating force and movement by interacting with myosin in the thick filaments. To determine whether *Actmap* loss affects thin filaments, we measured thin filament length in longitudinal sections of soleus muscle (*22*). Thin filaments in *Actmap*-knockout mice were on average ~8.4% shorter compared with WT (Fig. 4D). We next examined muscle morphology and observed an age-dependent, eightfold increase in centrally located nuclei within muscle fibers of 50-week-old *Actmap*-knockout mice compared with WT mice (Fig. 4, E and F). Centrally located nuclei in muscle fibers are a hallmark of ongoing muscle repair after injury and are often observed in progressive muscle pathologies (*23*). Thus, *Actmap* loss affects muscle strength, thin filament length, and the accumulation of centrally located nuclei. However, the current studies do not establish a causal relationship between these observations, and we cannot rule out a contribution of ACTMAP-binding proteins (such as PFNs) to these phenotypes.

This study identifies ACTMAP as the missing enzyme for cytoplasmic and muscle actin biosynthesis, demonstrating that it functions as a cysteine protease that specifically cleaves the actin N terminus but not the termini of other analyzed proteins. Unexpectedly, *Actmap*-knockout mice are viable despite the lack of actin N-terminal processing, although this comes at the cost of decreased muscle strength. It will be of interest to study whether the *Drosophila* homolog of *ACTMAP* is involved in the phenotype of a previously described *flightless* mutant displaying defective actin processing (*24*, *25*). Considering that *ACTMAP* is conserved across all species known to modify actin N termini (fig. S18), this factor most likely is the universal enzyme for the generation of mature actin.

REFERENCES AND NOTES

1. T. D. Pollard, J. A. Cooper, *Science* **326**, 1208–1212 (2009).
2. S. Varland, J. Vandekerckhove, A. Drazic, *Trends Biochem. Sci.* **44**, 502–516 (2019).
3. K. Redman, P. A. Rubenstein, *J. Biol. Chem.* **256**, 13226–13229 (1981).
4. P. A. Rubenstein, D. J. Martin, *J. Biol. Chem.* **258**, 3961–3966 (1983).
5. P. A. Rubenstein, D. J. Martin, *J. Biol. Chem.* **258**, 11354–11360 (1983).
6. L. R. Solomon, P. A. Rubenstein, *J. Biol. Chem.* **260**, 7659–7664 (1985).
7. G. Rebowski *et al.*, *Sci. Adv.* **6**, eaay8793 (2020).
8. A. Drazic *et al.*, *Proc. Natl. Acad. Sci. U.S.A.* **115**, 4399–4404 (2018).
9. M. Goris *et al.*, *Proc. Natl. Acad. Sci. U.S.A.* **115**, 4405–4410 (2018).
10. M. Brockmann *et al.*, *Nature* **546**, 307–311 (2017).
11. M. E. W. Logtenberg *et al.*, *Nat. Med.* **25**, 612–619 (2019).
12. J. Nieuwenhuis *et al.*, *Science* **358**, 1453–1456 (2017).
13. E. Wiame *et al.*, *FEBS J.* **285**, 3299–3316 (2018).
14. A. Drazic *et al.*, *J. Mol. Biol.* **434**, 167397 (2022).
15. M. Varadi *et al.*, *Nucleic Acids Res.* **50**, D439–D444 (2022).
16. L. Holm, *Methods Mol. Biol.* **2112**, 29–42 (2020).
17. Q. Xiao, F. Zhang, B. A. Nacev, J. O. Liu, D. Pei, *Biochemistry* **49**, 5588–5599 (2010).
18. M. Mirdita *et al.*, *Nat. Methods* **19**, 679–682 (2022).
19. R. Ree *et al.*, *J. Biol. Chem.* **295**, 16713–16731 (2020).
20. W. J. Metzler, A. J. Bell, E. Ernst, T. B. Lavoie, L. Mueller, *J. Biol. Chem.* **269**, 4620–4625 (1994).
21. J. M. de Winter *et al.*, *J. Clin. Invest.* **130**, 754–767 (2020).
22. J. M. Winter *et al.*, *Ann. Neurol.* **79**, 959–969 (2016).
23. H. Jungbluth *et al.*, *Nat. Rev. Neurol.* **14**, 151–167 (2018).
24. J. W. Mahaffey, M. D. Coutu, E. A. Fyrberg, W. Inwood, *Cell* **40**, 101–110 (1985).
25. S. Schmitz *et al.*, *J. Mol. Biol.* **295**, 1201–1210 (2000).

ACKNOWLEDGMENTS

We thank T. Sixma, A. Perrakis, A. Sonnenberg, K. Jalink J. Roix, G. L. McLelland, P. Bieling, and members of the Brummelkamp group for helpful discussions and critical reading of the manuscript; the Bioimaging, Flow Cytometry, Genomics Core, Animal & Animal pathology, Proteomics and Protein Facilities at NKI, especially P. Celie and A. Fish, for advice on protein biochemistry; and M. Mertz for assistance with live-cell imaging. O.B.B. acknowledges support from the X-omics Initiative, part of the NWO National Roadmap for Large-Scale Research Infrastructures. **Funding:** This work was supported by Nederlandse Organisatie voor Wetenschappelijk Onderzoek Vici grant 016.Vici.170.033 (T.R.B.), the Oncode Institute (T.R.B., M.V.), and the Novo Nordisk Foundation (P.H.). **Author contributions:** Conceptualization: P.H., T.R.B.; Funding acquisition: P.H., M.V., T.R.B.; Investigation: P.H., R.A.G., L.G.H., O.B.B., J.K., J.Y.S., L.K., M.P.B.; Methodology: P.H., R.A.G., L.G.H., O.B.B., J.K., J.Y.S., P.K., M.P.B., M.V., C.A.C.O., T.R.B.; Project administration: P.H., O.B.B., T.R.B.; Visualization: P.H., R.A.G. **Competing interests:** T.R.B. is a co-founder and scientific adviser at Scenic Biotech. The remaining authors declare no competing interests. **Data and materials availability:** Cell lines, the immature β-actin antibody, and *Actmap*-knockout mice are available from T.R.B. under a material transfer agreement with the Netherlands Cancer Institute. Screen data will be made available in the NCBI Sequence Read Archive (www.ncbi.nlm.nih.gov/sra/PRJNA858247) and on an interactive visualization platform (https://phenosaurus.nki.nl).

License information: Copyright © 2022 the authors, some rights reserved; exclusive licensee American Association for the Advancement of Science. No claim to original US government works. www.science.org/about/science-licenses-journal-article-reuse

SUPPLEMENTARY MATERIALS

science.org/doi/10.1126/science.abq5082
Materials and Methods
Figs. S1 to S18
Data S1 to S4
References (*26*–*33*)
MDAR Reproducibility Checklist

Submitted 12 April 2022; accepted 22 August 2022
10.1126/science.abq5082

SUPERCONDUCTIVITY

Promotion of superconductivity in magic-angle graphene multilayers

Yiran Zhang[1,2,3]†, Robert Polski[1,2]†, Cyprian Lewandowski[2,3], Alex Thomson[2,3,4], Yang Peng[5], Youngjoon Choi[1,2,3], Hyunjin Kim[1,2,3], Kenji Watanabe[6], Takashi Taniguchi[6], Jason Alicea[2,3], Felix von Oppen[7], Gil Refael[2,3], Stevan Nadj-Perge[1,2]*

Graphene moiré superlattices show an abundance of correlated insulating, topological, and superconducting phases. Whereas the origins of strong correlations and nontrivial topology can be directly linked to flat bands, the nature of superconductivity remains enigmatic. We demonstrate that magic-angle devices made of twisted tri-, quadri-, and pentalayer graphene placed on monolayer tungsten diselenide exhibit flavor polarization and superconductivity. We also observe insulating states in the tril- and quadrilayer arising at finite electric displacement fields. As the number of layers increases, superconductivity emerges over an enhanced filling-factor range, and in the pentalayer it extends well beyond the filling of four electrons per moiré unit cell. Our results highlight the role of the interplay between flat and more dispersive bands in extending superconducting regions in graphene moiré superlattices.

Rich phase diagrams of quantum electronic phases have been realized in many graphene superlattice structures but so far robust superconductivity has been exclusive to twisted bilayer graphene (TBG) (*1*, *2*) and twisted trilayer graphene (TTG) (*3*, *4*). Notably, TTG exhibits greater electric field tunability (*3*, *4*), Pauli limit violation (*5*), and more strongly coupled superconductivity (*3*, *4*) in comparison to TBG. Although these observed differences may serve as clues for identifying the superconducting origin of these systems, our ability to identify the truly universal features is ultimately limited by a lack of robust superconducting moiré materials, suggesting that further progress lies in the discovery of other moiré superconducting systems.

We investigate twisted graphene multilayers in which each successive layer is twisted by an angle ±θ relative to the previous one in an alternating sequence (Fig. 1A). For an even number n of layers, the spectrum at zero displacement field D is expected to separate into n / 2 independent TBG-like bands, each characterized by a different effective twist angle. When the number of layers n is odd, in addition to (n − 1) / 2 TBG-like bands, one monolayer graphene (MLG)-like band (essentially a Dirac cone) is expected (*6*) (see left column of Fig. 1B for examples when n is 3, 4, and 5). The system may be conveniently modified through the application of a displacement field D, which controllably hybridizes the different bands (Fig. 1B, right column). Experimentally, we explore the properties of alternating twisted tri-, quadri-, and pentalayer graphene (TTG, TQG, TPG, respectively) structures with $\theta = 1.52 \pm 0.02°$ (device D1, trilayer), $\theta = 1.80 \pm 0.04°$ (D2, quadrilayer), and $\theta = 1.82 \pm 0.05°$ (D3, pentalayer), respectively (*7*). These twist angles all lie close to the theoretically predicted "magic" values needed to obtain one set of flat TBG-like bands [$\theta_{TTG}^{magic} = \sqrt{2}\theta_{TBG}^{magic} \approx 1.53°$, $\theta_{TQG}^{magic} = (\sqrt{5}+1)\theta_{TBG}^{magic}/2 \approx 1.75°$, and $\theta_{TPG}^{magic} = \sqrt{3}\theta_{TBG}^{magic} \approx 1.87°$, assuming an effective TBG twist angle $\theta_{TBG}^{magic} = 1.08°$ (*6*); see section 4.1 in (*7*)]. We find that TTG, TQG, and TPG all exhibit hallmark signatures of strong correlations (Fig. 1, C to E), including robust superconductivity and flavor symmetry breaking as revealed by pronounced resistance peaks around certain integer filling factors ν [number of electrons per moiré site; see section 1 in (*7*) for assignment of ν].

In addition to the symmetry-breaking transitions previously reported in TTG (*3*, *4*, *8*), our TTG structure [coupled to a tungsten diselenide (WSe_2) monolayer] (*9*) exhibits a previously unobserved correlated insulating state near ν = +2 at finite D [Fig. 1C, inset; see also fig. S4, Fig. 1B right column, and sections 3 and 4 in (*7*)], which originates from the interplay between an interaction-driven cascade transition and hybridization induced by the D field [e.g., as captured by (*10*, *11*)]. We have also detected an insulating state developing at finite D fields in TQG near charge neutrality [Figs. 1D (inset) and 1G]. However, in contrast to TTG the TQG insulating state can be explained through the D-induced hybridization only. Notably, the detection of insulating gaps in TTG and TQG implies a low level of disorder in our samples (see also fig. S1).

The superconducting regions in all three structures extend over considerably larger filling factor ranges compared with TBG (*2*, *9*, *12*, *13*) where superconductivity is typically observed within $2 < |\nu| < 3$. Moreover, superconductivity emerges over successively broader regions of phase space, reaching ν ≈ +5 on the electron side for TPG (Fig. 1, C to E). Along with a zero longitudinal resistance R_{xx} observed in the characteristic ν versus T dome (Fig. 1, H to J), we also measure large critical currents (~400 nA) and occasionally see oscillations in critical current caused by superconducting interference, substantiating the robustness of phase coherence (*7*). Moreover, we measure high critical perpendicular magnetic fields B_c (typically ~0.8 T; see fig. S3), indicating that the corresponding Ginzburg–Landau coherence lengths ξ_{GL} (~10 to 30 nm) are substantially smaller than those observed in TBG and deviate from the weak-coupling prediction, $\xi_{GL} \approx \hbar v_F/\pi\Delta$ with $\Delta \approx 1.76 k_B T_c$; this suggests a strong-coupling origin of superconductivity (*3*, *4*) [see section 2 in (*7*)]. When combined with other recent experiments (*5*, *14*, *15*), these observations affirm the unconventional nature of superconductivity within the entire class of graphene moiré systems. Further, the measurements on three to five layers indicate that the addition of layers promotes superconductivity over a broader filling window despite the coexisting dispersive bands as well as the ostensibly increased vulnerability to disorder—both from the additional twist angles and from the sensitivity to the relative displacement between layers (fig. S14).

In addition to the pronounced ν-dependence, the observed superconducting pockets are highly tunable with electric displacement field D (Fig. 2). A comparison of the three structures reveals, however, that TQG and TPG are more tunable than TTG. This is apparent both in the D-dependent evolution of the filling range in which superconductivity is measured (Fig. 2, A to C) as well as in the critical temperature T_c (Fig. 2, D to F). Notably, superconductivity in TQG and TPG is fully quenched for all fillings at $D/\epsilon_0 = 0.75$ Vnm^{-1} and $D/\epsilon_0 = 0.6$ Vnm^{-1}, respectively. In the case of TTG, however, superconductivity is present up to the maximum accessible electric field $D/\epsilon_0 = 1$ Vnm^{-1}. Nevertheless, R_{xx} versus D and temperature measurements do show that superconductivity is suppressed for large D fields at optimal doping (the doping at which superconducting T_c is the highest) in all three heterostructures; further, they reveal that T_c forms a D symmetric dome maximized at small finite D (Fig. 2, D to F, for electron-side data showing similar behavior see fig. S5). We also note that TTG, TQG, and TPG all exhibit similar variation in T_c when

[1]T. J. Watson Laboratory of Applied Physics, California Institute of Technology, Pasadena, CA 91125, USA. [2]Institute for Quantum Information and Matter, Department of Physics, California Institute of Technology, Pasadena, CA 91125, USA. [3]Department of Physics, California Institute of Technology, Pasadena, CA 91125, USA. [4]Department of Physics, University of California, Davis, CA 95616, USA. [5]Department of Physics and Astronomy, California State University, Northridge, CA 91330, USA. [6]National Institute for Materials Science, Namiki 1-1, Tsukuba, Ibaraki 305 0044, Japan. [7]Dahlem Center for Complex Quantum Systems and Fachbereich Physik, Freie Universität Berlin, 14195 Berlin, Germany.
*Corresponding author. Email: s.nadj-perge@caltech.edu
†These authors contributed equally to this work.

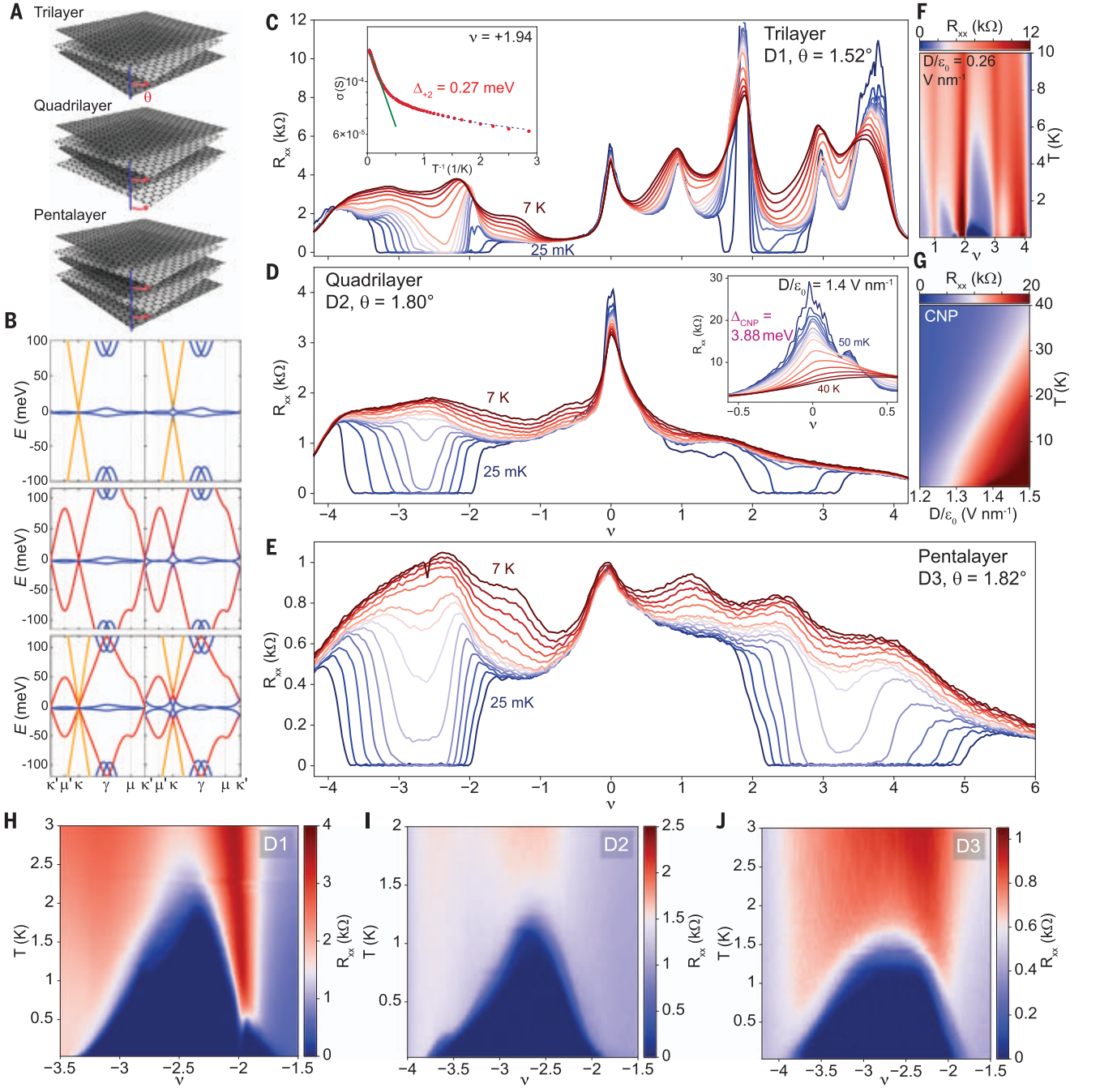


Fig. 1. Superconductivity and correlated insulators in alternating twisted graphene multilayers. (**A**) Schematics of the alternating twisted graphene multilayers in which each successive layer is twisted by an angle ±θ relative to the previous one in an alternating sequence. (**B**) Band structure of twisted tri-, quadri-, and pentalayer graphene (from top to bottom) for angles close to the theoretical magic angle at zero D field (left) and $D/\epsilon_0 \approx 0.4$ Vnm^{-1} (right) for valley K [section 4 in (*7*)]. (**C** to **E**) Line cuts of R_{xx} versus filling factor ν for a range of temperatures (shown are traces taken first at 25 mK, then every 0.25 K from 0.25 K to 2 K, followed by every 1 K from 3 K to 7 K), from top to bottom measured at $D/\epsilon_0 = 0.22$ Vnm^{-1} (C), −0.15 Vnm^{-1} (D), and 0 Vnm^{-1} (E), respectively. Inset of (C) is conductance versus T^{-1} for TTG showing thermal activation behavior [$D/\epsilon_0 = 0.26$ Vnm^{-1}, section 3 in (*7*)]. Inset of (D) shows charge-neutrality insulators in TQG at larger electric fields. (**F**) R_{xx} versus temperature and ν for the trilayer focusing around ν = +2 at $D/\epsilon_0 = 0.26$ Vnm^{-1}. (**G**) R_{xx} versus temperature and D field for the quadrilayer focusing near charge neutrality. (**H** to **J**) R_{xx} versus temperature and ν for hole doping, showing superconducting domes around ν = −2 in the same systems and for the same D fields as in (C) to (E).

viewed as a function of the potential difference U between the top and bottom layers [fig. S5, D and E; see also section 3 in (*7*) for the energy conversion from D to U]. This layer-number invariance is consistent with noninteracting continuum-model calculations tracking the evolution of the inverse of the flat-band bandwidth with U (Fig. 2G, bottom). The dependence of T_c on D in all devices qualitatively matches the predictions of (*16*) for TTG with one marked exception: the observed vanishing of superconductivity and the decay of T_c appears to be linear in D (Fig. 2, E and F, and fig. S5), in line with predictions for multilayer graphene with rhombohedral stacking

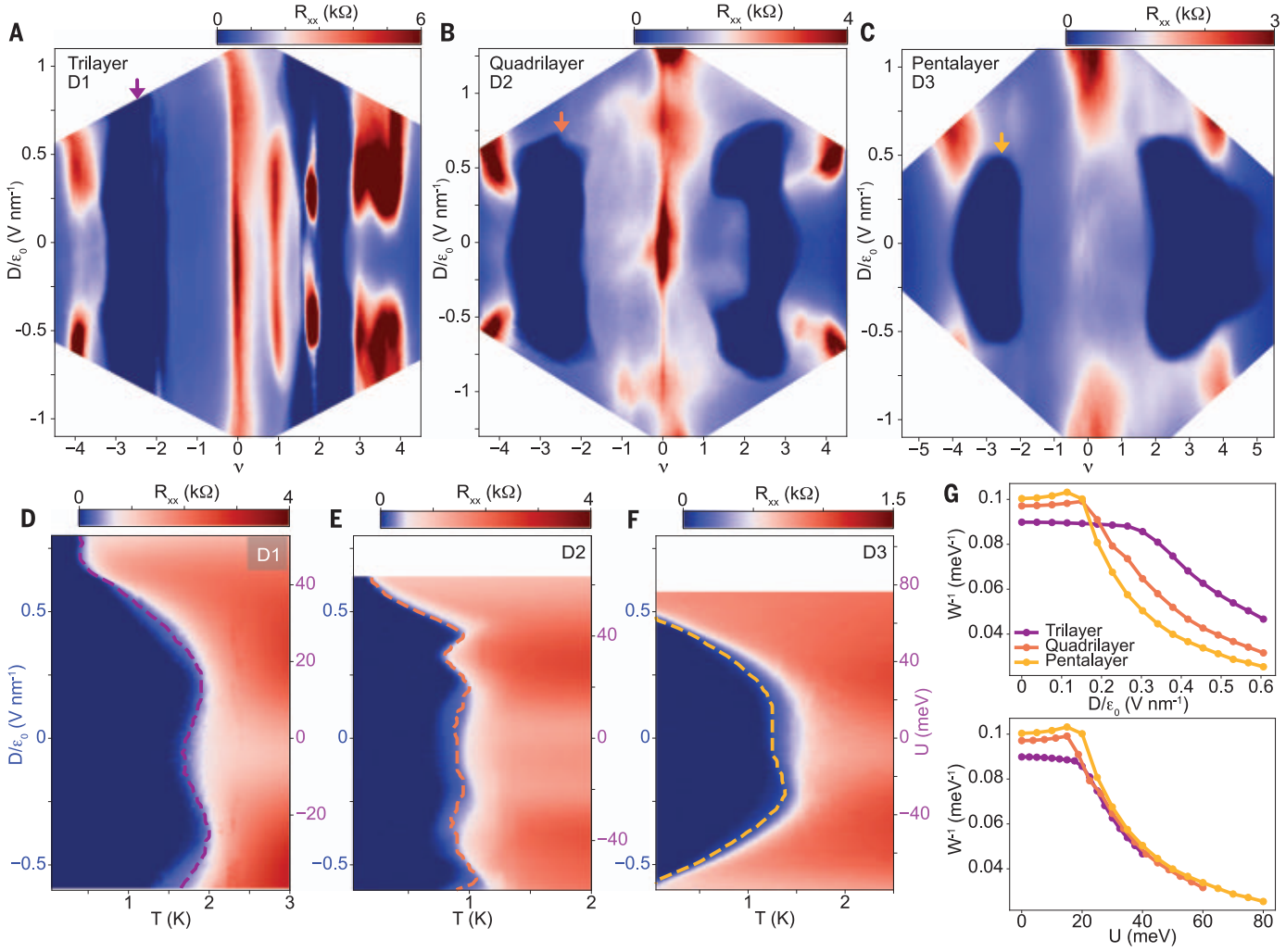


Fig. 2. TTG, TQG and TPG phase diagrams and electric field-tunable superconductivity. (**A** to **C**) R_{xx} versus filling factor ν and displacement field D for twisted trilayer (A), quadrilayer (B), and pentalayer (C) graphene, respectively. All data are taken at 25 mK, and the dark blue regions signal superconductivity. For electron-doped TTG and TQG, superconducting regions extend toward ν = +1 at intermediate D field. (**D** to **F**) R_{xx} versus temperature and D [or equivalent potential difference U between layers, see section 3 in (*7*)] for the filling factors indicated by arrows in (A) to (C). Critical temperature T_c is indicated by a dashed line that delineates 10% of the normal state resistance [section 2 in (*7*)]. T_c is maximized at finite D fields. Overall, superconductivity is suppressed more easily with D as the layer number is increased for both hole (D to F) and electron (fig. S5) doping. (**G**) Theoretical calculations of the inverse of the flat-band bandwidth for twisted trilayer, quadrilayer, and pentalayer graphene as a function of D/ϵ_0 (top) and potential difference U (bottom). For a fixed D, the bandwidth of the flat bands is larger for systems with more layers, but when expressed as a function of U, the flat-band broadening follows a similar trend across the different structures [section 4.1 in (*7*)].

(*17*) and in contrast to the exponential "tail" typically expected from the weak-coupling theory [and seen in the model of (*16*)].

Comparing the location of the superconducting regions with the evolution of the Hall density as a function of D and ν in TTG, TQG, and TPG provides further insight into the intricate relationship between the superconducting phase and the correlation-modified Fermi surface (Fig. 3). As in previous TBG and TTG measurements, we observe symmetry-breaking electronic transitions (a "cascade" of transitions) that are signaled by sudden drops in the Hall density magnitude (a "reset") without a change in sign. These resets (see dashed lines in Fig. 3, A to D) indicate a rearrangement of spin and valley sub-bands and typically occur near integer fillings of the flat bands (*18*, *19*). At low D fields, superconducting pockets onset around the $|\nu| = 2$ resets (purple dashed line), and the filling extent of superconductivity varies depending on the presence or absence of a $|\nu| = 3$ flavor symmetry-breaking transition (gray dashed line). For electron- and hole-doped TTG as well as for electron-doped TQG (Fig. 3, A, B, D), a flavor symmetry-breaking transition appears around $|\nu| = 3$ and superconductivity accordingly terminates, as previously noted in TTG (*3*). By contrast, when signatures of the $|\nu| = 3$ reset are completely absent (for example in hole-doped TQG, Fig. 3C, or TPG), superconductivity extends much further. Combined, these observations suggest that superconductivity is favored when only two out of the four flavors are predominantly populated ($|\nu| = 2$ cascade) and suppressed beyond $|\nu| = 3$ resets. This behavior can be understood within the simplest iteration of the cascade scenario: resets associated with $|\nu| = 3$ produce spin- and valley-polarized bands (*20*–*22*) and naturally disfavor Cooper pairing of time-reversed partners.

At high D fields, signatures of the cascade vanish and van Hove singularities (vHs) become more prominent instead, reflecting qualitative changes in the band structure (see yellow lines in Fig. 3, A to D and fig. S6 that track the vHs). Consistent with previous TTG measurements (*3*, *4*), the vHs in our TTG sample (as well as in TPG, see Fig. 3, E and F) crudely bound the superconducting regions. By contrast, the vHs

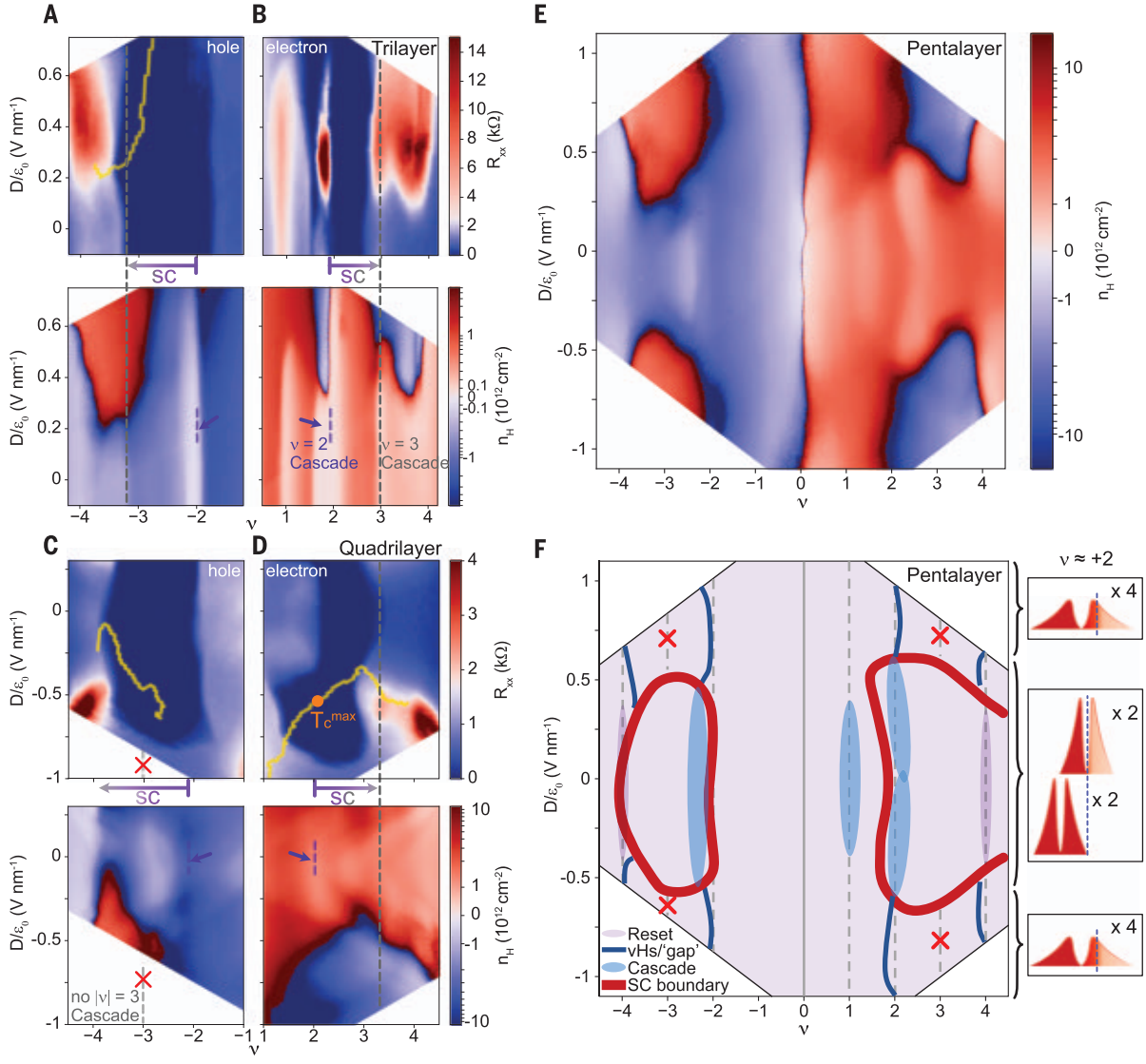


Fig. 3. Interplay between superconductivity, flavor symmetry-breaking transitions and van Hove singularities in TTG, TQG and TPG. (**A** and **B**) D field and ν dependence of R_{xx} (top) and Hall density (bottom, measured at B = 0.9 T) for TTG at 25 mK. Purple and gray dashed lines mark the filling factors in which flavor symmetry-breaking transitions associated with $|\nu| = 2$ and $|\nu| = 3$ happen, respectively. The yellow line in (A) delineates the evolution of the vHs. (**C** and **D**) D field and ν dependence of R_{xx} (top) and Hall density (bottom, measured at $B = 1.5$ T) for TQG at 25 mK. Superconducting T_c reaches its maximum [orange dot in (D)] exactly at the position of the vHs. When present, flavor symmetry-breaking transitions around $|\nu| \approx 3$ coincide with the termination of superconductivity [(A), (B), and (D)]. By contrast, superconductivity extends much further in the absence of a $|\nu| \approx 3$ reset (C). (**E**) D field- and ν-dependence of Hall density for TPG measured at T = 25 mK and B = 1.5 T. (**F**) Schematic of Hall density (E) and R_{xx} (Fig. 2C) features for the pentalayer, including the boundary of the superconducting region (red), vHs/"gap" (dark blue), cascade (light blue), and $|\nu_{flat}| = 4$ Hall density reset (light purple). Sketches of the DOS around ν = +2 for different D fields are shown on the right. The middle panel illustrates the flavor symmetry polarization observed in regions that support superconductivity. Flavor symmetry is preserved at higher D fields, as shown in the top and bottom panels.

in TQG cross well into the superconducting pockets—in fact, for electron doping, T_c reaches its maximum exactly at the position of the vHs (Fig. 3D, orange dot, and fig. S7, D to F). The interplay between the vHs and superconducting boundaries as revealed in Hall density measurements is complex: T_c can be both enhanced and suppressed at the vHs depending on the layer number and possibly other details such as the precise twist angle (see fig. S11 for data from the second TQG device).

Pentalayer measurements provide additional signatures that point toward a close relation between superconductivity and flavor symmetry-breaking cascades (Fig. 3, E and F). In contrast to TTG, in TPG we can access D fields that are large enough to stifle superconductivity, which occurs simultaneously with the onset of the vHs and the apparent suppression of the cascade transitions (see red and light blue lines in Fig. 3F that mark the superconducting boundaries and the cascade transitions, respectively). For example, at low D fields ($|D|/\epsilon_0 < 0.6$ Vnm^{-1}) around ν = +2, the Hall density resets close to zero, in line with a nearly complete flavor symmetry-breaking polarization. However, at higher D fields ($|D|/\epsilon_0 > 0.6$ Vnm^{-1}), the Hall density is dominated by a vHs around ν = +2 and the cascade signatures are diminished. Superconductivity accordingly also vanishes. For hole doping, the disappearance of superconductivity similarly coincides with the weakening of the cascade. This on and off

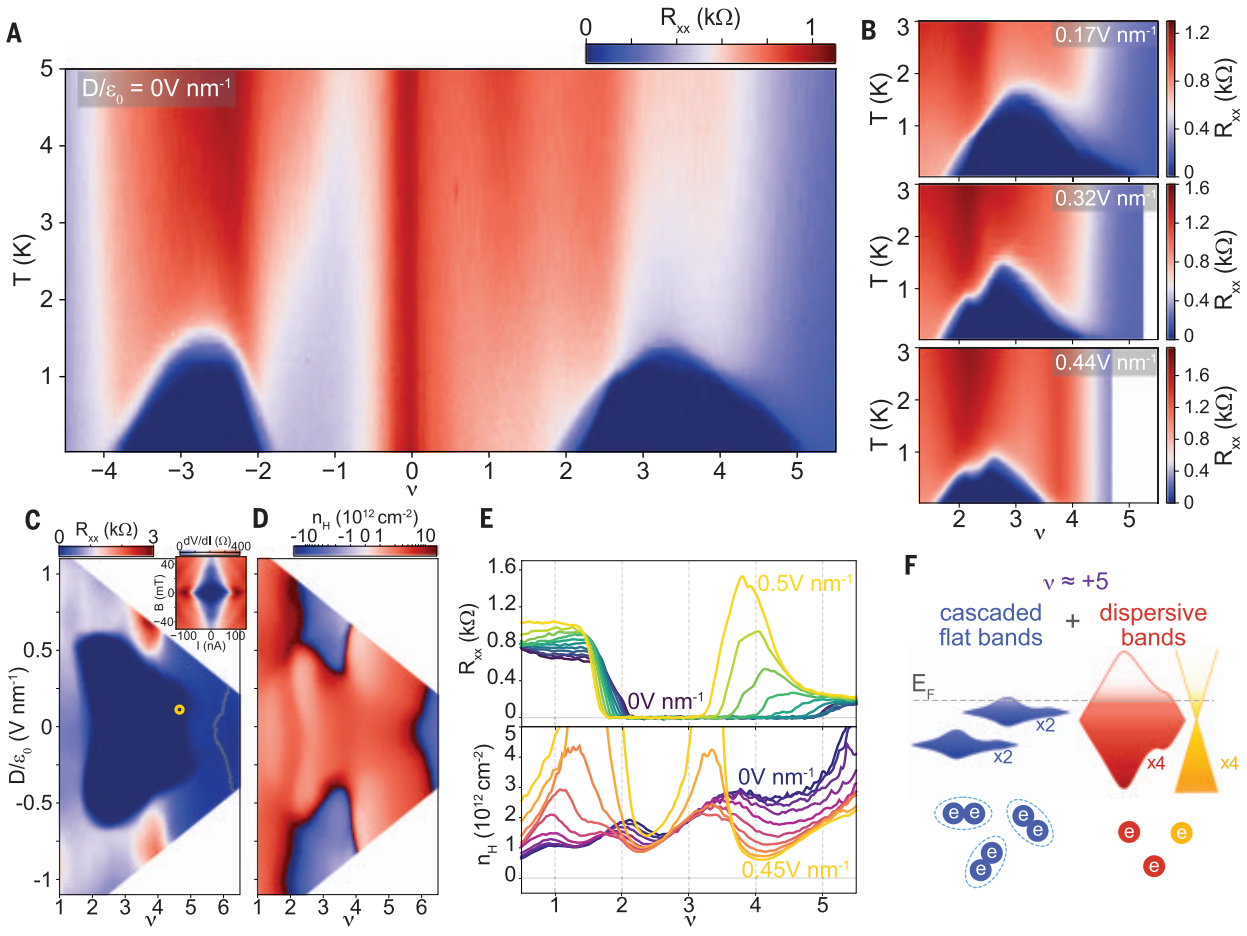


Fig. 4. Extended superconducting pockets in TPG. (**A**) R_{xx} versus ν and temperature at zero D field for twisted pentalayer graphene. (**B**) R_{xx} versus temperature and ν on the electron side at $D/\epsilon_0 = 0.17$, 0.32, and 0.44 Vnm^{-1}. The evolution of the superconducting domes and resistance peaks near ν = +2 and ν = +4 with D is shown. (**C** and **D**) D field and ν dependence of R_{xx} (C) and Hall density [(D), measured at B = 1.5 T)] at 25 mK, showing the region around the electron-side superconducting pocket. The gray line in (C) marks the vHs originating from the dispersive TBG-like bands (see also fig. S10). The inset shows the evolution of dV/dI as a function of I and B at $\nu = +4.6$, $D/\epsilon_0 = 0.12$ Vnm^{-1} (marked by a yellow dot in the main panel), confirming the robustness of the superconductivity above $\nu = +4$. (**E**) Line cuts of R_{xx} (top, measured at T = 25 mK) and Hall density (bottom, measured at T = 1.5 K, B = 0.5 T) versus ν for a range of D fields (traces are shown for every 0.05 for both R_{xx} and Hall density). Both the presence of Hall density resets around ν = +4 and the development of superconductivity extending from ν = +2 to +5 are shown to persist for a wide range of D fields. (**F**) Schematic of scenario (ii) with a Hartree correction for superconductivity at ν ≈ +5. The Hartree correction shifts the dispersive TBG- and MLG-like bands down in energy, which causes the flat TBG-like bands to fill more slowly with doping, thus allowing them to host superconductivity at ν > +4.

correspondence between the two phenomena suggests that they either share a common origin—such as a large DOS—or that the cascade serves as a prerequisite for robust superconductivity in graphene moiré superlattices.

As mentioned above, for low D fields in TPG, the superconducting pockets are extraordinarily large, spanning $-4 \lesssim \nu < -2$ for hole doping and $+2 \lesssim \nu \lesssim +5$ for electron doping (Figs. 1E, 2C, and 4). In particular, the electron-side range corresponds roughly to a density window of 6×10^{12} cm^{-2}, which is the largest filling range so far reported in a graphene-based superconductor. The observed superconductivity exhibits values of T_c and B_c (fig. S3) similar to that of the tri- and quadrilayer samples and is likewise accompanied by a weak oscillating pattern of critical current (Fig. 4C, inset), confirming superconducting phase coherence. We emphasize that the unprecedented persistence of superconductivity across a large filling factor range in TPG (and also TQG in comparison to TTG or TBG) cannot be explained in a minimal framework of alternating twisted graphene multilayers (*6*, *23*) without invoking the nontrivial role of the additional bands. The role of the additional bands in TPG deserves careful consideration because of the implications for the strength of interactions (such as Hartree effects) and the types of superconductivity the bands can plausibly support. Explanations for the enlarged superconducting intervals can generically be organized into three scenarios depending on the filling of the flat TBG-like bands ν_{flat}, relative to the total filling ν_{max} at which superconductivity terminates (ν_{max} = +5 for electron-doped TPG and $|\nu_{max}| = 4$ for TQG and hole-doped TPG). In scenario (i), ν_{max} corresponds to $\nu_{flat} \approx +3$, the flat band filling at which superconductivity is typically suppressed in TBG, suggesting that the superconducting phase space is largely the same for different multilayer magic-angle structures when considering just the flattest TBG-like bands. In scenario (ii), ν_{max} coincides with $\nu_{flat} \approx +4$, precluding any simple analogy with TBG, although superconductivity can still be attributed to the flat bands. Finally, scenario (iii) assumes full filling of the flat bands before superconductivity is suppressed at ν_{max}. This scenario includes the possibility that the distinction between the different TBG- and MLG-like bands breaks down even at D = 0 owing to

hybridization as well as potential multi-band superconductivity (*24*–*27*). In this case, superconductivity in TPG is a more general phenomenon than in TBG because it occurs in either mixed bands or new, more dispersive bands [see section 5 in (*7*)].

From the perspective of the noninteracting band structure, the three scenarios all seem implausible and therefore interactions must play a crucial role. In particular, although the presence of the dispersive bands implies that $|\nu| - |\nu_{\mathrm{flat}}| > 0$, this effect is much smaller than needed for either scenario (i) or (ii). Coulomb interactions can considerably enhance $|\nu| - |\nu_{\mathrm{flat}}|$, either by evening out the spatial charge distribution (*28*–*32*) or by symmetry breaking. A simple model for TPG incorporating these mechanisms [section 4.5 in (*7*)] suggests a minimal flat-band occupation $\nu_{\mathrm{flat}} \gtrsim +3.8$ at $\nu \approx +5$, diminishing the plausibility of scenario (i) for electron-doped TPG which has $\nu_{\mathrm{max}} \approx +5$. The relevance of this scenario is further undermined by the observation of vHs at $\nu \approx +5$ (fig. S10D): under the reasonable assumption that the noninteracting band structure remains valid for the dispersive TBG-like bands (apart from a Hartree shift), scenario (i) would instead place the observed vHs near $\nu \approx +5$. Taken together, these arguments effectively rule out scenario (i). Note, however, that the presented line of reasoning is not straightforward for the other superconducting pockets [see section 5 in (*7*)].

Both scenarios (ii) and (iii) are indicative of the nontrivial role of additional bands in stabilizing superconductivity. Assuming well-defined flat and dispersive bands, in scenario (iii) the former bands are completely filled and superconductivity is supported fully by the latter nonflat bands. This assertion is at odds with the large dispersion of the remaining TBG- and MLG-like bands. However, although the exact mechanism underlying scenario (iii) is difficult to pin down, it is not without experimental support. For instance, a natural interpretation of the Hall density minimum around $\nu \approx +4$ for $|D| \lesssim 0.4$ Vnm^{-1} is that it marks the complete filling of the flat bands, $\nu_{\mathrm{flat}} \approx +4$ [Fig. 4E, fig. S9, and section 5 in (*7*)].

One possible realization of scenario (iii) consistent with the experimental observations is that the division of the electronic states into simple TBG- and MLG-like bands fails—obviating our very definition of ν_{flat} and potentially allowing flavor polarization and accompanying superconductivity to persist well beyond $\nu \approx +4$. Although such hybridization is expected for finite D fields, mixing between flat, dispersive TBG- and MLG-like bands for $|\nu| < |\nu_{\mathrm{max}}|$ may occur even at $D = 0$ thanks to, for example, proximity to WSe_2, layer-to-layer charge inhomogeneity, or distant-layer coupling [see sections 4.4 and 4.5.3 in (*7*)].

Our measurements demonstrate the increasing predominance of superconductivity in twisted graphene multilayer structures as the number of layers is increased from three to five and highlight the close relationship between the flavor symmetry–breaking transitions and superconductivity. Moreover, our findings suggest a scenario in which the symmetry-broken $\nu = \pm 2$ state strongly favors the formation of the superconducting state whereas the cascade corresponding to $\nu = \pm 3$ suppresses it. Notably, this scenario is consistent not only with previous TBG (*2*, *9*, *12*, *13*, *33*, *34*) and TTG (*3*, *4*, *8*) observations but also in part with the recently investigated ABC trilayers (*35*) and Bernal bilayers with and without (*36*) a WSe_2 substrate (*37*) in which superconductivity is observed near or within phases with two out of four flavors being predominantly filled. These commonalities suggest that symmetry-broken states with similar types of polarization underlie superconductivity in all of these graphene-based superconductors. In this context, the discovery of superconductivity in TQG and TPG together with recent work on untwisted bi- and trilayers considerably expands the scope of graphene-based superconductors. This expansion holds promise for resolving ongoing questions related to the nature of the pairing mechanism in these systems and provides guidance for developing novel graphene-based superconductors and their applications.

Note added in proof: After submission of this report, we have become aware of related work (*38*).

REFERENCES AND NOTES

1. Y. Cao *et al*., *Nature* **556**, 80–84 (2018).
2. Y. Cao *et al*., *Nature* **556**, 43–50 (2018).
3. J. M. Park, Y. Cao, K. Watanabe, T. Taniguchi, P. Jarillo-Herrero, *Nature* **590**, 249–255 (2021).
4. Z. Hao *et al*., *Science* **371**, 1133–1138 (2021).
5. Y. Cao, J. M. Park, K. Watanabe, T. Taniguchi, P. Jarillo-Herrero, *Nature* **595**, 526–531 (2021).
6. E. Khalaf, A. J. Kruchkov, G. Tarnopolsky, A. Vishwanath, *Phys. Rev. B* **100**, 085109 (2019).
7. See the supplementary materials.
8. X. Liu, N. J. Zhang, K. Watanabe, T. Taniguchi, J. I. A. Li, *Nat. Phys.* **18**, 522–527 (2022).
9. H. S. Arora *et al*., *Nature* **583**, 379–384 (2020).
10. M. Christos, S. Sachdev, M. S. Scheurer, *Phys. Rev. X* **12**, 021018 (2022).
11. F. Xie, N. Regnault, D. Călugăru, B. A. Bernevig, B. Lian, *Phys. Rev. B* **104**, 115167 (2021).
12. M. Yankowitz *et al*., *Science* **363**, 1059–1064 (2019).
13. Y. Saito, J. Ge, K. Watanabe, T. Taniguchi, A. F. Young, *Nat. Phys.* **16**, 926–930 (2020).
14. M. Oh *et al*., *Nature* **600**, 240–245 (2021).
15. H. Kim *et al*., *Nature* **606**, 494–500 (2022).
16. W. Qin, A. H. MacDonald, *Phys. Rev. Lett.* **127**, 097001 (2021).
17. N. B. Kopnin, T. T. Heikkilä, G. E. Volovik, *Phys. Rev. B* **83**, 220503 (2011).
18. U. Zondiner *et al*., *Nature* **582**, 203–208 (2020).
19. D. Wong *et al*., *Nature* **582**, 198–202 (2020).
20. P. Potasz, M. Xie, A. H. MacDonald, *Phys. Rev. Lett.* **127**, 147203 (2021).
21. G. Shavit, E. Berg, A. Stern, Y. Oreg, *Phys. Rev. Lett.* **127**, 247703 (2021).
22. F. Xie *et al*., *Phys. Rev. B* **103**, 205416 (2021).
23. P. J. Ledwith *et al*., TB or not TB? Contrasting properties of twisted bilayer graphene and the alternating twist *n*-layer structures (n = 3, 4, 5, ...). arXiv:2111.11060 [cond-mat] (2021).
24. H. Suhl, B. T. Matthias, L. R. Walker, *Phys. Rev. Lett.* **3**, 552–554 (1959).
25. O. V. Dolgov, I. I. Mazin, D. Parker, A. A. Golubov, *Phys. Rev. B* **79**, 060502 (2009).
26. P. J. Hirschfeld, M. M. Korshunov, I. I. Mazin, *Rep. Prog. Phys.* **74**, 124508 (2011).
27. X. Chen, S. Maiti, A. Linscheid, P. J. Hirschfeld, *Phys. Rev. B* **92**, 224514 (2015).
28. F. Guinea, N. R. Walet, *Proc. Natl. Acad. Sci. U.S.A.* **115**, 13174–13179 (2018).
29. L. Rademaker, D. A. Abanin, P. Mellado, *Phys. Rev. B* **100**, 205114 (2019).
30. Z. A. H. Goodwin, V. Vitale, X. Liang, A. A. Mostofi, J. Lischner, *Electron. Struct.* **2**, 034001 (2020).
31. M. J. Calderón, E. Bascones, *Phys. Rev. B* **102**, 155149 (2020).
32. Y. Choi *et al*., *Nat. Phys.* **17**, 1375–1381 (2021).
33. P. Stepanov *et al*., *Nature* **583**, 375–378 (2020).
34. R. Polski *et al*., Hierarchy of Symmetry Breaking Correlated Phases in Twisted Bilayer Graphene. arXiv:2205.05225 [cond-mat.str-el] (2022).
35. H. Zhou, T. Xie, T. Taniguchi, K. Watanabe, A. F. Young, *Nature* **598**, 434–438 (2021).
36. H. Zhou *et al*., *Science* **375**, 774–778 (2022).
37. Y. Zhang *et al*., Spin-Orbit Enhanced Superconductivity in Bernal Bilayer Graphene. arXiv:2205.05087 [cond-mat.str-el] (2022).
38. J. M. Park *et al*., Magic-Angle Multilayer Graphene: A Robust Family of Moiré Superconductors. arXiv:2112.10760 [cond-mat.supr-con] (2021).
39. Y. Zhang *et al*., Superconductivity in Magic-Angle Graphene Multilayers, CaltechDATA, (2022).

ACKNOWLEDGMENTS

We thank H. Zhou and S. Mashahadi for fruitful discussions. **Funding:** This work has been primarily supported by NSF-CAREER award (DMR-1753306), Office of Naval Research (grant N142112635), and Army Research Office under Grant Award W911NF17-1-0323. Nanofabrication efforts have been in part supported by Department of Energy DOE-QIS program (DE-SC0019166). S.N-P. acknowledges support from the Sloan Foundation (grant FG-2020-13716). G.R., J.A., and S.N.-P. also acknowledge support of the Institute for Quantum Information and Matter, an NSF Physics Frontiers Center with support of the Gordon and Betty Moore Foundation through Grant GBMF1250. C.L. acknowledges support from the Gordon and Betty Moore Foundation's EPiQS Initiative, grant GBMF8682. Y.P. acknowledges support from the startup fund from California State University, Northridge. F.v.O. is supported by Deutsche Forschungsgemeinschaft within CRC 183 (project C02) as well as the project TWISTGRAPH. **Author contributions:** Y.Z. and R.P. performed the measurements, fabricated the devices, and analyzed the data. Y.C. and H.K. helped with device fabrication and data analysis. C.L., A.T., and Y.P. developed theoretical models and performed calculations in close collaboration and guidance by F.v.O., G.R., and J.A. K.W. and T.T. provided hBN crystals. S.N-P. supervised the project. Y.Z., R.P., C.L., A.T., Y.P., F.v.O., G.R., J.A., and S.N-P. wrote the manuscript with the input of other authors. **Competing interests:** The authors declare no competing interests. **Data and materials availability:** The data from this study are available via the CaltechDATA repository (*39*).

License information: Copyright © 2022 the authors, some rights reserved; exclusive licensee American Association for the Advancement of Science. No claim to original US government works. https://www.sciencemag.org/about/science-licenses-journal-article-reuse

SUPPLEMENTARY MATERIALS

science.org/doi/10.1126/science.abn8585
Materials and Methods
Supplementary Text
Figs. S1 to S14
References (*40*–*71*)

Submitted 24 December 2021; accepted 2 September 2022
10.1126/science.abn8585

OCEAN ACIDIFICATION

Climate change drives rapid decadal acidification in the Arctic Ocean from 1994 to 2020

Di Qi[1,2,3], Zhangxian Ouyang[4], Liqi Chen[1,2]*, Yingxu Wu[1], Ruibo Lei[5], Baoshan Chen[4], Richard A. Feely[6], Leif G. Anderson[7], Wenli Zhong[8], Hongmei Lin[2], Alexander Polukhin[9], Yixing Zhang[2], Yongli Zhang[10], Haibo Bi[3,11], Xinyu Lin[2], Yiming Luo[12], Yanpei Zhuang[1], Jianfeng He[5], Jianfang Chen[13], Wei-Jun Cai[4]*

The Arctic Ocean has experienced rapid warming and sea ice loss in recent decades, becoming the first open-ocean basin to experience widespread aragonite undersaturation [saturation state of aragonite (Ω_{arag}) < 1]. However, its trend toward long-term ocean acidification and the underlying mechanisms remain undocumented. Here, we report rapid acidification there, with rates three to four times higher than in other ocean basins, and attribute it to changing sea ice coverage on a decadal time scale. Sea ice melt exposes seawater to the atmosphere and promotes rapid uptake of atmospheric carbon dioxide, lowering its alkalinity and buffer capacity and thus leading to sharp declines in pH and Ω_{arag}. We predict a further decrease in pH, particularly at higher latitudes where sea ice retreat is active, whereas Arctic warming may counteract decreases in Ω_{arag} in the future.

In the global ocean, an increase in anthropogenic carbon dioxide (CO_2) has led to decreases in seawater pH based on the total hydrogen ion concentration scale (pH_T) and the saturation state of the calcium carbonate mineral aragonite (Ω_{arag}) in a process known as ocean acidification (*1*). Although substantial regional and decadal variability in ocean acidification, driven by climate-induced atmospheric and oceanic circulation changes, has been observed in low- and mid-latitude ocean basins (*2*–*4*) and in the Southern Ocean (*3*), long-term ocean acidification rates generally have followed the trends predicted from the increase in the concentration of CO_2 in the atmosphere (*2*, *3*). For the Arctic Ocean, although numerical models have predicted high acidification rates (*5*–*8*), observation-based decadal rates of surface water pH_T and Ω_{arag} change are sparse. Over the past three decades, climate warming has induced notable changes in the Arctic atmosphere-ice-ocean system (fig. S1). These changes include (i) a rapid sea ice retreat from a nearly fully ice-covered state before the 1990s to an ice-free state in the southern part of the Canada Basin and a partially ice-covered state in the northern part of the basin (*9*), (ii) a change from cyclonic circulation in the 1990s to an anomalous anticyclonic circulation pattern (*10*), and (iii) a spin-up of the Beaufort Gyre (*11*) over the past 20 years (fig. S1). There are also increases in freshwater storage (*11*), Pacific Summer Water inflow (*12*), biological production (*13*), stratification (*14*), air-sea CO_2 exchanges and carbon sinks (*15*, *16*), and nutricline depth (*17*) and decreases in surface nutrients (*18*) and subsurface anthropogenic CO_2 storage (*19*). In addition, pH_T and calcium carbonate saturation conditions have been substantially altered by these changes (*20*–*26*). For example, the Canada Basin was the first open-ocean basin where surface aragonite undersaturation (i.e., Ω_{arag} < 1) was detected (*20*, *22*) together with subsurface (*21*, *27*) and intermediate water (*28*, *29*) acidification. Thus, the Arctic Ocean is considered to be a bellwether of global climate change and ocean acidification (*30*).

Here, by using pH_T and Ω_{arag} estimates derived from data collected on 47 Arctic research cruises from 1994 to 2020 (see materials and methods), we document the high rates of long-term ocean acidification trends and basin-scale spatial expansion in terms of both pH_T and Ω_{arag} declines in the western Arctic Ocean. With this dataset, we further examine how sea ice loss and increasing atmospheric CO_2 have altered the sea-surface carbonate chemistry over the past two decades, and we propose an "ice melt–driven enhanced anthropogenic CO_2 acidification" mechanism to explain such rapid rates of regional ocean acidification.

The pH_T and Ω_{arag} values were calculated based on underway measurements of the partial pressure of CO_2 (P_{CO_2}) and salinity-derived total alkalinity (TA), together with sea surface temperature and salinity, from 1994 to 2020 (table S1). Data were supplemented with pH_T and Ω_{arag}, which were calculated from discrete measurements of TA and dissolved inorganic carbon (DIC) (see materials and methods). The salinity-derived TA and corresponding calculated DIC values match well with those of the discrete samples, yielding uncertainties of less than ±14 μmol kg^{-1} (fig. S2), which are further quality controlled as described in the materials and methods. The combined uncertainties of estimated pH_T and Ω_{arag} were 0.0113 and 0.0109, respectively, which were computed using the uncertainty propagation routine for CO2SYS (*31*).

Our results show that the area of sea surface with relatively low pH_T (<8.05) and Ω_{arag} (<1) expanded substantially (~0 to 0.88 × 10^6 km^2) from 1994 to 2020, not only increasing in areal coverage but also extending into higher latitudes in the western Arctic Ocean (Fig. 1). During the 1990s, more than 90% of the western Arctic Ocean basin waters were covered by sea ice, with a high pH_T (8.17 ± 0.05), and were supersaturated with respect to aragonite (Ω_{arag} = 1.46 ± 0.23) (Fig. 1, A and E). These initial conditions of the relatively higher pH_T and Ω_{arag} in the sea ice–covered period are due to the absence of gas exchange to replenish CO_2 from the atmosphere and low water temperature (i.e., for the same TA and DIC values, pH_T is higher in cold than warm waters). As sea ice in the western Arctic Ocean basin began to melt beyond the annual seasonal cycle of advance and retreat in the early 2000s, relatively lower pH_T (8.12 ± 0.04) and Ω_{arag} (1.21 ± 0.14) were observed in surface waters. This acidification happened first in the southern Canada Basin and slope and then extended northward to 76°N (Fig. 1, B and F). By the late 2000s, extreme summertime sea ice retreat mediated by both climate change and natural variability led to a broad ice-free area (~1.7 × 10^6 km^2) with a large-scale lower pH_T (8.04 ± 0.02) and aragonite undersaturation (Ω_{arag} = 0.97 ± 0.05) that extended into the central Canada Basin (Fig. 1, C and G). Whereas the pH_T decrease could be attributed to a combination of rapid warming and CO_2 uptake from the atmosphere, the Ω_{arag} decrease was mainly due to CO_2 uptake because warming would result in an opposite trend. From 2011 to 2020, although the overall sea ice concentration and pH_T and Ω_{arag} values were similar to those of the late 2000s, the areas of low-pH_T (8.02 ± 0.01) and Ω_{arag}-undersaturated (0.95 ± 0.05) waters continued to expand northwestward (Fig. 1, D and H). We attribute this acidification to the continuously increasing atmospheric CO_2 uptake over the expanded ice-free regions. Overall, from the 1990s to the 2010s, rapid sea ice loss and

[1]Polar and Marine Research Institute, College of Harbor and Coastal Engineering, Jimei University, Xiamen 361021, China. [2]Third Institute of Oceanography, Ministry of Natural Resources, Xiamen 361005, China. [3]Center for Ocean Mega-Science, Chinese Academy of Sciences, Qingdao 266071, China. [4]School of Marine Science and Policy, University of Delaware, Newark, DE, USA. [5]Key Laboratory for Polar Science of the Ministry of Natural Resources, Polar Research Institute of China, Shanghai 200136, China. [6]Pacific Marine Environmental Laboratory–National Oceanic and Atmospheric Administration, Seattle, WA, USA. [7]Department of Marine Sciences, University of Gothenburg, SE-412 96 Gothenburg, Sweden. [8]Key Laboratory of Physical Oceanography, Ocean University of China, Shandong, China. [9]P.P. Shirshov Institute of Oceanology, Russian Academy of Sciences, Moscow, Russia. [10]School of Marine Science and Technology, Tianjin University, Tianjin, China. [11]Key Laboratory of Marine Geology and Environment, Chinese Academy of Sciences, Qingdao 266071, China. [12]School of Marine Sciences, Sun Yat-Sen University, Zhuhai, China. [13]Second Institute of Oceanography, Ministry of Natural Resources, Hangzhou 310012, China.
***Corresponding author. Email: chenliqi@tio.org.cn (L.C.); wcai@udel.edu (W.-J.C.)**

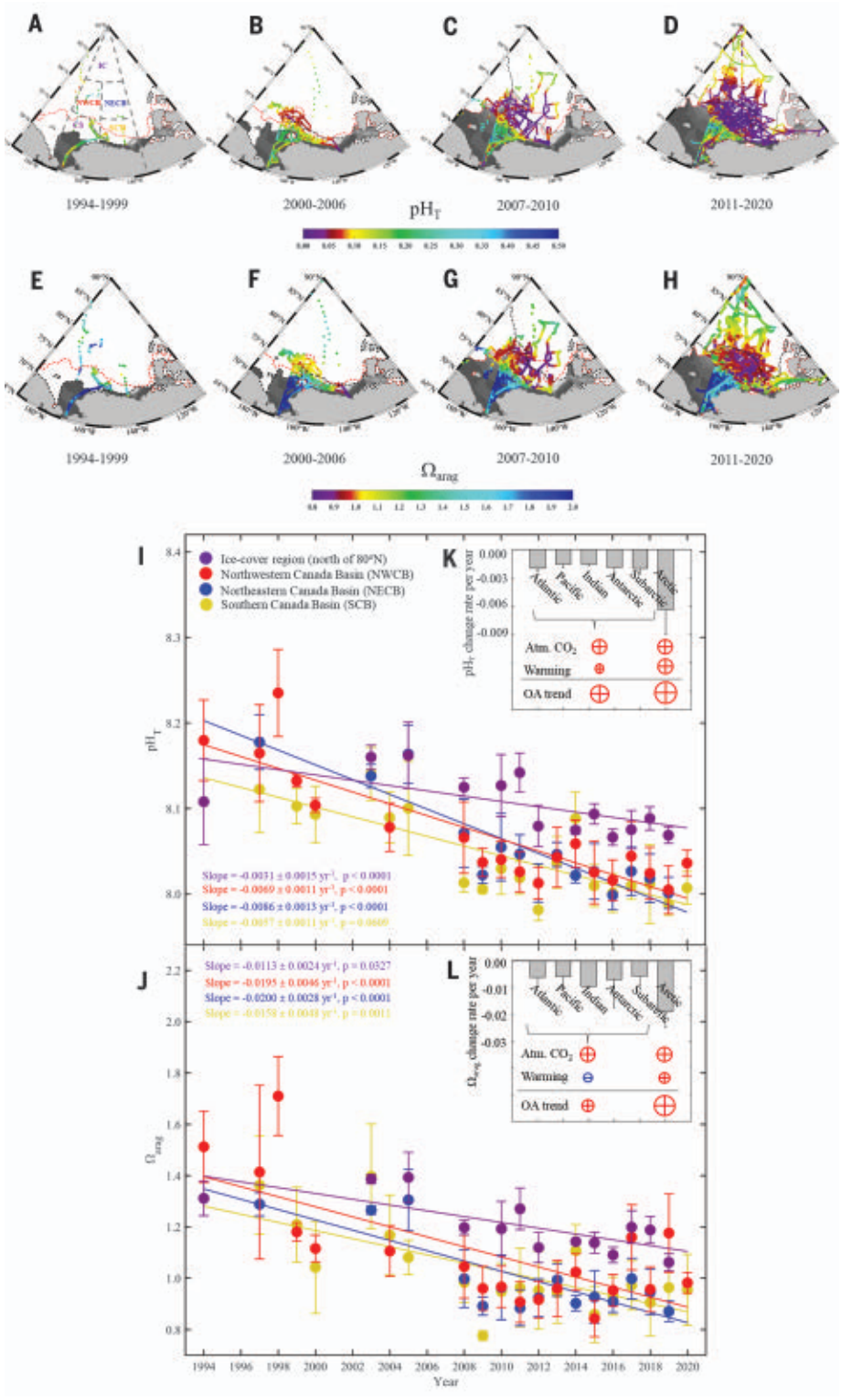


Fig. 1. Observations of ocean acidification and its decadal summertime trends in the western Arctic Ocean. (**A** to **H**) pH_T [(A) to D)] and Ω_{arag} [(E) to (H)] in the western Arctic Ocean during 1994 to 1999, 2000 to 2006, 2007 to 2010, and 2011 to 2020. The black dashed lines show the ice edge (with an ice concentration threshold of 15% and gray shading representing sea ice concentration) during the first week of September during the first year of the subperiod; the red dashed lines show the location of that edge during the final year of the subperiod. Cruise information is provided in table S1. Sea ice edge data are from the National Snow and Ice Data Center (https://nsidc.org/data/seaice_index/). (**I** and **J**) decadal summertime trends of pH_T and Ω_{arag}. Uncertainties associated with the trends were assessed by the Monte Carlo approach (see methods for detailed calculations). The error bars represent the combined uncertainty from sample measurements, carbonate system calculations, and the gridding-induced spatiotemporal variability. (**K** and **L**) Comparison of rates and mechanisms of acidification in the Arctic and other oceans. The gray vertical bars show annual rates, and the circles indicate the relative contributions of component mechanisms and their overall acidification effect. A red-plus circle indicates a positive contribution to acidification (or a positive net effect), and a blue-minus circle indicates an effect that counters acidification; the size of each circle indicates relative magnitude. The Arctic Ocean acidification rate was calculated as the average of the rates obtained in this study for the four western Arctic Ocean subregions (SCB, NECB, NWCB, and IC); decadal trend values for the other ocean basins were obtained from previous studies listed in table S2. Error bars represent the standard deviation of the mean rates. OA, ocean acidification.

acidification co-occurred in the western Arctic Ocean, but thereafter, relatively slow acidification occurred, accompanied by interannual fluctuation in sea ice coverage.

To quantify the long-term trends in pH_T and Ω_{arag}, we first divided the western Arctic Ocean into five subregions based on spatial patterns of decadal ice retreat and ocean acidification expansion: the Chukchi Sea shelf (CS), Southern Canada Basin (SCB), Northeastern Canada Basin (NECB), Northwestern Canada Basin (NWCB), and permanent ice-covered region (IC, north of 80°N) (i.e., where minimal sea ice concentration is >70%) (Fig. 1A). We then averaged pH_T and Ω_{arag} within each grid cell (0.1° latitude by 0.25° longitude) to obtain daily and monthly means for each cruise dataset. Finally, we averaged the gridded results within each subregion to obtain monthly and yearly (from June to October) means (see materials and methods).

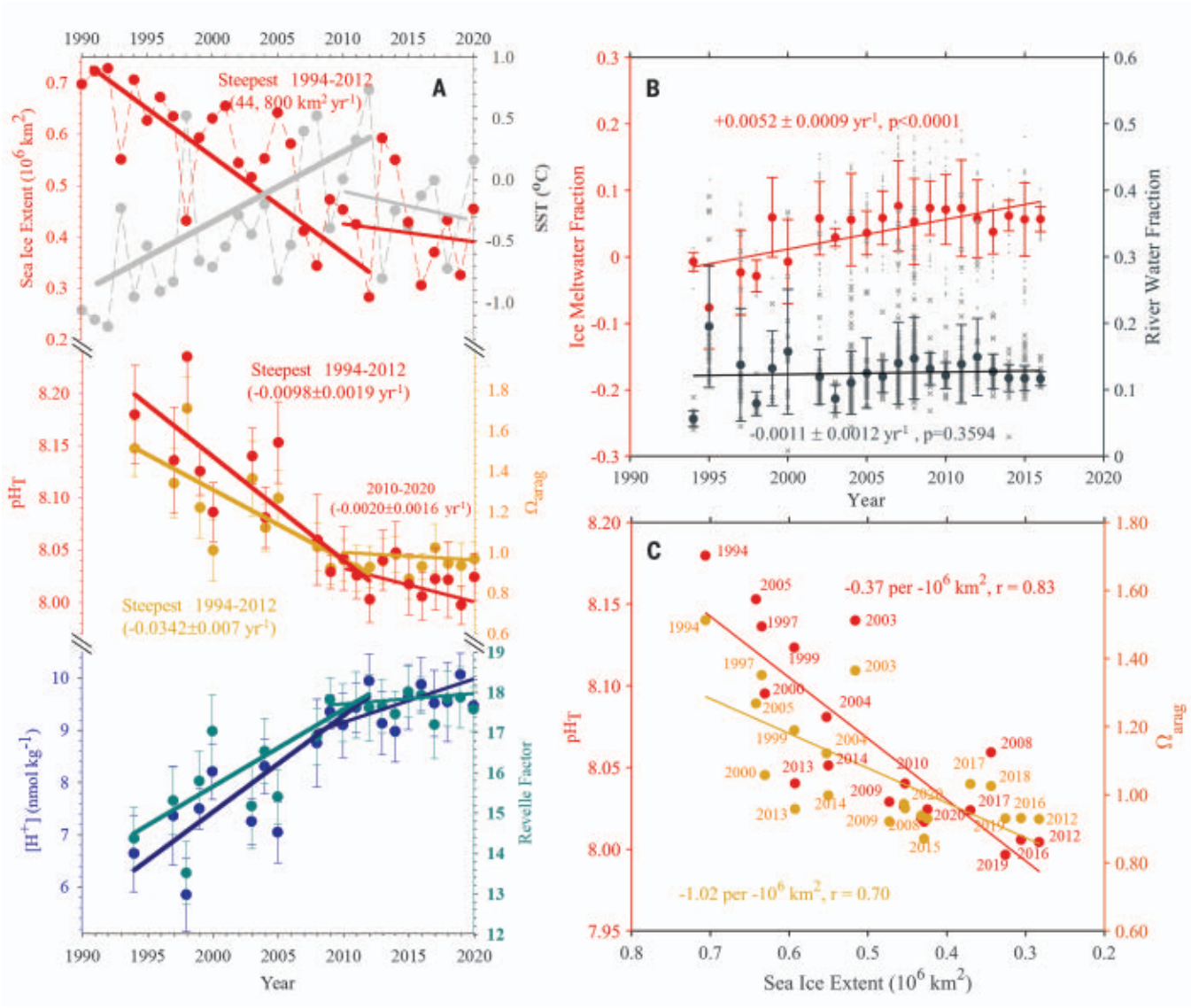


Fig. 2. Linking Arctic Ocean basin acidification to sea ice loss. (**A**) Sea ice loss, acidification status, and CO_2 buffer capacity (Revelle factor) in the rapid sea ice melt regions of the Canada Basin (including SCB, NECB, and NWCB). The Revelle factor (the ratio of $\partial P_{CO_2}/P_{CO_2}$ to $\partial DIC/DIC$) is a general measure of the ocean's sensitivity to an increase in CO_2. The sea surface temperature (SST) data were obtained from the Advanced Very High Resolution Radiometer (AVHRR) (*39*), whereas the sea ice extent data were obtained from the National Snow and Ice Data Center. Note that we use September monthly means to represent the decadal trends of sea ice extent. The middle and bottom panels show the mean decadal trends in the rapid ice melt area of the Canada Basin (south of 80°N), including the SCB, NECB, and NWCB regions. (**B**) Long-term change in fractions of meltwater and river water in the surface water (≤20 m) of the Canada Basin. The calculation methods follow those in (*20*, *21*). (**C**) Relationships between sea ice extent and pH_T and Ω_{arag}. The sea ice extent data are from https://nsidc.org/data/G02135/versions/3.

Different grid sizes, averaging schemes, deseasonalization treatments, and sensitivity tests (randomly removing 15 or 30% of measurements or cruises) were tested (figs. S3 to S11) for the determination of long-term trends. These various approaches yielded comparable and consistent rates of sea surface pH_T and Ω_{arag} decrease in all subregions except for the NWCB and CS, where undersampling in the former and the large natural spatiotemporal variability in the latter prohibit a good performance of deseasonalization.

Our results revealed rapid acidification in the western Arctic Ocean basins, with a mean annual rate of −0.0069 ± 0.0011 for pH_T and −0.0216 ± 0.0040 for Ω_{arag} from 1994 to 2020 (table S2). These rates are approximately four and three times faster, respectively, than the long-term decline rates in other ocean basins [Fig. 1, K and L, table S2, and (*32*)]. Similarly, the increase rate (0.128 ± 0.019 nmol kg^{-1} $year^{-1}$) of hydrogen ion [H^+] is also about four times faster than that in other ocean basins (table S2). The mean annual acidification rate was highest in the NECB (−0.0086 ± 0.0013 for pH_T and −0.020 ± 0.0028 for Ω_{arag}) and slowest in the ice-covered higher-latitude ocean basin (Fig. 1, I and J). These observational rates in the western Arctic basins are much faster than those projected by both regional and global models (e.g., −0.0025 to −0.0030 $year^{-1}$ for pH) (*5*–*8*). By contrast, we found a relatively slower rate of acidification on the CS than in the basins, with a mean annual rate of change of −0.0031 ± 0.0024 for pH_T and −0.0009 ± 0.0138 for Ω_{arag} (fig. S12).

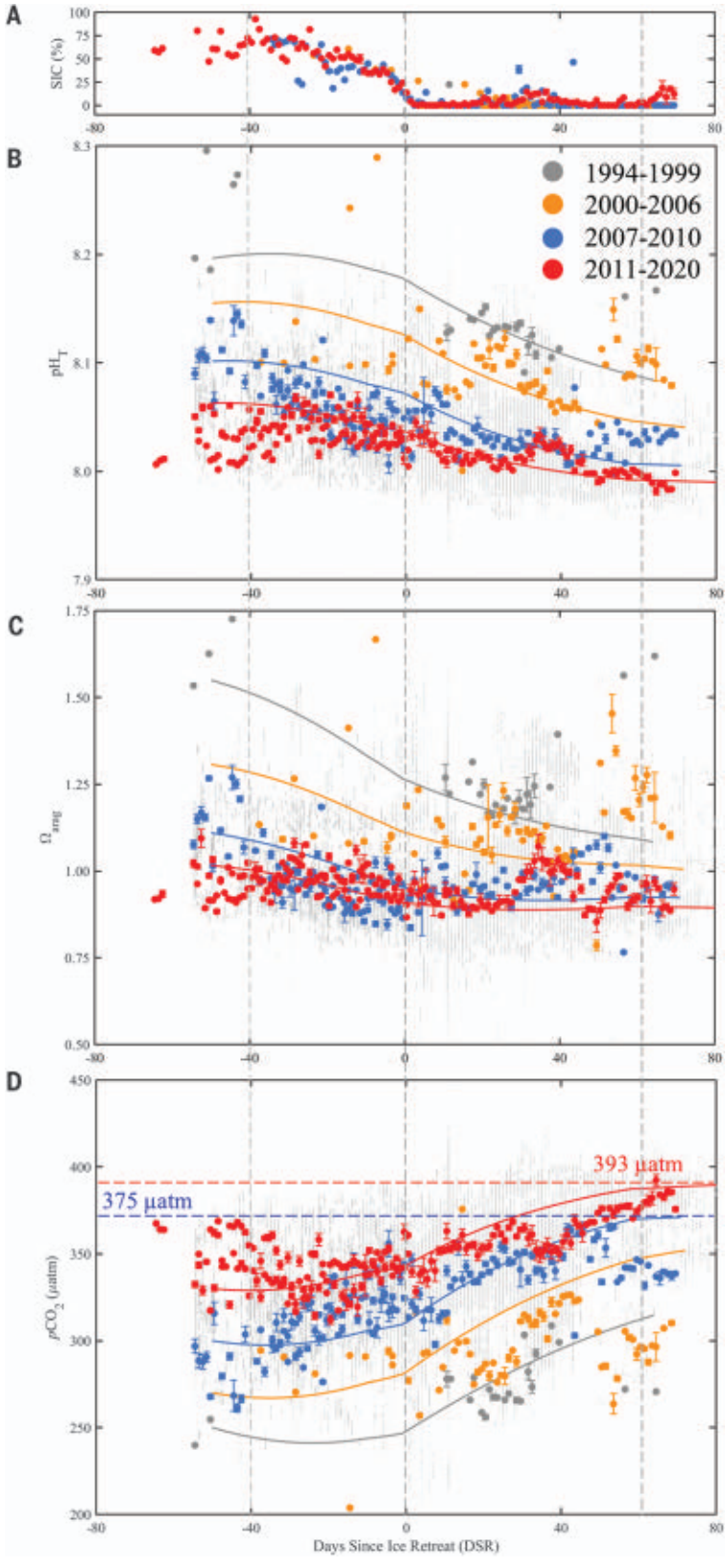


Fig. 3. Evolution of pH_T and Ω_{arag} as a function of days since ice retreat from 1994 to 2020 on the Arctic Ocean basin. (**A** to **D**) Sea ice concentration (SIC) (A), surface water pH_T (B), surface water Ω_{arag} (C), and surface water PCO_2 (D). The dots and error bars represent the means and standard deviations of SIC, pH_T, Ω_{arag}, and PCO_2 within 1 day's intervals. The "clouds" of gray dots in the background show individual data points. The solid lines show the 1D model–simulated days since ice retreat (DSR) dependences of these two CO_2 system parameters for four periods using a constant heating rate and panel until the DSR is 60, at which point the temperature is then held constant. The blue and red dashed lines represent the atmospheric CO_2 level in the 2007 to 2010 and 2011 to 2020 periods, respectively. See materials and methods for an explanation. The vertical dashed gray lines denote DSR of −40, 0, and 60 days.

The long-term acidification rates on the CS are likely mitigated by a strong and increasing biological CO_2 removal driven by nutrient inputs from the Pacific Ocean, which uses and counteracts CO_2 influx from the atmosphere (*13*, *16*, *33*).

When we focus on the regions of massive sea ice loss in the Canada Basin (including SCB, NWCB, and NECB), a notable finding appears—the decreases in pH_T and Ω_{arag} are strongly correlated with the decrease in sea ice extent over the past 26 years (Fig. 2). Notably, the

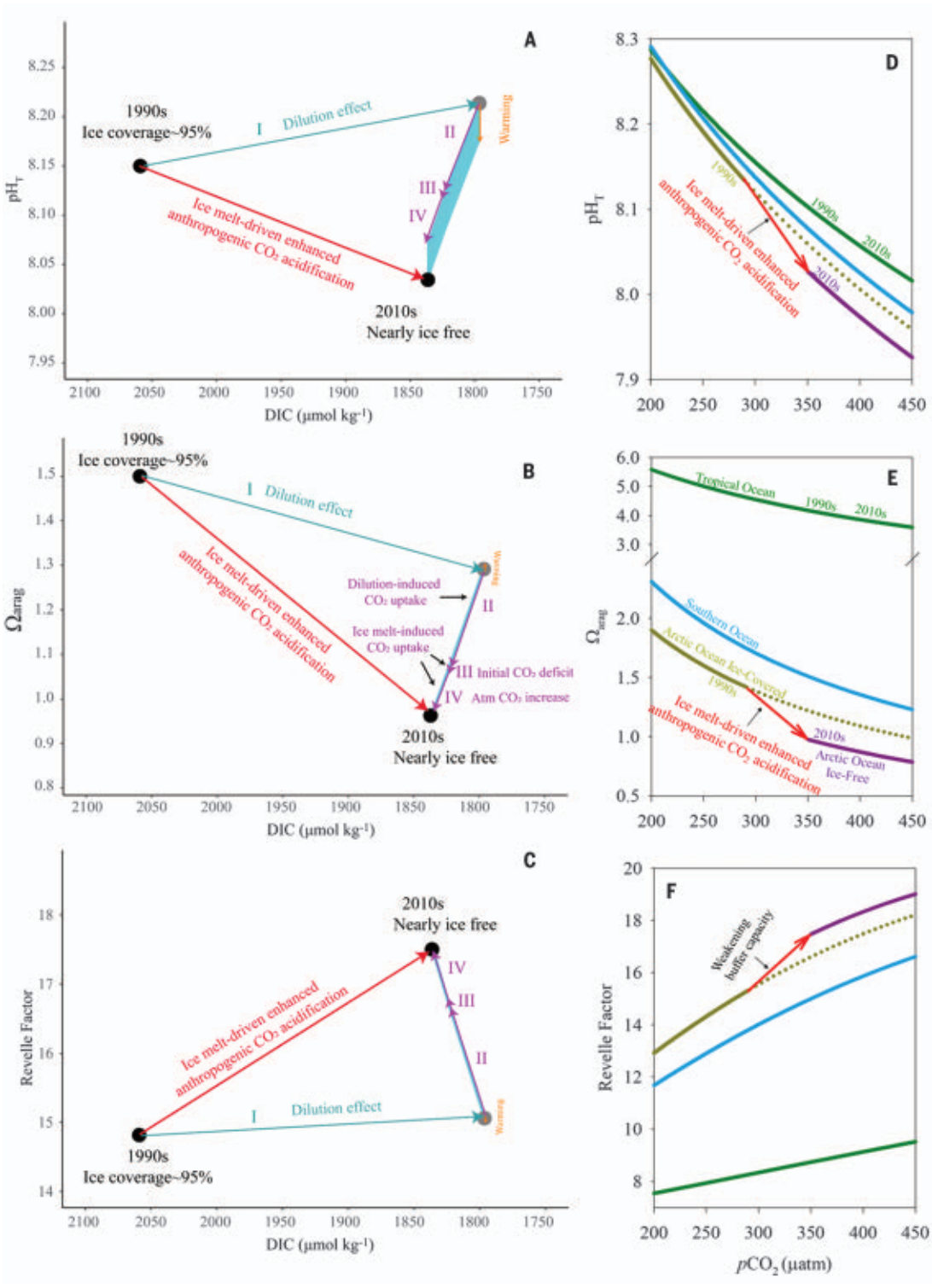


Fig. 4. Sea ice loss and melt are amplifying surface ocean acidification in the Arctic Ocean basin. (**A** to **C**) The decadal progression of ocean acidification with respect to pH_T (A), Ω_{arag} (B), and the Revelle factor (C). The black dots represent the observational conditions for pH_T, Ω_{arag}, and the Revelle factor (values calculated from decadal means; table S3). The gray dot represents the initial condition after sea ice melt [a two-endmember mixing model consisting of 1990s ice-covered seawater and ice-melt water was applied to calculate diluted TA and DIC and carbonate parameters; TA was used as a tracer, and the meltwater endmember was obtained from (*40*)]. The arrows indicate the processes of warming (orange), dilution (I, dark cyan), dilution-induced CO_2 uptake (II, magenta), and ice melt–induced CO_2 uptake (III and IV, magenta). The dilution-induced process (II) refers to the uptake of CO_2 to compensate for the dilution-lowered Pco_2 (increased up to the initial Pco_2 in the 1990s; fig. S15); the ice melt–induced process refers to the following CO_2 uptake from the atmosphere, where initial CO_2 deficit term (III) denotes the disequilibrium between 1990s Pco_2 and air Pco_2, and atmospheric (Atm) CO_2 increase term (IV) denotes acidification driven by the air Pco_2 increase from the 1990s to 2010s. The blue-shaded areas indicate the possible decadal variations in pH_T, Ω_{arag}, and the Revelle factor, which were synergistically affected by warming and CO_2 uptake. The initial status of the ice-covered Canada Basin in the 1990s is set as salinity (S) = 31.3, temperature (T) = −1.6°C, TA = 2192 μmol kg^{-1}, DIC = 2059 μmol kg^{-1}, and Pco_2 = 278 μatm (table S3). Dilution with a meltwater endmember of TA ≈ 70 μmol kg^{-1} (*40*) results in a lower TA of 1912 μmol kg^{-1}, DIC of 1792 μmol kg^{-1}, and Pco_2 of 214 μatm (and simultaneously lower Ω_{arag} owing to decreased salinity and carbonate ion concentration, but higher pH_T owing to decreased hydrogen ion concentration) (dilution effect I). When Pco_2 increases back to the initial Pco_2 level before ice melting in the 1990s (dilution-induced CO_2 uptake, II), it causes a decrease in pH_T of 0.10 and a decrease in Ω_{arag} of 0.25. These decreases will be driven by subsequent ice melt–induced CO_2 uptake (III and IV, where IV represents the air Pco_2 decadal increase of 38 μatm and corresponding changes in pH_T and Ω_{arag}), which leads to a further decrease in pH_T of 0.05 and a decrease in Ω_{arag} of 0.11. (**D** to **F**) Surface-water acidification parameters as a function of surface Pco_2 for the global tropical ocean, the Southern Ocean, and the Arctic Ocean (ice-covered and ice-free scenarios) from the multidecadal perspective. The dashed lines are linear extensions of the trendlines, which may not be realistic. Calculations were made using CO2SYS with the following input values: T = 26°C, S = 35, and TA = 2332 μmol kg^{-1} for the tropical ocean; T = −0.3°C, S = 34, and TA = 2297 μmol kg^{-1} for the Southern Ocean; T = −1.6°C, S = 31, and TA = 2192 for the Arctic Ocean, ice-covered scenario; and T = 0.72°C, S = 26, and TA = 1912 μmol kg^{-1} for the Arctic Ocean, ice-free scenario (table S3). The red arrows refer to the processes that regulate decadal changes in pH_T, Ω_{arag}, and the Revelle factor in (A) to (C).

earlier 18-year period (1994 to 2012) has the steepest decline trends in pH_T (-0.0098 ± 0.0019 year^{-1}) and Ω_{arag} (-0.0342 ± 0.0077 year^{-1}), which corresponds well with the steepest decrease in sea ice (Fig. 2). However, the decreasing trends of both pH_T and Ω_{arag} were slower during 2010 to 2020, which is consistent with the alleviated reduction of sea ice since 2008, though a strong interannual variability is apparent (Fig. 2A). Nevertheless, even during this period, the rate of pH_T decrease is still comparable to rates of other ocean basins (Fig. 2A and table S2), which are mainly driven by the increasing atmospheric CO_2. Unlike pH_T, no statistically significant trend for Ω_{arag} was found during 2010 to 2020, reflecting the counteracting effect of warming. Clearly, massive sea ice retreat, modulated by the large-scale climate change pattern, has played a critical role in the fast acidification in the Arctic Ocean over the past two to three decades.

To explain the link between rapid long-term pH_T and Ω_{arag} decline rates and the massive sea ice loss in the Arctic Ocean, a thorough understanding of the evolution of carbonate chemistry in response to the sea ice condition is required. In the 1990s, when most of the Arctic Ocean surface was covered by sea ice, the transfer of CO_2 from the atmosphere into the surface waters was impeded by sea ice (fig. S1A), resulting in a large deficit of DIC from the atmospheric equilibrium value ($\Delta DIC = -25$ μmol kg^{-1}; figs. S13C and S14). As a consequence, the cold surface seawater beneath the sea ice has a high potential to absorb atmospheric CO_2 once it is exposed to the atmosphere.

Since the 2000s, the Arctic Ocean has experienced accelerated warming and substantial sea ice retreat (e.g., ice extent was at its lowest in the summer of 2012) (Fig. 2A and fig. S1B). We used a simple one-dimensional (1D) dynamic model to simulate the response of pCO_2, pH, and Ω_{arag} to the decrease of sea ice (Fig. 3; see supplementary materials for a description of the model). We found that, under partially or newly ice-free conditions, the low-pCO_2 waters that were originally under the ice were exposed to higher atmospheric pCO_2 and rapidly took up CO_2 through air-sea gas exchange (Fig. 3D). In other words, the initial CO_2 deficit resulted in a CO_2 increase "boost" over that time period. The shallow surface mixed layer and strong stratification (*34*, *35*) also prevented the dilution of the absorbed CO_2, leading to rapid responses of the carbonate system parameters (Fig. 3, B and C, and fig. S1B).

The rapid decreases in pH_T and Ω_{arag} along with sea ice retreat are seen not only over a seasonal time scale but also over a decadal time scale (Fig. 3). We further quantified and decomposed the decadal drivers of acidification (table S7) and translated the results to a graphic illustration (Fig. 4, A to C). We found that the net increase in DIC due to CO_2 uptake plays the predominant role in regulating acidification, with minor contributions from warming and dilution. However, we further diagnosed that, indirectly, approximately half of the changes in pCO_2, pH_T, and Ω_{arag} that resulted from CO_2 uptake are attributable to the additional CO_2 deficit triggered by sea ice melt (i.e., dilution of TA and DIC leads to lower initial pCO_2; see Fig. 4, A to C, fig. S15, and table S7). Thus, the indirect effect of dilution on the seawater carbonate system through the promotion of CO_2 uptake is an important factor driving acidification and weakening buffer capacity in the western Arctic Ocean (Fig. 4, A to C).

The progression in sea ice loss represents a major change in seawater carbonate chemistry, from a state of well-buffered seawater with relatively high alkalinity and low pCO_2 underneath the sea ice (fig. S1A) to a meltwater-diluted state characterized by lower alkalinity, higher pCO_2, and lower buffer capacity under the partially or fully ice-free surface (Fig. 4, D to F, and fig. S1C). As a result, atmospheric CO_2 invasion would lead to a greater overall decrease in pH_T, Ω_{arag}, and buffer capacity in seawater diluted by meltwater than the original water (Fig. 4, A to C, and fig. S15), illustrated also as a jump from one pH_T-pCO_2 evolving locus along the high iso-alkalinity line in the 1990s to the low iso-alkalinity line in the 2010s (Fig. 4, D to F). We name this distinctive mechanism "ice melt–driven enhanced anthropogenic CO_2 acidification." The mechanism explains the amplified rapid acidification observed in the Arctic Ocean over the past two to three decades, in contrast to the slower acidification in other global oceans along only one alkalinity line (Fig. 4, D to F). This mechanism could conceivably also operate in the sea ice zone within the Southern Ocean, where seasonal sea ice melt also plays an important role in sea surface CO_2 dynamics and in air-sea CO_2 gas exchange (*36*).

We must also point out that further warming could result in contrasting impacts on pH_T and Ω_{arag} trends (fig. S16; see supplementary text for details). This phenomenon has emerged in late summer in ice-free southern regions since the 2010s, where both warming and CO_2 uptake from the atmosphere decreased pH_T (fig. S16A), whereas warming (when it exceeds +1°C) increased and CO_2 uptake decreased Ω_{arag} (fig. S16B). When temperature further increases, the net Ω_{arag} trend could even be positive, similar to what has been observed in some other parts of the world's oceans (*37*, *38*); this is also illustrated as the cancellation effect of the red-plus circle by the blue-minus circle in Fig. 1L).

Although Arctic sea ice coverage has fluctuated over the past decade, it is also shifting from multiyear ice to first-year ice (fig. S17). This thinning trend of sea ice implies that summer sea ice will continue to decline in extent and lower the seawater alkalinity and buffer capacity until the Arctic Ocean is turned into an ice-free region. Finally, although the overall freshwater increase, including that from rivers, has decreased the anthropogenic CO_2 inventory in the subsurface water (*19*), there is, at present, no significant decadal trend in river-water content in the surface layer (Fig. 2B). Therefore, both larger winter-to-summer meltwater-induced seawater alkalinity dilution and greater subsequent CO_2 uptake from the atmosphere are expected to be the dominant processes in surface waters. As a consequence, the "ice melt–driven enhanced anthropogenic CO_2 acidification" mechanism may continue to operate over the next few decades, becoming even more pronounced until the time that sea ice completely disappears during summer (at which time, Arctic Ocean surface seawater may reach its lowest alkalinity) (Fig. 4). Therefore, this greatly amplified summertime ocean acidification modulated by large-scale climate change may lead to long-lasting impacts on the biogeochemistry, ecosystem, and organisms in the Arctic Ocean basins.

REFERENCES AND NOTES

1. J. C. Orr *et al.*, *Nature* **437**, 681–686 (2005).
2. N. R. Bates *et al.*, *Oceanography* **27**, 126–141 (2014).
3. T. Takahashi *et al.*, *Mar. Chem.* **164**, 95–125 (2014).
4. L. Kwiatkowski, J. C. Orr, *Nat. Clim. Change* **8**, 141–145 (2018).
5. N. Gruber *et al.*, *Science* **337**, 220–223 (2012).
6. M. Steinacher, F. Joos, T. Frolicher, G.-K. Plattner, S. C. Doney, *Biogeosciences* **6**, 515–533 (2009).
7. L. Bopp *et al.*, *Biogeosciences* **10**, 6225–6245 (2013).
8. A. Yamamoto, M. Kawamiya, A. Ishida, Y. Yamanaka, S. Watanabe, *Biogeosciences* **9**, 2365–2375 (2012).
9. J. A. Screen, I. Simmonds, *Nature* **464**, 1334–1337 (2010).
10. A. Proshutinsky, D. Dukhovskoy, M. L. Timmermans, R. Krishfield, J. L. Bamber, *Philos. Trans. R. Soc. London Ser. A* **373**, 20140160 (2015).
11. K. A. Giles, S. W. Laxon, A. L. Ridout, D. J. Wingham, S. Bacon, *Nat. Geosci.* **5**, 194–197 (2012).
12. R. A. Woodgate, T. J. Weingartner, R. Lindsay, *Geophys. Res. Lett.* **39**, 2012GL054092 (2012).
13. K. M. Lewis, G. L. van Dijken, K. R. Arrigo, *Science* **369**, 198–202 (2020).
14. J. R. Farmer *et al.*, *Nat. Geosci.* **14**, 684–689 (2021).
15. W. J. Cai *et al.*, *Science* **329**, 556–559 (2010).
16. Z. Ouyang *et al.*, *Nat. Clim. Change* **10**, 678–684 (2020).
17. F. A. McLaughlin, E. C. Carmack, *Geophys. Res. Lett.* **37**, L24602 (2010).
18. Y. Zhuang *et al.*, *Environ. Res. Lett.* **16**, 054047 (2021).
19. R. J. Woosley, F. J. Millero, *Limnol. Oceanogr.* **65**, 1834–1846 (2020).
20. M. Yamamoto-Kawai, F. A. McLaughlin, E. C. Carmack, S. Nishino, K. Shimada, *Science* **326**, 1098–1100 (2009).
21. D. Qi *et al.*, *Nat. Clim. Change* **7**, 195–199 (2017).
22. L. L. Robbins *et al.*, *PLOS ONE* **8**, e73796 (2013).
23. J. N. Cross, J. T. Mathis, R. S. Pickart, N. R. Bates, *Deep Sea Res. Part II Top. Stud. Oceanogr.* **152**, 67–81 (2018).
24. I. Semiletov *et al.*, *Nat. Geosci.* **9**, 361–365 (2016).
25. J. T. Mathis *et al.*, *Geophys. Res. Lett.* **39**, L07606 (2012).
26. Y. Zhang, M. Yamamoto-Kawai, W. J. Williams, *Geophys. Res. Lett.* **47**, e60119 (2020).

27. J. G. Wynn, L. L. Robbins, L. G. Anderson, *J. Geophys. Res. Oceans* **121**, 8248–8267 (2016).
28. Y. Luo, B. P. Boudreau, A. Mucci, *Nat. Commun.* **7**, 12821 (2016).
29. J. Terhaar, L. Kwiatkowski, L. Bopp, *Nature* **582**, 379–383 (2020).
30. V. J. Fabry, J. B. McClintock, J. T. Mathis, J. M. Grebmeier, *Oceanography* **22**, 160–171 (2009).
31. J. C. Orr, J. M. Epitalon, A. G. Dickson, J. P. Gattuso, *Mar. Chem.* **207**, 84–107 (2018).
32. L. Gregor, N. Gruber, *Earth Syst. Sci. Data* **13**, 777–808 (2021).
33. Tu, Z. *et al*., *Geophys. Res. Lett.* **48**, e2021GL093844 (2021).
34. C. Peralta-Ferriz, R. A. Woodgate, *Prog. Oceanogr.* **134**, 19–53 (2015).
35. E. C. Fine, S. T. Cole, *J. Geophys. Res. Oceans* **127**, e2021JC018056 (2022).
36. M. S. Brown *et al*., *Nat. Clim. Change* **9**, 678–683 (2019).
37. W. J. Cai *et al*., *Nat. Commun.* **11**, 2691 (2020).
38. Y. Wu *et al*., *Geophys. Res. Lett.* **48**, e2021GL094473 (2021).
39. B. Huang *et al*., *J. Clim.* **34**, 2923–2939 (2020).
40. A. Mo *et al*., *Front. Mar. Sci.* **9**, 766810 (2022).

ACKNOWLEDGMENTS

We thank the many contributors to the CHINARE, SOCAT, OCADS, LDEO, R/V Mirai cruises (JAMSTEC), and WHOI datasets as well as the many research vessels and crews that contributed to the collection of data used in this study. This is Pacific Marine Environmental Laboratory (PMEL) contribution number 5115. We thank H. Sun, Z. Gao, T. Li, A. Collins, and Y. Zhang for data collection and L. Yuan, X. Chen, D. Gui, Z. Feng, and J. Zhao for data processing. We also thank T. Clayton for improving the language. We are also grateful to the three anonymous reviewers. **Funding:** This work was supported by the National Key Research and Development Program of China (2019YFE0114800); the National Natural Science Foundation of China (41941013, 42176230, 41630969, and 42188102); the Ocean Negative Carbon Emissions (ONCE) Program, Key Deployment Project of Centre for Ocean Mega-Research of Science; Chinese Academy of Sciences (CAS) (grant no. COMS2020Q12); Chinese Projects for Investigations and Assessments of the Arctic and Antarctic (CHINARE2017-2020); and the Natural Science Foundation of Fujian Province, China (2019Jo5148). The University of Delaware group has been supported by the National Science Foundation (NSF) (ARC-0909330, PLR-1304337, and OPP-1926158) and the National Oceanic and Atmospheric Administration (NOAA) (NA09OAR4310078). R.A.F. was supported by the NOAA Ocean Acidification Program and the Pacific Marine Environmental Laboratory. **Author contributions:** L.C., D.Q., and W.-J.C. designed the program, and D.Q. and Z.O. executed the fieldwork. D.Q., Y.W., Z.O., and W.-J.C. analyzed the data and prepared the paper. All authors contributed to discussion and writing of the manuscript. **Competing interests:** The authors declare that they have no competing interests. **Data and materials availability:** The CHINARE surface P_{CO_2} datasets are deposited in SOCAT (with 2008, 2010, 2012, 2014, 2016, and 2018 already archived in SOCATv2021 and 2017 and 2020 to be archived in SOCATv2023). These datasets are also accessible via the Ocean Carbon and Acidification Data System (OCADS) (https://www.ncei.noaa.gov/access/ocean-carbon-acidification-data-system/oceans/VOS_Program/Xuelong.html). The CHINARE bottle data have been submitted to the Global Ocean Data Analysis Project (GLODAP) and will be archived in v2023 as well. In addition, the integrated P_{CO_2} dataset used in this study is deposited in Mendeley Data (https://data.mendeley.com/datasets/2ccwgyf6cw/1). **License information:** Copyright © 2022 the authors, some rights reserved; exclusive licensee American Association for the Advancement of Science. No claim to original US government works. https://www.science.org/about/science-licenses-journal-article-reuse

SUPPLEMENTARY MATERIALS

science.org/doi/10.1126/science.abo0383
Materials and Methods
Supplementary Text
Figs. S1 to S20
Tables S1 to S7
References (*41*–*73*)

Submitted 9 January 2022; accepted 6 September 2022
10.1126/science.abo0383

SEA LEVEL CHANGE

A detection of the sea level fingerprint of Greenland Ice Sheet melt

Sophie Coulson[1]*, Sönke Dangendorf[2], Jerry X. Mitrovica[3], Mark E. Tamisiea[4], Linda Pan[3], David T. Sandwell[5]

Rapid melting of ice sheets and glaciers drives a unique geometry, or fingerprint, of sea level change. However, the detection of individual fingerprints has been challenging because of sparse observations at high latitudes and the difficulty of disentangling ocean dynamic variability from the signal. We predict the fingerprint of Greenland Ice Sheet (GrIS) melt using recent ice mass loss estimates from radar altimetry data and model reconstructions of nearby glaciers and compare this prediction to an independent, altimetry-derived sea surface height trend corrected for ocean dynamic variability in the region adjacent to the ice sheet. A statistically significant correlation between the two fields ($P < 0.001$) provides an unambiguous observational detection of the near-field sea level fingerprint of recent GrIS melting in our warming world.

As an ice sheet loses mass, its gravitational attraction on the nearby ocean is reduced, causing ocean water to migrate away from the ice sheet. Additionally, the solid Earth rebounds in response to the reduction in surface loading. This combination of geophysical processes leads to a relative sea level fall within ~2000 km of the melting ice sheet and a progressive sea level rise outside of this region (*1*–*11*). This nonuniform geometry of sea level change—commonly called a sea level fingerprint (*6*, *9*), but more recently referred to as a barystatic-GRD (gravity, rotation, and deformation) fingerprint (*12*)—suggests the possibility of using tide gauge and satellite measurements of sea level change to both improve estimates of global mean sea level (GMSL) rise (*13*) and constrain the individual sources of meltwater (*6*, *7*, *9*). However, sea level changes are also affected by large dynamic sea level signals associated with ocean and atmosphere circulation and steric effects (*14*, *15*), and by both natural and artificial variability in terrestrial water storage (*16*–*18*).

The detection of individual sea level fingerprints will, in general, require observations spanning multiple decades. For example, simulations of the sea level fingerprint and dynamic sea level changes in response to melting of the Greenland Ice Sheet (GrIS) at a rate of 0.5 mm/year in units of equivalent GMSL rise [in line with estimates of Greenland ice mass flux over the past 20 years (*19*)] suggest that the rigorous detection of the sea level fingerprint would require ~30 years of altimeter measurements if these were limited to latitudes lower than 66°N (*20*). The time scale of detection would, however, be reduced considerably if tide gauge or altimeter measurements were available at higher latitudes in proximity to GrIS, where the highest gradients in the predicted structure of the sea level fingerprint occur (*20*), or if ocean dynamic variability unrelated to the ice melt can be isolated from sea level records.

Detection efforts to date have largely focused on sea level records outside the zone of major sea level fall, where the gradients and amplitudes of the fingerprint signal are considerably lower (*21*–*23*). Notably, Hsu and Velicogna (*22*) compared Gravity Recovery and Climate Experiment (GRACE)–based global sea level fingerprint predictions with ocean bottom pressure data from sensors in the tropics and determined that the fingerprints agreed with the annual phase of data and differed from the barystatic estimate at two of eight stations. Davis and Vinogradova (*21*) demonstrated that the fingerprint of GrIS ice mass loss had measurable influence on tide gauge records of sea level acceleration along the eastern US coast since the mid-1990s. Moreira *et al*. (*23*) compared modeled sea level fingerprints with steric-corrected altimetry-based sea level data in the Atlantic Ocean surrounding south-eastern Greenland (among other regions) over a 10-year period. Despite low signal-to-noise ratios, they found that 25% of the variance in the altimetry-derived dataset is explained by a sea level fingerprint. However, observational datasets used in this study only extend to 65°N, and thus the majority of the ocean around Greenland was not captured. In this work, we built on these previous results to provide a statistically rigorous, unambiguous detection of the fingerprint signal from GrIS ice mass loss in sea surface height (SSH) trends encircling the ice sheet.

[1]Fluid Dynamics and Solid Mechanics Group, Los Alamos National Laboratory, Los Alamos, NM, USA. [2]Department of River-Coastal Science and Engineering, Tulane University, New Orleans, LA, USA. [3]Department of Earth and Planetary Sciences, Harvard University, Cambridge, MA, USA. [4]Center for Space Research, University of Texas, Austin, TX, USA. [5]Institute of Geophysics and Planetary Physics, University of California, San Diego, CA, USA.
***Corresponding author. Email: slcoulson@lanl.gov**

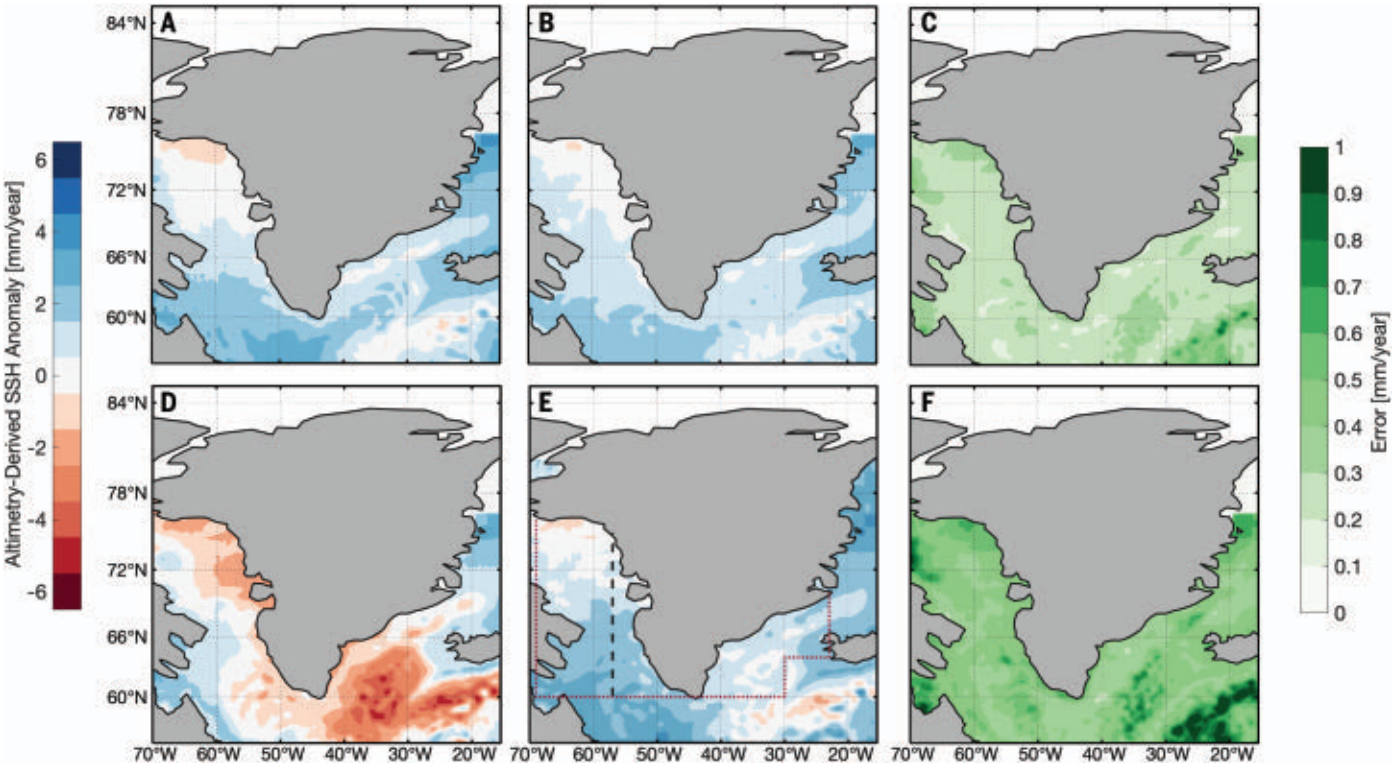


Fig. 1. Observed trends in SSH anomalies in the vicinity of Greenland. (**A**) Altimetry-derived mean SSH trends in millimeters per year over the period 1993–2019 (*26*–*28*). (**B**) As in (A), but corrected for ocean dynamic variability (Fig. 2). (**C**) The associated error estimate (based on an autoregressive process of the order 1) in this corrected signal. (**D** to **F**) As in (A) to (C), except for the shorter time period 2002–2019. The red dotted box and black dashed line in (E) denote a region and profile considered in the comparative analysis of Fig. 4.

We analyzed updated multimission altimetry records and corrected for the ocean dynamic variability signal to compute residual observational trends in sea surface height anomaly extending up to 80°N. We then compared these SSH trends with predicted sea level fingerprints using classical sea level modeling over a 27-year period and an 18-year period. The two time periods were considered separately to demonstrate robustness; the longer time range, from 1993 to 2019, includes the full observational period, taking advantage of all multimission altimetry data available, whereas the shorter time range, from 2002 to 2019, highlights a period of increased melting of the ice sheet (*19*, *24*–*26*).

Satellite altimetry has provided measurements of SSH anomalies since the early 1990s. The Copernicus Marine Environment and Monitoring Service (CMEMS) (*27*) reprocesses multimission altimetry records, and the most recent analysis is based on the Data Unification Altimeter Combination System (DUACS) DT2018 [see figure 1 of (*26*)]. After filling data gaps at higher latitudes (see supplementary materials), we used these observational records to compute mean trends over the periods 1993–2019 and 2002–2019 (Fig. 1, A and D). Notably, in the North Atlantic, the observations from the DUACS altimeter processing extend up to 80°N (Fig. 1), although their temporal availability decreases northward (fig. S1). The effective spatial resolution of the data is estimated to vary from ~100 km at the southern tip of Greenland, decreasing to ~250 km at 72°N in Baffin Bay on the west side of GrIS, and to ~150 km at 66°N on the east side between Greenland and Iceland (*28*). No estimate of resolution is provided for sites above 72°N in (*28*).

Over the 1993–2019 period, SSH anomaly rates off the west and south coast of Greenland trend downward toward the coastline in a concentric structure indicative of a Greenland ice melt fingerprint (Fig. 1A). Rates over the shorter 2002–2019 period (Fig. 1D) retain some of this spatial structure, but the SSH anomaly becomes generally noisier. The change in rates is particularly pronounced in the subpolar gyre region southeast of Greenland, where rates reverse sign from positive since 1993 to negative since 2002. These decadal rate changes in the subpolar gyre region have previously been linked to changes in (largely wind-driven) large-scale ocean circulation changes (*29*, *30*). Indeed, the subpolar gyre region has been transitioning from a period of strong warming between the early 1990s and mid-2000s to a cooling thereafter (*29*), and the signal has also been propagating up into the coastal zones of the northeastern Labrador Sea (Fig. 2).

One approach to isolating the nonuniform geometry of sea level fingerprints is by estimating depth-integrated steric height changes from temperature and salinity fields and removing them from altimetric SSH (*23*). Although this may work well in the deep ocean away from a melt source, SSH changes in the vicinity of an ice sheet can involve both deep and shallow ocean (fig. S1B). The latter is dominated by dynamic ocean mass redistribution, which is reflected in ocean bottom pressure changes rather than the steric height (fig. S2) (*14*). In the North Atlantic, this dynamic ocean mass variability has been shown to be tightly linked to variations in large-scale wind stress forcing (*31*). We therefore used an alternative approach, in which we identified common interannual variability between SSH and wind stress curl over the extratropical North Atlantic sector with a maximum covariance analysis and used the leading modes of wind stress curl as predictors for a regression with SSH (see supplementary materials). Depending on location, this regression explains up to 90% of the local SSH variability around Greenland (Fig. 2B; median explained variability over the entire domain is 69%) and captures well the decadal trends in the

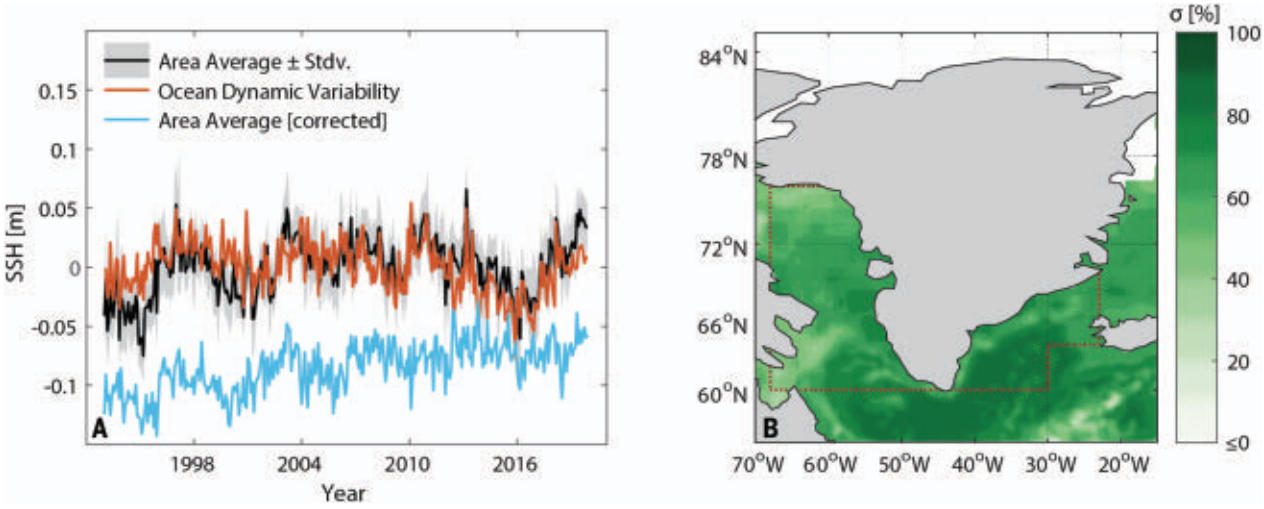


Fig. 2. Correction of ocean dynamic variability across the study area. (**A**) SSH time series before (gray and black) and after (blue) removing ocean dynamic variability associated with wind stress forcing (red) averaged over the area bounded by the red box in (B) over the period 1993–2019. Note that a vertical offset of ~0.08 m has been applied to the blue time series for better visibility. The correlation between the area average of SSH and ocean dynamic variability is 0.79. (**B**) Variance explained by the maximum covariance analysis regression (as an estimate of ocean dynamic variability) at each grid point around Greenland.

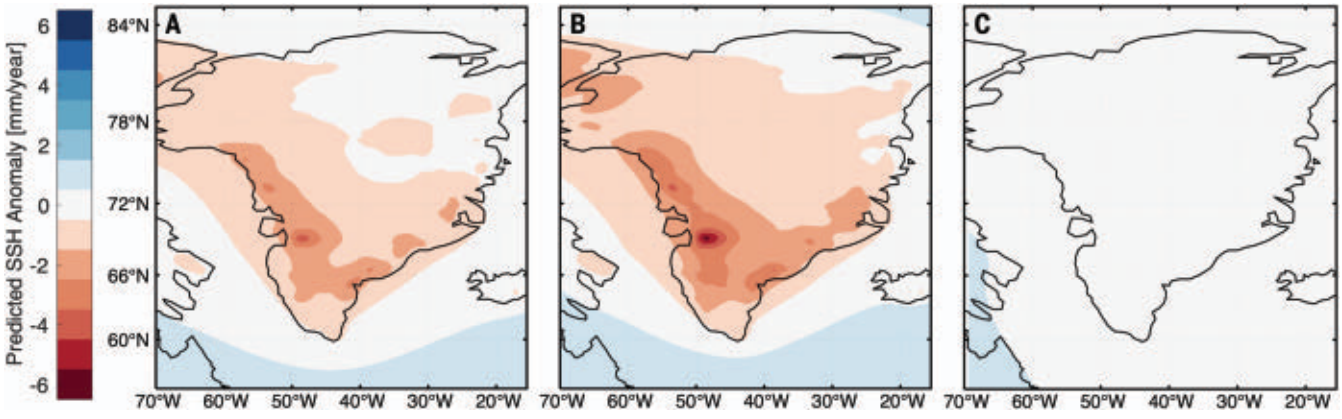


Fig. 3. Predicted trends in SSH anomalies in the vicinity of Greenland. Trend in SSH over the periods (**A**) 1993–2019 and (**B**) 2002–2019 (millimeters per year) computed using a radar altimetry–derived record of Greenland Ice Sheet mass balance over the same period (*19*) and model reconstructions of Greenland peripheral and nearby glaciers (*33*). (**C**) Ongoing trends in SSH due to ongoing glacial isostatic adjustment associated with the last ice age, computed using the ICE-6G_C/VM5a model of GIA (*37*).

extended subpolar gyre region (Fig. 2A). Thus, the regression accounts for a significant fraction of both spatiotemporal variability in steric height as well as ocean dynamic mass redistribution. When this signal is removed from the altimetric SSH field, the time series become less noisy (Fig. 2A) and the spatial trend patterns over the two time periods become more similar (Fig. 1, B and E). Additionally, because of the removal of ocean-internal variability, the trend estimation error is significantly reduced (the median reduction is ~45% over the entire region).

We predicted the rate of SSH change over the periods 1993–2019 and 2002–2019 by adopting a reconstruction of GrIS mass balance estimated from an analysis of multisatellite Ku-band altimetry measurements for the main ice sheet (*19*) and a model reconstruction of the glaciers at the periphery of the ice sheet and in nearby regions (Arctic Canada and Iceland) forced with the ERA5 global climate reanalysis (*32*, *33*). We calculated gravitationally self-consistent sea level changes using the theory and pseudo-spectral algorithm described in (*34*), with truncation at spherical harmonic degree and order 512 (Fig. 3, A and B), neglecting the effect of Earth's rotation to be consistent with the orientation of the reference frame assumed in altimetry. In addition to the recent ice history in Greenland, the simulation requires a model for the rheological structure of the solid Earth. For this purpose, we adopted a depth-varying Maxwell viscoelastic model in which the seismically inferred Preliminary Reference Earth Model (PREM) (*35*) provides depth-varying elastic and density profiles through Earth's crust and mantle. The model has an upper-mantle viscosity of 10^{20} Pa s, consistent with the inference of (*36*), which is based on the crustal response to recent ice mass flux, and a lower mantle viscosity of 5×10^{21} Pa s. The elastic response strongly dominates (to >90%) the total predicted signal. For direct comparison to the altimetry-derived datasets, we considered the modeled change in SSH rather than the full calculated sea level change, where the latter includes

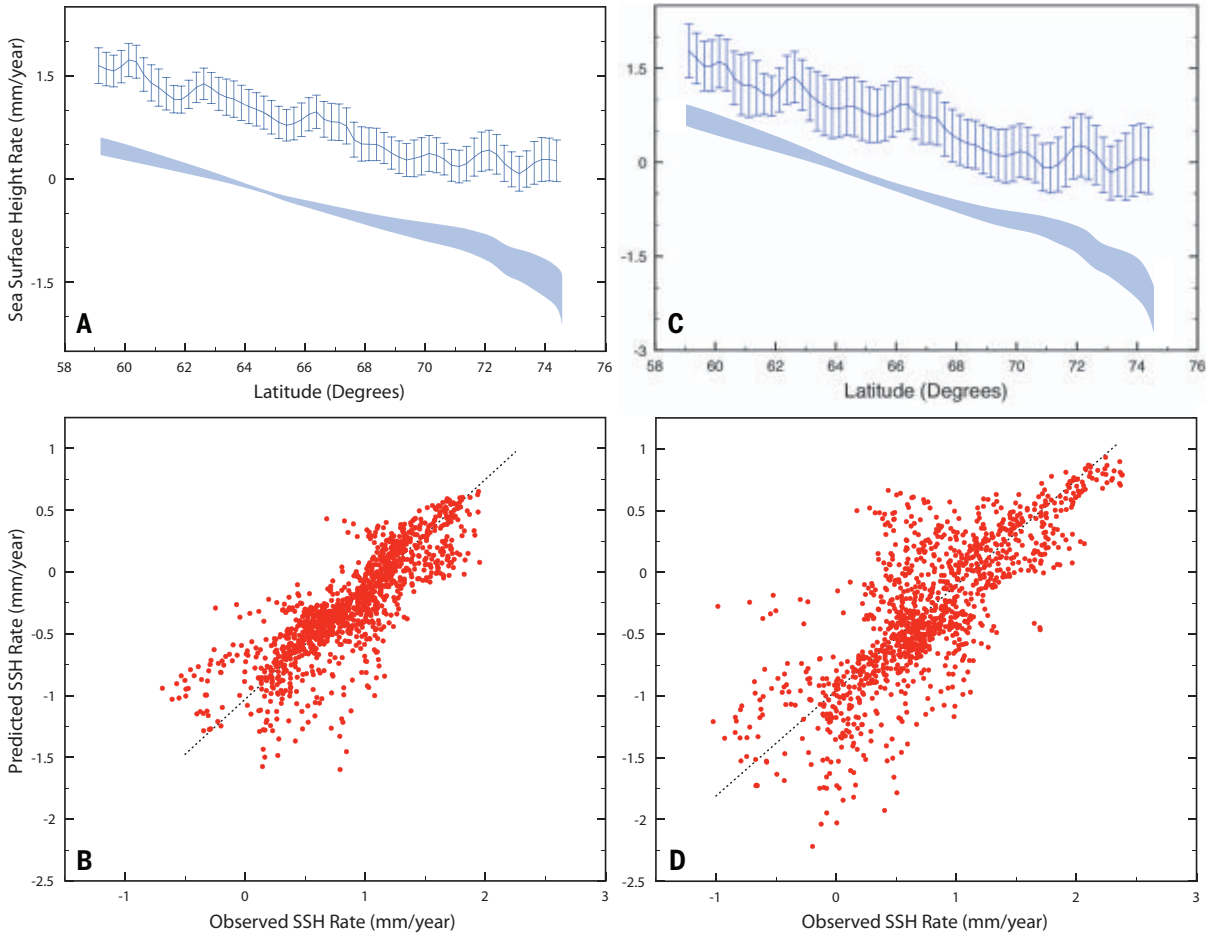


Fig. 4. Comparison of predicted and observed SSH trends in the vicinity of Greenland. Trends over the periods (**A** and **B**) 1993–2019 and (**C** and **D**) 2002–2019. [(A) and (C)] Altimetry-derived mean SSH trends [(*26*–*28*); corrected for ocean dynamic variability], corresponding to Fig. 1, B and E, respectively, along the black dashed profile shown in Fig. 1E (blue line, with error bars taken from Fig. 1, C and F). Trends along the same profile computed using a radar altimetry–derived record of GrIS mass balance (*19*) and model reconstructions of Greenland peripheral and nearby glaciers [(*33*); blue shading, corresponding to Fig. 3, A and B, respectively]. The shading accounts for errors in the ice mass history reported in (*19*, *33*). [(B) and (D)] Predicted SSH rates associated with modern melting of the GrIS (Fig. 3, A and B) versus observed rates (Fig. 1, B and E). Best-fitting slopes given in dashed black. The two fields are sampled within the red box shown in Fig. 1E.

changes in bathymetry not captured in satellite altimetry observations. We also performed a reference frame shift to the center of mass of the Earth system (i.e., a system including surfaces masses). The resulting trend maps (Fig. 3, A and B) reveal the typical fingerprint structure, with a predicted fall in SSH across most of the region covered by the figure, with progressively larger magnitude toward the site of the ice mass flux.

As we have noted, previous analyses of GrIS mass flux indicate that a major increase in melt rate of the Greenland ice sheet began in ~2002 (*19*, *24*–*26*). (The mean melt rates included in our calculation are 0.74 mm/year across the period 1993–2019 and 1.10 mm/year across the period 2002–2019, in units of equivalent GMSL rise.) This increase is apparent in the higher magnitude of the predicted signal in Fig. 3B relative to Fig. 3A. However, this difference is relatively localized to the zone of melting, and the signal over the ocean in the two cases is highly similar. This similarity explains the consistency of the corrected observational trends across the same two periods (Fig. 1, B and E).

In addition to predicting the impact of modern GrIS ice mass loss on SSH change, we performed a simulation to determine the ongoing impact of the last ice age on SSH in the region (Fig. 3C). We reserve the term glacial isostatic adjustment (GIA) for this signal. The GIA calculation was performed using the same sea level theory and algorithm as above (*34*) and is based on the paired models of the ICE-6G_C ice history from the Last Glacial Maximum onward and the VM5a viscosity model (*37*). The prediction based on this model shows little structure and varies by only ~0.2 mm/year across the entire region.

The observed SSH trends (Fig. 1, B and E) include all signals that contribute to the sea level field, including those associated with other areas of ice mass flux, long-term global-mean steric effects and terrestrial water storage. These additional signals are likely to be smooth across the North Atlantic region (low or zero gradient) (*15*). Thus, a positive offset between the observed trends and our prediction from recent GrIS (and neighboring) mass flux (Fig. 3, A and B) is expected. The detection of the latter fingerprint signal in the former must therefore be based on regional gradients in the signals. In this regard, a correlation between the maps of observed SSH trends and the predicted trends—both reflecting the hallmarks of a fingerprint geometry—is qualitatively apparent.

A preliminary examination of this correlation is provided in Fig. 4, A and C, in which the observed (blue line with vertical error bars) and predicted (blue shaded region) signals along the single north-south profile

shown in Fig. 1E are directly compared, for the time windows 1993–2019 and 2002–2019, respectively. The predicted signal in both frames accounts for the uncertainty in the altimetry-derived mass loss history (*19*, *33*). The two signals track each other closely over both time periods, showing comparable trends toward higher rates moving southward along the profiles.

Next, we extended the above analysis by sampling the observed and predicted SSH trends (Figs. 1, B and E, and 3, A and B) within a geographic region bounded by the red dotted box in Fig. 1E. The southern and eastern borders of the box are constrained to avoid the localized SSH anomaly in the subpolar gyre region (in the North Atlantic south of Greenland and Iceland). Moreover, any grid points associated with SSH observations within 30 km of the shoreline are omitted because of reduced data reliability in the vicinity of the coast (*38*). Figure 4, B and D, shows scatterplots of the results for time windows 1993–2019 and 2002–2019, respectively. The best-fitting slopes for the observed versus predicted SSH trends are 0.89 for the period 1993–2019 and 0.89 for the period 2002–2019. This analysis accounts for the variation in spatial resolution as a function of latitude (*28*) using a weighting approach. (As noted above, the resolution varies from ~100 km at the southern tip of Greenland, decreasing to ~150 km at 66°N and 250 km at 72°N. North of 72°N, we assume that the resolution remains at 250 km.) Accounting for errors in both the observed SSH trends and the model predictions (see supplementary materials), the Pearson correlation coefficient between the samples is 0.83 ± 0.26 for the 1993–2019 period and 0.77 ± 0.20 for the 2002–1993 period. Both the best-fit analysis and the correlation coefficients indicate a strong and statistically significant linear association ($P < 0.001$) between the predictions and the observations.

To gain insight into the origin of the scatter in Fig. 4, B and D, we computed maps of the distance between each point in these figure panels and the associated best-fit line (fig. S4). The result indicates that departures from the best-fit line are relatively small across the region, with the exception of sites close to the shoreline of Greenland and in the vicinity of the subpolar gyre. As noted above, the former may arise from the decrease in accuracy of the altimetry measurements of SSH close to shorelines. The latter suggests that a residual ocean dynamic signal exists in the vicinity of the subpolar gyre after the correction based on the maximum covariance analysis, particularly for the shorter time span 2002–2019.

Recent updates to multimission altimetry records (*26*–*28*) provide almost three decades of observations of SSH trends extending up to 80°N. This latitude range allows for examination of the largest amplitudes and gradients of the sea level fingerprint generated by GrIS melt. The analyses herein indicate that, after the removal of ocean dynamic variability, the geographic variation in the observed SSH trends in the oceans encircling Greenland, over the periods 1993–2019 and 2002–2019, are dominated by the sea level fingerprint produced by modern melting of GrIS and nearby glacier systems. These analyses provide a statistically significant detection of the sea level fingerprint of modern ice mass flux. Our results demonstrate that fingerprint geometries are rapidly established within the global oceans, they independently affirm the accuracy of altimetry-based constraints on SSH variations and polar ice mass flux, and they validate theoretical and numerical frameworks for predicting patterns of gravitationally self-consistent sea level change. Furthermore, the approach we have described that isolates decadal signals by means of a maximum covariance analysis regression with wind fields is universally applicable and markedly shortens the time scale necessary for fingerprint detection by overcoming several major obstacles; namely, that a steric height correction for ocean dynamic variability is inappropriate on shallow shelves and temperature and salinity data are generally more uncertain in polar regions. The combination of near-field sea level records with this analysis procedure can be applied in future efforts to detect sea level fingerprints of ice mass flux for all polar ice sheets and large-scale glacier systems, thus providing important additional constraints on their relative contributions to the budget of GMSL and on pressing efforts to perform accurate projections of the global geometry of sea level changes in our progressively warming world.

REFERENCES AND NOTES

1. J. Bamber, R. Riva, *Cryosphere* **4**, 621–627 (2010).
2. S. E. Brunnabend, J. Schröter, R. Rietbroek, J. Kusche, *J. Geophys. Res. Oceans* **120**, 7316–7328 (2015).
3. J. Clark, C. S. Lingle, *Nature* **269**, 206–209 (1977).
4. J. Clark, J. Primus, in *Sea-Level Changes*, M. J. Tooley, I. Shennan, Eds., vol. 20 of *Institute of British Geographers Special Publications* (Basil Blackwell, 1987), pp. 356–370.
5. C. P. Conrad, B. H. Hager, *Geophys. Res. Lett.* **24**, 1503–1506 (1997).
6. J. Mitrovica *et al.*, *Geophys. J. Int.* **187**, 729–742 (2011).
7. J. X. Mitrovica, M. E. Tamisiea, J. L. Davis, G. A. Milne, *Nature* **409**, 1026–1029 (2001).
8. H.-P. Plag, *Philos. Trans. A Math Phys. Eng. Sci.* **364**, 821–844 (2006).
9. H.-P. Plag, H.-U. Juettner, *Mem. Nat. Inst. Polar Res* **54**, 301–317 (2001).
10. G. Spada, G. Galassi, *Global Planet. Change* **143**, 34–49 (2016).
11. M. Tamisiea, J. Mitrovica, G. Milne, J. Davis, *J. Geophys. Res. Solid Earth* **106**, 30849–30863 (2001).
12. J. M. Gregory *et al.*, *Surv. Geophys.* **40**, 1251–1289 (2019).
13. C. C. Hay, E. Morrow, R. E. Kopp, J. X. Mitrovica, *Nature* **517**, 481–484 (2015).
14. S. Dangendorf *et al.*, *Nat. Clim. Chang.* **11**, 514–520 (2021).
15. B. D. Hamlington *et al.*, *Rev. Geophys.* **58**, RG000672 (2020).
16. WCRP Global Sea Level Budget Group, *Earth Syst. Sci. Data* **10**, 1551–1590 (2018).
17. J. W. Fiedler, C. P. Conrad, *Geophys. Res. Lett.* **37**, L12603 (2010).
18. W. B. Hawley, C. C. Hay, J. X. Mitrovica, R. E. Kopp, *Earths Future* **8**, EF001497 (2020).
19. S. B. Simonsen, V. R. Barletta, W. T. Colgan, L. S. Sørensen, *Geophys. Res. Lett.* **48**, e2020GL091216 (2021).
20. R. E. Kopp *et al.*, *Clim. Change* **103**, 619–625 (2010).
21. J. L. Davis, N. T. Vinogradova, *Geophys. Res. Lett.* **44**, 5133–5141 (2017).
22. C. W. Hsu, I. Velicogna, *Geophys. Res. Lett.* **44**, 8953–8961 (2017).
23. L. Moreira, A. Cazenave, A. Barnoud, J. Chen, *Remote Sens.* **13**, 4667 (2021).
24. W. Colgan *et al.*, *GEUS Bulletin* **43**, e2019430201 (2019).
25. J. Mouginot *et al.*, *Proc. Natl. Acad. Sci. U.S.A.* **116**, 9239–9244 (2019).
26. G. Taburet *et al.*, *Ocean Sci.* **15**, 1207–1224 (2019).
27. CMEMS, Global Ocean Mean Sea Level trend map from Observations Reprocessing: GLOBAL_OMI_SL_regional_trends, Copernicus Climate Change Service (2021); https://doi.org/10.48670/moi-00238.
28. M. Ballarotta *et al.*, *Ocean Sci.* **15**, 1091–1109 (2019).
29. L. Chafik, J. E. Ø. Nilsen, S. Dangendorf, G. Reverdin, T. Frederikse, *Sci. Rep.* **9**, 1041 (2019).
30. A. Ruiz-Barradas, L. Chafik, S. Nigam, S. Häkkinen, *Tellus A Dyn. Meterol. Oceanogr.* **70**, 1481688 (2018).
31. C. G. Piecuch, R. M. Ponte, *Geophys. Res. Lett.* **41**, 4261–4269 (2014).
32. H. Hersbach *et al.*, *Q. J. R. Meteorol. Soc.* **146**, 1999–2049 (2020).
33. J.-H. Malles, B. Marzeion, *Cryosphere* **15**, 3135–3157 (2021).
34. R. A. Kendall, J. X. Mitrovica, G. A. Milne, *Geophys. J. Int.* **161**, 679–706 (2005).
35. A. M. Dziewonski, D. L. Anderson, *Phys. Earth Planet. Inter.* **25**, 297–356 (1981).
36. S. Adhikari *et al.*, *Geophys. Res. Lett.* **48**, e2021GL094040 (2021).
37. W. R. Peltier, D. Argus, R. Drummond, *J. Geophys. Res. Solid Earth* **120**, 450–487 (2015).
38. Climate Change Initiative Coastal Sea Level Team, *Sci. Data* **7**, 357 (2020).
39. S. Coulson *et al.*, Datasets for "A Detection of the Sea Level Fingerprint of Greenland Ice Sheet Melt" Coulson *et al.*, 2022, Science, Zenodo (2022); https://doi.org/10.5281/zenodo.7041622.

ACKNOWLEDGMENTS

We thank S. Simonsen and J.-H. Malles for providing observational and modeled mass balance datasets and advice on how to use them. We acknowledge M. Hoffman for useful discussions on availability and use of ice sheet and glacier model predictions and ocean dynamic and steric datasets. We thank our two anonymous reviewers for constructive reviews that greatly improved the manuscript. **Funding:** S.C. is supported by a Los Alamos National Laboratory Director's Postdoctoral Fellowship. J.X.M. receives funding from the John D. and Catherine T. MacArthur Foundation and Harvard University. S.D. acknowledges NASA grant 80NSSC20K1241 and David and Jane Flowerree for funding. L.P. is supported by the Fonds de Recherche du Québec–Nature et technologies, the Natural Sciences and Engineering Research Council of Canada, and (with J.X.M.) the Star-Friedman Challenge. **Author contributions:** S.C. and J.X.M. designed the research after the original suggestion of D.T.S. S.C. processed ice mass balance datasets. S.C. and J.X.M. performed sea level simulations. M.E.T. advised on transforming the predictions to a reference frame consistent with altimetry datasets. S.D. processed the altimetry dataset and performed maximum covariance analysis to remove ocean dynamic variability. L.P. and J.X.M. performed statistical analyses with input from M.E.T. and S.D. S.C., J.X.M., and S.D. wrote the original manuscript text, which was revised with input from all the other coauthors. **Data and materials availability:** Grids of the altimetry-derived sea surface height trend corrected for ocean dynamic variability and model predicted trends in sea surface height (shown in Figs. 1 and 3, respectively) are available for download at Zenodo (*39*). **License information:** Copyright © 2022 the authors, some rights reserved; exclusive licensee American Association for the Advancement of Science. No claim to original US government works. https://www.science.org/about/science-licenses-journal-article-reuse

SUPPLEMENTARY MATERIALS

science.org/doi/10.1126/science.abo0926
Materials and Methods
Figs. S1 to S4
References (*40*–*54*)

Submitted 19 January 2022; accepted 6 September 2022
10.1126/science.abo0926

MEMBRANES

Hydrophobic polyamide nanofilms provide rapid transport for crude oil separation

Siyao Li[1], Ruijiao Dong[1,2], Valentina-Elena Musteata[3], Jihoon Kim[1,4,7], Neel D. Rangnekar[5], J. R. Johnson[5], Bennett D. Marshall[5], Stefan Chisca[3], Jia Xu[1,6], Scott Hoy[5]†, Benjamin A. McCool[5], Suzana P. Nunes[3], Zhiwei Jiang[1,7]*, Andrew G. Livingston[1,7]*

Hydrocarbon separation relies on energy-intensive distillation. Membrane technology can offer an energy-efficient alternative but requires selective differentiation of crude oil molecules with rapid liquid transport. We synthesized multiblock oligomer amines, which comprised a central amine segment with two hydrophobic oligomer blocks, and used them to fabricate hydrophobic polyamide nanofilms by interfacial polymerization from self-assembled vesicles. These polyamide nanofilms provide transport of hydrophobic liquids more than 100 times faster than that of conventional hydrophilic counterparts. In the fractionation of light crude oil, manipulation of the film thickness down to ~10 nanometers achieves permeance one order of magnitude higher than that of current state-of-the-art hydrophobic membranes while retaining comparable size- and class-based separation. This high permeance can markedly reduce plant footprint, which expands the potential for using membranes made of ultrathin nanofilms in crude oil fractionation.

Separation and purification play a crucial role in the oil and gas industry but rely on energy-intensive distillation processes, which account for 10 to 15% of global energy use (*1*). Membrane-based separation has emerged as a promising alternative because of its innate advantage of low energy consumption. One successful example is the production of fresh water from seawater by reverse osmosis (*2*). Thin-film composite membranes that are manufactured by means of interfacial polymerization show exceptional water permeance and high salt rejection, which is achieved through their thin and highly crosslinked polyamide selective layer (*2*). In search of a similar paradigm change, organic solvent reverse osmosis has been developed for molecular separations in organic liquids (*3*, *4*) and applied to the fractionation of crude oil (*5*, *6*).

However, thin-film composite membranes made from conventional chemistry exhibit limited permeance of hydrocarbon liquids, owing to the hydrophilic nature of polyamide or polyester networks in the separating layer (*7*–*9*). To enhance the hydrophobicity, attempts have been made to cap the polyamide layer with hydrophobic groups or introduce hydrophobic groups to the monomers used during the interfacial reaction (*10*–*15*). The permeance-selectivity range of the resulting membranes improved, but the permeance remains too low for industrial crude separation (*5*, *6*, *16*). Therefore, creating hydrophobic separating layers with high permeances for nonpolar liquids and tight selectivities for crude oil fractions remains of interest.

We report the fabrication of ultrathin hydrophobic polyamide nanofilms from vesicles of self-assembled multiblock oligomer amines (MOAs) by means of interfacial polymerization and their performance in hydrocarbon separations. Amphiphilic MOAs, which include a fluorine oligomer series and an alkane oligomer series, were synthesized by functionalizing the two ends of a hydrophilic precursor, pentaethylenehexamine (N_6), with hydrophobic inert oligomers containing R-OH (R = I to VI) (Fig. 1A and fig. S1). The two-step reaction used carbonyldiimidazole as a coupling agent, through which we tuned the MOA structure by attaching oligomers of increasing length. Nuclear magnetic resonance and Fourier transform infrared (FTIR) spectroscopy confirmed the formation of MOAs, including $F_5N_6F_5$, $F_9N_6F_9$, $F_{13}N_6F_{13}$, $C_3N_6C_3$, $C_6N_6C_6$, and $C_{10}N_6C_{10}$ (figs. S2 to S8).

MOAs were readily soluble in tetrahydrofuran (THF) and formed a clear solution (Fig. 1B). Upon the addition of water to reach a 95/5 water/THF mixture, when present above the critical aggregation concentration (CAC), the MOAs self-assemble into nanoscale micelles or vesicles (Fig. 1B and figs. S9 to S11) because of their inherent amphiphilicity (*17*). We conjecture that the spherical vesicles are composed of aggregated hydrophobic oligomers facing inward and extended hydrophilic amines facing outward to the aqueous solution (fig. S12) (*18*). Scanning electron microscope (SEM) and transmission electron microscope (TEM) images were consistent with the conjectured core-shell structure (Fig. 1B and figs. S13 and S14).

Amines on the outer shell of MOA vesicles can react with trimesoyl chloride at a free aqueous-organic interface to fabricate a highly cross-linked polyamide nanofilm (Fig. 1C). The nanofilm comprises smooth surfaces formed from the extended MOAs, with protuberances introduced by the vesicles present above the CAC. These nanofilms were flexible and robust, with no macroscopic defects observed while transferring them onto a water-air surface (Fig. 1D). When using more concentrated MOA solutions, nanofilms shrunk after transfer to the water surface (fig. S15 and movie S1), which is consistent with their hydrophobicity. Free-standing nanofilms were then adhered onto porous polymeric supports and used as composite membranes (fig. S16). Both SEM cross-sectional images (Fig. 1E) and atomic force microscopy (AFM) images (Fig. 1F) reveal the existence of vesicles in the nanofilms, with ~200-nm diameters (figs. S17 to S19), which matches well to the vesicle sizes measured in solution by using dynamic light scattering (fig. S11).

We hypothesized that the vesicles provide enhanced hydrophobicity across the nanofilm because of the aggregation of hydrophobic segments in MOAs. To verify this hypothesis, we produced smooth nanofilms without vesicles using an $F_5N_6F_5$ concentration below the CAC (Fig. 2A), which exhibited a water contact angle of ~74° (fig. S20). This increased to ~93° for membranes that incorporate vesicles by using concentrations above the CAC (Fig. 2B and fig. S20), which indicates high hydrophobicity (*19*) while retaining a similar cross-linking degree (fig. S21). TEM images and the corresponding element mapping demonstrate the fluorine distribution across the nanofilm (Fig. 2, C and D). The dispersed fluorine content in the smooth regions corresponded to nanofilms that were formed by extended MOAs, in contrast to concentrated fluorine intensity in the vesicles (Fig. 2C), which further enhanced with increasing MOA concentration (figs. S22 and S23). These results reveal the close proximity of fluorine oligomers inside the vesicles. The nanofilm was further stained with ruthenium tetroxide, which preferentially attaches to aromatic groups in the polyamide network (*20*). This enhances contrast and visibility of the polyamide separating layer under TEM (Fig. 2, E and F). A smooth nanofilm was formed at concentrations below the CAC, whereas flattened vesicles were observed in

[1]Barrer Center, Department of Chemical Engineering, Imperial College London, South Kensington Campus, London SW7 2AZ, UK. [2]Shanghai Center for Systems Biomedicine, Key Laboratory of Systems Biomedicine, Shanghai Jiao Tong University, Shanghai 200240, China. [3]King Abdullah University of Science and Technology, Biological and Environmental Science and Engineering Division, Advanced Membranes and Porous Materials Center, Thuwal 23955-6900, Saudi Arabia. [4]Process Design and Research Center, Chemical and Process Technology Division, Korea Research Institute of Chemical Technology, Daejeon 34114, South Korea. [5]Corporate Strategic Research, ExxonMobil Research and Engineering, Annandale, NJ 08801, USA. [6]Key Laboratory of Marine Chemistry Theory and Technology (Ministry of Education), School of Materials Science and Engineering, College of Chemistry and Chemical Engineering, Ocean University of China, Qingdao 266100, China. [7]School of Engineering and Materials Science, Queen Mary University of London, London E1 4NS, UK.
***Corresponding author. Email: zhiwei.jiang@qmul.ac.uk (Z.J.); a.livingston@qmul.ac.uk (A.G.L.)**
†Present address: Gas Phase Separations Division, Life Sciences and Applied Markets Group, Agilent Technologies, Wilmington, DE 19808, USA.

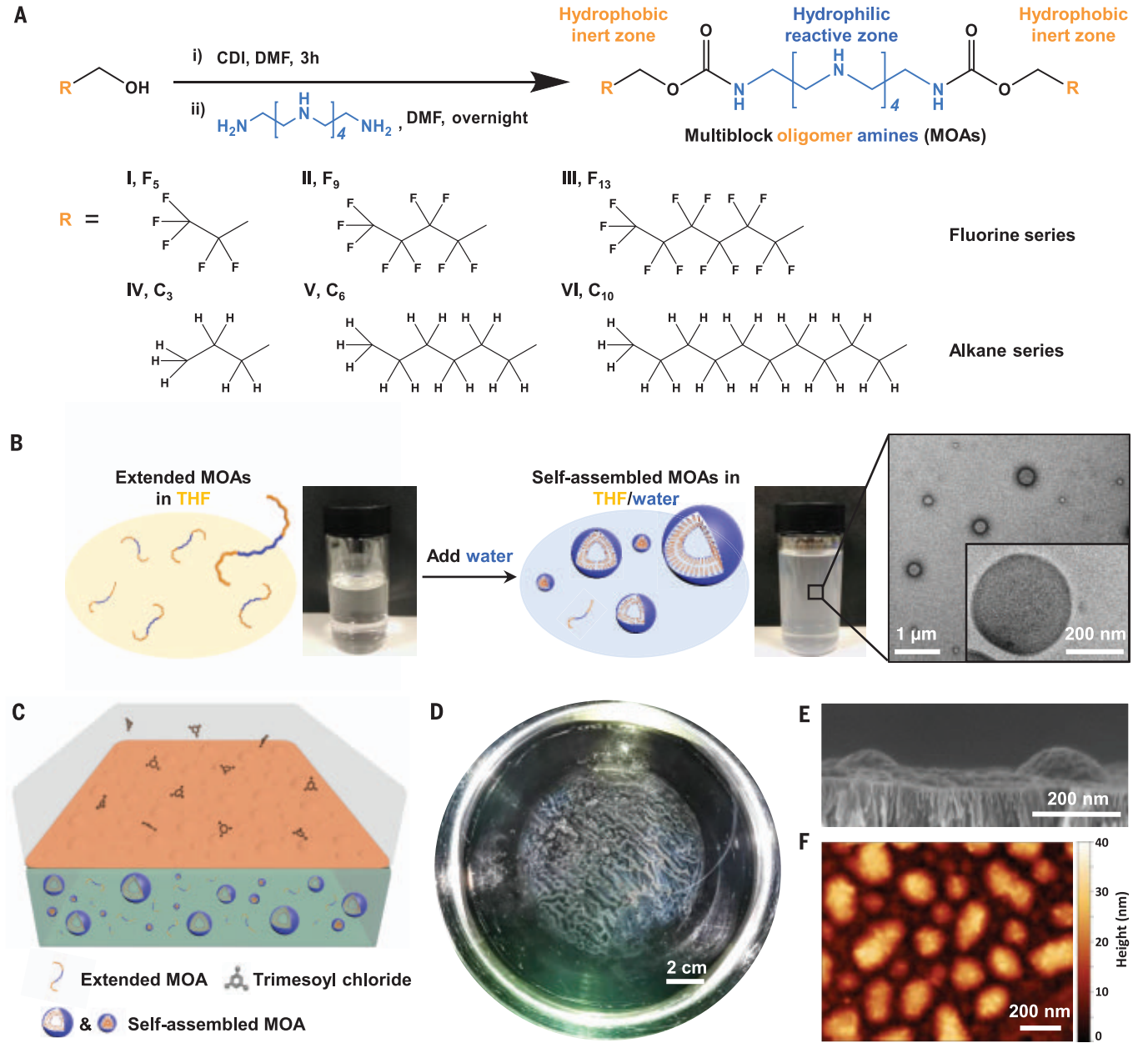


Fig. 1. Fabrication of hydrophobic polyamide nanofilms with MOAs. (**A**) Synthetic route to MOAs with different oligomers R-OH (R is I to VI) by using carbonyldiimidazole (CDI) as coupling agent. I = F_5, II = F_9, III = F_{13}, IV = C_3, V = C_6, and VI = C_{10}. (**B**) Schematic and photographs of extended MOAs in THF, which formed self-assembled micelles or vesicles by the addition of water. (Inset) A TEM image of $F_5N_6F_5$ (0.1 wt %) self-assembled MOAs with core-shell structure. (**C**) Fabrication of ultrathin polyamide nanofilms by interfacial polymerization at a free interface between a hexane phase containing trimesoyl chloride and an aqueous phase (95 wt % water and 5 wt % THF) containing MOAs. (**D**) Photograph of a free-standing nanofilm transferred from the free interface onto a water-air surface. (**E**) Cross-sectional SEM image of the ultrathin nanofilm transferred onto an alumina support. (**F**) AFM height image of the ultrathin nanofilm transferred onto a silicon wafer. Both images reveal the incorporation of MOA vesicles into the nanofilms.

nanofilms formed at MOA concentrations above the CAC. The high contrast across the vesicle surfaces reveals that the amines on the outer shell of vesicles reacted to form continuous cross-linked polyamide films during interfacial polymerization (Fig. 2F), which is chemically homogeneous with the smooth polyamide layer formed from extended MOAs. Furthermore, the interiors of the vesicles showed no signs of staining, which suggests a hollow structure beneath the ~30-nm-thick separating layer, despite the overall thickness of the vesicles being >100 nm. These vesicles were mechanically robust and conserved their structures after being pressurized at 10 bar (figs. S24 and S25). AFM images demonstrated that increasing the length of fluorine chains from $F_5N_6F_5$ to $F_{13}N_6F_{13}$ in MOA monomers led to a corresponding increase in the nanofilm thickness (Fig. 2, G and H, and figs. S26 to S28).

We hypothesized that the close proximity of hydrophobic chains in these vesicles provides rapid transport pathways for nonpolar liquids through the nanofilm. Further, MOA membranes could be activated by acetone to increase permeance. We assert that acetone activation rearranges the hydrophobic blocks

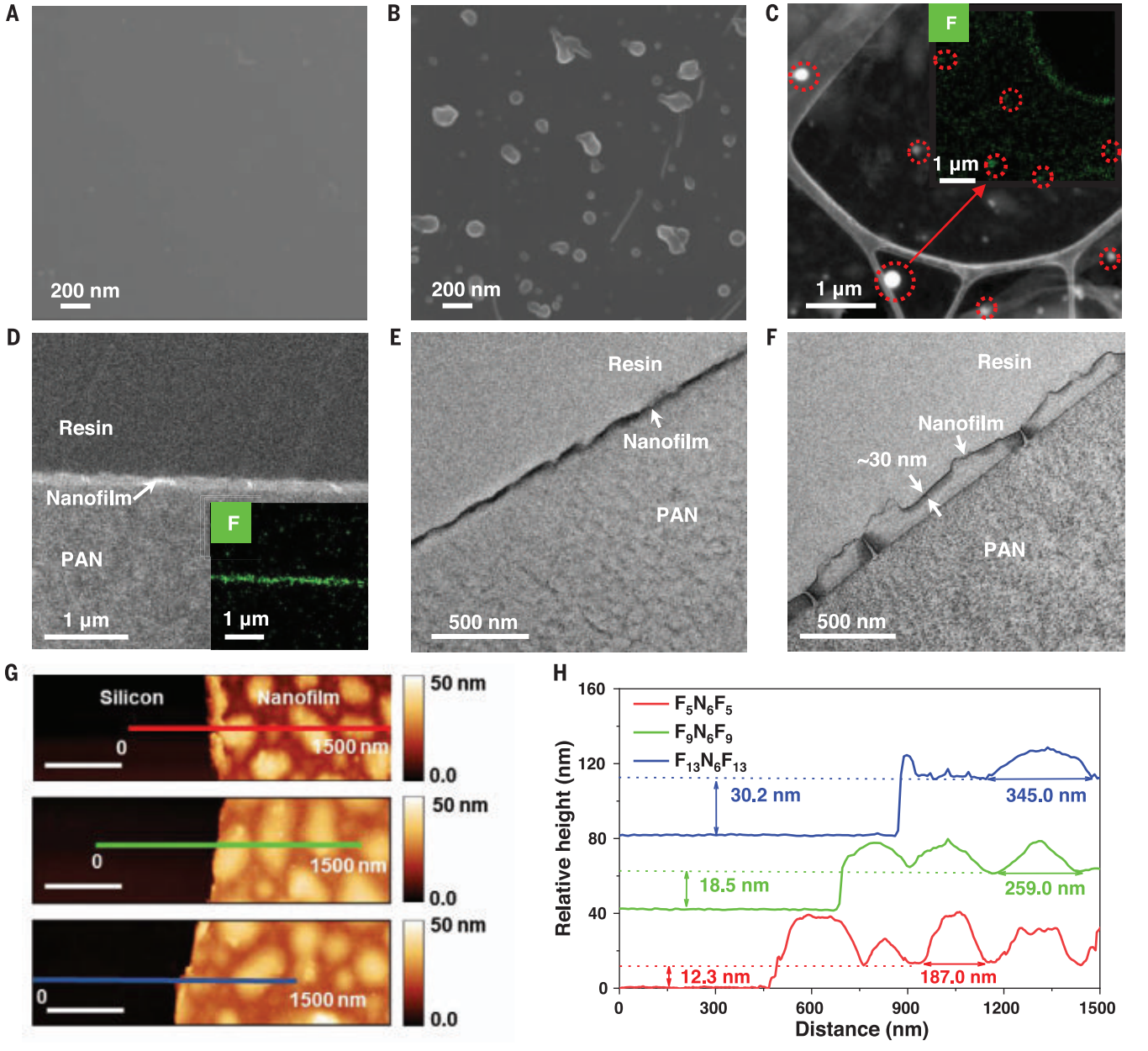


Fig. 2. Characterization of hydrophobic polyamide nanofilms fabricated from MOAs. (**A** and **B**) SEM surface images of MOA nanofilms fabricated at (A) $F_5N_6F_5$ concentration (0.005 wt %) below CAC and (B) $F_5N_6F_5$ concentration (0.02 wt %) above CAC. The protuberances correspond to the vesicles of self-assembled MOAs. (**C**) TEM images of nanofilms made by using 0.02 wt % $F_9N_6F_9$ and corresponding fluorine mapping from energy-dispersive x-ray (EDX) analysis (inset). (**D**) High-angle annular dark-field scanning TEM (HAADF-STEM) cross-sectional images of the nanofilm made by using 0.1 wt % $F_5N_6F_5$ and its EDX fluorine mapping (inset). PAN, polyacrylonitrile. (**E** and **F**) TEM cross-sectional images of the nanofilm made from $C_6N_6C_6$ at (E) low concentration (0.005 wt %) and (F) high concentration (0.1 wt %), in which the nanofilms were stained with ruthenium tetroxide to provide contrast for aromatic groups present in polyamide networks. The dense stripes in (F) reveal the active thickness of the nanofilm with hollow channels beneath. (**G** and **H**) AFM height (G) image and (H) profiles of $F_5N_6F_5$ (0.02 wt %), $F_9N_6F_9$ (0.02 wt %), and $F_{13}N_6F_{13}$ (0.025 wt %) nanofilms transferred onto silicon wafers for the measurement of nanofilm thickness. The profile lines across the protuberances provide width and height of MOA vesicles. Scale bar, 400 nm.

so that some of the initially inward-facing hydrophobic tails inside the vesicles extend from the outer surface (fig. S12). The activated $F_9N_6F_9$ membrane provided hexane permeance an order of magnitude higher as compared with the membrane before activation (Fig. 3A). This corresponded to an increase of the water contact angle from 82° to 98° after activation (Fig. 3A inset), which is consistent with exposure of the hydrophobic blocks (*11*). The net effect is creation of hydrophobic expressways for nonpolar solvents, which is similar to the ultrafast water transport through aquaporin membranes (*21*). Although conventional polyamide membranes exhibited enhanced permeance for all solvents after activation by dimethylformamide (DMF), MOA membranes showed a significant enhancement only for nonpolar solvents (figs. S29 and S30). Moreover, MOA membranes after DMF activation exhibited a relative increase in permeance approximnately eight times lower than those activated by acetone (fig. S31). Seeking to further explain this phenomenon, we examined the surface morphology, thickness,

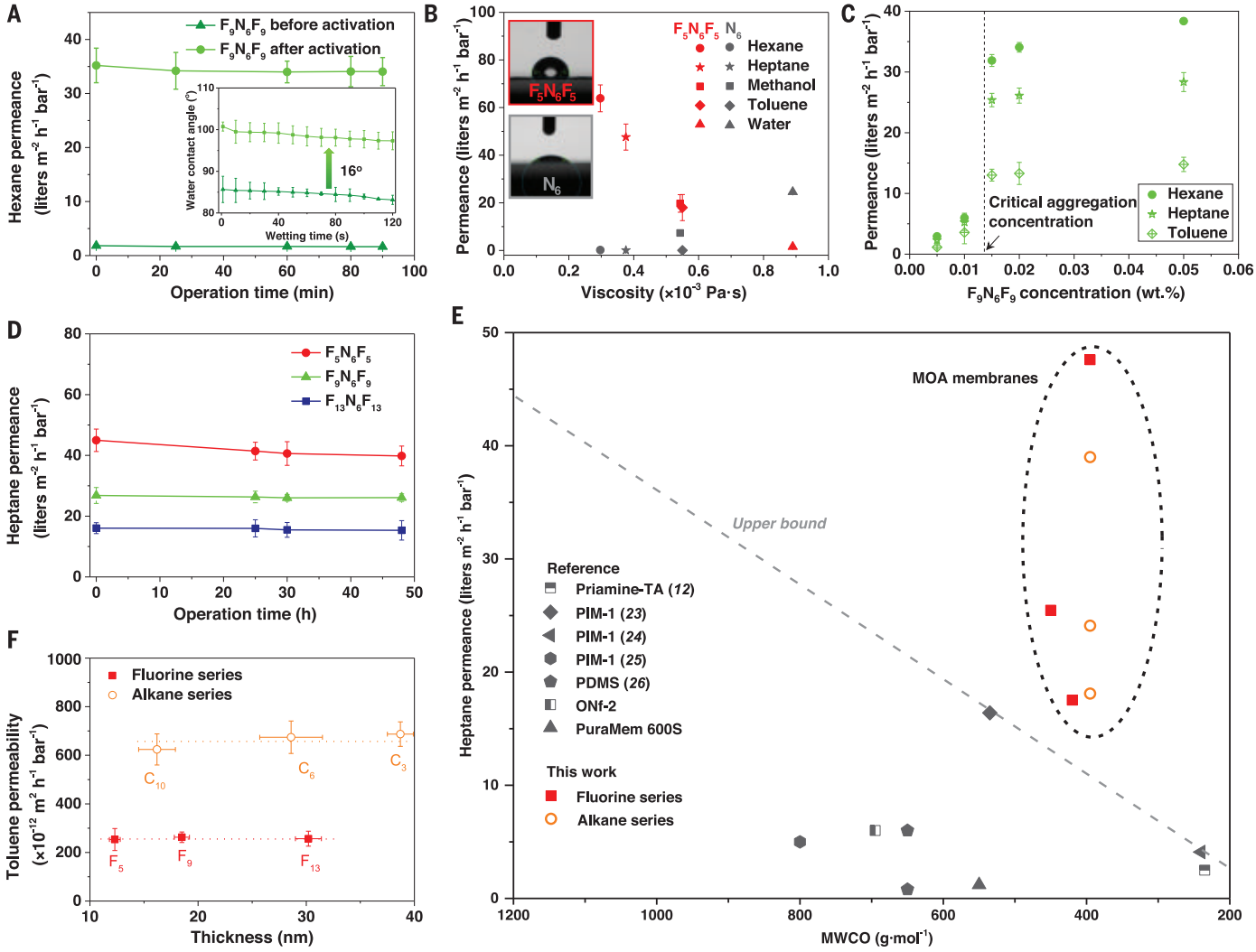


Fig. 3. Performance of nanofilms made from MOAs on PAN supports. (**A**) Hexane permeance for membranes made from 0.02 wt % $F_9N_6F_9$ before and after acetone activation. (Inset) The corresponding water contact angles. (**B**) Plot of solvent permeances through membranes made from 0.02 wt % $F_5N_6F_5$ and its precursor amine, pentaethylenehexamine (N_6), against the solvent viscosity, with both membranes being tested after acetone activation. (Inset) The water contact angle for both membranes. (**C**) Nonpolar solvent permeances including hexane, heptane, and toluene for $F_9N_6F_9$ membranes with increasing MOA concentrations. (**D**) Plot of heptane permeance against time for $F_5N_6F_5$, $F_9N_6F_9$, and $F_{13}N_6F_{13}$ membranes operating in a continuous crossflow rig. (**E**) Comparison of heptane permeance and molecular weight cut-offs for polystyrene markers between MOA membranes (this work) and membranes reported in the literature. MWCO, molecular weight cut-off; PDMS, polydimethylsiloxane; PIM-1, polymers of intrinsic microporosity–1. (**F**) Toluene permeability of membranes made from fluorine series ($F_5N_6F_5$, $F_9N_6F_9$, and $F_{13}N_6F_{13}$) and alkane series ($C_3N_6C_3$, $C_6N_6C_6$, and $C_{10}N_6C_{10}$) of MOAs. The error bars represent the standard deviation, which was calculated based on the results from three separate membranes.

and elemental composition of nanofilms before and after solvent activation (figs. S19, S21, and S28) and observed no notable differences. Therefore, we attribute the permeance boost to an increase in hydrophobicity that arises from the rearrangement of hydrophobic blocks at a molecular level upon acetone exposure.

To demonstrate the impact of hydrophobic oligomers, we used the precursor amine without oligomers, pentaethylenehexamine (N_6), to prepare hydrophilic polyamide nanofilms under identical conditions. This nanofilm was smooth, with no vesicles observed on the surface (fig. S19). Composite membranes comprising N_6 nanofilms showed no permeance increase after activation (fig. S32), exhibiting negligible permeances for nonpolar solvents, but showed high permeance for polar solvents, including water (Fig. 3B and table S1). By contrast, membranes that incorporated MOA vesicles reversed this trend, demonstrating fast transport for nonpolar solvents (Fig. 3B and fig. S33). For example, the hexane permeance reached 63.9 ± 5.6 liters m^{-2} hour^{-1} bar^{-1}, which is >100 times higher than that of N_6 membranes and other conventional hydrophilic polyamide membranes (*9*). This is consistent with the enhanced hydrophobicity of the MOA nanofilm, for which the water contact angle increased from 42° for the N_6 membrane to 93° for the $F_5N_6F_5$ membrane (Fig. 3B, inset).

To further evaluate the impact of vesicles, we prepared nanofilms with varying MOA concentrations (Fig. 3C and fig. S34). Below the CAC, no vesicles were formed in the aqueous phase, and the surface of the resulting nanofilms was relatively smooth (fig. S17) because the heat from the vigorous cross-linking reaction was efficiently dissipated through the bulk aqueous solution at the free interface (*22*). These pre-CAC membranes exhibited limited permeance increase after activation (fig. S35), with toluene permeance of 1.2 ± 0.3 liters m^{-2} hour^{-1} bar^{-1} recorded. This increased to

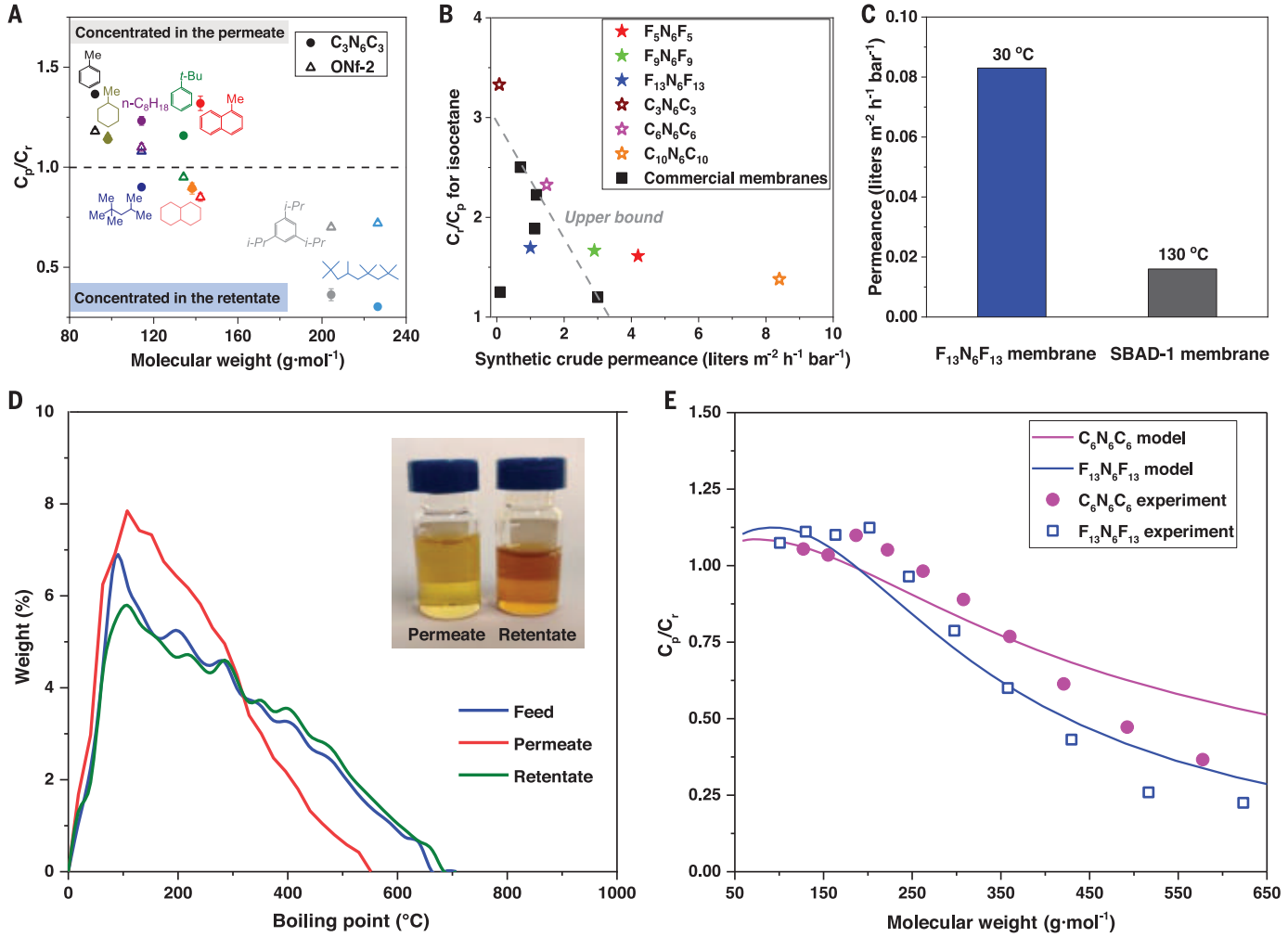


Fig. 4. Separation of synthetic and real crude oil by using nanofilm composite membranes made from MOAs. (**A**) Ratio of concentrations in permeate (C_p) versus retentate (C_r) of components in a synthetic crude oil fractionated by $C_3N_6C_3$ membrane and commercial benchmark, ONf-2 membrane (40 bar, 22°C, cross-flow conditions). Molecules above the reference dash line were more concentrated in the permeate as compared with the feed, whereas the molecules below the reference dash line were more concentrated in the retentate. (**B**) Comparison between membranes comprising MOAs ($F_5N_6F_5$, $F_9N_6F_9$, $F_{13}N_6F_{13}$, $C_3N_6C_3$, $C_6N_6C_6$, and $C_{10}N_6C_{10}$) and commercial membranes tested under the same conditions (40 bar, 22°C, cross-flow conditions), measured as C_r/C_p for iso-cetane (226.5 g mol^{-1}) and synthetic crude oil permeance. (**C**) Permeance of real light shale–based crude oil for $F_{13}N_6F_{13}$ membrane at 30°C and SBAD-1 membrane at 130°C, adapted from (*5*). (**D**) Boiling-point distribution of feed, permeate, and retentate from $F_{13}N_6F_{13}$ membrane fractionation of light shale–based crude oil. (Inset) Permeate (left) and retentate (right) solutions. (**E**) Comparison of C_p/C_r extracted from experimental simulated distillation curve of permeate and retentate to model predictions for $C_6N_6C_6$ membranes and $F_{13}N_6F_{13}$ membranes.

14.8 ± 1.2 liters m^{-2} hour^{-1} bar^{-1} for membranes incorporating vesicles made by using MOA concentrations above the CAC (Fig. 3C), despite thinner nanofilms and a similar cross-linking degree for the pre-CAC membranes (figs. S21 and S27). Although the permeance notably increased, the rejection performance remained unchanged (fig. S36).

One advantage of MOA membranes is the potential to manipulate their performance by tuning the oligomer length or chemistry. Heptane permeance increased as the fluorine chain length shortened from $F_{13}N_6F_{13}$ to $F_5N_6F_5$ (Fig. 3D) because of the thinner separating layer created (Fig. 2H). The permeances remained constant over 48 hours, which indicates no collapse of vesicles under 10 bar applied pressure (fig. S37). Polystyrene oligomers and dimer were dissolved in heptane to investigate their separation performance. The molecular weight cut-offs ranged from 395 to 450 g mol^{-1}, which is consistent with their dye rejections in methanol (fig. S38 and table S2). We plotted a trade-off between heptane permeance and molecular weight cut-off of polystyrene to compare the performance among MOA membranes, the commercial benchmarks ONf-2 and PuraMem 600S, and other membranes reported in literature (Fig. 3E and table S3) (*12*, *23*–*26*). MOA membranes exhibited separation performance well beyond the upper bound.

By tuning the chemistry of oligomers, composite membranes comprising a series of alkane MOA nanofilms were fabricated. The toluene permeability for MOA membranes comprising both fluorine and alkane series is shown in Fig. 3F. Within the same series, the toluene permeability remained unaltered, independent of the nanofilm thickness (Fig. 2H and fig. S27). Across different series, membranes made from the alkane MOAs provided more than double the permeability of the fluorine MOAs without compromising the rejection (fig. S38). This illustrates that the oligomer chemistry

in MOAs can tailor the permeance and permeability of the resulting membranes, which suggests that MOA membranes with designable oligomer functionality could be developed for dedicated separation tasks (*27*).

The ultrafast transport of nonpolar solvents and the material tunability make MOA membranes a promising candidate for fractionation of small hydrocarbon liquid molecules. Challenging the MOA membranes with a synthetic crude oil composed of a group of hydrocarbon molecules in a cross-flow filtration system (fig. S39 and table S4), we found that they demonstrated good separation of molecules on the basis of differences in size and class (Fig. 4A). In contrast to conventional binary separation systems such as polystyrenes in heptane, there is no designated solvent or solute in complex crude oil mixture fractionation. Thus, the membrane selectivity is presented as the ratio of permeate to retentate concentrations (C_p/C_r) for each component plotted against the molecular weight of the components. After >24 hours of continuous operation, the membranes made from MOAs, especially $C_3N_6C_3$ membranes, demonstrated much better size- and class-based selectivity compared with those of the ONf-2 membrane, which is the current commercial benchmark used for processing hydrocarbon liquids (Fig. 4A, fig. S40, and table S5). We speculate that the flexible alkane chains of $C_3N_6C_3$ in the membrane have a strong interaction with "structure-like" hydrocarbon molecules, which results in the retention of the larger species (*5*, *27*). Moreover, when elevating the system temperature from 22°C to 50°C, $C_3N_6C_3$ membranes displayed good thermal stability and increased permeance without compromising the selectivity, whereas ONf-2 membranes showed decreasing selectivity at high temperature (fig. S41). The trade-off between permeance and selectivity of the largest molecule, isocetane, for membranes tested with the synthetic crude oil is shown in Fig. 4B. The performance of most MOA membranes exceeded the upper bound compared with that of commercial membranes (table S6). This is due to the ultrathin MOA nanofilms formed through interfacial polymerization (*22*), which enable faster transport than that of commercial membranes with thick separating layers formed through phase inversion (*7*).

MOA membranes were further challenged with a real light shale–based crude oil. For this process, the SBAD-1 membrane is the current state-of-the-art membrane, with the highest permeance reported in literature (*5*, *6*). The permeance of the $F_{13}N_6F_{13}$ membrane was more than five times higher than that of SBAD-1 membrane, even operating at room temperature (30°C), whereas a high temperature (130°C) was needed for the SBAD-1 membrane to achieve comparable selectivity (Fig. 4C) (*5*). This is attributed to the ultrathin thickness of nanofilms fabricated by means of interfacial polymerization, whereas hundreds-of-nanometers-thick active layers were formed in the SBAD-1 membrane through the spin coating technique. The enhanced liquid permeance can substantially reduce the required membrane area, plant footprint, and hence the capital cost for any specific refinery capacity (*16*). The boiling point distribution of the feed, permeate, and retentate from the light shale–based crude is shown in Fig. 4D. The permeate has a cutoff at 550°C, whereas the feed and retentate boiling point range extends to 700°C. This demonstrates that the membrane rejects the heavy (residue) fraction of the crude oil. At the same time, the permeate was found to be appreciably enriched in the lighter molecules present in the feed so that >60 weight % (wt %) of the permeate had a boiling point below 400°C compared with 48 wt % observed in the feed. A two-dimensional gas chromotography (GC×GC) difference plot for the permeate and retentate samples further demonstrated that the permeate was lighter than the retentate, with high concentrations of light saturates and light aromatic molecules in the permeate, whereas there is rejection of heavier three- and four-ring aromatics (fig. S42). These results highlight the capabilities of MOA membranes in crude oil fractionation, providing enrichment of high-value light molecules and rejection of low-value heavy molecules while exhibiting the high permeances that industrial application demands. To demonstrate the scalability of this approach, conventional interfacial polymerization was carried out to fabricate in situ MOA membranes directly on the support (fig. S43). They showed satisfying separation performance in synthetic crude oil (fig. S44), which reinforces the potential for using these materials in large-scale industrial applications.

To understand the origin of the high selectivity by using MOA membranes in hydrocarbon separation systems, a modeling approach based on diffusion theory is proposed in the supplementary text, section 3. The model allows for the representation of membrane-based fractionation of crude oil on the basis of a single parameter, and it was applied to separations by using fluorine and alkane oligomers (tables S7 and S8). The model gives a good fit of the light shale–based crude oil separation data with the experimental results for the fluorine series ($F_{13}N_6F_{13}$ membranes) and alkane series ($C_6N_6C_6$ membranes), both having a crossover at molecular weight of ~200 g mol^{-1} (Fig. 4E). The $F_{13}N_6F_{13}$ membranes show a better retention for large hydrocarbon molecules than that of the $C_6N_6C_6$ membranes, which is consistent with the permeate boiling point cutoff results at 10% stage cut, 550°C for $F_{13}N_6F_{13}$ membranes and 590°C for $C_6N_6C_6$ membranes (fig. S45 and table S8). The increased retention of heavy species with $F_{13}N_6F_{13}$ membranes results from the low solubility of hydrocarbons in fluoropolymers (*28*).

By using MOAs for interfacial polymerization, we have fabricated ultrathin hydrophobic polyamide nanofilm membranes that incorporate vesicles from the self-assembled MOAs. In processing hydrocarbon liquids, these membranes are more permeable, selective, and stable than commercially available and other literature-reported membranes. We also highlight the feasibility of manipulating the crude oil separation performance at the molecular level by introducing oligomers with different chemistries into the MOA molecules. This work facilitates the development of the next-generation hydrophobic nanofilms created through interfacial polymerization by incorporating rational molecular-level design and with the potential for scaling up.

REFERENCES AND NOTES

1. D. S. Sholl, R. P. Lively, *Nature* **532**, 435–437 (2016).
2. M. Elimelech, W. A. Phillip, *Science* **333**, 712–717 (2011).
3. D. Y. Koh, B. A. McCool, H. W. Deckman, R. P. Lively, *Science* **353**, 804–807 (2016).
4. R. P. Lively, D. S. Sholl, *Nat. Mater.* **16**, 276–279 (2017).
5. K. A. Thompson *et al*., *Science* **369**, 310–315 (2020).
6. S. Chisca *et al*., *Science* **376**, 1105–1110 (2022).
7. P. Marchetti, M. F. Jimenez Solomon, G. Szekely, A. G. Livingston, *Chem. Rev.* **114**, 10735–10806 (2014).
8. M. F. Jimenez-Solomon, Q. Song, K. E. Jelfs, M. Munoz-Ibanez, A. G. Livingston, *Nat. Mater.* **15**, 760–767 (2016).
9. S. Karan, Z. Jiang, A. G. Livingston, *Science* **348**, 1347–1351 (2015).
10. M. F. Jimenez Solomon, Y. Bhole, A. G. Livingston, *J. Membr. Sci.* **434**, 193–203 (2013).
11. J. S. Trivedi, P. Bera, D. V. Bhalani, S. K. Jewrajka, *J. Membr. Sci.* **626**, 119155 (2021).
12. S.-H. Park *et al*., *Green Chem.* **23**, 1175–1184 (2021).
13. F. Alduraiei, P. Manchanda, B. Pulido, G. Szekely, S. P. Nunes, *Separ. Purif. Tech.* **279**, 119777 (2021).
14. F. Alduraiei, S. Kumar, J. Liu, S. P. Nunes, G. Szekely, *J. Membr. Sci.* **648**, 120345 (2022).
15. W. Kushida *et al*., *J. Mater. Chem. A Mater. Energy Sustain.* **10**, 4146–4156 (2022).
16. J. F. Brennecke, B. Freeman, *Science* **369**, 254–255 (2020).
17. F. Aydin *et al*., *J. Phys. Chem. B* **120**, 3666–3676 (2016).
18. W. Tao *et al*., *J. Am. Chem. Soc.* **134**, 762–764 (2012).
19. Y. Ma, X. Cao, X. Feng, Y. Ma, H. Zou, *Polymer* **48**, 7455–7460 (2007).
20. M. Di Vincenzo *et al*., *Nat. Nanotechnol.* **16**, 190–196 (2021).
21. K. Murata *et al*., *Nature* **407**, 599–605 (2000).
22. Z. Jiang, S. Karan, A. G. Livingston, *Adv. Mater.* **30**, e1705973 (2018).
23. P. Gorgojo *et al*., *Adv. Funct. Mater.* **24**, 4729–4737 (2014).
24. D. Fritsch, P. Merten, K. Heinrich, M. Lazar, M. Priske, *J. Membr. Sci.* **401–402**, 222–231 (2012).
25. M. Cook, P. R. J. Gaffney, L. G. Peeva, A. G. Livingston, *J. Membr. Sci.* **558**, 52–63 (2018).
26. M. Cook, L. Peeva, A. G. Livingston, *Ind. Eng. Chem. Res.* **57**, 730–739 (2018).
27. H. L. Castricum *et al*., *Adv. Funct. Mater.* **21**, 2319–2329 (2011).
28. B. D. Marshall, J. W. Allen, R. Lively, *SSRN*3976709.

ACKNOWLEDGMENTS

We thank A. Genovese (King Abdullah University of Science and Technology, Core Labs) for the EDX-TEM element mapping. A.G.L., Z.J., S.L., R.D., and J.X. are inventors on UK patent application no. 2005106.6 submitted by Imperial College London for the use of multi-oligomer monomers in interfacially polymerized film. **Funding:** This work was supported by ExxonMobil Research and Engineering. R.D. acknowledges support from UKRI EPSRC grant EP/M01486X; J.K. and A.G.L. acknowledge support from European Research Council (ERC) grant 786398; S.L. acknowledges support from King Abdullah University of Science and Technology (OSR-2017-CRG6-3441.01).

Z.J. acknowledges support from Engineering and Physical Sciences Research Council (CBET-EPSRC EP/R018847). **Author contributions:** S.L. and R.D. synthesized MOAs. S.L. performed NMR analysis and FTIR analysis, measured water contact angle, and captured SEM and AFM images. V.E.M. captured TEM images. N.D.R., J.R.J., S.H., and B.A.M. tested membrane performance in real crude oil system and performed boiling point measurement and GC×GC analysis. B.D.M performed model development and application. S.L. fabricated composite membranes and performed organic solvent nanofiltration (OSN) experiments. Z.J. tested membranes in synthetic crude system. J.K. built up the synthetic crude testing rig and tested the commercial membrane performance in synthetic crude system. S.C. performed x-ray photoelectron spectroscopy (XPS) test. S.L., R.D., N.D.R., J.R.J., J.X., B.A.M., S.P.N., Z.J., and A.G.L. conceived the research. All authors contributed to drafting the paper. **Competing interests:** Authors declare no competing interests. **Data and materials availability:** All data are available in the main text or the supplementary materials. **License information:** Copyright © 2022 the authors, some rights reserved; exclusive licensee American Association for the Advancement of Science. No claim to original US government works. https://www.science.org/about/science-licenses-journal-article-reuse

SUPPLEMENTARY MATERIALS

science.org/doi/10.1126/science.abq0598
Materials and Methods
Supplementary Text
Figs. S1 to S45
Tables S1 to S8
References (*29*–*35*)
Movie S1

Submitted 15 March 2022; accepted 26 August 2022
10.1126/science.abq0598

POLYMER CHEMISTRY

Catalytic deconstruction of waste polyethylene with ethylene to form propylene

Richard J. Conk[1,2]†, Steven Hanna[1,2]†, Jake X. Shi[1,2], Ji Yang[2], Nicodemo R. Ciccia[1,2], Liang Qi[2,3], Brandon J. Bloomer[1,2], Steffen Heuvel[1], Tyler Wills[1], Ji Su[2], Alexis T. Bell[2,3], John F. Hartwig[1,2]*

The conversion of polyolefins to monomers would create a valuable carbon feedstock from the largest fraction of waste plastic. However, breakdown of the main chains in these polymers requires the cleavage of carbon–carbon bonds that tend to resist selective chemical transformations. Here, we report the production of propylene by partial dehydrogenation of polyethylene and tandem isomerizing ethenolysis of the desaturated chain. Dehydrogenation of high-density polyethylene with either an iridium-pincer complex or platinum/zinc supported on silica as catalysts yielded dehydrogenated material containing up to 3.2% internal olefins; the combination of a second-generation Hoveyda-Grubbs metathesis catalyst and $[PdP(^tBu)_3(\mu\text{-}Br)]_2$ as an isomerization catalyst selectively degraded this unsaturated polymer to propylene in yields exceeding 80%. These results show promise for the application of mild catalysis to deconstruct otherwise stable polyolefins.

The mechanical durability and chemical inertness of commercial plastics have led to their widespread use in everyday life, but these same properties make them difficult to recycle. Polyolefins, which account for 36% of global plastic production (*1*), are particularly durable and inert, and only a small proportion of polyethylene (PE) waste is recovered by recycling (~14% in 2015) (*2*). Polyolefins are prepared with distinct molecular weights, molecular weight distributions, and microstructures for specific applications. Thus, a mixture of polyolefins individually produced for diverse applications lacks the properties of any one component; moreover, accumulated additives and contaminants, as well as chain scission induced by mechanical recycling, can degrade performance (*2*). Given the social, economic, and ecological threats from the accumulation of mixed polyolefin waste, innovative approaches to use this material as a carbon feedstock are needed (*2*–*4*).

Our group (*5*) and others (*6*–*8*) have been investigating catalytic chemistry that could occur with these polymers that contain only alkyl C–H and C–C bonds. Because the C–H bonds are more reactive than the C–C bonds, many efforts have focused on the introduction of functional groups onto the polymer chain to tune the properties of the plastic (*5*, *7*, *8*). More challenging are methods for "chemical recycling" of polyolefins, which entails the cleavage of polymer chains to regenerate monomers that can be repolymerized (*6*, *9*). Whereas processes are well established to cleave the C–O bonds of polyesters (*10*), methods to cleave the alkyl C–C bonds of PE are more limited. Pyrolysis (*4*), catalytic cracking (*11*), hydrogenolysis (*12*–*15*), tandem hydrogenolysis-aromatization (*16*), and alkane metathesis (*17*, *18*) have been reported for cleavage of PE chains. However, these processes form complex mixtures of hydrocarbons that are difficult to separate and have varying levels of utility (Fig. 1A). A process is needed by which PE undergoes depolymerization to form a single product for which the demand approaches the supply of PE waste. A method for the selective production of a commodity olefin from PE could thus render PE a valuable hydrocarbon feedstock.

We envisioned a cascade of catalytic processes that would introduce unsaturation to a PE chain and then unravel the chain to propylene. More specifically, dehydrogenation could be used to enable subsequent C–C bond cleavage by a combination of olefin metathesis and isomerization to form propylene (Fig. 1B) (*19*, *20*). We show that the combination of dehydrogenation of high-molecular-weight PE having high density (HDPE) or low density (LDPE) and subsequent isomerizing ethenolysis (I/E) of the resulting crude polymer containing internal alkenes converts PE with commercially relevant molecular weights to propene in yields as high as 80%. This dehydrogenation and isomerizing ethenolysis (DIE) process was successfully tested on both postconsumer and virgin PE dehydrogenated by either homogeneous or heterogeneous catalysts.

To determine whether the conversion of PE to propylene could be achieved by a cascade comprising DIE, a reliable dehydrogenation reaction was first needed. The formation and isolation of desaturated PE by catalytic dehydrogenation has been reported only with materials of low molecular weight [number-average molecular weight (M_n) = 606] to ensure solubility (*21*, *22*). Even a recently reported combination of stoichiometric halogenation and elimination was conducted with material with an M_n below 6.6 kDa (*18*). Many alkane dehydrogenation catalysts have been reported since these initial reports, and we investigated those containing phosphinous acid, bis(1,1-dimethylethyl)-, 5-methoxy-1,3-phenylene ester, which is a symmetric phosphinite pincer ligand containing an aryl backbone known as ^{tBu}POCOP, and related pincer ligands (*23*). Dehydrogenations of virgin HDPE and LDPE with more commercially relevant molecular weights (M_n 26.1 kDa, $Đ$ = 3.31 and M_n = 35.1 kDa, $Đ$ = 6.54, respectively) catalyzed by **Ir-^{tBu}POCOP** with *tert*-butyl ethylene (TBE) as the hydrogen acceptor in *p*-xylene solvent yielded unsaturated polymer containing exclusively internal olefins (<0.1% terminal and up to 3.2% internal), along with small amounts (<0.75%) of alkylarenes (Fig. 2A), as determined by ^{1}H nuclear magnetic resonance spectroscopy. The isomerization of terminal olefins (which might be the kinetic product) to internal olefins is well known from dehydrogenation of liquid alkanes with this catalyst (*24*). The 3.2% of unsaturated units corresponds to a modest 7.6 turnovers but was limited by consumption of the acceptor

[1]Department of Chemistry, University of California, Berkeley, Berkeley, CA 94720, USA. [2]Division of Chemical Sciences, Lawrence Berkeley National Laboratory, Berkeley, CA 94720, USA. [3]Department of Chemical and Biomolecular Engineering, University of California, Berkeley, Berkeley, CA 94720, USA.
***Corresponding author. Email: jhartwig@berkeley.edu**
†These authors contributed equally to this work.

and generated sufficient alkene units for the subsequent steps of the DIE process. Analysis of the molecular weight by gel-permeation chromatography revealed a decrease in M_n of the HDPE from 26.1 to 18.2 kDa upon dehydrogenation, but this change was not detrimental to our envisioned degradation to propylene.

To determine whether heterogeneous catalysts also could desaturate polyolefins, we investigated the dehydrogenation of PE with catalysts inspired by those in the Oleflex process of Honeywell UOP (formerly Universal Oil Products) for the dehydrogenation of long-chain paraffins (*25*). We tested the dehydrogenation of HDPE with established Pt/Sn (*25*) and a new type of heterogeneously supported Pt/Zn catalyst (*26*). Heating of the polymer melt over such catalysts under a flow of Ar at 350°C furnished unsaturated PE containing up to 0.6% olefins, along with ~0.25% arenes (Fig. 2B). Again, just a slight reduction in M_n was observed (from 26.1 to 21.7 kDa), and all of the olefin units were internal.

Having demonstrated the feasibility of the dehydrogenation of high-molecular-weight PE, we synthesized a series of dehydrogenated PEs with varying levels of unsaturation. To do so, we subjected laboratory-grade HDPE to dehydrogenation with Ir-^{tBu}POCOP and varying loadings of TBE as the sacrificial H_2 acceptor (see table S2 for full details). These reactions produced PE with degrees of unsaturation ranging from 0.6 to 3.2%.

It was unclear whether high-molecular-weight, unsaturated PE would undergo ethenolysis to form long-chain terminal alkenes for subsequent I/E. Subjecting the unsaturated HDPE containing 1.09% olefin units to ethenolysis with 3.6 mol % of second-generation Hoveyda-Grubbs catalyst **M1** resulted in a reduction of the M_n from 18.1 to 1.6 kDa. The M_n of the cleaved product corresponds to an average chain length of 114 carbons (Fig. 2C). To model the process of dehydrogenation and ethenolysis on a pure reactant and to gain information on the position of the alkene units and the resulting chain lengths, we conducted these reactions on tetracosane ($C_{24}H_{50}$), a pure, long-chain alkane. Initial dehydrogenation of tetracosane with 1 equivalent of TBE converted >95% of the acceptor to *tert*-butyl ethane and converted ~15% of the alkane to internal tetracosenes. Subsequent ethenolysis of the reaction mixture catalyzed by **M1** under 25 bar of ethylene formed the distribution of olefins, including a wide range of chain lengths shown in Fig. 2D. This result indicates that dehydrogenation of this long alkane with Ir-tBuPOCOP produces predominantly internal alkene, rather than terminal alkene, units.

Having shown that we could generate long-chain alkenes from PE, we investigated conditions for I/E of the resulting chains. I/E of

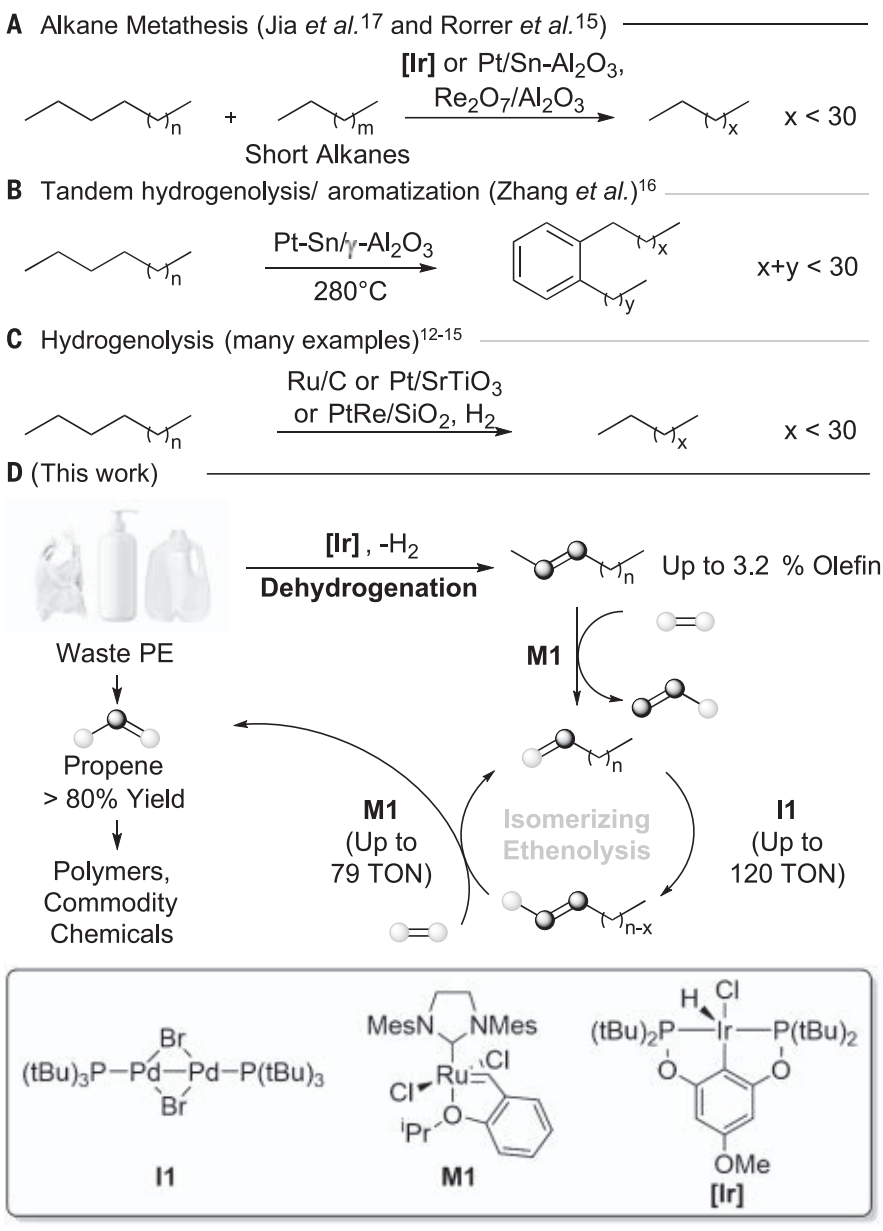


Fig. 1. Strategies for the valorization of PE waste. (**A**) Degradation of PE by alkane metathesis with n-hexane. (**B**) Conversion of PE to alkyl aromatics by tandem hydrogenolysis/aromatization. (**C**) Degradation of PE by hydrogenolysis. (**D**) Conversion of PE to propylene by DIE (where x is the number of I/E turnovers). Mes, mesitylene (2,4,6-trimethylbenzene).

hydrocarbons is known for the conversion of unsaturated alkylarenes to vinylarenes and for the conversion of 1-octadecene to propylene at low conversions. We sought an I/E that would transform the long-chain PE fragments to propylene in high yield by first seeking conditions for high conversion of 1-octadecene (**1a**) (*19*). Several combinations of complexes known to catalyze either olefin metathesis or isomerization were tested, and the results are summarized in table S1. The reaction of 1-octadecene with ethylene catalyzed by the combination of Hoveyda-Grubbs catalyst **M1** (6 mol % relative to alkene chains, 0.67 mol % relative to ethylene subunits) and the dimeric Pd(I) bromide catalyst **I1** (3 mol %, 0.33 mol % relative to ethylene subunits) at 60°C for 16 hours formed propylene in 95% yield.

Catalyst systems created from other combinations of individual metathesis and isomerization catalysts led to lower yields of propylene than those with **M1** and **I1**. Systems containing three alternative metathesis catalysts (**M2** to **M4** in table S1) with **I1** formed <60% propylene. Those containing the combination of **M1** and one of three other isomerization catalysts (**I2** to

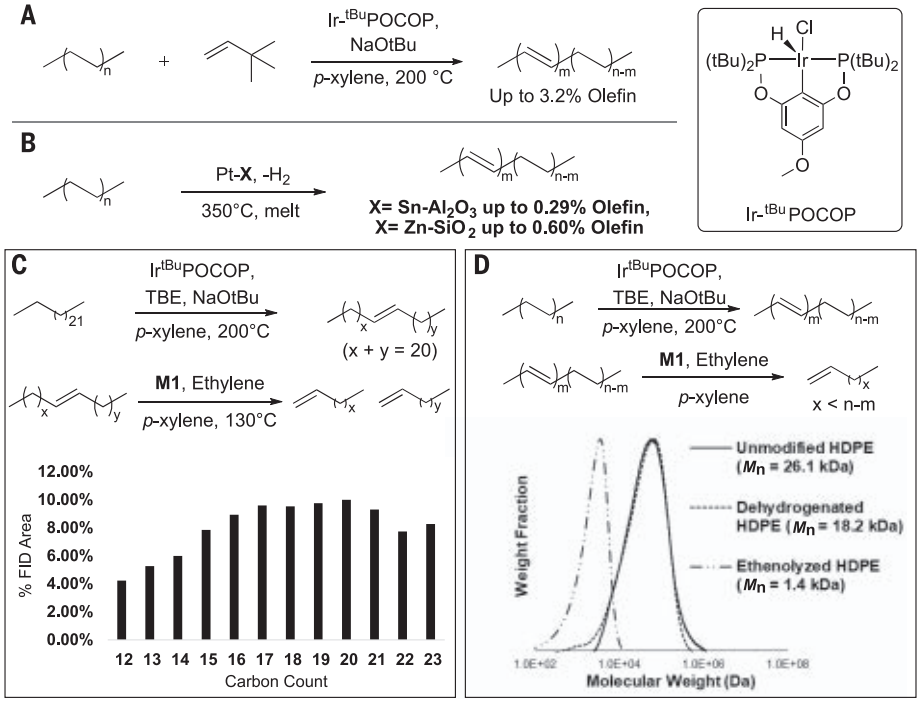


Fig. 2. Conditions tested for DIE. (**A**) Homogeneous dehydrogenation of PE: 0.42 mol % Ir-^{tBu}POCOP (9.8 wt %), 0.46 mol % NaOtBu, 0.6 M in PE; reactions were run for 12 hours with 0.4 equivalents of TBE. Mol %, equivalents. TBE and M of PE were calculated relative to PE monomer units. (**B**) HDPE (M_n = 26.1 kDa) with bimetallic catalysts supported on alumina. Conditions: 20 wt % catalyst, 350°C. Catalysts were first activated under H_2 flow for 1 hour, and then dehydrogenation was conducted for 16 hours under Ar flow. (**C**) Gel-permeation chromatogram of HDPE before and after ethenolysis with **M1**. Conditions for ethenolysis were 0.36 M in unsaturated PE 3.6 mol % **M1** in p-xylene (relative to PE monomer units), heated at 130°C for 16 hours under 25 bar ethylene. (**D**) Sequential dehydrogenation and ethenolysis of a long-chain paraffin (tetracosane). Initial dehydrogenation yields olefins in 10% yield, and subsequent ethenolysis with **M1** yields a statistical distribution of shorter-chain olefins.

I4 in table S1) formed <10% propylene. All of the isomerization catalysts furnished exclusively internal octadecenes from 1-octadecene in high or quantitative yield after 16 hours at 60°C in *p*-xylene, implying that incompatibility of the isomerization catalysts with the metathesis catalyst or with ethylene is the cause of the lower yields of propylene with alternative isomerization catalysts **I2** to **I4** (see table S1 for details).

The free energy of isomerizing ethenolysis is estimated to be negative but small (−1.52 kcal/mol of propylene formed under standard conditions; see the supplementary materials for details). Thus, our standard reactions that gave 95% yield of propylene were conducted in a pressure vessel with sufficient headspace to provide a large excess (64 equivalents per methylene unit) of ethylene to favor full consumption of the alkene chain. Consistent with the estimated thermodynamics, reactions with a smaller headspace providing just 3.5 equivalents of ethylene in the system also led to a high, albeit slightly lower, 72 ± 6% yield of propylene.

Finally, we tested the formation of propylene from ethylene and the unsaturated PE samples that we produced by dehydrogenation. The reactions of ethylene with the material from HDPE catalyzed by the two complexes in our I/E system formed propylene in yields shown in Fig. 3B. Reactions with HDPE containing only 0.68% unsaturation formed propylene in nearly 60% yield [turnover numbers (TONs) of 34 and 55 in **M1** and **I1**, respectively]. Reaction of the polymer in which 1.9% of the monomer units were unsaturated led to the formation of propylene in 87% yield (48 and 79 TON in **M1** and **I1**, respectively). The conversion of unsaturated LDPE to propylene also occurred under these conditions in yields up to 70% (39 and 64 TON in **M1** and **I1**, respectively).

We considered that ethylene could undergo dimerization or oligomerization, followed by ethenolysis, to form propylene without contribution from the polymer chains. Indeed, we did observe this background reactivity in the absence of long-chain olefins to form 0.13 mmol of propylene under our reaction conditions after 16 hours at 60°C and to form 1.01 mmol of propylene after the same reaction time at 130°C. Thus, to determine whether the observed propylene from the reactions with PE originated from dehydrogenated polymer or from the background conversion of ethylene to propylene, we designed an isotope-labeling experiment in which the production of propylene could be observed more directly. Because both dehydrogenation and I/E scramble ^{2}H labels, we conducted experiments with ^{13}C-labeled PE to assess the extent of formation of propylene from polymer clearly. The propylene arising from dehydrogenated PE by the proposed scheme would consist entirely of the singly ^{13}C-labeled isotopomer. This isotopic composition would be observed because scrambling would occur at the termini of propylene by olefin metathesis during the I/E, but scrambling at the 2 position would not (Fig. 3C). Accordingly, we subjected ^{13}C-labeled (99.9% ^{13}C) HDPE to DIE and characterized the resulting propylene by mass spectrometry. The mass spectrum revealed an isotopic enrichment of the propylene >70%, demonstrating that most of the propylene observed from the DIE of PE results from polymer chain degradation. Small amounts of propylene containing two ^{13}C carbons that results from metathesis of the initial propylene product with the ^{13}C ethene formed in situ were also detected, but this material accounted for just 1% of the propylene product.

We also conducted DIE on samples of postconsumer PE (Fig. 3E). Substantial yields of propylene were observed in all cases. Moreover, HDPE from a milk jug yielded 57% propylene, which is only 20% lower than the yield from virgin HDPE with a similar degree of unsaturation, and LDPE food packaging generated >50% yield of propylene. To investigate the effect of additives on the performance of the catalytic system, these experiments were conducted by two methods. In the first method, postconsumer samples were coarsely cut with scissors and dehydrogenated directly using Ir-^{tBu}POCOP under the conditions specified in Fig. 2A. In the second method, the cut samples were first dissolved in boiling xylenes and then precipitated from acetone to remove additives and impurities. In some cases, the additives and impurities had no effect, and in some cases, such as those from can tops and food packaging, the simple precipitation was needed for dehydrogenation to occur. These results show that postconsumer products comprising HDPE or LDPE can be converted to propylene by this protocol, and that our system is sufficiently robust to tolerate the additives present in postconsumer products while still furnishing substantial amounts of propylene.

The time courses of reactions for degrading octadecene at 60°C and degrading HDPE at 130°C are displayed in Fig. 4, A and B, respectively. These data revealed a lengthy induction period for the reaction of octadecene at 60°C, presumably because of the multiple stages of catalyst activation necessary for the reaction to

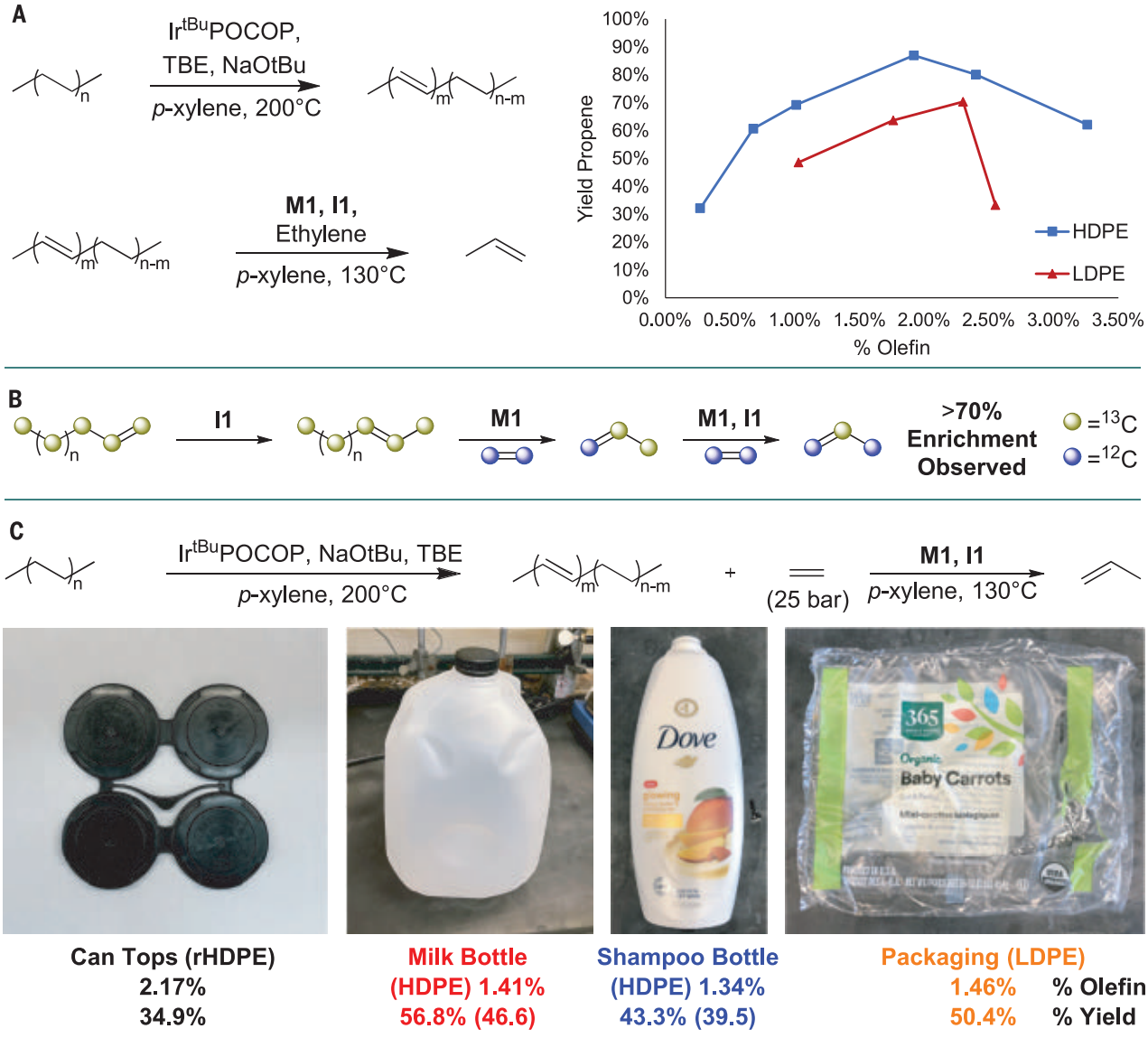


Fig. 3. Development of conditions for DIE of PE. (**A**) Application of I/E to dehydro-PE, with dehydro-HDPE yielding a maximum of 80% propylene with 1.96% dehydrogenation. Conditions for I/E of dehydrogenated PE: 3.6% **M1**, 2.2% **I1**, 1.78 M in PE, heated at 130°C in *p*-xylene for 16 hours under 25 bar of ethylene. Catalyst loadings are reported as mol % relative to total PE repeat units. (**B**) DIE of ^{13}C-labeled HDPE to check for background reactivity [conditions identical to those in (A)]. (**C**) DIE of postconsumer PE [conditions identical to those in (B)]. Propylene yields are reported as X% (Y) where X is the yield obtained from polymer purified by precipitation from acetone and Y is the yield obtained from unmodified polymer. Where a single yield is reported, dehydrogenation on unpurified samples failed.

occur at an appreciable rate. This plot fit well to an exponential formation of catalyst and a zero-order appearance of product until the substrate was depleted. The reaction of the unsaturated HDPE at 130°C occurred with a shorter induction period despite the need to first cleave the internal alkenes of the unsaturated HDPE, and a constant rate was then observed up to 85% of the total conversion. Presumably, the higher temperature diminishes the induction period. The linear formation of propylene suggest that the process occurs by a rate-determining reaction with the excess ethylene.

Additional data that we gathered on the degradation of PE by DIE point to future challenges. First, samples of dehydrogenated LDPE consistently furnished propylene in lower yields than did dehydrogenated HDPE with the same degree of unsaturation. We hypothesized that the significant degree of branching in LDPE led to the formation of trisubstituted alkenes during IE, and these more hindered alkenes underwent slower isomerization or slower ethenolysis. To test this hypothesis, we synthesized several substituted olefins and subjected them to I/E under conditions identical to those we used for the I/E of 1-octadecene (Fig. 4C). The I/E of substrates **1a** to **1d** demonstrate a clear trend of decreasing propylene yield with increasing olefin substitution.

Second, our experiments with virgin PE (Fig. 3B) showed that a high degree of unsaturation of PE chains was detrimental to the yield of I/E. We hypothesized from this observation that a high degree of polymer unsaturation leads to dienes and polyenes that isomerize during the I/E process to conjugated dienes that could poison the catalyst. Because there are multiple sites of unsaturation on each polymer chain, **I1** could isomerize such olefins to conjugated 1,3-dienes within the polymer, and such conjugated dienes could poison one or both catalysts. To test this hypothesis, we conducted I/E on one α,ω-diene, **1e** (1,9-decadiene), and one conjugated diene, **1f** (1,3-tetradecadiene) (Fig. 4D). These experiments showed that α-ω dienes separated by six methylene units (**1e**) formed propylene in

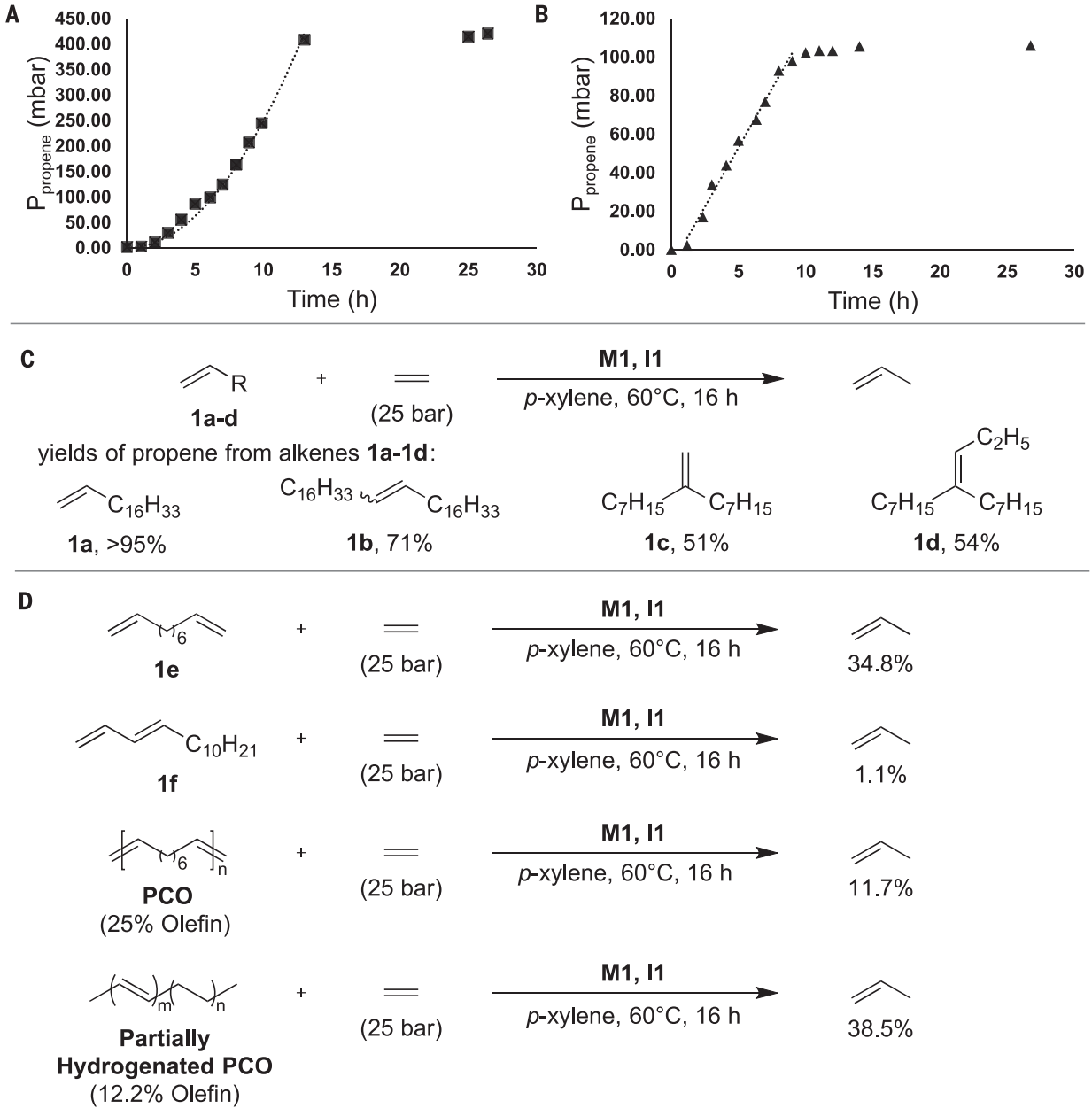


Fig. 4. Investigation of reaction scope and kinetics. (**A**) Time course of I/E with 1-octadecene (100% yield = 458.3 mbar). Conditions for I/E of 1-octadecene: 6.0 mol % **M1** (0.67 mol % relative to ethylene subunits), 3.0 mol % **I1** (0.33 mol % relative to ethylene subunits), 0.500 M in olefin, heated at 60°C in p-xylene for 16 hours under 25 bar of ethylene. A fit for the time course was conducted using COPASI by simulating an exponential appearance of catalyst and a zero-order reaction (R^2 = 0.993, k_{cat} = 0.071 s^{-1}, $k_{propylene}$ = 18.0 s^{-1}). (**B**) Time course of I/E with dehydrogenated HDPE (1.41% olefin) (100% yield = 193.5 mbar). A linear fit has been added to (B) to show the zero-order reaction after the short induction period and completion of the reaction (R^2 = 0.989). (**C**) Yields of I/E on small molecules **1a** to **1d** designed to assess the effect of branching on I/E. (**D**) Yields of I/E on small molecules **1e** and **1f** designed to test the effect of dienes on I/E [conditions identical to those specified in (A)] and on PCO (M_n= 5.2 kDa) designed to demonstrate the effect of polymer unsaturation on I/E yield in the absence of branching. Conditions for I/E in (C) and (D) were identical to those in Fig. 3C.

much higher yields than did 1,3-dienes. Consistent with our hypothesis, the addition of catalytic amounts of catalyst **I1** to conjugated diene **1f** without ethylene or the metathesis catalyst led to the immediate formation of a black precipitate (Fig. 4D).

We assessed this hypothesis further by applying I/E to poly(cyclooctene) (PCO). We synthesized PCO (M_n = 5.2 kDa, $Đ$ = 1.64) by ring-opening metathesis polymerization of cyclooctene (*27*). I/E of this substrate furnished propylene in significantly diminished yield, but I/E of a partially hydrogenated PCO (*28*) (with an olefin content of 12.2% versus 25% for the original polymer) furnished propylene in 38.5% yield (Fig. 4D). We concluded from these data that the formation of 1,3-dienes in situ was likely responsible for the lower yields of propylene from the more highly unsaturated polymers.

Propylene is used as a precursor to multiple commodity chemicals, including acrylic acid, acrylonitrile, and cumene, in addition to its use in the production of polypropylene plastic (*28*). Although it is produced primarily as a by-product of steam cracking or fluid catalytic cracking, the increasing demand for propylene

since the 1990s has motivated its "on-purpose" production through methanol-to-olefins technology, propane dehydrogenation, or the conproportionation of butene and ethylene (*29*). This on-purpose production is only expected to increase as increasing populations and standards of living heighten the demand for polypropylene.

The constituent reactions of the DIE process that we report on laboratory scale with homogeneous catalysts are closely related to reactions conducted on industrial scales with heterogeneous catalysts, and their combination draws analogies to the combination of reactions in the commodity-scale shell higher olefin process (SHOP) that forms long-chain alkenes from ethylene (*29*). The olefin metathesis and isomerization by which this degradation of the unsaturated polymer occurs are some of the most practiced industrial transformations and are routinely performed on commodity scales with heterogeneous catalysts (*30*, *31*). Thus, the capacity of such systems to catalyze the DIE processes would allow dehydrogenation and I/E to be conducted in continuous flow with less ethylene while removing the propylene product. The separation of propylene from ethylene is already conducted on the industrial scale by various methods, including low-temperature and extractive distillation (*32*). Thus, this initial report charts a path by which a DIE sequence could render polyolefin waste a hydrocarbon feedstock to generate a commodity chemical for which the demand is comparable to the available supply of recovered polyolefins. The use of heterogeneous catalysts is under development.

REFERENCES AND NOTES

1. R. Geyer, J. R. Jambeck, K. L. Law, *Sci. Adv.* **3**, e1700782 (2017).
2. G. W. Coates, Y. D. Y. L. Getzler, *Nat. Rev. Mater.* **5**, 501–516 (2020).
3. I. Vollmer *et al.*, *Angew. Chem. Int. Ed.* **59**, 15402–15423 (2020).
4. K. Ragaert, L. Delva, K. Van Geem, *Waste Manag.* **69**, 24–58 (2017).
5. L. Chen *et al.*, *Chem* **7**, 137–145 (2021).
6. M. Zeng *et al.*, *ACS Sustain. Chem. & Eng.* **9**, 13926–13936 (2021).
7. T. J. Fazekas *et al.*, *Science* **375**, 545–550 (2022).
8. J. B. Williamson, W. L. Czaplyski, E. J. Alexanian, F. A. Leibfarth, *Angew. Chem. Int. Ed.* **57**, 6261–6265 (2018).
9. L. T. J. Korley, T. H. Epps3rd, B. A. Helms, A. J. Ryan, *Science* **373**, 66–69 (2021).
10. M. Chu, Y. Liu, X. Lou, Q. Zhang, J. Chen, *ACS Catal.* **12**, 4659–4679 (2022).
11. D. P. Serrano, J. Aguado, J. M. Escola, *Ind. Eng. Chem. Res.* **39**, 1177–1184 (2000).
12. K. L. Sánchez-Rivera, G. W. Huber, *ACS Cent. Sci.* **7**, 17–19 (2021).
13. S. P. Ertem *et al.*, *Macromolecules* **53**, 6043–6055 (2020).
14. G. Celik *et al.*, *ACS Cent. Sci.* **5**, 1795–1803 (2019).
15. J. E. Rorrer, C. Troyano-Valls, G. T. Beckham, Y. Román-Leshkov, *ACS Sustain. Chem. & Eng.* **9**, 11661–11666 (2021).
16. F. Zhang *et al.*, *Science* **370**, 437–441 (2020).
17. X. Jia, C. Qin, T. Friedberger, Z. Guan, Z. Huang, *Sci. Adv.* **2**, e1501591 (2016).
18. L. D. Ellis *et al.*, *ACS Sustain. Chem. & Eng.* **9**, 623–628 (2021).
19. M. Nagyházi *et al.*, *Angew. Chem. Int. Ed.* **61**, e202204413 (2022).
20. S. Baader, D. M. Ohlmann, L. J. Gooßen, *Chemistry* **19**, 9807–9810 (2013).
21. A. Ray *et al.*, *Chem. Commun.* **27**, 3388–3390 (2005).
22. A. Ray *et al.*, *J. Mol. Catal. Chem.* **256**, 200–207 (2006).
23. I. Göttker-Schnetmann, P. White, M. Brookhart, *J. Am. Chem. Soc.* **126**, 1804–1811 (2004).
24. S. Biswas *et al.*, *J. Am. Chem. Soc.* **134**, 13276–13295 (2012).
25. S. He, K. R. Krishnamurthy, K. Seshan, in *Catalysis*, J. Spivey, Y.-F. Han, Eds. (The Royal Society of Chemistry, 2017), vol. 29, pp. 282–316.
26. L. Qi *et al.*, *J. Am. Chem. Soc.* **143**, 21364–21378 (2021).
27. R. Walker, R. M. Conrad, R. H. Grubbs, *Macromolecules* **42**, 599–605 (2009).
28. S. Kobayashi, L. M. Pitet, M. A. Hillmyer, *J. Am. Chem. Soc.* **133**, 5794–5797 (2011).
29. R. Schmidt *et al.*, in *Ullmann's Encyclopedia of Industrial Chemistry* (Wiley, 2014).
30. H. Zimmermann, in *Ullmann's Encyclopedia of Industrial Chemistr* (Wiley, 2014).
31. F. M. A. Geilen, G. Stochniol, S. Peitz, E. Schulte-Koerne, in *Ullmann's Encyclopedia of Industrial Chemistry* (Wiley, 2014).
32. R. B. Eldridge, *Ind. Eng. Chem. Res.* **32**, 2208–2212 (1993).

ACKNOWLEDGMENTS

We thank B. Abel for advice on cyclooctene polymerization; C. Delaney for many insightful discussions during the preparation of this manuscript; Z. Zhou in the QB3 mass spectrometry facility for help in acquiring and interpreting high-resolution mass spectra for isotopic labeling experiments; E. Dailing of the LBL Molecular Foundry for assistance in acquiring gel-permeation chromatograms of polyolefins reported herein; and C. Asokan of the LBNL Catalysis Laboratory for continuous technical support. R.C., N.C., S.H., and J.S. gratefully acknowledge the LBL Molecular Foundry (proposal nos. 7554 and 7515) for technical support. **Funding:** This work was supported by the Department of Energy (grant no. DOE-DE-AC02-05CH11231) and the National Science Foundation (Graduate Research Fellowship to J.X.S.). We acknowledge the UC Berkeley NMR Facility and the National Institutes of Health for providing funding for the cryoprobe for the AV-600 spectrometer under grant S10OD024998. S.H. gratefully acknowledges Chevron for a predoctoral fellowship. Work at the LBL Molecular Foundry was supported by the Office of Science, Office of Basic Energy Sciences, US Department of Energy, under contract no. DE-AC02-05CH11231. **Author contributions:** S.H. conceived of the overall reaction scheme. S.H., R.J.C., and J.F.H. conceived of the project directions. S.H., R.J.C., A.T.B., L.Q., and J.F.H. designed the experiments. S.H., R.J.C., J.X.S., N.R.C., B.J.B., S.H., L.Q., J.Y., and T.W. performed the experiments. R.J.C. wrote the manuscript. R.J.C., S.H., B.J.B., and J.F.H. reviewed the manuscript, which was approved by all authors. **Competing interests:** S.H., R.J.C., and J.F.H. are inventors on a US provisional patent application for the process described herein. The remaining authors declare no competing interests. **Data and materials availability:** All data are available in the main text or the supplementary materials. **License information:** Copyright © 2022 the authors, some rights reserved; exclusive licensee American Association for the Advancement of Science. No claim to original US government works. https://www.science.org/about/science-licenses-journal-article-reuse

SUPPLEMENTARY MATERIALS

science.org/doi/10.1126/science.add1088
Figs. S1 to S23
Tables S1 to S7
References (*33*–*37*)

Submitted 22 May 2022; accepted 6 September 2022
10.1126/science.add1088

METHANE EMISSIONS

Inefficient and unlit natural gas flares both emit large quantities of methane

Genevieve Plant[1]*, Eric A. Kort[1]*, Adam R. Brandt[2], Yuanlei Chen[2], Graham Fordice[1], Alan M. Gorchov Negron[1], Stefan Schwietzke[3], Mackenzie Smith[4], Daniel Zavala-Araiza[3,5]

Flaring is widely used by the fossil fuel industry to dispose of natural gas. Industry and governments generally assume that flares remain lit and destroy methane, the predominant component of natural gas, with 98% efficiency. Neither assumption, however, is based on real-world observations. We calculate flare efficiency using airborne sampling across three basins responsible for >80% of US flaring and combine these observations with unlit flare prevalence surveys. We find that both unlit flares and inefficient combustion contribute comparably to ineffective methane destruction, with flares effectively destroying only 91.1% (90.2, 91.8; 95% confidence interval) of methane. This represents a fivefold increase in methane emissions above present assumptions and constitutes 4 to 10% of total US oil and gas methane emissions, highlighting a previously underappreciated methane source and mitigation opportunity.

In oil and gas (O&G) production and processing, natural gas—most commonly, associated natural gas (a by-product of oil extraction)—is disposed of through flares for a variety of safety, infrastructure, regulatory, or economic reasons (*1*, *2*). Ideally, the combustion in a flare serves to convert the mostly hydrocarbon gas to carbon dioxide (CO_2) and water (*1*). The primary component of natural gas is typically methane (CH_4), the most important short-lived greenhouse gas owing to its high radiative forcing and global warming potential (*3*), relatively short atmospheric lifetime of 9 to 10 years (*4*, *5*), and contribution to formation of tropospheric ozone (*6*, *7*). The use of flares aims to reduce the climate and health impacts of the disposal of this waste gas. Global flaring activity is captured

[1]Climate and Space Sciences and Engineering, University of Michigan, Ann Arbor, MI, USA. [2]Department of Energy Science and Engineering, Stanford University, Stanford, CA, USA. [3]Environmental Defense Fund, Reguliersgracht 79, Amsterdam, Netherlands. [4]Scientific Aviation, Boulder, CO, USA. [5]Institute for Marine and Atmospheric Research Utrecht, Utrecht University, Utrecht, Netherlands.
***Corresponding author. Email: geplant@umich.edu (G.P.); eakort@umich.edu (E.A.K.)**

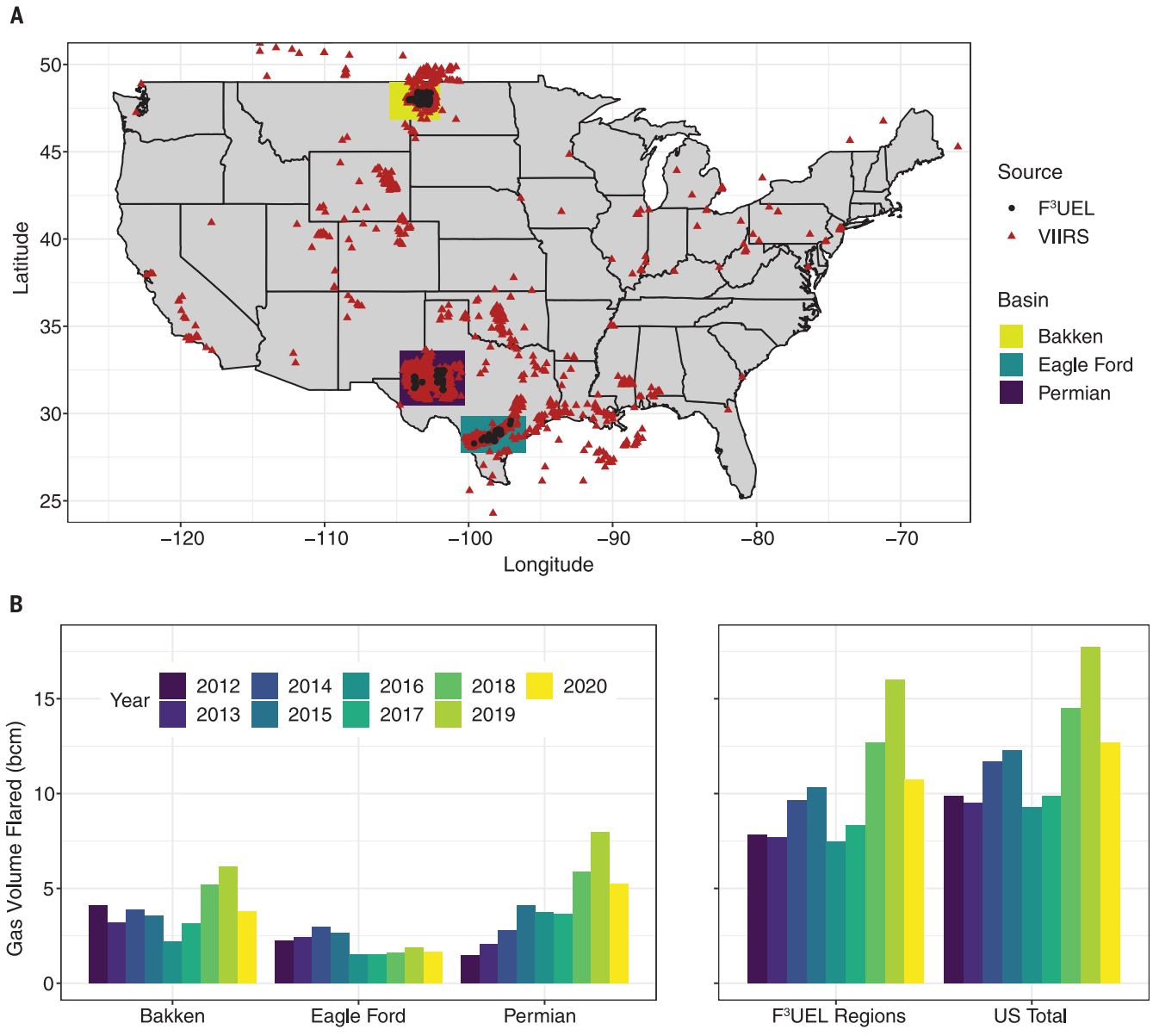


Fig. 1. Flaring activity in the United States. (**A**) Flaring locations in the contiguous US as seen from space (VIIRS, red triangles) for 2020 (*12*) and airborne sampling locations (F^3UEL, black circles), investigating the regions of the Bakken (yellow), Eagle Ford (green), and Permian (purple) from 25 August 2020 through 4 September 2020 and 28 June 2021 through 15 July 2021. (**B**) Temporal evolution of total gas volumes flared (bcm) in the VIIRS data product in the Bakken, Eagle Ford, and Permian, as delineated by the shaded regions in (A) (*13*). In 2020, VIIRS observed 665, 547, and 1710 flares in the Bakken, Eagle Ford, and Permian, respectively. The three areas in aggregate are the focus of this work (F^3UEL regions) and represent 80 to 90% of flared volumes in the US. At the national scale, flare volumes represent ~1% of natural gas gross withdrawals and generally track annual trends (fig. S1).

in the Visible Infrared Imaging Radiometer Suite (VIIRS) Nightfire dataset, where satellite-based nighttime imagery in five spectral bands is used to calculate the temperature, radiant heat, and source area of individual flares (*8*–*10*). From these measurements, flare gas volumes are inferred (*11*–*13*). Using these data, the World Bank estimates that 142 billion cubic meters (bcm) of gas was flared globally in 2020, with the United States having flared 11.8 bcm (*14*). The US consistently ranks among the top five flaring nations in the world (*14*), with >80% of gas volumes flared in the US occurring within three regions: the Permian Basin, the Bakken Formation in the Williston Basin, and the Eagle Ford Shale in the Western Gulf Basin (hereafter referred to as the Permian, the Bakken, and the Eagle Ford; Fig. 1A). These three regions, in aggregate, drive national flaring trends (Fig. 1B) and are the primary observational focus of measurements presented herein, collected as part of the Flaring & Fossil Fuels: Uncovering Emissions & Losses (F^3UEL) project (Fig. 1).

In 2018, Alvarez *et al.* presented a synthesis study considering field measurements made over the previous decade. They concluded that considerable upward revisions of CH_4 emissions estimates were needed for a variety of segments within the O&G sector (*15*). However, given a lack of real-world observations, estimates of flaring emissions were not re-evaluated. Estimates of flare-related emissions

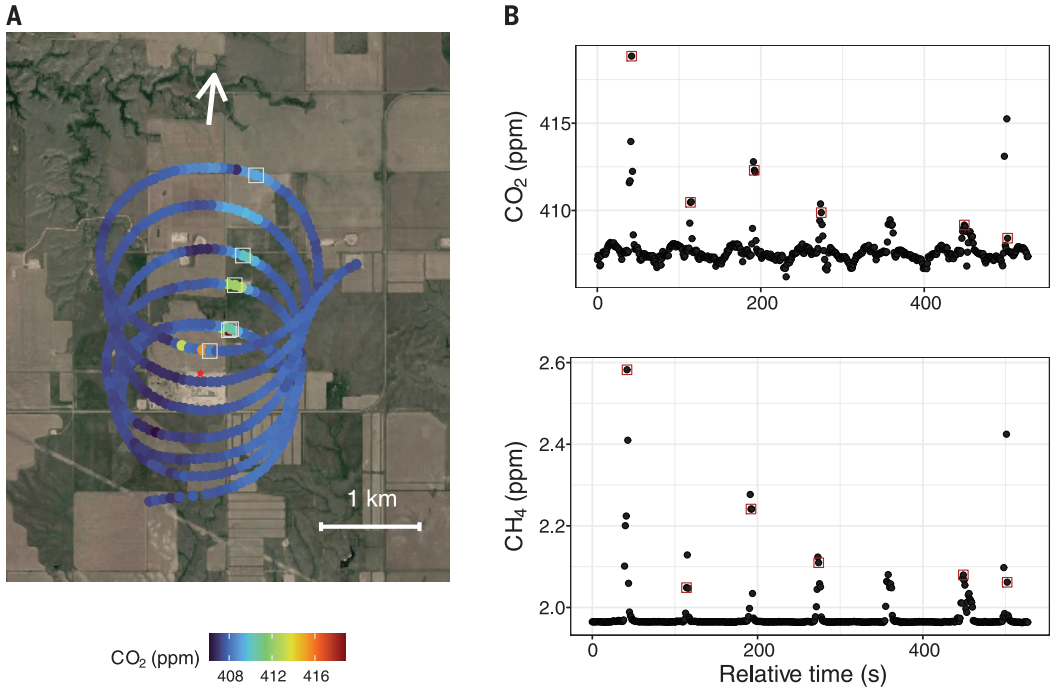


Fig. 2. Airborne flare sampling. (**A**) Flight track from the Bakken on 29 June 2021 colored by the CO_2 signal [parts per million (ppm)]. The white squares indicate the CO_2 peaks attributed to the upwind flare, with the wind direction (measured by the aircraft) indicated by the white arrow. The red star indicates the approximate location of the flare. (**B**) The corresponding time series of CO_2 (ppm) and CH_4 (ppm), with the red squares indicating the location of the combustion plume intercepts identified by the CO_2 peak–finding algorithm (further details in the materials and methods).

Table 1. Basin-level flare effective CH_4 destruction removal efficiency.

Region	Observed flare DRE		Unlit flares (%)	Total effective DRE*	
	Mean (%)	95% CI		Mean (%)	95% CI
Eagle Ford	96.5	95.4, 97.4	4.1†	92.4	91.3, 93.3
Bakken	97.3	96.9, 97.6	3.2	94.1	93.7, 94.4
Permian	91.7	90.5, 92.8	4.9	86.8	85.6, 87.9
Average	95.2	94.3, 95.9	4.1	91.1	90.2, 91.8

*Combines observed unlit flare statistics and DRE of lit flares work) and Permian surveys [Lyon *et al.* (*33*)]

†Average of unlit flare rate observed in the Bakken (this

are generally based on the dual assumptions that flares operate continuously and that 98% of the CH_4 in the flare gas is destroyed through combustion (*16*), a value based on limited US Environmental Protection Agency controlled studies conducted in the 1980s (*17*, *18*). Neither assumption is supported by measurements of real-world flare operations.

Although VIIRS provides global flare volume information for flares large enough to be viewed from space, this product does not evaluate flare performance. The operation of individual flares in response to specific environmental and gas composition variables has been evaluated in laboratory and testing facility studies (*19*–*25*), however, only a handful of in situ measurements to characterize performance (i.e., efficiency) have been made of real-world flares (*26*–*30*). A smaller subset of these studies estimate flaring efficiency in terms of CH_4 removal. An early work based on remote sensing of three flares found combustion efficiencies of >99% on average (*28*), whereas more recent airborne-based studies in the US have found mixed results. Caulton *et al.* sampled 10 flares in North Dakota and Pennsylvania, with a sampling bias toward the largest and brightest flares, and found that all were >99% efficient (*29*). Gvakharia *et al.* measured 37 flares in the Bakken and found that their efficiencies followed a skewed distribution with a median efficiency of 97% (mean: 95.2%), which, if representative of flare performance for the entire basin, would more than double the CH_4 flare emissions from the region (*30*). The limited statistics of these previous studies undermines the ability to extrapolate to larger scales, and, as such, this emission source has not received much attention as a methane emissions mitigation opportunity.

In addition to the efficiency of combusting flares, unlit flares (i.e., those that directly vent hydrocarbons to the atmosphere as a result of the flame extinguishing or never being lit) must also be considered. Data about the incidence rates of unlit flares remain incomplete. To date, the largest evaluation of unlit flares in the US is available through the Permian Methane Analysis Project (PermianMAP), an endeavor by the Environmental Defense Fund to quantify and locate CH_4 emissions in the Permian (*31*, *32*). Lyon *et al.* found that, on average, 4.9% of observed flares were unlit (*33*). It is not known, however, whether these statistics are representative of other regions and basins, particularly as the Permian has experienced unprecedented growth that has contributed to markedly high methane emissions (*34*). Also in the Permian, Cusworth *et al.* found that plumes from active and inactive flares accounted for 12.1% of the detected plume emissions captured in their aerial imaging study (*35*). In Canada, an airborne survey reported by Tyner and Johnson found that unlit flares accounted for 13% of the total CH_4 emissions quantified in their 2019 survey in northern British Columbia (*36*). These surveys highlight the important role unlit flares play in CH_4 emissions from the O&G sector, however, we do not presently know the relative importance to methane emissions of unlit flares compared with inefficient combustion. Knowledge of the full climate impact of flaring could help determine efficient and effective mitigation efforts, guiding efforts to address issues with combustion efficiency as well as with unlit flare prevalence.

As part of the F^{3}UEL project, we quantified the performance of flares across three regions

IMAGE: LANDSAT/COPERNICUS, MAXAR TECHNOLOGIES, USDA FARM SERVICE AGENCY (2022)

responsible for the bulk of flaring in the US, namely the Permian, Eagle Ford, and Bakken (Fig. 1A). Using an aircraft-based sampling approach over 12 research flights in 2020 and 2021, we directly measured methane, carbon dioxide, nitric oxide (NO), and nitrogen dioxide (NO_2) in flare combustion plumes, from which we quantified flare performance through calculation of the CH_4 destruction removal efficiency (DRE) for each plume intercept. The assessment of nitrogen oxides, or NOx ($NO + NO_2$), emissions and air quality implications will be the subject of forthcoming work. Consistent with previous airborne flare sampling campaigns (*29*, *30*), this method allows for direct measurement of the relative enhancements of the flare combustion plume without ground access to the flaring facility. An example flare-sampling flight track is shown in Fig. 2A, along with the accompanying concentration time series in Fig. 2B (details given in the materials and methods). With the airborne platform, we sampled more than 600 intercepts of flare combustion plumes, representing >300 distinct flares across the three basins (table S1). This represents an order-of-magnitude increase in the amount of data on in situ measurements of real-world flare performance.

Coincident measurements of CO_2 and CH_4 in the flare combustion plume allow for the calculation of CH_4 DRE, characterizing how well the flare's combustion destroys CH_4. DRE is distinct from combustion efficiency (CE)—DRE is the percentage of a specific species (e.g., CH_4) converted to another (e.g., CO_2), whereas CE is the percentage of total hydrocarbons in the gas that is converted to CO_2 (*16*). Following the methodology previously demonstrated in the literature (*29*, *30*), we estimate the DRE of CH_4 for each individual intercept of a flare combustion plume (materials and methods). The distribution of CH_4 DRE (%) values for flare intercepts across the three basins of study is shown in Fig. 3. In reporting and inventory estimates, 98% is a common default value used to quantify the efficiency at which flares convert CH_4 in the fuel gas to CO_2 (*1*), and this is shown in Fig. 3 as the dashed vertical line. Similar distributions result when flare intercepts are grouped and attributed to individual flares (fig. S2).

For all basins, the observed DRE values exhibit a skewed distribution, such that the median observed values are close to 98%, however, the effective efficiencies are much lower, with substantial contributions from flares whose DRE can drop as low as 60%. Lognormal distributions, which capture the heavy tail, fit the observed DREs far better than normal distributions (Fig. 3; fit parameters in table S3). This trend is consistent with results from a previous study in the Bakken that observed a similarly skewed DRE distribution among 37 flares (*30*). Investigations into possible drivers of reduced DRE, such as wind speed (measured at the aircraft), flare volume and temperature (VIIRS), and estimated well age and gas/oil ratio (*37*) did not yield compelling explanatory relationships, suggesting that the combination of our airborne sampling and these supplemental datasets cannot explain most of the observed flare CH_4 DRE variability. Improving attribution to flare design, operation, and environmental conditions would require a different study strategy, likely with more information on individual flare infrastructure and operation.

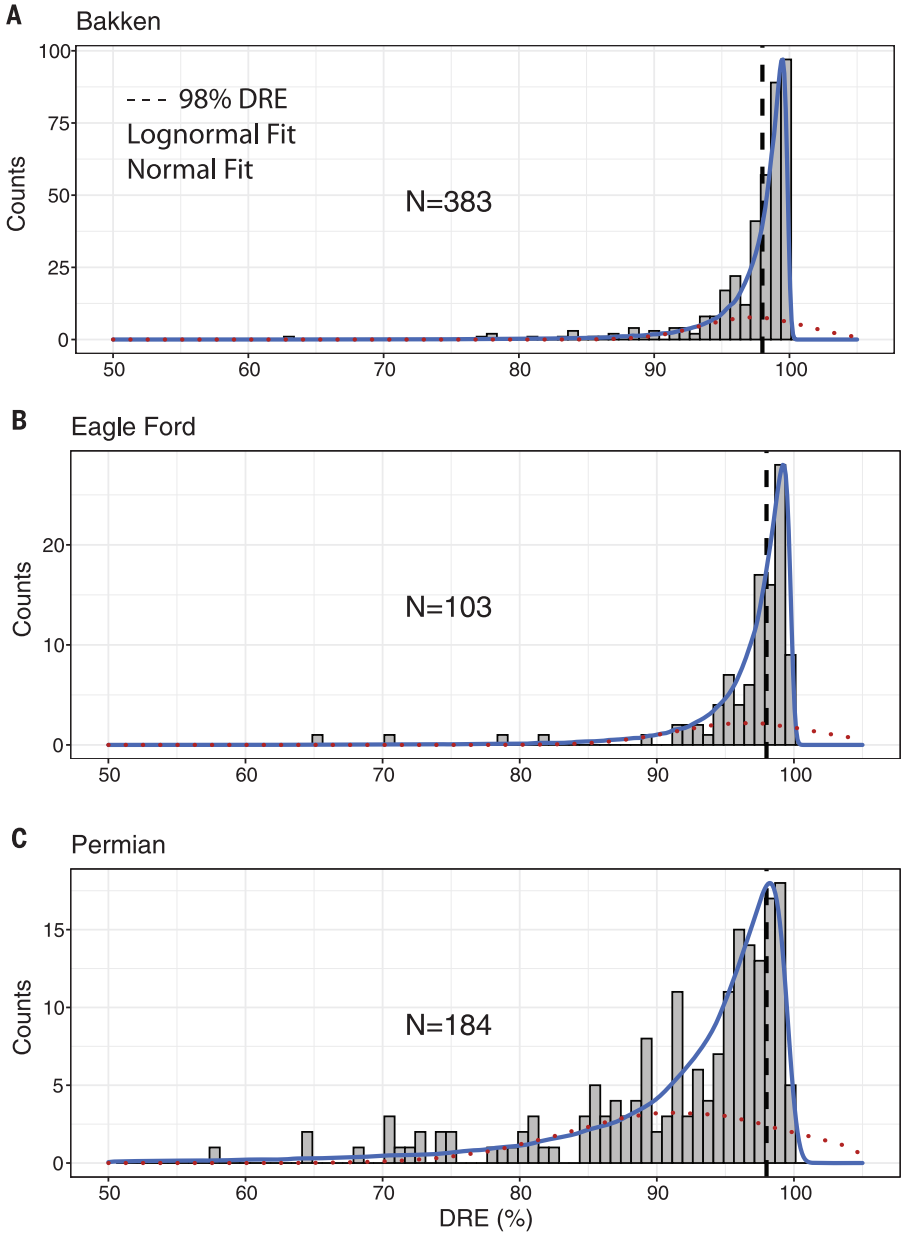


Fig. 3. Performance of active flares. Observed CH_4 DRE distributions of individual intercepts of lit flares for the (**A**) Bakken, (**B**) Eagle Ford, and (**C**) Permian. Normal (red dotted line) and lognormal (blue solid line) fits to the distributions are shown as normalized to the mean and maximum counts, respectively, to overlap with the observed data.

Unlit flares directly venting unburned gas to the atmosphere as a result of the flame being extinguished or never properly ignited have an additional impact on the flaring CH_4 budget. Across three infrared optical gas imaging surveys (onboard a helicopter platform), Lyon *et al.* found that, on average, 4.9% of surveyed flares in the Permian were unlit and venting (*33*). In 2021, we sampled 601 active flares in the Bakken as part of a ground-based infrared imaging survey and found that 3.2% of active flares were unlit (materials and methods and table S6). Owing to a lack of unlit flare observations in

the Eagle Ford, in this study we assume the percentage of unlit flares is 4.1%, the average of Bakken and Permian fractions (sensitivity study in material and methods).

To investigate CH_4 emissions from flares at the basin scale, we combined contributions of both inefficient performance and the prevalence of unlit flares into a total effective DRE (Table 1). We expanded our observed DRE estimates to the basin level by randomly resampling (with replacement) the observed DRE distributions and applying those efficiencies to the population of flares seen in VIIRS within each basin (delineated by the yellow, green, and purple regions shown in Fig. 1A), the results of which are shown in Table 1. We used a randomized approach, as we detected no relationship between observed DRE and flare size or temperature as quantified in the VIIRS product (see fig. S3). Additionally, we found that sampled flares represent the range of flare temperatures and sizes as seen by VIIRS (see fig. S4). From a bootstrap resampling (with replacement) of our observations, we inferred the uncertainty of our basin-average estimates, deriving 95% confidence intervals (CI). Unlit flares are assumed to have an efficiency of 0% (i.e., no combustion) and therefore directly reduce the effective DRE at the basin level by the unlit flare fraction (4.9%, Permian; 3.2%, Bakken; 4.1%, Eagle Ford).

The inefficiency of combusting flares in combination with the rate of unlit flares results in effective flare efficiencies that are considerably lower than 98% across all three basins. The standard value of 98% falls outside the confidence intervals for our basin-average DRE for lit flares. This indicates that flaring activities are a much larger part of the CH_4 O&G footprint than previously estimated. In addition, the relative contribution of both poorly combusting and unlit flares to total CH_4 flaring emissions is similar.

The average observed DRE across the study is 95.2%, and the average total effective DRE after accounting for unlit flares is 91.1%. Using flare volumes estimated from VIIRS for these regions (3.8, 1.6, and 5.2 bcm for the Bakken, Eagle Ford, and Permian, respectively, for 2020) (*12*, *13*), along with the basin-specific unlit flare fraction and average gas composition from the Greenhouse Gas Reporting Program (see fig. S5), we estimate a flaring CH_4 emissions rate from lit flares in these three basins of 0.27 (0.14, 0.38; 95% CI) Tg CH_4/year. Accounting for the presence of unlit flares increases that estimate to 0.49 (0.26, 0.72; 95% CI) Tg CH_4/year for these high-flaring areas. These emissions estimates are considerably larger (~5×) than if we assume 98% DRE for all flares quantified by VIIRS and no occurrences of unlit flares (0.10 Tg CH_4/year).

Flaring in the Bakken, Eagle Ford, and Permian represents the vast majority of activity in the US, ~84% (*12*, *13*). If we assume that the average effective DRE and a gas composition of 80% CH_4 is representative of the remaining flares, US CH_4 flaring emissions total 0.60 (0.31, 0.87) Tg CH_4/year, again five times larger than current assumptions would suggest (0.12 Tg CH_4/year), and a total emission magnitude comparable with notable O&G areas such as the Four Corners region (Colorado and New Mexico, US) at 0.54 Tg CH_4/year (± 0.20; 1σ) (*38*). The difference in US flare CH_4 emissions based on the observed effective DRE and 98%, 0.48 Tg CH_4/year, represents a substantial underaccounting of CH_4 emissions from flares. If measures were taken to ensure that US flares operated at 98% efficiency and remained lit, as current accounting assumes, this would be equivalent to removing 2.9 million cars from the road each year these mitigation measures were in place. This calculation uses a 100-year CH_4 global warming potential (GWP) of 28 and an annual emission of a typical passenger vehicle of 4.6 metric tons of CO_2 (*39*). Using a 20-year GWP of 84 (*40*) increases this mitigation measure's impact to the equivalent of removing 8.8 million cars. Our estimate for flaring emissions in the US represents 4 to 10% of total CH_4 emissions inventoried by the US Environmental Protection Agency for the O&G sector [8.4 Tg CH_4/year for 2020 in table 3-2 of (*41*)].

We do not know whether these US-based observations are globally representative. Flaring in other regions with differing regulations and oversight may perform better or worse. Nevertheless, our observationally derived performance characteristics are an improvement over simplified assumptions of 98% with no basis in real-world observations. Recently, the International Energy Agency (IEA) revised their estimate of global methane emission from flares to the assumption that flares operate at 92% efficiency, although the genesis of this value remains opaque (*42*). This assumed efficiency is similar to our US average effective CH_4 DRE of 91.1%. Using this updated efficiency assumption, the IEA estimated that flares were responsible for releasing 8 Tg (8 million tons) of CH_4 in 2020 (*42*), which would be on par with the world's methane ultra-emitters (*43*), equaling 8 to 11% of total global oil gas emissions (*44*). This highlights the need for more measurements of flare performance around the globe and represents a heretofore unrealized—or at least greatly underestimated—large source of methane emissions with known mitigation options. In the US, we find that both inefficient combustion and unlit flares contribute to substantial methane emissions greatly exceeding standard estimates for flares. As a result, mitigation efforts that address either combustion efficiency or unlit flares (such as operational practices on flare maintenance), in addition to reducing the usage of flares altogether (with alternatives such as reinjection or small-scale gas capture technology), would provide considerable methane emission benefits. Because flaring has long been treated as effective, there is little to no assessment of repair and maintenance costs, particularly for the issue of unlit flares. In principle, addressing unlit flares presents a simple and cost-effective CH_4 mitigation opportunity. Further investigation into the cause of flare malfunction could further inform mitigation measures and cost.

REFERENCES AND NOTES

1. U.S. Environmental Protection Agency, AP 42, Fifth Edition, Volume I Chapter 13: Miscellaneous Sources, Section 13.5 Industrial Flares (2018); https://www.epa.gov/air-emissions-factors-and-quantification/ap-42-fifth-edition-volume-i-chapter-13-miscellaneous-0.
2. The World Bank, Global Gas Flaring Reduction Partnership (GGFR): What is Gas Flaring?; https://www.worldbank.org/en/programs/gasflaringreduction/gas-flaring-explained.
3. G. Myhre *et al*., in *Climate Change 2013: The Physical Science Basis. Contribution of Working Group I to the Fifth Assessment Report of the Intergovernmental Panel on Climate Change*, T. F. Stocker *et al*., Eds. (Cambridge Univ. Press, 2013), chap. 8.
4. M. J. Prather, C. D. Holmes, J. Hsu, *Geophys. Res. Lett.* **39**, 2012GL051440 (2012).
5. A. Voulgarakis *et al*., *Atmos. Chem. Phys.* **13**, 2563–2587 (2013).
6. J. J. West, A. M. Fiore, L. W. Horowitz, D. L. Mauzerall, *Proc. Natl. Acad. Sci. U.S.A.* **103**, 3988–3993 (2006).
7. A. M. Fiore *et al*., *Geophys. Res. Lett.* **29**, 25-1–25-4 (2002).
8. C. D. Elvidge, M. Zhizhin, F.-C. Hsu, K. E. Baugh, *Remote Sens.* **5**, 4423–4449 (2013).
9. C. D. Elvidge, M. Zhizhin, K. Baugh, F. C. Hsu, T. Ghosh, *Remote Sens.* **11**, 395 (2019).
10. Earth Observation Group, VIIRS Nightfire; https://eogdata.mines.edu/products/vnf/.
11. C. D. Elvidge, M. Zhizhin, K. Baugh, F.-C. Hsu, T. Ghosh, *Energies* **9**, 14 (2016).
12. Earth Observation Group, Global Gas Flaring Observed from Space; https://eogdata.mines.edu/download_global_flare.html.
13. SkyTruth, Flaring Maps and Data (2021); https://skytruth.org/flaring/.
14. Global Gas Flaring Reduction Partnership, The World Bank, "Global Gas Flaring Tracker Report: April 2021" (2021); https://thedocs.worldbank.org/en/doc/1f7221545bf1b7c89b850dd85cb409b0-0400072021/original/WB-GGFR-Report-Design-05a.pdf.
15. R. A. Alvarez *et al*., *Science* **361**, 186–188 (2018).
16. U.S. EPA Office of Air Quality Planning and Standards (OAQPS), "Parameters for Properly Designed and Operated Flares: Report for Flare Review Panel April 2012" (2012); https://www3.epa.gov/airtoxics/flare/2012flaretechreport.pdf.
17. J. H. Pohl, B. A. Tichenor, J. Lee, R. Payne, *Combust. Sci. Technol.* **50**, 217–231 (1986).
18. M. McDaniel, Flare Efficiency Study (EPA/600/2-83/052, U.S. Environmental Protection Agency, 1983).
19. W. B. Knighton *et al*., *Ind. Eng. Chem. Res.* **51**, 12674–12684 (2012).
20. V. M. Torres, S. Herndon, Z. Kodesh, D. T. Allen, *Ind. Eng. Chem. Res.* **51**, 12559–12568 (2012).
21. V. M. Torres, S. Herndon, D. T. Allen, *Ind. Eng. Chem. Res.* **51**, 12569–12576 (2012).
22. V. M. Torres, S. Herndon, E. Wood, F. M. Al-Fadhli, D. T. Allen, *Ind. Eng. Chem. Res.* **51**, 12600–12605 (2012).
23. M. R. Johnson, L. W. Kostiuk, *Proc. Combust. Inst.* **29**, 1943–1950 (2002).
24. M. R. Johnson, L. W. Kostiuk, *Combust. Flame* **123**, 189–200 (2000).
25. S. P. Seymour, M. R. Johnson, *Atmos. Meas. Tech.* **14**, 5179–5197 (2021).
26. J. P. Schwarz *et al*., *Environ. Sci. Technol. Lett.* **2**, 281–285 (2015).
27. C. L. Weyant *et al*., *Environ. Sci. Technol.* **50**, 2075–2081 (2016).
28. R. Haus, R. Wilkinson, J. Heland, K. Schäfer, *Pure Appl. Opt.* **7**, 853–862 (1998).
29. D. R. Caulton *et al*., *Environ. Sci. Technol.* **48**, 9548–9554 (2014).

30. A. Gvakharia *et al*., . *Environ. Sci. Technol.* **51**, 5317–5325 (2017).
31. Environmental Defense Fund, Permian Methane Analysis Project (PermianMAP); https://www.permianmap.org.
32. Environmental Defense Fund, Flaring Aerial Survey Results; https://www.permianmap.org/flaring-emissions/.
33. D. R. Lyon *et al*., *Atmos. Chem. Phys.* **21**, 6605–6626 (2021).
34. Y. Zhang *et al*., *Sci. Adv.* **6**, eaaz5120 (2020).
35. D. H. Cusworth *et al*., *Environ. Sci. Technol. Lett.* **8**, 567–573 (2021).
36. D. R. Tyner, M. R. Johnson, *Environ. Sci. Technol.* **55**, 9773–9783 (2021).
37. Enverus, Drillinginfo (2021); https://www.enverus.com/.
38. E. A. Kort *et al*., *Geophys. Res. Lett.* **41**, 6898–6903 (2014).
39. U.S. Environmental Protection Agency, Greenhouse Gas Emissions from a Typical Passenger Vehicle (2016); https://www.epa.gov/greenvehicles/greenhouse-gas-emissions-typical-passenger-vehicle.
40. Core Writing Team, R. K. Pachauri, L. Mayer, Eds., *Climate Change 2014: Synthesis Report. Contribution of Working Groups I, II and III to the Fifth Assessment Report of the Intergovernmental Panel on Climate Change* (IPCC, 2015).
41. U.S. Environmental Protection Agency, Inventory of U.S. Greenhouse Gas Emissions and Sinks: 1990–2020 (2022); https://www.epa.gov/ghgemissions/inventory-us-greenhouse-gas-emissions-and-sinks-1990-2020.
42. International Energy Agency, Flaring Emissions (2021); https://www.iea.org/reports/flaring-emissions.
43. T. Lauvaux *et al*., *Science* **375**, 557–561 (2022).
44. M. Saunois *et al*., *Earth Syst. Sci. Data* **12**, 1561–1623 (2020).
45. E. A. Kort *et al*., Aircraft Data (2020) for Flaring & Fossil Fuels: Uncovering Emissions & Losses (F3UEL), University of Michigan Deep Blue Data (2022); https://doi.org/10.7302/1xjm-3v49.
46. E. A. Kort *et al*., Aircraft Data (2021) for Flaring & Fossil Fuels: Uncovering Emissions & Losses (F3UEL), University of Michigan Deep Blue Data (2022); https://doi.org/10.7302/6tgq-e116.

ACKNOWLEDGMENTS

We acknowledge T. Sullivan and P. Wliczak for piloting the airborne measurements campaigns presented here. We thank fellow F^3UEL team members Á. Adames-Corraliza for assistance with flight planning, and C. Hausman, M. Allan, and A. Stoltenberg for useful discussions throughout. We are grateful to B. Hmiel, D. Lyon, and J. Warren of the Environmental Defense Fund for their insightful discussions about their work in the Permian. **Funding:** This work was supported by the Alfred P. Sloan Foundation (G-2019-12451). **Author contributions:** Conceptualization: E.A.K. and G.P. Investigation: G.P., E.A.K., A.R.B., Y.C., G.F., A.M.G.N., S.S., and M.S. Writing – original draft: G.P. and E.A.K. Writing – review & editing: G.P., E.A.K., A.R.B., Y.C., A.M.G.N., M.S., and D.Z.-A. **Competing interests:** The authors declare that they have no competing interests. **Data and materials availability:** The airborne data presented in this work are available publicly in the University of Michigan Deep Blue Data Repository [2020 campaign (*45*) and 2021 campaign (*46*)]. Daily VIIRS data are available at https://eogdata.mines.edu/products/vnf/, and annual data are available at https://eogdata.mines.edu/download_global_flare.html. **License information:** Copyright © 2022 the authors, some rights reserved; exclusive licensee American Association for the Advancement of Science. No claim to original US government works. https://www.science.org/about/science-licenses-journal-article-reuse

SUPPLEMENTARY MATERIALS

science.org/doi/10.1126/science.abq0385
Materials and Methods
Figs. S1 to S10
Tables S1 to S7
References (*47*–*60*)

Submitted 23 March 2022; accepted 19 August 2022
10.1126/science.abq0385

ScienceCareers online @sciencecareers.org

INDIANA UNIVERSITY
BLOOMINGTON

TENURED/TENURE-TRACK FACULTY POSITION IN VIROLOGY
Department of Biology
https://biology.indiana.edu/index.html

The Microbiology Program in the Indiana University Department of Biology (https://biology.indiana.edu/graduate/microbiology/index.html) invites applications for a tenured/tenure-track position in Virology at the level of Assistant or Associate Professor. We are particularly interested in scientists studying emerging viruses. We encourage applications from candidates focused on the following areas of research: structure-function analysis of viral proteins, cell and molecular biology of events in viral replication, cellular responses to virus infection, and experimental approaches to virus evolution. Scientists working on model viral systems that inform our understanding of the biology of emerging viruses will also be considered. Start dates of Fall 2023 or Fall 2024 are possible.

This position is part of a significant, continuing expansion in the life sciences at IU Bloomington and represents an exceptional opportunity to join a strong Microbiology Program comprised of both Virologists and Bacteriologists. There also exists opportunities for interactions with programs in Molecular and Cellular Biochemistry, Genome, Cell and Developmental Biology, Evolutionary Biology, and Medical Sciences. The selected candidate will be provided with a competitive startup package and salary and will have access to outstanding research resources, including state-of-the-art facilities for genomics and bioinformatics, light and electron microscopy, flow cytometry, protein analysis, analytical chemistry, biophysical instrumentation, and crystallography. Applicants must hold a doctoral degree and have relevant postdoctoral experience with a strong record of research accomplishments. Successful candidates will be expected to develop a vigorous externally funded research program, and to participate in teaching at the undergraduate and graduate levels.

For more detailed application instructions and conditions, please see **https://indiana.peopleadmin.com/postings/13816**. Please address inquires to Jennifer Tarter jenjones@indiana.edu. Applications received by October 31, 2022 will be assured of full consideration; however, the search will remain open until a suitable candidate is found.

INDIANA UNIVERSITY
BLOOMINGTON

TENURED/TENURE TRACK FACULTY POSITION IN EVOLUTION
Indiana University Bloomington

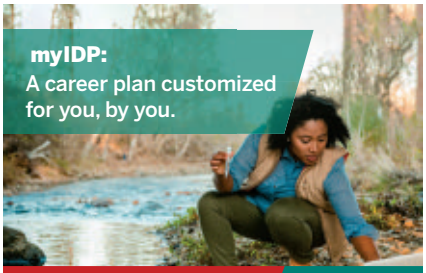
The Evolution, Ecology, and Behavior program in the Department of Biology at Indiana University Bloomington (IUB) invites applications for the newly endowed 'Olsen Chair in Evolutionary Biology', an open-rank tenured/tenure-track position at the Assistant, Associate, or Full Professor level. We welcome applicants who address fundamental evolutionary questions using integrative approaches and methods, in any system, including from organismal, genetic, and/or theoretical perspectives. Start date is flexible, from Aug 2023 to Aug 2024.

Applicants must hold a Ph.D. and have postdoctoral experience in relevant fields, with a strong record of research accomplishments. Successful candidates will be expected to develop a vigorous externally funded research program, and to participate in teaching at the undergraduate and graduate levels. The Department of Biology is committed to recruiting and retaining diverse faculty, and we strongly encourage applications from members of historically marginalized groups. We also welcome candidates who have demonstrated a commitment to working with people from groups that are underrepresented in STEM, through teaching, mentoring, or administration.

Apply online at **https://indiana.peopleadmin.com/postings/13961**, by November 1, 2022. Please address inquiries concerning the search to Jennifer Tarter at **812-856-3984** or **jenjones@indiana.edu**.

The Evolution, Ecology, and Behavior graduate program at IUB is a strong, integrative, and collegial group, ranked in the top 10 US EEB programs in 2022: **https://www.usnews.com/best-graduate-schools/top-science-schools/ecology-rankings**. Bloomington is a culturally diverse, welcoming city with a vibrant arts and music scene. The city is located among the hills, lakes, and forested landscape of south-central Indiana, with ample opportunities for outdoor activities and recreation. For information about the Department of Biology and for other links to the campus and the Bloomington community, see: **http://www.bio.indiana.edu**.





Features in myIDP include:

- Exercises to help you examine your skills, interests, and values.
- A list of 20 scientific career paths with a prediction of which ones best fit your skills and interests.

myIDP Visit the website and start planning today!
myIDP.sciencecareers.org

Science Careers In partnership with:

UCSF University of California San Francisco
UIC
BURROUGHS WELLCOME FUND
UMASS University of Massachusetts Medical School
FASEB Federation of American Societies for Experimental Biology

THE UNIVERSITY of NORTH CAROLINA at CHAPEL HILL

OPEN RANK FACULTY COMPUTATIONAL MEDICINE-PHARMACOLOGY-GENETICS

Position summary: The Computational Medicine Program and the Departments of Pharmacology and Genetics at the University of North Carolina at Chapel Hill (UNC-CH) invite applicants for two tenure-track faculty positions in Computational Medicine. The Computational Medicine Program at UNC-CH is a recently established research initiative that seeks to integrate modern computational approaches, including mathematical modeling, machine learning, computational genomics and network analysis, with cutting-edge experimental techniques to address problems relevant to human health. While the area of study is flexible, an ideal candidate would apply methods from systems biology and/or genomics to investigate molecular processes dysregulated in human diseases, and to eventually develop predictive models of these disease states. The successful candidate will hold a position, and research laboratory space, within the Computational Medicine Program, and also hold a position within either the Department of Genetics or Department of Pharmacology. They will be expected to direct an independent research program supported by extramural funding, and participate in team science projects initiated through the Computational Medicine Program. The successful candidate will also participate in graduate student mentoring and teaching at the graduate level. Applicant reviews will begin October 15 and continue until the positions are filled.

Minimum education and experience requirements: A Ph. D. or equivalent degree is required in Genetics, Pharmacology, Computational Biology, Computer Science, Statistics, Mathematics or related field. The successful candidates will have significant research experience applying computational approaches to problems in biomedical research. While postdoctoral experience is not required, 3-6 years of postdoctoral research is typical. Current Assistant and associate professors are also welcome to apply.

Preferred qualifications, competencies and experience: Strong training and experience in applying computational and quantitative approaches to problems in biomedical research. It is anticipated that some candidates may be entirely computational, while others will incorporate an experimental component into their research; both types are eligible and encouraged to apply.

Apply Here: Pharmacology: https://unc.peopleadmin.com/postings/239152
OR Genetics: https://unc.peopleadmin.com/postings/239062

Upload your C.V. to the "curriculum vitae/resume" tab, upload your Cover Letter to the "cover letter" tab, upload your research statement(statement of ongoing and planned research) to the "research statement:", and attached 2-3 recent publications to the "other document 2" and "other document 3" tabs.

The University of North Carolina at Chapel Hill is an equal opportunity and affirmative action employer. All qualified applicants will receive consideration for employment without regard to age, color, disability, gender, gender expression, gender identity, genetic information, national origin, race, religion, sex, sexual orientation, or status as a protected veteran.

KU THE UNIVERSITY OF KANSAS

DISTINGUISHED PROFESSOR, FULL PROFESSOR LEVEL
University of Kansas School of Pharmacy

Applications are invited for appointment as a tenured, Distinguished Professor at the Full Professor level in the Department of Pharmacology & Toxicology, School of Pharmacy at the University of Kansas. We are looking for an individual using a systems-based approach to understand mechanisms of disease and drug action, in order to advance disease prevention, diagnosis, and treatment for Alzheimer's disease or other neurological or neuropsychiatric disorder. The successful candidate must hold a PhD, MD, or DVM, have an exceptional record of externally funded research and previous teaching experience at the undergraduate and/or graduate level. The person appointed to this position is expected to lead and participate in collaborative research projects. The position comes with state-supported salary for nine-months and opportunity for grant-supported summer salary for an additional 3 months. Excellent University-shared core research facilities that house specialized scientific instruments and provide expert consultation and services to investigators, a generous start-up package and endowed funds support the position.

For more information and to apply, go to:
https://employment.ku.edu/academic/23365BR

Review of applications begins November 1, 2022 and will continue until the position is filled.

The University of Kansas is an EO/AAE, full policy at http://policy.ku.edu/IOA/nondiscrimination.

RUTGERS THE STATE UNIVERSITY OF NEW JERSEY

Faculty Tenure-track Assistant Professor

The Department of Biological Sciences at Rutgers University-Newark invites applications for two tenure-track Assistant Professor positions in the broadly defined field of cellular and molecular biology. Applicants using biochemical, molecular, genetic, bioinformatics (OMICS) and/or cellular approaches to study problems in the areas of neurobiology, cancer biology, developmental biology, stem cell biology, immunology, systems biology, microbiology, or related areas are encouraged to apply. Qualifications include a PhD degree or equivalent in the field of cell or molecular biology or related disciplines, and at least two years of postdoctoral research experience. Applicants must have a strong record of research accomplishments as demonstrated by publications in leading peer-reviewed journals. The successful applicant will receive generous start-up support and laboratory space in anticipation of developing a robust, externally-funded, independent research program and contributing to the teaching mission of the department.

Responsibilities Candidates are expected to develop an extramurally funded active research program that will incorporate graduate and undergraduate students. Candidates must be dedicated to providing quality instruction and undertake independent scholarly activity appropriate for advancement within Rutgers University. Responsibilities also include departmental and university service with a willingness to take on administrative responsibility.

Requirements Qualifications include a PhD degree or equivalent in cell or molecular biology or related disciplines and at least two years of postdoctoral research experience. Applications must have a strong record of research accomplishments as demonstrated by publications in leading peer-reviewed journals, demonstrating the ability to build a body of recognized work suitable for tenure at a research university.

Review of applications will begin December 1, 2022, and continue until the positions are filled.

Applications Please visit: https://jobs.rutgers.edu/postings/175954

Rutgers is an Affirmative Action/Equal Opportunity Employer.

WORKING LIFE

By **Naim Rashid**

Let's talk about authorship

As a Ph.D. student, I was excited when a friend proposed we collaborate on a project. I asked my supervisor for permission and he happily agreed, but advised that we should define our expected contributions and credit before starting. I didn't heed his words. I wasn't going to negotiate with a fast friend; I fully trusted my collaborator to give me fair credit, and I did not want to come across as entitled. Everything went fine. We completed and published the work as co-authors. Years passed, and I forgot my supervisor's advice.

As I moved into an assistant professor position, I knew publishing was crucial for my career. Initially I didn't have the funding or projects to recruit my own graduate students, so I co-supervised students who were under the primary supervision of other colleagues. I shared the intellectual burden and was a co-author on the resulting papers. My colleagues and I were quite satisfied with this win-win situation, and everything seemed to be going smoothly—until I moved to another institution.

Just a few months after leaving, I was browsing the literature and found a new article published by a student I had co-supervised. I was shocked and disappointed to see that I was not listed as an author or even acknowledged. I brought it up to the other supervisor, who was a close friend at the time. He told me they had just overlooked my contribution, but I doubted that. Plenty of other authors on the paper seemed to have contributed less to the work. We couldn't come to a happy resolution. We never collaborated again, and our relationship was ruined. Years passed, and I nearly forgot this difficult experience, which I saw as an unfortunate one-time dispute.

My career continued to progress through a number of countries and institutions, and at one point I was part of a team of investigators sharing funding and students. We agreed that any publication from our team would include the name of every team member. In hindsight I recognize this is not the best practice for ethical research and publishing, as some authors would get credit for minimal contributions, but we were not professionally mature enough to realize this.

Over the following years we all moved on to different institutions, and I noticed my colleagues no longer included me on papers about work that began during our time together. I took this to mean our agreement was concluded, and I stopped including them on my papers as well. So, I was surprised when I got a call from one of those colleagues, upset that I hadn't included him as a co-author. I tried to explain, but he felt wronged.



"I make sure to have a proactive discussion to clarify each team member's role."

Remembering the time I had been on the other side of the coin, I was overwhelmed with regret and doubt. Who was wrong in each dispute, I or my colleagues? For days, I told myself that I had done no wrong in either case—until, while I was out for a morning riverside walk, my supervisor's advice from years ago flashed to mind. "Naim—you can collaborate, but define your role and credit first."

I realized that in both cases, I had made a mistake. I should have initiated explicit conversations about authorship with my colleagues from the outset, regardless of our friendships. And we should have had follow-up discussions along the way, including when individuals changed institutions.

Thankfully, I was able to repair my relationship with my second colleague through further conversations. And since then, I have transformed my approach to collaboration and authorship. Before embarking on a project, I make sure to have a proactive discussion to clarify each team member's role and expected credit, acknowledging that contributions may change over the course of the project and we may need to revisit our agreement. Sometimes my colleagues seem offended, as if I am treating them not as a friendly partner, but as a cold professional, and I have lost several potential collaborations along the way. But painful experiences have shown me time and again that this is the best approach to foster long-term collaborations, ensure everyone gets the credit they are due, and ultimately protect our personal and professional relationships. ■

Naim Rashid is a researcher at Hamad Bin Khalifa University in Qatar. Send your career story to SciCareerEditor@aaas.org.

ILLUSTRATION: ROBERT NEUBECKER

Science
JOURNALS AAAS



Publish your research in the *Science* family of journals

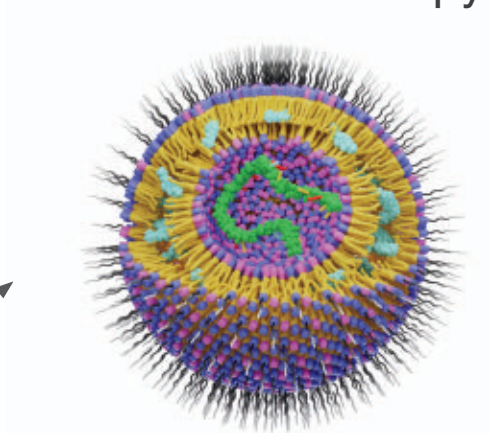
The *Science* family of journals (*Science, Science Advances, Science Immunology, Science Robotics, Science Signaling*, and *Science Translational Medicine)* are among the most highly-regarded journals in the world for quality and selectivity. Our peer-reviewed journals are committed to publishing cutting-edge research, incisive scientific commentary, and insights on what's important to the scientific world at the highest standards.

Submit your research today!

Learn more at **Science.org/journals**

mRNA-LNP Products & Services

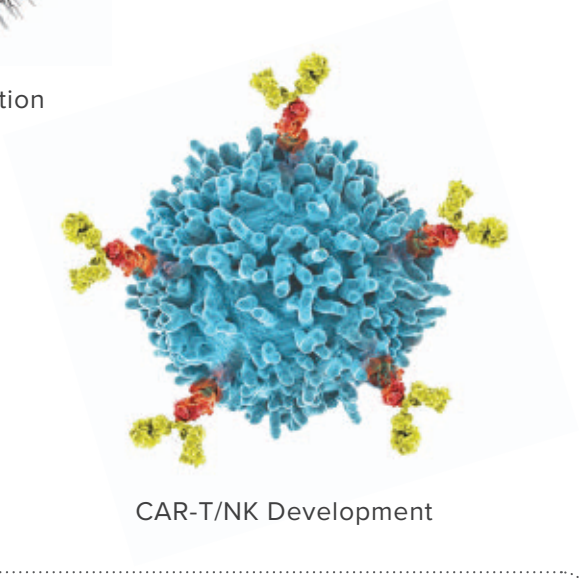
For Vaccine and Immunotherapy Development



mRNA-LNP Formulation



Antibody Engineering



CAR-T/NK Development

Antibody Services

- Monoclonal Ab Development
- Hybridoma Sequencing
- Human Antibody Screening
- Antibody Humanization
- Bispecific Antibody Engineering
- Stable Cell Line Generation

mRNA-LNP Services

- mRNA Design and Synthesis (IVT)
- mRNA Capping & Purification
- mRNA-LNP Encapsulation
- mRNA-LNP Scale Up and QC
- mRNA-LNP Validation In Vivo
- Ionizable Lipid Licensing

Immune Cell Services

- Lentivirus Production GMP
- CAR-T/NK Cell Generation
- CAR-T/NK Animal Model
- Immune Cell Engineering
- T/B/NK/Dendritic cell, Macrophages
- TCR knockout by CRISPR

All products are for research use only

Discover more | www.promab.com

ProMab Biotechnologies, Inc.

2600 Hilltop Dr, Building B, Richmond, CA 94806

1.866.339.0871 | info@promab.com

SCAN ME